WYDZIAŁ INŻYNIERII MATERIAŁOWEJ
POLITECHNIKA WARSZAWSKA
UL. WOŁOSKA 141A
02-507 WARSZAWA

za pośrednictwem:
Rady Doskonałości Naukowej
pl. Defilad 1
00-901 Warszawa
(Pałac Kultury i Nauki, p. XXIV, pok. 2401)

PIOTR BAZARNIK
Wydział Inżynierii Materiałowej
Politechnika Warszawska

Wniosek

z dnia 03.09.2025

o przeprowadzenie postępowania w sprawie nadania stopnia doktora habilitowanego

w dziedzinie **nauk inżynieryjno – technicznych** w dyscyplinie **inżynieria materiałowa**

Wnioskuję – na podstawie art. 221 ust. 10 ustawy z dnia 20 lipca 2018 r. Prawo o szkolnictwie wyższym i nauce – aby komisja habilitacyjna podejmowała uchwałę w sprawie nadania stopnia doktora habilitowanego w głosowaniu ~~**tajnym**~~**/jawnym***[1]

Zostałem poinformowany, że:

Administratorem w odniesieniu do danych osobowych pozyskanych w ramach postępowania w sprawie nadania stopnia doktora habilitowanego jest Przewodniczący Rady Doskonałości Naukowej z siedzibą w Warszawie (pl. Defilad 1, XXIV piętro, 00-901 Warszawa).

Kontakt za pośrednictwem e-mail: kancelaria@rdn.gov.pl , tel. 22 656 60 98 lub w siedzibie organu.

Dane osobowe będą przetwarzane w oparciu o przesłankę wskazaną w art. 6 ust. 1 lit. c) Rozporządzenia UE 2016/679 z dnia z dnia 27 kwietnia 2016 r. w związku z art. 220 - 221 oraz art. 232 – 240 ustawy z dnia 20 lipca 2018 roku - Prawo o szkolnictwie wyższym i nauce, w celu przeprowadzenie postępowania o nadanie stopnia doktora habilitowanego oraz realizacji praw i obowiązków oraz środków odwoławczych przewidzianych w tym postępowaniu.

Szczegółowa informacja na temat przetwarzania danych osobowych w postępowaniu dostępna jest na stronie www.rdn.gov.pl/klauzula-informacyjna-rodo.html

……..
(podpis wnioskodawcy)

[1] * Niepotrzebne skreślić.

Załączniki:

Załącznik 2: Dane wnioskodawcy w języku polskim

Załącznik 3: Kopia dokumentu potwierdzającego posiadanie stopnia doktora

Załącznik 4: Autoreferat w języku polskim

Załącznik 5: Publikacje A1-A9

Załącznik 6: Oświadczenia współautorów o ich zakresie prac w publikacjach współautorskich

Załącznik 7: Wykaz osiągnięć naukowych albo artystycznych, stanowiący znaczny wkład w rozwój określonej dyscypliny w języku polskim

Załącznik 8: Publikacje potwierdzające inne osiągnięcia naukowe

Załącznik 9: Dokumenty potwierdzające kierowanie projektami

Załącznik 10: Dokumenty potwierdzające odbyte staże zagraniczne

Załącznik 11: Dokumenty potwierdzające przyznane nagrody

Załącznik 12: Dokument potwierdzający przyznane stypendium ministra

Dane wnioskodawcy

1. Imię i Nazwisko: **Piotr Bazarnik**

2. Miejsce pracy: **Politechnika Warszawska, Wydział Inżynierii Materiałowej**

3. Adres korespondencyjny: [redacted]

4. Nr telefonu [redacted]

5. Adres e-mail: **Piotr.Bazarnik@pw.edu.pl**

6. Numer PESEL: [redacted]

……...…
(podpis wnioskodawcy)

POLITECHNIKA WARSZAWSKA

Wydział Inżynierii Materiałowej

DYPLOM

WYDANY W RZECZYPOSPOLITEJ POLSKIEJ

ODPIS

mgr inż. Piotr Marcin Bazarnik

urodzony dnia [redacted] w [redacted]

na podstawie przedstawionej rozprawy doktorskiej *„Rola granic ziaren w kształtowaniu właściwości mechanicznych stopu Al 5483 otrzymywanego metodami dużego odkształcenia plastycznego"*

oraz po złożeniu wymaganych egzaminów uzyskał stopień naukowy

DOKTORA

w dziedzinie *nauk technicznych*

w dyscyplinie *inżynieria materiałowa*

nadany uchwałą Rady *Wydziału Inżynierii Materiałowej*

z dnia *20 stycznia 2017 roku*

Promotor w przewodzie doktorskim:

prof. dr hab. inż. Małgorzata Lewandowska

Recenzenci w przewodzie doktorskim:

prof. dr hab. inż. Wojciech Przetakiewicz

dr hab. inż. Maria Sozańska, prof. Pol. Śl.

Warszawa, dnia *31 maja 2017 roku*

Nr *8045/2017*

Małgorzata Lewandowska

PROMOTOR

DZIEKAN
WYDZIAŁU INŻYNIERII MATERIAŁOWEJ
Jarosław Mizera
Prof. dr hab. inż. Jarosław Mizera

DZIEKAN

REKTOR
Politechniki Warszawskiej
prof. dr hab. inż. Jan Szmidt

REKTOR

AUTOREFERAT

dr inż. Piotr Marcin Bazarnik

Spis treści

Autoreferat

1. Imię i nazwisko.

Piotr Marcin Bazarnik

2. Posiadane dyplomy, stopnie naukowe lub artystyczne – z podaniem podmiotu nadającego stopień, roku ich uzyskania oraz tytułu rozprawy doktorskiej.

DOKTOR NAUK TECHNICZNYCH **2017** r., *Wydział Inżynierii Materiałowej, Politechnika Warszawska*
„Rola granic ziaren w kształtowaniu właściwości mechanicznych stopu Al 5483 otrzymywanego metodami dużego odkształcenia plastycznego”
Promotor: Prof. dr hab. inż. Małgorzata Lewandowska

MAGISTER INŻYNIER **2010** r., *Wydział Inżynierii Materiałowej, Politechnika Warszawska*
„Stabilność termiczna ultradrobnoziarnistego stopu Al-Mg otrzymanego różnymi technikami”
Promotor: Prof. dr hab. inż. Małgorzata Lewandowska

3. Informacja o dotychczasowym zatrudnieniu w jednostkach naukowych lub artystycznych.

11. 2017 – 10. 2019	*specjalista naukowo-techniczny* *Wydział Inżynierii Materiałowej, Politechnika Warszawska*
10.2019 – 06.2025	*adiunkt badawczo-dydaktyczny* *Wydział Inżynierii Materiałowej, Politechnika Warszawska*
07.2025 – teraz	*adiunkt badawczy* *Wydział Inżynierii Materiałowej, Politechnika Warszawska*

Informacja o odbytych stażach naukowych znajduje się w punkcie 5.

4. Omówienie osiągnięć, o których mowa w art. 219 ust. 1 pkt. 2 ustawy z dnia 20 lipca 2018 r. Prawo o szkolnictwie wyższym i nauce (Dz. U. z 2021 r. poz. 478 z późn. zm.).

Jako osiągnięcie naukowe wynikające z art. 219 ust. 1 pkt. 2 ustawy z dnia 20 lipca 2018 r. Prawo o szkolnictwie wyższym i nauce (Dz. U. z 2021 r. poz. 478 z późn. zm.) i stanowiące podstawę ubiegania się o uzyskanie stopnia naukowego doktora habilitowanego wskazuję jednotematyczny cykl 9 artykułów.

Artykuły zostały opublikowane w latach 2019-2025 w czasopismach z listy JCR należących do TOP10 najwyżej punktowanych czasopism. W 7 artykułach jestem pierwszym lub korespondencyjnym autorem. Wszystkie są efektem współpracy międzynarodowej i powstały w ramach 3 kierowanych przeze mnie projektów:

- **SONATINA-1** pt. “Synthesis of novel hybrid materials using High-Pressure Torsion” (artykuły **A1, A3, A6, A8, A9)**
- **OPUS-19** pt. “ Metal matrix composites fabricated by high-pressure torsion and reinforced with 2D and 3D nano-particles” (artykuły **A2, A4, A5)**

- **Technologie Materiałowe-1** – POB PW Inicjatywa Doskonałości, Uczelnia Badawcza, pt. „Stabilność termiczna i mechanizmy odkształcania hybrydowych materiałów nanokrystalicznych wytwarzanych technikami skręcania pod wysokim ciśnieniem (HPT)" (artykuły **A7)**

Dla każdej publikacji wskazano całkowitą liczbę cytowań wg. bazy Web of Science (Z_{WOS}) i Scopus (Z_S) - w nawiasach liczba cytowań po odrzuceniu cytowań własnych, impact factor (IF) czasopisma obowiązujący w roku opublikowania artykułu oraz liczbę punktów zgodnie z listą Ministerstwo Edukacji Narodowej obowiązującą w roku opublikowania artykułu MEN. Sumaryczny Impact Factor cyklu publikacji wynosi **53,271.**

4.1. Tytuł osiągnięcia naukowego

„Nowoczesne nanomateriały o podwyższonej wytrzymałości kształtowane techniką skręcenia pod wysokim ciśnieniem (HPT- high pressure torsion)"

4.2. Wykaz publikacji stanowiących osiągnięcie naukowe

Przedstawiony **cykl powiązanych tematycznie 9 publikacji** nie ma charakteru chronologicznego, a ujęty jest zagadnieniowo. Wynika to z faktu, że prace badawcze nad dwoma grupami materiałów – hybrydowymi i kompozytowymi otrzymywanymi w procesie HPT – były prowadzone równolegle.

[A.1] Huang Yi, **Bazarnik Piotr**, Wan Diqing, Luo Dan, Pereira Pedro Henrique R., Lewandowska Malgorzata, Yao Jin, Hayden Brian E., Langdon Terence G.; „The fabrication of graphene-reinforced Al-based nanocomposites using high-pressure torsion", Acta Materialia 164 (2019) 499 – 511 https://doi.org/10.1016/j.actamat.2018.10.060

IF-2019 – 7.656, punkty MNiSW – 200, Z_{WOS} – 142, Z_S – 147

W tym artykule pełniłem rolę jednego z dwóch wiodących autorów (wspólnie z dr Yi Huang). Po pierwsze byłem pomysłodawcą wytworzenia nanokrystalicznego materiału kompozytowego na osnowie aluminium wzmacnianego grafenem. Grafen był wtedy stosunkowo nowym materiałem i brak było publikacji na temat kompozytów wzmacnianych takim dodatkiem. Opublikowana praca, była pierwszą opisującą tego typu kompozyt wytwarzany techniką HPT. W artykule byłem odpowiedzialny za:

- opracowanie metodyki badań,
- przeprowadzenie obserwacji mikrostruktur otrzymanych nanokompozytów, używając skaningowej i transmisyjnej mikroskopii elektronowej oraz mikroskopii jonowej wraz z analizą uzyskanych wyników,
- napisałem i zredagowałem części artykułu poświęcone badaniom strukturalnym otrzymanych kompozytów,
- wszystkie rysunki związane z badaniami strukturalnymi są mojego autorstwa.

[A.2] Bazarnik Piotr, Emerla Maria, Bartkowska Aleksandra, Huang Yi, Lewandowska Małgorzata, Langdon Terence G.; „Using direct high-pressure torsion synthesis to produce aluminium matrix nanocomposites reinforced with carbon nanotubes", Journal of Alloys and Compounds, 968 (2023,) 171928 https://doi.org/10.1016/j.jallcom.2023.171928 i 10.1016/j.jallcom.2023.173067

IF-2023 – 6.371, punkty MNiSW – 140 Z_{WOS} – 11, Z_S – 12

Byłem pomysłodawcą koncepcji badania wpływu czystości użytego stopu na stopień dyspersji nanorurek węglowych (CNTs) podczas procesu HPT i ich wpływu na rozdrobnienie struktury oraz stabilność cieplną takich nanokompozytów. W tym artykule byłem odpowiedzialny za:

- opracowanie całościowej koncepcji artykułu,
- opracowanie metodyki badań mikrostruktury i właściwości mechanicznych,
- wykonanie obserwacji mikrostruktury przy użyciu transmisyjnej mikroskopii elektronowej oraz analizę uzyskanych mikrostruktur,
- analizę wyników badań wytrzymałościowych,
- zredagowanie i przygotowanie publikacji.

Materiały będą przedmiotem tego artykułu zostały wytworzone przeze mnie podczas stażu zagranicznego na Universytecie Southampton.

[A.3] Bazarnik Piotr, Nosewicz Szymon, Romelczyk-Baishya Barbara, Chmielewski Marcin, Strojny Nędza Agata, Maj Justyna, Huang Yi, Lewandowska Małgorzata, Langdon Terence G.; "Effect of spark plasma sintering and high-pressure torsion on the microstructural and mechanical properties of a Cu–SiC composite", Materials Science and Engineering A 766 (2019) 138350 https://doi.org/10.1016/j.msea.2019.138350

IF-2019 – 4.652, punkty MNiSW – 140, Z_{WOS} – 33, Z_S – 37

Byłem pomysłodawcą wytworzenia nanokrystalicznego materiału kompozytowego na osnowie miedzi wzmacnianego cząstkami SiC poddanego procesowi HPT. Opublikowana praca była jedną z pierwszych na świecie opisujących tą tematykę. W artykule byłem odpowiedzialny za:

- opracowanie całościowej koncepcji artykułu,
- opracowanie metodyki badań,
- przeprowadzenie obserwacji mikrostruktury przy użyciu skaningowej i transmisyjnej mikroskopii elektronowej oraz mikroskopii jonowej wraz z analizą uzyskanych wyników,
- przeprowadzenie pomiarów mikrotwardości oraz analiza wszystkich wyników badań mechanicznych, jakie były ujęte w artykule,
- napisałem i zredagowałem artykuł,
- wszystkie rysunki w artykule są mojego autorstwa,

[A.4] Emerla Maria, **Bazarnik Piotr**, Yi Huang, Wojciechowska Anita, Ciemiorek Marta, Pura Jarosław, Wieczorek-Czarnocka Monika, Kenichi Purbayanto Muhammad Abiyyu, Jastrzębsta Agnieszka, Lewandowska Małgorzata, Langdon Terence G.: „The influence of graphene oxide on the microstructure and properties of ultrafine-grained copper processed by high-pressure torsion", Journal of Alloys and Compounds, 2024, 1005, 176208 https://doi.org/10.1016/j.jallcom.2024.176208.

IF-2024 – 5.8, punkty MNiSW – 100 Z_{WOS} – 2, Z_S – 2

W tym artykule pełniłem rolę wiodącego autora. Jest to kontynuacja badań z 2019 nad kompozytami wzmacnianymi grafenowymi dodatkami. Byłem pomysłodawcą koncepcji badania wpływu tlenku grafenu na stopień rozdrobnienia struktury i stabilność cieplną w kompozytach na osnowie miedzi, wytworzonych techniką HPT. W tym artykule byłem odpowiedzialny za:

- opracowanie całościowej koncepcji artykułu,
- opracowanie metodyki badań mikrostruktury i właściwości mechanicznych,
- wykonanie obserwacji mikrostruktury przy użyciu transmisyjnej mikroskopii elektronowej oraz badaniami składu chemicznego,
- analizę uzyskanych mikrostruktur i wykonanie rysunków dotyczących badań strukturalnych
- analizę wyników badań wytrzymałościowych,
- pisanie i zredagowanie publikacji.

[A.5] Bazarnik Piotr, Emerla Maria, Yi Huang, Wojciechowska Anita, Ciemiorek Marta, Bednarczyk Wiktor, Jastrzębsta Agnieszka, Lewandowska Małgorzata, Langdon Terence G; „Enhanced thermal stability of nanocrystalline Cu composites processed by high-pressure torsion: The pinning effect of Al_2O_3, GO, and rGO/Al_2O_3 nanoparticles" Journal of Alloys and Compounds, 2025, 1033, 181283, https://doi.org/10.1016/j.jallcom.2025.181283,

IF-2025 – 5.8, punkty MNiSW – 140, Z_{WOS} – 0, Z_S – 0

Jest to rozwinięcie badań z poprzedniego artykułu. Byłem pomysłodawcą koncepcji badania wpływu trzech typów nanonapełniaczy na stopień rozdrobnienia struktury i stabilność cieplną w kompozytach na osnowie miedzi, wytworzonych techniką HPT. W tym artykule byłem odpowiedzialny za:

- opracowanie całościowej koncepcji artykułu,
- opracowanie metodyki badań mikrostruktury i właściwości mechanicznych,
- wykonanie obserwacji mikrostruktury przy użyciu transmisyjnej mikroskopii elektronowej oraz badaniami składu chemicznego,
- analizę uzyskanych mikrostruktur i wykonanie rysunków dotyczących badań strukturalnych
- analizę wyników badań wytrzymałościowych,
- pisanie i zredagowanie publikacji.

[A.6] Bartkowska Aleksandra, **Bazarnik Piotr**, Huang Yi, Lewandowska Malgorzata, Langdon Terence G.; "Using high-pressure torsion to fabricate an Al–Ti hybrid system with exceptional mechanical properties", Materials Science and Engineering A 799 (2021) 140114 https://doi.org/10.1016/j.msea.2020.140114

IF-2021 – 5,96, punkty MNiSW – 140, Z_{WOS} – 11, Z_S – 12

Jest to pierwszy z cyklu artykułów poświęconych wytarzaniu techniką HPT metalicznych materiałów hybrydowych. W tym artykule byłem odpowiedzialny za:

- opracowanie całościowej koncepcji artykułu oraz opracowanie części artykułu poświęconej badaniom strukturalnym,
- wytworzenie materiałów podczas mojego stażu zagranicznego na Universytecie Southampton,
- opracowanie metodyki badań mikrostruktury i właściwości mechanicznych,
- wykonanie obserwacji mikrostruktury przy użyciu transmisyjnej mikroskopii elektronowej oraz analizę składu chemicznego badanych materiałów,
- analizę uzyskanych mikrostruktur,
- analizę wyników badań wytrzymałościowych,

[A.7] Bazarnik Piotr, Bartkowska Aleksandra, Huang Yi, Szlązak Karol, Adamczyk-Cieślak Bogusława, Sort Jordi, Lewandowska Malgorzata, Langdon Terence G.; „Fabrication of hybrid nanocrystalline Al–Ti alloys by mechanical bonding through high-pressure torsion", Materials Science and Engineering A 833 (2022) 142549 https://doi.org/10.1016/j.msea.2021.142549

IF-2022 – 6.4 punkty MNiSW – 140, Z_{WOS} – 13, Z_S – 13

Jest to drugi z cyklu artykułów poświęconych wytarzaniu techniką HPT metalicznych materiałów hybrydowych. W tym artykule byłem odpowiedzialny za:

- opracowanie całościowej koncepcji artykułu oraz opracowanie części artykułu poświęconej badaniom strukturalnym,
- wytworzenie materiałów podczas mojego stażu zagranicznego na Universytecie Southampton
- opracowanie metodyki badań mikrostrukturalnych,
- wykonanie obserwacji mikrostruktury przy użyciu transmisyjnej mikroskopii elektronowej oraz analizę uzyskanych mikrostruktur,
- analizę wyników badań mikrotwardości,
- napisanie artykułu,

[A.8] Bazarnik Piotr, Bartkowska Aleksandra, Romelczyk-Baishya Barbara, Adamczyk-Cieślak Bogusława, Dai Jiaoyan, Huang Yi, Lewandowska Małgorzata, Langdon Terence G.; „Superior strength of tri-layered Al–Cu–Al nano-composites processed by high-pressure torsion", Journal of Alloys and Compounds 846 (2020) 156380 https://doi.org/10.1016/j.jallcom.2020.156380

IF-2020 – 5.316, punkty MNiSW – 100, Z_{WOS} – 22, Z_S – 27

Jest to trzeci z cyklu trzech artykułów poświęconych wytarzaniu techniką HPT metalicznych materiałów hybrydowych. W tym artykule byłem odpowiedzialny za:

- opracowanie całościowej koncepcji artykułu,
- wytworzenie materiałów podczas mojego stażu zagranicznego na Universytecie Southampton

- opracowanie metodyki badań mikrostruktury i właściwości mechanicznych,
- wykonanie obserwacji mikrostruktury przy użyciu transmisyjnej mikroskopii elektronowej oraz analizę uzyskanych mikrostruktur,
- analizę wyników badań wytrzymałościowych,
- redagowanie i przygotowanie publikacji wytworzenie wszystkich rysunków,

---

[A.9] Mousavi Tayebeh, Dai Jiaoyan, **Bazarnik Piotr**, Pereira Pedro Henrique R., Huang Yi, Lewandowska Malgorzata, Langdon Terence G.; "Fabrication and characterization of nanostructured immiscible Cu–Ta alloys processed by high-pressure torsion", Journal of Alloys and Compounds 832 (2020) 155007 https://doi.org/10.1016/j.jallcom.2020.155007

IF-2020 – 5.316, punkty MNiSW – 100, Z_{WOS} – 25, Z_S – 26

Artykuł ten był efektem współpracy, jaką nawiązałem z dr Dai Jiaoyan i dr Pedro Pereirą podczas mojego stażu naukowego w zespole Prof. Terrenca G. Langdona na Universytecie Southampton. Była to kontynuacja i rozwinięcie badań nad hybrydowymi układami metalicznymi o układy niemieszalne z układu Cu-Ta. Z mojej strony były to badania wstępne, które pozwoliły mi napisać wniosek o nowy projekt. Badania z tego zakresu będę kontynuował w ramach nowego projektu OPUS finansowanego przez NCN: „Synthesis of immiscible systems exhibiting unique physical and mechanical properties using high-pressure torsion technique". W tym artykule byłem odpowiedzialny za:

- wykonanie badań strukturalnych hybrydowych materiałów Cu–Ta, używając mikroskopii jonowej oraz skaningowej transmisyjnej mikroskopii elektronowej
- analizę TEM mikrostruktury po procesie HPT
- zredagowałam części artykułu poświęcone badaniom mikrostrukturalnym: fragmenty Introduction (1) oraz Materials and methods (2), Results from TEM and STEM observations (3.3) oraz części dyskusji (4)

---

*Publikacje [**A1-A9**] zestawiłem w **Załączniku 5**, zaś oświadczenia współautorów o ich zakresie prac w publikacjach współautorskich zawarłem w **Załączniku 6**.*

4.3. Omówienie celu naukowego ww. prac i osiągniętych wyników wraz z omówieniem ich ewentualnego wykorzystania

4.3.1. Wprowadzenie

Materiały o rozdrobnionej mikrostrukturze, w tym ultradrobnoziarniste (UFG, ang. ultrafine-grained) oraz nanokrystaliczne (NC, ang. nanocrystalline), stanowią nowoczesną klasę materiałów konstrukcyjnych i funkcjonalnych, które od wielu lat przyciągają uwagę grup badawczych na całym świecie.

Materiały te wykazują istotnie wyższe właściwości mechaniczne — nierzadko obserwuje się nawet 300% wzrost wytrzymałości w porównaniu z materiałem gruboziarnistym [1-6]. Zjawisko to wynika przede wszystkim z mechanizmu umocnienia granicami ziaren, które stanowią bariery dla ruchu dyslokacji. Im większy udział granic ziaren (czyli im mniejsza wielkość ziarna), tym więcej przeszkód dla ruchu dyslokacji, co prowadzi do wzrostu granicy plastyczności materiału. Ilościowo zależność tę opisuje równanie Halla-Petcha, zgodnie z którym granica plastyczności materiału wzrasta liniowo wraz z odwrotnością pierwiastka średniej wielkości ziarna [7,8].

Główną grupą technik pozwalających na wytworzenie tak silnie umocnionych materiałów są techniki dużego odkształcenia plastycznego (*SPD- ang.-severe plastic deformation*). Ich zasada działania opiera się na przekształceniu mikrokrystalicznej struktury materiału w nanokrystaliczną poprzez reorganizację struktur dyslokacyjnych powstałych w wyniku intensywnego odkształcenia plastycznego. W pierwszych etapach odkształcenia technikami SPD w materiale generowane są głownie dyslokacje, które początkowo są przypadkowo rozmieszczone. Po przekroczeniu pewnej krytycznej wartości odkształcenia dyslokacje ulegają przegrupowaniu, tworząc komórki i ściany dyslokacyjne. Wraz ze wzrostem odkształcenia zmniejsza się odległość pomiędzy tymi granicami, a ich kąt dezorientacji zwiększa się. W ten sposób powstaje nowa struktura o silnie zmniejszonych rozmiarach ziaren.

Do najważniejszych technik SPD należą:

- **Skręcanie pod wysokim ciśnieniem** (*high-pressure torsion*, HPT),
- **Przeciskanie przez zagięty kanał kątowy** (*equal-channel angular pressing*, ECAP),
- **Cykliczne walcowanie materiału wielowarstwowego** (*accumulative roll bonding*, ARB).

Technika HPT zasługuje na szczególną uwagę ze względu na swoją zdolność do wytwarzania mikrostruktur o wyjątkowo małych rozmiarach ziaren — często w zakresie nanometrycznym. Jest to jedna z najczęściej stosowanych metod SPD ze względu na możliwość

zadawania ekstremalnie dużego odkształcenia – np. dla 10 obrotów na krawędzi próbki równoważne odkształcenie skumulowane wynosi ponad 100. Dla porównania podobne odkształcenie techniką ECAP wymagałoby około 100 przeciśnięć próbki przez kanał matrycy. Początkowe prace z zakresu wykorzystania metody HPT do wytwarzania materiałów UFG i nanokrystalicznych dotyczyły czystych metali i jednofazowych stopów metali [1-5]. Pierwszy raz zetknąłem się z tą techniką podczas realizacji rozprawy doktorskiej. Badałem w niej wpływ rozdrobnienia mikrostruktury na kształtowanie właściwości mechanicznych stopu aluminium 5483. Szczególną uwagę poświęciłem wpływowi charakteru powstających granic ziaren na właściwości wytrzymałościowe materiału, czyli zmianom współczynnika nachylenia zależności Halla-Petcha. Wykazałem, że udział granic o dużych i małych kątach dezorientacji będzie miał istotny wpływ na kształtowanie właściwości mechaniczne metali [9,10].

Liczne badania procesu rozdrobnienia struktury podczas procesów SPD wykazały, że pomimo możliwości zadawania bardzo dużego (w teorii nieograniczonego) odkształcenia, możliwość rozdrobnienia ziarna w poszczególnych materiałach jest ograniczone i przejawia się **efektem stabilizacji mikrostruktury** (z ang. *saturation effect*) [11,12]. W praktyce oznacza to, że po przekroczeniu pewnej krytycznej wartości odkształcenia dalsze zmniejszanie rozmiaru ziarna staje się niemożliwe, a twardość materiału przestaje rosnąć. Wynika to z faktu, że przy bardzo drobnej, nanokrystalicznej strukturze dalsze generowanie dyslokacji staje się energetycznie nieopłacalne. Z termodynamicznego punktu widzenia zaczynają wówczas dominować procesy mniej energochłonne, takie jak anihilacja dyslokacji, dynamiczne zdrowienie czy częściowa rekrystalizacja. Prowadzi to do stabilizacji mikrostruktury mimo kontynuacji odkształcenia, ograniczając możliwość dalszego umocnienia materiału. Zwykle końcowa wielkość ziarna jest porównywalna z wielkością subziarn tworzących się w klasycznych metodach odkształcenia plastycznego.

Współczesne badania koncentrują się na próbach przesunięcia granicy wynikającej z efektu stabilizacji mikrostruktury i osiągnięcia jeszcze drobniejszych rozmiarów ziaren. Jednym z obiecujących podejść jest wprowadzanie do materiału nanocząstek drugiej fazy. Obecność takich cząstek sprzyja intensyfikacji rozdrabniania mikrostruktury, ograniczając mobilność dyslokacji oraz hamując procesy dynamicznego zdrowienia i rekrystalizacji [13-15]. W szczególności zastosowanie nanocząstek wzmacniających – takich jak węgliki, azotki czy tlenki – pozwala na dalsze zmniejszenie rozmiaru ziarna, często poniżej wartości uzyskiwanych w klasycznych procesach SPD [14-16]. Dodatkowo, cząstki te mogą przyczyniać się do zwiększenia stabilności cieplnej struktury, poprawy twardości, odporności na pełzanie czy zużycie ścierne. Tego rodzaju rozwiązania znajdują zastosowanie m.in. w klasycznych

gruboziarnistych stopach metalicznych, materiałach kompozytowych czy funkcjonalnych nanomateriałach.

Mimo rosnącego zainteresowania tym kierunkiem, wciąż brakuje kompleksowych i systematycznych badań dotyczących wpływu cząstek drugiej fazy na stopień rozdrobnienia struktury w warunkach intensywnego odkształcenia. Wymaga to zarówno dalszych eksperymentów, jak i analiz z wykorzystaniem technik wysokorozdzielczej mikroskopii elektronowej.

Kolejnym z kluczowym ograniczeniem nanometali pozostaje ich niska stabilność cieplna [3,6,17-21]. Wynika ona z wysokiej energii zgromadzonej w materiale w formie defektów strukturalnych takich jak granice ziaren czy dyslokacje. W rezultacie siła napędowa wzrostu ziarna jest kilkakrotnie większa niż w przypadku konwencjonalnych metali gruboziarnistych, co sprawia, że ich wygrzewanie w relatywnie niskiej temperaturze prowadzi do rekrystalizacji i wzrostu ziarna. W konsekwencji następuje znaczny spadek właściwości wytrzymałościowych materiału, co ogranicza jego zastosowanie w elementach pracujących w wysokich temperaturach. Stabilność cieplna nanometali jest szczególnie istotna w zastosowaniach przemysłowych, takich jak lotnictwo, motoryzacja czy energetyka, gdzie materiały muszą zachowywać swoje właściwości w podwyższonych temperaturach.

W swojej pracy podjąłem więc **wątek badawczy polegający na analizie wpływu dodatku nano-cząstek drugiej fazy w metalicznych nanomateriałach kompozytowych na stopień rozdrobnienia struktury oraz ich stabilność cieplną**. Zagadnieniu temu poświęcone są publikacje (**A.1-A.5**). Przed rozpoczęciem moich prac z tego zakresu badania nad stabilnością cieplną nanokompozytów były nieliczne. Wykazano w nich, że technika HPT pozwala na wytworzenie nanokompozytów z równomierne rozmieszczonymi stabilnymi cieplna nano-cząstkami w metalowej osnowie [14-16]. Efekt stabilizacyjny, określany jako pinning effect, polega na blokowaniu migracji granic ziaren w podwyższonej temperaturze, co zapobiega rozrostowi mikrostruktury [22-24]. Efekt stabilizacji mikrostruktury pokazano dla takich nanocząstek jak NbC, Al_2O_3 czy CNTs [14-16].

W ostatnich latach pojawiło się także nowe podejście do formowania tzw. **hybrydowych metalicznych materiałów wielowarstwowych** z wykorzystaniem techniki HPT. Koncepcja ta, zaproponowana przez prof. T.G. Langdona, została po raz pierwszy przedstawiona w pracy opublikowanej w 2014 roku [25], w której badano możliwość trwałego łączenia dysków ze stopów aluminium i magnezu za pomocą procesu HPT. W przeprowadzonym eksperymencie zastosowano układ kilku naprzemiennie ułożonych dysków o zbliżonej grubości, które poddano intensywnemu odkształceniu techniką HPT. Wyniki badań wykazały, że możliwe jest

uzyskanie jednorodnego i trwałego połączenia między warstwami obu metali, przy jednoczesnym znacznym rozdrobnieniu mikrostruktury w każdym z komponentów.

Połączenie materiałów o różnych właściwościach – jednych wykazujących efekt umocnieniowy, a innych efekt mięknięcia – doprowadziło do powstania nowego hybrydowego materiału. Dzięki swojej wielowarstwowej strukturze łączył on wysoką wytrzymałość z dobrą plastycznością. Dodatkowo, zarówno w tej, jak i w późniejszych pracach wykazano, że intensywne mieszanie podczas procesu HPT może prowadzić do formowania się twardych faz międzymetalicznych, które dodatkowo wzmacniają powstały materiał. W efekcie uzyskano materiał o złożonej, wielowarstwowej nanostrukturze oraz korzystnych właściwościach mechanicznych, wynikających zarówno z efektu umocnienia ziarnami, jak i z oddziaływań międzyfazowych. Uzyskane wyniki sugerowały, że intensywne mieszanie można wykorzystać nie tylko do wzmacniania hybrydowych układów za pomocą faz międzymetalicznych, ale także do syntezy materiałów, które w naturze nie tworzą stabilnych układów równowagi fazowej – takich jak systemy niemieszalne [26,27].

Dane literaturowe wskazują na duży potencjał tej metody w tworzeniu nowych hybrydowych układów metalicznych. Jednak ze względu na nowatorski charakter tego podejścia liczba dostępnych danych literaturowych była początkowo ograniczona, a testowane układy obejmowały jedynie kilka konfiguracji. Ponadto, koncentrowano się głównie na opisie zmian mikrostruktury otrzymanych złączy, pomijając zagadnienie ich właściwości mechanicznych. Dlatego w moich badaniach zaproponowałem wykorzystanie techniki HPT do **syntezy hybrydowych układów metalicznych na bazie Al, Cu i Ti oraz niemieszalnych układów Cu-Ta**. Zagadnieniu temu poświęcone były publikacje **(A.6-A.9).**

Wymienione wątki dotyczące nanostrukturalnych materiałów wytwarzanych techniką HPT wpisują się prezentowane przeze mnie osiągnięcie. **Celem ogólnym prowadzonych badań było projektowanie budowy oraz składu chemicznego materiałów: metalicznych, hybrydowych i kompozytowych wytworzonych techniką HPT i zrozumienie wpływu elementów mikrostruktury na właściwości mechaniczne, stopień rozdrobnienia struktury czy stabilność cieplną tych materiałów**.

4.3.2. Wpływ nano-cząstek na stopień rozdrobnienia struktury, efekt stabilizacji struktury, właściwości mechaniczne i stabilność cieplną (A.1-A.5).

Zagadnieniem, które podjąłem w mojej pracy, były badania nad kształtowaniem struktury i właściwości mechanicznych nanokompozytów metalicznych z wykorzystaniem techniki HPT. Prace koncentrowały się na dwóch głównych aspektach:

1) analiza wpływu cząstek dyspersyjnych w skali nano- i mikrometrycznej na stopień rozdrobnienia struktury oraz przesunięcie efektu nasycenia struktury w kierunku mniejszych rozmiarów ziarna.
2) badanie wpływu nanododatków na stabilność cieplną struktury i właściwości mechaniczne tych nanokompozytów.

Pierwszym wątkiem, którym się zajmowałem, było zbadanie możliwości wytwarzania techniką HPT nowej klasy nanokompozytów na bazie aluminium domieszkowanego grafenem (GNP – graphene nanoplates) **[A.1].** Grafen (*GNP- z ang graphene nanoplates*), dzięki swoim unikalnym właściwościom, takim jak:

- wysoka wytrzymałość (130 GPa) i moduł Younga (1 TPa),
- wysoki współczynnik przewodności cieplnej (4000 W/mK),
- doskonałe przewodnictwo elektryczne (15 000 $cm^2/V \cdot s$),

wydawał się idealnym materiałem do wzmacniania kompozytów metalicznych.

Temat kompozytów Al-GNP był wcześniej poruszany w literaturze [28-30], jednak dotyczył on tylko grubokrystalicznych materiałów, a badania wskazywały, że brak jest odpowiedniej techniki umożliwiającej równomierne rozmieszczenie grafenu w osnowie aluminiowej bez konieczności stosowania wysokich temperatur, które prowadzą do jego degradacji. Zastosowanie techniki HPT do syntezy tych układów oraz analiza wpływu grafenu na ich strukturę stanowiły oryginalny wkład w rozwój tej tematyki.

W eksperymencie wykorzystano mieszankę proszku aluminium (99,5%) i 5% wagowych grafenu (wielowarstwowego, 5–10 warstw atomowych), którą poddano skręcaniu techniką HPT pod ciśnieniem 6,0 GPa w temperaturach: pokojowej (25°C) i podwyższonej (125°C) i 200°C). Liczba obrotów wynosiła 0, 1, 5, 10 i 20.

Badania przeprowadziłem we współpracy z prof. Terence G. Langdonem oraz dr Yi Huang z Uniwersytetu Southampton. Wykazałem, że w wyniku odkształcenia techniką HPT doszło do intensywnego wymieszania aluminium z grafenem – efekt ten nasilał się wraz ze wzrostem liczby obrotów. Ponadto, średnia wielkość ziarna aluminium uległa znacznemu zmniejszeniu – z kilkudziesięciu mikrometrów do **70 nm** (dla próbki po 20 obrotach w 25°C) i **155 nm** (dla próbki po 20 obrotach w 200°C) (Rys. 1). Dla porównania, w przypadku czystego aluminium (99,5%) minimalna wielkość ziarna uzyskana po odkształceniu techniką HPT wynosiła **~300 nm** [31]. Dowiodło to, że zastosowane płatki grafenu jako nanododatek do kompozytów wspomagał spowalnianie procesów dynamicznego zdrowienia i rekrystalizacji, **przesuwając efekt nasycenia struktury** w kierunku mniejszych wielkości ziarna.

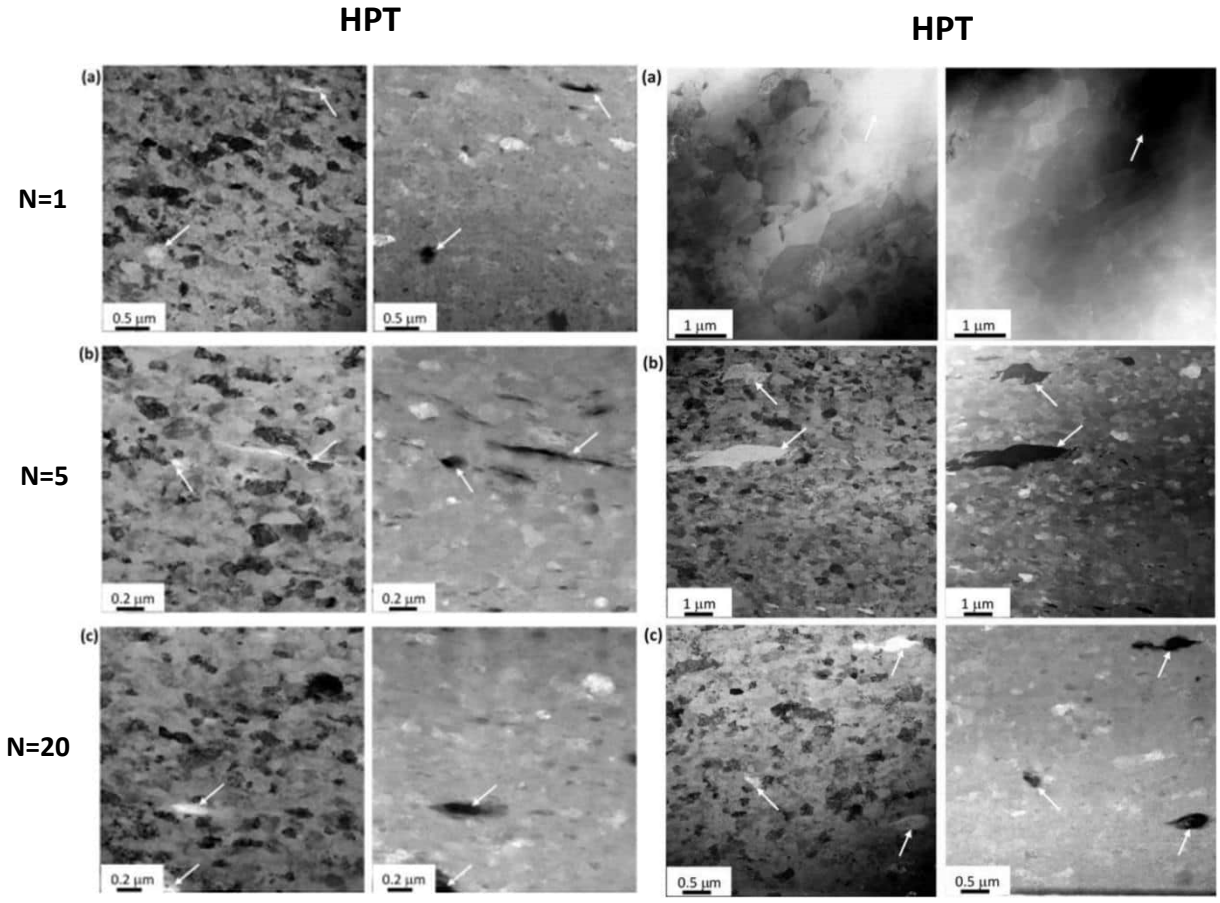

Rys. 1 *Obrazy STEM i Z-contrast przedstawiające mikrostruktury próbek przetworzonych metodą HPT w temperaturze 125°C i 200°C dla (a) N=1, (b) N=5 i (c) N=20. [A.1]*

Moje obserwacje pokazały, że w wyniku intensywnego odkształcenia dochodziło nie tylko do równomiernego rozmieszczenia aglomeratów GNP w osnowie aluminium, ale i do rozbijania tych aglomeratów. Wysokorozdzielcze analizy przeprowadzone dla próbek

poddanych 20 obrotom w temperaturach 25°C i 200°C wykazały, że pojedyncze płatki grafenu odrywają się od aglomeratów i wiążą z osnową (Rys. 2).

Wraz ze wzrostem liczby obrotów płatki grafenu ulegały znacznemu wygięciu, co było efektem silnych naprężeń wewnętrznych generowanych przez odkształcenie ścinające. Pomimo intensywnej deformacji grafen nie uległ rozpadowi ani nie tworzył faz Al_4C_3 w kontakcie z osnową aluminiową, co jest typowe dla układu Al-C. Fakt ten został potwierdzony zarówno w obserwacjach mikroskopowych, jak i w spektroskopii Ramana.

Wytworzone nanokompozyty, dzięki jednorodnemu rozmieszczeniu nanocząstek GNP, wykazywały znaczący wzrost twardości, osiągając wartości w zakresie 90–110 Hv (w porównaniu do ~50 Hv dla czystego aluminium po procesie HPT i 25 Hv dla gruboziarnistego Al), a także zwiększoną wytrzymałość na rozciąganie, przekraczającą 300 MPa. Dodatkowo, obecność GNP wpłynęła na poprawę przewodności elektrycznej uzyskanych kompozytów, która w najlepszym przypadku wynosiła $66{,}7 \pm 4{,}0\%$ IACS – dla porównania, czyste aluminium charakteryzuje się przewodnością na poziomie 62% IACS.

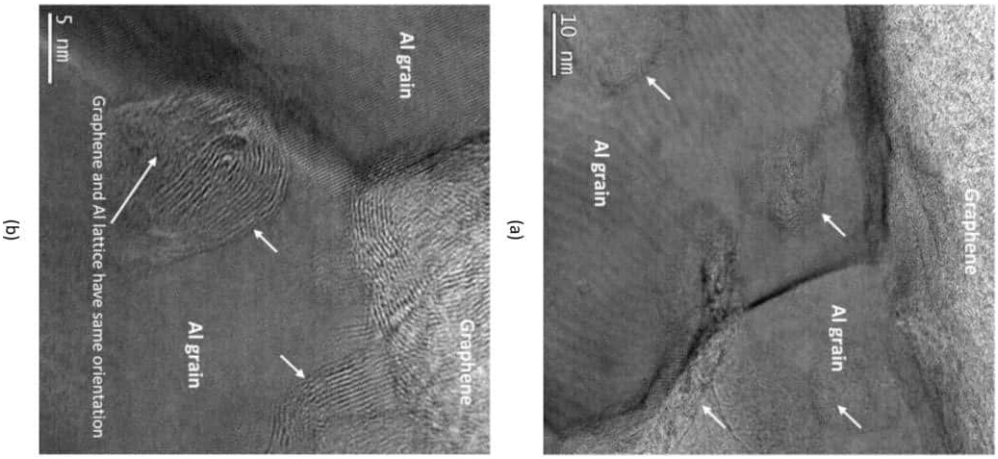

Rys. 2 *Wysokorozdzielcze obrazy STEM przedstawiające próbkę po 5 obrotach HPT w temperaturze 200°C, pokazujące interfejs między GNP a osnową Al., (a) obecność GNP nie tylko na granicy ziaren, ale również w osnową Al, (b) częściowe wyginanie płatków grafenu. [A.1]*

W moich dalszych badaniach kontynuowałem temat wytwarzania nanokompozytów na osnowie aluminium wzmacnianych węglowymi nanododatkami – tym razem wykorzystałem nanorurki węglowe (*CNTs – carbon nanotubes*). W literaturze istnieje stosunkowo duża liczba prac dotyczących nanokompozytów na bazie technicznie czystego aluminium wzmacnianego CNTs, które następnie poddawane są procesom mielenia, spiekania i dalszej obróbki za pomocą technik SPD [32,33]. W mojej pracy zaproponowałem wykorzystanie **nowego podejścia** do syntezy tych kompozytów oraz analizę **wpływu czystości użytego aluminium** (99.5% i

99.99%) na efekt stabilizacji struktury oraz stabilność cieplną tych kompozytów zawierających 0,5 i 1% CNTs **[A.2].**

Nowy sposób syntezy nanokompozytów polegał na umieszczeniu nanorurek węglowych między dwiema płytkami aluminium, a następnie odkształceniu techniką HPT pod ciśnieniem 1.0 GPa i przy 10, 20 i 50 obrotach. Takie rozwiązanie pozwoliło mi na ominięcie klasycznych etapów metalurgii proszków stosowanych przy wytwarzaniu tego typu kompozytów, takich jak mielenie proszków, ich zagęszczanie i spiekanie.

Badania strukturalne, jakie przeprowadziłem na testowanych układach, wykazały, że w obu analizowanych materiałach dodatek nanorurek węglowych pozytywnie wpłynął na rozdrobnienie ziarna aluminiowej osnowy (Rys.3). Zaobserwowałem przesunięcie nasycenia struktury do poziomu poniżej **200 nm** zarówno dla aluminium o mniejszej jak i większej czystości. Nanorurki węglowe ograniczały ruch dyslokacji w pasmach poślizgu i hamowały procesy dynamicznego zdrowienia, co prowadziło do aktywacji innych systemów poślizgu, intensyfikując rozdrobnienie strukturalne. W rezultacie następowało rozbijanie aglomeratów

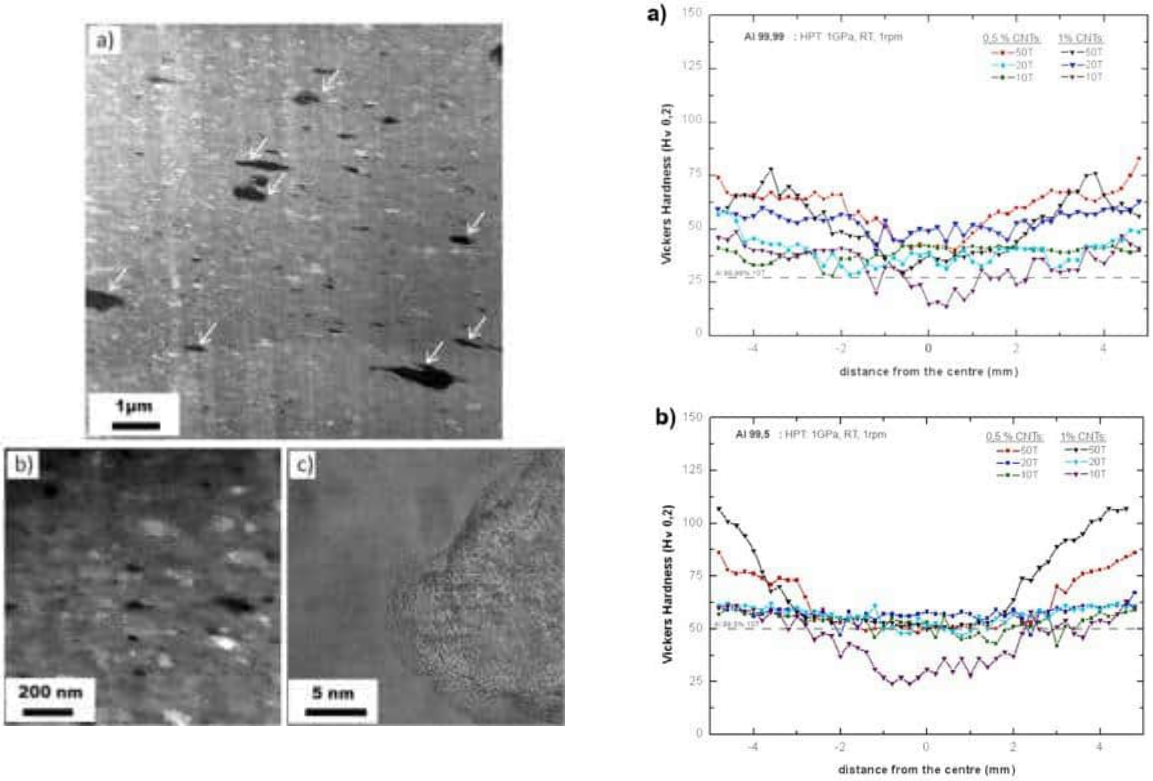

Rys. 3 *Obrazy STEM i HAADF a), b) pokazujące mikrostruktury próbek Al99,99 + 0,5 %CNTs po 50 obrotów HPT (z zaznaczonymi ciemnymi obszarami największych aglomeratów CNTs), wraz z obrazem STEM o wysokiej rozdzielczości c) pokazującym interfejs pomiędzy CNTs a osnową Al. Dodatkowo rozkłady twardości liniowej po średnicach przekrojów poprzecznych próbek: a) kompozyty Al 99,99, b) kompozyty Al 99,5. [A.2]*

nanorurek, oddzielanie pojedynczych CNTs oraz ich równomierne rozmieszczenie w osnowie (Rys. 3c), co sprzyjało ograniczeniu mobilności dyslokacji oraz hamowało procesy dynamicznego zdrowienia i rekrystalizacji. Dla porównania dla próbek referencyjnych bez dodatku nanorurek węglowych efekt nasycenia strukturalnego wynosił odpowiednio 450 nm (dla Al 99.5%) i 800 nm (dla Al 99.99%). Zaskakującym wynikiem okazał się fakt, że w kompozytach dla aluminium 99,5% po procesie HPT udział i wielkość aglomeratów były większe niż w przypadku kompozytów z aluminium 99,99%. Zjawisko to przypisano większej plastyczności stopu Al 99,99%, co ułatwiało równomierne rozmieszczenie aglomeratów CNTs oraz pojedynczych nanorurek w osnowie.

W swoich badaniach wykazałem, że kluczowym czynnikiem determinującym właściwości mechaniczne i stabilność cieplną nanokompozytów zawierających CNTs jest rozmieszczenie nanorurek węglowych w osnowie. Dodatek CNTs i intensywne rozdrobnienie struktury powodowało zwiększenie twardość nanokompozytu po procesie HPT, jednak efekt ten był widoczny wyłącznie przy wysokim stopniu rozproszenia cząstek wzmacniających w osnowie (Rys. 3). W nanokompozytach Al 99,99%, gdzie zaobserwowano najbardziej jednorodne rozmieszczenie CNT, wartości twardości przewyższały twardość czystego aluminium po HPT (nawet trzykrotnie) już po 10 obrotach. Natomiast w nanokompozytach na bazie Al 99,5% istotny wzrost twardości, wynikający z lepszego rozmieszczenia CNTs, był zauważalny dopiero w obszarach krawędzi dysków po 50 obrotach.

Jednorodne rozmieszczenie CNTs w osnowie aluminiowej miało kluczowe znaczenie nie tylko na stopień rozdrobnienia struktury i poprawę właściwości mechanicznych nanokompozytów, lecz także na ich stabilność cieplną. Moje badania wykazały, że kompozyty na osnowie aluminium 99,99% charakteryzowały się znakomitą stabilnością cieplną. Dopiero wygrzewanie w temperaturze 400°C spowodowało niewielki rozrost ziarna, co skutkowało spadkiem twardości z 75 HV do około 65 HV. Dla porównania, w kompozytach na bazie technicznie czystego aluminium 99,5% anormalny rozrost ziarna następował już w temperaturze 250–300°C. Zjawisko to przypisałem bezpośrednio **niejednorodnościom** strukturalnym w rozmieszczeniu CNTs w osnowie.

W kompozycie na bazie aluminium o czystości 99,99% udało się skutecznie rozbić większość aglomeratów nanorurek węglowych, co pozwoliło na ich względnie równomierne rozmieszczenie. Pojedyncze nanorurki, zlokalizowane głównie w pobliżu granic ziaren, skutecznie hamowały ich migrację i przeciwdziałały rozrostowi ziarna. Zjawisko to można interpretować jako działanie efektu Zenera, polegającego na blokowaniu ruchu granic ziaren przez cząstki drugiej fazy, co przyczynia się do stabilizacji mikrostruktury, zwłaszcza w

podwyższonych temperaturach [23,34]. Z drugiej strony, w próbkach aluminium o czystości 99,5% obecność dużych aglomeratów CNTs prowadziła do powstawania obszarów pozbawionych pojedynczych nanocząstek, które mogłyby skutecznie ograniczać ruch granic ziaren. W rezultacie tylko część granic była efektywnie blokowana, natomiast inne mogły przemieszczać się swobodnie, co prowadziło do **anormalnego wzrostu** ziarna [35]. W efekcie, w osnowie Al 99,5% obserwowano wyraźnie niejednorodną mikrostrukturę, cechującą się współistnieniem zarówno drobnych, jak i znacznie rozrośniętych ziaren.

Kolejną grupą materiałów kompozytowych, jakie były przedmiotem moich zainteresowań naukowych, są kompozyty na bazie miedzi. Pierwsza praca poświęcona była kompozytom Cu-SiC i kształtowaniu ich struktury techniką HPT [**A.3**]. **Kompozyty Cu-SiC** stanowią interesującą grupę materiałów, łączących doskonałą przewodność elektryczną i cieplną miedzi z wysoką wytrzymałością mechaniczną oraz odpornością na ścieranie, wynikającą z obecności twardych cząstek SiC. Mimo licznych zalet, kompozyty te wykazują pewne ograniczenia związane z metodami ich wytwarzania [36]. Wiele technologii ich wytwarzania, opartych jest na metalurgii proszków i następnie spiekaniu technikami hot pressing, natryskiwaniem cieplnym czy spiekaniem impulsowym. Wiążą się one ze stosowaniem wysokiej temperatury, co z kolei prowadzi do intensywnego rozrostu ziarna w osnowie miedzi i obniżenia jej wytrzymałości. Dodatkowo, istotnym problemem jest obecność porowatości szczątkowej, delaminacji cząstek SiC od osnowy oraz ich nierównomierne rozmieszczenie w materiale.

Aby przezwyciężyć te ograniczenia, zaproponowałem wykorzystanie techniki HPT do zagęszczania próbek wytworzonych metodą SPS, a także do rozdrobnienia struktury zarówno osnowy, jak i cząstek SiC, co wpłynęłoby pozytywnie na ich właściwości mechaniczne. W badaniach wykorzystałem dwa typy kompozytów, zawierające 10% i 20% objętościowych cząstek SiC oraz próbkę referencyjną z czystej miedzi po procesie SPS. Udało mi się wykazać, że technika HPT praktycznie całkowicie eliminuje porowatość szczątkową powstałą w procesie SPS oraz problem delaminacji pomiędzy cząstkami SiC a osnową (Rys. 4). Ponadto, naprężenia wygenerowane w próbce podczas odkształcenia techniką HPT doprowadziły do fragmentacji większych cząstek SiC (Rys. 4). Powstała duża frakcja cząstek SiC (ponad 10^4 mm^{-2}) o nanometrycznych rozmiarach, które zostały równomiernie rozmieszczone w osnowie. Jednocześnie we wszystkich próbkach struktura miedzi uległa rozdrobnieniu, a średnia wielkość ziarna była zbliżona dla wszystkich kompozytów i wynosiła ~300 nm,. Wynika z tego, że udział nanometrycznych cząstek SiC był zbyt mały, żeby doprowadzić do przesunięcia efektu nasycenia struktury w kierunku mniejszych rozmiarów ziaren.

Dodatek cząstek SiC przyczynił się do zwiększenia twardości o blisko 15% w porównaniu do czystej miedzi po procesie HPT. Zagęszczanie struktury w połączeniu z jej nanostrukturyzacją doprowadziło do zwiększenia wytrzymałości kompozytów z poziomu 70-100 MPa po procesie SPS do ponad 400 MPa po odkształceniu techniką HPT. Dodatkowo, materiały po procesie HPT wykazywały zwiększoną przewodność cieplną w porównaniu do materiałów wyjściowych.

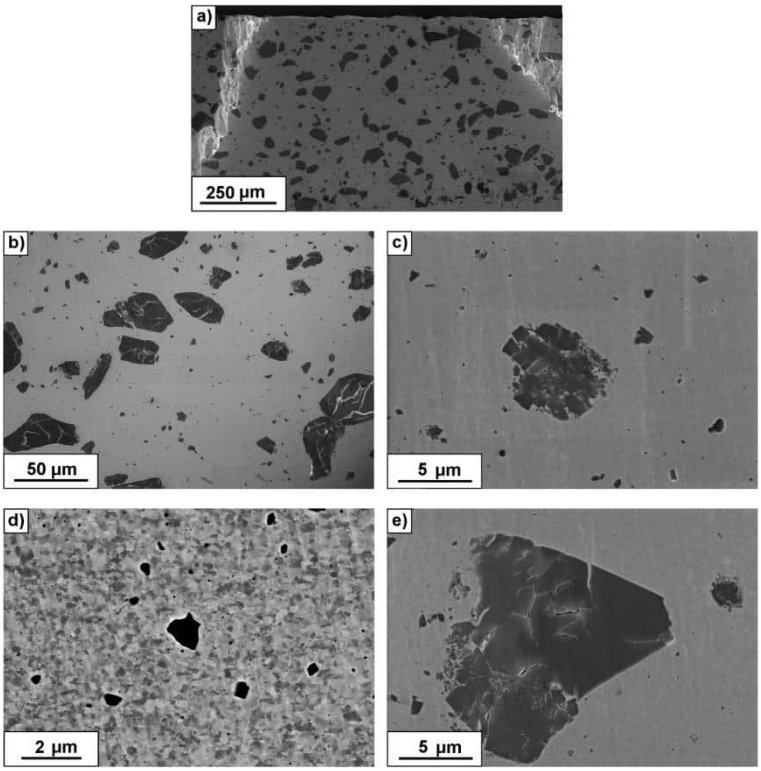

Rys. 4 *Obrazy SEM mikrostruktury kompozytu Cu–20SiC po procesie HPT. [A.3]*

Wątek nanostrukturyzacji i stabilizacji właściwości mechanicznych materiałów na bazie miedzi kontynuowałem dla nanokompozytów na bazie miedzi wzmacnianej **tlenkiem grafenu** (*GO – z ang. grafen oxide*) [**A.4**]. GO jest łatwiejszym i tańszym w produkcji materiałem niż grafen. Co więcej dane literaturowe wskazują, że ma on większy potencjał do tworzenia silnego wiązania z metaliczną osnową niż grafen. Wynika to z obecności grup tlenowych na powierzchni GO, które mają tendencję do tworzenia silnego wiązania z metalem osnowy [37]. Kompozyt Cu-GO zawierający 1% wagowy nanopłatków GO był wytworzony poprzez mielenie proszków, spiekanie techniką SPS i następnie skręcanie techniką HPT pod ciśnieniem 6.0 GPa i przy 20 obrotach.

W wyniku procesu HPT udało mi się uzyskać znaczące rozdrobnienie struktury miedzi i przesunięcie granicy nasycenia struktury z **210 nm** dla czystej miedzi bez nanododatków do poziomu **55 nm** dla kompozytu Cu-GO. Mikrostruktura po procesie HPT składała się głównie

z nanoziaren miedzi oraz drobnych fragmentów płatków grafenu (o wielkości od 5 do 30 nm), które były równomiernie rozmieszczone w osnowie (Rys. 5). Jednocześnie spektroskopia Ramana potwierdziła, że struktura tlenku grafenu jest silnie zdefektowana, jednak nadal zachowywała charakterystyczne właściwości GO.

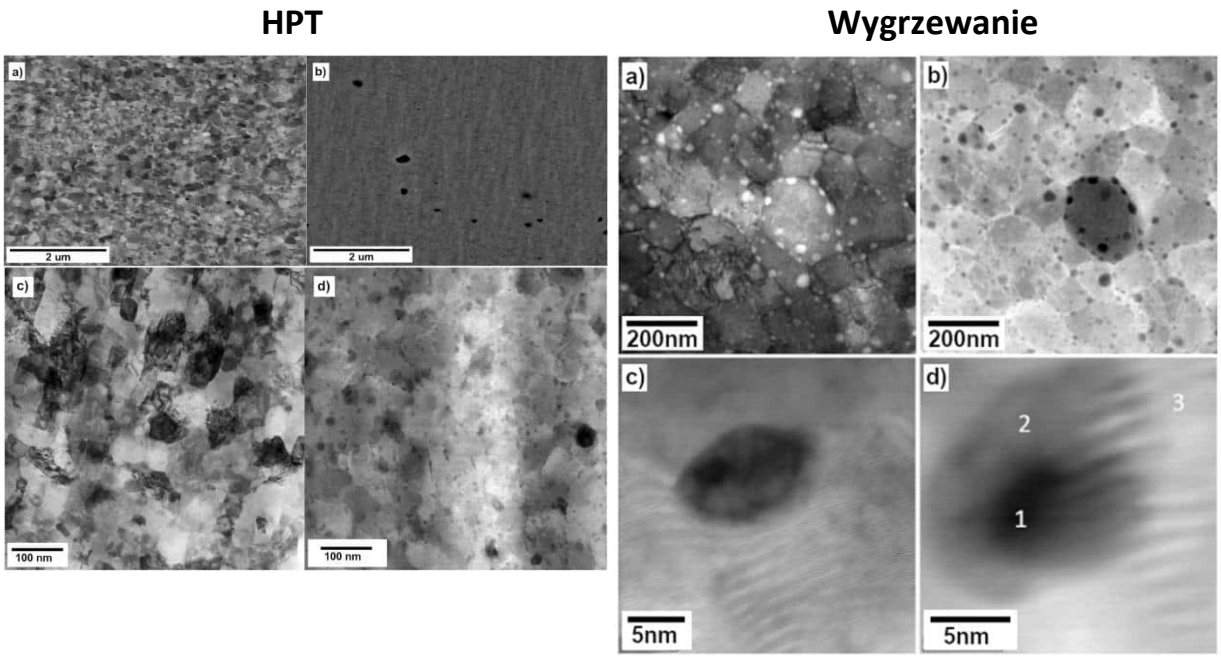

Rys. 5 *Obrazy SEM BSE czystej miedzi po HPT a); obraz SEM BSE Cu-GO po HPT b); obraz STEM Cu-GO w jasnym polu (BF) c) i obraz STEM Cu-GO w trybie HAADF d);. oraz obraz STEM kompozytu Cu-GO po procesie HPT i wyżarzeniu w temperaturze 500 ºC z widocznymi strukturami rdzenia i powłoki w osnowie Cu: a) BF i b) HAADF, c) i d) Obraz STEM punktów pomiaru EDS [A.4]*

Pogłębienie efektu nanostrukturyzacji osnowy miedzianej w połączeniu z umocnieniem drobnymi równomiernie rozmieszczonymi nanocząstkami miało istotny wpływ na właściwości mechaniczne takich kompozytów oraz ich stabilność cieplną. Wartość twardości dla kompozytu Cu-GO sięgały 250 HV, co stanowiło wzrost o ponad 75 jednostek w porównaniu do czystej miedzi poddanej procesowi HPT oraz niemal pięciokrotnie wyższą wartość niż w przypadku czystej, grubokrystalicznej miedzi. Kompozyt ten wykazywał wytrzymałość na poziomie 700 MPa, jednak ze względu na silne umocnienie oraz niewielkie rozmiary próbek próbki te zawsze ulegały zerwaniu w zakresie sprężystym.

Ponadto, badania stabilności cieplnej wykazały, że wytworzony kompozyt Cu-GO charakteryzował się wysoką stabilnością strukturalną nawet przy wygrzewaniu w temperaturze 500ºC (Rys. 5). W tej temperaturze nastąpił jedynie ograniczony wzrost ziarna, co spowodowało pewien spadek twardości (z 250 Hv do ~200Hv), jednak struktura wciąż

pozostawała w zakresie ultradrobnoziarnistym. Dla porównania, czysta miedź po HPT ulegała całkowitej rekrystalizacji już po wyżarzaniu w temperaturze 200–300°C. Wyjątkowa stabilność strukturalna nanokompozytu Cu-GO wynika z równomiernego rozmieszczenia nanocząstek GO, które skutecznie hamują ruch granic ziaren i blokują ich wzrost. Warto jednak podkreślić, że w próbce wyżarzanej w temperaturze 500°C zaobserwowano charakterystyczne zmiany mikrostrukturalne. W miejscach, gdzie pierwotnie znajdowały się cząstki GO, powstała struktura rdzenia i osnowy **(core-shell),** składająca się z rdzenia bogatego w węgiel oraz powłoki bogatej w tlen i miedź (Rys. 5). Zjawisko to powiązałem z termicznym rozkładem grup tlenowych obecnych w płatkach GO. Pod wpływem wysokiej temperatury grupy funkcyjne rozkładają się, uwalniając tlen [38], który następnie dyfunduje w materiale, prowadząc do powstania warstwy tlenków miedzi otaczających rdzeń bogaty w węgiel. Pomimo rozpadu GO, powstała struktura core-shell nadal stabilizuje mikrostrukturę kompozytu, ograniczając rozrost ziaren w podwyższonej temperaturze.

Wątek tworzenia nowych nanokompozytów na bazie miedzi kontynuowałem w kolejnej pracy [**A.5**], w której zaproponowałem porównanie wpływu trzech różnych nanonapełniaczy na mikrostrukturę oraz właściwości mechaniczne takich kompozytów. Były to: klasyczny nanododatek Al_2O_3 (często opisywany w literaturze i wykorzystany jako próbka referencyjna), tlenek grafenu (GO) omawiany w poprzedniej pracy oraz nowej klasy napełniacz **rGO/Al_2O_3** o strukturze typu hybrydowego - płatki GO były pokrywane nanocząstkami Al_2O_3. Tlen obecny na powierzchni GO został wykorzystany w procesie reakcji do powstania silnego wiązania z Al_2O_3, w wyniku czego doszło do redukcji GO do rGO. Struktura typu hybrydowego miała na celu zwiększenie sztywności płatków GO oraz poprawę ich stabilności cieplnej w wyższych temperaturach, co przełożyłoby się na lepszą stabilność cieplną wytworzonych z nim nanokompozytów. Wszystkie kompozyty zawierały 1% wagowy nanododatków i były wytworzone poprzez mielenie proszków, spiekanie techniką SPS i następnie skręcanie techniką HPT pod ciśnieniem 6.0 GPa i przy 20 obrotach.

Wyniki badań przeprowadzonych w celu charakterystyki mikrostruktury otrzymanych po procesie HPT nanokompozytów wykazały, że zastosowane nanododatki są dobrze połączone z osnową i równomiernie rozmieszczone w całej objętości — nie zaobserwowano obecności dużych, mikrometrycznych aglomeratów. Widoczne są jednak wyraźne różnice w wielkości oraz udziale objętościowym mniejszych aglomeratów/nanocząstek, zależne od rodzaju zastosowanego nanonapełniacza (Rys. 6). W próbce zawierającej Al_2O_3, aglomeraty cechowały się najmniejszymi rozmiarami (120 ± 45 nm) oraz najniższym udziałem powierzchniowym aglomeratów – zaledwie 0,5%. Dla kompozytu Cu-GO zaobserwowane aglomeraty

pokrywające około 1% powierzchni próbki. a ich średnia wielkość wynosiła 200 ± 160 nm. Natomiast w przypadku kompozytu Cu-rGO/Al_2O_3, aglomeraty zajmowały ponad 2,5% powierzchni analizowanego obrazu, a ich średnia wielkość wynosiła około 290 ± 160 nm.

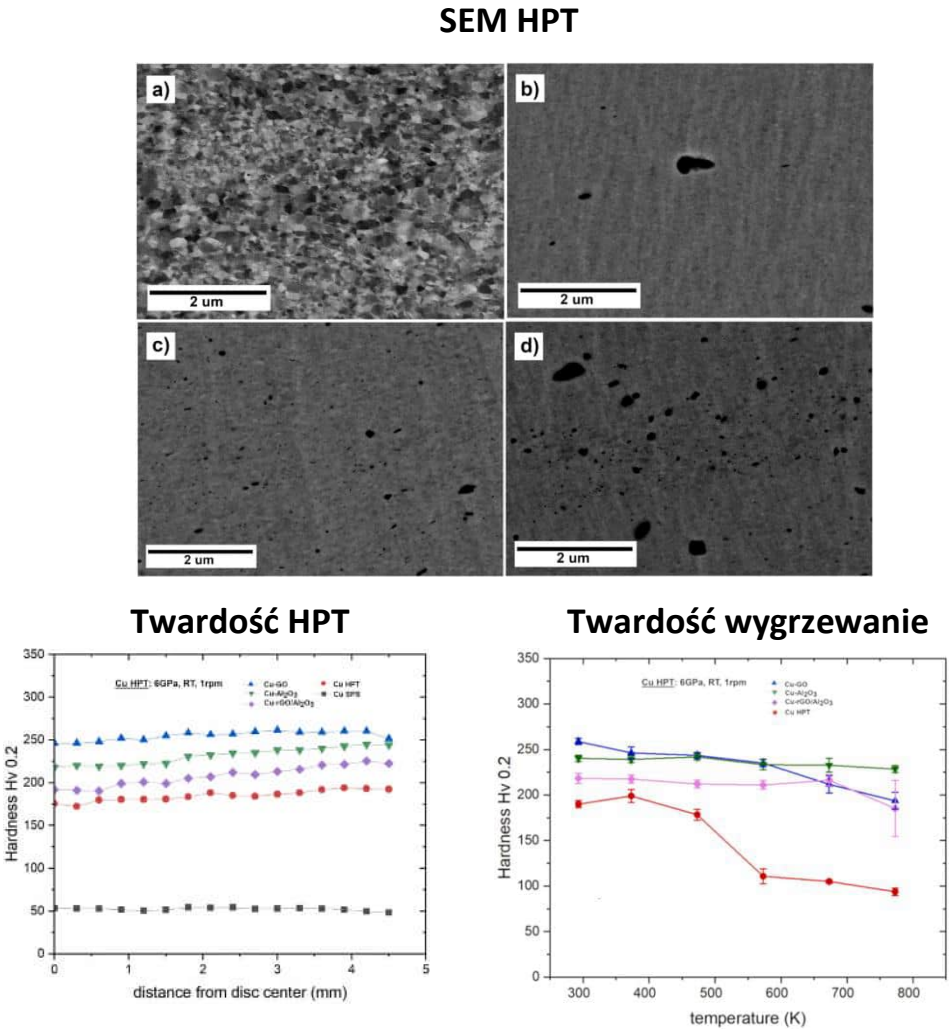

Rys. 6 *Obraz SEM BSE a) Cu po HPT; b) Cu-GO po HPT; c) Cu-Al_2O_3 po HPT; d) Cu-rGO/Al_2O_3 po HPT. Pomiary twardości wytworzonych materiałów w funkcji odległości od środków dysków, wraz z twardością jako funkcja temperatury wyżarzania.[A.5].*

W wyniku procesu HPT uzyskano znaczące rozdrobnienie struktury miedzi oraz przesunięcie efektu stabilizacji struktury. Średnie rozmiary ziarna dla kompozytów oszacowane na podstawie obrazów STEM wynosiło **~55 nm, ~65 nm i ~75 nm** odpowiednio dla kompozytów Cu-GO, Cu-Al_2O_3 i Cu-rGO/Al_2O_3. Dla porównania czysta miedź po procesie HPT miała ziarna o średniej wielkości < 300 nm. W pracy potwierdziłem tezę, że wprowadzenie stabilnych, twardych nanonapełniaczy oraz ich jednorodne rozmieszczenie w osnowie metalowej może skutecznie stabilizować granice ziaren. Nanocząstki skutecznie hamują

procesy dynamicznej rekrystalizacji i zdrowienia podczas intensywnego odkształcania plastycznego, co w konsekwencji przesuwa granicę nasycenia strukturalnego i przyczynia się do dalszego rozdrobnienia ziaren. Potwierdziłem także, że efekt przesunięcia stabilizacji strukturalnej zależy w dużej mierze od stopnia aglomeracji napełniaczy i ich rozmieszczenia w osnowie. Obserwowane różnice w wielkości ziarna w dużej mierze zależały od ilości aglomeratów, która była największa dla hybrydowego napełniacza.

Pogłębienie efektu nanostrukturyzacji osnowy miedzianej w połączeniu z umocnieniem drobnymi równomiernie rozmieszczonymi nanocząstkami miała istotny wpływ na właściwości mechaniczne takich kompozytów oraz na ich stabilność cieplną. Kompozyty wytworzone w ramach niniejszej pracy wykazywały unikalne wartości mechaniczne (Rys. 6) w porównaniu zarówno z gruboziarnistą, jak i nanokrystaliczną czystą miedzią. Zaobserwowano istotny wzrost twardości: o około 150 jednostek Hv dla kompozytu Cu–rGO/Al_2O_3, 170 jednostek Hv dla Cu–Al_2O_3 oraz ponad 200 jednostek Hv dla kompozytu Cu–GO, w odniesieniu do wartości twardości dla gruboziarnistej miedzi (50 Hv).

Za wyraźne zwiększenie właściwości mechanicznych odpowiada kilka współdziałających mechanizmów:

a) **Znaczne rozdrobnienie ziarna**, zgodne z zależnością Halla–Petcha [9], [10],

b) **Obecność twardych, jednorodnie rozmieszczonych nanocząstek** (GO, Al_2O_3 oraz rGO/Al_2O_3) w osnowie, ograniczając mobilność dyslokacji [13-15].

c) **Zwiększona gęstość dyslokacji**, wynikająca z obecności licznych przeszkód mikrostrukturalnych oraz intensywnego odkształcenia plastycznego.

Różnice w poziomach mikrotwardości pomiędzy poszczególnymi kompozytami można przypisać odmiennemu stopniowi rozdrobnienia ziarna, zróżnicowanemu rozkładowi fazy wzmacniającej w osnowie oraz różnym poziomom aglomeracji nanocząstek.

Dodatek nanocząstek wpływa nie tylko na rozdrobnienie mikrostruktury i poprawę właściwości mechanicznych, lecz również znacząco zwiększa **stabilność cieplną** wytworzonych kompozytów. Jak przedstawiono na Rys. 6, wszystkie opracowane materiały wykazują efekt podwyższonej stabilności cieplnej do poziomu co najmniej 400°C, co stanowi istotną poprawę względem czystej miedzi po procesie HPT, która ulega rekrystalizacji już przy 200°C.

W miarę dalszego wzrostu temperatury pojawiają się wyraźne różnice w zachowaniu poszczególnych kompozytów. Kompozyt Cu–Al_2O_3 wykazuje najwyższą stabilność cieplną – zachowując stabilną mikrostrukturę i mikrotwardość aż do 500°C. Efekt ten przypisuje się obecności jednorodnie rozprowadzonych ceramicznych nanocząstek Al_2O_3 w osnowie, które

dzięki swojej wysokiej stabilności cieplnej i niewielkim rozmiarom (średnio 6,5 nm) skutecznie hamują migrację granic ziaren [14].

Dodatek GO skutkował najsilniejszym rozdrobnieniem struktury spośród wszystkich wytworzonych kompozytów, co przełożyło się na najwyższą twardość tego materiału (260 Hv). Kompozyt Cu–GO wykazał jednak ciągły niewielki spadek twardości w miarę wzrostu temperatury wyżarzania. Po wyżarzaniu w temperaturze 500°C twardość materiału wynosi już jedynie 190 jednostek Hv. Efekt ten przypisałem termicznemu rozpadowi GO i tworzeniu struktury core-shell, co zaburzyło efekt hamowania rozrostu ziarna i doprowadziło do jego rozrostu do około 150 nm.

Kompozyt z dodatkiem rGO/Al_2O_3 wykazuje stabilność cieplną do temperatury 400°C K. Jednak wyżarzanie w temperaturze 500°C prowadzi do anormalnego rozrostu ziarna oraz formowania się **heterostruktury** składającej się z dużych, zrekrystalizowanych ziaren i regionów, gdzie nanostruktura dalej jest obecna. Powstanie heterostruktury przypisałem niejednorodnemu rozmieszczeniu cząstek rGO/Al_2O_3 w osnowie miedzianej. Stabilizowanie płatków GO nanocząstkami Al_2O_3 w istotny sposób zwiększyło sztywność oraz wytrzymałości mechaniczno-termiczne płatków rGO/Al_2O_3 (nie tworzą one struktury core-shell w podwyższonej temperaturze), jednak z drugiej strony uniemożliwiło ich fragmentację podczas intensywnego odkształcania HPT. W efekcie w mikrostrukturze pozostały stosunkowo duże aglomeraty, a w rezultacie zmniejszyła się efektywna liczba przeszkód blokujących migrację granic ziaren, umożliwiając lokalny wzrost ziaren i prowadząc do częściowej rekrystalizacji.

Przeprowadzone przeze mnie w tej części badania dowodzą, że efekt nasycenia strukturalnego i stabilność cieplna nanometali może być kontrolowane poprzez wprowadzanie rożnego rodzaju stabilnych nanododatków i ich równomierne rozmieszczenie w osnowie.

4.3.3. Określenie wpływu architektury, składu warstw i parametrów procesu HPT na strukturę i właściwości mechaniczne hybrydowych materiałów metalicznych (A.6-A.9).

W ramach tego wątku badawczego postawiłem sobie za cel zrozumienie mechanizmów oraz opisanie wpływu techniki HPT na możliwości wytwarzania nowych **hybrydowych** układów metalicznych. Moje prace koncentrowały się na wykorzystaniu nowatorskiej koncepcji wielowarstwowych materiałów, otrzymywanych poprzez naprzemienne układanie dysków różnych metali, a następnie ich skręcanie z zastosowaniem techniki HPT. Na owe czasy

idea tworzenia techniką HPT hybrydowych materiałów wielowarstwowych była stosunkowo nowym podejściem w projektowania materiałów i pozostawiała wiele pytań bez odpowiedzi, m.in.: jakie kombinacje materiałów są możliwe do połączenia oraz jaki wpływ na właściwości mechaniczne będzie miała struktura takiego układu?

W moich badaniach koncentrowałem się nad opisaniem wpływu takich czynników, jak: typy łączonych metali, architektura takich połączeń (liczba warstw i ich wzajemna grubość) czy parametrów procesu HPT (ciśnienia ściskającego, liczby obrotów, wygrzewania między procesami) na mikrostrukturę i właściwości wytrzymałościowe takich hybrydowych układów. Spośród wszystkich badanych przeze mnie układów najciekawsze wyniki uzyskałem dla trzech systemów: **Al-Ti (artykuły A.6, A.7), Al-Cu (artykuł A.8) i Cu-Ta (artykuł A.9).**

W moim podejściu badawczym w pierwszej kolejności skupiłem się na wpływie architektury układów, takich jak liczba warstw (dwie, trzy oraz ponad dziesięć), sposób ułożenia i ich grubości, a także na parametrach procesu HPT (np. ciśnienie i liczba obrotów) na możliwość uzyskania trwałego połączenia.

Pierwszym zaproponowanym przeze mnie układem był system Al–Ti, w którym wykorzystane metale zostały dobrane tak, aby cechowały się dużą różnicą we właściwościach mechanicznych. W początkowej fazie badań wykorzystałem klasyczny układ trójwarstwowy, z równą grubością każdej warstwy wynoszącą 0,3 mm. Przeanalizowałem wpływ ciśnienia ściskającego oraz konfiguracji warstw (Al–Ti–Al oraz Ti–Al–Ti) na efektywność procesu łączenia. Moje badania pokazały, że przy niskim ciśnieniu (1.0 GPa) nie dochodziło do utworzenia połączenia w żadnym z badanych układów. W związku z tym w dalszych etapach prac, również dla innych systemów, stosowano wyłącznie wysokie ciśnienie (6.0 GPa) i liczbę obrotów rzędu 50. Ustaliłem również, że konfiguracja warstw miała istotny wpływ na przebieg procesu. Układy zawierające dwie warstwy twardego tytanu oraz jedną warstwę miękkiego aluminium umieszczoną centralnie nie wykazywały efektu tworzenia połączenia — miękkie aluminium pełniło funkcję warstwy smarującej, po której tytanowe dyski ślizgały się, co potwierdzają dane także literaturowe dla innych układów. Z kolei w konfiguracji zawierającej jedną warstwę tytanu zaobserwowano intensywne wyginanie blaszki tytanowej, jej fragmentację oraz częściowe mieszanie się z aluminium, jednak proces ten zachodził jedynie w zewnętrznych partiach dysków. Poziom wymieszania oraz ewentualnego tworzenia się faz międzymetalicznych był niewielki, dlatego zaproponowałem zmianę podejścia: grubość warstwy tytanu została zmniejszona do **0,15 mm**, co miało ułatwić jej deformację, szybsze pękanie oraz intensyfikację procesu mieszania z aluminium, sprzyjając powstawaniu faz międzymetalicznych.

Zagadnienie to stanowiło temat pierwszego artykułu w prezentowanym w niniejszym rozdziale cyklu publikacji [**A.6**]. Przeprowadzone przeze mnie obserwacje strukturalne (Rys. 7) ujawniły silną fragmentację wewnętrznej tytanowej warstwy i jej mieszanie z aluminiową osnową. W rezultacie powstała typowa dla tego typu podejścia warstwowa budowa, w której można wyróżnić pasma osnowy aluminiowej o średniej wielkości ziarna wynoszącej około 160 nm oraz strefę mieszania, oznaczoną strzałką (obrazy STEM Rys. 7a). Dalsze badania strukturalne wykazały, że obszary te składają się z cienkich warstw o bardzo drobnych ziarnach, których średnia wielkość wynosi około 20 nm, co zilustrowano na Rys. 7c. Jest to wielkość ziarna niespotykana w porównaniu do materiałów wyjściowych po procesach SPD [31,39]. W porównaniu do czystego aluminium po procesie HPT jest ona o rząd wielkości mniejsza.

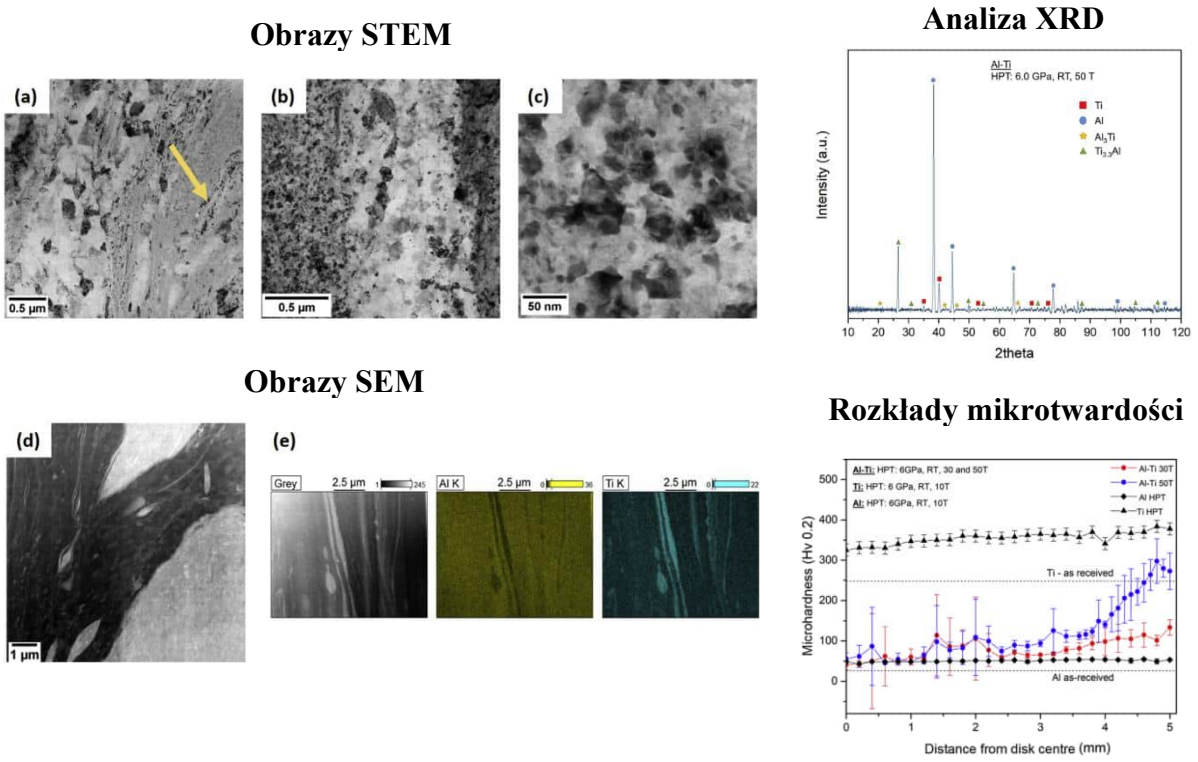

***Rys. 7** Mikrostruktura hybrydowego materiału z układu Al-Ti: a, b, c) zdjęcie STEM, d) SEM wraz z analizą składu chemicznego e) oraz badaniami składu fazowego XRD i rozkładami mikrotwardości dla układów hybrydowych i materiałów wyjściowych [A.6].*

Obserwacje SEM/EDX (Rys. 7e) wykazały, że obszary o silnie rozdrobnionej strukturze są bogate w tytan i aluminium, co sugeruje tworzenie się tam faz międzymetalicznych z układu Al-Ti. Potwierdziły to analizy XRD (Rys. 7), które wykazały powstawanie twardych faz międzymetalicznych Ti_3Al i Al_3Ti. Niespotykany dla tego typu materiałów efekt rozdrobnienia struktury w połączeniu z formowaniem się twardych faz międzymetalicznych z układu Al-Ti skutkowały silnym wzrostem twardości wytworzonych przeze mnie materiałów (Rys. 7).

Mikrotwardość dla badanego hybrydowego układu po 50 obrotach HPT w zewnętrznych częściach dysków (a więc w obszarach najintensywniejszego mieszania) przekraczała 300 jednostek Hv, a więc była niemal 10-krotnie wyższa niż dla czystego gruboziarnistego aluminium i o blisko 50 jednostek Hv wyższa niż dla czystego grubokrystalicznego tytanu. Nie udało się osiągnąć jednak twardości nanokrystalicznego tytanu. Niemniej, warto podkreślić, że w wytworzonym materiale hybrydowym użyto około ~24% wagowych tytanu, a resztę stanowiło miękkie aluminium.

Aby zintensyfikować tworzenie się wzmacniających faz międzymetalicznych oraz uzyskać jeszcze wyższy stopień rozdrobnienia mikrostruktury, w kolejnych etapach badań zaproponowałem zwiększenie udziału tytanu w składzie warstwowym układu. Jednakże, biorąc pod uwagę wcześniejsze wyniki eksperymentalne, zastosowanie blaszki tytanowej o grubości 0,3 mm okazało by się nieefektywne — jej wysoka wytrzymałość powodowała jedynie znaczne wyginanie oraz ograniczoną fragmentację i mieszanie, głównie w zewnętrznych partiach dysków. W związku z tym zaproponowałem zastosowanie nowej architektury układu, dzieląc blaszkę tytanową o grubości 0,3 mm na dwie cieńsze, każda o grubości 0,15 mm. Ostatecznie powstał układ składający się z **trzech warstw aluminium i dwóch warstw tytanu**, o sumarycznej grubości 1,2 mm, który został poddany procesowi skręcania metodą HPT pod ciśnieniem 6,0 GPa, przy różnych liczbach obrotów — aż do 50. W trakcie tego procesu aluminium, jako metal o większej plastyczności, wypływało z układu, zamykając tytanowe blaszki. Badania nad takim układem stanowiły temat drugiego artykułu w prezentowanym w niniejszym rozdziale cyklu publikacji [**artykuł A.7**].

Badania mikrostrukturalne wytworzonego materiału przeprowadziłem w szerokim zakresie skali wymiarowej. Obserwacje wykonane za pomocą mikroskopii świetlnej (MŚ) na przekrojach poprzecznych (Rys. 8) wykazały, że w próbkach poddanych niewielkiej liczbie obrotów dominują wygięte i pofragmentowane płytki Ti osadzone w osnowie Al, bez wyraźnego mieszania obu składników. Zwiększenie liczby obrotów do 50 prowadzi stopniowo do rozdrobnienia faz, ich wzajemnego mieszania oraz do niemal całkowitej eliminacji pęknięć i delaminacji w obrębie dysków. Mimo to, nawet po 50 obrotach metodą HPT struktura pozostaje niejednorodna, z wyraźnymi różnicami pomiędzy brzegiem a centrum dysku. W próbce poddanej 50 obrotom, fragmenty Ti i Al stają się nierozróżnialne w strefie brzegowej, co wskazuje na intensywne mieszanie się obu pierwiastków.

Uzupełnieniem tych badań była mikrotomografia rentgenowska (MicroCT) (Rys. 8). Uzyskane wyniki potwierdzają, że przy niskiej liczbie obrotów proces skręcania prowadzi głównie do zginania, przewężania, a w końcu do fragmentacji fazy tytanu (oznaczonej kolorem

czerwonym) wzdłuż średnicy dysku. Efekt ten wyraźnie narasta wraz ze wzrostem liczby obrotów, co szczególnie dobrze widoczne jest po 50 obrotach HPT — wówczas obserwuje się silną fragmentację tytanowej blaszki oraz tendencję do równomiernego rozmieszczenia jej fragmentów w osnowie aluminiowej. Należy jednak zaznaczyć, że zarówno mikroskopia świetlna, jak i mikrotomografia rentgenowska nie pozwalają na obserwację elementów o rozmiarach poniżej 1–2 μm. W związku z tym, w dalszej części badań strukturalnych zastosowałem techniki o wyższej zdolności rozdzielczej, takie jak SEM oraz TEM/STEM.

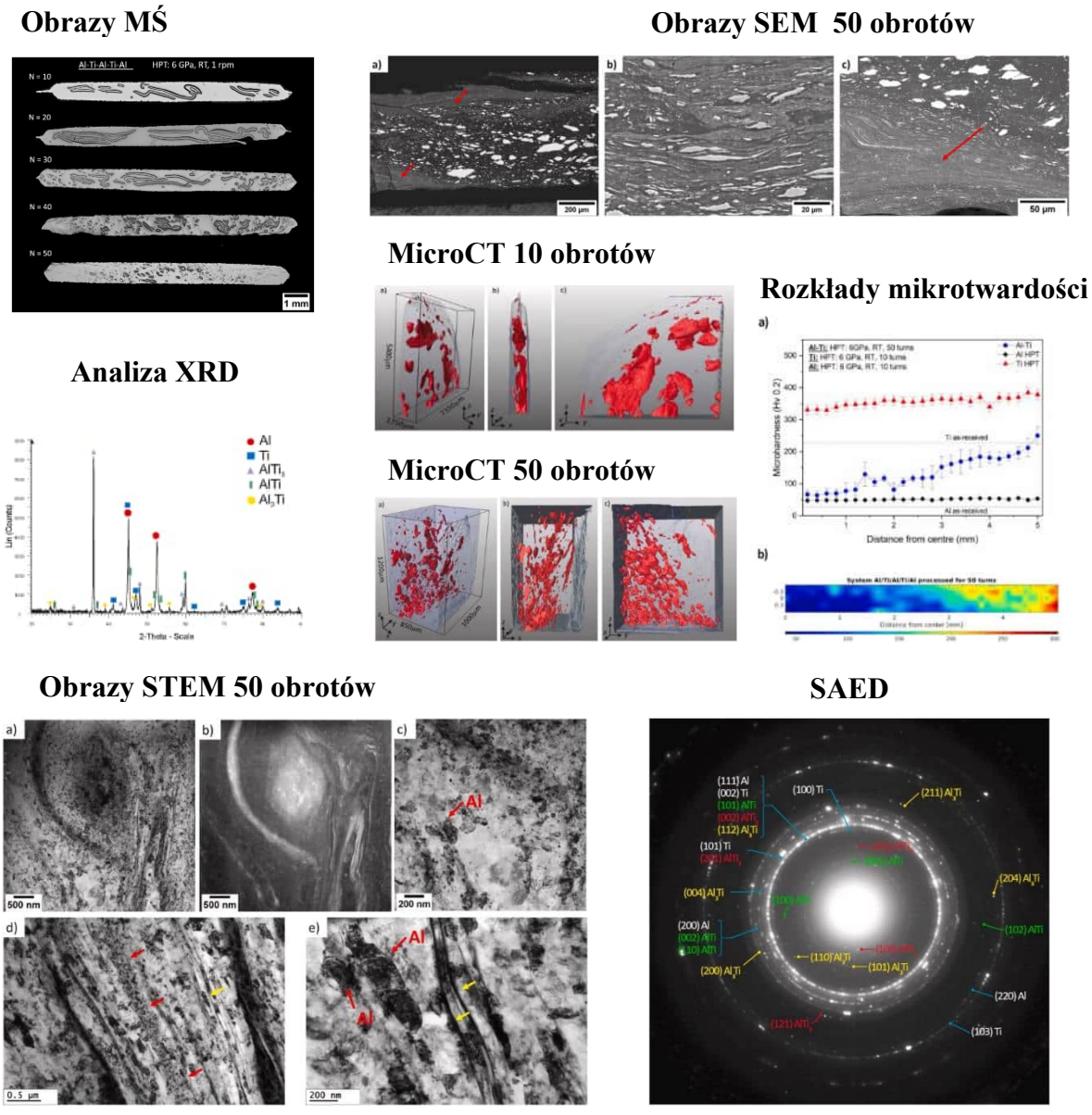

Rys. 8 *Mikrostruktura hybrydowego materiału pięcio-warstwowego z układu Al-Ti badana technikami mikroskopii świetlnej, tomografii komputerowej oraz mikroskopii SEM i STEM/TEM wraz z analizą składu fazowego XRD uzupełnioną o badania dyfrakcji elektronowej SAED i rozkładami mikrotwardości dla układów hybrydowych i materiałów wyjściowych [A.7].*

Obserwacje SEM potwierdziły efekt wyginania blaszek tytanowych przy małej liczbie obrotów, ale i obecność licznych delaminacji i nieciągłości pomiędzy tytanem a aluminium. Zwiększenie liczby obrotów do 50 prowadzi do silnej fragmentacji dysków Ti, domknięcia pęknięć oraz do jednorodnego rozmieszczenia fragmentów Ti w osnowie Al, szczególnie w obszarach brzegowych, co zilustrowano na Rys. 8 przedstawiającym obrazy SEM próbki Al–Ti po 50 obrotach. Wyraźnie widać, że po 50 obrotach dominującą część próbki stanowią stosunkowo drobne, pofragmentowane części dysku Ti w osnowie aluminiowej. Zwiększenie liczby obrotów do tego poziomu umożliwia więc zmniejszenie rozmiarów obszarów wzbogaconych w Ti. Widoczne są również obszary o podwyższonym stopniu wymieszania składników, w których obserwuje się zmiany kontrastu w obrazach BSE, co sugeruje zachodzenie procesu mieszania się Al i Ti oraz tworzenie faz międzymetalicznych.

W celu analizy procesu rozdrobnienia ziaren oraz mieszania składników w próbce po 50 obrotach przeprowadziłem badania z wykorzystaniem mikroskopii TEM/STEM oraz dyfrakcji elektronów (SAED) (Rys. 8). Analiza obrazów STENM pokazała, że w obszarach bogatych w aluminium średnia wielkość ziarna wynosiła około 200 nm i poniżej 100 nm w strefach tytanu. Widoczne są również liczne pasmowa (mieszania), w których ziarna mają rozmiary poniżej **30 nm**. Warto podkreślić, że średnia wielkość ziarna dla materiałów wyjściowych po procesie HPT wynosiła odpowiednio 700 nm dla aluminium i 100 nm dla tytanu. W tym kontekście zastosowanie takiego hybrydowego układu doprowadziło do dalszego rozdrobnienia struktury. Przeprowadzone przeze mnie badania SAED potwierdziły obecność faz międzymetalicznych w strefach mieszania (Rys. 8). Analiza obrazów dyfrakcyjnych potwierdzała obecność faz międzymetalicznych AlTi, Al_3Ti oraz $AlTi_3$ co zostało dodatkowo potwierdzone badaniami XRD (Rys. 8).

Zwiększenie stopnia rozdrobnienia struktury, a więc przesunięcie nasycenia strukturalnego w kierunku mniejszych rozmiarów ziaren, w połączeniu z formowaniem się twardych faz międzymetalicznych miało duży wpływ na właściwości mechaniczne otrzymanych materiałów hybrydowych. Wyniki pomiarów mikrotwardości dla opracowanego materiału hybrydowego (Rys. 8) wykazały, że w zewnętrznych obszarach dysków wartości twardości sięgają około 200 jednostek Hv, a miejscami dochodzą nawet do 250 Hv. Oznacza to niemal 10-krotny wzrost w porównaniu z czystym, gruboziarnistym aluminium (26 Hv). Dla porównania, po procesie HPT twardość aluminium wzrasta do 51 Hv, co nadal stanowi wartość niemal 5-krotnie niższą niż maksymalne wyniki uzyskane dla hybrydowego układu Al–Ti. Co więcej, mikrotwardość materiału hybrydowego jest tylko nieznacznie niższa niż w przypadku gruboziarnistego tytanu (219 Hv).

Na podstawie przeprowadzonych badań zaproponowałem mechanizm mieszania i formowania struktury lamelarnej w układach, w których różnice właściwości mechanicznych pomiędzy składnikami są znaczne. Wraz ze wzrostem liczby obrotów HPT ogólna twardość materiału hybrydowego rośnie, co związane jest z postępującym rozdrobnieniem struktury poszczególnych warstw i prowadzi do silnej lokalizacji odkształceń ścinających. Na początkowym etapie deformacji twardy dysk tytanowy ulega wyginaniu i pękaniu, a następnie z jego powierzchni odrywają się drobne fragmenty, które przechodzą do osnowy aluminiowej. Fragmenty te są dalej intensywnie deformowane, tworząc strukturę przypominającą wir, złożoną z bardzo cienkich warstw tytanu naprzemiennie rozmieszczonych w osnowie z aluminium. Po przekroczeniu pewnego krytycznego poziomu odkształcenia dochodzi do mechanicznego wymieszania Ti i Al, co prowadzi do powstania charakterystycznej struktury lamelarnej. W rezultacie, po 50 obrotach HPT, w obszarach brzegowych dysków udało mi się uzyskać niemal jednorodną strukturę, a w obrębie utworzonych struktur lamelarnych dochodziło do powstawania licznych faz międzymetalicznych z układu Al–Ti. Ich formowanie było możliwe dzięki intensywnym procesom dyfuzyjnym zachodzącym podczas deformacji HPT. Procesy te wynikają ze zwiększonej gęstości defektów sieciowych – takich jak wakanse, dyslokacje oraz znaczącego rozdrobnienia mikrostruktury, które prowadzą do skrócenia ścieżek dyfuzji. Skrócenie drogi dyfuzji sprzyja reakcjom w stanie stałym, co z kolei ułatwia tworzenie się twardych faz międzymetalicznych.

Wątek syntezy materiałów hybrydowych kontynuowałem w kolejnej pracy [**A.8**], w którym podjąłem dwa wątki badawcze:

- zbadanie możliwości wytworzenia techniką HPT hybrydowego układu Al-Cu.
- określenie wpływu stopnia odkształcenia metodą HPT na mikrostrukturę i zachodzące przemiany fazowe, a przez to właściwości mechaniczne uzyskanych dysków. Trzywarstwowe układy Al/Cu/Al (grubość każdej warstwy to 0.8 mm) były skręcane techniką HPT pod ciśnieniem 6.0 GPa przy różnej liczbie obrotów: 20, 50, 100 i 200.

Badania strukturalne, jakie przeprowadziłem na tym układzie, wykazały znaczące różnice w mikrostrukturze w zależności od liczny obrotów. Już po 20 obrotach struktura składa się z ultra-cienkich warstw bogatych w aluminium (Al) i miedź (Cu) (Rys. 9), z wyraźnymi oznakami znacznego rozdrobnienia ziaren we wszystkich warstwach. Analiza strukturalna wykazała, że ziarna w warstwach Al są wydłużone i zdecydowanie mniejsze (ok. 230 ± 20 nm) niż w pasmach Cu, gdzie ich wielkość silnie zależała od grubości poszczególnych warstw i wynosiła 310 ± 70 nm. Ponadto zaobserwowałem, że w wyniku procesu HPT na styku warstw

Al i Cu widoczna jest strefa dyfuzyjna (Rys. 9(c)), co zostało również potwierdzone liniową analizą EDX. Zjawisko dyfuzji zaobserwowano na niemal wszystkich granicach warstw Al–Cu. Dodatkowo, w niektórych miejscach najcieńsze warstwy Cu uległy całkowitemu wymieszaniu z aluminium tworząc strukturę o silnie rozdrobnionej wielkości ziarna (Rys. 9(b)) ok. 30 ± 20 nm.

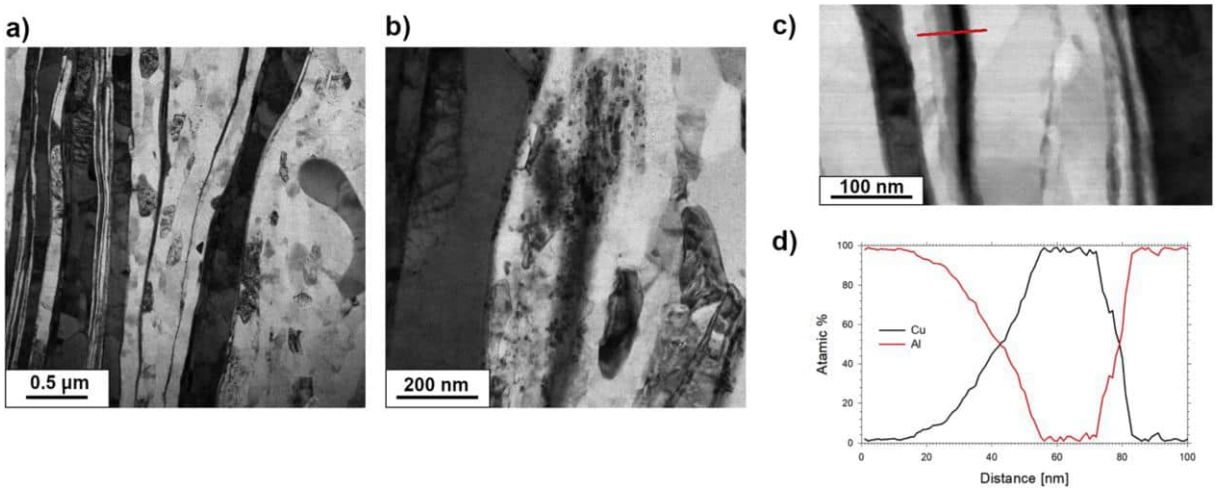

Rys. 9 *Obrazy mikrostruktury wykonane w trybie STEM (jasne pole) na krawędzi dysku po 20 obrotach HPT: (a) w małym powiększeniu oraz (b) w dużym powiększeniu. (c) Obraz HAADF mikrostruktury z zaznaczonym miejscem liniowego skanu EDX, którego wyniki przedstawiono na wykresie (d) w postaci udziału procentowego atomów w funkcji odległości skanowania dla pierwiastków Cu i Al.[A.8].*

Zastosowanie 200 obrotów doprowadziło do dalszego rozdrobnienia ziarna, (Rys. 10) z zachowaniem struktury warstwowej. Otrzymana struktura miała bimodalny charakter – w warstwach bogatych w Al występują ziarna o rozmiarze ok. **95 ± 15 nm** (Rys. 10), natomiast w strefach bogatych w Cu ziarna mają rozmiar rzędu **~5–20 nm**. Pierścienie dyfrakcyjne na obrazach dyfrakcji elektronów (SAED), przedstawione na Rys. 10, potwierdziły obecność Al i Cu oraz powstanie faz międzymetalicznych **Al_2Cu i Al_4Cu_9.** Obrazowanie w ciemnym polu z pierścienia Al_2Cu (110) (Rys. 10) potwierdziło, że faza ta występuje głównie w nanometrycznych pasmach bogatych w Cu i Al. Formowanie faz międzymetalicznych zostało również potwierdzone za pomocą dyfrakcji rentgenowskiej (XRD) (Rys. 10). Na dyfraktogramach wyraźne widać poszerzenie pików, spowodowane silnym rozdrobnieniem struktury, przy czym intensywność tego zjawiska wzrasta wraz z liczbą obrotów. Widoczne są piki dla Al i Cu oraz faz międzymetalicznych Al_2Cu i Al_4Cu_9. Obecność faz międzymetalicznych można zaobserwować już po 20 obrotach, a wzrost intensywności odpowiadających im pików dyfrakcyjnych wraz z dalszym zwiększaniem liczby obrotów wskazuje na rosnący udział tych faz w mikrostrukturze.

Kluczowa okazała się analiza kinetyki powstawania faz międzymetalicznych w tym układzie. Oba pierwiastki wykazują wzajemną dyfuzyjność i możliwość formowania przesyconych roztworów stałych Al(Cu) i Cu(Al). Ponieważ granica rozpuszczalności Cu w Al jest niemal dwa rzędy wielkości mniejsza niż rozpuszczalność Al w Cu [40-42], należy oczekiwać, że w pierwszej kolejności będzie formował się roztwór Al(Cu). Co więcej, współczynnik dyfuzji Cu w Al jest znacznie wyższy niż dyfuzji Al w Cu ($D_{(Cu)} \approx 1{,}78 \times 10^{-15}$ m²/s, $D_{(Al)} \approx 6{,}54 \times 10^{-19}$ m²/s) [41]. Atomy Cu mogą szybko dyfundować w Al, co prowadzi do przesycenia tej strony reakcji i w rezultacie do tworzenia się fazy Al_2Cu w strefie międzyfazowej. Jednocześnie faza Al_2Cu charakteryzuje się najbardziej ujemną wartością entalpię tworzenia, dlatego z punktu widzenia termodynamiki będzie to pierwsza faza powstająca w strefie międzyfazowej Al–Cu [42]. Faza Al_4Cu_9 będzie mniej uprzywilejowaną fazą pod względem kinetyki formowania. Wyjaśniało to większą intensywność pików dla fazy Al_2Cu na spektrach XRD i obrazach SAED.

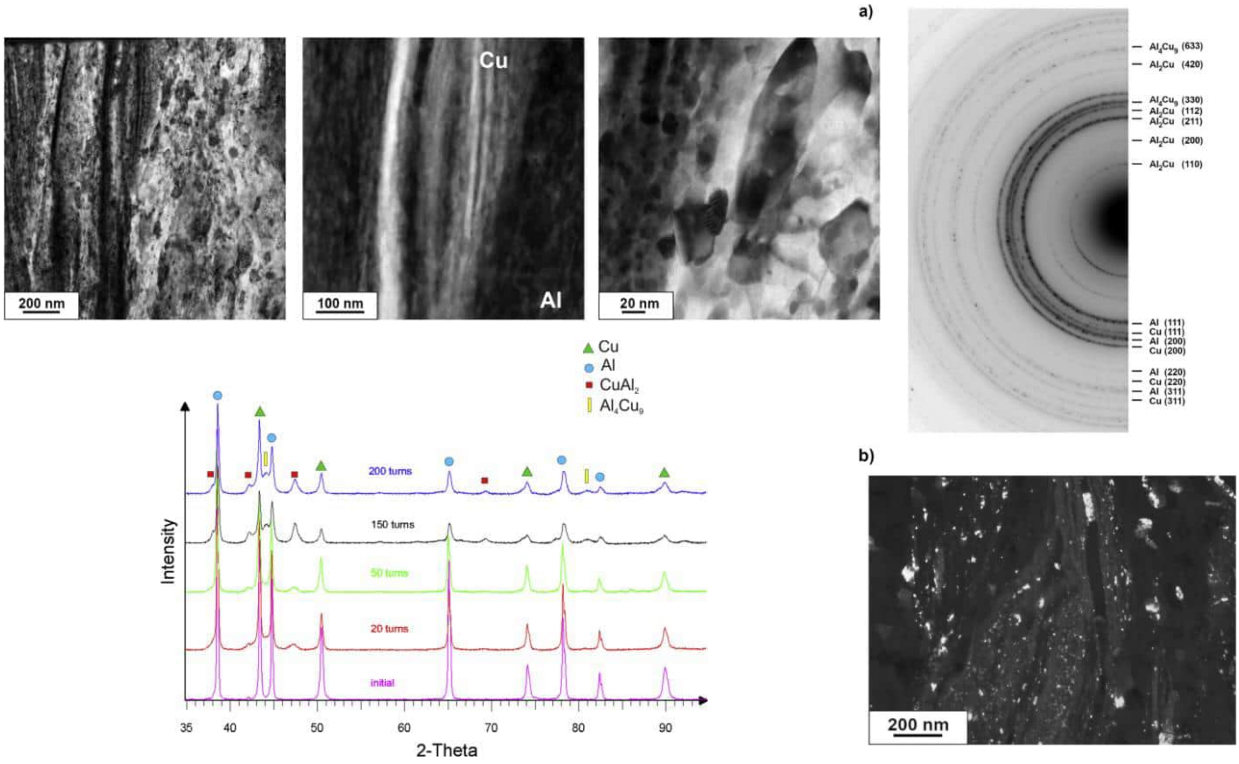

***Rys.* 10** *Obrazy STEM wykonane na krawędzi dysku po 200 obrotach HPT przedstawiają: (a) ogólny widok struktury lamelarnej, (b) obraz HAADF ukazujący rozkład pierwiastków Al i Cu w tej strukturze lamelarnej, (c) obraz w dużym powiększeniu przedstawiający strukturę bimodalną. Obrazy dyfrakcyjne SAED wykonane na krawędzi dysku po 200 obrotach HPT oraz (b) obraz w ciemnym polu pochodzący z pierścienia Al_2Cu (110). Spektra dyfrakcyjne XRD dla układu Al–Cu–Al w stanie początkowym oraz po obróbce HPT dla 20, 50, 150 i 200 obrotów. [A.8]*

W wytworzonych przeze mnie materiałach hybrydowych zaobserwowano skrajnie wysokie wzrosty twardości i wytrzymałości (Rys.11). Twardość układu Al–Cu po obróbce HPT osiągnęła wartość około 450 Hv po 200 obrotach, co jest wartością znacznie wyższą niż twardość nanokrystalicznego aluminium (ok. 50 Hv) oraz miedzi (ok. 130 Hv). Dodatkowo, po 200 obrotach zaobserwowano wysoką jednorodność strukturalną wzdłuż średnicy dysku, co miało istotny wpływ na rozkład mikrotwardości Vickersa – wartości te były względnie jednorodne w całym przekroju dysku. Wytrzymałość na rozciąganie materiału hybrydowego przekroczyła 900 MPa, co stanowi wartość o rząd wielkości wyższą niż dla gruboziarnistego aluminium (ok. 90 MPa) i ponad trzykrotnie wyższą niż dla gruboziarnistej miedzi (ok. 280 MPa).

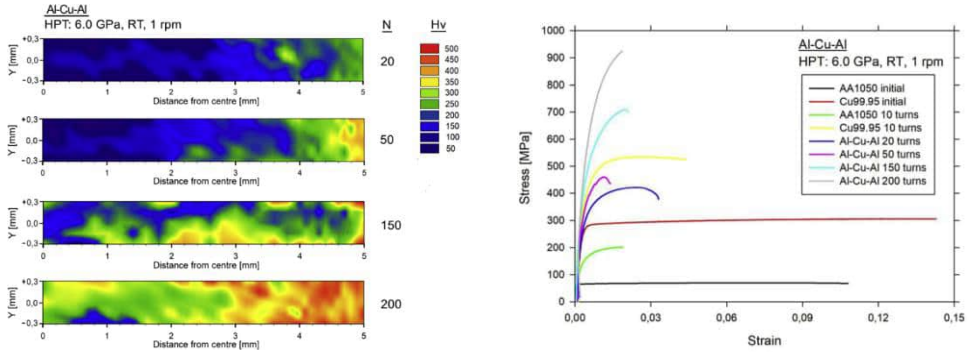

Rys. 11 *Mapy rozkładu mikrotwardości dla układu Al–Cu–Al po obróbce HPT z zastosowaniem 20, 50, 150 i 200 obrotów wraz z krzywymi ze statycznej próby rozciągania mini-próbek dla stopów Al-1050 i Cu 99,95% w stanie początkowym oraz po obróbce HPT, wraz z krzywymi dla układu Al–Cu–Al po 20, 50, 150 i 200 obrotach. [A.8]*

Na podstawie uzyskanych wyników wykazałem, że w układach hybrydowych otrzymanych metodą HPT, ogólna wytrzymałość materiału nie jest determinowana wyłącznie przez **rozdrobnienie ziarna zgodnie z zależnością Halla-Petcha** [9,10], lecz wynika także z kombinacji różnych mechanizmów umacniania, takich jak umocnienie roztworowe oraz umacnianie przez **twarde fazy międzymetaliczne** [43].

Zastosowanie efektu mieszania mechanicznego przy użyciu techniki HPT było przedmiotem współpracy jaką nawiązałem z dr Jiaoyan Dai z Ningbo University of Technology (Chiny), którą poznałem podczas mojego stażu na University of Southampton w 2018 roku. W ramach wspólnej pracy zajęliśmy się zagadnieniem syntezy niemieszalnych układów metalicznych z układu Cu–Ta, wykorzystując podejście opracowane wcześniej wraz z prof. Langdonem w badaniach nad metalicznymi materiałami hybrydowymi [artykuł **A.9**].

Wyniki przeprowadzonych badań strukturalnych wykazały wyraźne różnice w mikrostrukturze w zależności od liczby obrotów zastosowanych w procesie HPT. Już po 5 obrotach obserwowano początek fragmentacji tantalowych blaszek. Powyżej 100 obrotów fragmentacja i intensywne mieszanie były na tyle zaawansowane, że w mikroskopii optycznej nie było możliwe rozróżnienie poszczególnych komponentów układu.

Badania przeprowadzone przeze mnie z użyciem skaningowej mikroskopii elektronowej wykazały (Rys. 12), że zarówno w centralnej części dysków, jak i przy ich krawędziach, obecna jest wyraźna struktura warstwowa. W zewnętrznych częściach dysków mikrostruktura była drobniejsza, a warstwy przyjmowały pofalowany kształt, często tworząc wirujące układy charakterystyczne dla hybrydowych układów. W części centralnej natomiast warstwy były niemal prostoliniowe i równoległe. Zjawisko to przypisano gradientowi odkształcenia powstającemu podczas procesu HPT – intensywność odkształcenia rośnie w kierunku od środka ku krawędzi dysku.

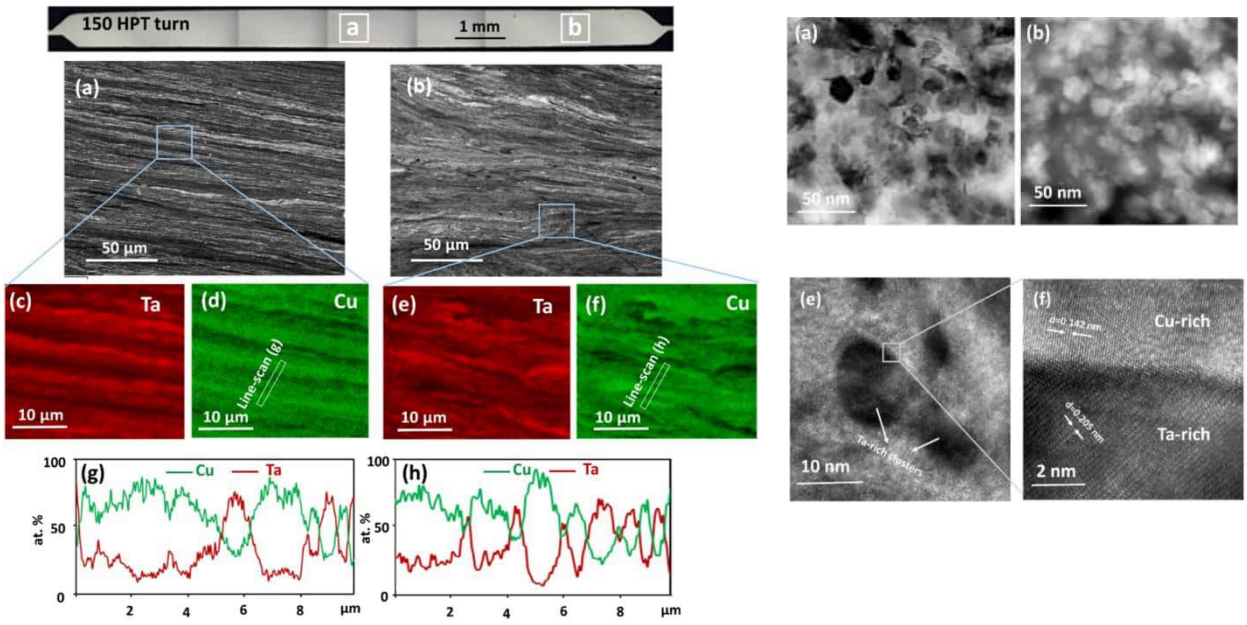

Rys. 12 *Obrazy SEM przekroju poprzecznego próbki po 150 obrotach wraz z mapami rozkładu pierwiastków Cu i Ta i liniowymi analizami, oraz obrazami STEM, HAADF i tymi o rozdzielczości atomowej przedstawiający interfejs pomiędzy obszarem bogatym w Ta i osnową bogatą w Cu. [A.9]*

Badania SEM zostały uzupełnione o obserwacje wykonane za pomocą mikroskopii TEM/STEM. Na podstawie przeprowadzonych przeze mnie analiz strukturalnych metodą STEM stwierdzono, że mikrostruktura we wszystkich badanych obszarach składa się z osnowy

bogatej w miedź, w której rozmieszczone są obszary bogate w tantal. Dodatkowo, wielkość ziarna w tym niemieszalnym układzie mieściła się w zakresie od 20 do 200 nm.

Wykonane przeze mnie obserwacje w dużym powiększeniu (Rys. 12), wykazują obecność bardzo drobnych ziaren i skupisk tantalu w osnowie Cu, o rozmiarach rzędu ∼5–10 nm. Obrazy STEM w rozdzielczości atomowej, ukazujące granice międzyfazowe, bez oznak porowatości czy mikropęknięć.

Wytworzony układ charakteryzował się unikalnymi właściwościami mechanicznymi. Pomiary wykazały, że po 150 obrotach HPT mikrotwardość była niemal jednorodna w całej średnicy dysku, a jej średnia wartość wynosiła około 350 Hv. Dla porównania, czysta miedź o rozmiarze ziarna ∼300 nm wykazuje twardość na poziomie jedynie ∼100 Hv [26].

Wytrzymałość na rozciąganie badanego układu osiągała niemal **1300 MPa** przy zachowaniu znacznego **wydłużenia rzędu 40%.** Dane literaturowe pokazują, że wytrzymałość czystego tantalu i czystej miedzi po obróbce metodą HPT wynosi odpowiednio ∼1300 MPa [44] i ∼460 MPa [45], co oznacza, że wytrzymałość wytworzonego przez nas układu hybrydowego Cu–Ta jest porównywalna z tą uzyskiwaną dla czystego nanokrystalicznego tantalu. Warto podkreślić, że zarówno dla czystego Cu, jak i Ta po procesie HPT wydłużenie do zerwania nigdy nie przekraczało 4%. Oznacza to, że w wytworzonym przez nas niemieszalnym systemie inne mechanizmy się odpowiedzialne za plastyczność układu. Postulowanym mechanizmem jest poślizg po granicach Cu–Ta, których charakter sprzyja przenoszeniu naprężeń oraz inicjacji dyslokacji. Zjawiska te mogą prowadzić finalnie przy większych nieprężeniach do poślizgu wzdłuż granic ziaren, a w efekcie – do znacznego zwiększenia wydłużenia do zerwania.

Pomimo że w opisywanym artykule byłem głównie odpowiedzialny za badania strukturalne, nawiązana współpraca pozwoliła mi na znaczące pogłębienie wiedzy na temat układów niemieszalnych oraz otworzyła nową perspektywę w zakresie ich syntezy techniką HPT. Bezpośrednim efektem tych działań było przygotowanie wniosku projektowego w konkursie OPUS 27 pt.: *„Synteza metodą skręcania pod wysokim ciśnieniem niemieszalnych układów wykazujących unikalne właściwości fizyczne i mechaniczne”,* który uzyskał finansowanie i którego realizację rozpoczynam (rok 2025). W ramach projektu planuję prowadzenie badań nad mechanizmami syntezy różnych układów niemieszalnych na bazie miedzi, co pozwoli na dalsze pogłębienie wiedzy o ich mikrostrukturze, właściwościach oraz potencjale aplikacyjnym.

Wyniki zamieszczone w pracach [**A.6-A.9**] wykazują, że metoda HPT ma duży potencjał do wytwarzania hybrydowych materiałów metalicznych i kształtowania ich

właściwości mechanicznych poprzez odpowiednie dobranie architektury układów i parametrów procesu.

4.3.4. Podsumowanie

Na podstawie analizy wyników badań przedstawionych w przedłożonym cyklu „**Nowoczesne nanomateriały o podwyższonej wytrzymałości kształtowane techniką skręcenia pod wysokim ciśnieniem (HPT- high pressure torsion)”** sformułowałem następujące wnioski:

Wnioski ogólne

- *Skręcanie pod wysokim ciśnieniem jako efektywna metoda syntezy nanokompozytów*.
  HPT umożliwia intensywną deformację plastyczną prowadzącą do znacznego rozdrobnienia ziarna oraz jednorodnego rozmieszczenia faz wzmacniających w osnowie metalicznej. W badanych systemach na bazie Al i Cu, proces ten skutkował wytworzeniem stabilnej nanokrystalicznej struktury. Nanododatki w istotny sposób ograniczają mobilność dyslokacji oraz hamują procesy dynamicznego zdrowienia i rekrystalizacji, w efekcie intensyfikując procesy rozdrobnienia strukturalnego przesuwając okno nasycenia struktury w kierunku mniejszych rozmiarów ziaren. HPT wykazuje więc duży potencjał w inżynierii materiałowej, szczególnie w zastosowaniach wymagających ultrawytrzymałych struktur.

- *Wpływ dodatków węglowych (grafen, GO, rGO, CNT) na właściwości kompozytów metalicznych*
  Dodatek nanostrukturalnych form węgla, takich jak grafen, tlenek grafenu czy nanorurki węglowe, w znaczący sposób wpływa na poprawę wytrzymałości, twardości oraz stabilności cieplnej takich nanomateriałów. Dowiodłem, że kluczowym czynnikiem jest równomierne rozmieszczenie nanododatków, możliwe dzięki intensywnej deformacji HPT. Ponadto, nanododatki węglowe poprawiają stabilność strukturalną w podwyższonych temperaturach, czyniąc takie kompozyty atrakcyjnymi dla zastosowań w ekstremalnych warunkach eksploatacyjnych. Wykazałem, że zastosowanie odpowiednich nanonapełniaczy istotnie zwiększa stabilność cieplną wytworzonych nanostruktur do poziomu nawet 600°C.

- *Zastosowanie techniki HPT do wytwarzania hybrydowych materiałów*

  Wykazałem, że nowa koncepcja zastosowania techniki HPT umożliwia wytwarzanie hybrydowych materiałów metalicznych z układów Al-Ti, Al-Cu i Cu-Ta. Co ważniejsze powstała struktura zależy od wielu czynników, jak: architektura układu czy parametry procesu. Struktury te wykazują synergiczne właściwości wynikające z obecności twardych faz międzymetalicznych oraz nanokrystalicznej osnowy, co skutkuje zwiększeniem twardości i wytrzymałości.

Wnioski szczegółowe

- *Synteza nanokompozytów Al–grafen*

  Synteza kompozytów Al z grafenem techniką HPT pozwoliła na równomierne rozmieszczenie grafenu w całej objętości materiału. Badania wykazały, że już niewielki dodatek (5% wag.) prowadzi do znacznego wzrostu twardości i zmniejszenia wielkości ziarna poniżej 100 nm. Dzięki temu kompozyt wykazuje lepszą wytrzymałość, a dodatek grafenu w pozytywny sposób wpływa na przewodność elektryczną takich kompozytów.
- *Bezpośrednia synteza techniką HPT kompozytów Al–nanorurki węglowe*

  Nowatorska metoda bezpośredniej syntezy kompozytów Al z nanorurkami węglowymi za pomocą HPT pozwoliła na uzyskanie jednorodnej mikrostruktury i znaczną poprawę właściwości mechanicznych w porównaniu do tradycyjnych materiałów. Na rozdrobnienie struktury w kompozytach aluminiowych wzmacnianych nanorurkami węglowymi w istoty sposób będzie wpływało zarówno udział objętościowy nanododatków jak i czystość użytego stopu.
- *Wpływ połączenia techniki SPS i HPT na strukturę kompozytu Cu–SiC*

  Wykorzystanie techniki HPT pozwala na wyeliminowanie wad kompozytów po procesie SPS. W przypadku kompozytów Cu–SiC technika HPT prowadzi do likwodacji porowatości i delaminacji pomiędzy osnową, a wzmocnieniem. Dodatkowo struktura ulega ujednorodnieniu, a duże cząstki SiC fragmentacji na mniejsze nawet nanometrycznej wielkości co ma pozytywny wpływ na właściwości mechanicznych i przewodność cieplną materiału.
- *Kompozyty na bazie miedzi wzmacniane nowoczesnymi nanododatkami*

  Rodzaj nanonapełniacza i jego rozmieszczenie w osnowie miedzianej ma znaczący wpływ na mikrostrukturę, właściwości mechaniczne i stabilność cieplną kompozytu. Analiza mikrostruktury pod względem wielkości ziarna wykazała, że największą różnicę

przypisuje się obecności nanonapełniaczy, ponieważ w czystej miedzi bez dodatków minimalna wielkość ziarna możliwa do uzyskania była rzędu ~210 nm, podczas gdy kompozyty Cu-GO, Cu-Al_2O_3 i Cu-rGO/Al_2O_3 miały odpowiednio wielkość ziarna ~55 nm, ~65 nm i ~75 nm. Dodatek tlenku grafenu w miedzi pozwala nie tylko na poprawę właściwości mechanicznych, ale też stabilności cieplnej. GO, dzięki obecności grup funkcyjnych, lepiej integruje się z osnową miedzianą. Kompozyty te wykazują też mniejsze ziarna oraz większą twardość w porównaniu do czystej miedzi po procesie HPT. Ponadto wszystkie kompozyty wykazywały również zwiększoną stabilność cieplną, przekraczającą ponad dwukrotnie tą dla miedzianej osnowy bez nanonapełniaczy.

- *Materiały hybrydowe z układu Al–Ti i Al-Cu*

  Zastosowanie HPT do tworzenia hybrydowych materiałów Al–Ti skutkuje powstawaniem struktur warstwowych bogatych w fazy międzymetaliczne, co przekłada się na wyjątkowe właściwości mechaniczne tych materiałów. Proces HPT tych bimetalicznych układów prowadzi do znacznego rozdrobnienia ziarna nawet do rozmiarów ~10–20 nm. Ponadto synteza mechaniczna prowadzi do powstawania twardych faz międzymetalicznych Al_2Cu, Al_4Cu_9, AlTi, Al_3Ti i $AlTi_3$. W rezultacie dochodzi do połączenia mechanizmu halla-Petcha i powstawania twardych faz międzymetalicznych, co prowadzi do uzyskania niespotykanej twardości i wytrzymałości tych systemów. W niektórych przypadkach właściwości te są o niemal rząd wielkości wyższe niż te dla materiałów wyjściowych

- *Synteza nanokrystalicznych systemów niemieszalnych Cu-Ta*

  Technika HPT umożliwia skuteczne wytworzenie systemów niemieszalnych Cu-Ta o nanokrystalicznej strukturze. W wyniku odkształcania w systemie Cu-Ta powstają silne naprężenia sprzyjające intensywnej fragmentacji tantalu. Cząstki tantalu intensyfikują procesy rozdrobnienia struktury (pinning effect). W rezultacie wielkość ziarna w miedzianej osnowie wynosi 35–45 nm, natomiast tantal tworzy równomiernie rozmieszczone w osnowie klastry o wielkości cząstek ~10 nm. Tak silne rozdrobnienie struktury skutkuje znacznym wzrostem twardości (300 Hv) i wytrzymałości na rozciąganie (1300 MPa) i jednoczesnym zachowaniu niespotykanie wysokiego jak na nanokrystaliczne metale wydłużenia do zerwania, rzędu 40%.

4.4. Wkład w rozwój dyscypliny

Przedstawiony do oceny cykl publikacji zawiera oryginalne wyniki i opisuje wykorzystanie techniki HPT do projektowania struktury i syntezy nowoczesnych nanokompozytów, układów hybrydowych i systemów niemieszalnych.

W toku badań **wykazałem, że zastosowanie HPT umożliwia otrzymywanie kompozytów i materiałów hybrydowych** o strukturach niedostępnych tradycyjnymi metodami — w tym jednorodnych nanostruktur w układach o ograniczonej mieszalności (np. Cu–Ta), przesyconych roztworów stałych oraz regularnych struktur warstwowych zawierających fazy międzymetaliczne (np. Al–Ti, Al–Cu). Istotnym elementem mojego wkładu jest udowodnienie, że mechanizmy dyfuzji w stanie stałym, zachodzące podczas intensywnej deformacji, umożliwiają syntezę faz międzymetalicznych już w temperaturze pokojowej.

Szczególną uwagę poświęciłem badaniom nad kompozytami z dodatkami nanostrukturalnych form węgla (grafen, tlenek grafenu, nanorurki węglowe), które wprowadzane do osnowy Al i Cu znacząco poprawiają właściwości mechaniczne, termiczne i elektryczne materiałów. Opracowana przeze mnie metoda integracji nanododatków z metaliczną osnową przy użyciu HPT pozwala uniknąć aglomeracji i prowadzi do jednorodnego rozmieszczenia faz wzmacniających, co zostało potwierdzone licznymi analizami mikrostrukturalnymi (SEM, TEM, EBSD).

Wkład mojej działalności naukowej w rozwój dyscypliny inżynieria materiałowa można podsumować w trzech kluczowych obszarach:

1. **Dowiodłem, że poprzez zastosowanie nanododatków do wytworzenia nanokompozytów bądź też właściwe projektowanie architektury hybrydowych układów możliwe jest osiągnięcie wyższego stopnia rozdrobnienia struktury, przesuwając efekt nasycenia w kierunku mniejszych rozmiarów ziaren**. Efekt ten może być na tyle intensywny, że w niektórych układach minimalna wielkość ziarna była nawet o rząd wielkości mniejsza niż w przypadku czystych metali po procesie HPT. Zjawisko to wynika z obecności twardych nanocząstek lub formowania się faz międzymetalicznych, które ograniczają mobilność dyslokacji oraz hamują procesy dynamicznego zdrowienia i rekrystalizacji, co z kolei intensyfikuje mechanizmy rozdrobnienia i umożliwia dalsze przesuwanie granic nasycenia struktury ku mniejszym wymiarom ziaren. Wykazałem, że ma to znaczący wpływ na zwiększenie twardości i wytrzymałości takich materiałów.

2. **Zaprezentowane przeze mnie podejście do syntezy materiałów hybrydowych było innowacyjne na tle dotychczasowych prac, ponieważ wykraczało poza klasyczne zastosowania techniki HPT (głównie do jedno- lub dwuskładnikowych materiałów jednorodnych) i otworzyło nowe możliwości syntezy materiałów o złożonej architekturze z układu Al-Ti, Al-Cu czy Cu-Ta.** W szczególności skoncentrowałem się na zależności pomiędzy architekturą układu (liczbą i grubością warstw, ich kolejnością), parametrami procesu HPT (ciśnienie, liczba obrotów), a efektywnością procesu łączenia i właściwościami mechanicznymi otrzymanych materiałów hybrydowych. Mechaniczna synteza wieloskładnikowych układów z wykorzystaniem techniki HPT prowadziła nie tylko do intensywnego rozdrobnienia ziarna, lecz również do powstawania twardych faz międzymetalicznych. Dodatkowo, moje badania strukturalne wykazały, że mechaniczna synteza z użyciem HPT umożliwia formowanie układów dotąd uznawanych za niemieszalne.

3. **Wykazałem, że zastosowanie nanododatków w roli fazy wzmacniającej istotnie zwiększa stabilność cieplną kompozytów metalicznych.** Kluczowe w tym kontekście okazało się równomierne rozmieszczenie nanonapełniaczy w osnowie. W swoich badaniach udowodniłem, że istnieje szereg czynników strukturalnych i technologicznych, które determinują poziom ujednorodnienia struktury. Na pierwszym planie znajduje się typ zastosowanego napełniacza oraz czystość osnowy metalowej. Zbyt sztywne cząstki (np. rGO/Al_2O_3) lub mniejsza czystość osnowy (np. CNTs w Al 99,5%) prowadzą do tworzenia większej gęstości aglomeratów, co skutkuje obniżeniem stabilności cieplnej kompozytu. Kluczowym czynnikiem wpływających na jednorodne rozmieszczenie nanonapełniacza jest skumulowane odkształcenie plastyczne w metodzie HPT, zależne od liczby obrotów w procesie. Ponadto dowiodłem, że różne typy nanonapełniaczy w odmienny sposób reagują z osnową podczas wyżarzania. Stabilne nanocząstki, takie jak ceramiki czy stabilizowane rGO/Al_2O_3, nie wchodzą w reakcje z osnową miedzianą w trakcie wygrzewania. Natomiast materiały zawierające grupy tlenowe, jak GO, mogą reagować z osnową, ulegając termicznemu rozpadowi i tworząc charakterystyczną strukturę typu core-shell. Mimo tych przemian, struktura ta nadal skutecznie stabilizuje kompozyt w warunkach podwyższonej temperatury.

4.5.Inne osiągnięcia

Oprócz przedstawionego cyklu publikacji wskazanego jako osiągnięcie, posiadam również inne osiągnięcia przedstawione w załączniku 7. W swojej karierze szczególną uwagę położyłem na współpracę z zagranicznymi naukowcami zajmującymi się technikami SPD, wytwarzając i charakteryzując liczne materiały metaliczne wytworzone tymi technikami. W rezultacie jestem autorem bądź współautorem **29** publikacji związanych tematycznie z technikami **SPD,** opublikowanych w międzynarodowych czasopismach naukowych (w tym wykluczając publikacje wskazane do osiągnięcia, 13 po uzyskaniu stopnia doktora).

Wśród nich na szczególną uwagę zasługuje wątek badawczy dotyczący wykorzystania techniki HPT do wytwarzania hybrydowych materiałów z układu Mg/Mg (AZ31/MgGd). Zagadnienie to było przedmiotem współpracy, jaką nawiązałem z Prof. Azzeddine Hiba (Universytet Mohamed Boudiaf, M'sila w Algierii) podczas mojego stażu naukowego w zespole Prof. Langdona na Uniwersytecie Southampton (2019). Przeprowadzone badania wykazały poprawę takich właściwości jak podatność na rozdrobnienie struktury, lepszą formowalność w niskich temperaturach oraz zwiększoną wytrzymałość i odporność na pełzanie w podwyższonych temperaturach. Ponadto odpowiednia obróbka cieplna takich stopów może prowadzić do powstania w stopie wydzieleń bogatych w pierwiastki ziem rzadkich, które wykazują efekt stabilizacji struktury w podwyższonych temperaturach, hamując procesy rekrystalizacji i rozrost ziarna. Efektem tej współpracy jest cykl czterech publikacji opisujących strukturę, właściwości mechaniczne i procesy rekrystalizacji tych materiałów:

- Ould Mohamed Ouarda, **Bazarnik Piotr**, Huang Yi, Azzeddine Hiba, Baudin Thierry, Brisset François, Langdon Terence G.; "A Comparative Study Between AZ31 and Mg-Gd Alloys After High-Pressure Torsion", Journal of Materials Engineering and Performance 33 (2024) 2860 - 2874 https://doi.org/10.1007/s11665-023-08856-8 IF-2024 – 2.52, punkty MNiSW – 70,
- Ould Mohamed Ouarda, Azzeddine Hiba, Huang Yi, Baudin Thierry, **Bazarnik Piotr**, Brisset François, Kawasaki Megumi, Langdon Terence G.; "Investigation of Microstructure and Texture Evolution in an AZ31/Mg–Gd Alloy Hybrid Metal Fabricated by High-Pressure Torsion", Advanced Engineering Materials, 2023, 25(11), 2201794 https://doi.org/10.1002/adem.202201794 IF-2023 – 3.6, punkty MNiSW – 100,
- Ould Mohamed Ouarda, **Bazarnik Piotr**, Huang Yi, Azzeddine Hiba, Baudin Thierry, Brisset François, Kawasaki Megumi, Langdon Terence G.; "Primary recrystallization of

a magnesium hybrid material fabricated by high-pressure torsion", Materials Today Communications, 38 (2024) 108305 https://doi.org/10.1016/j.mtcomm.2024.108305 IF-2024 – 1.859, punkty MNiSW – 70,

- Azzeddine Hiba, Avettand-Fènoël Marie-Noëlle, **Bazarnik Piotr**, Baudin Thierry, Huang Yi, Langdon Terence G.; "Recrystallization and grain growth activation energies in a hybrid magnesium material fabricated by high-pressure torsion", Thermochimica Acta, 738 (2024) 179805, https://doi.org/10.1016/j.tca.2024.179805 IF-2024 – 3.1, punkty MNiSW – 100

W przedstawionych pracach byłem odpowiedzialny za badania strukturalne zarówno materiałów wyjściowych, jak i wytworzonych materiałów hybrydowych oraz ocenę stabilności tych struktur w podwyższonej temperaturze. W prowadzonych analizach zastosowałem szeroki wachlarz technik, takich jak SEM, STEM i EDX, aby wykazać, w jaki sposób dodatek metali ziem rzadkich, a także obecność pierwiastków stopowych (takich jak Al, Mn czy Zn), wpływa na podatność stopów magnezu na odkształcenie plastyczne metodą HPT.

Udowodniłem, że obecność gadolinu w roztworze stałym sprzyja intensyfikacji rozdrabniania mikrostruktury, ograniczając mobilność dyslokacji oraz hamując procesy dynamicznego zdrowienia i rekrystalizacji. Dodatkowo, podczas badań stabilności cieplnej, zaobserwowałem, że w strefach wzbogaconych w gadolin pierwszym etapem wygrzewania było zarodkowanie wydzieleń bogatych w ten pierwiastek na granicach ziaren, co skutecznie hamowało rozrost ziarna. Natomiast w przypadku stopu AZ31, gdzie dominowały wydzielenia $Mg_{17}Al_{12}$, Mg_2Zn oraz Al_8Mn_5, efekt ograniczania rozrostu ziaren w podwyższonej temperaturze był znacznie słabszy.

Ważnym osiągnięciem w mojej dotychczasowej karierze naukowej było określenie wpływu nanostrukturyzacji na właściwości stopu aluminium z serii 5xxx domieszkowanego skandem. Tematyka ta była przedmiotem współpracy z dr. Pedro Henrique R. Pereirą z Uniwersytetu Federal de Minas Gerais (Brazylia), nawiązanej podczas mojego stażu naukowego w zespole prof. Langdona na Uniwersytecie w Southampton. Próbki stopu Al–3Mg–0,2Sc poddano intensywnej obróbce plastycznej metodą HPT, realizowanej w dwóch temperaturach: pokojowej (~25°C) oraz podwyższonej (175°C). Wyniki badań wykazały, że oba warianty materiału wykazywały zdolność do intensywnego odkształcenia nadplastycznego, jednak próbki przetworzone w temperaturze 175°C cechowały się znacznie wyższym wydłużeniem względnym – 1880% w porównaniu do 850% uzyskanych dla materiału formowanego w temperaturze 25°C.

Celem moich badań było zidentyfikowanie mikrostrukturalnych czynników odpowiedzialnych za to zróżnicowanie właściwości nadplastycznych. Analiza mikrostruktury wykazała, że średnia wielkość ziarna w obu przypadkach była porównywalna i wynosiła odpowiednio 140 nm dla obróbki w 25°C oraz 150 nm dla HPT w 175°C. Istotne różnice zaobserwowano jednak w morfologii ziaren: po przetwarzaniu w temperaturze pokojowej ziarna miały wydłużony kształt, natomiast po obróbce w 175°C były równoosiowe. Kluczowym wnioskiem płynącym z badań było stwierdzenie, że w wyniku formowania w wyższej temperaturze w strukturze materiału pojawiają się drobne, stabilne wydzielenia fazy Al_3Sc, które skutecznie hamują rozrost ziaren podczas testów w warunkach nadplastycznych. Obecność tych wydzieleń przyczyniała się do zwiększenia stabilności mikrostrukturalnej oraz umożliwiała bardziej intensywną deformację, co tłumaczy wyraźnie wyższy poziom nadplastyczności uzyskany dla materiału obrabianego w temperaturze 175°C. Wyniki przeprowadzonych w tym zakresie badań zawarte są w dwóch publikacjach:

- Pereira Pedro Henrique R., **Bazarnik Piotr**, Huang Yi, Lewandowska Malgorzata, Langdon Terence G., „The role of processing temperature for achieving superplastic properties in an Al-3Mg-0.2Sc alloy processed by high-pressure torsion” Materials Science and Engineering: A, 916 (2024) 147320. https://doi.org/10.1016/j.msea.2024.147320 IF-2024 – 6.8, punkty MNiSW – 140

- Pereira Pedro Henrique R., **Bazarnik Piotr**, Huang Yi, Lewandowska Malgorzata, Langdon Terence G., „Flow behaviour and microstructural stability in an Al–3Mg-0.2Sc alloy processed by high-pressure torsion at different temperatures”, Materials Science and Engineering: A 887 (2023) 145766. https://doi.org/10.1016/j.msea.2023.145766 IF-2023 – 6.4, punkty MNiSW – 140

5. Informacja o wykazywaniu się istotną aktywnością naukową albo artystyczną realizowaną w więcej niż jednej uczelni, instytucji naukowej lub instytucji kultury, w szczególności zagranicznej.

Efektem mojej dotychczasowej działalności naukowej jest **69** publikacji (54 po uzyskaniu stopnia doktora) w międzynarodowych czasopismach w zdecydowanej większości (**65**) z listy JCR, z czego **73%** z nich zostało opublikowanych w czasopismach z **TOP25%** (dane ze Scopus). **57%** wszystkich moich publikacji było realizowanych we współpracy z zagranicznymi jednostkami naukowymi (dane ze Scopus).

Po uzyskaniu stopnia doktora brałem udział w 13 konferencjach krajowych i międzynarodowych, podczas których wygłosiłem 9 referatów i zaprezentowałem 4 postery.

Byłem lub jestem kierownikiem 5 projektów finansowanych przez NCN (Preludium, Etiuda, Sonatina, 2x Opus) i 3 grantów badawczych finansowanych z subwencji Politechniki Warszawskiej, a także brałem udział w realizacji na Wydziale Inżynierii Materiałowej ponad 20 innych projektów finansowanych przez NCN i NCBR.

W mojej pracy kładę szczególny nacisk na systematyczne pogłębianie mojej wiedzy z zakresu mikroskopii elektronowej, zarówno w wymiarze teoretycznym, jak i praktycznym. Stale doskonalę umiejętność doboru odpowiednich technik badawczych do analizowanych materiałów, interpretacji uzyskanych wyników oraz rozwijania własnych kompetencji w pracy z zaawansowaną aparaturą badawczą. Samodzielnie wykorzystuję szereg mikroskopów elektronowych dostępnych na Wydziale Inżynierii Materiałowej Politechniki Warszawskiej, w tym m.in.:

- skaningowy transmisyjny mikroskop (STEM) Thermo Fisher SPECTRA 200 wyposażony w detektor EDX Super-X
- skaningowy transmisyjny mikroskop elektronowy (STEM) firmy Hitachi model HD2700
- skaningowy transmisyjny mikroskop elektronowy (STEM) firmy Hitachi model S 5500
- skaningowy mikroskop elektronowy (SEM) firmy Hitachi model SU 8000,
- skaningowy mikroskop elektronowy (SEM) firmy Hitachi model SU 70,
- mikroskop jonowy (FIB) firmy Hitachi model FB-2100,
- mikroskop jonowy (FIB) firmy Hitachi model NB-5000 nanoDUET, na którym prowadzę szkolenia doktorantów i pracowników.
- transmisyjny mikroskop elektronowy (TEM) firmy Jeol model 1200.

Jestem promotorem pomocniczym mgr inż. Marii Emerli, która w ramach mojego projektu OPUS-19 realizuje rozprawę doktorską, pt.: „Nowoczesne materiały kompozytowe na bazie miedzi kształtowane techniką skręcania pod wysokim ciśnieniem" (obrona przewidywana na początek roku 2026).

Swoją działalność naukową realizuję w swojej macierzystej jednostce – Politechnice Warszawskiej oraz w ramach staży zagranicznych. Już podczas studiów doktoranckich, które realizowałem na Wydziale Inżynierii Materiałowej Politechniki Warszawskiej odbyłem **trzy-miesięczny** (09-11 2014) staż naukowy na **Uniwersytecie Southampton** w Anglii w ramach Programu Rozwojowego Politechniki Warszawskiej CAS 29. Staż odbyłem pod opieką **Prof. Terence'a G. Langdona**, który jest wybitnym przedstawicielem środowiska skupionego wokół technik SPD. Podczas tego stażu przeprowadzałem eksperymenty z wykorzystaniem technik HPT i ECAP, wykonywałem pomiary mikrotwardości i badania wytrzymałości. W efekcie udało mi się nawiązać ścisłą współpracę z grupą Prof. Langdona, która trwa do dzisiaj i skutkowała powstaniem licznych artykułów naukowych (w tym miejscu wymieniam tylko te nie wymienione wcześniej):

- **Piotr Bazarnik**, Barbara Romelczyk, Yi Huang, Małgorzata Lewandowska, Terence G. Langdon, Effect of applied pressure on microstructure development and homogeneity in an aluminium alloy processed by high-pressure torsion, J. Alloy. Comp. 688 (2016) 736-745
- **Piotr Bazarnik**, Yi Huang, Małgorzata Lewandowska, Terence G. Langdon, Structural impact on the Hall–Petch relationship in an Al–5Mg alloy processed by high-pressure torsion, Mater. Sci. Eng. A 626 (2015) 9-15
- Katarzyna Sharman, **Piotr Bazarnik**, Tomasz Brynk, Asli Gunay Bulutsuz, Malgorzata Lewandowska, Yi Huang, Terence G. Langdon, Enhancement in mechanical properties of a β-titanium alloy by high-pressure torsion, J. Mater. Res. Tech. 4 (2015) 79-83
- Saad A. Alsubaie, **Piotr Bazarnik**, Yi Huang, Małgorzata Lewandowska, Terence G. Langdon, Evolution of microstructure and hardness in an AZ80 magnesium alloy processed by high-pressure torsion, J. Mater. Res. Tech. 5 (2016) 152-158
- **Piotr Bazarnik**, Yi Huang, Małgorzata Lewandowska, Terence G. Langdon, Enhanced grain refinement and microhardness by hybrid processing using hydrostatic extrusion and high-pressure torsion, Mater. Sci. Eng. A 712 (2018) 513-520
- Hsuan-Kai Lin, Guan Yuan Li, Sarah Mortier, **Piotr Bazarnik**, Yi Huang, Malgorzata Lewandowska, Terence G. Langdon, Processing of CP-Ti by high-pressure torsion and the

effect of surface modification using a post-HPT laser treatment, J. Alloy. Comp. 784 (2019) 653-659

- Hsuan-Kai Lin, Yi-Hong Cheng, Guan Yuan Li, Ying-Chi Chen, **Piotr Bazarnik**, Jessica Muzy, Yi Huang, Terence G. Langdon, Study on the Surface Modification of Nanostructured Ti Alloys and Coarse-Grained Ti Alloys, Metals 12 (2022) 948
- Saad A. Alsubaie, **Piotr Bazarnik**, Yi Huang, Małgorzata Lewandowska, Terence G. Langdon, Achieving Superplastic Elongations in an AZ80 Magnesium Alloy Processed by High-Pressure Torsion, Adv. Eng. Mater. 24 (2022) 2200620

Podczas doktoratu przyznano mi projekt w konkursie ETIUDA organizowanym przez Narodowego Centrum Nauki, w trakcie którego odbyłem **trzy-miesięczny** staż badawczy w **Interdyscyplinarnym Centrum Mikroskopii Elektronowej** (Interdisciplinary Centre for Electron Microscopy - CIME) na L'École Polytechnique Fédérale de Lausanne (Politechnice w Lozannie) w Szwajcarii, w grupie **dr Marco Cantoniego**, gdzie zwiększałem swoje umiejętności z zakresu mikroskopii elektronowej. Zdobyłem doświadczenie w pracy na dedykowanym skaningowo-transmisyjnym mikroskopie elektronowym FEI Tecnai OSIRIS oraz FEI TALOS, a także transmisyjnym mikroskopie elektronowym JEOL 2200FS wyposażonym w system ASTAR do analizy orientacji ziaren i mapowania fazowego z rozdzielczością przestrzenną 2-3 nm. Brałem też udział w pracach na wysokorozdzielczym mikroskopie FEI TITAN, którego obecnie używam na Politechnice Warszawskiej. Prowadziłem liczne badania fluktuacji składu chemicznego w materiałach po procesach SPD i łączeniu wybuchowym. Prowadziłem też badania zmian charakteru granic ziaren (kąta dezorientacji) w zależności od stopnia odkształcenia próbki w metodzie SPD wykorzystując system ASTAR. W efekcie współpracy powstał artykuł:

- **Piotr Bazarnik**, Bogusława Adamczyk-Cieślak, Aleksander Gałka, Bartłomiej Płonka, Lucjan Snieżek, Marco Cantoni, Małgorzata Lewandowska, Mechanical and microstructural characteristics of Ti6Al4V/AA2519 and Ti6Al4V/AA1050/AA2519 laminates manufactured by explosive welding, Mater. Des. 111 (2016) 146 – 157

Bezpośrednio po obronie doktoratu przyznano mi projekt SONATINA (UMO-2017/24/C/ST8/00145), w ramach którego ponownie wyjechałem na **Uniwersytet Southampton** w Anglii, gdzie odbyłem: **dwu-miesięczny** (02-03. 2018) i **miesięczny** (08. 2019) staż naukowy w **grupie Prof. Langdona**. W ramach staży opracowywałem i wytwarzałem przy użyciu techniki HPT nowe typy hybrydowych i kompozytowych

nanokrystalicznych materiałów o dużej wytrzymałości. W ramach współpracy opracowaliśmy nowe klasy materiałów: nanokrystaliczne aluminium wzmocnione grafenem i nanorurkami węglowymi oraz nanokrystaliczne układy wielowarstwowe/hybrydowe: Al-Ti, Cu-Ta, Al-Cu. Efektem moich działań był udział w 5 konferencjach międzynarodowych oraz opublikowanie licznych artykułów naukowych wchodzących w skład opisywanego w punkcie 4.1 osiągnięcia.

6. Informacja o osiągnięciach dydaktycznych, organizacyjnych oraz popularyzujących naukę lub sztukę.

6.1. Osiągnięcia dydaktyczne

Równolegle do działalności naukowej prowadzę działalność dydaktyczną adresowaną głównie do słuchaczy studiujących w trybie stacjonarnym zarówno dla I (inżynierskie) jak i II (magisterskie) stopnia kształcenia, ale także w ramach programu studiów anglojęzycznych:

- Po uzyskaniu stopnia doktora nauk technicznych, od 2018 roku prowadzę zajęcia na kierunku Inżynieria Materiałowa realizując ćwiczenia z Laboratorium Podstawy Nauk o Materiałach, laboratorium Mechanizmy Niszczenia Materiałów. Od 2024 prowadzę ćwiczenia z laboratorium Materiały i ich Zastosowanie.
- Od 2020 uczestniczę w realizacji przedmiotu Projekt badawczy - nanomateriały i nanotechnologie, wykonując ze studentami realne obróbki technikami SPD różnych materiałów metalicznych, hybrydowych i kompozytowych, a następnie badając ich strukturę i właściwości mechaniczne.
- Od 2020 roku prowadzę wykłady: Nanomateriały i nanotechnologie oraz dla anglojęzycznych studentów wykłady Nanomaterials and Nanotechnology.
- Jednocześnie w 2020 roku prowadziłem laboratorium Structural Materials Laboratory dla anglojęzycznego kierunku na Wydziale SIMR PW.

Pod moją opieką oraz w ramach prowadzonych przeze mnie projektów zostały zrealizowane lub są realizowane następujące prace inżynierskie i magisterskie:

Promotor prac:

- Jakub Maliszewski, praca magisterska pt.: „Wytwarzanie katalizatorów do reakcji redukcji tlenu stosowanych w ogniwach paliwowych zasilanych kwasem mrówkowym”, 2023

- Paulina Jaskulska, praca magisterska pt. : „Nanodruty InP wytwarzane z wykorzystaniem złota oraz indu jako katalizatora wzrostu – porównanie właściwości”, w trakcie realizacji

Opiekun naukowy:

- Mateusz Mostowy praca inżynierska pt.: „Mikrostruktura i właściwości blach ze stopu aluminium 5483 łączonych wybuchowo” 2016
- Aleksandra Bartkowska praca magisterska pt.: “Fabrication of novel Al-Ti hybrid materials using high-pressure torsion” 2020
- Ewa Moskała praca magisterska pt.: „Wpływ obróbki cieplnej na mikrostrukturę i właściwości złącz tytan-aluminium wytwarzanych metodą łączenia wybuchowego” 2015

Biorę również aktywny udział w pracach Laboratorium Mikroskopii Elektronowej na Wydziale Inżynierii Materiałowej, prowadząc zajęcia ze studentami oraz szkolenia dla doktorantów i pracowników wydziału z zakresu pracy na mikroskopach elektronowych i jonowych: Hitachi Su-70, Hitachi Su-8000, Hitachi FB-2100, Hitachi NB-5000, JEOL 1200, Hitachi HD-2700, SPECTRA 200.

6.2.Osiągnięcia organizacyjne

Od 2022 jestem członkiem Polskiego Towarzystwa Mikroskopii.
Od 2020 roku jestem recenzent Narodowego Centrum Nauki biorąc udział w recenzji projektów w konkursie Miniatura.
Członek Odwoławczej Komisji Dyscyplinarnej ds. Studentów Politechniki Warszawskiej, kadencja 2020-2024 i 2024-2028.
Członek rady dyscypliny naukowej Inżynieria Materiałowa na Politechnice Warszawskiej w kadencji 2020-2024.
Od 2022 Członek wydziałowej komisji do spraw oceny śródokresowej doktorantów

Organizacja konferencji naukowych:

- Członek Komitetu Organizacyjnego XVI Konferencji Mikroskopii Elektronowej, Jachranka, wrzesień 2017.

- Od 2015 roku biorę co roku udział w organizacji międzynarodowej konferencji EMRS Fall Meeting w Warszawie.

7. Oprócz kwestii wymienionych w pkt. 1-6, wnioskodawca może podać inne informacje, ważne z jego punktu widzenia, dotyczące jego kariery zawodowej.

Nagrody i wyróżnienia:

- Laureat stypendium ministra dla wybitnych młodych naukowców, finansowane przez Ministra Nauki i Szkolnictwa Wyższego (załącznik 12)
- W roku 2019 wchodziłem w skład zespołu, który otrzymał Nagrodę zespołową I stopnia Rektora Politechniki Warszawskiej za osiągnięcia naukowe (załącznik 11)
- W roku, 2021 wchodziłem w skład zespołu, który otrzymał Nagrodę zespołową I stopnia Rektora Politechniki Warszawskiej za osiągnięcia naukowe (załącznik 11)
- W roku 2023 wchodziłem w skład zespołu, który otrzymał Nagrodę zespołową I stopnia Rektora Politechniki Warszawskiej za osiągnięcia naukowe (z załącznik 11)
- W roku 2025 wchodziłem w skład zespołu, który otrzymał Nagrodę zespołową I stopnia Rektora Politechniki Warszawskiej za osiągnięcia naukowe (wręczenie dyplomów nastąpiło po złożeniu rozprawy habilitacyjnej)

- Laureat nagrody uczelnianej w konkursie BEST PAPER za publikację artykułu "The fabrication of graphene-reinforced Al-based nanocomposites using high-pressure torsion" w czasopiśmie Acta Materialia (załącznik 11)

Wskaźniki bibliometryczne (stan na dzień 03.09.2025)

Wskaźniki bibliometryczne		
	Wg. Scopus	Wg. Web of Science
Indeks Hirsha bez autocytowań	22	22
Liczba publikacji	70	68
Liczba cytowań	1474	1391
Liczba cytowań bez autocytowań	1368	1283
Liczba publikacji jako pierwszy autor bądź autor korespondencyjny	16	15

Literatura do rozdziału 4

[1] R.Z. Valiev, Y. Estrin, Z. Horita, T.G. Langdon, M.J. Zehetbauer, Y.T. Zhu, Fundamentals of superior properties in bulk NanoSPD materials, Mater. Res. Lett., 4 (2016), pp. 1-21.

[2] A.P. Zhilyaev, T.G. Langdon, Using high-pressure torsion for metal processing: fundamentals and applications, Prog. Mater. Sci., 53 (2008), pp. 893-979

[3] Valiev RZ, Zhilyaev AP, Langdon TG. Bulk nanostructured materials: fundamentals and applications. Hoboken, NJ: Wiley; 2014.

[4] T.G. Langdon, Twenty-five years of ultrafine-grained materials: Achieving exceptional properties through grain refinement, Acta Mater., 61 (2013), pp. 7035-7059

[5] R.Z. Valiev, R.K. Islamgaliev, I.V. Alexandrov, Bulk nanostructured materials from severe plastic deformation, Prog. Mater. Sci., 45 (2000) pp. 103-189

[6] R.Z. Valiev, T.G. Langdon, Principles of equal-channel angular pressing as a processing tool for grain refinement, Prog. Mater. Sci., 51 (2006), pp. 881-981

[7] E.O. Hall, The Deformation and Ageing of Mild Steel: III Discussion of Results, Proc. Phys. Soc. B, 64 (1951), pp. 747-753

[8] N.J. Petch, he Cleavage Strength of Polycrystals, J Iron Steel Inst., 174 (1953), pp. 25-28

[9] P. Bazarnik, Y. Huang, M. Lewandowska, T.G. Langdon, Enhanced grain refinement and microhardness by hybrid processing using hydrostatic extrusion and high-pressure torsion, Mater Sci. Eng. A, 712 (2018), pp. 513-520

[10] P. Bazarnik, Y. Huang, M. Lewandowska, T.G. Langdon, Structural impact on the Hall–Petch relationship in an Al–5Mg alloy processed by high-pressure torsion Mater Sci. Eng. A, 626 (2015), pp. 9-15

[11] M. Kawasaki, H.-J. Lee, B. Ahn, A.P. Zhilyaev, T.G. Langdon, Evolution of hardness in ultrafine-grained metals processed by high-pressure torsion, J. Mater. Res. Tech., 3 (2014), pp. 311–318.

[12] M. Kawasaki, R.B. Figueiredo, T.G. Langdon, An investigation of hardness homogeneity throughout disks processed by high-pressure torsion, Acta Mater. 59, (2011) pp. 308–316.

[13] K.A. Darling, M. Rajagopalan, M. Komarasamy, M.A. Bhatia, B.C. Hornbuckle, R.S. Mishra, K.N. Solanki, Extreme creep resistance in a microstructurally stable nanocrystalline alloy, Nature, 537 (2016), pp. 378-381

[14] R.Z. Valiev, R.K. Islamgaliev, N.F. Kuzmina, Y. Li, T.G. Langdon, Strengthening and grain refinement in an Al-6061 metal matrix composite through intense plastic straining, Scripta Materi. 40 (1999), 117–122

[15] B. D. Long, M. Umemoto, Y. Todaka, R. Othman, H. Zuhailawati, Fabrication of high strength Cu–NbC composite conductor by high pressure torsion, Materials Science and Engineering: A, 528 (2011), 1750-1756.

[16] Y. Xue, B. Jiang, L. Bourgeois, P. Dai, M. Mitome, C. Zhang, M. Yamaguchi, A. Matveev, C. Tang, Y. Bando, K. Tsuchiya, Dmitri Golberg, Aluminum matrix composites reinforced with multi-walled boron nitride nanotubes fabricated by a high-pressure torsion technique, Materials & Design, 88 (2015), 451-460.

[17] R.K. Islamgaliev, F. Chmelik, R. Kuzel, Thermal structure changes in copper and nickel processed by severe plastic deformation, Materials Science and Engineering A, 234–236 (1997) 335-338.

[18] E. Schafler and R. Pippan, Effect of thermal treatment on microstructure in high pressure torsion (HPT) deformed nickel, Materials Science and Engineering A, 387–389 (2004), 799-804.

[19] P. Bazarnik, M. Lewandowska, M. Andrzejczuk, K.J. Kurzydlowski, The strength and thermal stability of Al–5Mg alloys nano-engineered using methods of metal forming, Materials Science and Engineering: A, 556 (2012), 134-139.

[20] N. Lugo, N. Llorca, J.J. Suñol, J.M. Cabrera, Thermal stability of ultrafine grains size of pure copper obtained by equal-channel angular pressing, J. Mater. Sci., 45 (2010), pp. 2264-2273

[21] H. Jiang, Y.T. Zhu, D.P. Butt, I.V. Alexandrov, T.C. Lowe, Microstructural evolution, microhardness and thermal stability of HPT-processed Cu, Mater. Sci. Eng. A, 290 (2000), pp. 128-138

[22] H.R. Peng, M.M. Gong, Y.Z. Chen, F. Liu, Thermal stability of nanocrystalline materials: thermodynamics and kinetics, Int. Mater. Rev., 62 (2017), pp. 303-333

[23] P.A. Manohar, M. Ferry, T. Chandra, Five decades of the Zener Equation, ISIJ Int, 38 (1998), pp. 913-924

[24] N. Wang, Y. Wen, L.Q. Chen, Pinning force from multiple second-phase particles in grain growth, Comput. Mater. Sci., 93 (2014), pp. 81-85,

[25] M. Kawasaki, H.-J. Lee, B. Ahn, A.P. Zhilyaev, T.G. Langdon, Evolution of hardness in ultrafine-grained metals processed by high-pressure torsion, Journal of Materials Research Technology, 3 (2014), 311–318.

[26] N. Ibrahim, M. Peterlechner, F. Emeis, M. Wegner, S.V. Divinski, G. Wilde Mechanical alloying via high-pressure torsion of the immiscible Cu50Ta50 system Mater. Sci. Eng. A, 685 (2017), pp. 19-30

[27] A. Bachmaier, H. Aboulfadl , M. Pfaff , F. Mücklich , C. Motz, Structural evolution and strain induced mixing in Cu–Co composites studied by transmission electron microscopy and atom probe tomography, Mater. Charact. 100, 2015, Pages 178-191

[28] M. Alipour, R. Eslami-Farsani Synthesis and characterization of graphene nanoplatelets reinforced AA7068 matrix nanocomposites produced by liquid metallurgy route, Mater. Sci. Eng., A, 706 (2017), p. 71

[29] J. Wang, Z. Li, G. Fan, H. Pan, Z. Chen, D. Zhang, Reinforcement with graphene nanosheets in aluminum matrix composites, Scripta Mater., 66 (2012), pp. 594-597

[30] S.N. Alam, L. Kumar, Mechanical properties of aluminium based metal matrix composites reinforced with graphite nanoplatelets, Mater. Sci. Eng., A, 667 (2016), pp. 16-32

[31] Y. Ito, K. Edalati, Z. Horita, High-pressure torsion of aluminum with ultrahigh purity (99.9999%) and occurrence of inverse Hall-Petch relationship, Mater. Sci. Eng. A., 679 (2017), pp. 428-434,

[32] P. Jenei, E.Y. Yoon, J. Gubicza, H.S. Kim, J.L. Lábár, T. Ungár, Microstructure and hardness of copper-carbon nanotube composites consolidated by High Pressure Torsion, Mater. Sci. Eng. A., 528 (2011), pp. 4690-4695

[33] S.K. Tiwari, H. Singh, A. Midathada, S. Sharma, U.K. Ravella, Study of Fabrication Processes and Properties of Al-CNT Composites Reinforced by Carbon Nano tubes-A Review, Mater. Today Proc., 5 (2018), pp. 28262-28270

[34] E. Nes, N. Ryum, O. Hunderi, On the Zener Drag, Acta Matallurgica, 33 (1985), pp. 11-22

[35] Z. Wang, L. Chen, J. Tang, C. Zhang, G. Zhao, Strategy for suppressing abnormal grain growth of ZK60 Mg alloy during solution by pre-compression: A quasi-in-situ study, J. Mater. Sci. Tech. 171 (2024) pp. 115-128

[36] M. Chmielewski, K. Pietrzak, A. Strojny-Nędza, K. Kaszyca, R. Zybała, P. Bazarnik, M. Lewandowska, S. Nosewicz, Microstructure and thermal properties of Cu-SiC composite materials depending on the sintering technique, Sci. Sinter., 49 (2017), pp. 11-22

[37] P. Hidalgo-Manrique, X. Lei, R. Xu, M. Zhou, I.A. Kinloch, R.J. Young, Copper/graphene composites: a review, J. Mater. Sci., 54 (2019), pp. 12236-12289,

[38] L. Hu, A. Wang, W. Wang, Structural evolution of graphene oxide and its thermal stability during high temperature sintering, J. Wuhan. Univ. Technol. Mater. Sci. Ed., 37 (2022), pp. 342-349

[39] H.-K. Lin, G. Y. Li, S. Mortier, P. Bazarnik, Y.i Huang, M. Lewandowska, T.G. Langdon, Processing of CP-Ti by high-pressure torsion and the effect of surface modification using a post-HPT laser treatment, J Alloy Comp. 784 (2019) pp 653-659

[40] C.C. Hsieh, M.S. Shi, W. Wu, Growth of intermetallic phases in Al/Cu composites at various annealing temperatures during the ARB process, Met. Mater. Int., 18 (2012), pp. 1-6

[41] G. Huang, W. Hou, J. Li, Y. Shen, Development of surface composite based on Al-Cu system by friction stir processing: evaluation of microstructure, formation mechanism and wear behaviour, Surf. Coating. Technol., 344 (2018), pp. 30-42

[42] L. Yang, B.X. Mi, L. Lin, H.J. Huang, X.P. Lin, X.G. Yuan, Formation sequence of interface intermetallic phases of cold rolling Cu/Al clad metal sheet in annealing process, Mater. Sci. Forum (2013), pp. 600-605

[43] T. Shanmugasundaram, M. Heilmaier, B.S. Murty, V. Subramanya Sarma, On the Hall–Petch relationship in a nanostructured Al–Cu alloy, Mater. Sci. Eng., 527 (2010), pp. 7821-7825

[44] N. Maury, N.X. Zhang, Y. Huang, A.P. Zhilyaev, T.G. Langdon, A Critical examination of pure tantalum processed by high-pressure torsion, Mater. Sci. Eng. A, 638 (2015), pp. 174-182

[45] M.Y. Alawadhi, S. Sabbaghianrad, Y. Huang, T.G. Langdon, Direct influence of recovery behaviour on mechanical properties in oxygen-free copper processed using different SPD techniques: HPT and ECAP, J. Mater, Res, Technol., 6 (4) (2017), pp. 369-377

……..……..…….
(podpis wnioskodawcy)

,

Acta Materialia 164 (2019) 499–511

Contents lists available at ScienceDirect

Acta Materialia

journal homepage: www.elsevier.com/locate/actamat

Full length article

The fabrication of graphene-reinforced Al-based nanocomposites using high-pressure torsion

Yi Huang [a, b, *], Piotr Bazarnik [c], Diqing Wan [d], Dan Luo [e], Pedro Henrique R. Pereira [f], Malgorzata Lewandowska [c], Jin Yao [g], Brian E. Hayden [g], Terence G. Langdon [b]

[a] Department of Design and Engineering, Faculty of Science and Technology, Bournemouth University, Poole, Dorset, BH12 5BB, UK
[b] Materials Research Group, Department of Mechanical Engineering, University of Southampton, Southampton, SO17 1BJ, UK
[c] Faculty of Materials Science and Engineering, Warsaw University of Technology, Woloska 141, 02-507 Warsaw, Poland
[d] School of Mechanical and Electronical Engineering, East China Jiaotong University, Nanchang, Jiangxi Province, 330013, PR China
[e] LiME BCAST, Brunel University London, Uxbridge, Middlesex, UB8 3PH, UK
[f] Department of Metallurgical and Materials Engineering, Universidade Federal de Minas Gerais, Belo Horizonte, MG 31270-901, Brazil
[g] Advanced Composite Materials Facility, Department of Chemistry, University of Southampton, Southampton, SO17 1BJ, UK

ARTICLE INFO

Article history:
Received 17 August 2018
Received in revised form
26 October 2018
Accepted 29 October 2018
Available online 1 November 2018

Keywords:
Aluminium
Graphene
High-pressure torsion
Nanocomposites
Ultrafine grains

ABSTRACT

Metal matrix nanocomposites were fabricated by high-pressure torsion (HPT) using 5% graphene nanoplates as a reinforcement contained within an Al matrix. Powders were mixed and compacted at room temperature and then processed by HPT at three different temperatures of 298, 373 and 473 K. After processing, microstructural observations were undertaken to reveal the distributions of graphene in the matrix, the grain refinement in the aluminium and the nature of the graphene-aluminium interfaces. Tests were performed to measure the microhardness, the tensile stress-strain curves and the electrical conductivity. The results show that processing by HPT is advantageous because it avoids the sintering and high temperature deformation associated with other processing routes.

1. Introduction

Metal matrix composites (MMCs) are lightweight structural materials having wide applications in the aerospace, automotive and electronic sectors [1]. Boron, carbon and silicon carbide (SiC) are often used as continuous fibre reinforcements and silicon carbide (SiC_p), alumina (Al_2O_3) and boron carbide (B_4C) are conventional particle reinforcements [2]. Aluminium-based MMCs have attracted much interest due to the strengthening effects from different reinforcements such as Al_2O_3 and SiC [3]. An alternative reinforcement is graphene which was discovered in the last 15 years [4] and has a low mass density of 0.77 mg m^{-2} [5], outstanding mechanical properties with a 1 TPa Young's modulus and 130 GPa tensile strength [6], as well as high thermal conductivity above 4000 W mK^{-1} [7] and high electronic conductivity above 15000 cm V^{-2} [8]. The 2D geometry of graphene nanosheets and nanoplates is responsible for producing maximum values for their surface-to-volume ratios so that graphene appears as an ideal candidate for incorporation in an aluminium matrix to achieve high strength and conductivity. Graphene nanoplates (GNPs), which consist of multilayer graphene, are much cheaper and easier to produce than single layer graphene [9] but the high van der Waals forces between the graphene layers tends to limit the uniform dispersion of GNPs within the metal matrix.

The traditional fabrication routes for MMCs can be divided into liquid state (liquid metal infiltration and casting techniques) and solid state (powder metallurgy) methods [10]. Liquid metal infiltration and casting involves an incorporation of a dispersed particulate into a molten matrix metal, followed by its solidification. However, due to the large density difference between graphene and the metal matrix, it is difficult to disperse graphene uniformly within the matrix and the liquid processing methods usually produce agglomerated particles in the ductile matrix which lead to an unwanted brittle nature. Furthermore, the agglomeration is more severe when the particulate size is in the submicrometer or

* Corresponding author. Department of Design and Engineering, Faculty of Science and Technology, Bournemouth University, Poole, Dorset, BH12 5BB, UK.
E-mail address: yhuang2@bournemouth.ac.uk (Y. Huang).

https://doi.org/10.1016/j.actamat.2018.10.060

nanoscale range [11] which is the case when using graphene as the reinforcement. The alternative of powder metallurgy (PM) processing techniques generally involve sintering, cold isostatic pressing, hot isostatic pressing or spark plasma sintering, and in some cases secondary deformation such as hot extrusion, hot forging, hot rolling and/or friction stir processing. The PM processing has two major disadvantages. The first disadvantage is an oxidation of the metal matrix and the production of unclean interfaces between the particulates and the matrix which lead to a weak bonding and consequent low mechanical strength [12]. In addition, processing at elevated temperatures aids the chemical reactions between the matrix and particles which may produce brittle secondary phases [13]. The second disadvantage is that high temperature sintering can produce unexpected grain growth in the matrix [14]. Nevertheless, it is generally easier to achieve uniformity of the reinforcement distributions using PM processing rather than liquid processing [15].

Several recent reports have described the synthesis of graphene-reinforced Al matrix composites [16–28] including using a liquid method [16], ball milling plus hot isostatic pressing, hot pressing or hot extrusion [17–21], ball milling plus sintering [22], sintering or sintering plus extrusion [23–25], spark plasma sintering [26,27] or an ultrasonic treatment plus friction stir processing [28]. In practice, these various investigations all involve high temperature processing steps which may cause oxidation of the metal matrix and/or reactions between the graphene and the matrix. Thermodynamic calculations show that the Al and graphite may react to form Al_4C_3 at high temperature [29]. Therefore, in order to overcome these technical challenges, it is important to consider developing the composites using a low temperature approach. One possibility is to use high-pressure torsion (HPT) which is a severe plastic deformation technique that introduces significant grain refinement and corresponding strength enhancement in bulk metals in particular when processing at relatively low temperatures [30,31]. Currently, there are reports on the HPT processing of powder materials such as pure metals [32–36], composites reinforced with Al_2O_3 and SiC particulates [37–40] and composites reinforced with carbon-based particles such as fullerenes (C_{60}) and carbon nanotubes (CNTs) [41–48]. These MMCs can be effectively processed by HPT at temperatures between 298 and 473 K and this range is much lower than the typical sintering temperatures of 863–893 K for Al alloys. Furthermore, the use of low temperature HPT processing will avoid oxidation and the formation of second phases. There is also mass transfer within the samples due to the development of turbulent eddy currents in the sample cross-sections during HPT processing, as confirmed by computer modelling [49] and experimental observations in immiscible alloys [50,51], and this will help in the redistribution of reinforcements within the metal matrix. In addition, there are currently no reports on using HPT to fabricate graphene-reinforced Al-based MMCs (henceforth designated graphene-Al composites).

The present research was therefore initiated in order to evaluate the use of HPT processing in the fabrication of graphene-Al composites at temperatures ranging from 298 to 473 K, to develop a comprehensive understanding of the microstructural developments in both the Al matrix and the graphene, and to measure experimentally the strength and conductivity in the fabricated composites.

2. Experimental materials and procedures

Aluminium powder with a mean particle size of 125 μm was purchased from Goodfellow (Cambridge, UK). The purity of the powder, as provided by the supplier, was 99.5% with Cu < 200, Fe < 3500, Mn < 200, and Si < 2500 ppm; this composition is similar to the specifications for commercial purity Al-1050 aluminium in ASTM B491. Graphene nanoplates (GNPs) were purchased from Sigma-Aldrich (Gillingham, Dorset, UK) with Raman D/G (the ratio of D band peak to G band peak) and D/D′ (the ratio of D band peak to D′ band peak) values of 0.28 and 5.0, respectively. The 2D band shape indicates the presence of graphene flakes of a few layers with an average of ~5–7 atomic layers. Fig. 1(a) shows the scanning electron microscope (SEM) images of the as-received GNPs and the higher magnification image in Fig. 1(b) shows an agglomeration of GNPs.

The aluminium powder was initially mixed with 5% of GNPs in weight percentage and the mixed powders were then poured into a glass bottle and rotated on a rotation rack for 30 min to improve the homogeneity of GNPs in the Al powder. The mixed powders were

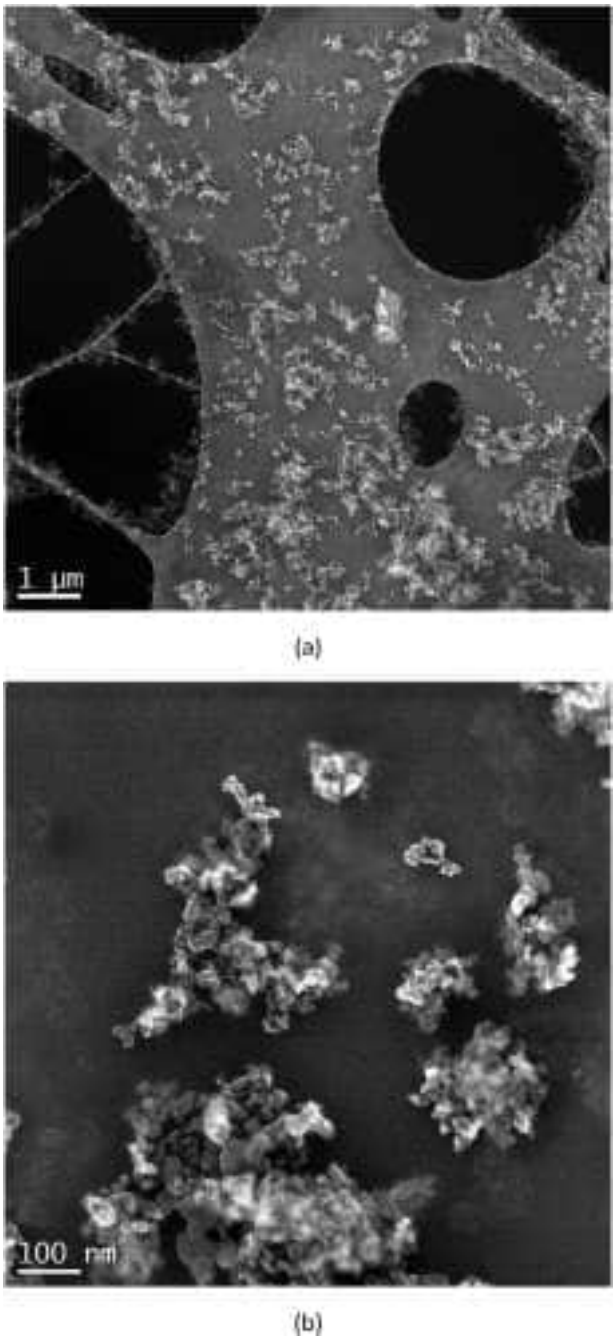

Fig. 1. SEM images of as-received GNPs powder at (a) low and (b) high magnifications.

compacted in a die at room temperature under a pressure ~40 MPa for 1 min to provide disc-shaped tablets with diameters of 10 mm and heights of ~1.2 mm.

The HPT processing was conducted at temperatures of 298, 373 and 473 K under quasi-constrained conditions where there is a small outflow of material around the periphery of the disc during processing [52]. At each temperature, the pre-compacted disc-shaped tablets were initially subjected to a pressure of 6.0 GPa for 1 min without any shear deformation where this processing condition is henceforth designated 0 turns. Thereafter, the samples were processed by torsional straining through numbers of rotations, *N*, of 1, 5, 10 and 20 turns.

After processing, each disc was cut into two halves along a diameter using a diamond wafering saw. The cross-sections of each disc were examined using SEM with the specimens prepared by grinding and ion polishing using an Hitachi Ion Milling System IM-4000. Since ion milling is a damageless process, this polishing eliminates all deformation and oxide layers and the surface quality was sufficiently good that the structure was examined by SEM using channelling contrast. Microstructure examinations were conducted using an Hitachi SU-8000 SEM operating at 10 kV. The images were taken in secondary electron (SE) imaging and in back-scattered electron (BSE) modes. The SEM observations were performed on cross-section planes in the middle region close to the disc centre and in the edge region at ~0.5 mm from the disc edge. Detailed microstructural observations from selected areas were recorded using a Cs-corrected dedicated high resolution scanning transmission electron microscope (STEM) Hitachi HD-2700 operating at an accelerating voltage of 200 kV. The STEM thin foils were extracted from the peripheral parts of each disc using a focused ion beam (FIB) Hitachi NB 5000 microscope. The STEM observations were taken in bright-field (BF) and high-angle annular dark field (HAADF or Z-contrast) modes. The grain size of the HPT-processed Al matrix was measured using the linear intercept method with Image J software based on the SEM and STEM images.

XploRA confocal Raman spectroscopy was used to examine the structure change of the graphene during HPT processing. The Raman spectra were acquired with a selected laser wavelength of 532 nm at room temperature.

The mechanical properties of HPT-processed samples were evaluated using microhardness measurements and tensile testing. The Vickers microhardness, Hv, was measured along radial directions on the polished disc surfaces using an FM-300 microhardness tester with a load of 200 g (equivalent to 1.96 N) and a dwell time of 15 s. Miniature tensile specimens having gauge lengths of 1.1 mm, widths of 0.95 mm and thicknesses of ~0.7 mm were cut from the HPT-processed discs. These specimens were tested in tension at 298 K using a Zwick 30 kN Proline facility operating at a constant rate of cross-head displacement with an initial strain rate of 1.0×10^{-3} s^{-1}. The constant cross-head velocity testing machine applies a constant strain rate that is the sum of the elastic and plastic strain rates in the specimen and the strain rate resulting from the elasticity of the testing machine [53]. The load and displacement data were converted to engineering stress and engineering strain using the method described elsewhere [54] where the influence of the elastic deformation of the testing apparatus was minimised by equating the elastic portion of the stress-strain curves to the theoretical elastic modulus of aluminium. To check on reproducibility, four samples were tested for each condition.

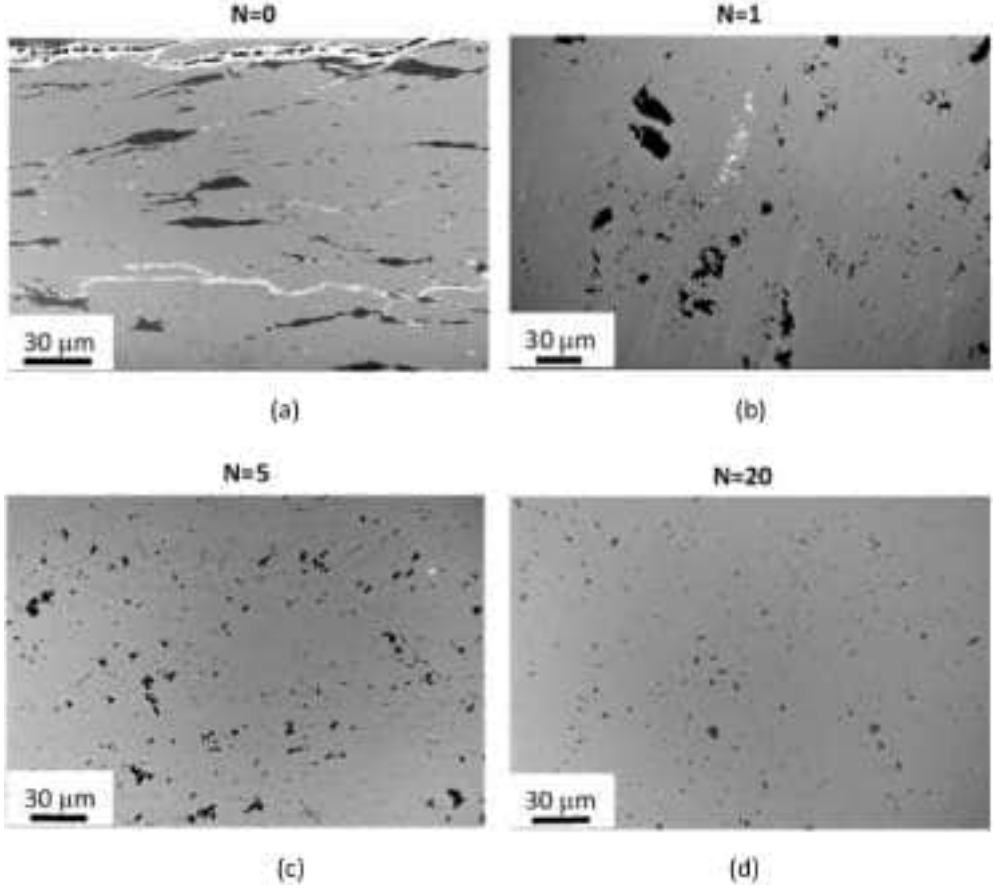

Fig. 2. The distribution of 5% GNPs in the Al matrix processed by HPT at 298 K with (a) $N = 0$, (b) $N = 1$, (c) $N = 5$ and (d) $N = 20$.

The bulk electrical resistivity (ohms-cm) of HPT-processed disc samples was measured on a 4D automatic four-points probe meter (Model 280) using a linear probe with a probe size of 500 μm and a probe-to-probe distance of 1 mm. For each disc sample, the bulk electrical resistivity was measured at 5 or more positions within the disc half-radius area. The measured bulk resistivity (ohms-cm) was compared with the bulk resistivity of annealed commercial pure Cu (1.72×10^{-6} Ω-cm), and then it was converted to the electrical conductivity represented by the IACS (International Annealed Copper Standard) using the expression IACS (%) = 1.72×10^{-6} Ω-cm/(the measured bulk electrical resistivity in ohm-cm) [55].

3. Experimental results

3.1. The evolution of the GNPs distributions in the Al matrix during HPT processing

The polished cross-sectional surfaces of samples processed by HPT at 298 K were observed by SEM and the SE images giving the GNPs distributions in the Al matrix are shown in Fig. 2 after 0, 1, 5 and 20 turns, where the GNPs have a black colour in these images. In the sample compressed under 6.0 GPa for 1 min (0 turns sample), large cracks with shining reflections appear at the upper and lower regions of the disc in Fig. 2(a) and the GNPs are in the form of agglomerates displaying flow tendencies. By contrast, no cracks are visible in samples processed to 1, 5 and 20 turns in Fig. 2(b–d). Furthermore, with increasing numbers of turns there is less evidence for a flow tendency in the agglomerated GNPs, and the size of the agglomerates is reduced significantly as N increases from 5 to 20 turns.

Similar polished cross-sectional surfaces were examined after HPT at 473 K and the results are shown in Fig. 3(a–d). No large cracks are visible in the 0 turns sample in Fig. 3(a) although there are some very short cracks in the top area of the SE image but the agglomerated GNPs have no obvious flow tendency. Comparing Figs. 3(a) and 2(a), it is apparent that HPT processing at 473 K promotes diffusion and plastic flow which reduces the cracking in the 0 turns sample. The agglomeration of GNPs in the Al matrix also changes with increasing numbers of turns as shown in Fig. 3(b–d) such that the agglomerated GNPs are fragmented to much smaller sizes after 5 and 20 turns by comparison with the samples processed at 298 K. This shows that the shear deformation induced by HPT processing is effective in reducing cracking and in prompting the material flow and the fragmentation of the agglomerates of GNPs in the Al matrix.

3.2. Microstructure development in the Al matrix during HPT processing

The polished surfaces of the 0 turns samples processed by HPT at 298 and 473 K were further observed by SEM at higher magnifications to reveal the grain structure in the Al matrix and the occurrence of local bonding between the GNPs and the Al matrix. Fig. 4(a) and (b) show the same area observed by the SE and BSE mode for the 0 turns sample processed at 298 K. The SE image in Fig. 4(a) demonstrates that most of the agglomerated GNPs have good bonding with the metal matrix and some of them have comet-tails which confirm the strong flow tendency after compression at 6.0 GPa for 1 min. Some cracks formed around the GNPs and also

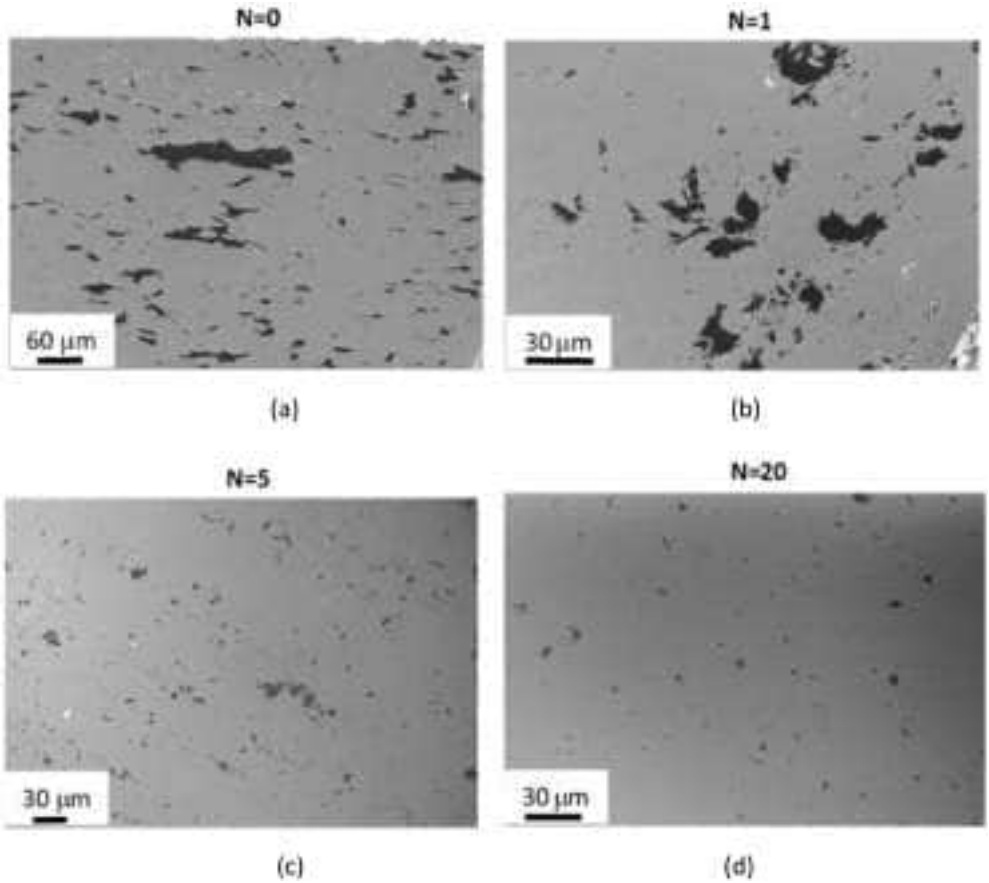

Fig. 3. The distribution of 5% GNPs in the Al matrix processed by HPT at 473 K with (a) $N = 0$, (b) $N = 1$, (c) $N = 5$ and (d) $N = 20$.

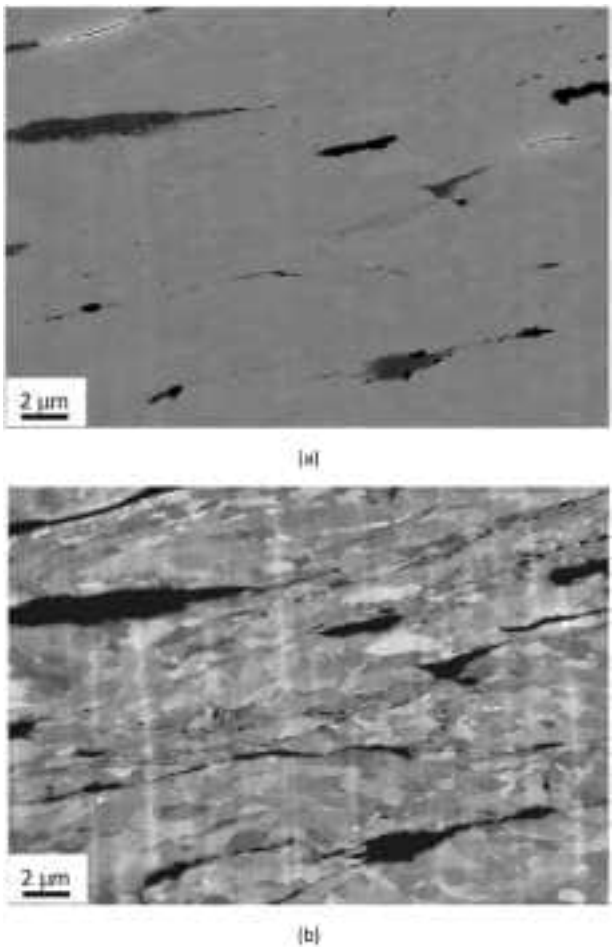

Fig. 4. Microstructures of 0 turns sample processed by HPT at 298 K: same area observed using different SEM modes of (a) secondary electron image and (b) back scattered image.

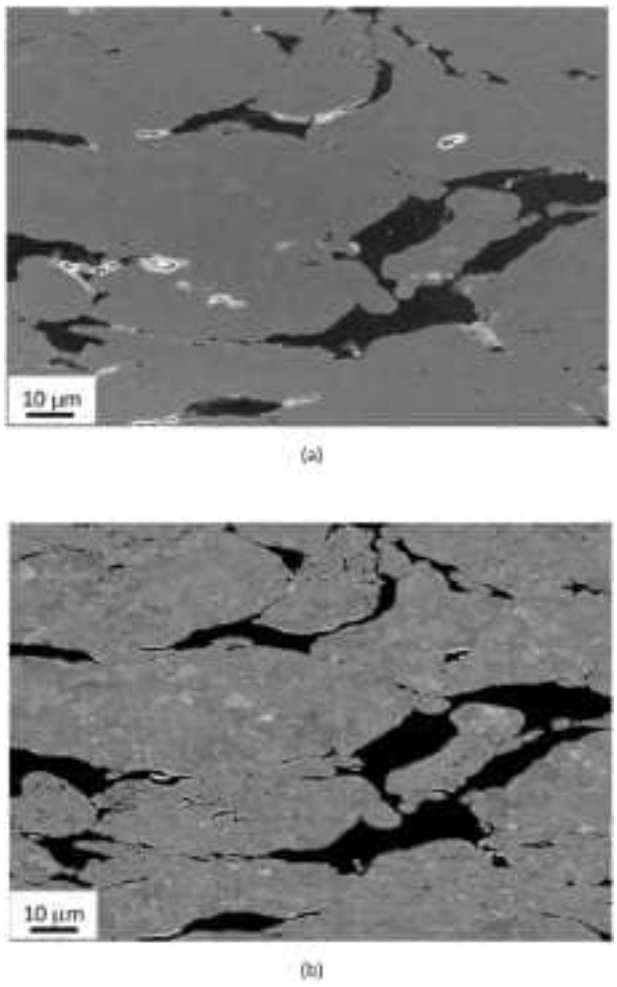

Fig. 5. Microstructures of 0 turns sample processed by HPT at 473 K: same area observed using different SEM modes of (a) secondary electron image and (b) back scattered image.

some isolated cracks formed within the Al matrix. The BSE image in Fig. 4(b) reveals the grain structure and the white regions of lines or dots were identified by EDX analysis as Fe-Si rich phases which is consistent with the compositional analysis of the Al powder. When the compact tablet is subjected only to compression as at 0 turns, the axial compression gives a radial flow tendency so that most of the grain structure tends to be elongated with a measured average grain size of ~0.5 μm along the shorter axes of the grains. It is important to note that the cracks and GNPs both appear as a black colour in the BSE image in Fig. 4(b) so that the cracks and GNPs can be identified only in the SE image in Fig. 4(a). Similar observations were recorded for the 0 turns sample processed by HPT at 473 K in Fig. 5 where the GNPs have no obvious flow tendency and there is a network-like bonding with the Al matrix. It is evident from Fig. 5(b) that the grains are reasonably equiaxed in structure with an average grain size of ~1.5 μm.

Fig. 6 shows the STEM images of samples processed to (a) 1, (b) 5 and (c) 20 turns of HPT at 298 K: each row shows two images where the left column is a high resolution STEM image so that the GNPs appear white and the right column is a HAADF image (or Z-contrast image) of the same area where the GNPs are black based on the compositional difference. Normally, heavy elements are brighter in Z-contrast images and, since the carbon atoms in graphene are lighter than the aluminium atoms, the graphene appears dark in the Z-contrast images. For convenience, the observable GNPs are marked with white arrows in both the STEM and Z-contrast images. By comparing the two sets of images for each sample, it is apparent that the presence of GNPs is resolved more clearly in the Z-contrast images. No cracks or voids exist between the GNPs and the Al matrix after processing to 1, 5 and 20 turns but with increasing through 1, 5 and 20 turns at 298 K the average grain size of the Al matrix is reduced through ~180, ~90 and ~70 nm, respectively. Fig. 7 shows comparable images after processing at 473 K for (a) 1, (b) 5 and (c) 20 turns: as in Fig. 6, the observable GNPs are marked with white arrows. Thus, the GNPs show good bonding with the Al matrix without the detection of any cracks or voids. The average grain sizes after 1, 5 and 20 turns at 473 K were ~700, ~295 and ~155 nm, respectively, and these values are larger than at 298 K.

3.3. The nature of the interfaces between the GNPs and the Al matrix during HPT processing

Samples processed by HPT at 298 and 473 K were observed under high resolution STEM to reveal the bonding interface and the surface features of the GNPs: representative STEM images are presented in Figs. 8 and 9.

Fig. 8 shows STEM images of 1 turn samples processed by HPT at 298 K. Thus, when the graphene (0001) nanoplates have a different orientation from the (111) crystal plane of the Al matrix, there is an interface transition zone in which the C and Al atoms accommodate

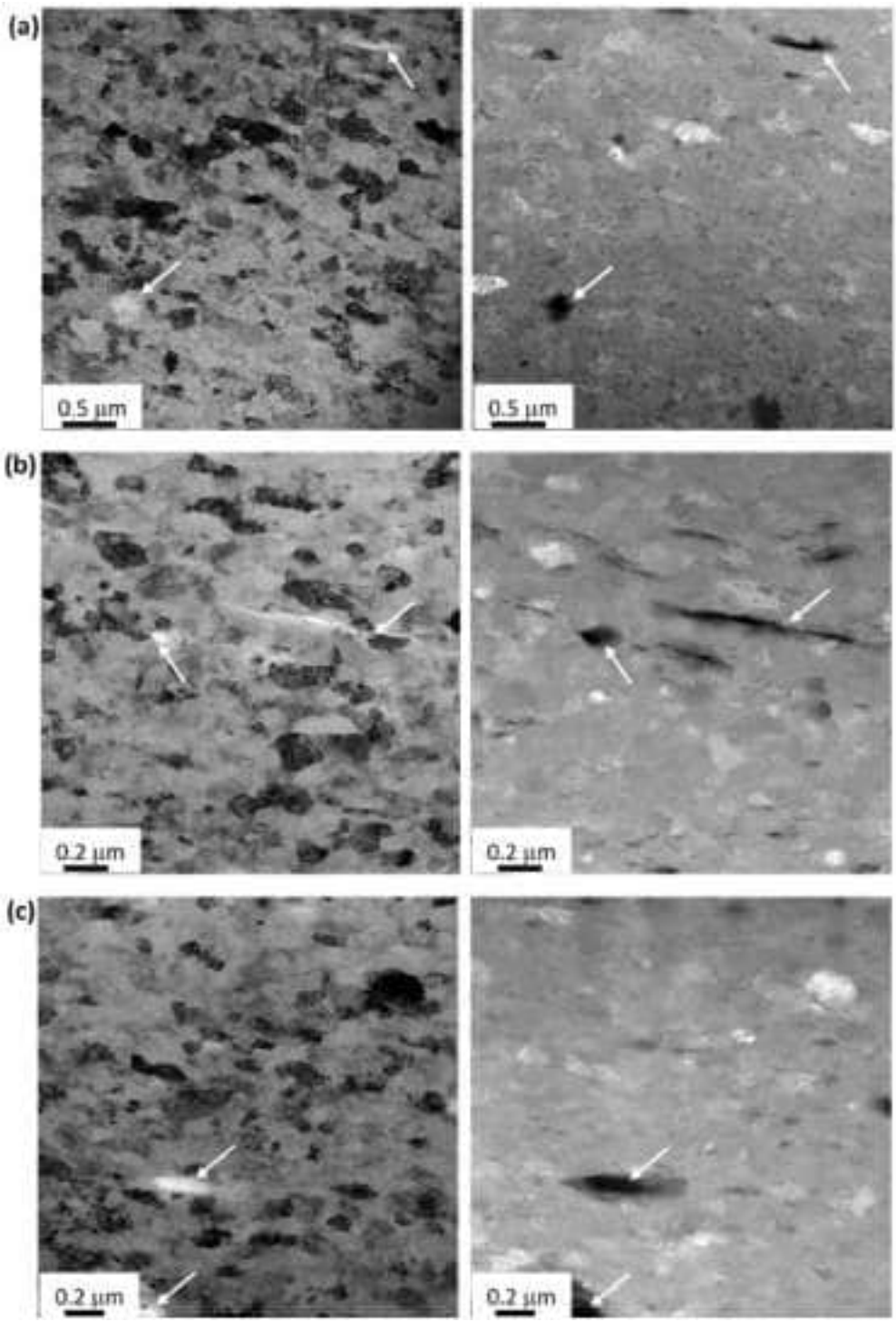

Fig. 6. STEM and Z-contrast images showing the microstructures of samples processed by HPT at 298 K for (a) $N = 1$, (b) $N = 5$ and (c) $N = 20$.

each other as shown in Fig. 8(a). The measured layer-to-layer distance of the GNPs is ~0.35 nm in Fig. 8(a) which is similar to the layer-to-layer distance reported for carbon nanotubes [48] whereas the Al (111) interplanar spacing is ~0.23 nm. The GNPs show a long intact layered structure and there are only slight bends as indicated by white arrows in Fig. 8(b). These results are reasonable because of the small amounts of shear strain applied to the graphene-Al composite in 1 turn of HPT processing.

Comparable STEM images are shown in Fig. 9 for 5 turns samples processed by HPT at 473 K. Thus, the GNPs exist not only in the grain boundary area in Fig. 9(a) but also within the Al matrix in Fig. 9(b) as highlighted by white arrows. The GNPs embedded within these ultrafine grains are critical for achieving a significant strength enhancement in the graphene-Al composites. Based on these observations of samples processed by HPT at 298 and 473 K, it is concluded that the GNPs display more bending as the numbers of turns increase and this is consistent with the high levels of internal stress introduced by the heavy shear deformation.

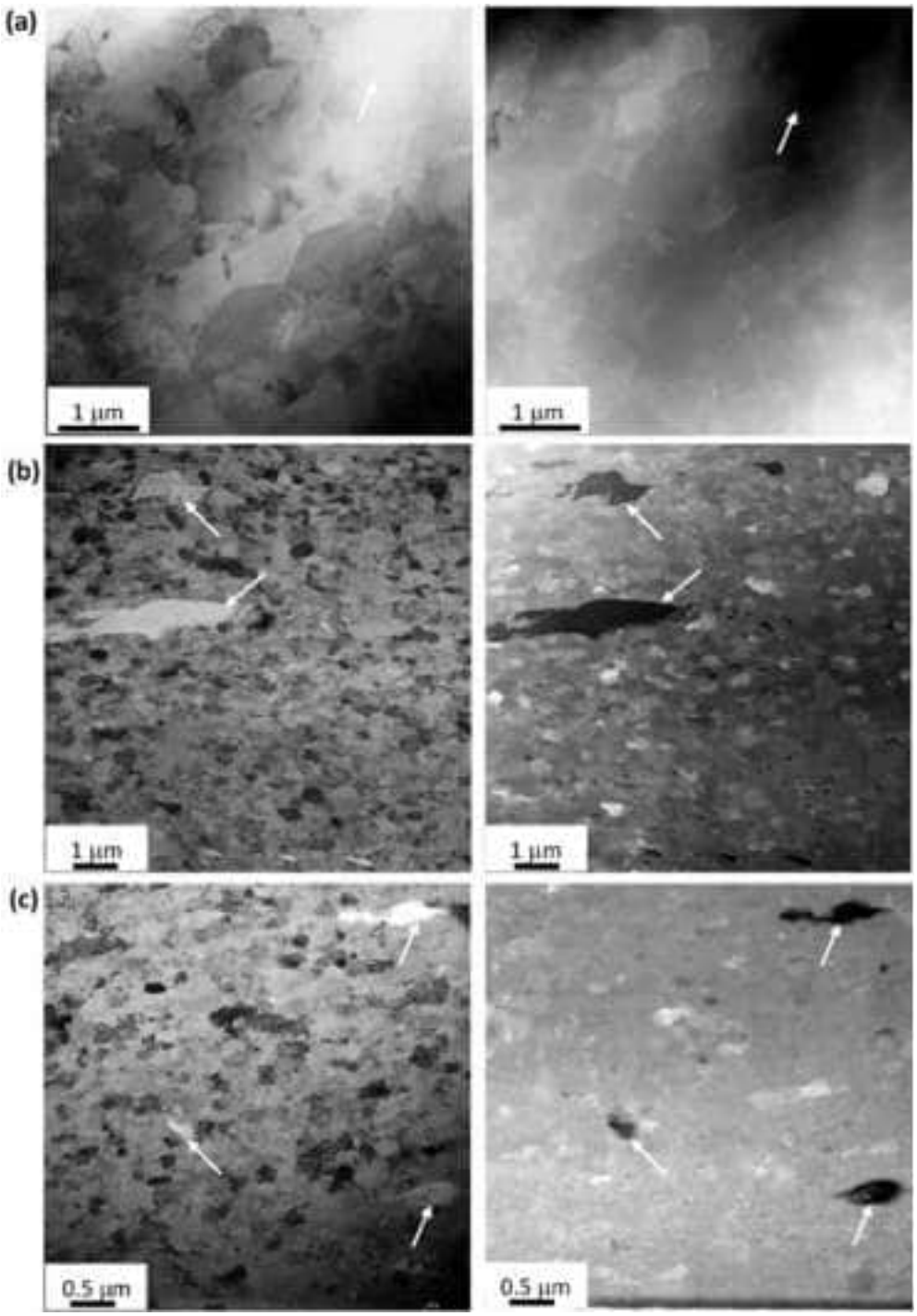

Fig. 7. STEM and Z-contrast images showing the microstructures of samples processed by HPT at 473 K for (a) $N = 1$, (b) $N = 5$ and (c) $N = 20$.

Raman spectroscopy is a convenient and effective method for characterizing carbon materials and Fig. 10 shows the Raman spectra of GNPs in the 20 turns sample processed by HPT at 298 K. The characteristic peaks of the disorder-induced D band (~1353 cm^{-1}) and G band (1580 cm^{-1}) were detected, where the D band is associated with non-sp^2 disorders (sp^3-hybridized carbon) which are present in the network of sp^2-hybridized carbon, whereas the G band is a typical ordered graphite structure that is attributed to the degree of crystallinity of sp^2-bonded carbon materials [56]. The intensity ratio of the D band to G band (I_D/I_G) is a measure of the defects present in the GNPs after HPT processing, where a high ratio indicates a higher defect density in carbon materials [57]. In Fig. 10, the ratio is ~1.15 indicating that some defects exist in the GNPs after 20 turns, where this is consistent with the observed bends of the GNPs in the STEM images in Figs. 8 and 9.

3.4. Mechanical properties of HPT-processed graphene-Al nanocomposites

Fig. 11 shows the evolution of microhardness in the composites processed by HPT at (a) 298, (b) 373 and (d) 473 K, respectively. At 298 K, there is no large difference in hardness between the 0 turns

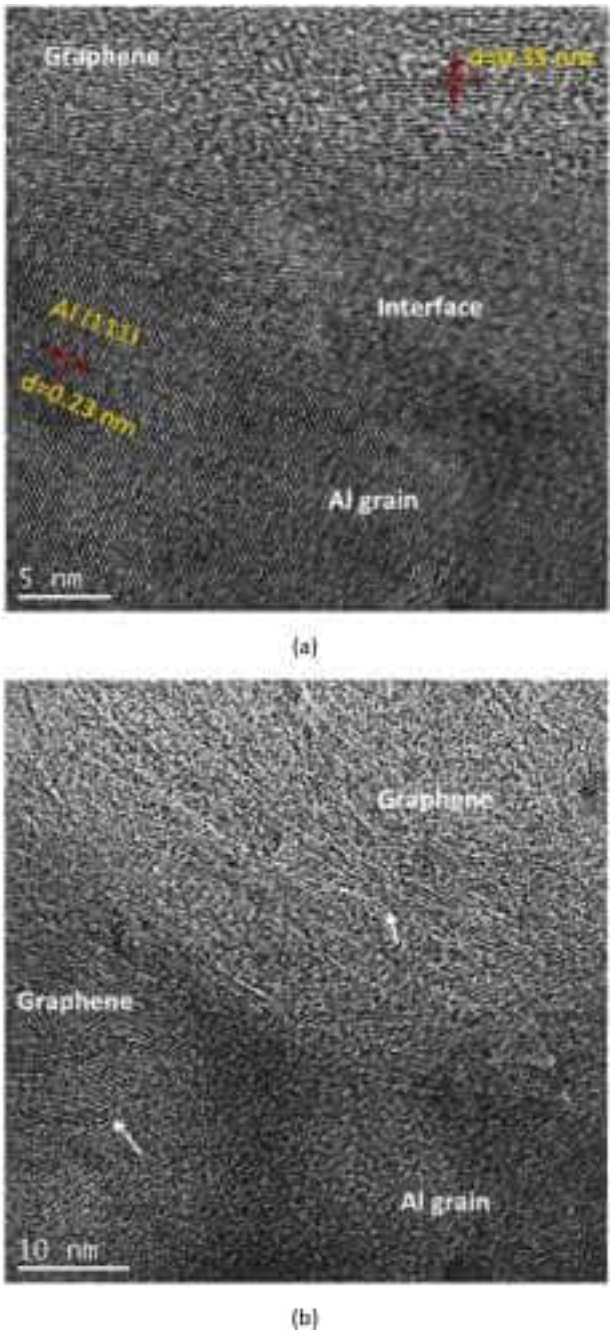

Fig. 8. High resolution STEM images of 1 turn sample processed by HPT at 298 K showing the interface between GNPs and the Al matrix under the condition of (a) graphene nanoplates and Al matrix having different orientations, (b) the existence of long straight and slightly curved GNPs in the Al matrix.

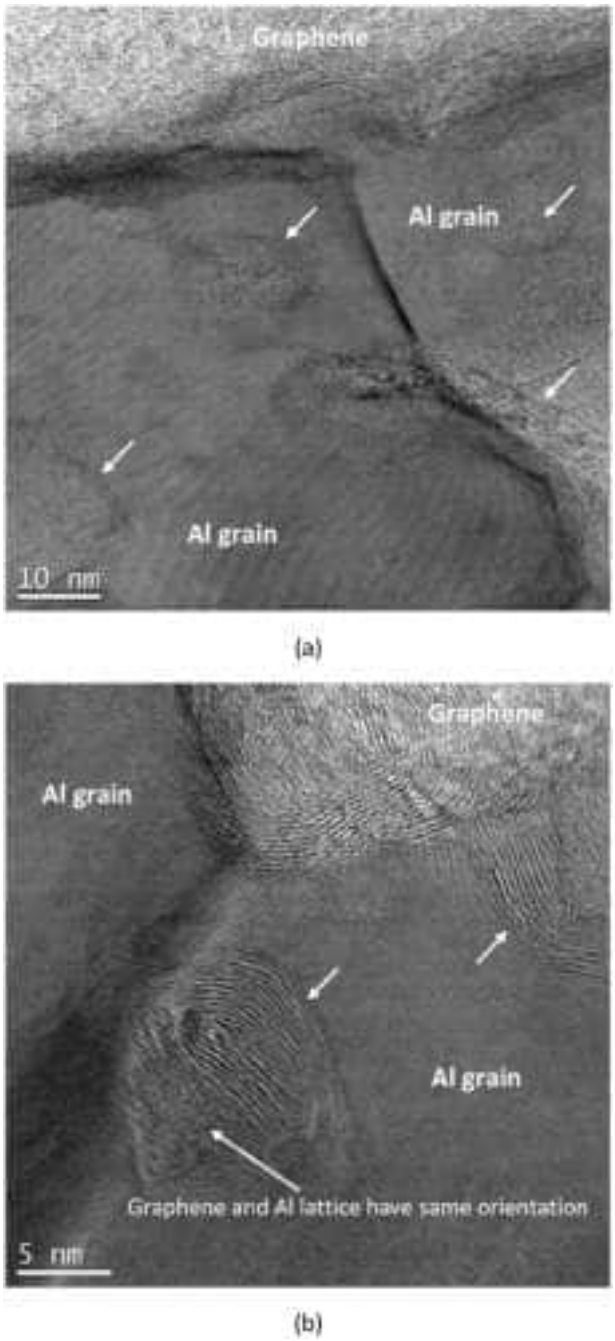

Fig. 9. High resolution STEM images of 5 turns sample processed by HPT at 473 K showing the interface between GNPs and the Al matrix under the condition of (a) the existence of GNPs not only in the grain boundary area but also within the Al matrix, (b) part of the curved graphene nanoplates having the same orientation with Al matrix.

and 1 turn samples in Fig. 11(a) and all values are in the range ~40–60 Hv which shows that 1 turn of HPT introduces no significant deformation in the Al matrix. As the numbers of turns increases to 5 and 10, the hardness distributions show the typical trends observed in most bulk metals with lower hardness values in the disc centre areas and higher hardness values in the disc outer areas [58]. With a further increase in the numbers of turns to 20, the centre area shows only a slight increase in hardness but from the half-radius position to the disc edge the hardness values lie around a plateau with a value of ~110 Hv which confirms that heavy straining introduces a saturation state. At 373 K, hardness distributions in Fig. 11(b) are similar except there is no well-defined plateau distribution after 20 turns. In Fig. 11(c) for HPT at 473 K the maximum hardness values are ~90 Hv after 20 turns and the hardness values for the samples processed to 10 and 20 turns are almost identical.

Tensile testing was conducted at room temperature with an initial strain rate of 1.0×10^{-3} s^{-1} on samples processed by 20 turns at three different temperatures. As shown in Fig. 12, the strength of the graphene-Al nanocomposite decreases with increasing processing temperature and the maximum strengths are ~350, ~340 and ~290 MPa after processing at 298, 373 and 473 K, respectively.

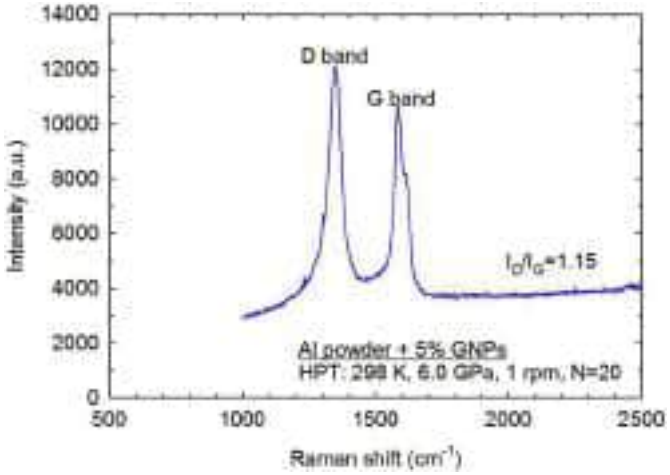

Fig. 10. Raman spectroscopy of GNPs after HPT processing to 20 turns at 298 K.

Inspection shows that the elongations exhibit no simple variation with processing temperature and the measured elongations for these three temperatures are ~1.8%, ~3.9% and ~2.1%, respectively.

3.5. Electrical conductivity of the HPT-processed graphene-Al composites

For comparison purposes, Table 1 shows electrical conductivity measurements in the HPT-processed graphene-Al composite. The electrical conductivity of commercial purity Al is 62% IACS [59]. When graphene-Al composites are processed by HPT at 298 K, the average electrical conductivity in samples taken through 5 and 20 turns are 66.7 ± 4.0% and 64.9 ± 2.1% IACS, respectively. Considering the relatively large error bar ranges, the conductivity in the sample with the larger shear deformation is only slightly lower than the sample with the smaller shear deformation. To check whether the HPT processing temperature has an influence, the electrical conductivity was also measured after processing by HPT for 20 turns at 473 K. The result is shown in Table 1 and it confirms there is an increase in conductivity with increasing HPT processing temperature which is consistent with data reported for the processing of a Cu-Cr alloy by HPT [60]. It is also consistent with the result for a Cu-Cr alloy showing that the conductivity is increased when samples are subjected to heat treatments after HPT [61].

4. Discussion

4.1. The use of HPT in dispersing agglomerated GNPs within an Al matrix

The generally accepted theory of HPT is based on the assumptions of a uniformity of simple shear deformation through the height of the specimen but with the localized shear strain proportional to the distance from the disc centre [62]. However, several recent investigations show deviations from this simple model. For example, in the HPT processing of a duplex stainless steel there is evidence for the formation of significant local turbulence including the presence of double-swirl patterns and local shear strain vortices [63–67]. Double-swirl flow patterns were reported also in a Cu-28% Ag alloy after HPT processing [68] and there are recent simulations demonstrating that non-laminar or turbulent flow causes intensive mass transfer and a mixing of the deformed material [49,69]. This explains the improved uniformity of particle size distribution in an Al-6061 matrix alloy reinforced with Al_2O_3

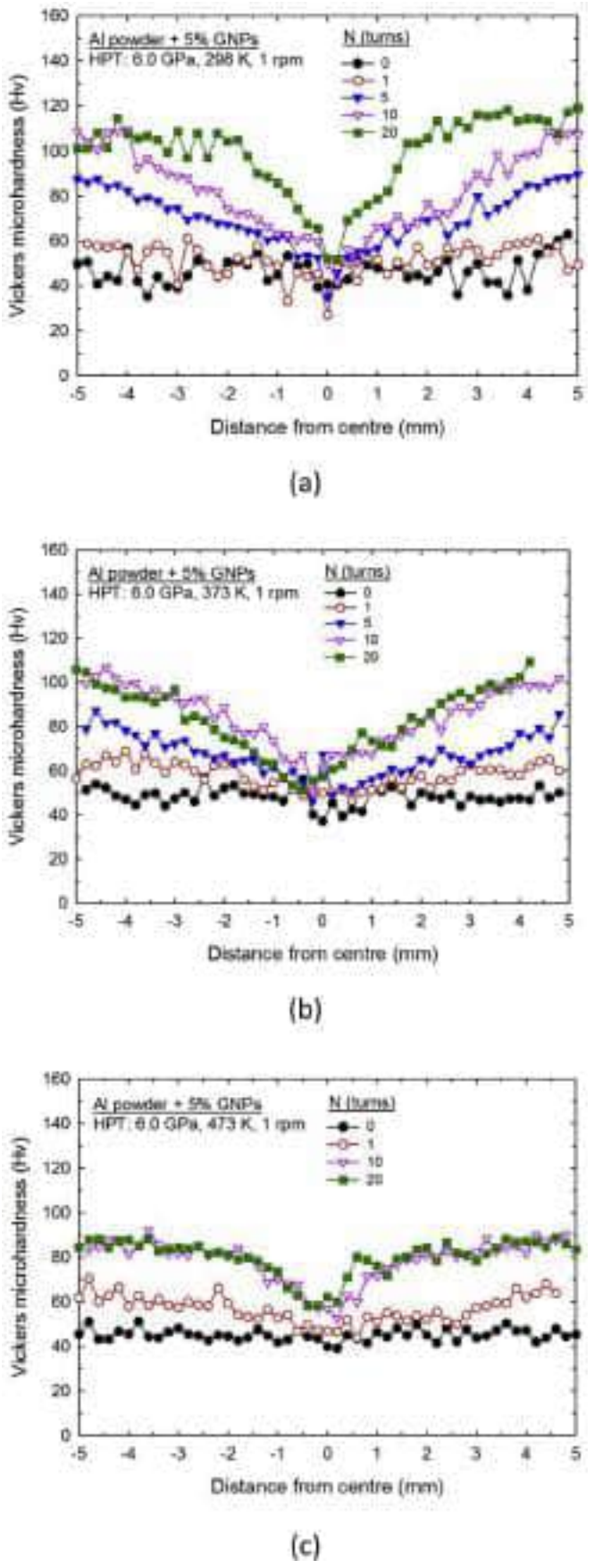

Fig. 11. Microhardness distributions along disc diameter in samples processed by HPT at (a) 298 K, (b) 373 K and (c) 473 K.

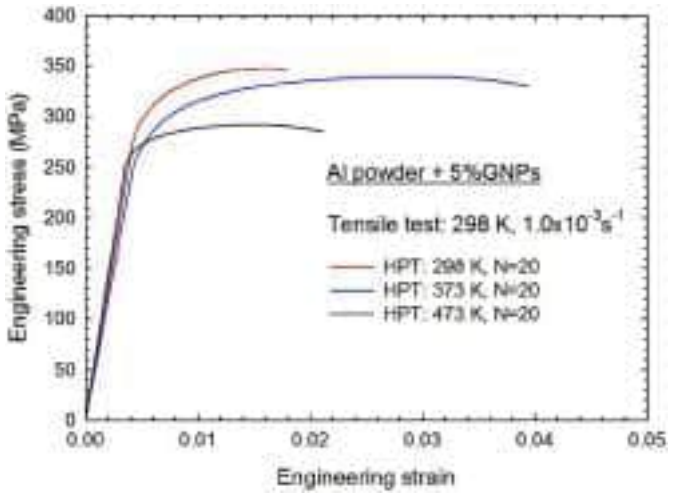

Fig. 12. Tensile results of 20 turns samples processed by HPT at different processing temperatures of 298, 373 and 473 K, and testing at 298 K.

particulates after heavy shear deformation [33,70] and the good homogeneity achieved in a nanocrystalline Cu-Cr alloy with an average grain size of less than 20 nm from an initial mixture of coarse Cu and Cr particles [71]. The successful processing of immiscible alloys by HPT also provides evidence of turbulent flow, mass transfer and the mixing of the deformed materials since a very high degree of chemical mixing was produced in the immiscible $Cu_{50}Ta_{50}$ system by the HPT deformation to high strains of stacks of Cu and Ta thin foils [51].

Based on these experimental observations and the simulations, it is reasonable to anticipate that the heavy shear strain applied by HPT will fragment the agglomerated GNPs in the Al matrix and redistribute the particles reasonably homogenously through the advent of turbulent flow. Figs. 2 and 3 confirms this trend for materials processed at 298 and 473 K, with a reduction in the extent of the GNPs agglomeration with increasing numbers of turns. This suggests that HPT may provide a powerful manufacturing route for obtaining uniform distributions of GNPs in an Al matrix through heavy shear deformation. This approach also overcomes the problem of the wettability between GNPs in an Al matrix which is an inherent feature of traditional liquid casting methods.

Furthermore, we noted that some graphene agglomerations remained even after high numbers of turns of HPT processing and this may limit any additional strength enhancement in the graphene-Al composites. Thus, the procedure for achieving a fully homogenous dispersion of graphene nanoplates in the Al matrix remains a challenge.

4.2. The effect of GNPs in improving the strength of HPT-processed graphene-Al nanocomposites

It was noted earlier that the composition of the Al powder is similar to that of the commercial purity (99.5%) Al-1050 alloy. Therefore, it is interesting to compare the strength of the HPT-processed graphene-Al nanocomposites with the Al-1050 alloy. After 5 turns of HPT at 298 K, the Al-1050 alloy shows a saturation hardness of ~65 Hv across the disc diameter [72,73] whereas in Fig. 11(a) the nanocomposite has not achieved saturation after 5 turns at 298 K with hardness values of ~40 Hv in the disc central area and ~90 Hv at the edge. There is also no saturation in the nanocomposite after 20 turns but with a maximum hardness of ~110 Hv from the disc half-radius to the edge. Thus, a much higher hardness is achieved at the edge of the nanocomposite which confirms the significant strengthening contribution from the GNPs.

It is well established that the equivalent von Mises strain, ε, imposed in HPT may be estimated from the relationship

$$\varepsilon = \frac{2\pi Nr}{h\sqrt{3}} \quad (1)$$

where N is the number of HPT processing turns and r and h are the radius and height (or thickness) of the disc, respectively [62]. An early report demonstrated that all hardness datum points derived in HPT processing may be conveniently correlated by plotting against the equivalent strain [74]. Fig. 13 shows these plots for the nanocomposite at the three temperatures of (a) 298, (b) 373 and (c) 473 K. The saturation hardness at 298 K is ~110 Hv at equivalent strains above ~200, at 373 K the behaviour is similar to 298 K but with a saturation hardness of ~100 Hv at equivalent strains above ~200 and at 473 K there is a well-defined saturation at ~80 Hv at equivalent strains above ~50. These hardness distributions are similar to many other bulk metals except that the saturation then occurs at lower equivalent strains of ~30 in Al-1% Mg [75], ~50 in AZ31 alloy [76] and ~20 in tantalum [77]. This suggests the GNPs may interfere with dislocation slip in the Al matrix so that there is little or no recovery during the HPT processing.

Commercial purity Al-1050 sheet in an H14 state (work hardened by rolling) should have a tensile strength of ~105–145 MPa with a minimum of 12% elongation. Fig. 12 show that the graphene-Al nanocomposite has maximum strengths of ~350, ~340 and ~290 MPa after processing by HPT through 20 turns at 298, 373 and 473 K, respectively, and then testing in tension at 298 K. These values are therefore significantly higher than for the Al-1050 sheet. A comparison of grain refinement in the Al matrix when processing by HPT at 298 and 473 K is given in Fig. 14 and it is apparent that processing at 473 K produces a coarser grain structure with final grain sizes after 20 turns of ~70 and ~155 nm at 298 and 473 K, respectively. Thus, the HPT-processed graphene-Al nanocomposite has much higher strength than the commercial purity Al-1050 alloy but with limited ductility, where this strength enhancement may arise from the synergistic effect of grain size refinement, dislocation strengthening, GNPs reinforcement and stress transfer [78].

Table 1
Electrical conductivity of HPT-processed graphene-Al composite at 298 and 473 K.

Sample condition	Electrical conductivity, IACS%
HPT processing at 298 K, N = 5	66.7 ± 4.0
HPT processing at 298 K, N = 20	64.9 ± 2.1
HPT processing at 473 K, N = 20	69.5 ± 2.3

4.3. The nature of the graphene-Al interface after HPT processing

There is an *ab initio* simulation on the interaction between a graphene (0001) sheet and Al (111) layer in carbon-aluminium (C-Al) nanocomposite systems with a calculated cohesive energy of ~0.185 eV for the C-Al interface and an equilibrium separation distance of ~0.248 nm between the graphene and Al layers [79]. This calculated cohesive energy at the C-Al interface is much larger than the value of 0.0417 eV for the bulk C-Al system [80] and suggests that the interface bonding of the C-Al nanostructure is not simply a van der Waals type but rather it is metallic or semi-metallic in nature [81]. The calculated equilibrium separation distance of 0.248 nm between the graphene (0001) layers and the Al (111) layers is smaller than the GNPs interlayer separation of 0.35 nm but larger than the Al (111) interplanar distance of 0.231 nm. In order to form coherent interfaces between the

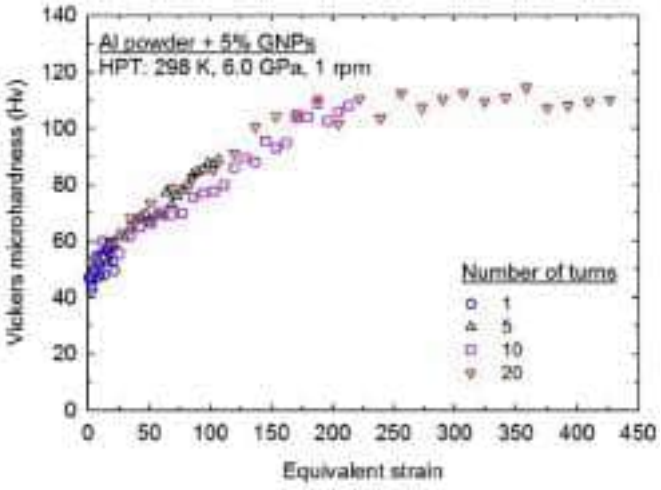

(a)

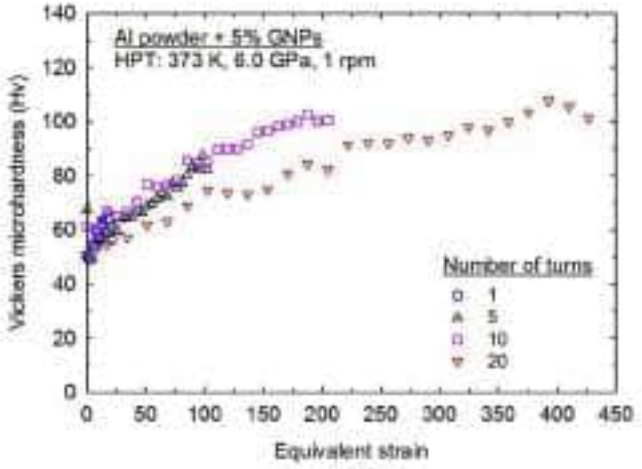

(b)

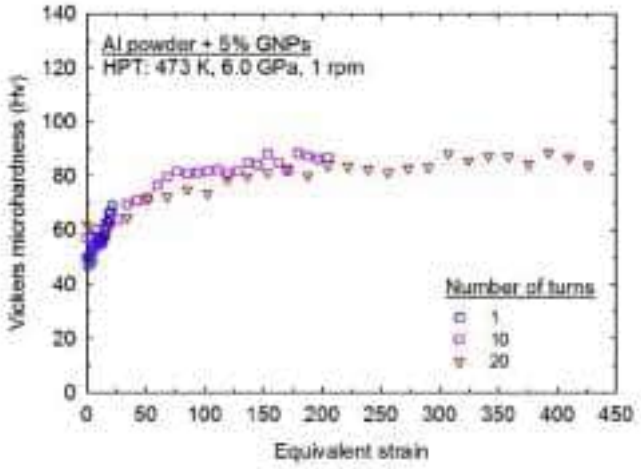

(c)

Fig. 13. Values of the Vickers microhardness plotted as a function of the equivalent strain for HPT-processed nanocomposites at (a) 298 K, (b) 373 K and (c) 473 K.

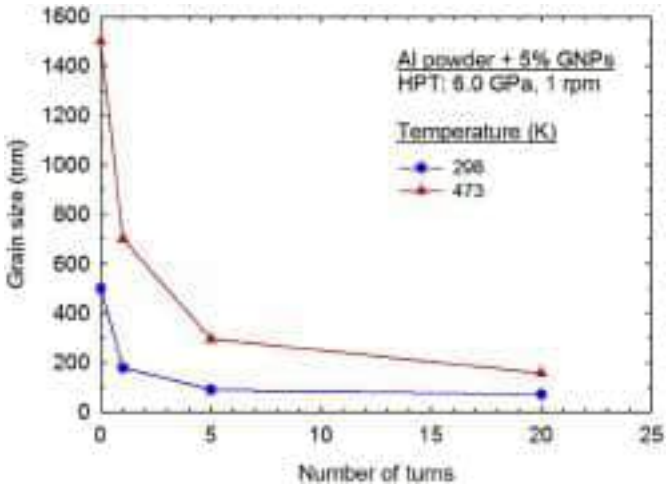

Fig. 14. Grain size comparison in graphene-Al composites processed at 298 and 473 K.

graphene (0001) sheets and the Al (111) planes, it is reasonable to assume that the interfacial spacing of the Al (111) layer near the interface is larger than the area without GNPs so that this interfacial area has a high dislocation density and microstrain within the Al lattice.

For a sample processed to 1 turn by HPT at 298 K as shown in Fig. 8(a), the graphene nanoplates have large orientation differences with the Al matrix (111) planes at lower numbers of turns which is consistent with the wide interfacial area. Due to the low shear strain induced at 1 turn of HPT, long straight and slightly curved GNPs are visible in the Al matrix in Fig. 8(b). At 473 K for 5 turns, the GNPs are dispersed and embedded within the grains, along the grain boundaries and in relatively large agglomerates in Fig. 9. The curvatures of the GNPs in Fig. 9 indicate heavy levels of local strain. Nevertheless, when the Al lattice (001) planes have the same orientation as the GNPs (0001) nanoplates, they merge together and it becomes difficult to clearly reveal the graphene nanoplates as in Fig. 9(b).

4.4. Factors affecting the electrical conductivity

The electrical conductivity is very sensitive to the microstructure of the metallic materials [81]. In practice, the electrical resistance of metals can be represented by Matthiessen's rule [59]:

$$\rho_{total} = \rho + \rho_{ss} + \rho_p + \rho_d + \rho_{gb} \quad (2)$$

where ρ_{total} is the total electrical resistance, ρ is the electrical resistivity of the lattice, ρ_{ss} is the resistivity due to solute atoms dissolved in the matrix, ρ_p is the resistivity added by second-phase precipitates, ρ_d is the resistivity due to dislocations present in the microstructure and ρ_{gb} is the resistivity due to grain boundaries.

The electrical conductivity of commercial purity Al in an annealed state with a coarse-grained structure is 62% IACS [82]. After HPT processing to 10 turns at 300 K, the electrical resistivity of commercial purity Al (99.5 wt%) was 30.5 nΩm [83], equivalent to 57.5% IACS. The drop of electrical conductivity in commercial purity Al arises from an electrical resistance increase due to the increased numbers of dislocations and grain boundaries ($\rho_d + \rho_{gb}$) after HPT processing.

In the fabricated graphene-Al nanocomposites, there is no significant effect from solute atoms (ρ_{ss}) and this term can be neglected. The GNPs as a reinforcement are different from second-phase precipitates and it is expected that the pi (π) electrons of

graphene will help to improve the conductivity. By contrast, the high dislocation densities and the significant grain refinement introduced by HPT processing increases the electrical resistance through ρ_d and ρ_{gb} and thereby reduces the electrical conductivity. This means the measured conductivity of the graphene-Al nanocomposite will arise from these competing factors.

The electrical conductivities recorded in Table 1 show that in HPT processing at 298 K for 5 and 20 turns the average conductivities are higher than the reported conductivity of 57.5% IACS in commercial purity Al when processed to 10 turns by HPT at 300 K [83]. This suggests that the reinforcement by graphene produces a small improvement in the conductivity. There is also a further increase when the nanocomposite is processed by HPT at 473 K for 20 turns. In practice, HPT processing at 473 K may introduce some oxidation and this will increase the resistivity [84] but, in addition, processing at 473 K produces a lower dislocation density and a coarser grain structure when compared to HPT processing at 298 K as shown in Fig. 7 and this will effectively reduce the resistivity. Finally, it should be noted that, although the electrical conductivity is increased after processing by HPT at 473 K (Table 1), the tensile strength (Fig. 12) and the hardness (Fig. 13) are reduced at this processing temperature and this may limit the use of this material in practical applications.

5. Summary and conclusions

1. Graphene-Al nanocomposites with 5% GNPs reinforced in an Al matrix were successfully fabricated using HPT processing at 298, 373 and 473 K. Agglomerated GNPs were fragmented during HPT processing and tended to become more dispersed in the Al matrix as the numbers of turns increased.
2. Significant microstructural refinement was achieved in the Al matrix with average grain sizes of ~70 and ~155 nm after processing through 20 turns at 298 and 473 K, respectively.
3. The interface between graphene and the Al matrix showed long aligned graphene nanoplates at low numbers of turns and curved graphene plates after higher numbers of turns. The graphene nanoplates were present both within the Al grains and along the grain boundaries.
4. The HPT-processed graphene-Al nanocomposites have improved hardness and tensile strength by comparison with HPT-processed commercial purity Al. Therefore, the graphene reinforcement effectively improves the material strength.
5. These nanocomposites show a small improvement in conductivity compared with HPT-processed commercial purity Al at 298 K which suggests that graphene tends to improve the material conductivity.

Acknowledgements

This work was supported by the European Research Council under ERC Grant Agreement no. 267464-SPDMETALS. The work was also supported by the National Science Centre, Poland, within the project SONATINA 1 “Synthesis of novel hybrid materials using High-Pressure Torsion”, under Grant Agreement No. 2017/24/C/ST8/00145.

References

[1] K.U. Kainer (Ed.), Metal Matrix Composites: Custom-made Materials for Automotive and Aerospace Engineering, Wiley-VCH, Weinheim, Germany, 2006.
[2] A.P. Mouritz (Ed.), Introduction to Aerospace Materials, Woodhead Publishing, Cambridge, U.K., 2012.
[3] Y. Huang, T.G. Langdon, The creep behaviour of discontinuously reinforced metal-matrix composites, JOM 55 (1) (2003) 15–20.
[4] E.P. Randviir, D.A.C. Brownson, C.E. Banks, A decade of graphene research: production, application and outlook, Mater. Today 17 (2014) 426–432.
[5] The Nobel Prize in Physics 2010, in: Graphene Compiled by the Class for Physics of Royal Swedish Academy of Sciences, The Nobel Foundation, Stockholm, Sweden, 5 October 2010.
[6] C. Lee, X. Wei, J.W. Kysar, J. Hone, Measurement of the elastic properties and intrinsic strength of monolayer graphene, Science 321 (2008) 385–388.
[7] A.A. Balandin, S. Ghosh, I. Bao, W. Calizo, D. Teweldebrhan, F. Miao, C. Lau, Superior thermal conductivity of single-layer graphene, Nano Lett. 8 (2008) 902–907.
[8] A.K. Geim, K.S. Novoselov, The rise of graphene, Nat. Mater. 6 (2007) 183–191.
[9] B. Li, W.H. Zhong, Review on polymer/graphite nanoplatelet nanocomposites, J. Mater. Sci. 46 (2011) 5595–5614.
[10] B.C. Kandpal, J. Kumar, H. Singh, Production technologies of metal matrix composite: a review, Int. J. Res. Mech. Eng. Technol. 4 (20) (2014) 27–32.
[11] N.H. Babu, S. Tzamtzis, B. Barekar, J.B. Patel, Z. Fan, Fabrication of metal matrix composites under intensive shearing, Solid State Phenom. 141–143 (2008) 373–378.
[12] I.A. Ibrahim, F.A. Mohamed, E.J. Lavernia, Particulate reinforced metal matrix composites – a review, J. Mater. Sci. 26 (1991) 1137–1156.
[13] R.S. Rana, R. Purohit, S. Das, Review of recent studies in Al matrix composites, Int. J. Sci. Eng. Res. 3 (6) (2012) 1–16.
[14] V. Viswanathan, T. Laha, K. Balani, A. Agarwal, S. Seal, Challenges and advances in nanocomposite processing techniques, Mater. Sci. Eng. R 54 (2006) 121–285.
[15] A. Feest, Materials and processing technology for PM MMCs, Met. Powder Rep. 47 (10) (1992) 40–45.
[16] M. Alipour, R. Eslami-Farsani, Synthesis and characterization of graphene nanoplatelets reinforced AA7068 matrix nanocomposites produced by liquid metallurgy route, Mater. Sci. Eng., A 706 (2017) 71, 28.
[17] H. Zhang, C. Xu, W. Xiao, K. Ameyama, C. Ma, Enhanced mechanical properties of Al5083 alloy with graphene nanoplates prepared by ball milling and hot extrusion, Mater. Sci. Eng., A 658 (2016) 8–15.
[18] J. Wang, Z. Li, G. Fan, H. Pan, Z. Chen, D. Zhang, Reinforcement with graphene nanosheets in aluminum matrix composites, Scripta Mater. 66 (2012) 594–597.
[19] P. Hidalgo-Manrique, S. Yan, F. Lin, Q. Hong, I.A. Kinloch, X. Chen, R.J. Young, X. Zhang, S. Dai, Microstructure and mechanical behaviour of aluminium matrix composites reinforced with graphene oxide and carbon nanotubes, J. Mater. Sci. 52 (2017) 13466–13477.
[20] G. Liu, B. Xiong, Effects of graphene content on microstructures and tensile property of graphene-nanosheets/aluminum composites, J. Alloy. Comp. 697 (2017) 31–36.
[21] S.J. Yan, S.L. Dai, X.Y. Zhang, C. Yang, Q.H. Hong, J.Z. Chen, Z.M. Lin, Investigating aluminium alloy reinforced by graphene nanoflakes, Mater. Sci. Eng., A 612 (2014) 440–444.
[22] X. Yang, T. Zou, C. Shi, E. Liu, C. He, Effect of carbon nanotube (CNT) content on the properties of in-situ synthesis CNT reinforced Al composites, Mater. Sci. Eng., A 660 (2016) 11–18.
[23] S.N. Alam, L. Kumar, Mechanical properties of aluminium based metal matrix composites reinforced with graphite nanoplatelets, Mater. Sci. Eng., A 667 (2016) 16–32.
[24] M. Rashad, F. Pan, Z. Yu, M. Asif, H. Lin, R. Pan, Investigation on microstructural , mechanical and electrochemical properties of aluminium composites reinforced with graphene nanoplatelets, Prog. Nat. Sci.: Met. Mater. Int. 25 (2015) 460–470.
[25] B. Chen, K. Kondoh, H. Imai, J. Umeda, M. Takahashi, Simultaneous enhancing strength and ductility of carbon nanotube/aluminium composites by improving bonding condition, Scripta Mater. 113 (2016) 158–162.
[26] A. Bhadauria, L.K. Singh, T. Laha, Effect of physio-chemically functionalized graphene nanoplatelet reinforcement on tensile properties of aluminum nanocomposite synthesized via spark plasma sintering, J. Alloy. Comp. 748 (2018) 783–793.
[27] A. Bisht, M. Srivastava, R.M. Kumar, I. Lahiri, D. Lahiri, Strengthening mechanism in graphene nanoplatelets reinforced aluminium composite fabricated through spark plasma sintering, Mater. Sci. Eng., A 695 (2017) 20–28.
[28] R. Rajeshkumar, V. Udhayabanu, A. Srinivasan, K.R. Ravi, Microstructural evolution in ultrafine grained Al-graphite composite synthesized via combined use of ultrasonic treatment and friction stir processing, J. Alloy. Comp. 726 (2017) 358–366.
[29] R.A. Rapp, X. Zheng, Thermodynamic consideration of grain refinement of aluminum alloys by titanium and carbon, Metall. Trans. A 22A (1991) 3071–3075.
[30] Y. Huang, T.G. Langdon, Advances in ultrafine-grained materials, Mater. Today 16 (3) (2013) 85–92.
[31] A. Bachmaier, R. Pippan, New procedure to generate stable nanocrystallites by severe plastic deformation, Intl Mater. Res. 58 (2013) 41–62.
[32] M. Khajouei-Nezhad, M.H. Paydar, R. Ebrahimi, P. Jenei, P. Nagy, J. Gubicza, Microstructure and mechanical properties of ultrafine-grained aluminum consolidated by high-pressure torsion, Mater. Sci. Eng., A 682 (2017) 501–508.
[33] A. Bachmaier, A. Hohenwarter, R. Pippan, New procedure to generate stable nanocrystallites by severe plastic deformation, Scripta Mater. 61 (2009) 1016–1019.
[34] R.Z. Valiev, R.S. Mishra, J. Groza, A.K. Mukherjee, Processing of nanostructured

nickel by severe plastic deformation consolidation of ball-milled powder, Scripta Mater. 34 (1996) 1443–1448.
[35] K. Edalati, Z. Horita, H. Fujiwara, K. Ameyama, Cold consolidation of ball-milled *titanium powders* using high-pressure torsion, Metall. Mater. Trans. 41A (2010) 3308–3317.
[36] A.P. Zhilyaev, G. Ringot, Y. Huang, J.M. Cabrera, T.G. Langdon, Mechanical behavior and microstructure properties of titanium powder consolidated by high-pressure torsion, Mater. Sci. Eng., A 688 (2017) 498–504.
[37] E. Menendez, G. Salazar-Alvarez, A.P. Zhilyaev, S. Surinach, M.D. Baro, J. Nogues, J. Sort, Cold Consolidation of metal-ceramic nanocomposite powders with large ceramic fractions, Adv. Funct. Mater. 18 (2008) 3293–3298.
[38] I. Sabirov, O. Kolednik, R. Pippan, Homogenization of metal matrix composites by high-pressure torsion, Metall. Mater. Trans. 36A (2005) 2861–2870.
[39] R.K. Islamgaliev, W. Buchgraber, Y.R. Kolobov, N.M. Amirkhanov, A.V. Sergueeva, K.V. Ivanov, G.P. Grabovetskaya, Deformation behavior of Cu-based nanocomposite processed by severe plastic deformation, Mater. Sci. Eng., A 319–321 (2001) 872–876.
[40] I.V. Alexandrov, Y.T. Zhu, T.C. Lowe, R.K. Islamgaliev, R.Z. Valiev, Consolidation of nanometer sized powders using severe plastic torsional straining, Nanostruct. Mater. 10 (1998) 45–54.
[41] T. Tokunaga, K. Kaneko, K. Sato, Z. Horita, Microstructure and mechanical properties of aluminum-fullerene composite fabricated by high pressure torsion, Scripta Mater. 58 (2008) 735–738.
[42] T. Tokunaga, K. Kaneko, Z. Horita, Production of aluminium-matrix carbon nanotube composite using high pressure torsion, Mater. Sci. Eng., A 490 (2008) 300–304.
[43] H. Asgharzadeh, S.-Y. Joo, H.S. Kim, Al/C60 nanocomposites fabricated by high-pressure torsion, Metall. Mater. Trans. 46A (2015) 1838–1842.
[44] S.H. Joo, S.C. Yoon, C.S. Lee, D.H. Nam, S.H. Hong, H.S. Kim, Microstructure and tensile behaviour of Al and Al-matrix carbon nanotube composites processed by high pressure torsion of the powders, J. Mater. Sci. 45 (2010) 4652–4658.
[45] M.R. Akbarpour, M. Farvizi, D.J. Lee, H. Rezaei, H.S. Kim, Effect of high-pressure torsion on the microstructure and strengthening mechanism of hot-consolidated Cu-CNT nanocomposite, Mater. Sci. Eng., A 638 (2015) 289–295.
[46] P. Jenei, J. Gubicza, E.Y. Yoon, H.S. Kim, J.L. Lábár, High temperature thermal stability of pure copper and copper-carbon nanotube composites consolidated by high pressure torsion, Composites Part A 51 (2013) 71–79.
[47] P. Jenei, E.Y. Yoon, J. Gubicza, H.S. Kim, J.L. Lábár, T. Ungár, Microstructure and hardness of copper-carbon nanotube composites consolidated by high pressure torsion, Mater. Sci. Eng., A 528 (2011) 4690–4695.
[48] H. Li, A. Misra, Y. Zhu, Z. Horita, C.C. Koch, T.G. Holesinger, Processing and characterization of nanostructured Cu-carbon nanotube composites, Mater. Sci. Eng., A 523 (2009) 60–64.
[49] R. Kulagin, Y. Beygelzimer, Y. Ivanisenko, A. Mazilkin, H. Hahn, High pressure torsion: from laminar flow to turbulence, IOP Conf. Ser. Mater. Sci. Eng. 194 (1–6) (2017), 012045.
[50] K. Edalati, H. Emami, Y. Ikeda, H. Iwaoka, I. Tanaka, E. Akiba, Z. Horita, New nanostructured phases with reversible hydrogen storage capability in immiscible magnesium-zirconium system produced by high-pressure torsion, Acta Mater. 108 (2016) 293–303.
[51] N. Ibrahim, M. Peterlechner, F. Emeis, M. Wegner, S.V. Divinski, G. Wilde, Mechanical alloying via high-pressure torsion of the immiscible $Cu_{50}Ta_{50}$ system, Mater. Sci. Eng., A 685 (2017) 19–30.
[52] R.B. Figueiredo, P.R. Cetlin, T.G. Langdon, Using finite element modeling to examine the flow processes in quasi-constrained high-pressure torsion, Mater Sci Eng. A 528 (2011) 8198–8204.
[53] G.E. Dieter, Mechanical Metallurgy, McGraw-Hill, New York, NY, USA, 1988, p. 304.
[54] R.B. Figueiredo, S. Sabbaghianrad, A. Giwa, J.R. Greer, T.G. Langdon, Evidence for exceptional low temperature ductility in polycrystalline magnesium processed by severe plastic deformation, Acta Mater. 122 (2017) 322–331.
[55] Copper Wire Tables (Technical report), Circular of the Bureau of Standards No.31, 3d ed., United States Department of Commerce, Washington DC, October 1914.
[56] A.C. Ferrari, J.C. Meyer, V. Scardaci, C. Casiraghi, M. Lazzeri, F. Mauri, S. Piscanec, D. Jiang, K.S. Novoselov, S. North, A.K. Gem, Raman spectrum of graphene and graphene layers, Phys. Rev. Lett. 97 (2006), 187401-18704.
[57] C. He, N. Zhao, C. Shi, X. Du, J. Li, H. Li, Q. Cui, An approach to obtaining homogeneously dispersed carbon nanotubes in Al powders for preparing reinforced Al-matrix composites, Adv. Mater. 19 (2007) 1128–1132.
[58] M. Kawasaki, Different models of hardness evolution in ultrafine-grained materials processed by high-pressure torsion, J. Mater. Sci. 49 (2014) 18–34.
[59] P.L. Rositter, The Electrical Resistavity of Metals and Alloys, Cambridge University Press, Cambridge, U.K., 2003.
[60] R.K. Islamgaliev, K.M. Nesterov, Y. Champion, R.Z. Valiev, Enhanced strength and electrical conductivity in ultrafine-grained Cu-Cr alloy processed by severe plastic deformation, IOP Conf. Ser. Mater. Sci. Eng. 63 (1–6) (2014), 012118.
[61] S.V. Dobatkin, J. Gubicza, D.V. Shangina, N.R. Bochvar, N.Y. Tabachkova, High strength and good electrical conductivity in Cu-Cr alloys processed by severe plastic deformation, Mater. Lett. 153 (2015) 5–9.
[62] R.Z. Valiev, YuV. Ivanisenko, E.F. Rauch, B. Baudelet, Structure and deformation behaviour of Armco iron subjected to severe plastic deformation, Acta Mater. 44 (1996) 4705–4712.
[63] Y. Cao, Y.B. Wang, S.N. Alhajeri, X.Z. Liao, W.L. Zheng, S.P. Ringer, T.G. Langdon, Y.T. Zhu, A visualization of shear strain in processing by high-pressure torsion, J. Mater. Sci. 45 (2010) 765–770.
[64] Y. Cao, M. Kawasaki, Y.B. Wang, S.N. Alhajeri, X.Z. Liao, W.L. Zheng, S.P. Ringer, Y.T. Zhu, T.G. Langdon, Unusual macroscopic shearing patterns observed in metals processed by high-pressure torsion, J. Mater. Sci. 45 (2010) 4545–4553.
[65] Y. Cao, Y.B. Wang, R.B. Figueiredo, L. Chang, X.Z. Liao, M. Kawasaki, W.L. Zheng, S.P. Ringer, T.G. Langdon, Y.T. Zhu, Three-dimensional shear-strain patterns induced by high-pressure torsion and their impact on hardness evolution, Acta Mater. 59 (2011) 3903–3914.
[66] Y. Huang, M. Kawasaki, T.G. Langdon, Influence of anvil alignment on shearing patterns in high-pressure torsion, Adv. Eng. Mater. 15 (2013) 747, 655.
[67] Y. Huang, M. Kawasaki, T.G. Langdon, An investigation of flow pattern and hardness distribution using different anvil alignments in high-pressure torsion, J. Mater. Sci. 48 (2013) 4533–4542.
[68] Y.Z. Tian, X.H. An, S.D. Wu, Z.F. Zhang, R.B. Figueiredo, N. Gao, T.G. Langdon, Direct observations of microstructural evolution in a two-phase Cu-Ag alloy processed by high-pressure torsion, Scripta Mater. 63 (2010) 65–68.
[69] M. Pouryazdan, B.J.P. Kaus, A. Rack, A. Ershov, H. Hahn, Mixing instabilities during shearing of metals, Nat. Commun. 8 (1–7) (2017) 1611.
[70] I. Sabirov, O. Kolednik, R.Z. Valiev, R. Pippan, Equal channel angular pressing of metal matrix composites: effect on particle distribution and fracture toughness, Acta Mater. 53 (2005) 4919–4930.
[71] J. Guo, J.M. Rosalie, R. Pippan, Z. Zhang, Revealing the microstructural evolution in Cu-Cr nanocrystalline alloys during high pressure torsion, Mater. Sci. Eng., A 695 (2017) 350–359.
[72] S.N. Alhajeri, M. Kawasaki, N. Gao, T.G. Langdon, The evolution of homogeneity during processing of aluminium alloys by HPT, Mater. Sci. Forum 667–669 (2011) 277–282.
[73] M. Kawasaki, S.N. Alhajeri, C. Xu, T.G. Langdon, The development of hardness homogeneity in pure aluminum and aluminum alloy disks processed by high-pressure torsion, Mater. Sci. Eng., A 529 (2011) 345, 251.
[74] A. Vorhauer, R. Pippan, On the homogeneity of deformation by high pressure torsion, Scripta Mater. 51 (2004) 921–925.
[75] O. Andreau, J. Gubicza, N.X. Zhang, Y. Huang, P. Jenei, T.G. Langdon, Effect of short-term annealing on the microstructures and flow properties of an Al-1% Mg alloy processed by high-pressure torsion, Mater. Sci. Eng., A 615 (2014) 231–239.
[76] Y. Huang, R.B. Figueiredo, T. Baudin, F. Brisset, T.G. Langdon, Evolution of strength and homogenity in a magnesium AZ31 alloy processed by high-pressure torsion at different temperatures, Adv. Eng. Mater. 14 (2012) 1018–1026.
[77] N. Maury, N.X. Zhang, Y. Huang, A.P. Zhilyaev, T.G. Langdon, A critical examination of pure tantalum processed by high-pressure torsion, Mater. Sci. Eng., A 638 (2015) 174–182.
[78] J. Wang, Z. Li, G. Fan, H. Pan, Z. Chen, D. Zhang, Reinforcement with graphene nanosheets in aluminium matrix composites, Scripta Mater. 66 (2012) 594–597.
[79] W. Lee, S. Jang, M.J. Kim, J.-M. Myoung, Interfacial interactions and dispersion relations in carbon-aluminium nanocomposite systems, Nanotechnology 19 (1–13) (2008) 285701.
[80] Y. Qiu, L.G. Hector, N. Ooi, J.B. Adams, A first principles study of adhesion and adhesive transfer at Al (111)/graphite (0001), Surf. Sci. 581 (2005) 155–168.
[81] R.Z. Valiev, M.Yu Murashkin, I. Sabirov, A nanostructureal design to produce high-strength Al alloys with enhanced electrical conductivity, Scripta Mater. 76 (2014) 13–16.
[82] E.V. Bobruk, M.Yu Murashkin, V.U. Kazykhanov, R.Z. Valiev, Aging behavior and properties of ultrafine-grained aluminum alloys of Al-Mg-Si system, Rev. Adv. Mater. Sci. 31 (2012) 109–115.
[83] A.M. Mavlyutov, A.S. Bondarenko, M.Yu Murashkin, E.V. Boltynjuk, R.Z. Valiev, T.S. Orlova, Effect of annealing on microhardness and electrical resistivity of nanostructured SPD aluminium, J. Alloy. Comp. 698 (2017) 539–546.
[84] Y. Miyajima, S.-Y. Komatsu, M. Mitsuhara, S. Hata, H. Nakashima, N. Tsuji, Change in electrical resistivity of commercial purity aluminium severely plastic deformed, Phil. Mag. 90 (2010) 4475–4488.

Journal of Alloys and Compounds 968 (2023) 171928

Contents lists available at ScienceDirect

Journal of Alloys and Compounds

journal homepage: www.elsevier.com/locate/jalcom

Using direct high-pressure torsion synthesis to produce aluminium matrix nanocomposites reinforced with carbon nanotubes

Maria Emerla [a], Piotr Bazarnik [a,*], Yi Huang [b,c], Małgorzata Lewandowska [a], Terence G. Langdon [b]

[a] Warsaw University of Technology, Faculty of Materials Science and Engineering, Woloska 141, 02-507 Warsaw, Poland
[b] Materials Research Group, Department of Mechanical Engineering, University of Southampton, Southampton SO17 1BJ, United Kingdom
[c] Department of Design and Engineering, Faculty of Science and Technology, Bournemouth University, Poole, Dorset BH12 5BB, United Kingdom

ARTICLE INFO

Keywords:
Aluminium
Carbon nanotubes
High-pressure torsion
Nanocomposites
Thermal stability

ABSTRACT

Aluminium matrix nanocomposites reinforced with carbon nanotubes were fabricated in a new way by direct synthesis using high-pressure torsion (HPT). Aluminium of 99.99 % and 99.5 % purities were used as matrix materials with carbon nanotubes in amounts of 0.5 and 1 wt% as reinforcement. The HPT processing led to extensive grain size refinement which was significantly higher than for pure metals and to a relatively uniform distribution of the fillers. The grain size of the matrix was smaller for Al99.5 compared to Al99.99 while the particle spatial distribution was more homogenous for the Al99.99 matrix. This was attributed to a lower hardness and higher plasticity of Al 99.99 alloy. The addition of carbon nanotubes also improved the thermal stability of the ultrafine-grained structure, especially if homogenously distributed as for the Al99.99 matrix nanocomposites.

1. Introduction

The continuous development of applied technologies in the automotive, aerospace and electronics industries, as well as contemporary efforts to protect the natural environment by reducing emissions of exhaust and greenhouse gases, have contributed to numerous studies seeking effective methods to significantly improve the mechanical properties of metal alloys and composites with favourable strength-to-density ratios [1–4]. One of the developmental paths leading to the improvement of strength, hardness and wear resistance of such metallic materials is a significant refinement of their grain structure where this can be achieved by, among others, the use of processing through the application of severe plastic deformation (SPD) [5–9]. Among a number of SPD methods, High-Pressure Torsion (HPT) is considered the most effective in terms of grain size refinement due to the large plastic strains introduced to the material [5,7].

Several studies have demonstrated that HPT processing leads to a significant increase in hardness and tensile strength in many engineering materials [7,10,11] due to the production of severe grain refinement to the sub-micrometric and nanometric sizes. Nevertheless, the ability of each material to achieve grain refinement is limited so that ultimately the grain size saturates at a certain level [11–17]. Moreover, the purity level of metals also has a significant impact on the final structural refinement. For example, high purity Al (99.9999 %) undergoes HPT-induced softening due to grain growth during the processing whereas a commercial purity Al (99.5 %) exhibits a strain hardening during processing [18]. This softening effect is caused by the high mobility of dislocations and the role of grain boundaries as dislocations sinks which are significantly influenced by the presence of impurity atoms [19].

Additionally, ultra-fine grained (UFG) and nanocrystalline (NC) metals are inherently thermally unstable so that annealing, even at low temperatures, leads to recrystallisation and grain growth of the microstructure and this is deleterious to the material properties [20–22].

In order to improve the thermal stability of these types of materials and stabilise the grain sizes at elevated temperature, some limited attempts have been made to create metal matrix nanocomposites reinforced with various particles such as Al_2O_3, multi-walled boron nitride nanotubes (BNNTs),or carbon nanotubes (CNTs) [23–25]. Nano-particles uniformly distributed within the metallic matrix constitute a pinning effect on lattice defects, such as dislocations and grain boundaries, thereby stabilising the UFG microstructure and expanding

* Corresponding author.
E-mail address: piotr.bazarnik@pw.edu.pl (P. Bazarnik).

https://doi.org/10.1016/j.jallcom.2023.171928
Received 6 June 2023; Received in revised form 8 August 2023; Accepted 27 August 2023
Available online 28 August 2023

the temperature window for their potential technological applications.

There are only a few reports describing Al-CNTs nanocomposites subjected to HPT processing [26–28]. Furthermore, a review of these reports shows that all of the nanocomposites were fabricated in multi-stage procedures in which the HPT processing was always preceded by powder metallurgy synthesis such as ball milling of the powders followed by conventional sintering [29,30], hot pressing [31,32], spark plasma sintering [33,34] or hot extrusion[34]. The aim of the present work was to remove this time-consuming pre-treatment step and to produce an Al-CNTs nanocomposite using HPT as a direct mixing method by forming a sandwich of CNTs between two pure Al plates with different purity levels ranging from 99.5 % to 99.99 %. This objective was inspired by recent publications describing the fabrication of metal composites and metastable alloys by directly packing alternating disks of different metals for the HPT processing [35–37]. To date, only some limited publications describe any thermal stability studies of these types of materials [28,38]. Accordingly, the present report provides a detailed description of the mechanical properties, thermal stability and microstructural characteristics of Al-CNTs nanocomposites produced by this new procedure of direct HPT processing.

2. Experimental material and procedures

High and commercial purity aluminium, Al99.99 and Al99.5 %, respectively, in the form of rods of 10 mm diameter were used as a matrix while multi-walled CNTs with tube diameters of 2–5 nm were used as the reinforcement. The Al-CNTs nanocomposites with 0.5 and 1 wt% of CNTs were produced by direct HPT synthesis. Specifically, a stack of two aluminium disks with diameters of 10 mm and thicknesses of 0.4 mm, with CNTs placed between them, were subjected to HPT processing under a pressure of 1 GPa through a total number of 50 turns. Fig. 1 schematically illustrates the process for the direct synthesis of nanocomposites by HPT. In addition, 1 mm thick aluminium disks of both purities were HPT processed under the same pressure for up to 10 revolutions and these disks served as reference samples.

To investigate the thermal stability, the HPT-processed Al-CNTs nanocomposites and HPT-processed aluminium disks were annealed for 1 h at temperatures of 100ºC, 150ºC, 200ºC, 250ºC, 300ºC, 350ºC or 400ºC. The annealing was conducted in a protective argon atmosphere and the accuracy of maintaining the set temperature was ± 5°C.

Initial observations of cross-sections of the disk samples were made using a Zeiss Axio Observer optical microscope (OM). These observations were carried out on disk samples after 10, 20 and 50 revolutions in order to determine the level of mixing of the CNTs with the matrix material and also to evaluate the quality of bonding along the diameter of the disk. Images of the entire cross-sections of each sample were obtained by assembling a series of photographs using the Adobe Photoshop graphics program. The samples for OM observations were prepared by cutting the disks along their diameters using a circular saw, encapsulating the samples in resin, grinding the samples on sandpaper and then polishing the samples using a 1 μm diamond suspension.

Advanced structural observations of the fabricated nanocomposites

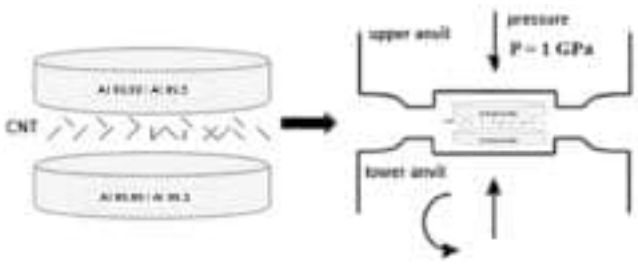

Fig. 1. Schematic of sandwich carbon nanotubes between two aluminium disks for HPT processing.

before and after annealing were collected using a scanning electron microscope (SEM) Hitachi Su8000 operating in back-scattered electron (BSE) mode. Observations were carried out on cross-sectional planes approximately 1 mm from the edges of the disks. Samples for SEM investigations were prepared using an Hitachi IM4000 ion milling system. This procedure gives high-quality surfaces for observation due to the ion beam polishing which eliminates any deformation, stresses and/or the formation of oxide layers. The surface quality after the ion milling process permitted the structure to be observed in so-called channel contrast in the SEM.

The average grain sizes together with the standard deviations, were measured based on SEM/BSE image analysis. NIS-Elements BR 3.2 software was used to analyse the grain size and its variability and GIMP 2 software was used to prepare the SEM images for analysis. Detailed microstructural observations were performed using a scanning-transmission electron microscope (STEM) Hitachi HD-2700 operating at an accelerating voltage of 200 kV. Samples for the STEM observations were prepared using a focused ion beam facility (FIB) Hitachi NB5000.

A Falcon 503 hardness tester was employed to determine the Vickers hardness of the samples before and after annealing using a 200 g load for each measurement. Hardness values were recorded on cross-sections of the specimens with a 0.3 mm distance between each indentation. Hardness measurements for the annealed specimens were taken approximately 1 mm from the edge of the disk with a 0.2 mm spacing between indentations. Prior to these hardness measurements, the specimens were encapsulated in resin and the cross-sectional surfaces of the disks were mechanically ground and then polished using a 3 μm anhydrous diamond suspension in order to remove any oxides.

3. Experimental results

3.1. Microstructure of Al-CNTs nanocomposites

Fig. 2 shows a series of OM images of the cross-sectional areas of Al99.5 and Al99.99 with 0.5 % and 1 % of CNTs nanocomposites after HPT processing through 10, 20 and 50 turns. These images provide clear evidence for the gradual evolution towards nanocomposites. A large structural variation can be observed depending on the number of rotations. With increasing numbers of HPT turns, there is an obvious improvement in the distribution of CNTs in the aluminium matrix and thus a reduction in the number of large and visible CNTs agglomerates. Since the CNTs were applied directly between two aluminium disks, they tended to accumulate along the horizonal axis of the disk sample especially near the centre of each disk. For all nanocomposites, more dispersed CNT particles in the aluminium matrix are observed with higher numbers of turns and increasing distance from the disk centres. Inspection shows that samples of all nanocomposite types after 10 and 20 HPT rotations have visible long bands of CNTs agglomerates while in the samples after 50 rotations such bands are much less visible so that there is an improved dispersion of CNTs throughout the samples. The only exception is the Al99.5–1 % CNTs sample for which a significant proportion of CNTs agglomerates remains visible in the central regions. In addition, it is noticeable that in the nanocomposites based on Al99.99 the CNTs particles exhibit a higher tendency to be uniformly distributed in the matrix by comparison with Al99.5.

The polished surfaces of the Al-CNTs samples were further observed by SEM at higher magnifications to reveal the grain structure. The results are presented in Fig. 3 and for comparative reasons were complemented with images for pure aluminium samples of both purities processed through 10 HPT turns. These microstructures were evaluated quantitatively using a computer-aided image analyser. The grain sizes described in terms of the equivalent grain diameter (d) and the standard deviation (SD) are summarised in Table 1.

The average grain sizes in pure Al99.5 and Al99.99 after 10 HPT turns were 670 and 830 nm (Fig. 3), respectively, and this is consistent with results reported for materials processed using conventional SPD

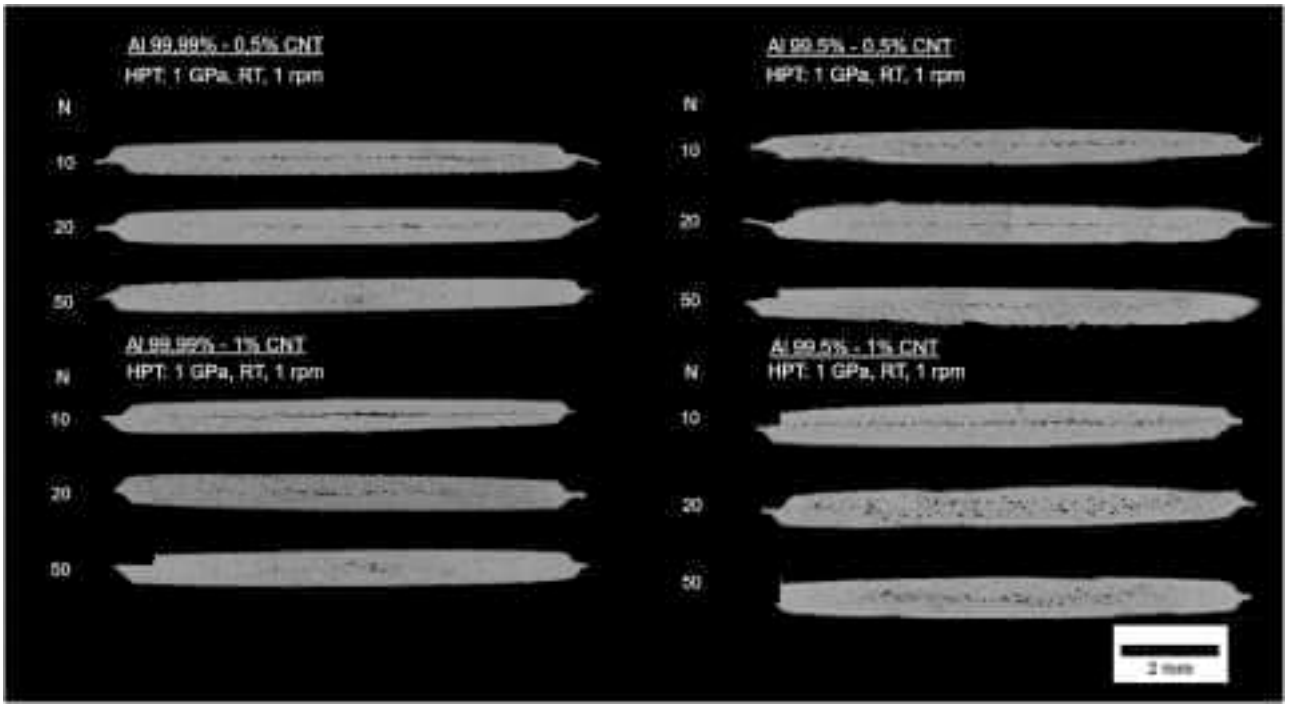

Fig. 2. Light microscopy views of cross-sections of HPT-processed composites.

methods [18,39,40]. The addition of CNTs led to more intense grain refinement in the metal matrix in both nanocomposites, as is evident from Fig. 3 and Table 1. After 10 HPT revolutions, the grain size was reduced to ~800 nm in the Al99.99 matrix nanocomposites and below ~450 nm in the Al99.5 matrix nanocomposites. A further decrease in grain size was observed with increasing numbers of turns such that, after 50 turns, the average grain sizes of the aluminium matrices for all nanocomposites was below ~250 nm (Table 1). The matrix structure in all nanocomposites consisted of equiaxed grains and the grain size scatter was typical for fairly homogenous materials. The smallest grain size in the aluminium matrix of ~190 nm was obtained for the Al99.5 matrix nanocomposite containing 1 % of CNTs.

It is important to note that, although the structure of the matrix is reasonably homogeneous, the distribution of CNTs is not homogeneous. Fig. 4a and b show SEM images of the edge region for Al99.99 containing 0.5 % of CNT after 10 and 50 HPT turns, respectively. It is apparent that the CNTs are mostly distributed in the form of micro-sized agglomerates and in the form of chains along grain boundaries after 10 revolutions whereas after 50 revolutions many of these larger agglomerates are fragmented to sizes of ~20–200 nm and they become uniformly distributed in the aluminium matrix. However, the size and the density of the CNTs agglomerates strongly depends on the purity of the aluminium matrix. Fig. 4c and d were taken at the same magnification and they illustrate the microstructures after 50 HPT revolutions for Al99.99 – 0.5 % CNTs and Al99.5–0.5 % CNTs, respectively. These images show that the agglomerates are smaller and their density is lower in the purer metal and this tendency was observed in all samples.

In order to better describe the distribution of CNTs in the matrix, a series of SEM images was analysed in terms of the average size and the surface fraction of CNTs agglomerates that were larger than ~150 nm and the results are summarised in Table 2. In general, for small numbers of revolutions it is apparent that mostly large agglomerates dominate the structures with their size and surface fraction associated with the amount of CNTs used. With increasing numbers of revolutions, there is an observed decrease in both the size of the agglomerates and their surface fraction. It is also be noted that this tendency is less for the Al99.5 matrix than for the Al99.99 matrix.

Figs. 5 and 6 shows exemplary STEM images of, respectively, Al99.99 and Al99.5 samples containing 0.5 % of CNTs processed through 50 HPT revolutions. The comparative HAADF and BF images of Al99.99 (Fig. 5a, b) and Al99.5 (Fig. 6a, b) matrix nanocomposites confirmed the significant grain refinement with an average grain size of ~200 nm in both aluminium matrices and large differences in the size and distribution of CNTs agglomerates which are shown black in the HAADF contrast. The agglomerates in the Al99.5 matrix nanocomposite are larger and their number is greater than in the Al99.99 matrix nanocomposite. At the same time, only a fraction of individual CNTs are visible in the matrix of the Al99.5 nanocomposite (Fig. 6c) whereas in the Al99.99 nanocomposite there are a number of small (<100 nm) uniformly distributed agglomerates (Fig. 5b) as well as individual CNTs (Fig. 5c) within the matrix.

3.2. *Mechanical properties of Al-CNTs nanocomposites*

The microhardness of the fabricated nanocomposites were measured on the cross-sections of the disks and the results are shown in Fig. 7a and b as a function of distance from the disk centres. These plots demonstrate that HPT processing has enhanced the hardness in both types of nanocomposites and, in general, the hardness of the nanocomposites increases with increasing numbers of revolutions and concentration of CNTs. The highest values of hardness were obtained in samples containing 1 wt% of CNTs subjected to 50 HPT rotations. Thus, the hardness values increased from 25 and 50 Hv for HPT-processed Al99.99 and Al99.5 pure metallic samples to 80 and 110 Hv, respectively, at the edges of the HPT-processed nanocomposites containing 1 wt% of CNTs. Although the hardness after 50 HPT turns was higher for the Al99.5 matrix nanocomposites, the hardness distribution was more homogeneous for the Al99.99 matrices.

The hardness for the Al99.99 matrix nanocomposites rises rapidly during HPT and already after 10 turns it is almost two times higher in the edge regions than in the pure metal after HPT (Fig. 7a). It is also apparent that there is a significant impact of the CNTs content on the hardness distribution for lower numbers of turns. Nanocomposites containing 1 wt% of CNTs exhibit higher hardness than those with 0.5 %

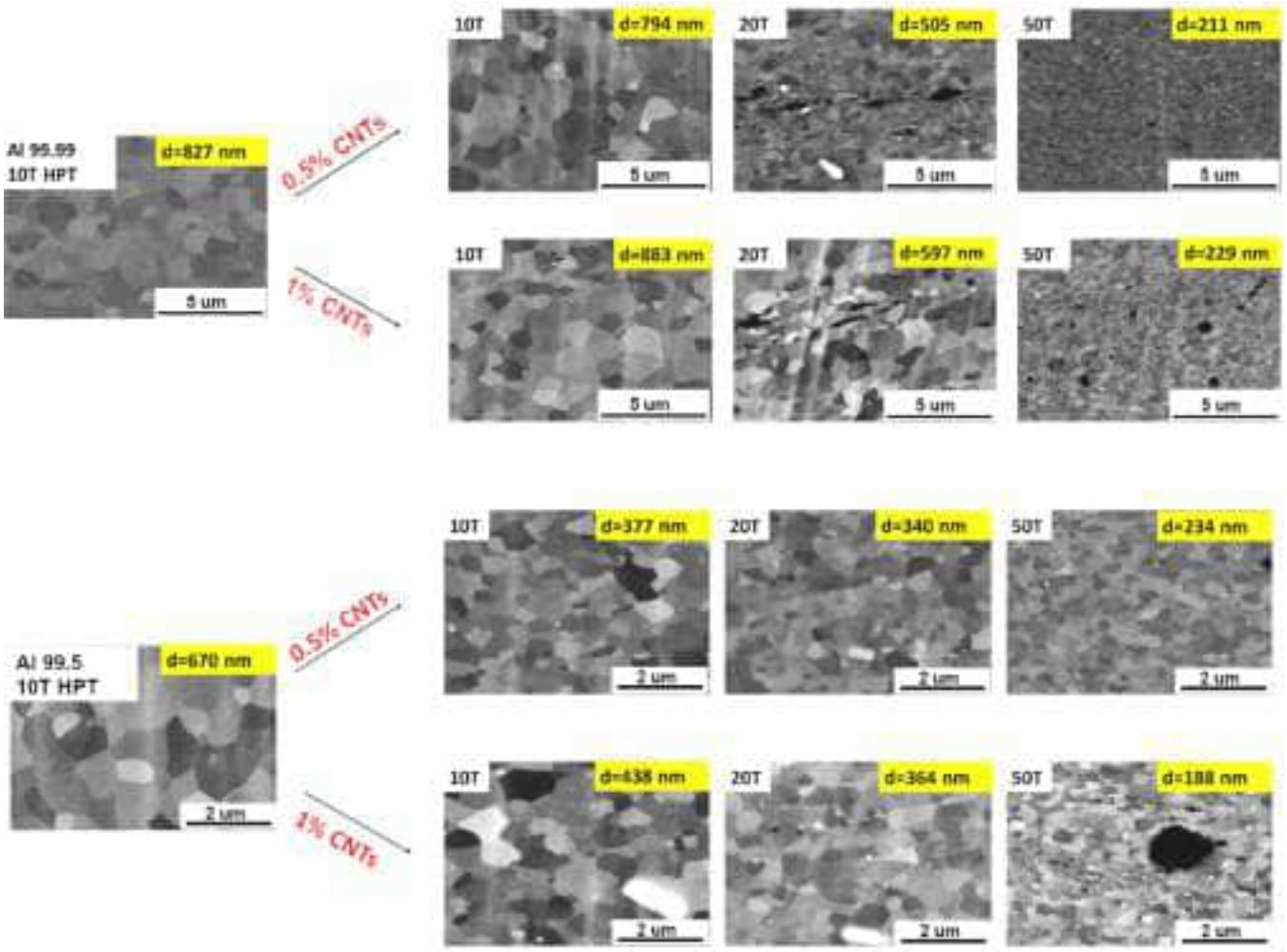

Fig. 3. Microstructure of Al 99.99 and Al 99.5 alloys after HPT processing and the microstructure of their composites containing 0.5 % and 1 % of CNTs after various numbers of HPT revolutions.

Table 1
Summary of grain sizes and standard deviations from grain sizes for individual samples.

Sample	Turns nr.	d [nm]	SD [nm]
Al 99,5 %	10	670	216
Al 99,5 % 0,5 % CNT	10	377	150
	20	340	136
	50	234	95
Al 99,5 % 1 % CNT	10	438	176
	20	364	137
	50	188	72
Al 99,99 %	10	827	352
Al 99,99 % 0,5 % CNT	10	794	377
	20	506	138
	50	211	77
Al 99,99 % 1 % CNT	10	883	417
	20	597	262
	50	229	84

which is clearly visible in the samples after 20 HPT turns for which the difference in hardness was higher than 15 Hv. Further processing up to 50 turns gave an additional hardness increase up to ~75 Hv in the edge regions with some small areas of lower hardness near the centre of the disk.

In the Al99.5 matrix nanocomposites, the results of hardness in the samples having 0.5 and 1 wt% of CNTs after 10 and 20 turns are close and only ~10 Hv higher than for pure aluminium after HPT processing and the hardness values are almost homogeneous across the disk diameters. By contrast, after 50 revolutions there is a further increase in hardness values in the edge regions such that the hardness values reach ~75 and ~100 Hv for nanocomposites containing 0.5 and 1 wt% of CNTs, respectively.

3.3. Thermal stability of Al-CNTs nanocomposites

Fig. 8 shows the average hardness measured at the disk edges for the nanocomposites after 50 HPT turns and subsequent annealing at temperatures ranging from 100 °C to 400 °C for 1 h. These results are also complemented with the hardness values for the initial materials after 10 HPT turns. The results show that UFG Al99.99 and UFG Al99.5 are thermally stable up to 150 °C and 200 °C, respectively, and these results are in agreement with earlier reports [28,41]. As can be seen, the addition of CNTs contributes to increases in the hardness for both types of nanocomposites compared to the matrix as well as to their thermal stability.

The results for the Al99.99 matrix nanocomposites indicate that the hardness remains stable until annealing at a temperature of 400 °C where there is a small drop in the hardness values (Fig. 8a). The thermal stability of the Al99.5 based nanocomposite is not as good as the Al99.99 material. Furthermore, the hardness changes more significantly and the drop strongly depends on the concentration of the CNTs. Thus, the average hardness of the Al99.5 composites is reduced after annealing at 250 °C for 0.5 wt% of CNTs by ~ 16 % and for 1 wt% of CNTs composite

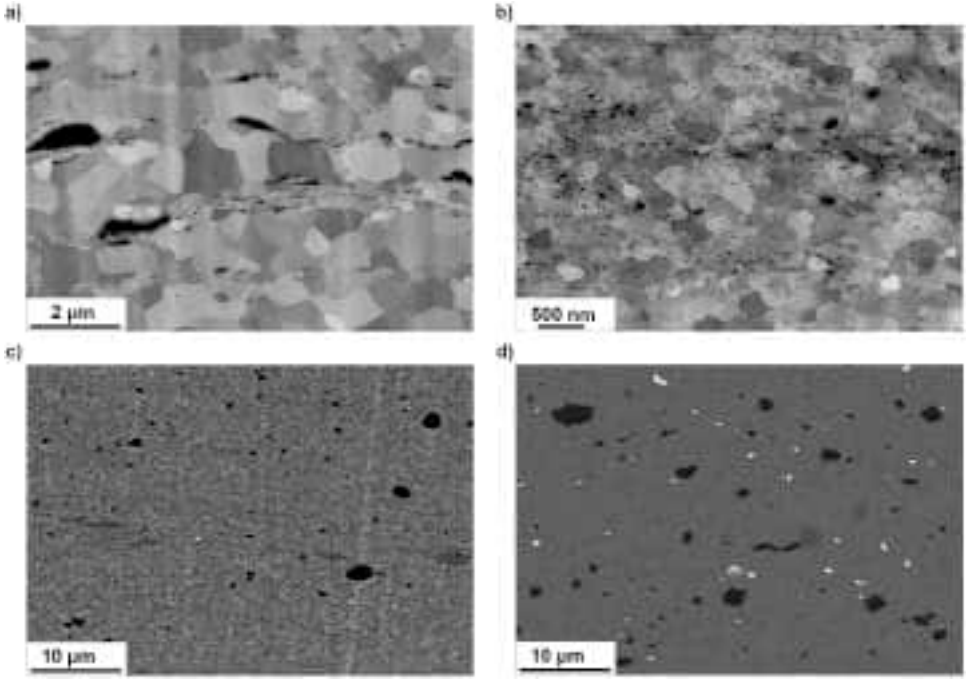

Fig. 4. SEM images of Al99.99 + 0.5 % CNTs composite after a) 10 and b) 50 HPT turns, together with comparative microstructural images taken at the same magnification for c) Al99.99 + 0.5 % CNTs and d) Al99.5 + 0.5 % CNTs, where dark regions are CNTs agglomerates.

Table 2
The average size of CNTs agglomerates and their fraction surface.

Sample		d [nm]	SD [nm]	surface fraction [%]
99.99	0.5 % CNT 10 T	590	3100	5.7
	0.5 % CNT 20 T	440	550	-
	0.5 % CNT 50 T	300	260	1.2
99.99	1 % CNT 10 T	740	4580	8.9
	1 % CNT 20 T	580	890	-
	1 % CNT 50 T	360	707	1.8
99.5	0.5 % CNT 10 T	910	8410	6.8
	0.5 % CNT 20 T	620	1550	-
	0.5 % CNT 50 T	520	950	3.4
99.5II	1 % CNT 10 T	1355	9560	9.2
	1 % CNT 20 T	750	2125	-
	1 % CNT 50 T	550	1045	4.5

after annealing at 350 °C by ~ 30 %, respectively, and a further drop of hardness is observed with annealing temperature. Nevertheless, it is interesting to note the standard deviations of the values for these results which are marked in Fig. 8b since, although the results for the nanocomposites having 0.5 % of CNTs seem to be stable up to 300 °C, at the same time they show a very large standard deviation by up to 18 Hv.

Such behaviour is explained by conducting microstructural observations. An SEM analyses of the Al99.99 matrix nanocomposites revealed their excellent thermal stability as illustrated in Fig. 9. Thus, the grain structure was stable up to a temperature of 400 °C where only slight grain growth was observed in both nanocomposites by only 10–15 % compared to the composites after HPT processing. The Al99.5 matrix nanocomposites maintained a homogeneous ultrafine-grained structure with an average grain size comparable to the material before annealing up to temperatures of 350 °C and 250 °C for the nanocomposites containing 0.5 % and 1 % of CNTs, respectively (see Figs. 10 and 11). Above these temperatures, there was an onset in the formation of a heterogeneous structure in both nanocomposites such that single large recrystallised grains, up to tens to hundreds of μm in size, surrounded by nanosized regions were observed in these structures. As the temperature increased, more regions of heterogeneous grain growth appeared in the microstructure. Moreover, it should be emphasised that in the sample

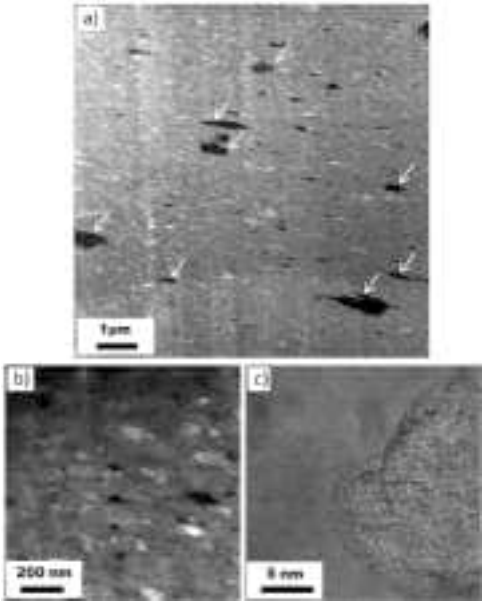

Fig. 5. STEM and HAADF a), b) images showing the microstructures of samples Al99.99 + 0.5 %CNTs processed by 50 HPT turns (with marked dark regions of CNTs biggest agglomerates), together with high resolution STEM image c) showing the interface between CNTs and the Al matrix.

containing 1 % of CNTs heterogeneous grain growth was more intense than in the sample containing 0.5 % of CNTs. After annealing at 400 °C, most of microstructure consisted of fully recrystallised large grains but there remained some places with highly refined grains although their fraction was small. Fig. 12 shows an STEM image of such a heterostructure cut from the Al99.5 sample containing 0.5 % of CNTs annealed at 350 °C. In this image there are regions with large recrystallised grains coexisting with those having UFG dimensions. In addition, there are large agglomerates (marked with arrows) of CNTs and single tubes

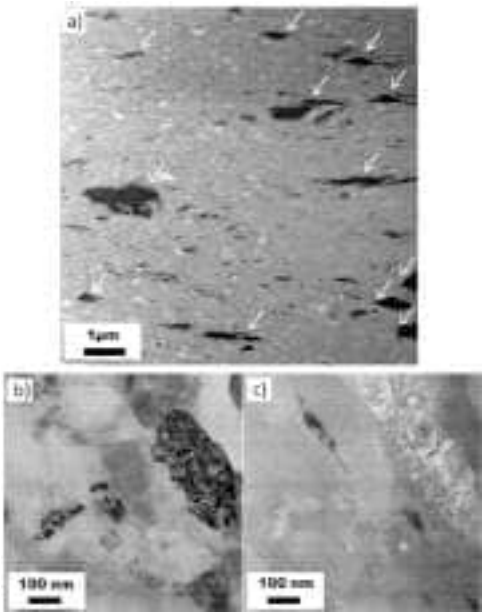

Fig. 6. STEM and HAADF images showing the microstructures of samples Al99.5 + 0.5 %CNTs processed by 50 HPT turns (with marked dark regions of CNTs biggest agglomerates), together with high resolution STEM image.

located at grain boundaries within the microstructure. At the same time it should be noted that these single CNTs are located mainly in areas with small grains.

4. Discussion

4.1. Fabrication of Al-CNTs nanocomposites via direct HPT synthesis

The results of this research demonstrate that Al-CNTs nanocomposites with fairly homogenous microstructures may be achieved by direct mixing in HPT processing. Comparing the microstructures of the processed nanocomposites with the matrix materials (Al99.99 and Al99.5) after HPT, it is shown that the addition of CNTs leads to a significantly smaller grain size in the HPT process. The effect of the addition of second phase particles on enhanced grain refinement in HPT processing was previously reported for other systems [6,30] but the present results are the first demonstration using a direct synthesis method. This phenomenon is explained by the pinning effect imposed by nanoparticles on lattice defects, such as dislocations and grain boundaries, which effectively reduces the ability of a material to exhibit recovery and recrystallisation during processing [42–44].

In these nanocomposites, the purity of the matrix material (Al99.99 and Al99.5) had a noticeable effect on the distribution of CNT particles within the matrix. For the Al99.99 matrix, which is characterised by lower hardness and thus higher ductility than Al99.5, fewer CNTs agglomerates were observed and their sizes were smaller. Numerical and experimental studies indicate that the turbulent flow of the material during the HPT deformation plays a crucial role in the fragmentation of agglomerates and the distribution of individual reinforcing phases in the matrix [45,46]. Blocking of the shear deformation in the sample undergoing HPT leads to the mixing of the material and thus an improved distribution of reinforcement phases. It is probable that the higher ductility of the Al99.99 matrix was associated with easier and faster mixing of CNTs into the matrix during HPT processing which thereby led to their more uniform distribution in the matrix. It should be noted that, besides breaking of the CNTs agglomerates during HPT processing, a fragmentation of individual CNTs also occurred. Despite this, many of them have retained their tubular structure, as shown in Fig. 5c.

It is worth noting that the improved distribution of CNTs in the Al99.99 matrix enhanced the process of grain refinement such that the grain size was ~830 nm and ~220 nm for the pure matrix and the nanocomposite, respectively, but smaller grain sizes of ~190 nm were achieved for the nanocomposites based on Al99.5 1 %CNT. This relationship is also reflected in the hardness measurements as the nanocomposites based on Al99.5 exhibited higher values of hardness in the edge areas of disk samples. This is in agreement with earlier studies on the effect of the degree of purity of the aluminium alloy on the fragmentation of the structure during the HPT process [18,47]. It should be emphasised that the addition of CNTs benefits in increasing the hardness of the nanocomposite after HPT but only if a high degree of dispersion of the reinforcing particles is achieved within the matrix. For Al99.99 matrix nanocomposites where a good distribution of the CNTs was observed, the hardness values increase even after 10 revolutions, whereas in the Al99.5 matrix nanocomposites a significant increase in hardness, associated with a better distribution of CNTs), was observed only at the disk sample edge area after 50 revolutions.

4.2. Tailoring of the mechanical properties in Al-CNTs nanocomposites

In general, the hardness of the fabricated nanocomposites depends on four factors: (1) the purity of the aluminium matrix [18], (2) the grain size as described by the Hall-Petch relationship [5], (3) density of dislocations and (4) the dispersion of CNTs. The Al99.99 matrix

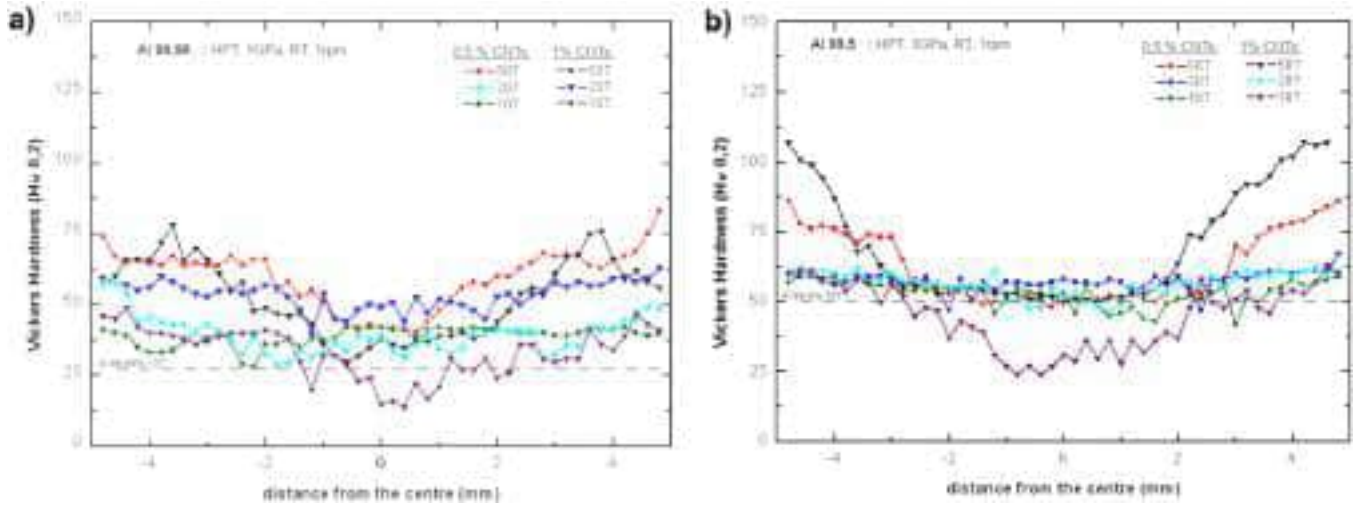

Fig. 7. Linear Hardness on the diameters of the cross-sections of samples: a) Al 99,99 composites b) Al 99,5 composites.

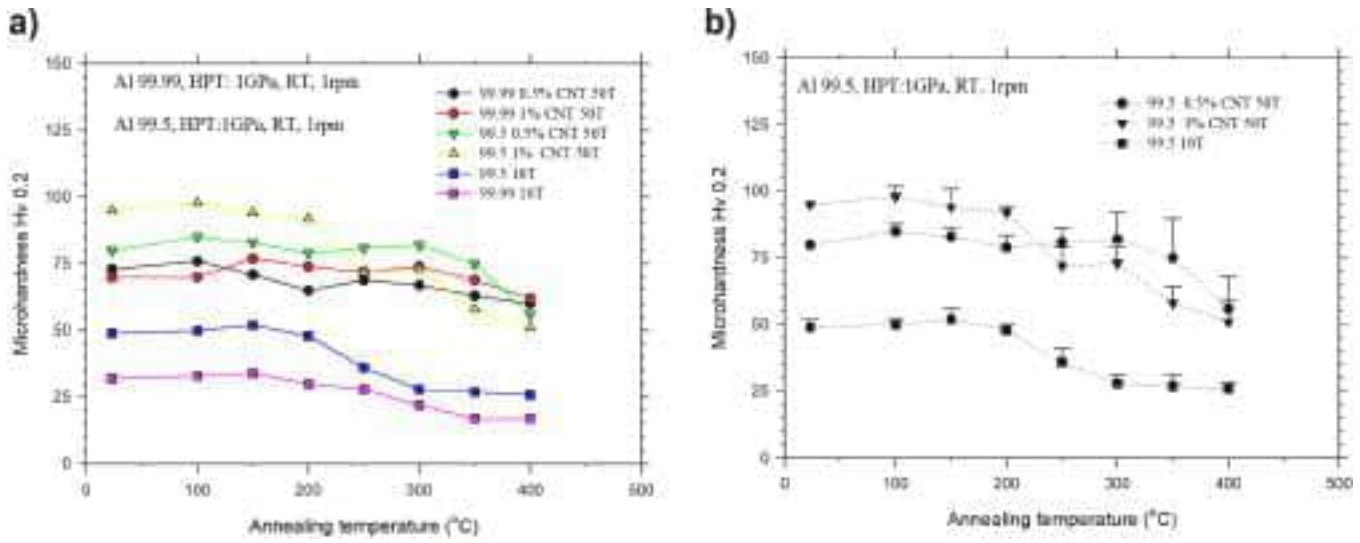

Fig. 8. The hardness of a) the Al99.99 and Al99.5 composites as a function of annealing temperature and b) hardness results for Al99.5 composites complemented with standard deviation bars.

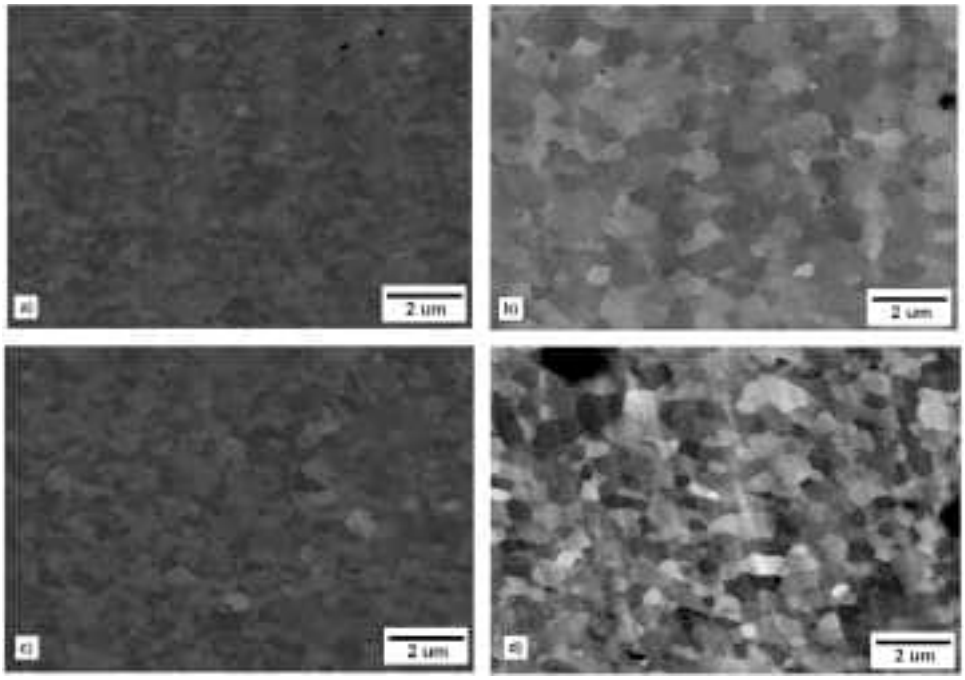

Fig. 9. Representative microstructural images of Al 99,99 0,5 % CNT composite after annealing at a) 250ºC and b) 400ºC; and Al 99,99 1 % CNT composite after annealing at c) 250ºC and d) 400ºC.

nanocomposites exhibit lower hardness when compared with the Al99.5 matrix nanocomposites mainly due to the higher purity and larger grain size of the matrix so that the better dispersion of CNTs is unable to compensate this loss. Nevertheless, the present results clearly indicate that this new approach for the production of nanocomposites using direct mixing by HPT is probably at least competitive, if not superior, to the traditional methods consisting of several stages of milling and sintering followed by HPT.

To place the results of this work in a broader perspective, Table 3 summarises the mechanical properties of the fabricated Al-CNTs nanocomposites with various Al-C alloys produced by traditional methods [10,26,27,48]. A careful review of these data provides clear confirmation that the direct processing via HPT of Al-CNTs nanocomposites presented in this work produces a material with a comparable microstructure and mechanical properties to other nanocomposites [10, 26,27,48].

It was shown in many earlier studies that the microstructural fragmentation and increase in hardness during HPT processing for many materials occur up to a certain strain and thereafter a saturation effect occurs so that at higher strains there is no additional increase in hardness or further grain size reduction [8,14,15]. The experimental points in Fig. 7 tend to be scattered but it was noted in a very early investigation of HPT that it should be possible to correlate these various points by plotting the data in the form of the values of Hv against the equivalent strain (Fig. 13) and this type of plot should also provide a direct measure of the saturation hardness [11,49]. It is apparent from Fig. 13 that the saturation effect was strongly related to the type of matrix used to produce the nanocomposites. In the nanocomposites with the Al99.99

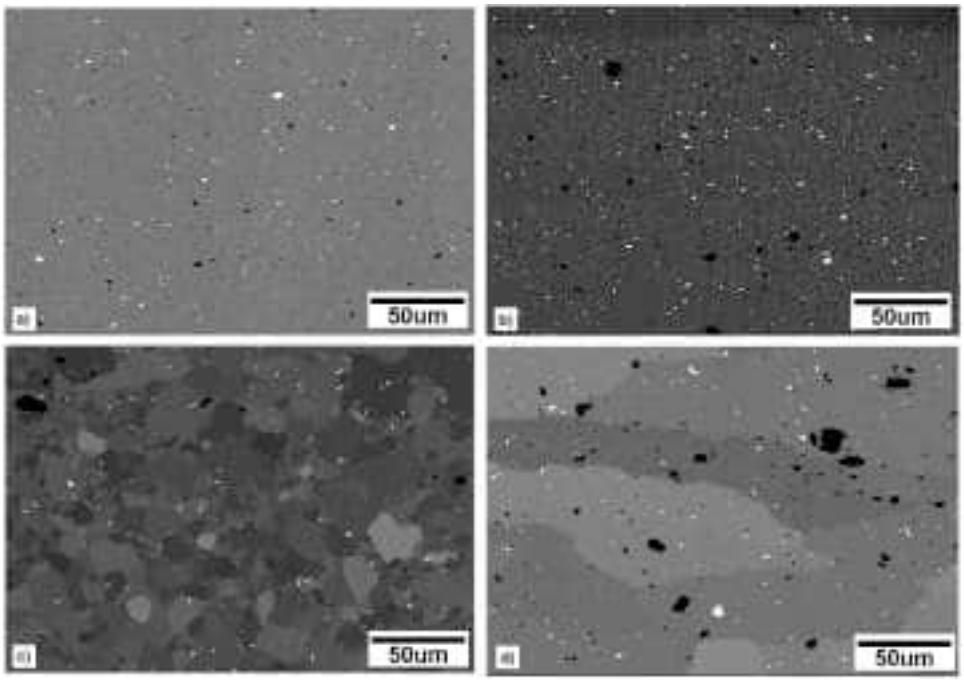

Fig. 10. Representative microstructural images of Al 99,5 0,5 % CNT after annealing at: a) 250ºC; b) 300ºC; c) 350ºC; d) 400ºC.

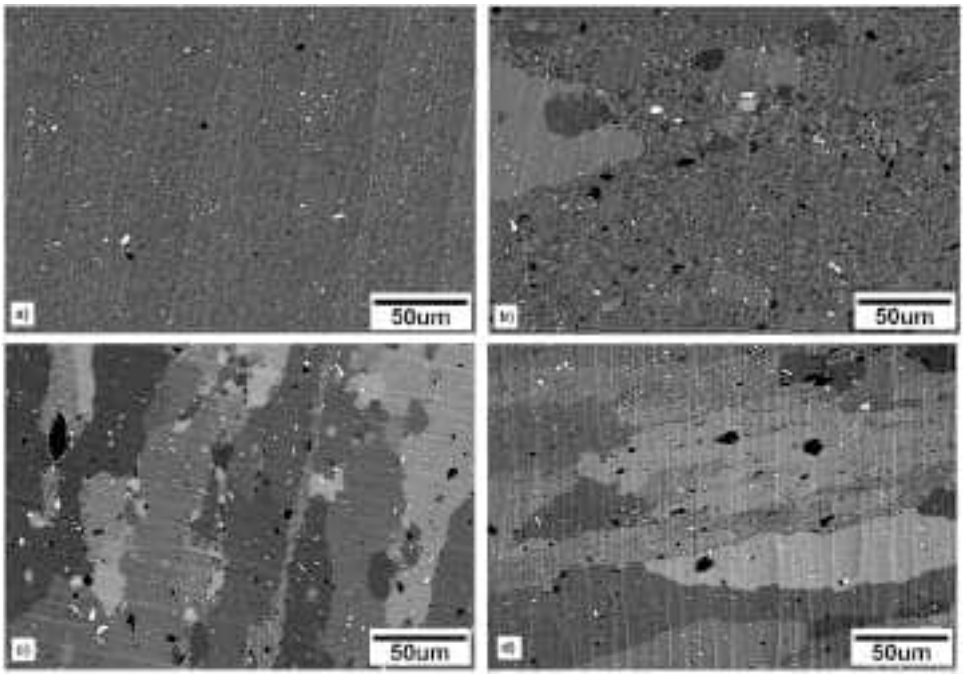

Fig. 11. Representative microstructural images of Al 99,5 1 % CNT composite after annealing at: a) 200ºC; b) 250ºC; c) 300ºC; d) 350ºC.

matrix in Fig. 13a, the increase in hardness is visible from the beginning of processing and the microhardness was not saturated until the equivalent strain exceeded ~1000. This indicates that the Al99.99 nanocomposites possess a stronger strain hardening ability than pure metal during HPT processing [5]. For the Al99.5 nanocomposites, the hardening behaviour is different as shown in Fig. 13b since the microhardness values tend to saturate in the first stage but then, after exceeding an equivalent strain of ~800, there is a strong increase in hardness which is probably associated with the dispersion of CNTs in the matrix. In materials with a good dispersion of CNTs, such as Al99.99, a significant grain refinement was observed even at 10 revolutions as in Fig. 2 whereas in the Al99.5 nanocomposites, in which a small number of revolutions such as 10 and 20 turns failed to produce a good distribution of CNTs as in Fig. 2, the hardness values saturated at a level of ~55 Hv. Thereafter, a good distribution of CNTs was achieved after exceeding a certain critical level of equivalent strain and this led to a reduction in grain size and a further increase in the microhardness values.

The present results in Fig. 3 and Table 1 show that the use of HPT processing to fabricate Al-CNTs nanocomposites leads to a pronounced microstructural refinement and an enhancement in the mechanical properties. However, such a significant increase in hardness of the nanocomposites cannot be explained only by Hall-Petch strengthening

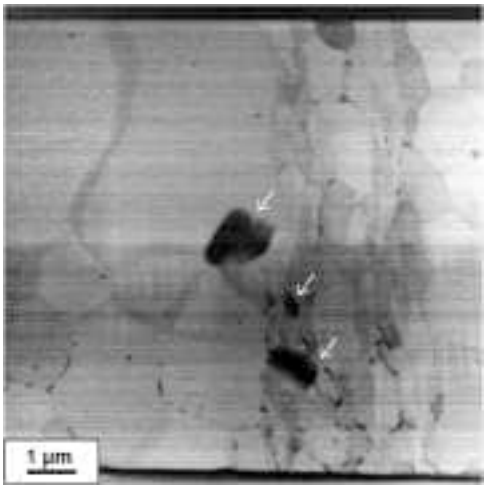

Fig. 12. HAADF image of Al99.5 with 0.5 % of CNTs composite after HPT processing and annealing at 350ºC showing the distribution of individual CNTs (black in HAADF contrast) and their agglomerates (marked with arrows).

Table 3
Grain size and mechanical properties of Al-C nanocomposites composites [10,26,27,48].

Sample	Processing	Grain size [nm]	Hardness [Hv]	Ref.
Al 99.99 + 0.5 % CNTs and 1 %CNTs	• Direct mixing 50 turns	210 230	75 75	Present work
Al 99.5 + 0.5 % CNTs and 1 %CNTs	• Direct mixing 50 turns	235 190	95 105	Present work
Al 99.99 % powder + 5 wt % CNTs	• Plastic consolidation of powders • Followed by HPT at RT, 2.5 GPa, 30 turns	170	76	[26]
Al 1050 powder + 5 wt% CNTs modified with Cu	• Plastic consolidation of powders • Followed by HPT at 473 K, 6.0 GPa, 10 turns	100	150	[27]
Al 1050 powder + 1.5 and 2 wt % CNTs	• Consolidation of powders using HIP • Followed by HPT at RT, 5.0 GPa, 5 turns	150	100	[48]
Al1050 powder + 5 wt% GNPs	• Compaction of powders • Followed by HPT at 298 K, 373 K, and 473 K, 6.0 GPa, 1, 5, 10 and 20 turns	160	110	[10]
Al 99,99 % + 5mass% CNT	• Al powder + CNT mixted in ethanol under ultrasonic condition 5 min, then ethanol evaporated • Mixted powders 0,35 g put into HPT anvil, HPT processed 2,5 GPa 1 rpm, 30 T	100	76	[26]

[50,51] as given by the following relationship which is reformulated in terms of hardness to give

$$H = H_o + k_H d^{-1/2} \quad (1)$$

where H is the hardness, H_o and k_H are material constants and d is the average grain size.

To further check on the applicability of the Hall-Petch relationship for the aluminium nanocomposites fabricated by HPT processing, the microhardness values obtained at the edges of the disks were plotted in Fig. 14 as a function of $d^{-1/2}$ together with datum points obtained from the initial coarser-grained alloys and the initial alloys after 10 HPT revolutions. In addition, trend lines for the Hall-Petch relationship for pure materials are also included. It is apparent that there is a clear difference in the distributions of the experimental points between the Al99.99 and Al99.5 nanocomposites and the trend lines for pure metals. For Al99.99 nanocomposites, the results are significantly shifted, even after 10 revolutions, from the linear relationship and this shift is the greater the higher the numbers of HPT revolutions. The hardness results for the samples after 20 and 50 revolutions are close to the trend line obtained for pure Al99.5. In addition, for Al99.5 matrix nanocomposites the results for 10 and 20 revolutions are close to the linear relationship for the pure alloy and there is a shift from the linear relationship only in the sample after 50 revolutions. It is important to note also that the data in Fig. 14 do not display the abrupt changes in slope that have been reported for several materials including Al alloys processed by HPT [52].

It is evident from these results that the key factor determining the strength of these nanocomposites is the good dispersion of nanofillers within the matrix. In the Al99.99 matrix nanocomposites, where the CNTs were uniformly distributed in the matrix even after only 10 turns, the mechanical properties were influenced not only by the increased grain refinement level according to the Hall-Petch relationship [50,51] but also by the individual CNTs which made a large contribution to the final strength of the nanocomposites. By contrast, the structure of the Al99.5 nanocomposites was determined primarily by the large CNTs agglomerates which favoured the fragmentation of the structure but contributed little to the overall strength. As a result, the linear trend was maintained for the samples after 10 and 20 revolutions and it was only after 50 rotations that there was a clear shift from linearity due to the improved distribution of CNTs in the matrix.

4.3. Thermal stability

The uniform distribution of CNTs in the aluminium matrix had a major impact not only on the grain refinement and mechanical properties of these nanocomposites but also on their thermal stability. In practice, the Al99.99 matrix nanocomposites had smaller CNT agglomerates than the Al99.5 matrix. Thus, Table 2 shows the proportion of visible agglomerates in the sample surfaces and for the Al99.99 matrix nanocomposites these values are significantly smaller (1.2 % and 1.8 % for 0.5 % and 1 % CNTs) than for the Al99.5 matrix nanocomposites (3.4 % and 4.5 % for 0.5 % and 1 % CNTs). The larger size of the visible agglomerates, for the same amount of added nanotubes, is associated with the poorer distribution of nanotubes in the metal matrix, where this had a significant effect on the role of these particles in blocking the movement of dislocations and grain boundaries. Fine particles located at grain boundaries may apply a pinning pressure thereby impeding the mobility of grain boundaries and blocking grain growth in addition to the overall effect of these CNTs, where this is described as the Zener pinning effect [53]. At the same time, the presence of large CNT agglomerates in the Al99.5 matrix samples leaves some areas without any particles to impede grain growth so that, as a result, some grains are blocked from growing whereas others are not blocked. This contributes to the abnormal growth of grains not blocked by CNTs, as described by the theory of abnormal grain growth due to the contribution from second phase particles [54], and this leads to heterogeneous microstructures in the Al99.5 matrix nanocomposites after annealing at 300ºC and 250ºC for 0.5 % and 1 % CNT additions.

In conclusion, the addition of CNTs has a positive effect on limiting the growth of aluminium grains during annealing but only when the CNT particles do not form large and numerous agglomerates but are instead sufficiently well distributed within the aluminium matrix. In the present direct synthesis procedure, the distribution of these CNTs is related both to the ductility of the matrix material and to the extent of

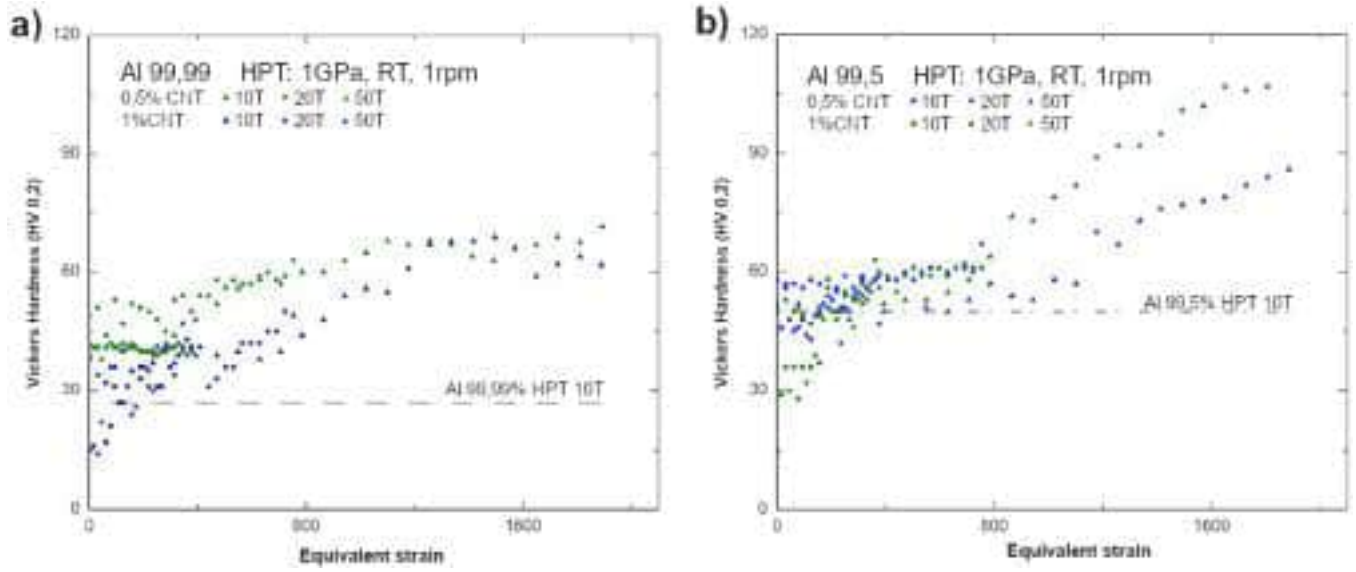

Fig. 13. Vickers microhardness plotted against equivalent strain for produced composites and reference literature data for Al 99.99 and Al 99.5 alloys.

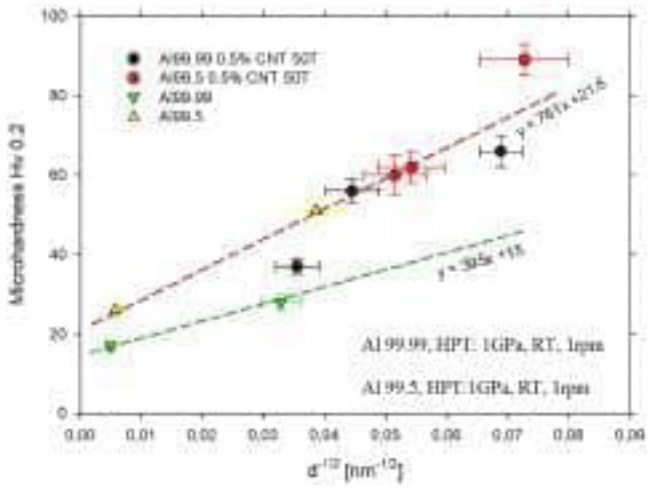

Fig. 14. Hall–Petch relationship for initial alloys in coarse-grained state and after processing through 10 HPT turns together with the data for Al-CNT composites fabricated in this work.

the applied deformation.

5. Summary and conclusions

- Al-CNTs nanocomposites were successfully produced by a direct synthesis procedure using HPT processing.
- A relatively good dispersion of CNTs was obtained within the Al matrix, especially for Al99.99.
- The addition of CNTs contributed to an increased grain size refinement by comparison with the matrix and this, together with the reinforcing effect of the CNTs, gave a significantly higher hardness of the nanocomposites compared to the matrix materials.
- For Al99.99 matrix nanocomposites, the hardness and microstructure remained stable even after annealing for 1 h at 400 °C. By contrast, the HPT-processed Al99.5 lost its UFG structure and enhanced mechanical properties after annealing at 150 °C. These results were associated with the good dispersion of CNTs in the Al99.99 matrix.
- For the Al99.5 matrix nanocomposites, the hardness was higher than for the pure metal for the total range of annealing temperatures. Nevertheless, there was noticeable grain growth accompanied by a decrease in hardness after annealing at 250 °C for the nanocomposite with 1 % CNTs and at 300 °C for the nanocomposite with 0.5 % CNTs and this was due to the poorer dispersion of CNTs and the increased number of large agglomerates.

CRediT authorship contribution statement

P. Bazarnik: Conceptualization, Methodology, Investigation, Data curation, Writing – original draft, Project administration, Funding acquisition. **M. Emerla:** Conceptualization, Methodology, Investigation, Validation, Writing – review & editing. **Y. Huang:** Processing, Investigation, data calculation. **M. Lewandowska:** Conceptualization, Writing – review & editing. **T.G. Langdon:** Conceptualization, Supervision, Writing – review & editing.

Declaration of Competing Interest

The authors declare that they have no known competing financial interests or personal relationships that could have appeared to influence the work reported in this paper.

Data availability

Data will be made available on request.

Acknowledgements

This work was carried out within an OPUS 19 project, Metal matrix composites fabricated by high-pressure torsion and reinforced with 2D and 3D nano-particles, funded by National Science Centre Poland under nb. 2020/37/B/ST5/01837. Two of the authors were supported by the European Research Council under ERC Grant Agreement No. 267464-SPDMETALS (YH and TGL).

References

[1] W. Zhang, J. Xu, Advanced lightweight materials for automobiles: a review, Mater. Des. 221 (2022), 110994, https://doi.org/10.1016/j.matdes.2022.110994.
[2] J. Hirsch, Recent development in aluminium for automotive applications, in: Trans. Nonferrous Met. Soc. China (English Ed., 24, 2014, pp. 1995–2002, https://doi.org/10.1016/S1003-6326(14)63305-7.
[3] V. Ferreira, P. Egizabal, V. Popov, M. García de Cortázar, A. Irazustabarrena, A. M. López-Sabirón, G. Ferreira, Lightweight automotive components based on

nanodiamond-reinforced aluminium alloy: a technical and environmental evaluation, Diam. Relat. Mater. 92 (2019) 174–186, https://doi.org/10.1016/j.diamond.2018.12.015.
[4] M.S. Sarfraz, H. Hong, S.S. Kim, Recent developments in the manufacturing technologies of composite components and their cost-effectiveness in the automotive industry: a review study, Compos. Struct. 266 (2021), 113864, https://doi.org/10.1016/j.compstruct.2021.113864.
[5] R.Z. Valiev, A.P. Zhilyaev, T.G. Langdon, Bulk Nanostructured Materials: Fundamentals and Applications, John Wiley & Sons, Inc, Hoboken, New Jersey, USA, 2014, https://doi.org/10.1142/9789814397988_0011.
[6] R.Z. Valiev, Y. Estrin, Z. Horita, T.G. Langdon, M.J. Zehetbauer, Y.T. Zhu, Fundamentals of superior properties in bulk NanoSPD materials, Mater. Res. Lett. 4 (2016) 1–21, https://doi.org/10.1080/21663831.2015.1060543.
[7] A.P. Zhilyaev, T.G. Langdon, Using high-pressure torsion for metal processing: fundamentals and applications, Prog. Mater. Sci. 53 (2008) 893–979, https://doi.org/10.1016/j.pmatsci.2008.03.002.
[8] P. Bazarnik, Y. Huang, M. Lewandowska, T.G. Langdon, Enhanced grain refinement and microhardness by hybrid processing using hydrostatic extrusion and high-pressure torsion, Mater. Sci. Eng. A 712 (2018) 513–520, https://doi.org/10.1016/j.msea.2017.12.007.
[9] M.I.A. El Aal, H.S. Kim, Wear properties of high pressure torsion processed ultrafine grained Al-7%Si alloy, Mater. Des. 53 (2014) 373–382, https://doi.org/10.1016/j.matdes.2013.07.045.
[10] Y. Huang, P. Bazarnik, D. Wan, D. Luo, P.H.R. Pereira, M. Lewandowska, J. Yao, B. E. Hayden, T.G. Langdon, The fabrication of graphene-reinforced Al-based nanocomposites using high-pressure torsion, Acta Mater. 164 (2019) 499–511, https://doi.org/10.1016/j.actamat.2018.10.060.
[11] P. Bazarnik, Y. Huang, M. Lewandowska, T.G. Langdon, Structural impact on the Hall-Petch relationship in an Al-5Mg alloy processed by high-pressure torsion, Mater. Sci. Eng. A. 626 (2015) 9–15, https://doi.org/10.1016/j.msea.2014.12.027.
[12] M. Kawasaki, H.J. Lee, B. Ahn, A.P. Zhilyaev, T.G. Langdon, Evolution of hardness in ultrafine-grained metals processed by high-pressure torsion, J. Mater. Res. Technol. 3 (2014) 311–318, https://doi.org/10.1016/j.jmrt.2014.06.002.
[13] P. Král, J. Staněk, L. Kunčická, F. Seitl, L. Petrich, V. Schmidt, V. Beneš, V. Sklenička, Microstructure changes in HPT-processed copper occurring at room temperature, Mater. Charact. 151 (2019) 602–611, https://doi.org/10.1016/j.matchar.2019.03.046.
[14] V.V. Popov, E.N. Popova, A.V. Stolbovskiy, Nanostructuring Nb by various techniques of severe plastic deformation, Mater. Sci. Eng. A 539 (2012) 22–29, https://doi.org/10.1016/j.msea.2011.12.082.
[15] S. Sabbaghianrad, J. Wongsa-Ngam, M. Kawasaki, T.G. Langdon, An examination of the saturation microstructures achieved in ultrafine-grained metals processed by high-pressure torsion, J. Mater. Res. Technol. 3 (2014) 319–326, https://doi.org/10.1016/j.jmrt.2014.10.002.
[16] S. Sabbaghianrad, T.G. Langdon, Microstructural saturation, hardness stability and superplasticity in ultrafine-grained metals processed by a combination of severe plastic deformation techniques, Lett. Mater. 5 (2015) 335–340, https://doi.org/10.22226/2410-3535-2015-3-335-340.
[17] S. Sabbaghianrad, T.G. Langdon, An evaluation of the saturation hardness in an ultrafine-grained aluminum 7075 alloy processed using different techniques, J. Mater. Sci. 50 (2015) 4357–4365, https://doi.org/10.1007/s10853-015-8989-x.
[18] Y. Ito, K. Edalati, Z. Horita, High-pressure torsion of aluminum with ultrahigh purity (99.9999%) and occurrence of inverse Hall-Petch relationship, Mater. Sci. Eng. A. 679 (2017) 428–434, https://doi.org/10.1016/j.msea.2016.10.066.
[19] K. Edalati, Z. Horita, Significance of homologous temperature in softening behavior and grain size of pure metals processed by high-pressure torsion, Mater. Sci. Eng. A 528 (2011) 7514–7523, https://doi.org/10.1016/j.msea.2011.06.080.
[20] R.K. Islamgaliev, F. Chmelik, R. Kuzel, Thermal structure changes in copper and nickel processed by severe plastic deformation, Mater. Sci. Eng. A 234–236 (1997) 335–338, https://doi.org/10.1016/s0921-5093(97)00247-5.
[21] E. Schafler, R. Pippan, Effect of thermal treatment on microstructure in high pressure torsion (HPT) deformed nickel, Mater. Sci. Eng. A 387–389 (2004) 799–804, https://doi.org/10.1016/j.msea.2004.01.112.
[22] P. Bazarnik, M. Lewandowska, M. Andrzejczuk, K.J. Kurzydlowski, The strength and thermal stability of Al-5Mg alloys nano-engineered using methods of metal forming, Mater. Sci. Eng. A. 556 (2012) 134–139, https://doi.org/10.1016/j.msea.2012.06.068.
[23] R.Z. Valiev, R.K. Islamgaliev, N.F. Kuzmina, Y. Li, T.G. Langdon, Strengthening and grain refinement in an Al-6061 metal matrix composite through intense plastic straining, Scr. Mater. 40 (1999) 117–122, https://doi.org/10.1016/S1359-6462(98)00398-4.
[24] I. Sabirov, O. Kolednik, R. Pippan, Homogenization of metal matrix composites by high-pressure torsion, Metall. Mater. Trans. A Phys. Metall. Mater. Sci. 36 (2005) 2861–2870, https://doi.org/10.1007/s11661-005-0281-2.
[25] Y. Xue, B. Jiang, L. Bourgeois, P. Dai, M. Mitome, C. Zhang, M. Yamaguchi, A. Matveev, C. Tang, Y. Bando, K. Tsuchiya, D. Golberg, Aluminum matrix composites reinforced with multi-walled boron nitride nanotubes fabricated by a high-pressure torsion technique, Mater. Des. 88 (2015) 451–460, https://doi.org/10.1016/j.matdes.2015.08.162.
[26] T. Tokunaga, K. Kaneko, Z. Horita, Production of aluminum-matrix carbon nanotube composite using high pressure torsion, Mater. Sci. Eng. A 490 (2008) 300–304, https://doi.org/10.1016/j.msea.2008.02.022.
[27] S.H. Joo, S.C. Yoon, C.S. Lee, D.H. Nam, S.H. Hong, H.S. Kim, Microstructure and tensile behavior of Al and Al-matrix carbon nanotube composites processed by high pressure torsion of the powders, J. Mater. Sci. 45 (2010) 4652–4658, https://doi.org/10.1007/s10853-010-4382-y.
[28] D.D. Phuong, P. Van Trinh, N. Van An, N. Van Luan, P.N. Minh, R.K. Khisamov, K. S. Nazarov, L.R. Zubairov, R.R. Mulyukov, A.A. Nazarov, Effects of carbon nanotube content and annealing temperature on the hardness of CNT reinforced aluminum nanocomposites processed by the high pressure torsion technique, J. Alloy. Compd. 613 (2014) 68–73, https://doi.org/10.1016/j.jallcom.2014.05.219.
[29] S. Suárez, E. Ramos-Moore, B. Lechthaler, F. Mücklich, Grain growth analysis of multiwalled carbon nanotube-reinforced bulk Ni composites, Carbon 70 (2014) 173–178, https://doi.org/10.1016/j.carbon.2013.12.089.
[30] M. Darabi, M. Rajabi, B. Junipour, M.T. Noghani, The effect of sintering temperature on Cu-Cnts nano composites properties produced by pm method, Sci. Sinter. 50 (2018) 477–486, https://doi.org/10.2298/SOS1804477D.
[31] A.K. Shukla, N. Nayan, S.V.S.N. Murty, S.C. Sharma, P. Chandran, S.R. Bakshi, K. M. George, Processing of copper-carbon nanotube composites by vacuum hot pressing technique, Mater. Sci. Eng. A. 560 (2013) 365–371, https://doi.org/10.1016/j.msea.2012.09.080.
[32] M. Jafari, M.H. Abbasi, M.H. Enayati, F. Karimzadeh, Mechanical properties of nanostructured Al2024-MWCNT composite prepared by optimized mechanical milling and hot pressing methods, Adv. Powder Technol. 23 (2012) 205–210, https://doi.org/10.1016/j.apt.2011.02.008.
[33] C. Guiderdoni, C. Estournès, A. Peigney, A. Weibel, V. Turq, C. Laurent, The preparation of double-walled carbon nanotube/Cu composites by spark plasma sintering, and their hardness and friction properties, Carbon 49 (2011) 4535–4543, https://doi.org/10.1016/j.carbon.2011.06.063.
[34] H. Kurita, H. Kwon, M. Estili, A. Kawasaki, Multi-walled carbon nanotube-aluminum matrix composites prepared by combination of hetero-agglomeration method, spark plasma sintering and hot extrusion, Mater. Trans. 52 (2011) 1960–1965, https://doi.org/10.2320/matertrans.M2011146.
[35] G.F. Korznikova, K.S. Nazarov, R.K. Khisamov, S.N. Sergeev, R.U. Shayachmetov, G.R. Khalikova, J.A. Baimova, A.M. Glezer, R.R. Mulyukov, Intermetallic growth kinetics and microstructure evolution in Al-Cu-Al metal-matrix composite processed by high pressure torsion, Mater. Lett. 253 (2019) 412–415, https://doi.org/10.1016/j.matlet.2019.07.124.
[36] B. Ahn, A.P. Zhilyaev, H.J. Lee, M. Kawasaki, T.G. Langdon, Rapid synthesis of an extra hard metal matrix nanocomposite at ambient temperature, Mater. Sci. Eng. A 635 (2015) 109–117, https://doi.org/10.1016/j.msea.2015.03.042.
[37] J.K. Han, K.D. Liss, T.G. Langdon, M. Kawasaki, Synthesis of a bulk nanostructured metastable Al alloy with extreme supersaturation of Mg, Sci. Rep. 9 (2019) 1–7, https://doi.org/10.1038/s41598-019-53614-3.
[38] J. Lipecka, M. Andrzejczuk, M. Lewandowska, J. Janczak-Rusch, K. J. Kurzydłowski, Evaluation of thermal stability of ultrafine grained aluminium matrix composites reinforced with carbon nanotubes, Compos. Sci. Technol. 71 (2011) 1881–1885, https://doi.org/10.1016/j.compscitech.2011.09.001.
[39] Y. Liu, C. Lu, H. Wang, A.K. Tieu, B. Liu, Microstructure evolution, lattice rotation retardation and grain orientation fragmentation in commercial purity aluminium deformed by high pressure torsion, J. Mater. Res. Technol. 9 (2020) 6642–6654, https://doi.org/10.1016/j.jmrt.2020.04.056.
[40] Y. Iwahashi, Z. Horita, M. Nemoto, T.G. Langdon, The process of grain refinement in equal-channel angular pressing, Acta Met. 46 (1998) 3317–3331, https://doi.org/10.1007/978-3-319-35107-0_5.
[41] Z. Horita, T. Fujinami, M. Nemoto, T.G. Langdon, Equal-channel angular pressing of commercial aluminum alloys: grain refinement, thermal stability and tensile properties, Metall. Mater. Trans. A Phys. Metall. Mater. Sci. 31 (2000) 691–701, https://doi.org/10.1007/s11661-000-0011-8.
[42] N. Wang, Y. Wen, L.Q. Chen, Pinning force from multiple second-phase particles in grain growth, Comput. Mater. Sci. 93 (2014) 81–85, https://doi.org/10.1016/j.commatsci.2014.06.030.
[43] J.H. Driver, Stability of nanostructured metals and alloys, Scr. Mater. 51 (2004) 819–823, https://doi.org/10.1016/j.scriptamat.2004.05.014.
[44] Z. Li, J. Wang, H. Huang, Influences of grain/particle interfacial energies on second-phase particle pinning grain coarsening of polycrystalline, J. Alloy. Compd. 818 (2020), https://doi.org/10.1016/j.jallcom.2019.152848.
[45] R. Kulagin, Y. Beygelzimer, Y. Ivanisenko, A. Mazilkin, H. Hahn, Modelling of High Pressure Torsion using FEM, Procedia Eng. 207 (2017) 1445–1450, https://doi.org/10.1016/j.proeng.2017.10.911.
[46] R. Sundeev, A. Shalimova, S. Rogachev, O. Chernogorova, A. Glezer, A. Ovcharov, I. Karateev, N. Tabachkova, Structural aspects of the formation of multilayer composites from dissimilar materials upon high-pressure torsion, Materials 16 (2023), https://doi.org/10.3390/ma16103849.
[47] Y. Beygelzimer, Vortices and mixing in metals during severe plastic deformation, Mater. Sci. Forum 683 (2011) 213–224, https://doi.org/10.4028/www.scientific.net/MSF.683.213.
[48] X. Yang, T. Zou, C. Shi, E. Liu, C. He, N. Zhao, Effect of carbon nanotube (CNT) content on the properties of in-situ synthesis CNT reinforced Al composites, Mater. Sci. Eng. A 660 (2016) 11–18, https://doi.org/10.1016/j.msea.2016.02.062.
[49] A. Vorhauer, R. Pippan, On the homogeneity of deformation by high pressure torsion, Scr. Mater. 51 (2004) 921–925, https://doi.org/10.1016/j.scriptamat.2004.04.025.
[50] E.O. Hall, The deformation and ageing of mild steel III discussion of results, Proc. Phys. Soc. Sect. B 64 (1951) 747–753.
[51] N.J. Petch, The cleavage strength of polycrystals, J. Iron Steel Inst. 174 (1953) 25–28.

[52] S. Dangwal, K. Edalati, R.Z. Valiev, T.G. Langdon, Breaks in the Hall–Petch relationship after severe plastic deformation of magnesium, aluminum, copper, and iron, Crystals 13 (2023) 413, https://doi.org/10.3390/cryst13030413.

[53] P.A. Manohar, M. Ferry, T. Chandra, Five decades of the Zener equation, ISIJ Int. 38 (1998) 913–924, https://doi.org/10.2355/isijinternational.38.913.

[54] A.J. McEvily, Fail. Fatigue (1974), https://doi.org/10.1016/b978-0-08-025437-1.50014-0.

Materials Science & Engineering A 766 (2019) 138350

Contents lists available at ScienceDirect

Materials Science & Engineering A

journal homepage: www.elsevier.com/locate/msea

Effect of spark plasma sintering and high-pressure torsion on the microstructural and mechanical properties of a Cu–SiC composite

P. Bazarnik[a,*], S. Nosewicz[b], B. Romelczyk-Baishya[a], M. Chmielewski[c], A. Strojny Nędza[c], J. Maj[b], Y. Huang[d,e], M. Lewandowska[a], T.G. Langdon[e]

[a] Warsaw University of Technology, 141 Woloska Str., 02-507, Warsaw, Poland
[b] Institute of Fundamental Technological Research, Polish Academy of Sciences, 5B Pawinskiego, 02-106, Warsaw, Poland
[c] Institute of Electronic Materials Technology, 133 Wolczynska Str, 01-919, Warsaw, Poland
[d] Department of Design and Engineering, Faculty of Science and Technology, Bournemouth University, Poole, Dorset, BH12 5BB, UK
[e] Materials Research Group, Department of Mechanical Engineering, University of Southampton, Southampton, SO17 1BJ, UK

ARTICLE INFO

Keywords:
Copper
Silicon carbide
High-pressure torsion
Spark plasma sintering
Thermal conductivity

ABSTRACT

This investigation examines the problem of homogenization in metal matrix composites (MMCs) and the methods of increasing their strength using severe plastic deformation (SPD). In this research MMCs of pure copper and silicon carbide were synthesized by spark plasma sintering (SPS) and then further processed via high-pressure torsion (HPT). The microstructures in the sintered and in the deformed materials were investigated using Scanning Electron Microscopy (SEM) and Scanning Transmission Electron Microscopy (STEM). The mechanical properties were evaluated in microhardness tests and in tensile testing. The thermal conductivity of the composites was measured with the use of a laser pulse technique. Microstructural analysis revealed that HPT processing leads to an improved densification of the SPS-produced composites with significant grain refinement in the copper matrix and with fragmentation of the SiC particles and their homogeneous distribution in the copper matrix. The HPT processing of Cu and the Cu–SiC samples enhanced their mechanical properties at the expense of limiting their plasticity. Processing by HPT also had a major influence on the thermal conductivity of materials. It is demonstrated that the deformed samples exhibit higher thermal conductivity than the initial coarse-grained samples.

1. Introduction

Metal matrix composites (MMCs) are lightweight structural materials which often exhibit unique properties such as enhanced strength and hardness [1,2], wear [3] and corrosion resistance [4–6] together with excellent electrical and thermal properties [6–8]. Various MMC systems have been studied and an enhancement of a range of material properties was reported thereby making these materials attractive for use in a wide range of applications including in the aerospace, automotive and electronics sectors [9,10].

Recently, significant interest has been directed towards the fabrication of copper-based composites [4,6–8,11–14]. Copper and its alloys exhibit excellent thermal and electrical conductive properties but, due to their poor mechanical properties of very low wear resistance and low yield strength, especially at elevated temperature, their use is restricted in many industrial applications. Therefore, Cu-based MMCs reinforced with ceramic particles are now under consideration as promising candidate materials for applications requiring high thermal conductivity and thermal stability together with excellent wear resistance. The incorporation of ceramic particulate reinforcements, such as SiC, may significantly improve the thermal and some of the mechanical properties as well as the wear resistance without any major deterioration in the thermal and electrical conductivities of the matrix [5,15,16]. The Cu–SiC MMCs appear to be promising engineering materials because they offer a combination of both the superior ductility and toughness of the copper matrix together with the high strength, high Young's modulus and exellent wear resistance of the SiC reinforcement. To date, Cu–SiC composites have been used extensively as welding electrodes, electrical contacts, and switches and in electronic packaging [17].

Several different techniques have been developed to synthesize MMCs where these methods include stir casting [18,19], spray forming [18,20], squeeze casting [18,21] and powder metallurgy [18,22]. In practice, powder metallurgy techniques such as hot isostatic pressing

* Corresponding author.
E-mail address: Piotr.Bazarnik@pw.edu.pl (P. Bazarnik).

https://doi.org/10.1016/j.msea.2019.138350
Received 21 July 2019; Received in revised form 26 August 2019; Accepted 27 August 2019
Available online 28 August 2019
0921-5093/

(HIP) [23], hot pressing (HP) [24] and spark plasma sintering (SPS) [18,25] are especially promising because of the attractive properties of the processed samples. In an earlier study, it was demonstrated that the microstructure and mechanical properties of Cu–SiC MMCs depend strongly on the nature of the sintering technique [15,26]. Specifically, the optimum densification, and therefore the best mechanical properties of Cu–SiC MMCs, was reported after SPS processing [15]. Nevertheless, MMCs obtained via powder metallurgy processing may have some disadvantages, including large microstructural inhomogeneities in the particle distributions, the presence of some residual porosity even after SPS processing [15] and in many cases a weak connection between the particles and the metal matrix. It is well established that structural inhomogeneity and residual porosity will significantly degrade the formability and ductility, thereby making these materials prone to premature failure.

In order to uniformly distribute the ceramic reinforcing particles within the metal matrix and to densify the sintered materials, it is feasible to use conventional deformation processes such as rolling or hot extrusion. However, in many cases the deformation level generated through these techniques is not sufficient to improve the microstructural homogeneity. For example, there is evidence that the improvement of homogeneity in MMCs requires strains higher than ~4 [27–29] which cannot be obtained in conventional rolling and hot extrusion processes.

Recently, severe plastic deformation (SPD) processes were used to fabricate MMCs and improve their homogeneity [30–45]. Moreover, SPD procedures increase the strength of the composites through a reduction in grain size in the matrix metal. A number of SPD methods were developed, such as high-pressure torsion (HPT) [46], equal-channel angular pressing (ECAP) [47], accumulative roll bonding (ARB) [48] and hydrostatic extrusion (HE) [49,50]. Among these methods, HPT is regarded as reasonably ideal for achieving good homogenization of the MMCs because of the ability to generate extremely high strains of typically more than 200 at 10 revolutions. This process has been widely used in the processing of nano- and micro-sized metals, metal alloys and their powders [51–57], intermetallics [58,59] and MMCs [30–32,38–45,60,61]. However, there are to date only a limited number of experimental studies on the HPT processing of Cu–SiC composites [62–64]. Moreover, there is a lack of information regarding the thermal conductivity of MMCs fabricated by SPD techniques.

Therefore, the purpose of this study was to investigate the fabrication of novel MMCs using HPT to provide homogenization of sintered Cu–SiC composites having different volume fractions of the SiC reinforcement. The strength, microhardness and thermal conductivity were examined and the effect of refinement of the matrix grains and the SiC particles on the thermal conductivity and mechanical properties was also evaluated.

2. Experimental

A regular-shaped copper powder (produced by NewMet Koch) with a purity of 99.99% and 40 μm average particle size was used as a matrix. The composites were reinforced by silicon carbide particles with a purity of 99.99% (Saint-Gobain, France) having average particle sizes of about 80 μm and theparticle size ranges from 30 μm to 130 μm.

The powders were mixed in a planetary mill (Pulverisette 6) using processing parameters of a rotational speed of 100 rpm, a time of mixing of 2 h and a ball-to-powder ratio (BPR) of 5:1. A milling medium was not used during the mixing. Two compositions of the powder mixtures were prepared with the following Cu to ceramic phase content (vol%): 90%Cu–10%SiC, 80%Cu–20%SiC.

The powders were consolidated by the SPS technique using a graphite die with a sample diameter of 10 mm and height of 10 mm. The sintering process was carried out at a temperature of 950 °C in an argon atmosphere with a heating rate of 100 °C/min and a 10 min holding time at maximum temperature at a pressure of 150 MPa. As a reference, a sample of pure copper was sintered under the same conditions.

The sintered samples were cut to discs with thicknesses of 1 mm and then subjected to HPT processing. This processing was conducted under an applied pressure of 6.0 GPa at room temperature under quasi-constrained conditions [65] where there is a small outflow of material around the periphery of the disc during the processing operation. Discs were torsionally strained by rotating the lower anvil at 1 rpm through 20 revolutions each.

The microstructures of the Cu and Cu–SiC composites were examined using scanning electron microscopy (SEM) (Hitachi SU-8000) operating at 10 kV. The images were taken in secondary electron (SE) and in back-scattered electron (BSE) modes. The SEM observations were performed on cross-sectional planes in the edge regions and also at ~0.5 mm from the disc edge. Detailed microstructural observations from selected areas were performed using a Cs-corrected dedicated high-resolution scanning transmission electron microscope (STEM) (Hitachi HD-2700). The STEM images were taken in bright-field (BF) and high-angle annular dark field (HAADF) modes. The samples for STEM observations were cut using the focussed ion beam (FIB) technique with a Hitachi NB5000 microscope. All microstructures were evaluated quantitatively using a computer-aided image analyser. The grain size was described by the equivalent grain diameter, d_{eq}, defined as the diameter of a circle with a surface area equal to the surface area of the grain.

To evaluate the changes in the mechanical properties after HPT processing, microhardness tests were performed on the polished surfaces of discs using an FM-300 microhardness tester equipped with a Vickers indenter. Measurements were taken under a load of 200 g and a dwell time of 10 s along randomly-selected diameters on each disc with a spacing of 0.3 mm between the measuring points. The results were plotted in the form of the hardness profiles. The study of mechanical properties was complemented by tensile testing conducted at room temperature using a Zwick 005 universal testing machine under displacement control at a strain rate of $1.0 \times 10^{-3}\,s^{-1}$. For proper strain estimation, Digital Image Correlation (DIC) was applied [66]. A CCD camera operating at 4fps with a Pentax lens was placed in front of the sample. The image acquisition by AVT software was synchronized with the beginning of each tensile test. Based on the load - displacement data, the yield stress (YS), ultimate stress (UTS) and the elongation to failure were determined.

The thermal conductivity of the processed composites was measured with the use of a laser pulse technique [67]. This was performed using an LFA 457 device by Netzsch over the temperature range of 50–300 °C in an argon atmosphere. The value of the thermal conductivity (TC) was calculated using the following equation:

$$\lambda = \rho \cdot c_p \cdot D \quad (1)$$

where λ is the thermal conductivity in W/mK, ρ is the density in g/cm^3, c_p is the specific heat in J/gK and D is the diffusivity in mm^2/s. The value of the specific heat was determined based on the rule of mixtures.

All of the results obtained for the samples after HPT processing were compared with data for the initial material after SPS processing.

3. Results

3.1. Microstructure evolution

Figs. 1–2 show representative images of the initial microstructures of pure Cu, Cu–10SiC and Cu–20SiC samples after SPS processing. The microstructure in the pure Cu sample after SPS is inhomogeneous and exhibits a bimodal character as illustrated in Fig. 1a with low magnification. The grain structure consists of two types of grains: (1) coarse grains having diameters of ~210 μm and occupying ~70% of the sample volume and (2) fine grains with an average grain size of

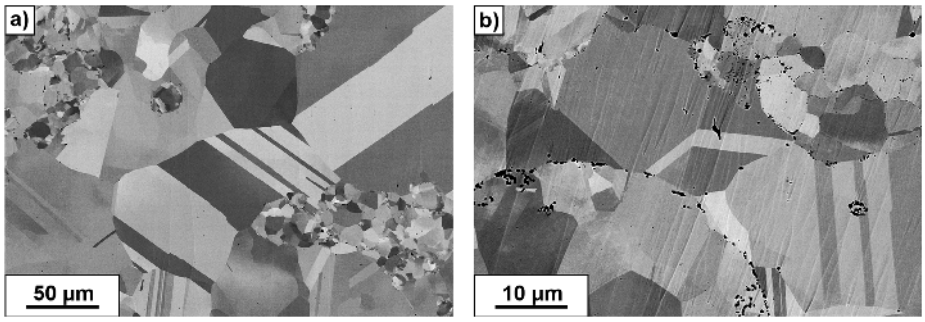

Fig. 1. SEM images of the microstructures of pure Cu after SPS processing at low (a) and high (b) magnifications.

~3.4 µm. Also, numerous twins are visible in the microstructure. Some residual porosity is visible in the copper matrix, as presented in Fig. 1b with high magnification where the black regions in the BSE image are pores. These pores have size ranges between ~0.5–2.0 µm and they are located mainly at the contact surfaces of the primary powder particles.

The structures of the Cu–10SiC and Cu–20SiC composites in Fig. 2 were more uniform. Microstructure observations show that the SiC reinforcement phase is fairly uniformly distributed throughout the sample volume with only a few clusters of SiC particles visible in the Cu matrix in Fig. 2a and b. The SiC particles embedded in the Cu matrix have sizes from ~10 to ~100 µm with a majority of particles having sizes of the order of ~100 µm. In both samples the grain size distributions in the copper matrix are more uniform (Fig. 2c) with an average grain size of ~130 µm. However, some discontinuities are visible in the microstructures, such as the presence of pores in the Cu matrix which appear as white dots in the SE image in Fig. 2d and the lack of bonding between the copper matrix and some SiC particles which are visible as empty spaces on the contact surfaces in Fig. 2d.

The use of HPT processing has a significant impact on the structures of the sintered samples, as illustrated in Figs. 3–5 for Cu, Cu–10SiC and Cu–20SiC samples, respectively. In the pure copper, the HPT processing produces a significant reduction in the pore density. Thus, as can be seen in the SEM image in Fig. 3a, only very fine pores can be identified in the microstructure (marked by arrows). In addition, SEM images taken in orientation contrast mode revealed a significant grain size reduction as shown in Fig. 3b. These grains are relatively equiaxial and with sizes below ~1 µm.

After HPT processing, the microstructures in the samples with the 10% SiC and 20% SiC reinforcements are similar, as shown in Figs. 4 and 5, but there is a significant grain size reduction in the Cu matrix and a decrease in porosity. These SEM observations confirm there is a considerable fragmentation of the SiC particles during the HPT processing (Figs. 4a and 5a). Moreover, the quality of the bonding between the particles and the Cu matrix has improved as is evident in Figs. 4b and Fig. 5b–c. No pores and voids are visible at the interfaces between the SiC particles and the Cu matrix. Nevertheless, the degree of fragmentation appears to be strongly correlated to the original size of the SiC particles. For the largest particles having sizes of ~100 µm, a number of cracks and discontinuities are observed in the Cu–20SiC sample in Fig. 5e. In addition, for most of these particles their outer parts are fragmented into clusters of smaller particles embedded within the Cu matrix and this phenomenon is visible in Fig. 5c and e. At the same time, the fraction of smaller fragmented particles having sizes of ~20–40 µm increased after HPT processing. Some of these particles were fragmented and formed clusters of particles having sizes in the range of ~0.05–1.0 µm (Figs. 4c and 5c). At the same time, a high fraction of fine SiC particles with sizes of ~50–700 nm is found in the Cu matrix (Fig. 5d) where these particles are dispersed in the Cu matrix. Observations by SEM indicate that the fragmentation effect is more intense in the sample with 20% of SiC reinforcement, where there are numerous small particles and clusters of particles in the copper matrix.

The particle sizes were quantitatively analysed in the Cu–10SiC and Cu–20SiC samples and Fig. 6 shows the particles size distributions per unit area for the as-sintered samples (Fig. 6a–c) and HPT-processed

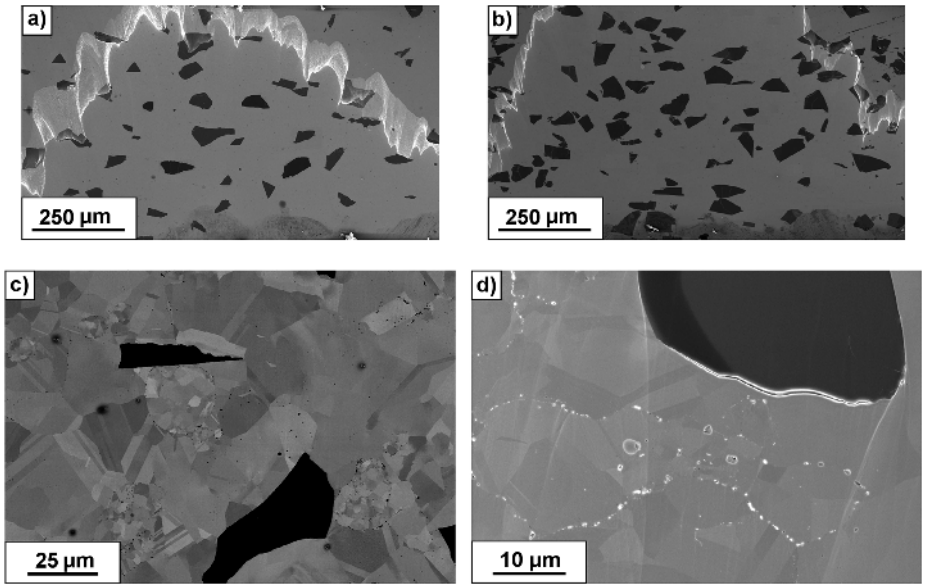

Fig. 2. SEM images of the microstructures of Cu–SiC composites after SPS processing: with 10% (a) at low magnification (c) at high magnification in BSE mode and 20% at (b) low magnification (d) at high magnification in SE mode (the white dots are pores).

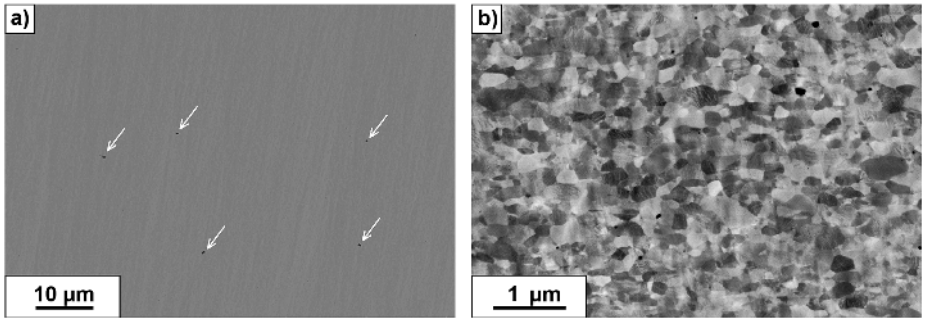

Fig. 3. SEM images of the microstructure of pure Cu after HPT processing.

samples (Fig. 6b–d). In both the Cu–10SiC and Cu–20SiC samples, the numbers of the largest SiC particles after HPT processing decreases when compared with the as-sintered state. At the same time, the fraction of small particles, smaller than 2 μm, increases significantly especially in the sample with 20% of SiC reinforcement where the numbers of particles having sizes in the range of ~50–700 nm reaches ~10^4 per mm^2.

The SEM observations in Figs. 4c and 5d gives clear evidence for grain size refinement in the Cu matrix during HPT processing. However, in order to precisely determine the grain size distributions after HPT processing it was necessary to conduct more detailed investigations. Fig. 7 shows representative STEM images for Cu and the Cu–10SiC and Cu–20SiC samples after HPT processing. The microstructure is generally similar for all samples with the Cu matrix containing both elongated and equiaxial grains with a relatively small density of internal dislocations as shown in Fig. 7 a-c. The average grain size for these conditions was ~360 nm and there were clusters of fragmented SiC particles as in Fig. 7d and undeformed larger particles as in Fig. 7e.

3.2. Mechanical properties

The microhardness distributions across the disc diameters for the SPS-processed samples and samples processed by HPT through 20 turns are presented in Fig. 8. In addition, the average microhardness values with their standard deviations for all samples are given in Table 1. It should be noted that the microhardness measurements were undertaken using a procedure that avoided impinging or hitting any of the large SiC particles with the indenter.

The average microhardness of pure Cu after SPS process is ~58 Hv with a large scatter in the experimental results whereas in the SPS-processed samples with the SiC reinforcement the microhardness of the Cu matrix was at a level of ~65 Hv. After HPT processing, the hardness along the discs diameters in all samples tended to distribute homogenously with only a small depression in the values in the central regions as shown in Fig. 8. In pure Cu, the microhardness increased from ~58 Hv to ~178 Hv. In the samples with the SiC reinforcement, the hardness values were at levels of ~200 Hv and ~230 Hv for the HPT-processed Cu–10SiC and Cu–20SiC samples, respectively. It should be noted that the standard deviation for the SiC-reinforced samples was larger than for the pure Cu sample.

The results of tensile tests for the HPT-processed samples are illustrated in Fig. 9 where these data were complemented with the results for SPS-processed samples. The results and summarised in Table 2 showing the ultimate tensile strength (UTS), yield strength (YS) and elongation to failure. For the sintered Cu material, the YS is at a level of ~130 MPa with a UTS of ~235 MPa. In addition, the material exhibits a large elongation to failure of ~40%. The UTS of samples with the SiC reinforcement is much lower and the values are not larger than ~140 and ~75 MPa for the Cu–10SiC and Cu–20SiC samples, respectively. These samples also exhibited lower elongations to failure with values below 10%.

Processing by HPT has a strong impact on the mechanical behaviour in all samples. Thus, the UTS in pure copper increases from ~235 MPa to ~560 MPa. In the Cu–SiC samples, the UTS increases from ~140 MPa

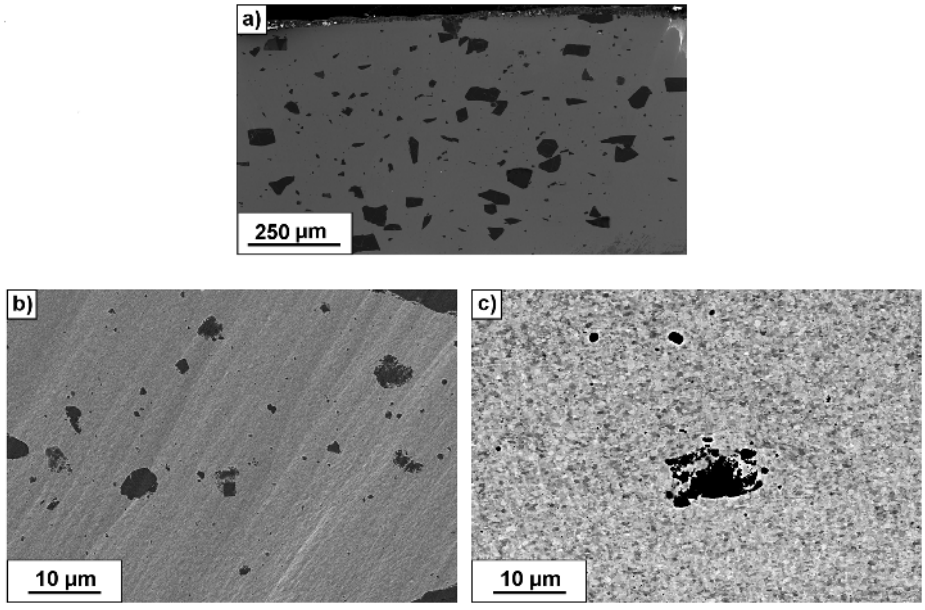

Fig. 4. SEM images of the microstructure of Cu–10SiC composite after HPT processing.

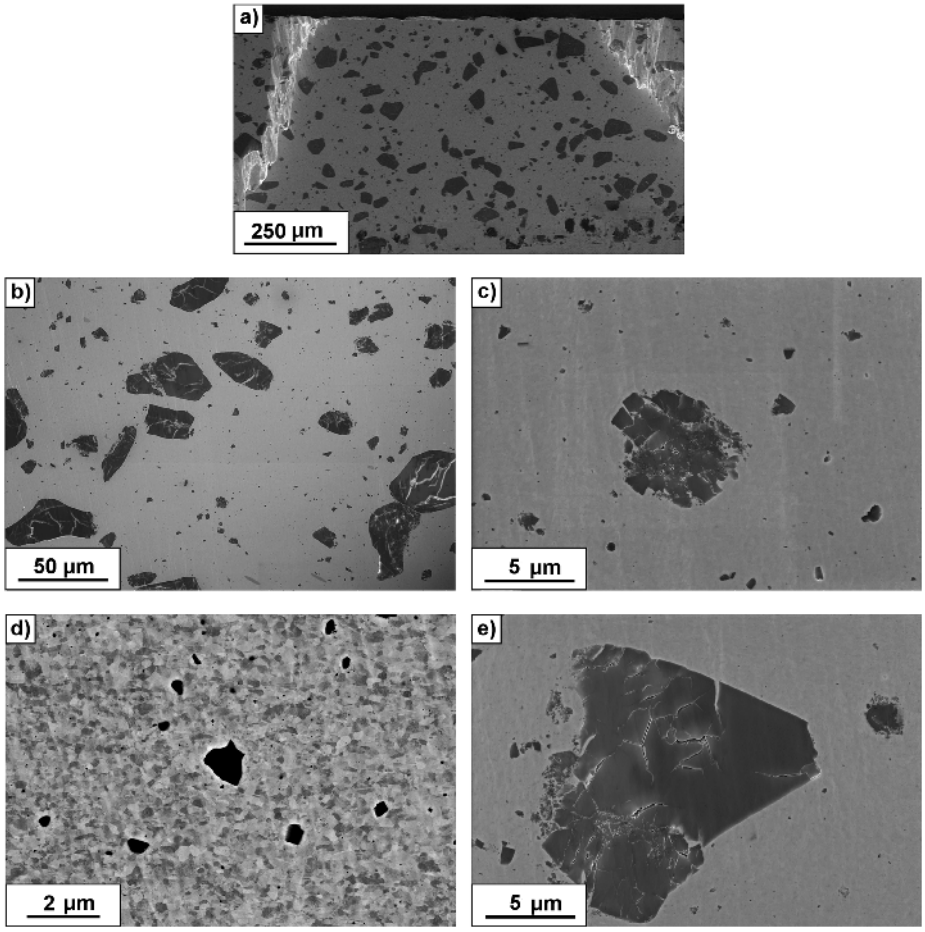

Fig. 5. SEM images of the microstructure of Cu–20SiC composite after HPT processing.

to ~420 MPa in Cu–10SiC and from ~75 MPa to ~440 MPa in Cu–20SiC. This high strength was at the expense of ductility and the elongations to failure dropped to ~10% and ~2% in the pure copper and SiC-reinforced samples, respectively.

3.3. Thermal conductivity

The thermal properties of Cu and the Cu–SiC composites were examined before and after HPT processing. Based on measurements of the thermal diffusivity, the thermal conductivity was estimated and the results are presented in Fig. 10. These data indicate that the fraction volume of SiC and the use of HPT processing have a significant impact on the thermal properties of these materials. The highest values of thermal conductivity were obtained for the SPS-processed copper and HPT-processed copper. As can be seen, the thermal conductivity of the HPT-processed Cu sample, measured at 50 °C, reached a value of ~450 W/mK which is almost 15% higher than the value of ~400 W/mK for the SPS-processed Cu sample. The conductivity values decrease with increasing testing temperature but the observed trend remains visible up to 150 °C. With a testing temperature above 150 °C, the results for the thermal conductivity of SPS-processed Cu and HPT-processed Cu are almost equal at ~375 W/mK.

A similar tendency is observed for the Cu–SiC composite samples. The thermal conductivity of the HPT-processed Cu–10SiC sample, measured at 50 °C, is almost equal to that of pure copper in the SPS state (~385 W/mK). The thermal conductivity values for the SPS-processed and HPT-processed Cu–10SiC samples decrease with increasing testing temperature. In addition, the conductivity values for the HPT-processed samples are higher than for the SPS-processed samples. The largest difference is observed up to 150 °C. At higher temperatures the results are almost equal although the conductivity for the composite samples after HPT processing is always higher by several units.

In the Cu–20SiC samples, the thermal conductivity at 50 °C for the HPT-processed sample is higher than for the SPS-processed sample and it is also higher than for the SPS-processed Cu–10SiC sample. In addition, for both SPS-processed and HPT-processed Cu–20SiC samples the conductivity decreases with increasing temperature but their values never become equal. These thermal conductivity values for the HPT-processed sample are higher by ~100 W/mK at 50 °C and by ~30 W/mK at 300 °C.

4. Discussion

4.1. Microstructures of SPS-processed samples and their evolution during HPT processing

SPS-processed samples exhibit some structural differences depending on their composition. In the pure copper sample the microstructure was highly inhomogeneous in terms of grain size whereas in the Cu–SiC samples the grain size in the copper matrix was more uniform. These structural differences are due to the inhomogeneous recrystallization and grain growth processes occurring during sintering and the inhibition in grain boundary mobility caused by the presence of pores and second phase particles [68,69]. One of the main factors limiting grain growth is the size of the powder particles used in the sintering. Therefore, for pure Cu sample there were large powder particles and it is reasonable to expect significant grain growth. However, a high fraction of fine-grained regions was also observed in this sample and it is worth emphasizing that these refined structures were observed mainly in the regions where there were high densities of pores. Thus,

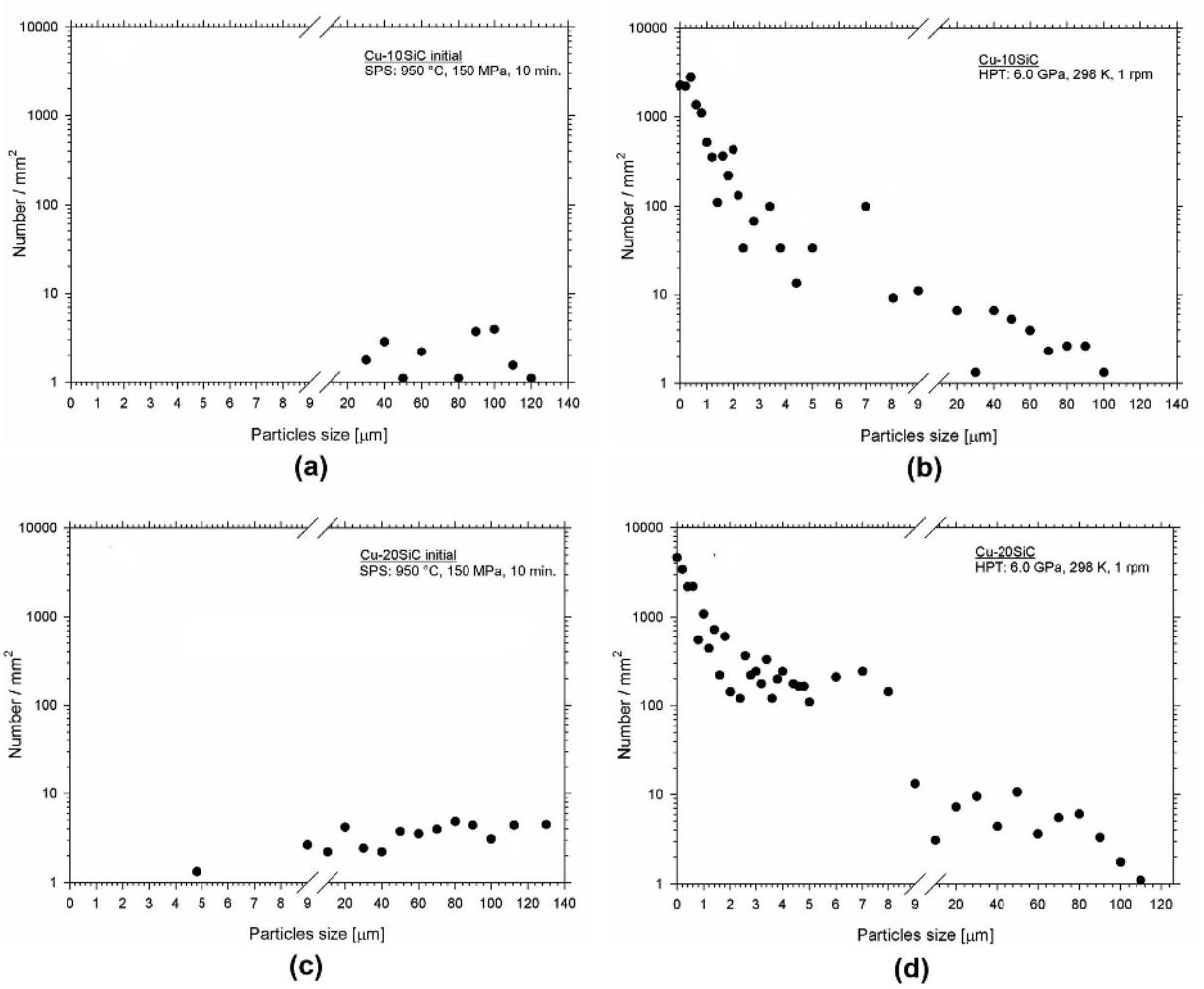

Fig. 6. Particles size distributions in Cu–SiC samples after SPS processing (a, c) and after HPT processing (b, d).

the presence of porosity significantly inhibits diffusion and grain growth by reducing the diffusion area [68,69]. Moreover, the surface area of the powder particles is always slightly oxidized and this oxidation also inhibits grain growth. Both factors play a significant role in the formation of fine-grained structures in the copper sample.

The addition of SiC particles acts to homogenise the grain size distribution in the Cu matrix. The SiC particles are thermally stable elements and they play a role as barriers impeding grain growth and recrystallization processes [70,71]. The inhibition of grain growth by dispersed particles, combined with the effects resulting from residual porosity and oxidation, leads to a more homogeneous average grain size in the copper matrix. In addition, it is worth noting that there were numerous discontinuities and voids at the interface between the SiC particles and the Cu matrix in these samples and this indicates that the SiC particles exhibit a poor wettability during sintering.

The results show also that HPT processing of Cu and Cu–SiC composites produces significant changes in the microstructure.

Firstly, it has a beneficial influence on the reduction of residual porosity. The SEM images in Fig. 3 show the presence of only single pores in all microstructures and no voids were observed at the interfaces between the SiC particles and the Cu matrix after HPT processing. The closure of pores is related to the processing parameters and is a direct consequence of the high imposed compressive pressure of 6.0 GPa and the high shear strains of more than ~400 generated in the outer parts of the discs during HPT. Both factors contribute to the closure of the remaining voids and pores in the samples [62,72,73] leading to further densification.

Secondly, the HPT processing causes a significant grain refinement in pure copper and the copper matrix as in Figs. 3–4 and the average grain size in all samples was of the order of ~360 nm. This is similar to the grain size in pure copper after 10 HPT revolutions which was reported as ~300 nm [74].

Thirdly, the HPT processing has a dual effect on the evolution of SiC particles in the composite samples. It leads to a significant fragmentation of the SiC particles as confirmed by SEM observations (Figs. 4 and 5) and quantitative analysis (Fig. 6). The number density of large SiC particles decreased and the number density of nanometric fragmented SiC particles significantly increased. In addition, after a large number of HPT turns there was a homogeneous distribution of fragmented SiC particles in the Cu matrix. A fragmentation of the hard ceramic phase during SPD processing was reported earlier for various MMCs, such as ZnO in a Cu matrix [73], Al_2O_3 in an aluminium matrix [75,76], SiC in an Al matrix [76], Al_3Ti in an aluminium matrix [77], TiB in Al and Ti matrices [78,79] and SiC in a Cu matrix [62]. These various reports demonstrate that the combination of a high compressive pressure with the high shear strains generated during torsional straining in HPT and the low fracture toughness of the SiC reinforcing phase favours particle fragmentation during processing [62,80]. The SiC ceramic particles embedded in the Cu matrix undergo an unusually high extent of plastic deformation during the HPT processing. Thus, extremely high shear strains are generated during HPT and this promotes dislocation formation in the ceramic phase (Fig. 7e), an activation of their movement by slip and then facilitates the transformation of slip bands to microcracks causing the fragmentation of the ceramic phase [62,80].

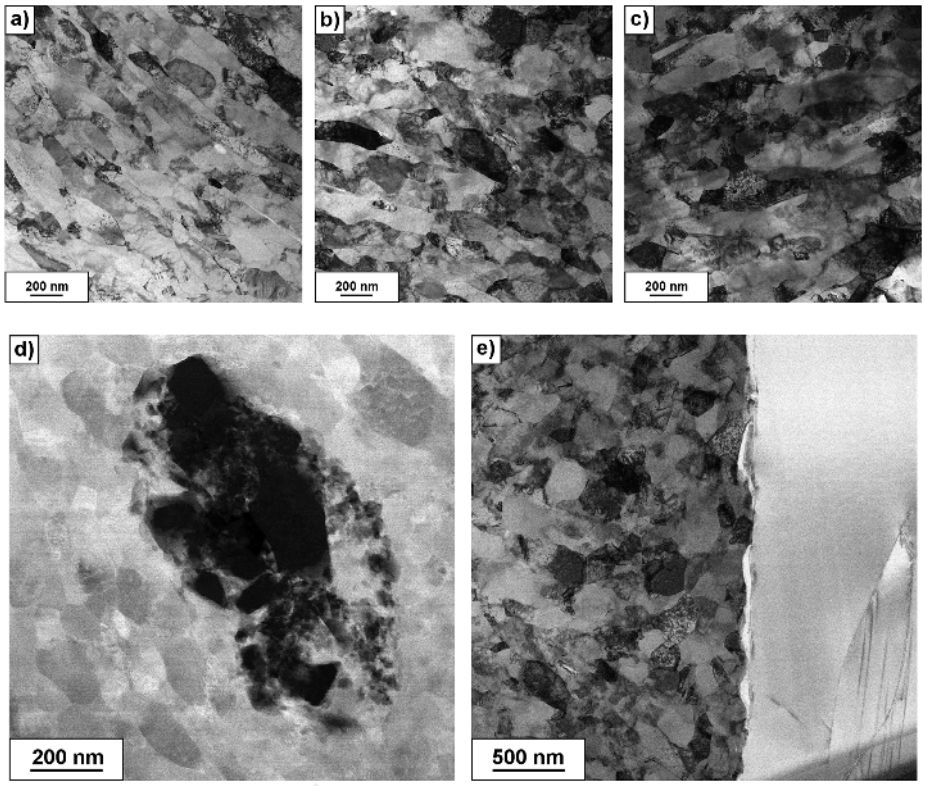

Fig. 7. STEM images of the Cu–SiC microstructure after HPT processing: (a) pure Cu, (b) Cu10SiC, (c) Cu20SiC, (d) a cluster of fine SiC particles embedded in Cu matrix, (e) interface between big SiC particle and Cu matrix.

It is worth emphasizing that the fragmentation effects reported in these experiments were not fully completed and high numbers of large SiC particles were observed in the microstructures after HPT processing (Figs. 4–6) which are a consequence of the insufficient strain that was imposed during HPT processing. Moreover, most of these particles contained numerous cracks and voids. By contrast, it was demonstrated that the size of SiC particles may be drastically reduced after 15 HPT revolutions [62] but in those studies powder particles were smaller than ~30 μm and therefore easier to fragment. These experiments also employed a higher compressive pressure of 10 GPa which again favours the formation of higher stresses in the material.

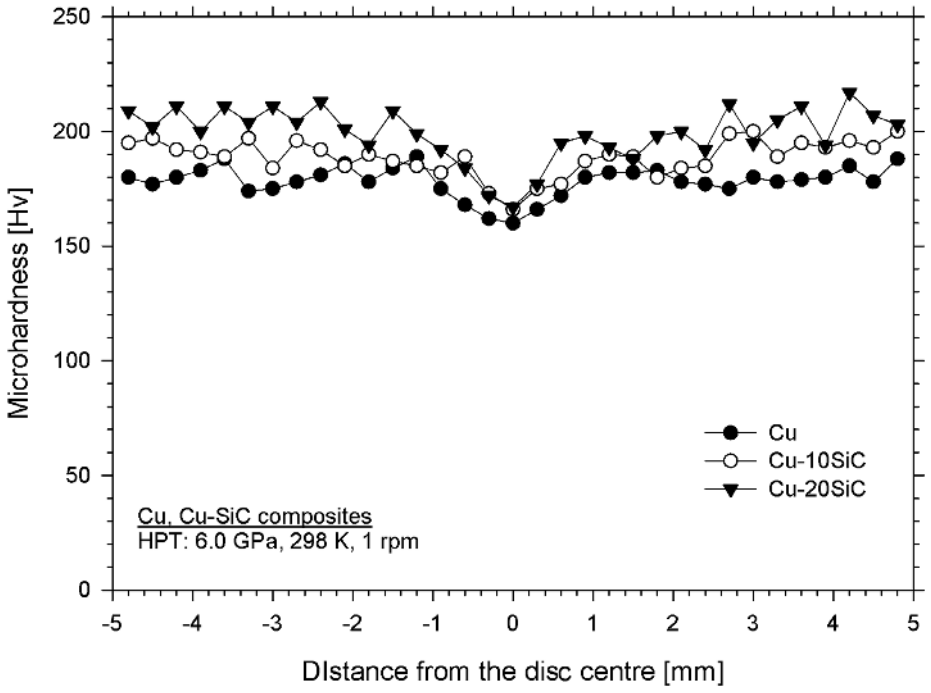

Fig. 8. Variations of hardness with distance from the disc centre for Cu and Cu–SiC samples after HPT processing.

Table 1
Showing average microhardness of studied samples together with their standard deviation.

Sample	Microhardness	Standard deviation
Cu sintered	58	7.6
Cu–10SiC sintered	65	3.4
Cu–20SiC sintered	66	2.5
Cu HPT	178	6.7
Cu–10SiC HPT	199	7.9
Cu–20SiC HPT	228	13.1

Table 2
Mechanical properties determined in tensile tests.

Sample	UTS [MPa]	YS [MPa]	Elongation [%]
Cu sintered	235	130	40
Cu–10SiC sintered	140	110	9
Cu–20SiC sintered	75	68	2.3
Cu HPT	560	480	10.3
Cu–10SiC HPT	440	395	2.9
Cu–20SiC HPT	420	385	1.9

4.2. The effect of HPT processing on the mechanical properties

The experimental results in these experiments prove that a combination of SPS and HPT processing is effective in producing MMC samples with exceptionally high strength. The SPS samples exhibited significant differences in the microhardness results with ~58 Hv and high scatter for pure copper and ~65 Hv for the MMCs with 10% and 20% of SiC reinforcement. The observed differences are related to the microstructures of these samples. Thus, in the pure copper sample a high grain size inhomogeneity was observed and this gave a reduced hardness and a large scatter in the experimental results. In the MMCs samples, where the SiC particles inhibited grain growth, the microstructure was homogeneous in terms of grain size and the hardness values were higher and more uniform.

In the samples processed by HPT, the microhardness increased more than three times and there was a reasonable level of homogeneity throughout the disc with only a small drop in hardness in the central regions. This indicates that the materials reached a saturation state [81]. After HPT processing, the average microhardness values increased to ~178 Hv for pure Cu and ~200 Hv and ~230 Hv for Cu–10SiC and Cu–20SiC, respectively. Such an increase in microhardness after HPT processing is related to the grain refinement in the Cu matrix, the increased density of dislocations and, for the MMCs, with the presence of fragmented fine SiC particles which act as obstacles to dislocation motion according to the Orowan model [82]. The fragmentation of the ceramic phase generates a high fraction of homogeneously distributed SiC nano-particles, as shown by the microstructure images presented in Figs. 4–5 and the particle size distributions in Fig. 6. The fragmentation of SiC particles is more intense for the sample containing 20% of reinforcement and this leads to the higher microhardness values in this sample.

The presence of an SiC reinforcement also has a major impact on the mechanical properties as measured in the tensile testing. In the SPS samples, the highest strength was obtained for pure copper (~200 MPa) whereas in the Cu–10SiC and Cu–20SiC samples the UTS values were ~130 MPa and ~75 MPa, respectively. This large reduction in strength is attributed to the presence of numerous pores and discontinuities at the interfaces between the Cu matrix and the SiC particles, as visible in Figs. 1 and 2, which act as stress concentrators leading to the propagation of cracks [83] and giving material failure at lower stresses. These results are consistent with earlier studies on Cu–SiC composites fabricated by various powder metallurgy techniques [15,26]. The poor wettability of SiC by copper significantly reduces the strength of the sintered samples [84].

The samples processed by HPT exhibited higher strength than those of the coarse-grained materials. The improvement in UTS of the pure Cu and Cu–SiC samples is associated with matrix strengthening through the grain refinement according to the Hall–Petch relationship [85,86]. In addition, the increased number density of fragmented nano-sized SiC particles [14,62] also plays a beneficial role contributing to the increase in the UTS. In earlier work a UTS as high as 850 MPa was reported for Cu–20SiC after 15 HPT revolutions [62]. However, the SiC particles used in the earlier experiments were smaller and therefore easier to fragment whereas the SiC particles in this study had diameters of ~100 μm. As presented in the SEM images in Figs. 4 and 5, even 20 HPT

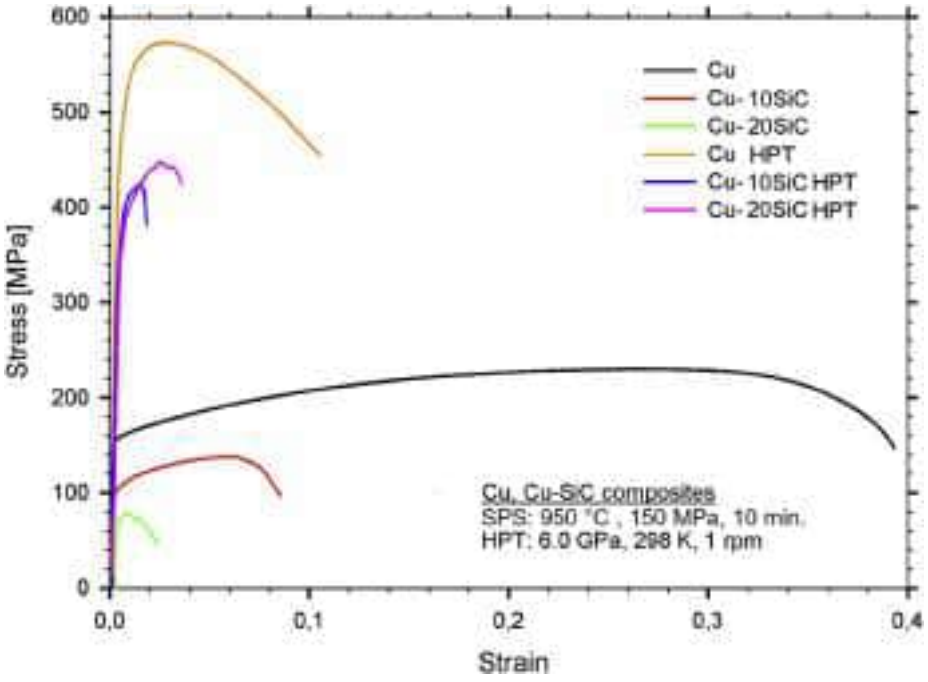

Fig. 9. Plots of stress versus strain for tensile specimens processed by HPT.

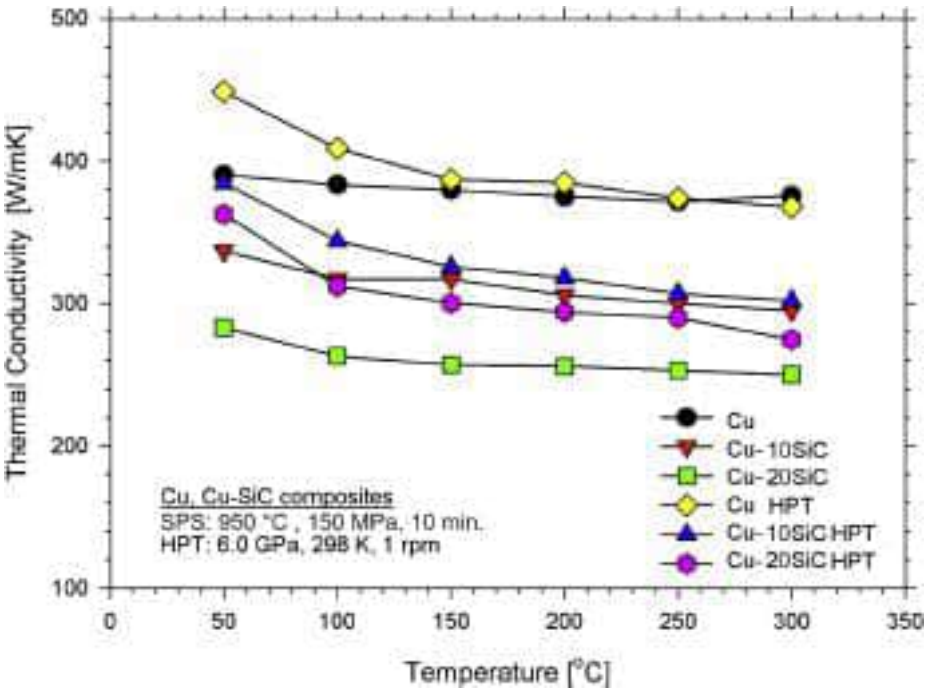

Fig. 10. Thermal conductivity as a function of temperature for SPS-processed samples and HPT-processed samples.

revolutions under a pressure of 6.0 GPa failed to produce sufficient shear forces to fully fragment such large particles (Fig. 6). Moreover, after HPT processing most of the remaining large particles were cracked (Fig. 5) which may also have a negative effect on the strength [83].

4.3. Effect of plastic deformation on thermal conductivity

No data on the effect of HPT on the thermal conductivity of Cu and Cu–SiC composites were reported so far. Therefore, it is important to provide a basic explanation of the thermal conductivity changes observed in Fig. 10. The results clearly show that the high plastic deformation introduced during HPT processing enhances the thermal conductivity. Thus, its value for pure copper subjected to 20 turns of HPT was ~445 W/(mK) while the thermal conductivity of sintered copper was only ~390 W/(mK). The results for the Cu–SiC MMCs are lower than those for the pure metal which is reasonable since the conductivity of SiC is 360 W/(mK). However, even in these samples there was an observable increase in the conductivity after HPT processing. Several factors may be responsible for this behaviour.

The first factor is associated with the further densification of the sample during HPT processing. The pores and other discontinuities are structural barriers to heat flow. Therefore, intense plastic deformation closes most of these defects, as in Figs. 3–5, thereby increasing the thermal conductivity.

The second factor is associated with structural changes in the Cu matrix. A large amount of cold working makes the samples thermally unstable and the rate of heat emission is enhanced [87,88]. As a consequence of plastic deformation and residual stresses, the lattice parameter may be slightly changed. Thus, atoms are more densely packed and the heat transfer is enhanced by physical or atomic contact between the conducting atoms. As a result, the absorbed heat is quickly transferred from one atom to the other [89,90]. It is also worth examining the density of defects generated during the SPD processing. In general, all structural defects are considered as structural barriers for heat flow. Some investigations suggest that dislocations are a source of anharmonic phonon–phonon scattering and this reduces the relaxation time of longitudinal acoustic phonons [91]. Increased phonon scattering by dislocations has been suggested as an explanation for the thermal conductivity reduction [91,92]. At some point, the numbers of scattering dislocations may be reduced due to dislocation annihilation [81]. Pure metals, such as the 99.99Cu used in this study, have a strong tendency for recovery processes and the density of defects is lower than in their alloys. This means that the effect of dislocation scattering on the thermal properties is probably essentially negligible.

5. Summary and conclusions

1) Samples of Cu, Cu–10SiC and Cu–20SiC were successfully consolidated by the SPS technique. Nevertheless, pores and voids remained at the interfaces between the Cu matrix and the SiC particles. Further processing by HPT made it possible to substantially reduce the residual porosity as well as increasing the bonding between the Cu matrix and the SiC particles.
2) Processing by HPT with a pressure of 6.0 GPa and 20 revolutions produced an ultrafine-grained structure in the Cu matrix for all samples with an average grain size of ~360 nm. It also led to the fragmentation of the SiC phase. As a result, high numbers of nano-sized SiC particles were observed after processing.
3) The presence of SiC nanoparticles and a refined microstructure in the Cu matrix contributed to an increase in the microhardness in the Cu and Cu–SiC samples.
4) The use of HPT processing significantly improves the strength of Cu–SiC composites but the presence of some remaining cracked large SiC particles had a negative impact on the strength of the MMCs which remained not higher than ~450 MPa.
5) It is shown that the thermal conductivity of Cu-based MMCs may be enhanced by subjecting these samples to intensive plastic deformation.

Acknowledgments

The work was supported by the National Science Centre, Poland, within the project SONATINA 1 “Synthesis of novel hybrid materials using High-Pressure Torsion”, under Grant Agreement No. UMO-2017/24/C/ST8/00145.

References

[1] W. Bai, A. Roy, R. Sun, V.V. Silberschmidt, Enhanced machinability of SiC-reinforced metal-matrix composite with hybrid turning, J. Mater. Process. Technol. 268 (2019) 149–161 https://doi.org/10.1016/j.jmatprotec.2019.01.017.

[2] J. Lin, K. Ma, H. Yang, M. Li, E.J. Lavernia, J.M. Schoenung, The microstructural design of trimodal aluminum composites, JOM 66 (2014) 898–908 https://doi.org/10.1007/s11837-014-0906-2.

[3] Ri. Gecu, Y. Yurekturk, E. Tekoglu, F. Muhaffel, A. Karaaslan, Improving wear resistance of 304 stainless steel reinforced AA7075 aluminum matrix composite by micro-arc oxidation, Surf. Coat. Technol. 368 (2019) 15–24 https://doi.org/10.1016/j.surfcoat.2019.04.029.

[4] B. Jin, D.-B. Xiong, Zhanqiu Tan, G. Fan, D. Zhang, Enhanced corrosion resistance in metal matrix composites assembled from graphene encapsulated copper nanoflakes, Carbon 142 (2019) 482–490 https://doi.org/10.1016/j.carbon.2018.10.088.

[5] S. Sivakumar, S.K. Thimmappa, B.R. Golla, Corrosion behavior of extremely hard Al-Cu/Mg-SiC light metal alloy composites, J. Alloy. Comp. 767 (2018) 703–711 https://doi.org/10.1016/j.jallcom.2018.07.117.

[6] R. Venkatesh, V.S. Rao, Thermal, corrosion and wear analysis of copper based metal matrix composites reinforced with alumina and graphite, Def Technol. 14 (2018) 346–355 https://doi.org/10.1016/j.dt.2018.05.003.

[7] K.E. Pappacena, M.T. Johnson, H. Wang, W.D. Porter, K.T. Faber, Thermal properties of wood-derived copper–silicon carbide composites fabricated via electrodeposition, Compos. Sci. Technol. 70 (2010) 478–484 https://doi.org/10.1016/j.compscitech.2009.11.011.

[8] M. Barmouz, M.K.B. Givi, Fabrication of in situ Cu/SiC composites using multi-pass friction stir processing: evaluation of microstructural, porosity, mechanical and electrical behaviour, Compos. Part A 42 (2011) 1445–1453 https://doi.org/10.1016/j.compositesa.2011.06.010.

[9] Z. Liao, A. Abdelhafeez, H. Li, Y. Yang, D. Axinte, State-of-the-art of surface integrity in machining of metal matrix composites, Int. J. Mach. Tool Manuf. 143 (2019) 63–91 https://doi.org/10.1016/j.ijmachtools.2019.05.006.

[10] G. Sdanghi, G. Maranzana, A. Celzard, V. Fierro, Review of the current technologies and performances of hydrogen compression for stationary and automotive applications, Renew. Sustain. Energy Rev. 102 (2019) 150–170 https://doi.org/10.1016/j.rser.2018.11.028.

[11] F. Shehata, A. Fathy, M. Abdelhameed, S.F. Moustafa, Preparation and properties of Al2O3 nanoparticle reinforced copper matrix composites by in situ processing, Mater. Des. 30 (2009) 2756–2762 https://doi.org/10.1016/j.matdes.2008.10.005.

[12] S.F. Moustafa, Z. Abbel-Hamid, A.M. Abd-Elhay, Copper matrix SiC and Al2O3 particulate composites by powder metallurgy technique, Mater. Lett. 53 (2002) 244–249 https://doi.org/10.1016/S0167-577X(01)00485-2.

[13] M. López, D. Corredor, C. Camurri, V. Vergara, J. Jiménez, Performance and characterization of dispersion strengthened Cu–TiB2 composite for electrical use, Mater. Char. 55 (2005) 252–262 https://doi.org/10.1016/j.matchar.2005.04.006.

[14] M.R. Akbarpour, E. Salahi, F. Alikhani Hesari, E.Y. Yoon, H.S. Kim, A. Simchi, Microstructural development and mechanical properties of nanostructured copper reinforced with SiC nanoparticle, Mater. Sci. Eng. A 568 (2013) 33–39 https://doi.org/10.1016/j.msea.2013.01.010.

[15] M. Chmielewski, K. Pietrzak, A. Strojny-Nędza, K. Kaszyca, R. Zybała, P. Bazarnik, M. Lewandowska, S. Nosewicz, Microstructure and thermal properties of Cu-SiC composite materials depending on the sintering technique, Sci. Sinter. 49 (2017) 11–22 https://doi.org/10.2298/SOS1701011C.

[16] S.T.K. Rajan, A.N. Balaji, P. Narayanasamy, S.C. Vettivel, Microstructural, electrical, thermal and tribological studies of copper-fly ash composites through powder metallurgy, Bull. Pol. Acad.: Technol. 66 (2018) 935–940 https://doi.org/10.24425/bpas.2018.125941.

[17] G.C. Efe, I. Altinsoy, M. Ipek, S. Zeytin, C. Bindal, Effects of SiC on properties of Cu-SiC metal matrix composites, AIP Conf. Proc. 1400 (2011) 529–534 https://doi.org/10.1063/1.3663176.

[18] A. Ramanathan, P.K. Krishnan, R. Muraliraja, A review on the production of metal matrix composites through stir casting – furnace design, properties, challenges, and research opportunities, J. Manuf. Process. 42 (2019) 213–245 https://doi.org/10.1016/j.jmapro.2019.04.017.

[19] B.C. Kandpal, J. Kumar, H. Singh, Manufacturing and technological challenges in Stir casting of metal matrix composites– A review, Mater. Today Proc. 5 (2018) 5–10 https://doi.org/10.1016/j.matpr.2017.01.130.

[20] T.S. Srivatsan, E.J. Lavernia, Use of spray techniques to synthesize particulate-reinforced metal-matrix composites, J. Mater. Sci. 27 (1992) 5965–5981, https://doi.org/10.1007/BF01133739.

[21] J. Maj, M. Basista, W. Węglewski, K. Bochenek, A. Strojny-Nędza, K. Naplocha, T. Panzner, M. Tatarková, F. Fiori, Effect of microstructure on mechanical properties and residual stresses in interpenetrating aluminum-alumina composites fabricated by squeeze casting, Mater. Sci. Eng. A 715 (2018) 154–162, https://doi.org/10.1016/j.msea.2017.12.091.

[22] D. Apelian, Particulate Processing (Powder Metallurgy), Encyclopedia of Materials: Science and Technology, second ed., Elsevier, Pergamon, 2001, pp. 6761–6768 https://doi.org/10.1016/B0-08-043152-6/01197-9.

[23] N.P. Hung, C.S. Lim, Y.K. Ho, Y.C. Tan, W.G. Tan, Cumulative creep and hot isostatic pressing of particle-reinforced metal matrix composites, J. Mater. Process. Technol. 101 (2000) 104–109 https://doi.org/10.1016/S0924-0136(00)00399-X.

[24] G. Miranda, A. Araújo, F. Bartolomeu, M. Buciumeanu, O. Carvalho, J.C.M. Souza, F.S. Silva, B. Henriques, Design of Ti6Al4V-HA composites produced by hot pressing for biomedical applications, Mater. Des. 108 (2016) 488–493 https://doi.org/10.1016/j.matdes.2016.07.023.

[25] M. Razavi, A.R. Farajipour, M. Zakeri, M.R. Rahimipour, A.R. Firouzbakht, Production of Al2O3–SiC nano-composites by spark plasma sintering, Boletín La Soc Española Cerámica Y Vidr 56 (2017) 186–194, https://doi.org/10.1016/j.bsecv.2017.01.002.

[26] M. Chmielewski, S. Nosewicz, E. Wyszkowska, Ł. Kurpaska, A. Strojny-Nędza, A. Piątkowska, P. Bazarnik, K. Pietrzak, Analysis of the micromechanical properties of copper-silicon carbide composites using nanoindentation measurements, Ceram. Int. 45 (2019) 9164–9173 https://doi.org/10.1016/j.ceramint.2019.01.257.

[27] M.J. Tan, X. Zhang, Powder metal matrix composites: selection and processing, Mater. Sci. Eng. A 244 (1998) 80–85 https://doi.org/10.1016/S0921-5093(97)00829-0.

[28] I. Sabirov, O. Kolednik, R.Z. Valiev, R. Pippan, Equal channel angular pressing of metal matrix composites: effect on particle distribution and fracture toughness, Acta Mater. 53 (2005) 4919–4930 https://doi.org/10.1016/j.actamat.2005.07.010.

[29] I. Sabirov, O. Kolednik, R. Pippan, Homogenization of metal matrix composites by high-pressure torsion, Metall. Mater. Trans. A 36 (2005) 2861–2870 https://doi.org/10.1007/s11661-005-0281-2.

[30] Y. Huang, P. Bazarnik, D. Wan, D. Luo, P.H.R. Pereira, M. Lewandowska, J. Yao, B.E. Hayden, T.G. Langdon, The fabrication of graphene-reinforced Al-based nanocomposites using high-pressure torsion, Acta Mater. 164 (2019) 499–511 https://doi.org/10.1016/j.actamat.2018.10.060.

[31] S.N. Alhajeri, K.J. Al-Fadhalah, A.I. Almazrouee, T.G. Langdon, Microstructure and microhardness of an Al-6061 metal matrix composite processed by high-pressure torsion, Mater. Char. 118 (2016) 270–278 https://doi.org/10.1016/j.matchar.2016.06.003.

[32] M. Kawasaki, Y. Huang, C. Xu, M. Furukawa, Z. Horita, T.G. Langdon, A quantitative study of cavity development in the tensile testing of an aluminum metal matrix composite processed by equal-channel angular pressing, Mater. Sci. Eng. A 410–411 (2005) 402–407.

[33] D. Ma, J. Wang, K. Xu, Equal channel angular pressing of a SiCw reinforced aluminum-based composite, Mater. Lett. 56 (2002) 999–1002, https://doi.org/10.1016/S0167-577X(02)00662-6.

[34] B.Q. Han, T.G. Langdon, Achieving enhanced tensile ductility in an Al-6061 composite processed by severe plastic deformation, Mater. Sci. Eng. A 410–411 (2005) 430–434.

[35] M.A. Muñoz-Morris, N. Calderón, I. Gutierrez-Urrutia, D.G. Morris, Matrix grain refinement in Al–TiAl composites by severe plastic deformation: influence of particle size and processing route, Mater. Sci. Eng. A 425 (2006) 131–137.

[36] G. Ramu, R. Bauri, Effect of equal channel angular pressing (ECAP) on microstructure and properties of Al–SiCp composites, Mater. Des. 30 (2009) 3554–3559.

[37] L. Bian, W. Liang, G. Xie, W. Zhang, J. Xue, Enhanced ductility in an Al–Mg2Si in situ composite processed by ECAP using a modified BC route, Mater. Sci. Eng. A 528 (2011) 3463–3467.

[38] I. Sabirov, R. Pippan, Formation of a W–25% Cu nanocomposite during high pressure torsion, Scr. Mater. 52 (2005) 1293–1298.

[39] X. Sauvage, R. Pippan, Nanoscaled structure of a Cu–Fe composite processed by high-pressure torsion, Mater. Sci. Eng. A 410–411 (2005) 345–347.

[40] I. Sabirov, R. Pippan, Characterization of tungsten fragmentation in a W–25% Cu composite after high-pressure torsion, Mater. Char. 58 (2007) 848–853.

[41] X. Quelennec, A. Menand, J.M. Le Breton, R. Pippan, X. Sauvage, Homogeneous Cu–Fe supersaturated solid solutions prepared by severe plastic deformation, Philos. Mag. 90 (2010) 1179–1195.

[42] Y.Z. Tian, Z.F. Zhang, T.G. Langdon, Achieving homogeneity in a two-phase Cu–Ag composite during high-pressure torsion, J. Mater. Sci. 48 (2013) 4606–4612.

[43] C. Gode, H. Yilmazer, I. Ozdemir, Y. Todaka, Microstructural refinement and wear property of Al–Si–Cu composite subjected to extrusion and high-pressure torsion, Mater. Sci. Eng. A 618 (2014) 377–384.

[44] M.R. Akbarpour, M. Farvizi, D.J. Lee, H. Rezaei, H.S. Kim, Effect of high-pressure torsion on the microstructure and strengthening mechanisms of hot-consolidated Cu–CNT nanocomposite, Mater. Sci. Eng. A 638 (2015) 289–295.

[45] S. Sabbaghianrad, T.G. Langdon, Developing superplasticity in an aluminum matrix composite processed by high-pressure torsion, Mater. Sci. Eng. A 655 (2016) 36–43 https://doi.org/10.1016/j.msea.2015.12.078.

[46] A.P. Zhilyaev, T.G. Langdon, Using high-pressure torsion for metal processing: fundamentals and applications, Prog. Mater. Sci. 53 (2008) 893–979.

[47] R.Z. Valiev, T.G. Langdon, Principles of equal-channel angular pressing as a processing tool for grain refinement, Prog. Mater. Sci. 51 (2006) 881–981.

[48] Y. Saito, H. Utsunomiya, N. Tsuji, T. Sakai, Novel ultra-high straining process for bulk materials—development of the accumulative roll-bonding (ARB) process, Acta Mater. 47 (1999) 579–583 https://doi.org/10.1016/S1359-6454(98)00365-6.

[49] M. Lewandowska, H. Garbacz, W. Pachla, K.J. Kurzydlowski, Hydrostatic extrusion and nanostructure formation in an aluminium alloy, Solid State Phenom. 101–102 (2005) 65–69.

[50] P. Bazarnik, M. Lewandowska, K.J. Kurzydlowsk, Mechanical behaviour of ultrafine grained AI-Mg alloys obtained by different processing routes, Arch. Metall. Mater. 57 (2012) 869–876, https://doi.org/10.2478/V10172-012-0096-2.

[51] P. Bazarnik, Y. Huang, M. Lewandowska, T.G. Langdon, Structural impact on the Hall–Petch relationship in an Al–5Mg alloy processed by high-pressure torsion, Mater. Sci. Eng. A 626 (2015) 9–15 https://doi.org/10.1016/j.msea.2014.12.027.

[52] A.T. Krawczynska, S. Gierlotka, P. Suchecki, D. Setman, B. Adamczyk-Cieslak, M. Gloc, W. Chrominski, M. Lewandowska, M. Zehetbauer, Phenomena occurring in nanostructured stainless steel 316LVM during annealing under high hydrostatic pressure, Adv. Eng. Mater. 21 (2019) 1800101 https://doi.org/10.1002/adem.201800101.

[53] V.V. Stolyarov, Y.T. Zhu, T.C. Lowe, R.K. Islamgaliev, R.Z. Valiev, Processing nanocrystalline Ti and its nanocomposites from micrometer-sized Ti powder using

high pressure torsion, Mater. Sci. Eng. A 282 (2000) 78–85 https://doi.org/10.1016/S0921-5093(99)00764-9.
[54] A.P. Zhilyaev, G. Ringot, Y. Huang, J.M. Cabrera, T.G. Langdon, Mechanical behavior and microstructure properties of titanium powder consolidated by high-pressure torsion, Mater. Sci. Eng. A 688 (2017) 498–504 https://doi.org/10.1016/j.msea.2017.02.032.
[55] S. Sabbaghianrad, M. Kawasaki, T.G. Langdon, Microstructural evolution and the mechanical properties of an aluminum alloy processed by high-pressure torsion, J. Mater. Sci. 47 (2012) 7789–7795.
[56] A.P. Zhilyaev, A.A. Gimazov, G.I. Raab, T.G. Langdon, Using high-pressure torsion for the cold-consolidation of copper chips produced by machining, Mater. Sci. Eng. A 486 (2008) 123–126.
[57] M.M. de Castro, A.P. Carvalho, P.H.R. Pereira, A.C. Isaac Neta, R.B. Figueiredo, T.G. Langdon, Consolidation of magnesium and magnesium alloy machne chips using high-pressure torsion, Mater. Sci. Forum 941 (2018) 851–856.
[58] J.-K. Han, X. Li, R. Dippenaar, K.-D. Liss, M. Kawasaki, Microscopic plastic response in a bulk nano-structured TiAl intermetallic compound processed by high-pressure torsion, Mater. Sci. Eng. A 714 (2018) 84–92 https://doi.org/10.1016/j.msea.2017.12.065.
[59] K. Edalati, S. Toh, M. Watanabe, Z. Horita, In situ production of bulk intermetallic-based nanocomposites and nanostructured intermetallics by high-pressure torsion, Scr. Mater. 66 (2012) 386–389 https://doi.org/10.1016/j.scriptamat.2011.11.039.
[60] M.M. Castro, P.H.R. Pereira, A. Isaac, R.B. Figueiredo, T.G. Langdon, Development of a magnesium/alumina composite through cold consolidation of machining chips by high-pressure torsion, J. Alloy. Comp. 780 (2019) 422–427.
[61] M.M. Castro, S. Sabbaghianrad, P.H.R. Pereira, E.M. Mazzer, A. Isaac, T.G. Langdon, R.B. Figueiredo, A magnesium-aluminium composite produced by high-pressure torsion, J. Alloy. Comp. 804 (2019) 421–426.
[62] M.I.A. El Aal, Effect of high-pressure torsion processing on the microstructure evolution and mechanical properties of consolidated micro size Cu and Cu-SiC powders, Adv. Powder Technol. 28 (2017) 2135–2150 https://doi.org/10.1016/j.apt.2017.05.020.
[63] O. Ghaderi, M.R. Toroghinejad, A. Najafizadeh, Investigation of microstructure and mechanical properties of Cu–SiCP composite produced by continual annealing and roll-bonding process, Mater. Sci. Eng. A 565 (2013) 243–249 https://doi.org/10.1016/j.msea.2012.11.004.
[64] M. Jahedi, M.H. Paydar, M. Knezevic, Enhanced microstructural homogeneity in metal-matrix composites developed under high-pressure-double-torsion, Mater. Char. 104 (2015) 92–100 https://doi.org/10.1016/j.matchar.2015.04.012.
[65] R.B. Figueiredo, P.R. Cetlin, T.G. Langdon, Using finite element modelling to examine the flow processes in quasi-constrained high-pressure torsion, Mater. Sci. Eng. A 528 (2011) 8198–8204.
[66] R.M. Molak, K. Paradowski, T. Brynk, L. Ciupinski, Z. Pakiela, K.J. Kurzydlowski, Measurement of mechanical properties in a 316L stainless steel welded joint, Int. J. Press. Vessel. Pip. 86 (2009) 43–47.
[67] S. Min, J. Blumm, A. Lindemann, A new laser flash method for measurement of the thermophysical properties, Thermochim. Acta 455 (2007) 46–49.
[68] N.A. Rawashdeh, W. Khraisat, H. Borgström, Pinning effect of pores on grain growth in sintered steel, Jordan J. Mech. Ind. Eng. 11 (2017) 73–78.
[69] V. Rehn, J. Hötzer, W. Rheinheimer, M. Seiz, C. Serr, B. Nestler, Phase-field study of grain growth in porous polycrystals, Acta Mater. 174 (2019) 439–449 https://doi.org/10.1016/j.actamat.2019.05.059.
[70] S. Farag, I. Konyashin, B. Ries, The influence of grain growth inhibitors on the microstructure and properties of submicron, ultrafine and nano-structured hard-metals – a review, Int. J. Refract. Metals Hard 77 (2018) 12–30 https://doi.org/10.1016/j.ijrmhm.2018.07.003.
[71] M. Ao, H. Liu, C. Dong, The effect of La2O3 addition on intermetallic-free aluminium matrix composites reinforced with TiC and Al2O3 ceramic particles, Ceram. Int. 45 (2019) 12001–12009 https://doi.org/10.1016/j.ceramint.2019.03.093.
[72] Y. Qi, A. Kosinova, A.R. Kilmametov, B.B. Straumal, E. Rabkin, Generation and healing of porosity in high purity copper by high-pressure torsion, Mater. Char. 145 (2018) 1–9 https://doi.org/10.1016/j.matchar.2018.08.023.
[73] Y. Qi, A. Kosinova, A.R. Kilmametov, B.B. Straumal, E. Rabkin, Plastic flow and microstructural instabilities during high-pressure torsion of Cu/ZnO composites, Mater. Char. 145 (2018) 389–401 https://doi.org/10.1016/j.matchar.2018.09.001.
[74] Z. Horita, T.G. Langdon, Microstructures and microhardness of an aluminum alloy and pure copper after processing by high-pressure torsion, Mater. Sci. Eng. A 410–411 (2005) 422–425 https://doi.org/10.1016/j.msea.2005.08.133.
[75] K. Edalati, M. Ashida, Z. Horita, T. Matsui, H. Kato, Wear resistance and tribological features of pure aluminum and Al–Al2O3 composites consolidated by high-pressure torsion, Wear 310 (2014) 83–89 https://doi.org/10.1016/j.wear.2013.12.022.
[76] K.C. Nayak, P.P. Date, Hot deformation flow behavior of powder metallurgy based Al-SiC and Al-Al2O3 composite in a single step and two-step uni-axial compression, Mater. Char. 151 (2019) 563–581 https://doi.org/10.1016/j.matchar.2019.03.047.
[77] H. Sato, Y. Watanabe, Three-dimensional microstructural analysis of fragmentation behavior of platelet Al3Ti particles in Al-Al3Ti composite deformed by equal-channel angular pressing, Mater. Char. 144 (2018) 305–315 https://doi.org/10.1016/j.matchar.2018.07.005.
[78] Y. Han, J. Li, G. Huang, Y. Lv, X. Shao, W. Lu, D. Zhang, Effect of ECAP numbers on microstructure and properties of titanium matrix composite, Mater. Des. 75 (2015) 113–119 https://doi.org/10.1016/j.matdes.2015.03.018.
[79] R. Shobha, C. Siddaraju, K.R. Suresh, H.B. Niranjan, Mechanical property evaluation of heat treated insitu Al- TiB2 composite after severe plastic deformation, Mater. Today Proc. 5 (2018) 2534–2540.
[80] R. Pippan, S. Scheriau, A. Taylor, M. Hafok, A. Hohenwarter, A. Bachmaier, Saturation of fragmentation during severe plastic deformation, Annu. Rev. Mater. Res. 40 (2010) 319–343, https://doi.org/10.1146/annurev-matsci-070909-104445.
[81] M. Kawasaki, R.B. Figueiredo, T.G. Langdon, An investigation of hardness homogeneity throughout disks processed by high-pressure torsion, Acta Mater. 59 (2011) 308–316.
[82] Z. Zhang, D.L. Chen, Consideration of Orowan strengthening effect in particulate-reinforced metal matrix nanocomposites: a model for predicting their yield strength, Scr. Mater. 54 (2006) 1321–1326.
[83] Walter D. Pilkey, Deborah F. Pilkey, Peterson's Stress Concentration Factors, third ed., A Wiley-Interscience Publications, 978-0-470-04824-5, 2008.
[84] M. Chmielewski, K. Pietrzak, M. Teodorczyk, S. Nosewicz, D. Jarzabek, R. Zybała, P. Bazarnik, M. Lewandowska, A. Strojny-Nedza, Effect of metallic coating on the properties of copper-silicon carbide composites, Appl. Surf. Sci. 421A (2017) 159–169.
[85] E.O. Hall, The deformation and ageing of mild steel III discussion of results, Proc. Phys. Soc. Sect. B 64 (1951) 747–753.
[86] N.J. Petch, The cleavage strength of polycrystals, J. Iron Steel Inst. 174 (1953) 25–28.
[87] J. Omotoyinbo, I.O. Oladele, W. Shokoya, Effect of the degree of plastic deformation on the electrical resistance and thermal conductivity of Al-Mg-Si alloy, Leonardo Electron. J. Pract. Technol. 13 (2014) 37–50.
[88] O.V. Gendelman, M. Shapiro, Y. Estrin, R.J. Hellmig, S. Lekhtmakher, Grain size distribution and heat conductivity of copper processed by equal channel angular pressing, Mater. Sci. Eng. A 434 (2006) 88–94 https://doi.org/10.1016/j.msea.2006.06.091.
[89] P.J. Bolt, N.A.P.M. Lamboo, P.J.C.M. Rozier, Feasibility of warm drawing of Aluminium products, J. Mater. Process. Technol. 115 (1) (2001) 118–121.
[90] R. Riahifar, S. Serajzadeh, Three dimensional model for hot rolling of aluminium alloys - thermal conductivity of 6063 aluminium alloy, Mater. Des. 28 (8) (2007) 2366–2372.
[91] K. Termentzidis, M. Isaiev, A. Salnikova, I. Belabbas, D. Lacroix, J. Kioseoglou, Impact of screw and edge dislocations on the thermal conductivity of individual nanowires and bulk GaN: a molecular dynamics study, Phys. Chem. Chem. Phys. 20 (2018) 5159–5172, https://doi.org/10.1039/C7CP07821H.
[92] S.I. Kim, K.H. Lee, H.A. Mun, H.S. Kim, S.W. Hwang, J.W. Roh, D.J. Yang, W.H. Shin, X.S. Li, Y.H. Lee, G.J. Snyder, S.W. Kim, Dense dislocation arrays embedded in grain boundaries for high-performance bulk thermoelectrics, Science 348 (2015) 109–114, https://doi.org/10.1126/science.aaa4166.

Journal of Alloys and Compounds 1005 (2024) 176208

Contents lists available at ScienceDirect

Journal of Alloys and Compounds

journal homepage: www.elsevier.com/locate/jalcom

The influence of graphene oxide on the microstructure and properties of ultrafine-grained copper processed by high-pressure torsion

Maria Emerla [a], Piotr Bazarnik [a,*], Yi Huang [b,c], Anita Wojciechowska [a], Marta Ciemiorek [a], Jarosław Pura [a], Monika Wieczorek-Czarnocka [a], Purbayanto Muhammad Abiyyu Kenichi [a], Agnieszka Jastrzębska [a], Małgorzata Lewandowska [a], Terence G. Langdon [b]

[a] Warsaw University of Technology, Faculty of Materials Science and Engineering, Wołoska 141, Warsaw 02-507, Poland
[b] Materials Research Group, Department of Mechanical Engineering, University of Southampton, Southampton SO17 1BJ, United Kingdom
[c] Department of Design and Engineering, Faculty of Science and Technology, Bournemouth University, Poole, Dorset BH12 5BB, United Kingdom

ARTICLE INFO

Keywords:
Copper
High-pressure torsion
Metal matrix composites
Thermal stability
Graphene Oxide

ABSTRACT

New metal matrix nanocomposites with enhanced thermal stability were produced in a three step process consisting of mechanical milling, spark plasma sintering and High-Pressure Torsion (HPT). The nanocomposites consisted of a copper matrix and the addition of 1 wt% Graphene Oxide (GO) as a reinforcement. A nanocrystalline microstructure, enhanced hardness and improved thermal stability were achieved. The grain size of the nanocomposites was ~55 nm which is almost four time smaller than for Cu HPT at 210 nm. Hardnes and ultimate tensile strength of the nanocomposites reach 250 Hv and 700 MPa, respectively, which was more than three times higher than for the initial material. The most important result is that the nanocomposites remained ultrafine-grained up to 500 °C whereas the Cu HPT fully recrystalized after annealing at 300 °C The report also includes an investigation of the electrical conductivity of the copper-based composite which was slightly better than for copper after HPT together with the wear behaviour of this material. This is one of the first reports on copper reinforced with graphene oxide composites produced by HPT and it gives information on its thermal stability, electrical conductivity and wear behaviour together with the microstructural characteristics and mechanical properties.

1. Introduction

The modern industry places increasing demands on structural materials so that new approaches to materials development are a pressing requirement. Novel fabrication techniques allow combined properties and provide a potential for new functionalities. One of the directions in this field is to increase the strength of the metals through grain size reduction [1–4]. It is well known that intense grain refinement to the ultrafine-grained (UFG) or nanocrystalline (NC) level leads to a significant increase in strength, as described by the Hall–Petch relationship [5,6]. In practice, UFG and NC materials are most readily produced in bulk form by subjecting materials to severe plastic deformation (SPD). A number of techniques are now available for the SPD processing of metals [2–4,7–11] The most promising in terms of producing novel metallic structures with the smallest possible grain sizes is high-pressure torsion (HPT) [2,4]. HPT is considered the most effective for achieving UFG and NC structures because of the processing ability to generate extremely high strains [12,13].

Despite a very significant increase in strength, UFG and NC materials generally exhibit some disadvantages. For example, it was proven that in SPD processing the grain size decreases with increasing strain until it reaches a stable minimum which is designated the saturation state. This limitation in grain refinement has attracted much attention [14–19] and it appears to be an inherent feature of each material depending upon the crystallographic structure, stacking-fault energy, purity level of the alloy or the presence of intermetallic impurities. Moreover, the commercial applications of the UFG/NC alloys are limited due to their low microstructural stability at elevated temperatures which complicates the processing of final products in industry. Due to the high energy stored in these materials in the form of defects such as grain boundaries or dislocations, they are inherently thermally unstable and annealing, even at low temperatures, leads to recrystallization and coarsening of the

* Corresponding author.
E-mail address: piotr.bazarnik@pw.edu.pl (P. Bazarnik).

https://doi.org/10.1016/j.jallcom.2024.176208
Received 25 June 2024; Received in revised form 26 August 2024; Accepted 27 August 2024
Available online 29 August 2024

microstructure, which in turn degrades the material properties [20–22]. In extreme cases, as in ultra-pure copper after HPT processing, the material recrystallizes already at room temperature [15].

Overcoming the problem of insufficient thermal stability and grain refinement limitations in UFG and NC materials is currently a challenge in materials science. Different physical phenomena could allow the control of grain growth and the stabilization of the structure. One of the most effective approaches is to use nano-particles uniformly distributed within the metal matrix that will have a pinning effect on any lattice defects, such as dislocations and grain boundaries, thereby stabilizing the UFG microstructure and expanding the temperature window for their potential technological applications [23–25]. Moreover, it has been proven that the addition of dispersed nanoparticles can overcome the saturation effect, leading to a further grain size reduction during SPD processing [26]. However, most studies omit the thermal stability of metal matrix composites (MMCs) while focusing on the synthesis and impact of reinforcement on the microstructural development. By contrast, only a few reports focus on systematic studies to improve the thermal stability in UFG/NC metals reinforced with dispersed particles [23,24,27].

There are several reports regarding HPT processing of composites reinforced with various oxide and carbide particles [23,24,28–32] and composites reinforced with carbon-based particles such as fullerenes [33] or carbon nanotubes [27,34]. Recently, a new group of composites was introduced reinforced with graphene nanoparticles (GNPs) [35–37] or graphene-oxide (GO) nanoparticles [38]. Research on Al-GNPs [37] and Cu-GNPs [39] fabricated by HPT processing shows the general trend that the addition of even small amounts (1–2 %) of graphene produces a remarkable increase in the mechanical properties, a decrease in the coefficient of friction, an improvement in the electrical conductivity [39] and even an improvement in the wear resistance [39], when compared with pure metals after HPT processing [40,41]. In practice, GO is easier to produce and easier to uniformly distribute in a Cu matrix than graphene due to oxide functional groups on the GO surface. Moreover, it has been reported that the oxygen groups in GO have a tendency to create a strong bonding with the metallic matrix whereas in graphene-based composites this connection is weakened [39,42–44]. At the same time, there are only a few publications covering copper-based composites reinforced with GO and none of them focuses on composites produced by HPT. Accordingly, the present study was therefore initiated to evaluate the use of HPT processing in the fabrication of Cu-GO composites as well as evaluating their mechanical properties, electrical conductivity and thermal stability.

2. Materials and methods

2.1. Materials

The Cu-GO nanocomposites were produced in a three-step process consisting of: 1) a mixing of the powders by mechanical milling, and then 2) sintering by a Spark Plasma Sintering (SPS) method and finally 3) processing by HPT.

A regular-shaped copper powder (produced by ABCR company) with a purity of 99 % and a particle size of ~50 ± 13 μm was used as the matrix. The composites were reinforced by adding 1 wt% of GO flakes produced by modification of Hummers method which was described in another report [45]. The powders were mixed in a planetary ball milling system (Retsch PM100) in an argon protective atmosphere with a speed of 300 rpm and time of 1 h. The weight ratio of powder to ball was 1:10. The milling chamber and balls were made of ZrO_2.

2.2. Fabrication

The powders were consolidated by the SPS technique using a graphite die with a sample diameter of 10 mm and a height of 10 mm. The sintering process was carried out at a temperature of 950 °C in an argon atmosphere with a heating rate of 100 °C/min and a 15 min holding time at maximum temperature and a pressure of 50 MPa. As a reference, a sample of pure copper (denoted as Cu SPS) was sintered under the same conditions. Fig. 1 illustrates the microstructure of this sample where it consists of large grains of about 27 ± 10 μm with twins and many round-shaped pores with average diameters of about 1μm. The density of this sample measured by the Archimedes' method was 8.44 g/cm^3 which is about 95 % of the theoretical density of copper.

The sintered samples were cut with a circular saw into discs of 10 mm diameter and 1 mm height and then subjected to HPT processing. This processing was conducted under an applied pressure of 6.0 GPa at room temperature under quasi-constrained conditions [46]. Discs were torsionally strained by rotating the lower anvil at 1 rpm through 20 revolutions for the Cu-GO nanocomposite and for the Cu reference sample. Potential slippage and temperature rise during HPT were controlled according to standards from previous studies [47–49].

2.3. Characterization

The microstructures of Cu and the Cu-GO composites were examined using scanning electron microscopy (SEM) (Hitachi Su8000) operating at an accelerating voltage of 10 kV in back-scattered electron (BSE) mode and secondary electron (SE) mode. The SEM observations were carried out on cross-sectional planes of the discs in an area ~1 mm from the disc edge. The samples for SEM observations were prepared by ion milling polishing on Hitachi IM4000. This procedure gives a high quality surface without any deformation, stresses and/or the formation of oxide layers, and it allows the structure to be observed in so-called channel contrast in the SEM. Detailed structural investigations were complemented using scanning electron transmission microscopy (STEM) Thermo-Fisher Scientific SPECTRA 200, with a dedicated Cs-corrected high resolution microscope operating under an accelerating voltage of 200 kV and equipped with Super-X energy dispersion spectroscopy (EDS) detectors. The samples for STEM observations were cut using a focus ion beam (FIB) microscope Hitachi NB-5000. Structural investigations were complemented with Raman spectroscopy in order to confirm the presence of GO particles in the composites. Firstly, the GO flakes were tested, then the mixed powders and finally the composites after HPT. The tests were conduct on a spectroscope produced by Renishaw company with a laser wavelength of 514 nm.

The mechanical properties of HPT-processed samples were evaluated using microhardness measurements, tensile testing and wear testing. The Vickers microhardness, Hv, was measured along radial directions on the polished disc surfaces using a Falcon 503 microhardness tester. The measurements were taken under a load of 200 g and dwelling time 10 s along randomly selected diameters on each disc with a spacing of 0.3 mm between the measuring points. The results were plotted in the form of the hardness profiles. The tensile tests were carried out on microsamples cut from discs by electrical discharge using a universal testing machine Zwick Z005 with an initial strain rate of 10^{-3} s^{-1}. For

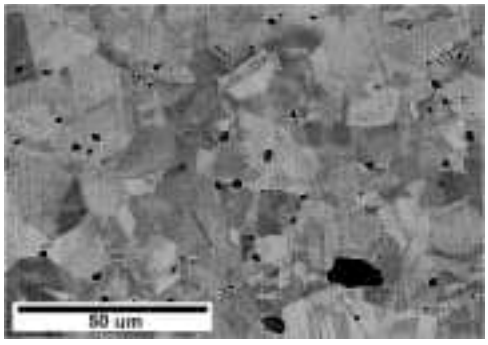

Fig. 1. SEM BSE image of microstructure of Cu SPS.

each state at least two samples were cut and tested. The gauge sections of the samples were 4 mm long and the cross-sections were 0.6×0.8 mm^2. A Digital Image Correlation system was used for the tests in order to accurately measure the elongations.

The wear behaviour was examined in a reciprocating sliding condition by pin-on-plate testing with the use of NC6 steel as the contra material with a hardness of 270 Hv (PN-EN ISO 4957). The pin diameter was 3 mm and its surface was prepared by grinding on 1000 paper. The test was conducted under a load of 3 kg and time of 8 h at room temperature in an air atmosphere without the use of a lubricant. The range of motion of the pin along the disc was 8 mm, the number of cycles was 28800, the frequency was 1 Hz and the total friction path was 345.6 m. All samples were weighed before and after the wear test. After the test, the abrasion surface was examined using a profilometer (Wyko NT9300 optical profilometer from Veeco) and SEM method. For comparative reasons the friction coefficient and wear rate were calculated. The friction force was measured directly by the wear test device in N and the friction coefficient was then calculated by dividing the friction force in N by using the load in N. The wear rate was calculated by dividing the volume of the wiped sample material by the pressing force multiplied by the friction distance.

Samples for the electrical conductivity test were prepared by grinding and finishing the surface by polishing with a diamond suspension of 1 μm. The electroconductivity measurements were conducted by a four-point method using a digital multimeter (Keithley DAQ6510, USA). The measurements were taken at three different spots and the reported electrical conductivity was obtained by taking the average of these values. This method involves the use of four probes in a single line with known equal spacing between them of 2 mm. The flow of current between the two outer probes causes a reduction in the voltage between the two inner probes and, by measuring this change, it is possible to determine the resistance of the sample and thus determine its electrical conductivity. The resistance was measured in Ohm and related to the dimensions of the probes in meters, and the inverse of this value is then the conductivity of the probes expressed in Simens per metre.

The thermal stability was investigated by annealing the samples for 1 hour in a 100–500 °C temperature range. After annealing, the hardness of the samples was measured in the same manner as for the samples before annealing. Thereafter, the microstructure was investigated by SEM and STEM with the sample preparation and the observations made in the same way as for the unannealed samples.

3. Results

3.1. Microstructure characterization

Fig. 2a, b shows SEM BSE microstructural images of the pure Cu and Cu-GO nanocomposite both after HPT. The average grain size in pure copper (Fig. 2a) was 210 nm and this is consistent with the results reported for materials processed using conventional SPD methods [40]. The addition of GO led to more intense grain refinement (Fig. 2b) and the resultant grain size was too small to be visible in the SEM images. At the same time, some GO agglomerates were detected in the microstructure (black in BSE contrast in Fig. 2b) but their sizes was not larger than ~500 nm and they covered less than 1.5 % of the composite surface area.

The SEM structural investigations of the Cu-GO nanocomposite were complemented with STEM studies. Fig. 2c, d shows exemplary STEM images of the microstructure of the Cu-GO composite in bright-field (BF) and high-angle annular dark field (HAADF) modes, respectively. The BF mode image (Fig. 2c) shows a highly refined structure of the Cu matrix consisting of equiaxed grains containing a high concentration of dislocations. The average grain size determined from these images was ~55 nm. On the other hand, the HAADF image (Fig. 2d) demonstrates

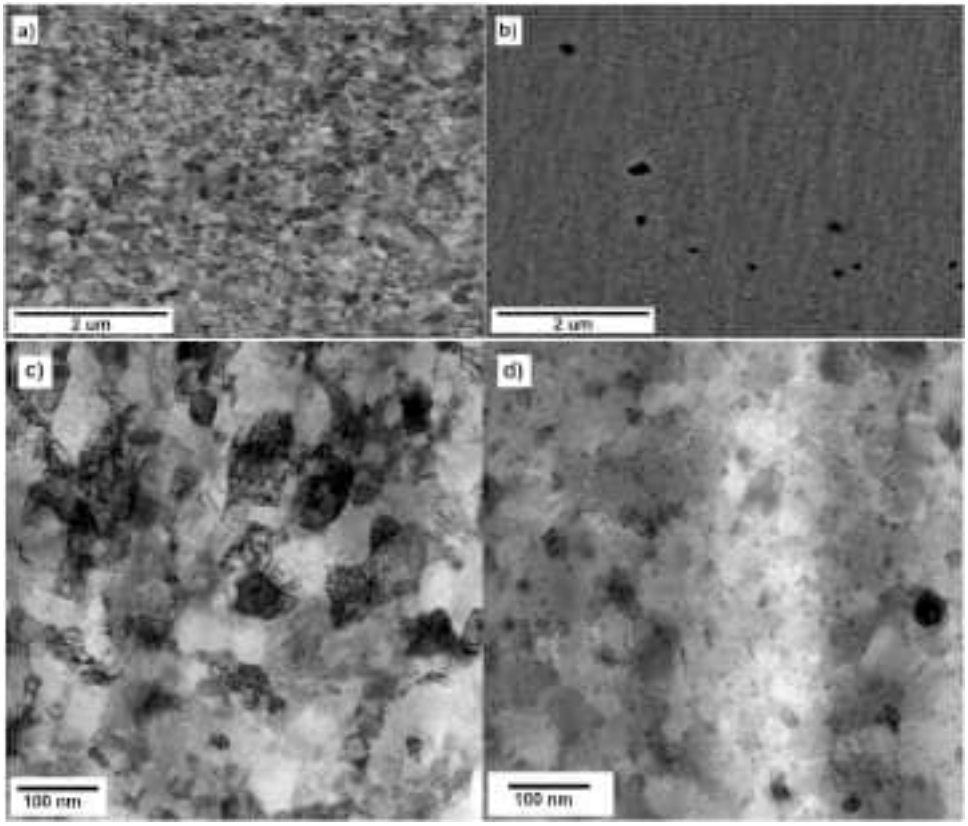

Fig. 2. a) SEM BSE image of Cu after HPT; b) SEM BSE image of Cu-GO after HPT; c) STEM image of Cu-GO in bright-field (BF) and d) STEM image of Cu-GO in high-angle annular dark field (HAADF) mode.

the distribution of GO nanoparticles (the dark regions in the HAADF image) in the matrix. It is apparent that the large GO flakes were fragmented during milling and HPT processing and this reduced them to smaller flakes that were uniformly distributed in the Cu matrix. The size of these particles varied in the range of 5–30 nm.

In order to prove that the particles visible in the SEM and STEM images are GO, Raman spectroscopy studies were conducted. Based on the literature data [50–54] graphene oxide may exhibit a few characteristic peaks in Raman spectroscopy where the disorder band arises from a tangential stretch and sp^3 – hybridized carbon called D band approximately at 1355 cm^{-1} and a second band called G at 1575 cm^{-1} representing the crystalline graphite [55]. It is also found in the literature that the 2D band can be located at about 2700 cm^{-1} [51] but this is not considered in the present analysis because the most significant changes occur within the G and D peaks. When it comes to analysing the GO Raman spectra, the ratio between the D and G band intensity (ID/IG) is the most important. Thus, for GO the ID/IG is lower than 1 (0.85) and the increasing value of the ID/IG ratio is connected with the higher defect level resulting in the degradation of GO [50,51,56].

Fig. 3 represents the Raman spectra collected for the GO flakes, for a mixture of copper powder and GO after mechanical milling and on the samples after HPT. It is apparent that GO was detected in all three samples but the ratio ID/IG was different. Initially GO was lower than 1 and it increased with further processing steps such as ball milling (1.03) and HPT (1.37). This means that the mechanical milling of GO with Cu powder, SPS and HPT processing led to an increase in the density of defects in the GO structure and therefore to its partial degradation.

3.2. Mechanical properties of Cu-GO nanocomposites

The results of microhardness measurements on the disc cross-sections are presented in Fig. 4 as a function of distance from the disc centre for the Cu-GO nanocomposite together with data for pure Cu after SPS and after HPT processing. The hardness for pure Cu samples after HPT rose more than three times from 55 Hv units to more than 180 Hv units compared with the sample after SPS. It is also apparent that the addition of GO significantly impacts the microhardness leading to its further increase by 70–80 Hv units compared to pure Cu after HPT. The microhardness of the Cu-GO nanocomposite exceeds 260 Hv units.

The results of tensile testing for the HPT-processed composite are illustrated in Fig. 5 where these data are complemented by including results for Cu samples both after SPS and after 20 HPT revolutions. The HPT processing leads to a more than two-fold improvement in the mechanical strength of Cu SPS such that its yield strength increased from

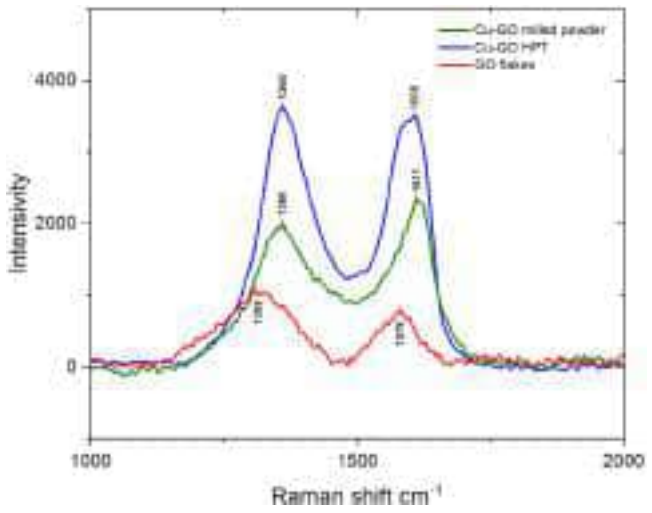

Fig. 3. Raman spectra of: GO flakes, powder mixture of GO and Cu after mechanical milling, and Cu-GO HPT nanocomposite.

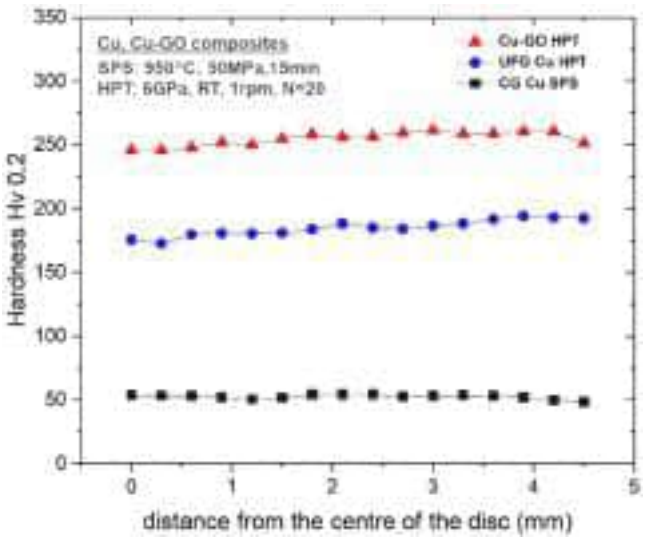

Fig. 4. Hardness of the samples (Cu SPS, Cu HPT, and Cu-GO HPT) as the function of distance from disc centre.

140 MPa for the sample after SPS to 640 MPa after HPT processing. The highest mechanical strength was observed for the Cu-GO nanocomposite sample at almost 700 MPa. However, this sample underwent a brittle fracture with no plastic deformation in tension. Nevertheless, the maximum stress at which the fracture occurred was higher than the ultimate tensile strength of the HPT processed Cu where these values were 675 and 640 MPa, respectively. Another difference in mechanical properties of the analysed materials can be observed for the strain hardening ability. The curve for Cu after SPS is typical for materials with excellent strain hardening ability but HPT processing decreases this ability and a decrease of stress is observed for strains higher than approximately 0.02. A further decrease in strain hardening ability is observed for the Cu-GO composite which is not capable of any plastic strain.

3.3. Electrical conductivity

Because of the use of Cu-based nanocomposites in electrical contact materials, their electrical conductivity is considered as a critical property. The results of electrical conductivity of the fabricated Cu-GO nanocomposite, together with the conductivity for Cu SPS and Cu HPT, are presented in Fig. 6. The tests show that for Cu after SPS there is a significant decrease of conductivity when compared to the literature data for Cu 99 % after casting (a drop from 4.2 E7 S/m [57] to 1.1 E7 S/m) but after HPT processing the electrical conductivity rises to 1.5 E7 S/m. The addition of GO to copper contributes to a further improvement in the conductivity when compared with pure Cu after HPT, as shown in Fig. 6.

3.4. Wear properties

The results obtained in wear tests for Cu SPS, Cu–HPT and the Cu-GO HPT nanocomposite are summarised in Table 1. After the tests, the abrasion surfaces were examined using an optical profilometer and SEM method and the results are presented in Figs. 7 and 8, respectively.

The results suggest that the friction coefficient for the Cu SPS and Cu HPT samples are similar but the wear rate was the smallest for the Cu HPT sample. The highest wear rate was observed for the sample after SPS processing but the mass reduction for this sample was the smallest of all analysed materials. This can be explained by the higher porosity of the material after the SPS process. The Cu-GO sample after HPT exhibited a higher friction coefficient, wear rate and mass loss than the Cu sample after HPT processing.

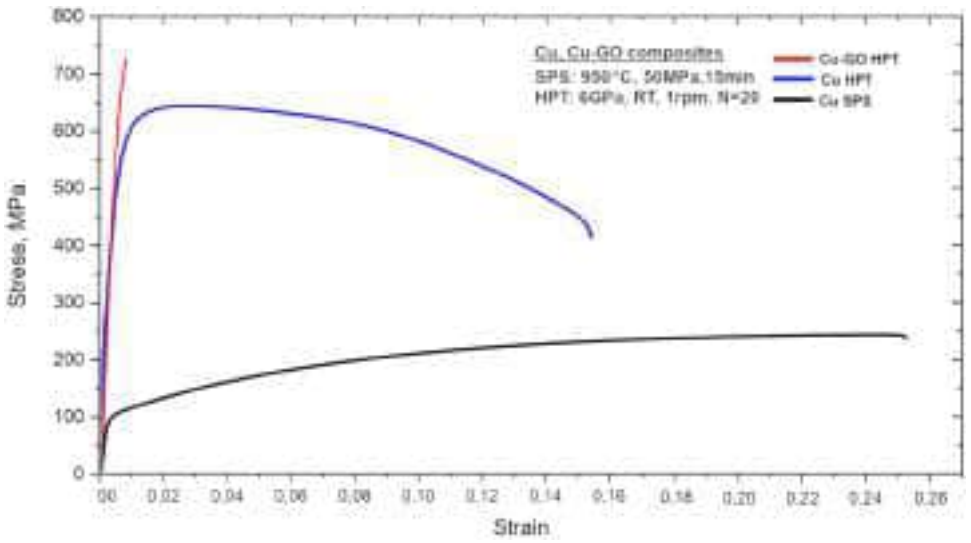

Fig. 5. Tensile strength curves of Cu SPS, Cu HPT and Cu-GO HPT.

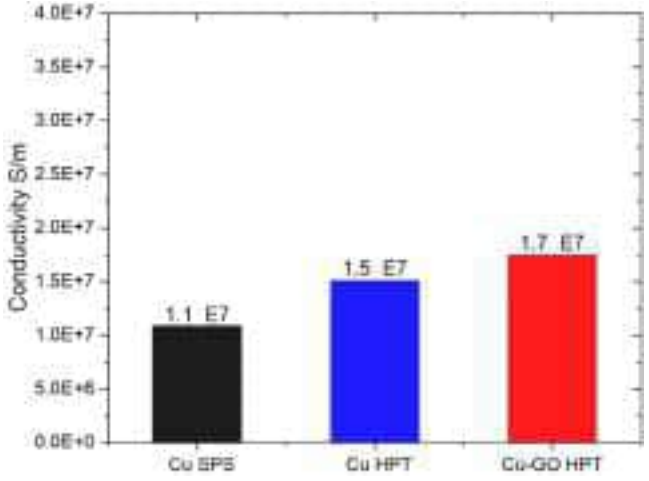

Fig. 6. Electrical conductivity of tested samples (Cu SPS, Cu HPT, and Cu-GO HPT).

Table 1
Wear test results.

Sample	Friction coeficient	Wear rate mm3/N*m	Mass reduction mg
Cu SPS	0.73	4.49×10^{-4}	25
Cu HPT	0.72	2.62×10^{-4}	28
Cu-GO HPT	0.80	3.89×10^{-4}	32

Fig. 7 shows profilometer images of the surfaces after wear tests and this illustrates differences in the wear behaviour of the individual samples. The wipe/scar on the Cu SPS sample had almost a constant depth of about 200 μm along its entire length (Fig. 7a). At the same time, a high outflow of material at the edges of the abrasion was observed in this sample. The bottom of the scar, despite being slightly tilted, was mostly flat, and this contrasts with samples after the HPT process. Wipes on samples after the HPT process (Cu HPT and Cu-GO HPT in Fig. 7b and 7c, respectively) were deeper in the middle sections and shallower at the edge regions of the wipes. This characteristic strengthening of the edges of the HPT discs resulted also in an overall reduction of wear, including a maximum abrasion depth and abrasion volume.

The main difference between the two samples produced by the HPT process was that most wear products from pure Cu remained attached to one end of the scar (Fig. 7b), whereas the material from the Cu with 1 % GO was entirely separated from the sample (Fig. 7c) and the edge was smoother. The bottoms of the scars also showed differences in the wear mechanisms. The entire length of the scar bottom on Cu SPS was covered by deep parallel scratches and a very similar topography appeared on the middle part of the scar on pure Cu after the HPT process. On the sample with 1 % GO, however, the bottom of the scar appeared smoother, less scratched, and consisted mostly of small sharp pits/cracks but also it was placed along the direction of the run.

A more in-depth analysis of abrasion marks was performed using a Scanning Electron Microscope. Fig. 8 shows the wear marks visible in the SEM images for coarse-grained copper after SPS, copper after HPT and copper with GO after HPT. The wear marks on the Cu SPS and the Cu produced by HPT processing show typical features of abrasive wear such as furrowing and longitudinal scratching. In some areas the surface appears flattened and larger cavities seem to be closed by a strongly deformed material. The surface of the Cu-GO sample exhibits similar topographical features but with pits or cavities, and in some cases cracks, arranged transverse to the direction of the run to form river-like meandering patterns. These observations suggest that samples with 1 % GO exhibit a different wear mechanism which probably involves a different adhesive component.

3.5. *Thermal stability*

Fig. 9 shows the average hardness measured at the disk edges for the Cu-GO nanocomposites after HPT processing and subsequent annealing at temperatures ranging from 100 °C to 500 °C for 1 h. These results are also complemented with the hardness values for Cu HPT sample. The results show that the Cu HPT sample is thermally stable up to 200 °C which is in agreement with an earlier report [22]. The Cu-GO sample exhibits a different tendency since the hardness values in this sample decrease slightly with increasing temperature. Nevertheless, even after annealing at 500 °C, the hardness values are at the level of 200 Hv units which is similar to copper after the HPT processing before annealing.

Microstructural observations were carried out in order to explain this phenomenon. A SEM analysis shows that pure copper after HPT recrystalizes at 300 °C (Fig. 10a), whereas the Cu-GO nanocomposite was structurally stable even at 400 °C (Fig. 10b) and starts coarsening of grains at 500 °C (Fig. 10c) but nevertheless it maintains a UFG structure. Moreover, despite grain growth in this sample, it is apparent that there are a number of uniformly distributed darker spots which correspond to

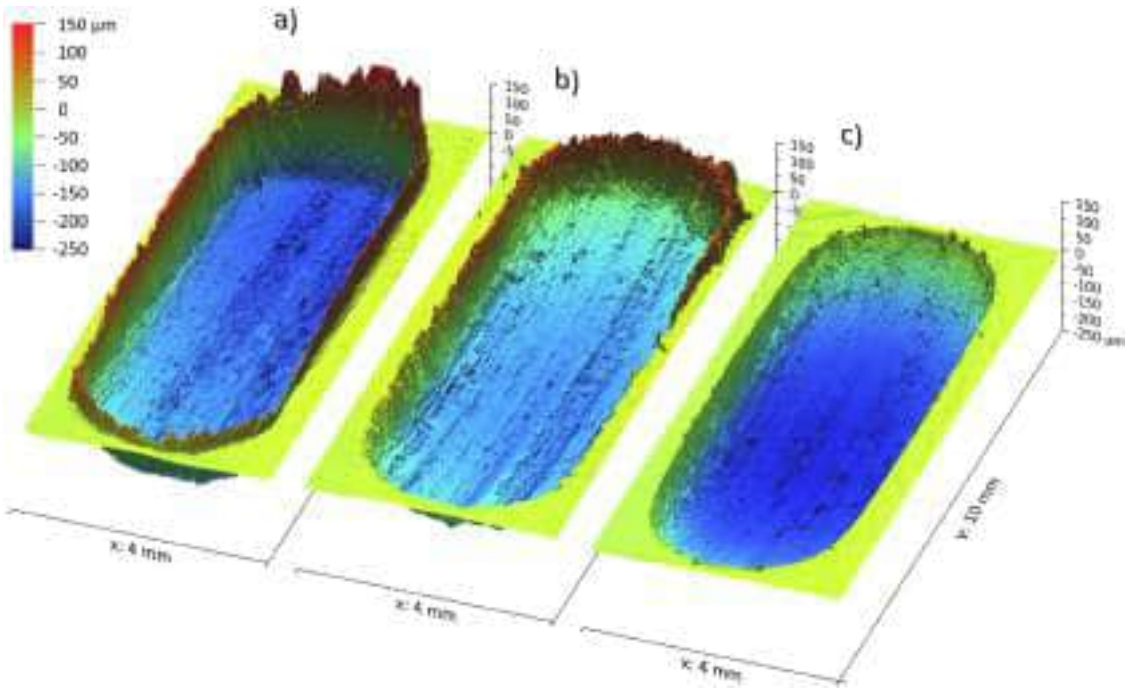

Fig. 7. Profilometry images of the tested materials a) Cu SPS; b) Cu HPT; c) Cu-GO HPT.

the GO flakes in the initial sample. In order to study this effect in more detail, detailed structural investigations were carried out using a STEM microscope. Fig. 11 shows exemplary STEM images of the Cu-GO sample after annealing at 500 °C. The comparative BF and HAADF (Fig. 11a and b) images confirm the grain growth observed in SEM with an average grain size of ~200 nm and uniformly distributed particles with sizes from 10 to even 50 nm. Closer investigations of these structures (Fig. 11c and d) revealed that they have a core-shell structure. EDS analyses of these regions (Fig. 11d), summarised in Table 2, indicates that these structures consist of a carbon-rich core and an oxygen-rich shell zone embedded within the Cu matrix.

4. Discussion

4.1. Fabrication of Cu-GO nanocomposites

A bulk Cu-GO composite with uniformly dispersed GO nanoparticles was obtained by a three-step fabrication processing including the use of quasi-constrained HPT. This processing introduced a remarkable refinement of the GO agglomerates and grains in the Cu matrix. A combination of milling and HPT processing led to a uniform distribution of GO particles having sizes of tens of nanometres while only a small fraction of fine agglomerates remained in the structure. An analysis of the SEM images (Fig. 2) indicated that the surface area fraction of the GO agglomerates with sizes greater than 100 nm was not higher than ~1.5 % of the entire surface of the observed samples. The formation of Cu–O–C chemical bonds, whose origin lies is in the reaction between the Cu and the carboxyl or hydroxyl groups on the surface of the GO, may also play a key role in producing a good dispersion of GO nanoparticles in the Cu matrix. It was shown in previous studies that the oxygen atoms on the surface of GO enhance its connection with Cu which, in the case of Cu pure graphene composites, was reported to be much weaker [39,42–44].

The addition of GO particles also has a beneficial effect on the enhanced grain refinement of the Cu matrix. The fabricated composite has a nanocrystalline structure with a grain size of around 55 nm (Fig. 2c) while for pure Cu after HPT the grain size is about 210 nm (Fig. 2a). The grain size obtained in this study is one of the smallest reported for Cu and Cu nanocomposites fabricated by SPD processing [58] and the graphene oxide phase enhances the thermal stability of the nanocomposite I

An enhanced grain refinement effect occurring in composite materials during SPD processing is well known and was reported in many earlier studies [2,26,59]. Hard nanoparticles uniformly distributed in the metal matrix produce a pinning effect on the movement of dislocations and grain boundaries, thereby promoting grain refinement and reducing the tendency for dynamic recovery and recrystallization during processing [60,61].

The nanocomposites in this research exhibit unique strength (Fig. 5) and hardness (Fig. 4) when compared with pure coarse-grained and nanostructured copper. This is due to several factors: (1) the enhanced grain size reduction and the relevant Hall-Petch relationship [5,6], (2) the presence of hard, uniformly distributed GO nanoparticles in the matrix [25,27,29] and (3) the increased density of dislocations resulting from the presence of additional obstacles (GO) to their movement [23,62].

4.2. Electrical conductivity and wear properties

This part of the research was designed to investigate the effect of the addition of GO particles on the electrical conductivity of the fabricated nanocomposites. First of all, it was shown that the electrical conductivity of the Cu SPS sample is lower than that for Cu 99 % after casting [57]. This is connected with two factors: the high porosity after SPS processing as visible in Fig. 1 [63,64] and the potential oxide impurities introduced during sintering or milling. In powder metallurgy, a protective atmosphere generally plays a key role in shaping the properties of the final product. Despite using the best available protective atmospheres, an oxidation of the powder surface may occur which in turn may affect the electrical conductivity.

The electrical conductivity of pure Cu after HPT processing and the Cu-GO composite (Fig. 5) was found to be higher by 36 % and 54 %, respectively, although it remained lower than reported for Cu 99 % after casting [57]. The Cu HPT and Cu-GO HPT samples had no visible pores during the SEM observation (Fig. 2) so that the HPT process effectively densifies the material and removes the porosity created during the

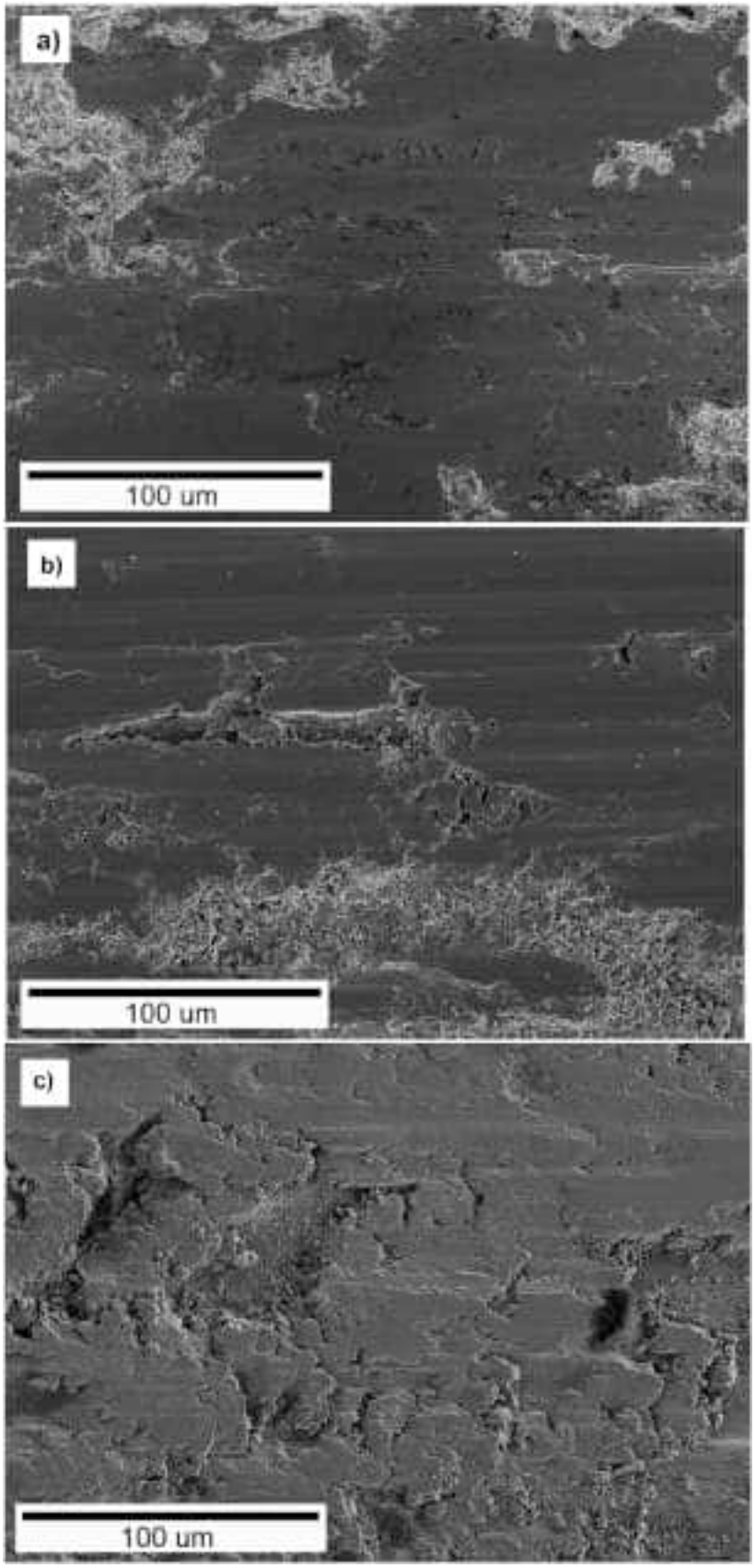

Fig. 8. Surface after wear sliding test in SEM SE image: a) Cu SPS; b) Cu HPT; c) Cu-GO HPT.

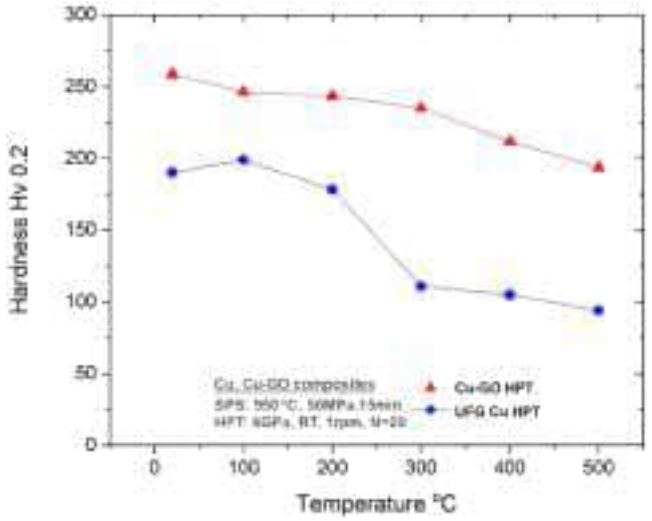

Fig. 9. Hardness of the Cu-GO HPT nanocomposite and Cu HPT as a function of the annealing temperature.

sintering process. At the same time, these materials may have small amounts of oxides formed during the sintering process. The best electrical conductivity was obtained for the Cu-GO HPT where the addition of 1 % GO improved the electrical conductivity.

Regarding the wear properties, Cu after HPT has the highest wear resistance from all of the tested samples (Fig. 7, Table 1). From the traditional Archard equation [56], the increase in hardness should improve the wear resistance. The results for Cu SPS and Cu HPT are in accordance with this law but the results for the Cu HPT and Cu-GO HPT samples are contrary. Furthermore, previous studies have shown more contradictory results whereby surface strengthening through microstructure refinement either increased [65–68] or decreased [40,69–71] the wear resistance. For materials processed by HPT, most of the published results show a decrease in wear resistance compared to the coarse-grained materials [40,69–72]. However, in the present research, the coarse-grained material was produced by sintering of powders which produced a high porosity in the material. These pores may be the starting points for slicing of the material during the wear test and this may explain the better wear resistance of the Cu HPT samples.

By contrast, a different wear behaviour was observed in the Cu-GO HPT sample. Literature data suggests any correlation between the material hardness and wear is limited since the hardness is only one of many material parameters that influence the wear [72]. For example, there are several possible reasons for reducing wear resistance in HPT-processed samples including a low ductility and plasticity of the material, a low strain hardening capability, a higher oxidation rate and the presence of non-equilibrium grain boundaries [66]. Results from the present research suggest that the lower ductility (Fig. 5) and the lack of a strain hardening capability led to a lower wear rate for the Cu-GO HPT than for the Cu HPT. It is interesting that the GO particles in the fabricated composite failed to improve the wear resistance as was expected from earlier studies [39]. This is probably due to the amount and size of the GO particles which were relatively uniformly distributed in the composite matrix but were too small to result in a self-lubricity of the material. However, the addition of GO to the Cu matrix changes the wear surface in Fig. 8 from an extensive brittle crack delamination in Cu after HPT to a more plastic delamination and river-like surface in the composite.

4.3. Thermal stability of UFG structure

The uniform distribution of GO nanoparticles in the Cu matrix had a major influence not only on the enhanced grain refinement and improvement of mechanical properties of this nanocomposite but also on its thermal stability. The fabricated Cu-GO composite had a stable microstructure up to 500 ℃ (Fig. 8, Fig. 9). At this temperature, limited grain growth occurred but the microstructure remained UFG. By contrast, pure Cu after HPT fully recrystalized after annealing at 200–300 ℃ so that the addition of GO extended the stable temperature window by 200 ℃. The remarkable structural stability in the Cu-GO nanocomposite is connected with the uniform distribution of nano-sized GO particles which inhibits grain boundary movement and blocks grain growth [23,61,73,74]. It should be mentioned that similar grain sizes was reported by Horita et al. by subjecting high-purity Cu (99.99 % and 99.99999 %) to a cryogenic-HPT process [75]. Nevertheless, the thermal stability of these samples after cryogenic-HPT was so poor that they exhibited a self-annealing and significant drop of mechanical properties within a few hours after the HPT processing. This confirms the importance of the presence of the second (in this case GO) phase to ensure the thermal stability of nanometals.

Despite such a significant increase in the thermal stability of the Cu-GO nanocomposite, it is important to note some characteristic microstructural changes occurring in this sample after annealing at 500 °C (Fig. 10 and Fig. 11). A characteristic core-shell structure was observed composed of a C-rich core and an O-rich shell embedded in the Cu matrix. The transformation of GO particles into core-shell structures may be connected with the thermal decomposition of GO at high temperatures [56,76–78]. Graphene oxide has functional groups such as hydroxyl, carbonyl epoxy on its surface and edges [79,80]. When exposed to sufficiently high temperatures, these functional groups separate from GO in the form of gases such as CO and CO_2 vapours. This rapid escape of gases leads to a separation of the thicker carbon layers in places where GO was previously located [81,82] and a thermally enhanced diffusion of O-rich gases into the matrix. This produces a generation of copper oxides (CuO and Cu_2O) as intermediate products surrounding the C-rich core. All these processes lead to an increase in the space previously occupied by GO, where this is evident in the present composites through the appearance of numerous small black dots in the structural images (Figs. 10 and 11).

5. Summary and conclusions

- Cu – GO nanocomposites were successfully produced using HPT processing.
- A relatively good dispersion of GO was obtained within the Cu matrix.
- The GO addition led to an enhanced grain refinement compared to the matrix material. The reduction of grain size and reinforcing effect led to a higher hardness for the composite compared to the matrix material.
- The addition of GO slightly improved the electrical conductivity of copper after HPT processing.
- The fabricated composite was thermally stable up to 400 °C whereas at 500 °C the microstructure of the composite changed, but remained UFG.
- Annealing of the composite at 500 °C led to a slight reduction of hardness by about 50 Hv.

CRediT authorship contribution statement

Jarosław Pura: Investigation. **Purbayanto Kenichi:** Investigation, Conceptualization. **Monika Wieczorek-Czarnocka:** Investigation. **Marta Ciemiorek:** Investigation. **Maria Emerla:** Writing – original draft, Methodology, Investigation, Data curation, Conceptualization. **Terence Langdon:** Writing – review & editing, Supervision, Conceptualization. **Małgorzata Lewandowska:** Writing – review & editing, Conceptualization. **Agnieszka Jastrzębska:** Writing – review & editing. **Anita Wojciechowska:** Investigation. **Yi Huang:** Writing – review & editing, Validation, Investigation. **Piotr Bazarnik:** Writing – original

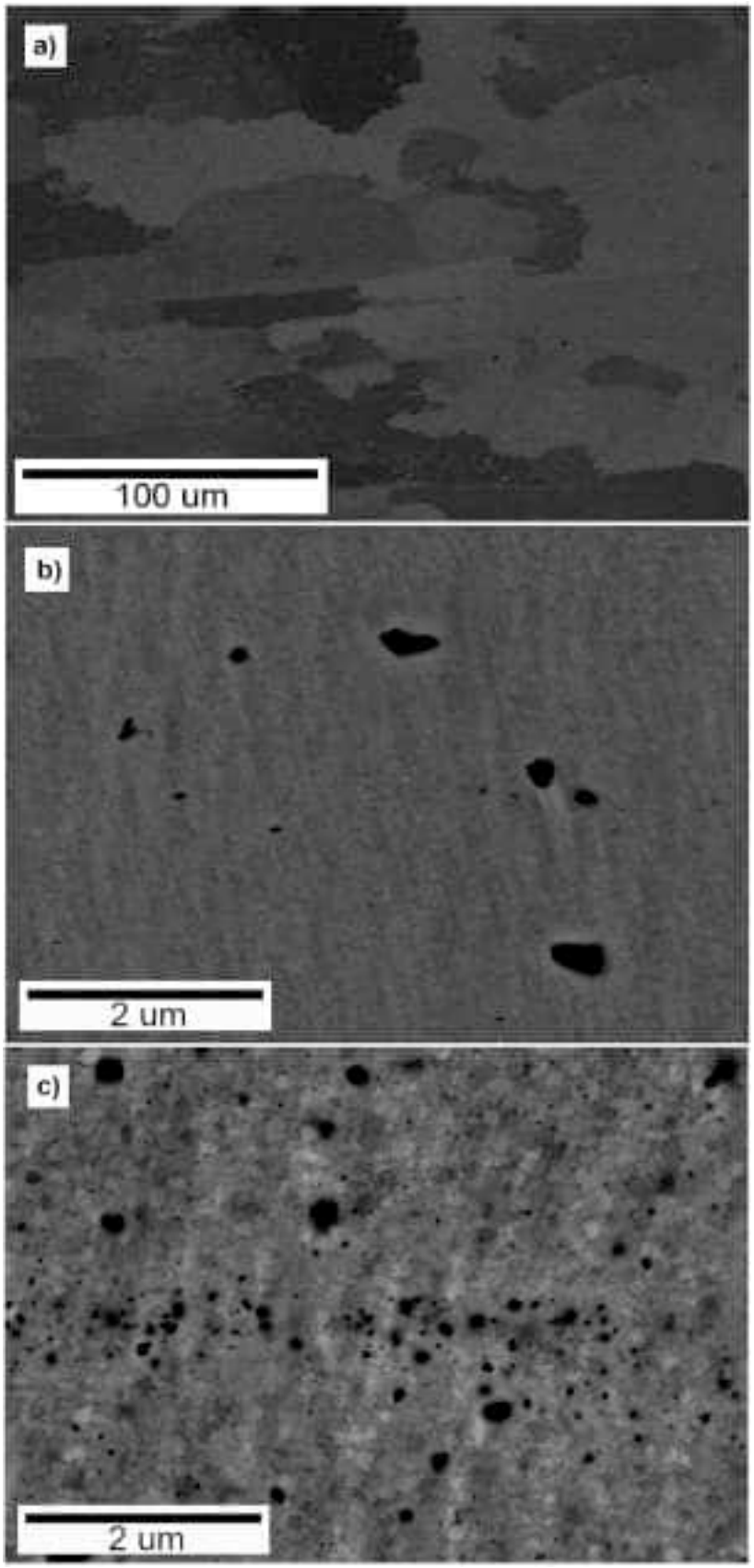

Fig. 10. SEM BSE image: a) Cu HPT after annealing at 300 °C; b) Cu 1 % GO HPT after annealing at 400 °C; c) Cu 1 % GO HPT after annealing at 500 °C.

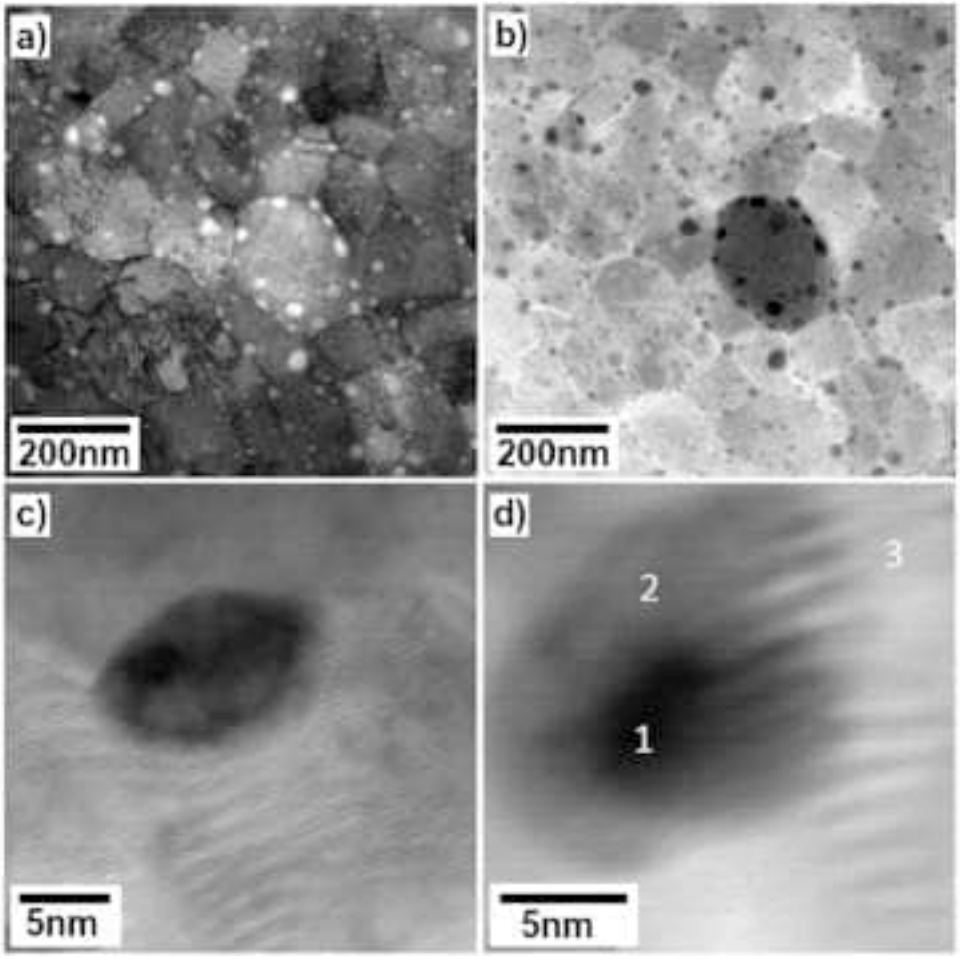

Fig. 11. STEM image Cu-GO HPT after annealing at 500 °C with visible core shell structures trapped in Cu matrix: a) BF and b) HAADF, c) and d) STEM image of EDS measure points – core shell structure with carbon core, oxygen shell, trapped in Cu matrix.

Table 2
EDS measurements for Cu-GO sample after HPT processing and annealing.

	C-K	O-K	Cu-K
Point 1	14.3	43.4	45.3
Point 2	2.5	33.2	64.3
Point 3	0.9	3.4	95.7

draft, Project administration, Methodology, Investigation, Funding acquisition, Data curation, Conceptualization.

Declaration of Competing Interest

The authors declare that they have no known competing financial interests or personal relationships that could have appeared to influence the work reported in this paper.

Data availability

Data will be made available on request.

Acknowledgments

This work was carried out within an OPUS 19 project "Metal matrix composites fabricated by high-pressure torsion and reinforced with 2D and 3D nano-particles" funded by National Science Centre under nb. 2020/37/B/ST5/01837.

References

[1] R.Z. Valiev, I.V. Alexandrov, M. Kawasaki, T.G. Langdon, Ultrafine-Grained Materials, in: Miner. Met. Mater. Ser., Springer Nature, Cham, Switzerland, 2024: pp. 1–29. https://doi.org/10.1007/978-3-031-31729-3.
[2] T.G. Langdon, R.Z. Valiev, A.P. Zhilyaev, Bulk Nanostructured Materials. Fundamentals and Applications, John Wiley & Sons, Inc, Hoboken, New Jersey, USA, 2013, https://doi.org/10.1142/9789814397988_0011.
[3] R.Z. Valiev, Y. Estrin, Z. Horita, T.G. Langdon, M.J. Zehetbauer, Y.T. Zhu, Fundamentals of superior properties in bulk NanoSPD materials, Mater. Res. Lett. 4 (2016) 1–21, https://doi.org/10.1080/21663831.2015.1060543.
[4] A.P. Zhilyaev, T.G. Langdon, Using high-pressure torsion for metal processing: fundamentals and applications, Prog. Mater. Sci. 53 (2008) 893–979, https://doi.org/10.1016/j.pmatsci.2008.03.002.
[5] E.O. Hall, The deformation and ageing of mild steel III discussion of results, Proc. Phys. Soc. Sect. B 64 (1951) 747–753.
[6] N.J. Petch, The cleavage strength of polycrystals, J. Iron Steel Inst. 174 (1953) 25–28.
[7] K. Edalati, A.Q. Ahmed, S. Akrami, K. Ameyama, V. Aptukov, R.N. Asfandiyarov, M. Ashida, V. Astanin, A. Bachmaier, V. Beloshenko, E.V. Bobruk, K. Bryła, J. M. Cabrera, A.P. Carvalho, N.Q. Chinh, I.C. Choi, R. Chulist, J.M. Cubero-Sesin, G. Davdian, M. Demirtas, S. Divinski, K. Durst, J. Dvorak, P. Edalati, S. Emura, N. A. Enikeev, G. Faraji, R.B. Figueiredo, R. Floriano, M. Fouladvind, D. Fruchart, M. Fuji, H. Fujiwara, M. Gajdics, D. Gheorghe, L. Gondek, J.E. González-Hernández, A. Gornakova, T. Grosdidier, J. Gubicza, D. Gunderov, L. He, O. F. Higuera, S. Hirosawa, A. Hohenwarter, Z. Horita, J. Horky, Y. Huang, J. Huot, Y. Ikoma, T. Ishihara, Y. Ivanisenko, J. il Jang, A.M. Jorge, M. Kawabata-Ota, M. Kawasaki, T. Khelfa, J. Kobayashi, L. Kommel, A. Korneva, P. Kral, N. Kudriashova, S. Kuramoto, T.G. Langdon, D.H. Lee, V.I. Levitas, C. Li, H.W. Li, Y. Li, Z. Li, H.J. Lin, K.D. Liss, Y. Liu, D.M.M. Cardona, K. Matsuda, A. Mazilkin, Y. Mine, H. Miyamoto, S.C. Moon, T. Müller, J.A. Muñoz, M.Y. Murashkin, M. Naeem, M. Novelli, D. Olasz, R. Pippan, V.V. Popov, E.N. Popova, G. Purcek, P. de Rango, O. Renk, D. Retraint, Á. Révész, V. Roche, P. Rodriguez-Calvillo, L. Romero-Resendiz, X. Sauvage, T. Sawaguchi, H. Sena, H. Shahmir, X. Shi, V. Sklenicka, W. Skrotzki, N. Skryabina, F. Staab, B. Straumal, Z. Sun, M. Szczerba,

Y. Takizawa, Y. Tang, R.Z. Valiev, A. Vozniak, A. Voznyak, B. Wang, J.T. Wang, G. Wilde, F. Zhang, M. Zhang, P. Zhang, J. Zhou, X. Zhu, Y.T. Zhu, Severe plastic deformation for producing superfunctional ultrafine-grained and heterostructured materials: an interdisciplinary review, J. Alloy. Compd. 1002 (2024), https://doi.org/10.1016/j.jallcom.2024.174667.

[8] K. Edalati, A. Bachmaier, V.A. Beloshenko, Y. Beygelzimer, V.D. Blank, W.J. Botta, K. Bryła, J. Čížek, S. Divinski, N.A. Enikeev, Y. Estrin, G. Faraji, R.B. Figueiredo, M. Fuji, T. Furuta, T. Grosdidier, J. Gubicza, A. Hohenwarter, Z. Horita, J. Huot, Y. Ikoma, M. Janeček, M. Kawasaki, P. Král, S. Kuramoto, T.G. Langdon, D. R. Leiva, V.I. Levitas, A. Mazilkin, M. Mito, H. Miyamoto, T. Nishizaki, R. Pippan, V.V. Popov, E.N. Popova, G. Purcek, O. Renk, Á. Révész, X. Sauvage, V. Sklenicka, W. Skrotzki, B.B. Straumal, S. Suwas, L.S. Toth, N. Tsuji, R.Z. Valiev, G. Wilde, M. J. Zehetbauer, X. Zhu, Nanomaterials by severe plastic deformation: review of historical developments and recent advances, Mater. Res. Lett. 10 (2022) 163–256, https://doi.org/10.1080/21663831.2022.2029779.

[9] R.Z. Valiev, Y. Estrin, Z. Horita, T.G. Langdon, M.J. Zehetbauer, Y. Zhu, Producing bulk ultrafine-grained materials by severe plastic deformation: ten years later, JOM 68 (2006) 1216–1226, https://doi.org/10.1007/s11837-016-1820-6.

[10] P. Bazarnik, Y. Huang, M. Lewandowska, T.G. Langdon, Enhanced grain refinement and microhardness by hybrid processing using hydrostatic extrusion and high-pressure torsion, Mater. Sci. Eng. A 712 (2018) 513–520, https://doi.org/10.1016/j.msea.2017.12.007.

[11] M. Kawasaki, Z. Horita, T.G. Langdon, Microstructural evolution in high purity aluminum processed by ECAP, Mater. Sci. Eng. A 524 (2009) 143–150, https://doi.org/10.1016/j.msea.2009.06.032.

[12] J.J. Jonas, C. Ghosh, L.S. Toth, The equivalent strain in high pressure torsion, Mater. Sci. Eng. A 607 (2014) 530–535, https://doi.org/10.1016/j.msea.2014.04.046.

[13] V.V. Popov, E.N. Popova, A.V. Stolbovskiy, Nanostructuring Nb by various techniques of severe plastic deformation, Mater. Sci. Eng. A 539 (2012) 22–29, https://doi.org/10.1016/j.msea.2011.12.082.

[14] T. Hebesberger, H.P. Stüwe, A. Vorhauer, F. Wetscher, R. Pippan, Structure of Cu deformed by high pressure torsion, Acta Mater. 53 (2005) 393–402, https://doi.org/10.1016/j.actamat.2004.09.043.

[15] P. Král, J. Staněk, L. Kunčická, F. Seitl, L. Petrich, V. Schmidt, V. Beneš, V. Sklenička, Microstructure changes in HPT-processed copper occurring at room temperature, Mater. Charact. 151 (2019) 602–611, https://doi.org/10.1016/j.matchar.2019.03.046.

[16] S. Sabbaghianrad, T.G. Langdon, Microstructural saturation, hardness stability and superplasticity in ultrafine-grained metals processed by a combination of severe plastic deformation techniques, Lett. Mater. 5 (2015) 335–340, https://doi.org/10.22226/2410-3535-2015-3-335-340.

[17] S. Sabbaghianrad, T.G. Langdon, An evaluation of the saturation hardness in an ultrafine-grained aluminum 7075 alloy processed using different techniques, J. Mater. Sci. 50 (2015) 4357–4365, https://doi.org/10.1007/s10853-015-8989-x.

[18] S. Sabbaghianrad, J. Wongsa-Ngam, M. Kawasaki, T.G. Langdon, An examination of the saturation microstructures achieved in ultrafine-grained metals processed by high-pressure torsion, J. Mater. Res. Technol. 3 (2014) 319–326, https://doi.org/10.1016/j.jmrt.2014.10.002.

[19] P. Jenei, E.Y. Yoon, J. Gubicza, H.S. Kim, J.L. Lábár, T. Ungár, Microstructure and hardness of copper-carbon nanotube composites consolidated by High Pressure Torsion, Mater. Sci. Eng. A 528 (2011) 4690–4695, https://doi.org/10.1016/j.msea.2011.02.066.

[20] A. Dhal, B. Prathyusha, R. Kumar, S.K. Panigrahi, Twin evolution and work-hardening phenomenon of a bulk ultrafine grained copper with high thermal stability and strength-ductility synergy, Mater. Sci. Eng. A 802 (2021) 140622, https://doi.org/10.1016/j.msea.2020.140622.

[21] H. Jiang, Y.T. Zhu, D.P. Butt, I.V. Alexandrov, T.C. Lowe, Microstructural evolution, microhardness and thermal stability of HPT-processed Cu, Mater. Sci. Eng. A 290 (2000) 128–138, https://doi.org/10.1016/S0921-5093(00)00919-9.

[22] R.K. Islamgaliev, F. Chmelik, R. Kuzel, Thermal structure changes in copper and nickel processed by severe plastic deformation, Mater. Sci. Eng. A (1997) 234–236, https://doi.org/10.1016/s0921-5093(97)00247-5.

[23] D. Zhou, D. Zhang, C. Kong, P. Munroe, R. Torrens, Grain and nanoparticle coarsening of an ultrafine structured Cu-5 vol%Al_2O_3 nanocomposite during isochronal annealing, J. Alloy. Compd. 642 (2015) 83–91, https://doi.org/10.1016/j.jallcom.2015.04.106.

[24] B. Tian, P. Liu, K. Song, Y. Li, Y. Liu, F. Ren, J. Su, Microstructure and properties at elevated temperature of a nano-Al_2O_3 particles dispersion-strengthened copper base composite, Mater. Sci. Eng. A (2006) 705–710, https://doi.org/10.1016/j.msea.2006.07.129.

[25] J. Naser, H. Ferkel, W. Riehemann, Grain stabilisation of copper with nanoscaled Al2O3-powder, Mater. Sci. Eng. A (1997) 470–473, https://doi.org/10.1016/s0921-5093(97)00263-3.

[26] M. Emerla, P. Bazarnik, A. Bartokwska, Y. Huang, M. Lewandowska, T.G. Langdon, Using direct high-pressure torsion synthesis to produce aluminium matrix nanocomposites reinforced with carbon nanotubes, J. Alloy. Compd. 968 (2023), https://doi.org/10.1016/j.jallcom.2023.171928.

[27] J. Lipecka, M. Andrzejczuk, M. Lewandowska, J. Janczak-Rusch, K. J. Kurzydłowski, Evaluation of thermal stability of ultrafine grained aluminium matrix composites reinforced with carbon nanotubes, Compos. Sci. Technol. 71 (2011) 1881–1885, https://doi.org/10.1016/j.compscitech.2011.09.001.

[28] M. Jahedi, M.H. Paydar, M. Knezevic, Enhanced microstructural homogeneity in metal-matrix composites developed under high-pressure-double-torsion, Mater. Charact. 104 (2015) 92–100, https://doi.org/10.1016/j.matchar.2015.04.012.

[29] M.I. Abd El Aal, Effect of high-pressure torsion processing on the microstructure evolution and mechanical properties of consolidated micro size Cu and Cu-SiC powders, Adv. Powder Technol. 28 (2017) 2135–2150, https://doi.org/10.1016/j.apt.2017.05.020.

[30] D. Shen, P. Gao, Y. He, J. Gong, J. Du, A Cu-Al_2O_3 composite with ultrahigh tensile strength prepared by high-pressure torsion, J. Mater. Eng. Perform. (2022) 1–6, https://doi.org/10.1007/s11665-022-06936-9.

[31] K. Edalati, M. Ashida, Z. Horita, T. Matsui, H. Kato, Wear resistance and tribological features of pure aluminum and Al-Al_2O_3 composites consolidated by high-pressure torsion, Wear 310 (2014) 83–89, https://doi.org/10.1016/j.wear.2013.12.022.

[32] P. Bazarnik, S. Nosewicz, B. Romelczyk-Baishya, M. Chmielewski, A. Strojny Nędza, J. Maj, Y. Huang, M. Lewandowska, T.G. Langdon, Effect of spark plasma sintering and high-pressure torsion on the microstructural and mechanical properties of a Cu–SiC composite, Mater. Sci. Eng. A 766 (2019), https://doi.org/10.1016/j.msea.2019.138350.

[33] T. Tokunaga, K. Kaneko, K. Sato, Z. Horita, Microstructure and mechanical properties of aluminum-fullerene composite fabricated by high pressure torsion, Scr. Mater. 58 (2008) 735–738, https://doi.org/10.1016/j.scriptamat.2007.12.010.

[34] D.D. Phuong, P.Van Trinh, N.Van An, N.Van Luan, P.N. Minh, R.K. Khisamov, K. S. Nazarov, L.R. Zubairov, R.R. Mulyukov, A.A. Nazarov, Effects of carbon nanotube content and annealing temperature on the hardness of CNT reinforced aluminum nanocomposites processed by the high pressure torsion technique, J. Alloy. Compd. 613 (2014) 68–73, https://doi.org/10.1016/j.jallcom.2014.05.219.

[35] G. Korznikova, T. Czeppe, G. Khalikova, D. Gunderov, E. Korznikova, L. Litynska-Dobrzynska, M. Szlezynger, Microstructure and mechanical properties of Cu-graphene composites produced by two high pressure torsion procedures, Mater. Charact. 161 (2020) 110122, https://doi.org/10.1016/j.matchar.2020.110122.

[36] Y. Huang, P. Bazarnik, D. Wan, D. Luo, P.H.R. Pereira, M. Lewandowska, J. Yao, B. E. Hayden, T.G. Langdon, The fabrication of graphene-reinforced Al-based nanocomposites using high-pressure torsion, Acta Mater. 164 (2019) 499–511, https://doi.org/10.1016/j.actamat.2018.10.060.

[37] Z. Zheng, X. Xia Yang, J. Ch. LI, X. xX Zhang, I. Muhammad, L. Geng, Preparation and properties of graphene nanoplatelets reinforced aluminum composites, Trans. Nonferrous Met. Soc. 31 (2021) 878–886, https://doi.org/10.1016/S1003-6326(21)65546-2.

[38] N. Khobragade, K. Sikdar, B. Kumar, S. Bera, D. Roy, Mechanical and electrical properties of copper-graphene nanocomposite fabricated by high pressure torsion, J. Alloy. Compd. 776 (2019) 123–132, https://doi.org/10.1016/j.jallcom.2018.10.139.

[39] P. Hidalgo-Manrique, X. Lei, R. Xu, M. Zhou, I.A. Kinloch, R.J. Young, Copper/graphene composites: a review, J. Mater. Sci. 54 (2019) 12236–12289, https://doi.org/10.1007/s10853-019-03703-5.

[40] A.P. Zhilyaev, I. Shakhova, A. Belyakov, R. Kaibyshev, T.G. Langdon, Wear resistance and electroconductivity in copper processed by severe plastic deformation, Wear 305 (2013) 89–99, https://doi.org/10.1016/j.wear.2013.06.001.

[41] A.P. Zhilyaev, I. Shakhova, A. Belyakov, R. Kaibyshev, T.G. Langdon, Effect of annealing on wear resistance and electroconductivity of copper processed by high-pressure torsion, J. Mater. Sci. 49 (2014) 2270–2278, https://doi.org/10.1007/s10853-013-7923-3.

[42] G. Giovannetti, P.A. Khomyakov, G. Brocks, V.M. Karpan, J. Van Den Brink, P. J. Kelly, Doping graphene with metal contacts, Phys. Rev. Lett. 101 (2008) 4–7, https://doi.org/10.1103/PhysRevLett.101.026803.

[43] P.A. Khomyakov, G. Giovannetti, P.C. Rusu, G. Brocks, J. Van Den Brink, P.J. Kelly, First-principles study of the interaction and charge transfer between graphene and metals, Phys. Rev. B Condens. Matter Mater. Phys. 79 (2009) 1–12, https://doi.org/10.1103/PhysRevB.79.195425.

[44] L. Zhang, E. Pollak, W.C. Wang, P. Jiang, P.A. Glans, Y. Zhang, J. Cabana, R. Kostecki, C. Chang, M. Salmeron, J. Zhu, J. Guo, Electronic structure study of ordering and interfacial interaction in graphene/Cu composites, Carbon N. Y 50 (2012) 5316–5322, https://doi.org/10.1016/j.carbon.2012.07.020.

[45] N. Kurantowicz, E. Sawosz, S. Jaworski, M. Kutwin, B. Strojny, M. Wierzbicki, J. Szeliga, A. Hotowy, L. Lipińska, R. Kozinski, J. Jagiełło, A. Chwalibog, Interaction of graphene family materials with Listeria monocytogenes and Salmonella enterica, Nanoscale Res. Lett. 10 (2015) 1–12, https://doi.org/10.1186/s11671-015-0749-y.

[46] Roberto B. Figueiredo, Paulo R. Cetlin, Terence G. Langdon, Using finite element modeling to examine the flow processes in quasi-constrained high-pressure torsion, Mater. Sci. Eng. A 527 (2011) 8198–8204, https://doi.org/10.1016/j.msea.2011.07.040.

[47] K. Edalati, Z. Horita, T.G. Langdon, The significance of slippage in processing by high-pressure torsion, Scr. Mater. 60 (2009) 9–12, https://doi.org/10.1016/j.scriptamat.2008.08.042.

[48] K. Edalati, Y. Hashiguchi, P.H.R. Pereira, Z. Horita, T.G. Langdon, Effect of temperature rise on microstructural evolution during high-pressure torsion, Mater. Sci. Eng. A 714 (2018) 167–171, https://doi.org/10.1016/j.msea.2017.12.095.

[49] P.H.R. Pereira, R.B. Figueiredo, Y. Huang, P.R. Cetlin, T.G. Langdon, Modeling the temperature rise in high-pressure torsion, Mater. Sci. Eng. A 593 (2014) 185–188, https://doi.org/10.1016/j.msea.2013.11.015.

[50] J. Chen, C. Li, W. Cao, S. Sang, Q. Wu, H. Liu, K. Liu, Conductive and high anticorrosive rGO-modified copper foil prepared by electrocoagulation and chemical reduction, Ionics 25 (2019) 2935–2944, https://doi.org/10.1007/s11581-018-2702-4.

[51] V.B. Mohan, R. Brown, K. Jayaraman, D. Bhattacharyya, Characterisation of reduced graphene oxide: effects of reduction variables on electrical conductivity, Mater. Sci. Eng. B 193 (2015) 49–60, https://doi.org/10.1016/j.mseb.2014.11.002.
[52] J.Bin Wu, M.L. Lin, X. Cong, H.N. Liu, P.H. Tan, Raman spectroscopy of graphene-based materials and its applications in related devices, Chem. Soc. Rev. 47 (2018) 1822–1873, https://doi.org/10.1039/c6cs00915h.
[53] A.C. Ferrari, Raman spectroscopy of graphene and graphite: disorder, electron-phonon coupling, doping and nonadiabatic effects, Solid State Commun. 143 (2007) 47–57, https://doi.org/10.1016/j.ssc.2007.03.052.
[54] K.N. Kudin, B. Ozbas, H.C. Schniepp, R.K. Prud'homme, I.A. Aksay, R. Car, Raman spectra of graphite oxide and functionalized graphene sheets, Nano Lett. 8 (2008) 36–41, https://doi.org/10.1021/nl071822y.
[55] J. Song, L. Xu, C. Zhou, R. Xing, Q. Dai, D. Liu, H. Song, Synthesis of graphene oxide based cuo nanoparticles composite electrode for highly enhanced nonenzymatic glucose detection, ACS Appl. Mater. Interfaces 5 (2013) 12928–12934, https://doi.org/10.1021/am403508f.
[56] I. Sengupta, S.S.S. Sharat Kumar, S.K. Pal, S. Chakraborty, Characterization of structural transformation of graphene oxide to reduced graphene oxide during thermal annealing, J. Mater. Res. 35 (2020) 1197–1204, https://doi.org/10.1557/jmr.2020.55.
[57] J. Li, H. Ding, B. Li, L. Wang, Microstructure evolution and properties of a Cu–Cr–Zr alloy with high strength and high conductivity, Mater. Sci. Eng. A 819 (2021), https://doi.org/10.1016/j.msea.2021.141464.
[58] P. Jenei, J. Gubicza, E.Y. Yoon, H.S. Kim, J.L. Lábár, High temperature thermal stability of pure copper and copper-carbon nanotube composites consolidated by high pressure torsion, Compos. Part A Appl. Sci. Manuf. 51 (2013) 71–79, https://doi.org/10.1016/j.compositesa.2013.04.007.
[59] M. Darabi, M. Rajabi, B. Junipour, M.T. Noghani, The effect of sintering temperature on Cu-CNTsnano composites properties produced by pm method, Sci. Sinter. 50 (2018) 477–486, https://doi.org/10.2298/SOS1804477D.
[60] N. Wang, Y. Wen, L.Q. Chen, Pinning force from multiple second-phase particles in grain growth, Comput. Mater. Sci. 93 (2014) 81–85, https://doi.org/10.1016/j.commatsci.2014.06.030.
[61] Z. Li, J. Wang, H. Huang, Influences of grain/particle interfacial energies on second-phase particle pinning grain coarsening of polycrystalline, J. Alloy. Compd. 818 (2020), https://doi.org/10.1016/j.jallcom.2019.152848.
[62] S. Dangwal, K. Edalati, R.Z. Valiev, T.G. Langdon, Breaks in the Hall-Petch relationship after severe plastic deformation of magnesium, aluminum, copper, and iron, Crystals 13 (2023) 413, https://doi.org/10.3390/cryst13030413.
[63] F. Ternero, L.G. Rosa, P. Urban, J.M. Montes, F.G. Cuevas, Influence of the total porosity on the properties of sintered materials—a review, Metals 11 (2021), https://doi.org/10.3390/met11050730.
[64] T. Kaiser, G. Dehm, C. Kirchlechner, A. Menzel, H. Bishara, Probing porosity in metals by electrical conductivity: nanoscale experiments and multiscale simulations, Eur. J. Mech. 97 (2023) 104777, https://doi.org/10.1016/j.euromechsol.2022.104777.
[65] M.I. Abd El Aal, Wear properties of copper and copper composites powders consolidated by high-pressure torsion, Friction 8 (2020) 433–450, https://doi.org/10.1007/s40544-019-0285-3.
[66] F.A. Sadykov, N.P. Barykin, I.R. Aslanyan, The influence of strain-heat processing on copper wear, Wear 212 (1997) 160–164, https://doi.org/10.1016/S0043-1648(97)00164-6.
[67] Z. Zhang, S. Hosoda, I.S. Kim, Y. Watanabe, Grain refining performance for Al and Al-Si alloy casts by addition of equal-channel angular pressed Al-5 mass% Ti alloy, Mater. Sci. Eng. A 425 (2006) 55–63, https://doi.org/10.1016/j.msea.2006.03.018.
[68] M. Chegini, A. Fallahi, M.H. Shaeri, Effect of equal channel angular pressing (ECAP) on wear behavior of Al-7075 alloy, Procedia Mater. Sci. 11 (2015) 95–100, https://doi.org/10.1016/j.mspro.2015.11.116.
[69] C.T. Wang, N. Gao, R.J.K. Wood, T.G. Langdon, Wear behavior of an aluminum alloy processed by equal-channel angular pressing, J. Mater. Sci. 46 (2011) 123–130, https://doi.org/10.1007/s10853-010-4862-0.
[70] H. Garbacz, M. Gradzka-Dahlke, K.J. Kurzydłowski, The tribological properties of nano-titanium obtained by hydrostatic extrusion, Wear 263 (2007) 572–578, https://doi.org/10.1016/j.wear.2006.11.047.
[71] N. Gao, C.T. Wang, R.J.K. Wood, T.G. Langdon, Wear resistance of SPD-processed alloys, Mater. Sci. Forum 667-669 (2011) 1095–1100, https://doi.org/10.4028/www.scientific.net/MSF.667-669.1095.
[72] N. Gao, C.T. Wang, R.J.K. Wood, T.G. Langdon, Tribological properties of ultrafine-grained materials processed by severe plastic deformation, J. Mater. Sci. 47 (2012) 4779–4797, https://doi.org/10.1007/s10853-011-6231-z.
[73] P.A. Manohar, M. Ferry, T. Chandra, Five decades of the zener equation, ISIJ Int 38 (1998) 913–924, https://doi.org/10.2355/isijinternational.38.913.
[74] S. Suárez, E. Ramos-Moore, B. Lechthaler, F. Mücklich, Grain growth analysis of multiwalled carbon nanotube-reinforced bulk Ni composites, Carbon N. Y 70 (2014) 173–178, https://doi.org/10.1016/j.carbon.2013.12.089.
[75] K. Edalati, J.M. Cubero-Sesin, A. Alhamidi, I.F. Mohamed, Z. Horita, Influence of severe plastic deformation at cryogenic temperature on grain refinement and softening of pure metals: investigation using high-pressure torsion, Mater. Sci. Eng. A 613 (2014) 103–110, https://doi.org/10.1016/j.msea.2014.06.084.
[76] K. Raidongia, A.T.L. Tan, J. Huang, Graphene Oxide: Some New Insights into an Old Material. Second Edi, Elsevier Ltd, 2014, https://doi.org/10.1016/B978-0-08-098232-8.00014-0.
[77] S.H. Huh, Thermal reduction of graphene oxide, Phys. Appl. Graph. Exp. (2011) 73–90.
[78] L. Hu, A. Wang, W. Wang, Structural evolution of graphene oxide and its thermal stability during high temperature sintering, J. Wuhan. Univ. Technol. Mater. Sci. Ed. 37 (2022) 342–349, https://doi.org/10.1007/s11595-022-2537-8.
[79] T. Szabó, O. Berkesi, P. Forgó, K. Josepovits, Y. Sanakis, D. Petridis, I. Dékány, Evolution of surface functional groups in a series of progressively oxidized graphite oxides, Chem. Mater. 18 (2006) 2740–2749, https://doi.org/10.1021/cm060258+.
[80] A. Lerf, H. He, M. Forster, J. Klinowski, Structure of graphite oxide revisited, J. Phys. Chem. B 102 (1998) 4477–4482, https://doi.org/10.1021/jp9731821.
[81] I. Sengupta, S. Chakraborty, M. Talukdar, S.K. Pal, S. Chakraborty, Thermal reduction of graphene oxide: How temperature influences purity, J. Mater. Res. 33 (2018) 4113–4122, https://doi.org/10.1557/jmr.2018.338.
[82] H.C. Schniepp, J.L. Li, M.J. McAllister, H. Sai, M. Herrera-Alonson, D.H. Adamson, R.K. Prud'homme, R. Car, D.A. Seville, I.A. Aksay, Functionalized single graphene sheets derived from splitting graphite oxide, J. Phys. Chem. B 110 (2006) 8535–8539, https://doi.org/10.1021/jp060936f.

Journal of Alloys and Compounds 1033 (2025) 181283

Contents lists available at ScienceDirect

Journal of Alloys and Compounds

journal homepage: www.elsevier.com/locate/jalcom

Enhanced thermal stability of nanocrystalline Cu composites processed by high-pressure torsion: The pinning effect of Al_2O_3, GO, and rGO/Al_2O_3 nanoparticles

Piotr Bazarnik [a], Maria Emerla [a,*], Yi Huang [b], Anita Wojciechowska [a], Marta Ciemiorek [a], Wiktor Bednarczyk [c], Agnieszka Jastrzębska [d], Małgorzata Lewandowska [a], Terence G. Langdon [e]

[a] Warsaw University of Technology, Faculty of Materials Science and Engineering, Wołoska 141, Warsaw 02-507, Poland
[b] Department of Design and Engineering, Faculty of Science and Technology, Bournemouth University, Poole, Dorset BH12 5BB, United Kingdom
[c] Faculty of Metals Engineering and Industrial Computer Science, AGH University of Krakow, al. A. Mickiewicza 30, Krakow 30-059, Poland
[d] Warsaw University of Technology, Faculty of Mechatronics, św. Andrzeja Boboli 8, Warsaw 02-525, Poland
[e] Department of Aerospace & Mechanical Engineering University of Southern California, Los Angeles, CA 90089-1453, USA

ARTICLE INFO

Keywords:
Aluminium oxide
Graphene oxide
High-pressure torsion
Metal matrix composites
Reduced graphene oxide
Thermal stability

ABSTRACT

Metal matrix composites with improved mechanical properties and thermal stability were produced using mechanical milling, spark plasma sintering (SPS) and high-pressure torsion (HPT). Three types of reinforcing particles were used, i.e., GO, Al_2O_3 and rGO/Al_2O_3. All of the produced composites exhibit higher hardness and tensile strength than pure copper, reaching values of 250 Hv for Cu-GO, 240 Hv for Cu- Al_2O_3, 210 Hv for Cu-rGO/Al_2O_3 and 185 Hv for Cu after HPT. STEM analyses reveal that the HPT significantly refines the grain size of pure copper to ~210 nm, and even more in the Cu-based composites achieving grain sizes as small as ~55–75 nm. Pure Cu after HPT recrystallizes after annealing at 573 K. The Cu- Al_2O_3 composite demonstrated the best thermal stability with a hardness after annealing at 773 K of 220 Hv and a grain size of ~100 nm. The composite of Cu-GO after annealing at 773 K showed slight grain growth up to ~150 nm. The composite Cu-GO/Al_2O_3 exhibits improved microhardness and tensile strength up to 673 K and annealing of this composite at 773 K which led to a bimodal microstructure. All of the composites annealed at 773 K showed hardness above 180 Hv.

1. Introduction

Pure copper exhibits excellent electrical and thermal conductivity which makes it an optimum material for electrical applications. Unfortunately, its tensile properties and hardness are relatively low, and this restricts its use in more advanced applications. One of the possible ways to improve the strength of pure copper, and at the same time to maintain a reasonably high electrical conductivity, lies in refining the grain size [1,2]. Materials with ultrafine (below 1 μm) or nanocrystalline (below 100 nm) grains are most often produced by severe plastic deformation (SPD) techniques such as equal channel angular pressing (ECAP) [3], accumulative roll bonding (ARB) [4] and high-pressure torsion (HPT) [5,6] with the latter considered as the most efficient in terms of the final grain size [7–9]. Earlier studies of copper deformed by various SPD methods showed that the grain size reduction in these methods produced a significant increase in hardness (by about 270 %) with only a slight decrease in electrical conductivity (by about 12 %) [10].

Despite great improvement in the microhardness and tensile strength, the ultrafine grained (UFG) and nanocrystalline (NC) metals are inherently thermally unstable due to the high energy stored in the form of dislocations and grain boundaries. Thus, in practice UFG and NC metals exhibit a strong tendency for recrystallization at relatively low temperatures compared to their coarse-grained equivalents [11–15] thereby limiting their potential industrial applications at elevated temperatures. Several concepts were proposed to improve the thermal stability of UFG materials but the most promising is to create metal matrix composites (MMCs) by adding thermally stable nanosized particles and uniformly distributing them within the metal matrix [16–19]. These thermally stable nanoparticles have a strong pinning effect which blocks the movement of grain boundaries during annealing and thus limits the

* Corresponding author.
E-mail address: maria.wolna.dokt@pw.edu.pl (M. Emerla).

https://doi.org/10.1016/j.jallcom.2025.181283
Received 27 March 2025; Received in revised form 7 May 2025; Accepted 28 May 2025
Available online 29 May 2025

recrystallization and grain growth processes [20–24].

There are a number of investigations on the fabrication of UFG/NC MMCs but they were mostly reinforced with different types of oxides such as Al_2O_3 [16,25–27] or carbides such as SiC [28–30]. Recently, carbon-based nano-particles have attracted growing attention due to their potential to strongly improve the mechanical properties, promote grain refinement, stabilise the microstructure during annealing and at the same time increase the electrical and thermal properties [31]. As a result, MMCs reinforced with carbon nanotubes (CNTs) [32–34], graphene [35–37] and graphene oxide (GO) [38,39] have been successfully synthesized. However, there are drawbacks regarding the fabrication of carbon reinforced MMCs. In particular, CNTs and graphene flakes exhibit low wettability by metals, which leads to a strong tendency to form agglomeration in the metal matrix [31,40]. Nevertheless, due to the presence of oxygen functional groups GO particles are a promising material to fabricate composites with a good distribution and connection of particles with the matrix [31]. It was shown that oxygen groups on the surface of GO also enhance the connection between GO and metal through the formation of oxygen-mediated chemical bonds which are stronger than conventional adhesive bonding between the graphene and the metal [41–43]. However, it should be emphasized that GO exhibits a lower thermal resistance than graphene and decomposes in the air atmosphere in the temperature range of 573 K – 673 K [44–46]. No results are at present available to establish the behaviour of GO in the composite when heated to such temperatures.

GO flakes can be stabilized by covalent bonding with other nanoparticles such as Au [47], Ag [48], Cu [38], TiO_2 [49] or Al_2O_3 [50] and forming a core-shell structure. The stabilization with Al_2O_3 seems to be very promising since GO has a number of functional groups capable of forming the aluminium–oxygen bonds, such as C═O (1730 cm^{-1}), C-O-C (1280 cm^{-1}) and C-O (1225 cm^{-1}) as measured on FTIR and Raman [50]. It was shown that the intensities of these peaks decreased due to the formation of the Al–O bond that stabilized the GO structure [50]. In addition, this functionalization leads to reduction of GO and formation of reduced GO (rGO). The rGO/Al_2O_3 composite nanoparticles are a new type of material that have not been tested yet as a filler to form composites, especially the composites having a UFG/NC structure.

Therefore, the purpose of the present study was to fabricate novel thermally stable Cu-based nanocomposites using HPT processing and to investigate the effect of three different types of reinforcement, i.e., Al_2O_3, GO and modified rGO/Al_2O_3, on the microstructural development, the mechanical properties and the thermal stability.

2. Experimental

The following three types of composites were produced in this study containing 1 wt% of nanofillers: Cu-GO, Cu-Al_2O_3 and Cu-rGO/Al_2O_3. The GO and Al_2O_3 represent 2D and 3D nanofillers, respectively, whereas the rGO/Al_2O_3 is a mixture of both. A regular-shaped copper powder (produced by ABCR company) with a purity of 99 % was used as the matrix. All nano-fillers were synthesized at Warsaw University of Technology using the methods described in earlier reports for GO [51], rGO/Al_2O_3 [50] and Al_2O_3 [52]. The average nanoparticle size measured from SEM images was 150 + /- 16 nm, 230 + /- 50 nm and 50 + /- 20 nm for the GO, rGO/Al_2O_3 and Al_2O_3, respectively.

The composites were manufactured using the procedure of the mechanical milling of powders followed by sintering using Spark Plasma Sintering (SPS) and subsequent processing by HPT. The mechanical milling of copper powders with selected particles was performed in a planetary ball milling system (Retsch PM100) in a protective argon atmosphere. The processing parameters for the ball milling were a speed of rotation of 300 rpm, a grinding time of 1 h and a weight ratio of powder to balls of 1:10. The material for the milling chamber and balls was ZrO_2. Mixed powders were sintered using the SPS method with a 10 mm diameter graphite mould. The process was carried out in a protective argon atmosphere with a heating rate of 373 K/min and the maximum sintering temperature was 1223 K at which the samples were held for 15 min under a pressure of 50 MPa. The material obtained after sintering was cut into discs of 10 mm in diameter and 1 mm in height and the surfaces of these discs were levelled by grinding on 800 papers. The discs were subjected to HPT processing under a compressive pressure of 6 GPa at room temperature with a rotation speed of 1 rpm. Each sample was processed to 20 revolutions through HPT processing using quasi-constrained conditions where there is a small outflow of material around the periphery of the disk during the HPT operation [53]. Additionally, a reference sample of pure copper was produced under the same conditions as the composites.

The fabricated composites were studied in terms of the microstructure using scanning electron microscopy (SEM) (Hitachi SU8000). Observations were conducted in the secondary electron (SE) and backscattered electron (BSE) modes. All observations were carried out on the cross-sectional surfaces of the disc from an area approximately 1 mm from the edge of each disc. The surface of the samples for the SEM observations was prepared by ion milling using a Hitachi IM4000 instrument. Ion polishing is a method that produces a very high-quality surface that is free of surface deformation, stresses or oxide layers and which allows a study of the grain structure and the distribution of particle agglomerates using channel contrast in the SEM.

More detailed observations of the microstructure were carried out using a Thermo-Fisher Scientific SPECTRA 200 scanning transmission electron microscope (STEM) operating at an accelerating voltage of 200 kV and equipped with Super-X energy dispersion spectroscopy (EDX) detectors which permitted additional chemical analyses of the samples. The thin samples for STEM observations were cut using a focused ion beam (FIB) microscope Hitachi NB-5000.

The average grain size of the composites and copper was determined from STEM and SEM images. Visible grain boundaries were marked in ImageJ software, which then calculated the area of each grain and its equivalent diameter. Based on the measurement of at least 150 grains, the average value of the equivalent diameter of the grains of the material was determined. The term grain size, used in this article, means the value of the average equivalent diameter of the grains of a particular material.

The mechanical properties of the composites after HPT processing were studied by microhardness measurements and tensile tests. The Vickers microhardness was measured using a Falcon 503 microhardness tester with a load of 200 g and dwelling time of 10 s. The hardness was measured on the polished disc surfaces along radial directions with a spacing of 0.3 mm between indentations. The tensile tests were performed on miniature tensile specimens cut from the discs via electrical discharge. A Zwick Z005 universal testing machine with an initial strain rate of 10^{-3} s^{-1} was used and at least two tensile specimens were prepared and tested for each material. The gauge length of the tensile specimen was 4 mm, and the cross-sectional dimensions were 0.6×0.8 mm^2. A Digital Image Correlation system was employed during the tests to precisely measure the elongations.

The thermal stability of the produced composites was evaluated by annealing the samples in the temperature range from 373 K to 773 K for 1 hour. The annealing time and temperature range were established on the basis of previous studies [54]. After annealing, the samples were evaluated in terms of the microhardness and microstructural changes in the same way as for the composites after HPT. For the sample annealed at 773 K, Electron Backscatter Diffraction (EBSD) measurements were made using Hitachi SU-70 analytical microscope. The accelerating voltage was 25 kV, the working distance was 20 mm, the step size was 40 nm and the map size was 51×38 μm^2.

3. Results

3.1. Microstructure

Fig. 1 shows representative SEM BSE micrographs of the fabricated nanocomposites and Cu reference sample after HPT. In practice, the HPT processing led to significant grain size refinement in all materials. The average grain size in pure copper was ~210 nm (Fig. 1a) while for the nanocomposites the grain size was much smaller and cannot be determined from these images. However, there are clear agglomerates of nanoparticles whose size and volume fraction depend on the type of filler. For the Cu-GO composite (Fig. 1b) the visible agglomerates cover about 1 % of the sample area and their average size is 200 + /- 160 nm. In the case of the Cu-Al_2O_3 composite (Fig. 1c), the volume fraction of agglomerates is smaller at about 0.5 % and their average size is 120 + /- 45 nm. For the Cu-rGO/Al_2O_3 composite (Fig. 1d), the agglomerates cover more than 2.5 % of the entire image surface and their average size is about 290 + /- 160 nm. Moreover, in the Cu-GO and Cu-Al_2O_3 composites the agglomerates are uniformly distributed over the entire composites (Fig. 1b and c) whereas in the Cu-rGO/Al_2O_3 composite they tend to be grouped into bands (Fig. 1d).

STEM analysis was conducted to analyse the grain structure in detail and nanoparticle distributions in the composites after 20 HPT turns. Obtained results are presented in Figs. 2–4. In all cases the STEM images in bright field (BF) mode show significant grain refinement in the matrix structure. The average grain sizes of the composites were estimated to be ~55, ~65 and ~75 nm for Cu-GO (Fig. 2a), Cu-Al_2O_3 (Fig. 3a), and Cu-rGO/Al_2O_3 (Fig. 4a), respectively. By contrast, the HPT-processed pure Cu has an average grain size of ~210 nm, as shown in Fig. 1a. Obviously, the addition of the GO, Al_2O_3 and rGO/Al_2O_3 nanofillers led to a greater grain size reduction in the Cu matrix than in pure Cu processed by HPT. The images of Figs. 2b, 3b and 4b also show the distribution of nanoparticles in the matrix. Apart from the large agglomerates visible in the SEM BSE images (Fig. 1b-d), a large fraction of the nanoparticles is homogenously distributed in copper in the form of either individual nanoparticles or small agglomerates having average sizes of ~6.5, ~7.0 and ~12.0 nm for the Cu-Al_2O_3, Cu-GO and Cu-rGO/Al_2O_3 composites, respectively.

It is worth noting that, despite the application of intensive plastic deformation via mechanical milling and HPT processing during the synthesis of these nanocomposites, the fillers largely remain intact and do not undergo significant degradation. The EDX chemical distribution maps (Figs. 2c, 3c, 4c) confirm that the chemical compositions of the observed nanoparticles and the agglomerates correspond to the composition of the added fillers. For the Cu-GO (Fig. 2c) and Cu-Al_2O_3 (Fig. 3c) composites, the EDX maps show that the C, O and Al elements are precisely located where the nanoparticles were observed in the HAADF images. In the rGO/Al_2O_3 composite (Fig. 4), the chemical composition of the nanoparticles varies. Some particles contain C, Al and O elements especially in agglomerates whereas others contain only C or only Al and O. This suggests that, in this composite, the Al_2O_3 nanoparticles may have been torn off from the rGO/Al_2O_3 flakes during the HPT processing. At the same time, the intensive deformation does not destroy the GO structure, as confirmed in an earlier study using Raman spectroscopy [54].

3.2. Mechanical properties

The microhardness measurement results are presented in Fig. 5 as a function of the distance from the disc centres. Starting from the results for pure Cu, the microhardness of the samples processed by HPT is more than 100 Hv units higher than the microhardness of the copper in the coarse-grained state after SPS. All of the produced composites exhibit higher microhardness than for Cu after HPT. The highest microhardness values were achieved for the composite with the addition of GO nanoflakes where it is more than 250 Hv units. The lowest hardness value among the composites was obtained for Cu- rGO/Al_2O_3, while the average hardness obtained for this sample was 210 Hv. Moreover, the Cu-GO composite exhibits a homogeneous distribution of microhardness results across the entire disc diameter which indicates that the grain refinement level and the distribution of the nanofillers are quite homogeneous throughout the sample. Composites with the addition of Al_2O_3 and rGO/Al_2O_3 exhibit a small but gradual increase in the microhardness values from the central region to the edge from 220 Hv to

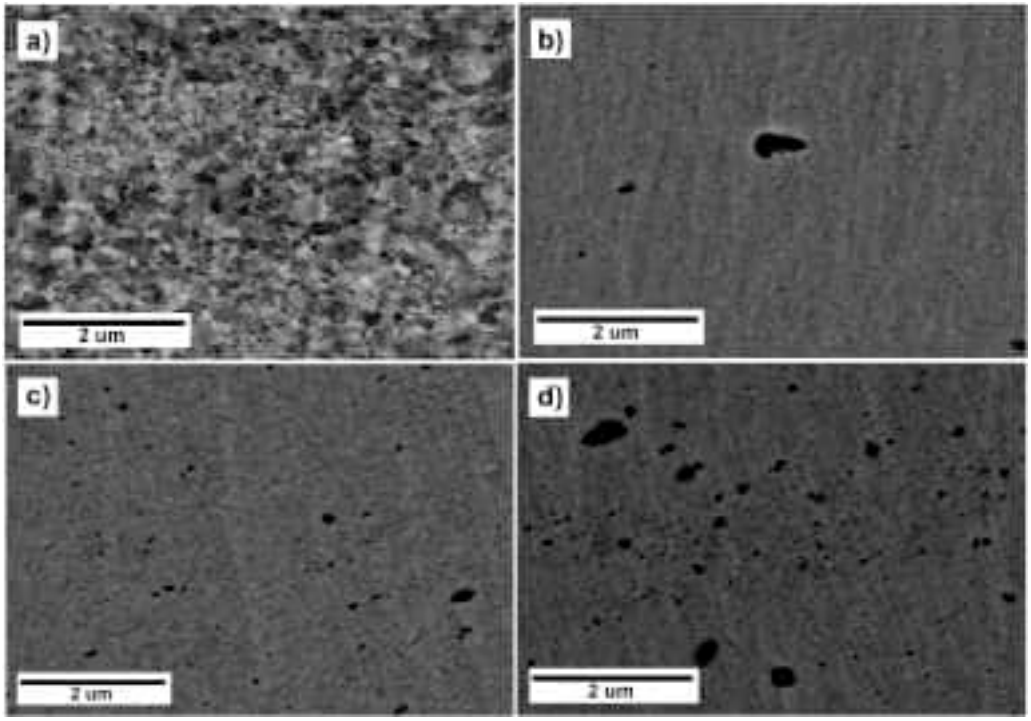

Fig. 1. SEM BSE image of a) Cu after HPT; b) Cu-GO after HPT; c) Cu-Al_2O_3 after HPT; d) Cu-rGO/Al_2O_3 after HPT.

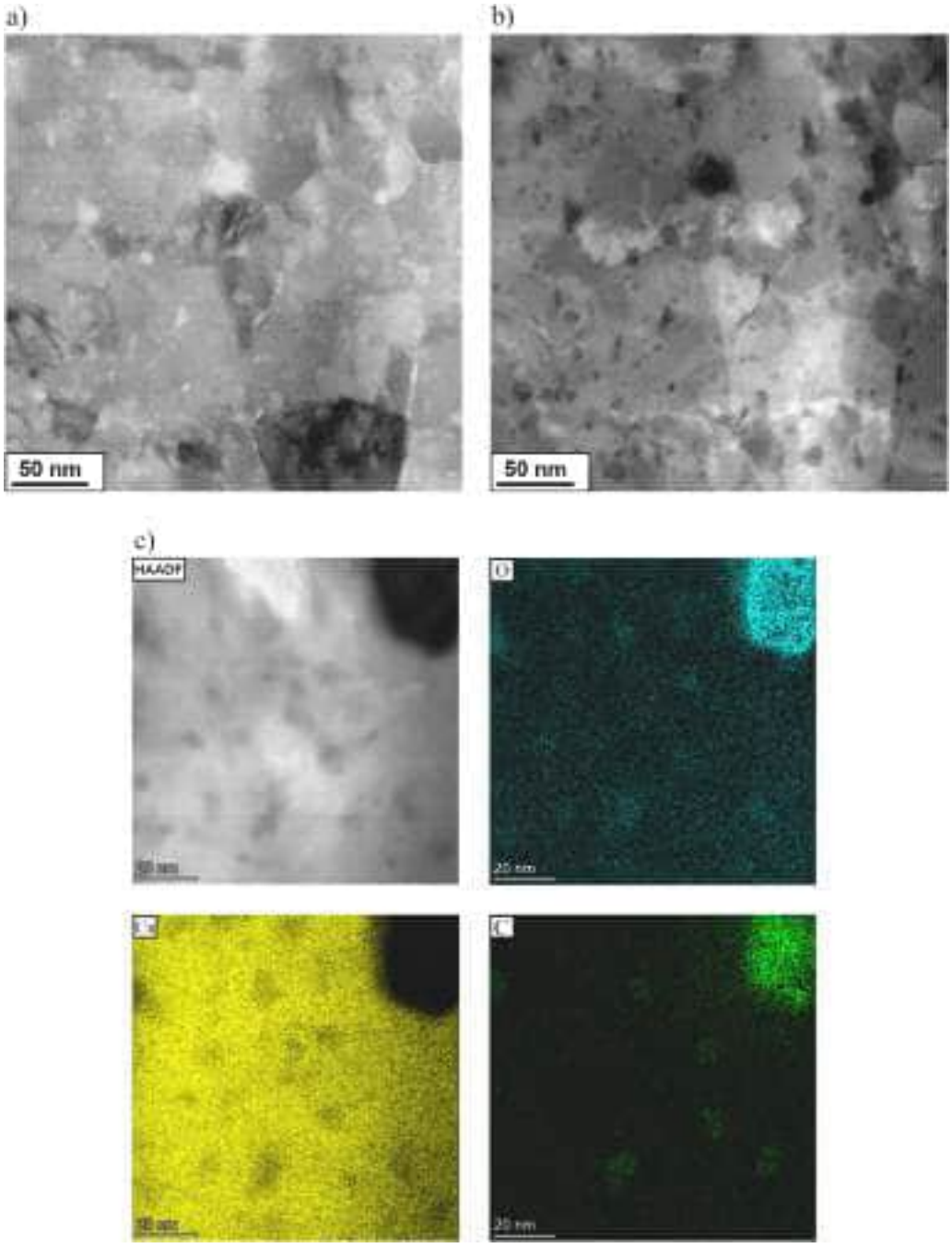

Fig. 2. STEM image of Cu-GO a) bright field, b) HAADF image, c) EDX map.

245 Hv and 190 Hv to 225 Hv, respectively.

The results of the tensile testing for the HPT-processed composite materials are illustrated in Fig. 6. The ultimate tensile strength (UTS) of the HPT-processed pure Cu is ~640 MPa which in general is consistent with the available published data [55]. The UTS of the coarse-grained copper after SPS is ~250 MPa. The results for the composite samples clearly demonstrate the beneficial role of the nanofillers since the strength consistently increases compared with pure Cu. A highest UTS of ~780 ± 12 MPa was recorded for the Cu-Al_2O_3 composite which was a value higher by ~140 MPa than for HPT-processed Cu and ~500 ± 2 MPa higher than for coarse-grained Cu. The Cu-rGO/Al_2O_3 and Cu-GO composites exhibit slightly lower values of UTS of ~690 ± 5 MPa and ~675 ± 2 MPa, respectively. Nevertheless, the high strength of the composites is at the expense of ductility since the elongation to failure is smaller than 10 % and the Cu-GO composite exhibits brittle fracture in the elastic region.

3.3. Thermal stability

Fig. 7 presents the changes in hardness measured at the disc edges for the nanocomposites after 20 HPT turns with subsequent annealing at temperatures ranging from 373 K to 773 K for 1 h. These results are also complemented with the microhardness changes for the Cu HPT sample. The results show that the Cu HPT sample is thermally stable up to 473 K which agrees with published data [40]. The microhardness decreases dramatically from ~170 Hv units to ~110 Hv units after annealing at 573 K.

By contrast, the microhardness of the fabricated nanocomposites

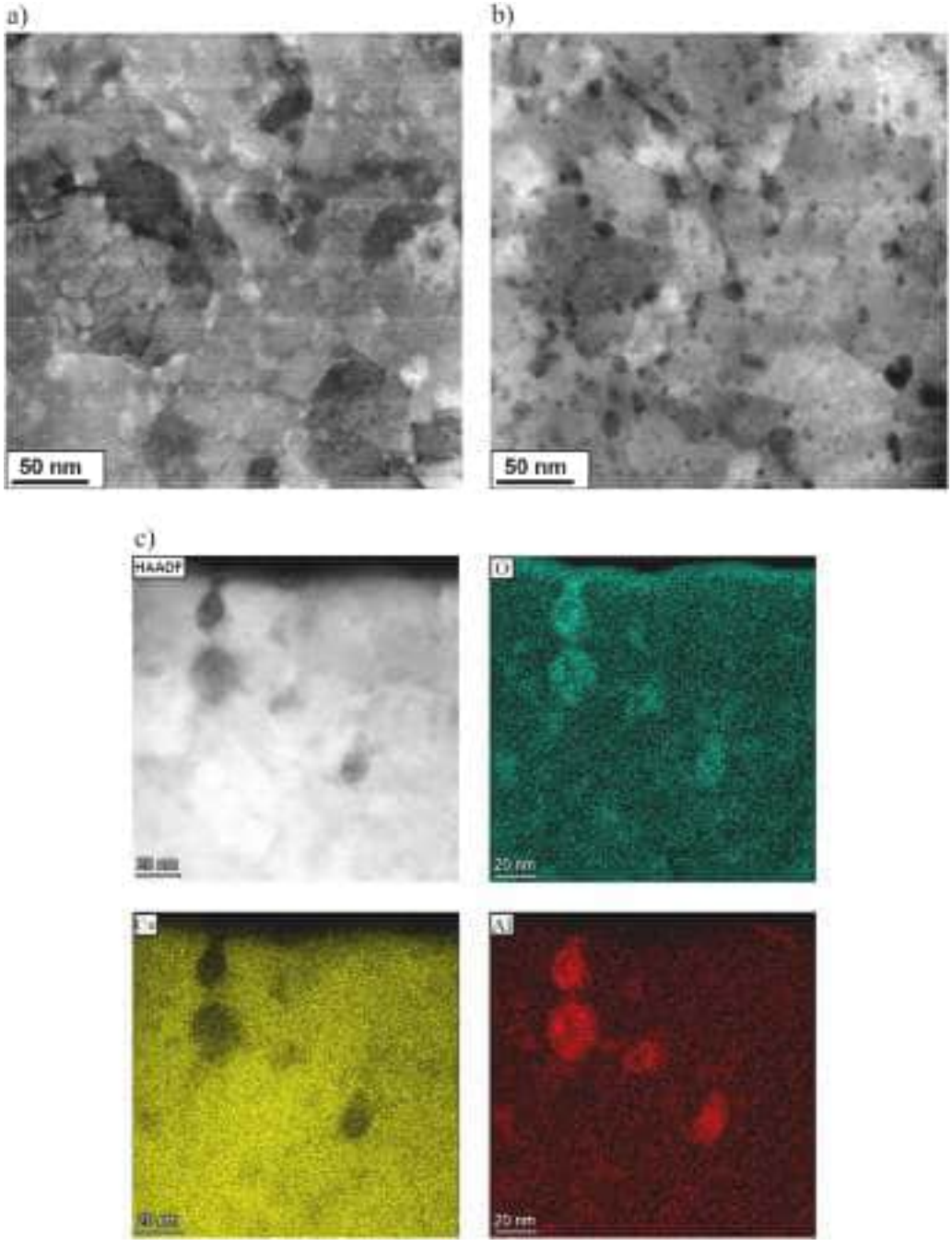

Fig. 3. STEM image of Cu-Al_2O_3 a) bright field, b) HAADF image, c) EDX map.

does not decrease significantly even after annealing at 773 K. Furthermore, even if a drop of microhardness is observed at a higher temperature, the microhardness values are higher than the microhardness of the HPT-processed pure Cu without any post-HPT annealing. In the Cu-GO composite, a gradual decrease in microhardness is observed with increasing annealing temperature but this drop is no larger than ~60 Hv for 773 K. On the other hand, the Cu-Al_2O_3 nanocomposite demonstrates excellent thermal stability with the hardness values remaining steady at ~240 Hv across the entire temperature range. An interesting result was observed in the Cu-rGO/Al_2O_3 composite, for which the microhardness values are stable up to 573 K and after annealing at 773 K the microhardness drops to ~185 Hv units which remains higher than for the Cu HPT sample.

To understand the thermal stability of the HPT-processed nanocomposites, SEM and STEM studies of the annealed samples were carried out. Fig. 8 shows representative SEM images taken in tunnelling contrast to study grain size coarsening during annealing. The reference Cu HPT sample undergoes recrystallization during annealing at 573 K, leading to the formation of grains which are larger than 100 μm (Fig. 8a). By contrast, the microstructures of the Cu-GO and Cu-Al_2O_3 nanocomposites remain relatively stable at high temperatures (Figs. 8b and 8c). However, in the Cu-GO sample a slight grain coarsening is observed after annealing at 773 K (Fig. 8b) whereas this is not evident for the Cu-Al_2O_3 composite. The Cu-rGO/Al_2O_3 composite after annealing at 773 K exhibits abnormal grain growth leading to the formation of a distinct heterostructure (Fig. 8d). The microstructure in this sample consists of large grains having sizes above ~100 μm and these are surrounded by regions of nanocrystalline grains. Additionally, these large

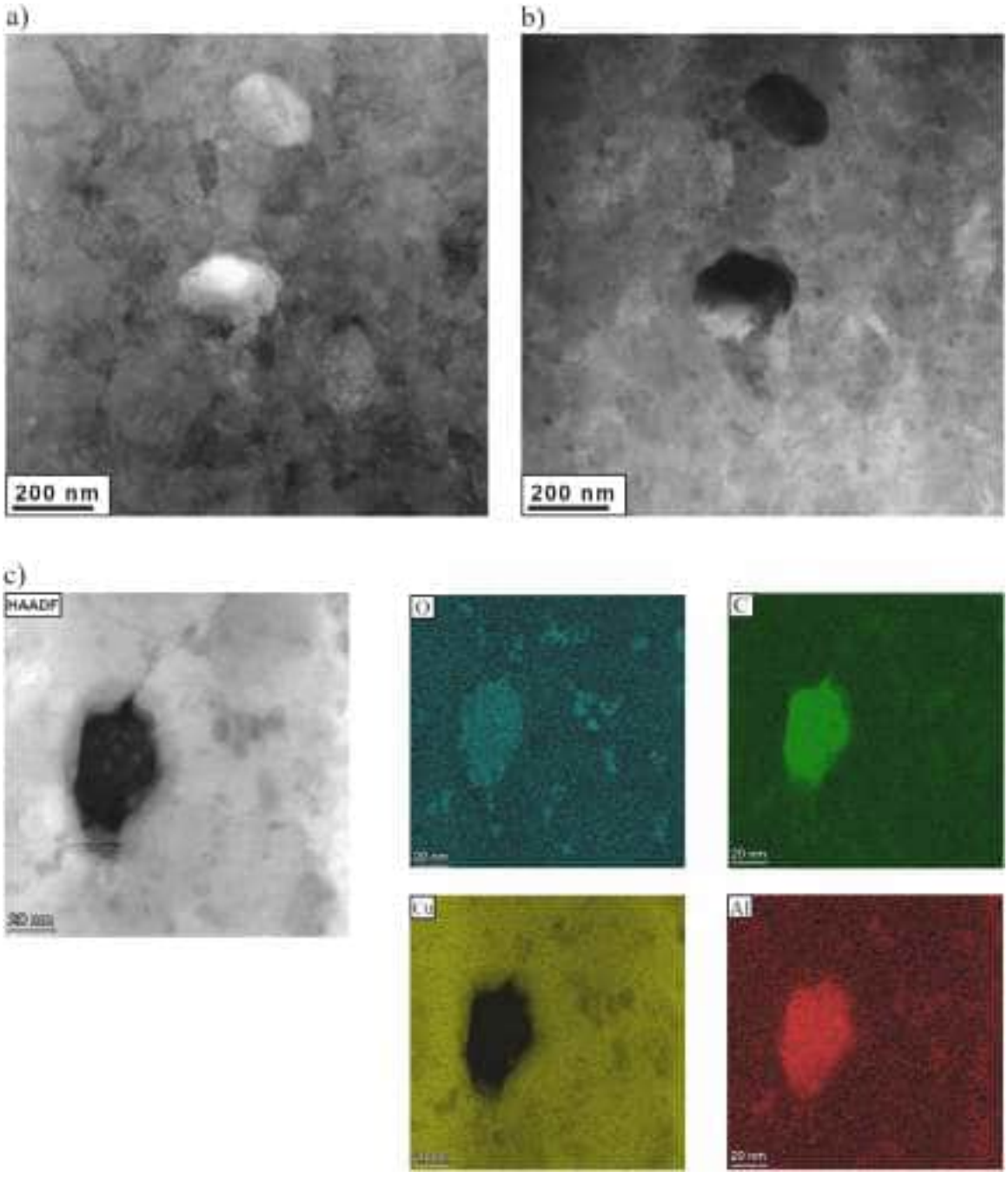

Fig. 4. STEM image of Cu-rGO/Al_2O_3 a) bright field, b) HAADF image, c) EDX map.

recrystallized grains are filled with small partial twins which are visible in the SEM image in Fig. 8d and were identified on the EBSD maps in Fig. 8(e-g). The EBSD maps presented in Fig. 8(e–g) reveal a very high density (85.4 %) of Σ3{111} twin boundaries, characterized by a misorientation angle of 60° ± 5°. Simultaneously, the grain orientation spread (GOS) and Kernel average misorientation (KAM) maps clearly indicate the absence of internal deformation within the observed grains. Both parameters exhibit very low values, confirming complete recrystallization. Furthermore, the presence of parallel, thin twin laths is typical of annealing twins. Considering the limitations of the EBSD technique, the dark lines observed in the band contrast maps are probably nanometric twins. However, due to the resolution limits of EBSD, these features cannot be directly detected.

In order to study the microstructural changes during annealing in more detail, advanced investigations were carried out using STEM microscope. Fig. 9 presents representative STEM images of the Cu-GO, Cu-Al_2O_3 and Cu-rGO/Al_2O_3 microstructures after annealing at 773 K. In the Cu-GO composite (Fig. 9a) after annealing at 773 K there is minor grain growth, and the grain size increased from the HPT-processed value of ~55 nm to ~150 nm. In the microstructure of the Cu-GO composite, there is evidence for the formation of core-shell structures which are visible as dark regions on the HAADF images (Fig. 9a) and presented at higher magnification in Fig. 9b. The EDX analyses of these structures, summarized in Table 1, indicate that they consist of a carbon-rich core and an oxygen-rich shell zone embedded within the Cu matrix. The STEM images of the Cu-Al_2O_3 sample (Fig. 9c) demonstrate the excellent thermal stability of this composite with only a slight grain growth from the HPT-processed ~65 nm to ~110 nm after annealing at 773 K. The

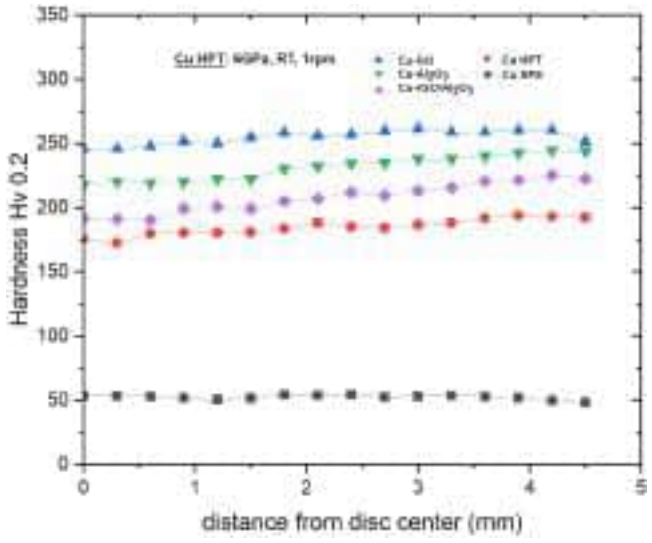

Fig. 5. Hardness measurements of the produced materials as a function of the distance from the disc centres.

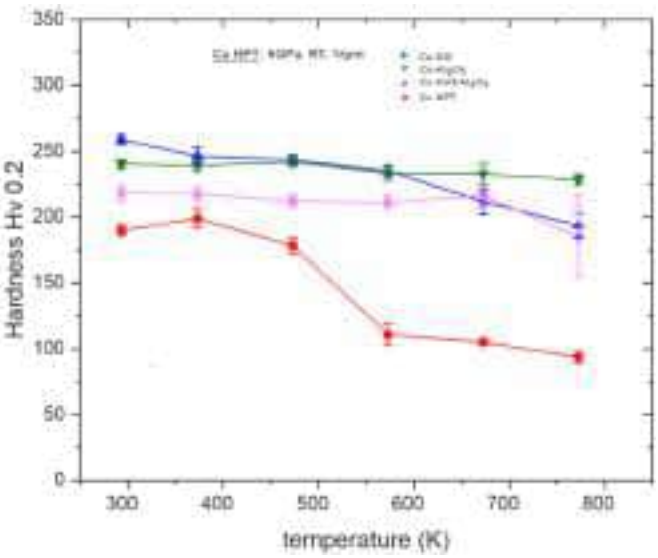

Fig. 7. Hardness as a function of annealing temperature.

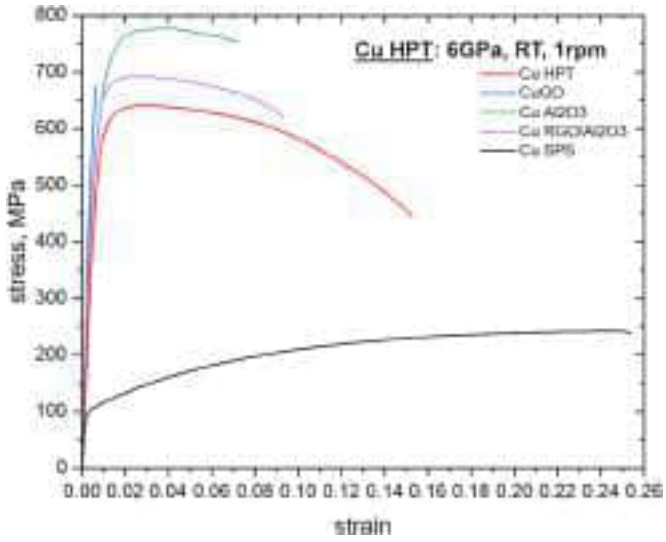

Fig. 6. Tensile strength results.

STEM images for the Cu-rGO/Al_2O_3 composite (Fig. 9d) reveal abnormal grain growth after annealing at 773 K and it is possible to distinguish a zone of finely refined grains with uniformly distributed nanoparticles together with the zone where recrystallization occurred. In these recrystallized regions numerous partial twins are observed, within which there are nanoparticles along the grain boundaries. In the nanocrystalline regions more rGO/Al_2O_3 particles are visible than in the recrystalized zones. Unlike the Cu-GO sample, where the core-shell structure of the C-rich core and the Cu-oxide layer were visible after annealing, in the Cu-rGO/Al_2O_3 composite this effect was not evident after the annealing.

4. Discussion

4.1. Effect of nanoparticle type on the microstructure and properties of composites

The addition of nanoparticles to a copper matrix has a great influence on the microstructure development during HPT processing and in the subsequent properties of the nanocomposites. The nanoparticles added in this study were GO, Al_2O_3 and rGO/Al_2O_3 and they all enhanced the grain refinement. The fabricated composites had nanocrystalline structures with average grain sizes ranging from ~55 to ~75 nm for Cu-GO, Cu- Al_2O_3 and Cu-rGO/Al_2O_3, respectively, while for pure Cu after HPT the grain size was ~210 nm. The substantial grain refinement observed in the composite materials during SPD processing is well-established and has been reported in various earlier studies [12,14,16]. The incorporation of stable, hard nanofillers and their uniform distribution within the metal matrix can restrict dislocation movement and pin grain boundaries, thereby effectively limiting their mobility. This suppresses dynamic recrystallization and recovery processes which occur during intense plastic deformation, shifting the structural saturation point [56] and ultimately enhancing the grain size refinement. It is worth noting that the saturation effect depends on the type of material, its purity, melting point or stacking fault energy. Furthermore, the saturation effect applies not only to the size of the grains, but also to the particles of the second phase. Research has shown that for a given material subjected to the HPT process, there is a certain level of saturation to which the material will aspire from both 'above' and 'below' [57–59].

Additionally, the uniform distribution of the reinforcing phase within the copper matrix has a crucial impact on both the microstructure and the mechanical properties. The Cu-GO and Cu-Al_2O_3 samples displayed the best reinforcement distribution, corresponding to the smallest grain sizes of the matrix. By contrast, the Cu-rGO/Al_2O_3 composite showed a higher degree of agglomeration, and this led to a less effective structural refinement.

These differences are primarily attributed to the distinct characteristics and structures of the reinforcing phases. Previous studies have shown that GO is less prone to agglomeration in a metal matrix compared to graphene or carbon nanotubes due to the presence of carboxyl and hydroxyl groups on the surface of GO [28–31]. These groups form Cu-O-C chemical bonds with the matrix, improving the dispersion of GO within the matrix and strengthening the bonding between the Cu matrix and the GO reinforcing phase. For composites reinforced with Al_2O_3 particles, the particles were initially nanosized with an average size of ~50 nm. As a result, the combination of milling and 20 HPT turns was sufficient to break most of the agglomerates and achieve an essentially uniform distribution of the Al_2O_3 particles in the Cu matrix. By contrast, for the rGO/Al_2O_3 particles, most of the carboxyl and hydroxyl groups originally present on the GO surface are used during the synthesis of the rGO/Al_2O_3 flakes as they form Al_2O_3-C bonds. This limits the ability of the rGO/Al_2O_3 flakes to bond effectively with the Cu matrix and, moreover, the rGO/Al_2O_3 flakes are stiffer and

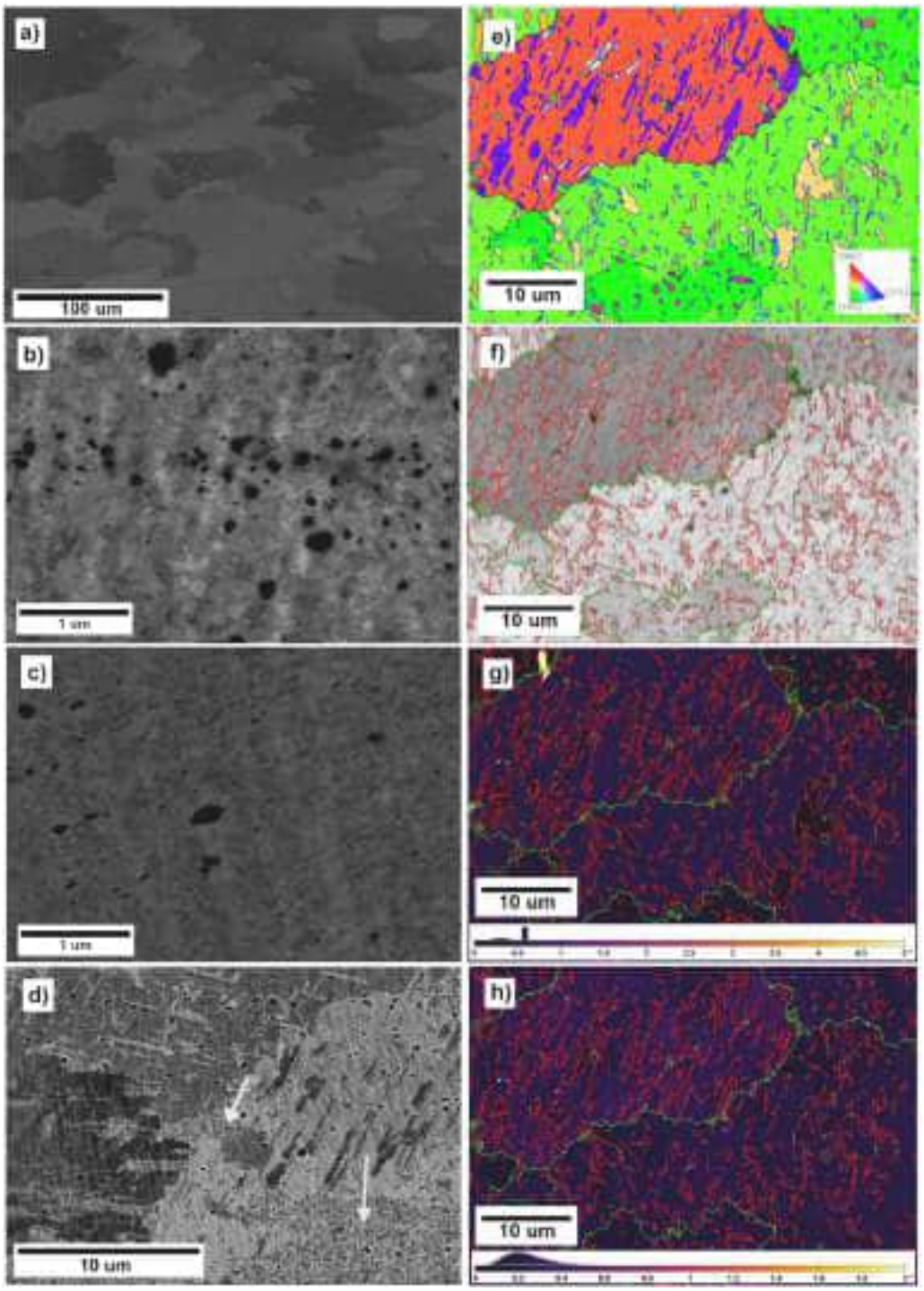

Fig. 8. SEM images of samples after annealing: a) Cu after HPT annealed at 573 K; b) Cu-GO annealed at 773 K; C) Cu-Al2O3 annealed at 773 K; d) Cu-RGO/Al2O3 annealed at 773 K; e) EBSD map of Cu-RGO/Al2O3 annealed at 773 K; f) EBSD band contrast map with marked Σ3 twin boundaries (red), HAGB (green) and LAGB (yellow); g) EBSD grain orientation spread (GOS) map with marked Σ3 twin boundaries (red), HAGB (green) and LAGB (yellow); h) EBSD Kernel average misorientation (KAM) map with marked Σ3 twin boundaries (red), HAGB (green) and LAGB (yellow).

more difficult to break during processing so that their agglomerates are harder to fragment and uniformly distribute within the Cu matrix [60].

The composites fabricated in this research exhibit unique hardness (Fig. 5) when compared with the coarse-grained and nanostructured pure copper. The hardness values increased by appropriately 200 % for the Cu-rGO/Al_2O_3 composite, 230 % for Cu-Al_2O_3 and 250 % for the Cu-GO composite relative to the initial coarse-grained copper. This unique enhancement in mechanical properties is attributed to several factors: a) the significant grain size reduction which is consistent with the Hall-Petch relationship [57,61], b) the presence of hard, uniformly distributed GO, Al_2O_3 and rGO/Al_2O_3 nanoparticles within the matrix [58] and c) the increased dislocation density caused by additional obstacles to dislocation movement. The observed differences in microhardness values between the samples are a consequence of the varying degrees of grain size reduction, the distribution of the reinforcement phase within the matrix and the level of nanoparticle agglomeration.

The UTS of the fabricated nanocomposites (Fig. 6) ranged from 675 MPa to 780 MPa and these values are nearly three times higher than

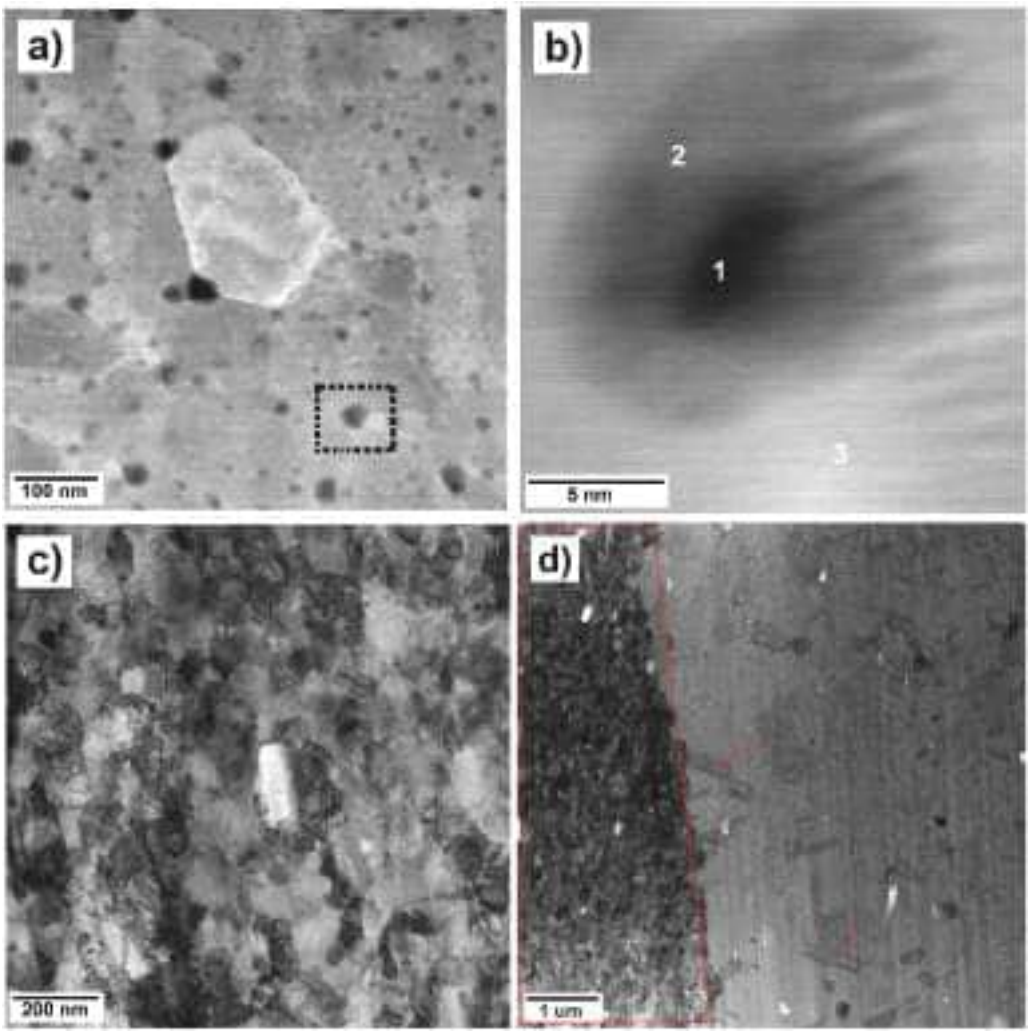

Fig. 9. SETM images of samples after annealing at 773 K: a) Cu-GO; b) higher magnification of the area marked by the square in a), numbers indicate Cu-GO EDS measure points (1 - C; 2 - O; 3 - Cu); C) Cu-Al_2O_3; d) Cu-RGO/Al_2O_3.

Table 1
EDX measurements correlated with STEM image - Fig. 9b.

	C-K	O-K	Cu-K
Point 1	14.3	43.4	45.3
Point 2	2.5	33.2	64.3
Point 3	0.9	3.4	95.7

for unprocessed copper (~250 MPa) and 40 MPa to 140 MPa higher than HPT-processed Cu. The highest UTS was observed in the Cu-Al_2O_3 sample (~780 MPa) and the Cu-rGO/Al_2O_3 sample (~690 MPa). Both samples also demonstrated plasticity in the range of 6–8 %. This enhanced strength is attributed to significant grain refinement and the presence of hard particles that hinder dislocation movement. The sample with the GO addition, despite exhibiting the highest hardness, could not be evaluated in tensile testing due to their failure in the elastic region. This problem has been widely discussed and is generally attributed to two factors. First, the Cu-GO microstructure experiences intense grain size reduction, with the smallest grain size of 55 nm reported for this sample, and this leads to a lack of accommodation of stress through plastic deformation and therefore to premature failure during testing [59]. Second, the exceptionally small sizes of the tensile test samples (4.0 ×0.6 ×0.8 mm^3) which were cut using an EDM machine. The surface roughness of such tensile samples is enhanced and this, combined with their small dimensions, may have led to the formation of localized stress concentrations causing early failure under tension.

4.2. Thermal stability of the composites

The addition of nanoparticles to the copper matrix significantly influences not only grain refinement and the mechanical properties but also the thermal stability of the composites. The particles restrict the movement of grain boundaries during annealing and actively inhibit recrystallization in the Zener pinning effect [62]. In this context, the thermal behaviour of the fillers and their uniform distribution within the copper matrix are critical factors determining the thermal stability of these nanocomposites.

As shown in Fig. 7, the produced composites are thermally stable up to at least 673 K where this is significantly greater than for pure copper after HPT (473 K). At elevated temperatures, notable differences begin to emerge between the composites. Starting from the Cu-Al_2O_3 composite, it remains thermally stable up to 773 K with both the microstructure and the microhardness remaining stable throughout the entire temperature range. This is attributed to the presence of a uniformly distributed Al_2O_3 in the matrix (Fig. 3) and thermally stable Al_2O_3 nanoparticles with a diameter of 6.5 nm which act as effective barriers for grain growth. This mechanism is well documented in the literature [20,26,63,23].

The addition of GO gave the highest hardness and the smallest grain

size among all fabricated composites. However, the Cu-GO composite exhibited a slight drop of hardness as the temperature increased. After annealing at 773 K the hardness dropped from 260 Hv units to approximately 190 Hv units. It is worth noting that this value is comparable to that of pure copper after HPT processing. The drop of mechanical properties is associated with specific microstructural changes occurring in the sample after annealing at 773 K (Fig. 8 and Fig. 9). Firstly, limited grain growth was observed, with the grain size increasing from the HPT-processed ~55 nm to ~150 nm. Secondly, the GO nanoparticles transformed into core-shell structures embedded within the metal matrix, consisting of an oxygen-rich outer layer and a carbon-rich core (Fig. 9). These core-shell structures are less effective in inhibiting grain growth compared to the Al_2O_3 nanoparticles and their formation is linked to the degradation of GO at higher temperatures. During heating, oxygen functional groups on the GO surface react with the Cu matrix to form diffusive layers of CuO and CuO_2. Subsequently, the hexagonal graphene structure degrades, leading to the formation of a graphite core [54,64-66].

The composite with the addition of rGO/Al_2O_3 seems to be thermally stable up to 673 K and the annealing at 773 K produced abnormal grain growth and the formation of a heterostructure composed of large recrystalized grains (Fig. 8d) containing partial recrystallization twins (marked with red arrows Fig. 9d) which were identified based on the EBSD analysis (Fig. 8e) and some nanocrystalline regions (indicated by white arrows on Fig. 8d and red frame Fig. 9d). This heterostructure formation is attributed to an inhomogeneous distribution of rGO/Al_2O_3 particles in the matrix. The fabrication of rGO/Al_2O_3 nanoparticles significantly increased the stiffness and strength of the GO flakes preventing many of them from fragmenting during the HPT processing (Fig. 1d and Fig. 4). Therefore, large agglomerates remained in the microstructure, and this reduced the number of obstacles to recrystallization leading to a partial recrystallization. Moreover, there was no trace of the formation of a core-shell structure typical of the GO sample. This is associated with the production route of rGO/Al_2O_3 which already included a thermal treatment at 553 K for 2 h which effectively decomposed the organic precursor to Al_2O_3 and reduced the GO to rGO [50]. The GO poses oxygen-containing functional groups on its surface such as carbonyl, epoxy, carboxylic acid and hydroxyl which decompose during annealing [64] and cause the formation of a core-shell structure in the Cu-GO sample. When these oxygen groups are reduced, the material becomes rGO and this material is thermally stable even above 1273 K [64]. For the rGO/Al_2O_3 nanoparticles, there are no free oxygen-containing functional groups which are capable of decomposing during annealing of the Cu-rGO/Al_2O_3 samples.

5. Conclusions

The type of nanofiller and its distribution in the copper matrix has a significant effect on the microstructure, mechanical properties and thermal stability of the composite. Analysis of the microstructure in terms of grain size showed that the greatest difference is attributed to the presence of nanofillers as the copper without additives had grain sizes of the order of ~210 nm whereas the composites had grain sizes of ~55 nm, ~65 nm and ~75 nm for Cu-GO, Cu-Al_2O_3 and Cu-rGO/Al_2O_3, respectively.

The type of additive influenced the extent by which the hardness improved by comparison with copper after HPT. These improvements increased by 65 Hv, 45 Hv and 25 Hv for Cu-GO, Cu-Al_2O_3 and Cu-rGO/Al_2O_3, respectively. Significant differences were also seen in the tensile tests where the Cu-GO composite cracked in the elastic range while the other composites showed some plastic deformation range with higher UTS values of ~780 MPa in Cu-Al_2O_3 and ~690 MPa in Cu-rGO/Al_2O_3 compared with ~640 MPa in Cu after HPT.

The greatest difference between the additives was observed in the thermal stability tests. The Cu-Al_2O_3 composite annealed at 373 – 773 K had almost the same hardness and its microstructure changed slightly such that, after annealing at 773 K, the average grain size increased to ~100 nm. The Cu-GO composite showed a slow and minor decrease in hardness with increasing annealing temperature and the hardness decreased to ~180 Hv after annealing at 773 K. There were more observable changes in the microstructure of this composite related to the thermal decomposition of GO but the grain size increased to only ~150 nm and therefore the material remained in the UFG condition. The Cu-rGO/Al_2O_3 composite remained stable in terms of hardness and microstructure up to 673 K but annealing at 773 K led to a decrease in hardness to ~185 Hv associated with microstructural growth. It is noteworthy that the composite underwent abnormal grain growth resulting in a bimodal structure caused by an uneven distribution of reinforcing particles in the matrix.

It is also worth emphasising that all the produced composites had better thermal stability than the HPT-processed pure Cu and their hardness values after annealing at 773 K were higher than for Cu after HPT without subsequent annealing.

CRediT authorship contribution statement

Bednarczyk Witor: Investigation. **Marta Ciemiorek:** Investigation. **Anita Wojciechowska:** Investigation. **Yi Huang:** Writing – review & editing, Validation, Investigation. **Terence G. Langdon:** Writing – review & editing, Supervision, Conceptualization. **Małgorzata Lewandowska:** Writing – review & editing, Conceptualization. **Agnieszka Jastrzębska:** Writing – review & editing. **Maria Emerla:** Writing – original draft, Methodology, Investigation, Data curation. **Piotr Bazarnik:** Writing – original draft, Project administration, Methodology, Investigation, Funding acquisition, Data curation, Conceptualization.

Declaration of Competing Interest

The authors declare that they have no known competing financial interests or personal relationships that could have appeared to influence the work reported in this paper.

Acknowledgments

This work was carried out within an OPUS 19 project “Metal matrix composites fabricated by high-pressure torsion and reinforced with 2D and 3D nano-particles” funded by National Science Centre under nb. 2020/37/B/ST5/01837.

Data availability

Most of the data on which this article is based has been included. Other measurement data and numerous microscopic images produced during the research can be made available on request to the reader by contacting the corresponding author.

References

[1] Q. Mao, Y. Liu, Y. Zhao, A review on copper alloys with high strength and high electrical conductivity, J. Alloy. Compd. 990 (2024) 174456, https://doi.org/10.1016/j.jallcom.2024.174456.
[2] M. Lipińska, P. Bazarnik, M. Lewandowska, The influence of severe plastic deformation processes on electrical conductivity of commercially pure aluminium and 5483 aluminium alloy, Arch. Civ. Mech. Eng. 16 (2016) 717–723, https://doi.org/10.1016/j.acme.2016.04.013.
[3] Y. Iwahashi, Z. Horita, M. Nemoto, T.G. Langdon, The process of grain refinement in equal-channel angular pressing, Acta Met. 46 (1998) 3317–3331, https://doi.org/10.1016/S1359-6454(97)00494-1.
[4] H.N. Omran, A.R. Eivani, M. Farbakhti, H.R. Jafarian, Tribological properties of copper-graphene (CuG) composite fabricated by accumulative roll bonding, J. Mater. Res. Technol. 25 (2023) 4650–4657, https://doi.org/10.1016/j.jmrt.2023.06.261.
[5] A. Vorhauer, R. Pippan, On the homogeneity of deformation by high pressure torsion, Scr. Mater. 51 (2004) 921–925, https://doi.org/10.1016/j.scriptamat.2004.04.025.

[6] S. Sabbaghianrad, J. Wongsa-Ngam, M. Kawasaki, T.G. Langdon, An examination of the saturation microstructures achieved in ultrafine-grained metals processed by high-pressure torsion, J. Mater. Res. Technol. 3 (2014) 319–326, https://doi.org/10.1016/j.jmrt.2014.10.002.
[7] Y. Ito, K. Edalati, Z. Horita, High-pressure torsion of aluminum with ultrahigh purity (99.9999%) and occurrence of inverse Hall-Petch relationship, Mater. Sci. Eng. A 679 (2017) 428–434, https://doi.org/10.1016/j.msea.2016.10.066.
[8] A.P. Zhilyaev, T.G. Langdon, Using high-pressure torsion for metal processing: Fundamentals and applications, Prog. Mater. Sci. 53 (2008) 893–979, https://doi.org/10.1016/j.pmatsci.2008.03.002.
[9] M. Kawasaki, H.J. Lee, B. Ahn, A.P. Zhilyaev, T.G. Langdon, Evolution of hardness in ultrafine-grained metals processed by high-pressure torsion, J. Mater. Res. Technol. 3 (2014) 311–318, https://doi.org/10.1016/j.jmrt.2014.06.002.
[10] K. Edalati, K. Imamura, T. Kiss, Z. Horita, Equal-channel angular pressing and high-pressure torsion of pure copper: evolution of electrical conductivity and hardness with strain, Mater. Trans. 53 (2012) 123–127, https://doi.org/10.2320/matertrans.MD201109.
[11] H. Jiang, Y.T. Zhu, D.P. Butt, I.V. Alexandrov, T.C. Lowe, Microstructural evolution, microhardness and thermal stability of HPT-processed Cu, Mater. Sci. Eng. A 290 (2000) 128–138, https://doi.org/10.1016/S0921-5093(00)00919-9.
[12] R.Z. Valiev, R.K. Islamgaliev, I.V. Alexandrov, 2000, Bulk nanostructured materials from severe plastic deformation, 2000. https://doi.org/10.1016/S0079-6425(99)00007-9..
[13] R.K. Islamgaliev, F. Chmelik, R. Kuzel, Thermal structure changes in copper and nickel processed by severe plastic deformation, 335–338, Mater. Sci. Eng. A (1997) 234–236, https://doi.org/10.1016/s0921-5093(97)00247-5.
[14] J. Čížek, I. Procházka, M. Cieslar, R. Kužel, J. Kuriplach, F. Chmelík, I. Stulíková, F. Bečvář, O. Melikhova, R.K. Islamgaliev, Thermal stability of ultrafine grained copper, Phys. Rev. B - Condens. Matter Mater. Phys. 65 (2002) 1–16, https://doi.org/10.1103/PhysRevB.65.094106.
[15] N. Lugo, N. Llorca, J.J. Suñol, J.M. Cabrera, Thermal stability of ultrafine grains size of pure copper obtained by equal-channel angular pressing, J. Mater. Sci. 45 (2010) 2264–2273, https://doi.org/10.1007/s10853-009-4139-7.
[16] J. Čížek, I. Procházka, M. Cieslar, R.K. Islamgaliev, O. Kulyasova, Influence of ceramic nanoparticles on thermal stability of ultra fine grained copper, Acta Phys. Pol. A 113 (2008) 1285–1292, https://doi.org/10.12693/APhysPolA.113.1285.
[17] B. Tian, P. Liu, K. Song, Y. Li, Y. Liu, F. Ren, J. Su, Microstructure and properties at elevated temperature of a nano-Al2O3 particles dispersion-strengthened copper base composite, 705–710, Mater. Sci. Eng. A (2006) 435–436, https://doi.org/10.1016/j.msea.2006.07.129.
[18] D. Shen, P. Gao, Y. He, J. Gong, J. Du, A Cu-Al2O3 composite with ultrahigh tensile strength prepared by high-pressure torsion, J. Mater. Eng. Perform. (2022) 1–6, https://doi.org/10.1007/s11665-022-06936-9.
[19] J. Naser, H. Ferkel, W. Riehemann, Grain stabilisation of copper with nanoscaled Al_2O_3-powder, 470–473, Mater. Sci. Eng. A. (1997) 234–236, https://doi.org/10.1016/s0921-5093(97)00263-3.
[20] H.R. Peng, M.M. Gong, Y.Z. Chen, F. Liu, Thermal stability of nanocrystalline materials: thermodynamics and kinetics, Int. Mater. Rev. 62 (2017) 303–333, https://doi.org/10.1080/09506608.2016.1257536.
[21] P.A. Manohar, M. Ferry, T. Chandra, Five decades of the Zener Equation, ISIJ Int 38 (1998) 913–924, https://doi.org/10.2355/isijinternational.38.913.
[22] N. Wang, Y. Wen, L.Q. Chen, Pinning force from multiple second-phase particles in grain growth, Comput. Mater. Sci. 93 (2014) 81–85, https://doi.org/10.1016/j.commatsci.2014.06.030.
[23] E. Nes, N. Ryum, O. Hunderi, On the Zener Drag, Acta Matallurgica 33 (1985) 11–22.
[24] D. Li, S. Zhou, P. Li, W. Lü, X. Zhu, Research progresses on thermal stabilization of metal nanocrystalline alloys, Xiyou Jinshu Cailiao Yu Gongcheng/Rare Met. Mater. Eng. 44 (2015) 1075–1081. https://doi.org/10.1016/s1875-5372(15)30070-9.
[25] R.Z. Valiev, R.K. Islamgaliev, N.F. Kuzmina, Y. Li, T.G. Langdon, Strengthening and grain refinement in an Al-6061 metal matrix composite through intense plastic straining, Scr. Mater. 40 (1999) 117–122, https://doi.org/10.1016/S1359-6462(98)00398-4.
[26] D. Zhou, D. Zhang, C. Kong, P. Munroe, R. Torrens, Grain and nanoparticle coarsening of an ultrafine structured Cu-5 vol%Al_2O_3 nanocomposite during isochronal annealing, J. Alloy. Compd. 642 (2015) 83–91, https://doi.org/10.1016/j.jallcom.2015.04.106.
[27] K. Edalati, M. Ashida, Z. Horita, T. Matsui, H. Kato, Wear resistance and tribological features of pure aluminum and Al-Al_2O_3 composites consolidated by high-pressure torsion, Wear 310 (2014) 83–89, https://doi.org/10.1016/j.wear.2013.12.022.
[28] M.I. Abd El Aal, Wear properties of copper and copper composites powders consolidated by high-pressure torsion, Friction 8 (2020) 433–450, https://doi.org/10.1007/s40544-019-0285-3.
[29] M. Jahedi, M.H. Paydar, M. Knezevic, Enhanced microstructural homogeneity in metal-matrix composites developed under high-pressure-double-torsion, Mater. Charact. 104 (2015) 92–100, https://doi.org/10.1016/j.matchar.2015.04.012.
[30] M.I. Abd El Aal, Effect of high-pressure torsion processing on the microstructure evolution and mechanical properties of consolidated micro size Cu and Cu-SiC powders, Adv. Powder Technol. 28 (2017) 2135–2150, https://doi.org/10.1016/j.apt.2017.05.020.
[31] P. Hidalgo-Manrique, X. Lei, R. Xu, M. Zhou, I.A. Kinloch, R.J. Young, Copper/graphene composites: a review, J. Mater. Sci. 54 (2019) 12236–12289, https://doi.org/10.1007/s10853-019-03703-5.
[32] P. Jenei, E.Y. Yoon, J. Gubicza, H.S. Kim, J.L. Lábár, T. Ungár, Microstructure and hardness of copper-carbon nanotube composites consolidated by High Pressure Torsion, Mater. Sci. Eng. A. 528 (2011) 4690–4695, https://doi.org/10.1016/j.msea.2011.02.066.
[33] S.K. Tiwari, H. Singh, A. Midathada, S. Sharma, U.K. Ravella, Study of Fabrication Processes and Properties of Al-CNT Composites Reinforced by Carbon Nano tubes-A Review, Mater. Today Proc. 5 (2018) 28262–28270, https://doi.org/10.1016/j.matpr.2018.10.109.
[34] T. Tokunaga, K. Kaneko, Z. Horita, Production of aluminum-matrix carbon nanotube composite using high pressure torsion, Mater. Sci. Eng. A. 490 (2008) 300–304, https://doi.org/10.1016/j.msea.2008.02.022.
[35] C. Xiong, D. Li, S. Song, Y. Ye, Z. Ye, D. Zuo, Research on the performance of rGO-CNTs synergistically enhanced copper matrix composites, Powder Technol. 394 (2021) 1–9, https://doi.org/10.1016/j.powtec.2021.08.007.
[36] N. Khobragade, K. Sikdar, B. Kumar, S. Bera, D. Roy, Mechanical and electrical properties of copper-graphene nanocomposite fabricated by high pressure torsion, J. Alloy. Compd. 776 (2019) 123–132, https://doi.org/10.1016/j.jallcom.2018.10.139.
[37] J. Hwang, T. Yoon, S.H. Jin, J. Lee, T.S. Kim, S.H. Hong, S. Jeon, Enhanced mechanical properties of graphene/copper nanocomposites using a molecular-level mixing process, Adv. Mater. 25 (2013) 6724–6729, https://doi.org/10.1002/adma.201302495.
[38] K. Zhang, Fabrication of copper nanoparticles/graphene oxide composites for surface-enhanced Raman scattering, Appl. Surf. Sci. 258 (2012) 7327–7329, https://doi.org/10.1016/j.apsusc.2012.04.002.
[39] F. Lin, R. Xu, M. Zhou, R.J. Young, I.A. Kinloch, Y. Ding, Mechanical and Electrical Properties of Graphene Oxide Reinforced Copper–Tungsten Composites Produced via Ball Milling of Metal Flakes, Mater. (Basel) 15 (2022), https://doi.org/10.3390/ma15217736.
[40] P. Jenei, J. Gubicza, E.Y. Yoon, H.S. Kim, J.L. Lábár, High temperature thermal stability of pure copper and copper-carbon nanotube composites consolidated by High Pressure Torsion, Compos. Part A Appl. Sci. Manuf. 51 (2013) 71–79, https://doi.org/10.1016/j.compositesa.2013.04.007.
[41] G. Giovannetti, P.A. Khomyakov, G. Brocks, V.M. Karpan, J. Van Den Brink, P. J. Kelly, Doping graphene with metal contacts, Phys. Rev. Lett. 101 (2008) 4–7, https://doi.org/10.1103/PhysRevLett.101.026803.
[42] P.A. Khomyakov, G. Giovannetti, P.C. Rusu, G. Brocks, J. Van Den Brink, P.J. Kelly, First-principles study of the interaction and charge transfer between graphene and metals, Phys. Rev. B - Condens. Matter Mater. Phys. 79 (2009) 1–12, https://doi.org/10.1103/PhysRevB.79.195425.
[43] L. Zhang, E. Pollak, W.C. Wang, P. Jiang, P.A. Glans, Y. Zhang, J. Cabana, R. Kostecki, C. Chang, M. Salmeron, J. Zhu, J. Guo, Electronic structure study of ordering and interfacial interaction in graphene/Cu composites, Carbon N. Y 50 (2012) 5316–5322, https://doi.org/10.1016/j.carbon.2012.07.020.
[44] K. Raidongia, A.T.L. Tan, J. Huang. Graphene Oxide: Some New Insights into an Old Material, Second Edi, Elsevier Ltd, 2014, https://doi.org/10.1016/B978-0-08-098232-8.00014-0.
[45] I. Sengupta, S. Chakraborty, M. Talukdar, S.K. Pal, S. Chakraborty, Thermal reduction of graphene oxide: How temperature influences purity, J. Mater. Res. 33 (2018) 4113–4122, https://doi.org/10.1557/jmr.2018.338.
[46] I. Sengupta, S.S.S. Sharat Kumar, S.K. Pal, S. Chakraborty, Characterization of structural transformation of graphene oxide to reduced graphene oxide during thermal annealing, J. Mater. Res. 35 (2020) 1197–1204, https://doi.org/10.1557/jmr.2020.55.
[47] B.S. Kong, J. Geng, H.T. Jung, Layer-by-layer assembly of graphene and gold nanoparticles by vacuum filtration and spontaneous reduction of gold ions, Chem. Commun. (2009) 2174–2176, https://doi.org/10.1039/b821920f.
[48] X. Zhou, X. Huang, X. Qi, S. Wu, C. Xue, F.Y.C. Boey, Q. Yan, P. Chen, H. Zhang, In situ synthesis of metal nanoparticles on single-layer graphene oxide and reduced graphene oxide surfaces, J. Phys. Chem. C 113 (2009) 10842–10846, https://doi.org/10.1021/jp903821n.
[49] Y. Liang, H. Wang, H.S. Casalongue, Z. Chen, H. Dai, TiO2 nanocrystals grown on graphene as advanced photocatalytic hybrid materials, Nano Res. 3 (2010) 701–705, https://doi.org/10.1007/s12274-010-0033-5.
[50] A.M. Jastrzębska, J. Karcz, R. Letmanowski, D. Zabost, E. Ciecierska, J. Zdunek, E. Karwowska, M. Siekierski, A. Olszyna, A. Kunicki, Synthesis of the RGO/Al_2O_3 core-shell nanocomposite flakes and characterization of their unique electrostatic properties using zeta potential measurements, Appl. Surf. Sci. 362 (2016) 577–594, https://doi.org/10.1016/j.apsusc.2015.10.125.
[51] N. Kurantowicz, E. Sawosz, S. Jaworski, M. Kutwin, B. Strojny, M. Wierzbicki, J. Szeliga, A. Hotowy, L. Lipińska, R. Koziński, J. Jagiełło, A. Chwalibog, Interaction of graphene family materials with Listeria monocytogenes and Salmonella enterica, Nanoscale Res. Lett. 10 (2015) 1–12, https://doi.org/10.1186/s11671-015-0749-y.
[52] A.M. Jastrzębska, E. Karwowska, A. Tabernacka, P. Mosdorf, P. Polis, P. Kurtycz, A. Olszyna, A.R. Kunicki, New non phyto- and eco-toxic alumina-stabilized silver and praseodymium nanoparticles, Int. J. Appl. Ceram. Technol. 10 (2013) 908–916, https://doi.org/10.1111/j.1744-7402.2012.02834.x.
[53] R.B. Figueiredo, P.H.R. Pereira, M.T.P. Aguilar, P.R. Cetlin, T.G. Langdon, Using finite element modeling to examine the temperature distribution in quasi-constrained high-pressure torsion, Acta Mater. 60 (2012) 3190–3198, https://doi.org/10.1016/j.actamat.2012.02.027.
[54] V.V. Popova, A.V. Stolbovkiy, E.N. Popova, V.P. Pilyugin, Structure and thermal stability of Cu after severe plastic deformation, 1312–1321, Defect Diffus. Forum (2010) 297–301, https://doi.org/10.4028/www.scientific.net/DDF.297-301.1312.
[55] M. Emerla, P. Bazarnik, Y. Huang, A. Wojciechowska, M. Ciemiorek, J. Pura, M. Wieczorek-Czarnocka, P.M.A. Kenichi, A. Jastrzębska, M. Lewandowska, T. G. Langdon, The influence of graphene oxide on the microstructure and properties

of ultrafine-grained copper processed by high-pressure torsion, J. Alloy. Compd. 1005 (2024), https://doi.org/10.1016/j.jallcom.2024.176208.
[56] P. Bazarnik, S. Nosewicz, B. Romelczyk-Baishya, M. Chmielewski, A. Strojny Nędza, J. Maj, Y. Huang, M. Lewandowska, T.G. Langdon, Effect of spark plasma sintering and high-pressure torsion on the microstructural and mechanical properties of a Cu–SiC composite, Mater. Sci. Eng. A 766 (2019), https://doi.org/10.1016/j.msea.2019.138350.
[57] H. Wen, R.K. Islamgaliev, K.M. Nesterov, R.Z. Valiev, E.J. Lavernia, Dynamic balance between grain refinement and grain growth during high-pressure torsion of Cu powders, Philos. Mag. Lett. 93 (2013) 481–489, https://doi.org/10.1080/09500839.2013.805268.
[58] B.B. Straumal, R. Kulagin, L. Klinger, E. Rabkin, P.B. Straumal, O.A. Kogtenkova, B. Baretzky, Structure refinement and fragmentation of precipitates under severe plastic deformation: a review, Mater. (Basel) 15 (2022), https://doi.org/10.3390/ma15020601.
[59] L. Upadhayay, S. Nilawar, C. Kumar, K. Chatterjee, P. Kumar, Effect of processing Mg–6Zn–0.2Ce through high-pressure torsion on its use as a biomaterial, J. Mater. Sci. 59 (2024) 5872–5890, https://doi.org/10.1007/s10853-024-09460-4.
[60] Y. Hu, Y. Xie, H. Xin, J. Chen, shizhong, Y. Liu, C. Li, Xu, Nano/microstructures and mechanical properties of Al_2O_3–TiC ceramic composites reinforced with Al_2O_3@RGO nanohybrids, Ceram. Int. 48 (2022) 27536–27549, https://doi.org/10.1016/j.ceramint.2022.06.047.
[61] M. Emerla, P. Bazarnik, Y. Huang, M. Lewandowska, T.G. Langdon, Using direct high-pressure torsion synthesis to produce aluminium matrix nanocomposites reinforced with carbon nanotubes, J. Alloy. Compd. 968 (2023), https://doi.org/10.1016/j.jallcom.2023.171928.
[62] E.O. Hall, The deformation and ageing of mild steel III discussion of results, Proc. Phys. Soc. Sect. B. 64 (1951) 747–753.
[63] N.J. Petch, The cleavage strength of polycrystals, J. Iron Steel Inst. 174 (1953) 25–28.
[64] Y. Nishida, Introduction to Metal Matrix Composites, Springer Japan, Japan, 2013, https://doi.org/10.1007/978-4-431-54237-7.
[65] Y. Estrin, A. Vinogradov, Extreme grain refinement by severe plastic deformation: A wealth of challenging science, Acta Mater. 61 (2013) 782–817, https://doi.org/10.1016/j.actamat.2012.10.038.
[66] L. Hu, A. Wang, W. Wang, Structural Evolution of Graphene Oxide and Its Thermal Stability During High Temperature Sintering, J. Wuhan. Univ. Technol. Mater. Sci. Ed. 37 (2022) 342–349, https://doi.org/10.1007/s11595-022-2537-8.

Materials Science & Engineering A 799 (2021) 140114

Contents lists available at ScienceDirect

Materials Science & Engineering A

journal homepage: http://www.elsevier.com/locate/msea

Short communication

Using high-pressure torsion to fabricate an Al–Ti hybrid system with exceptional mechanical properties

Aleksandra Bartkowska [a], Piotr Bazarnik [a,*], Yi Huang [b,c], Malgorzata Lewandowska [a], Terence G. Langdon [c]

[a] Warsaw University of Technology, Faculty of Materials Science and Engineering, Woloska, 141, 02-507, Poland
[b] Department of Design and Engineering, Faculty of Science and Technology, Bournemouth University, Poole, Dorset, BH12 5BB, UK
[c] Materials Research Group, Department of Mechanical Engineering, University of Southampton, Southampton, SO17 1BJ, UK

ARTICLE INFO

Keywords:
Aluminium
High-pressure torsion
Hybrid materials
Titanium
Ultrafine grains

ABSTRACT

A novel hybrid material was fabricated from the Al–Ti system using high-pressure torsion up to 50 turns. Microstructural observations revealed intermetallic phases and mixing zones enriched in Ti, consisting of grains of ~20 nm within an Al matrix. Microhardness measurements gave values higher than in the HPT-processed bulk aluminium alloy.

The fabrication of multi-layered hybrid materials is a new concept that may be used to enhance the strength of ultrafine-grained (UFG) materials without losing their ductility. The earliest research was conducted by using high-pressure torsion (HPT) to process semi-circular disks of Ag-Ni [1], Nb-Zr [1] and Al–Cu [2] or quarter disks of Al-Cu [3] where these partial disks were placed to form whole disks within the HPT facility. Later, a new approach was developed by separately stacking disks for HPT processing using Al-Mg [4–7], Cu-Sn [8] and Al–Cu, Al–Fe and to perform some preliminary tests on Al-Ti [9]. The Al–Ti system is especially interesting due to the excellent mechanical properties such as high strength, toughness and stiffness combined with a low density which makes it a good candidate material for use in automotive and aerospace applications [10–12]. Therefore, several attempts have been made to fabricate Al–Ti composites using different techniques such as cold-roll bonding [10,11,13], accumulative roll bonding [14–16], explosive welding [17] and powder consolidation by HPT [18]. The present research was initiated to evaluate the potential for achieving high mechanical properties by processing a stacking of Al/Ti/Al disks by HPT.

The initial disks of 10 mm diameter were cut from a commercial purity aluminium alloy (Al-1050) and titanium (CP–Ti). The initial grain sizes were 44 and 25 μm for these two materials, respectively. The aluminium disks were mechanically polished to a final thickness of ~0.4 mm and titanium to a final thickness of ~0.15 mm. These disks were then stacked in a sequence of one Ti disk between two Al disks using the procedure described earlier [4,5]. The stacks of three disks were then processed by HPT at room temperature under a pressure of 6.0 GPa for 10, 30 and 50 turns. After every 10 rotations, excepting only after the last 10, a heat treatment was applied consisting of annealing the samples in a furnace for 30 min at 300 °C to soften the Al alloy and allow further deformation. It should be emphasized that the temperature of 300 °C is too low to have any major impact on phase transformations in the Al–Ti system.

After processing, each disk was cut vertically along a diameter to give two semi-circular disks and then examined on the cross-sections using light microscopy (LM) with a Zeiss Axio Observer. Panoramic images were made of the overall cross-sections in order to permit a preliminarily examination of the quality of bonding between the individual components. Thereafter, observations were undertaken by scanning electron microscopy (SEM) in back-scatter electron (BSE) mode in the peripheral regions. Detailed microstructural observations were performed using a scanning-transmission electron microscope (STEM) Hitachi HD-2700 operating at an accelerating voltage of 200 kV. Samples for the STEM observations were prepared using a focused ion beam facility (FIB) Hitachi NB5000. X-ray diffraction analysis was undertaken at room temperature to analyse the phase composition of the sample processed by HPT for 50 turns. Diffraction patterns were recorded using a Bruker D8 Advance X-ray diffractometer with filtered radiation of

* Corresponding author.
E-mail address: Piotr.Bazarnik@pw.edu.pl (P. Bazarnik).

https://doi.org/10.1016/j.msea.2020.140114
Received 17 April 2020; Received in revised form 12 August 2020; Accepted 13 August 2020
Available online 19 August 2020

CuKα. Microhardness measurements were recorded using a Zwick/Roell Z2.5 hardness testing machine with a load of 200 g. Linear analysis was performed on one-half of the cross-section with distances between consecutive measurement points of 0.2 mm. The initial coarse-grained materials and the initial materials after 10 HPT revolutions were used as reference samples.

The LM panoramic images of the Al–Ti composites are presented in Fig. 1 after 10, 30 and 50 turns. In the sample after 10 turns there was no intensive bonding between the components with some delamination in the central regions and the Ti disk was only slightly fragmented, whereas after 30 and 50 turns monolithic samples were obtained without evidence for any pores or defects at the Al/Ti interfaces. It is readily apparent that increasing the numbers of HPT turns produces successive fragmentation of the Ti disk. In the sample after 50 turns, there is a continuous bond between components throughout the cross-section but with a gradient in Ti fragmentation moving away from the edge of the sample where the deformation is the highest. The size of the fragmented Ti increases after 50 turns and reaches a maximum size near the centre of the disk. At the edges of the sample, where the applied strain is the largest at the macroscopic scale, it is hard to distinguish between the Al and Ti phases, thereby confirming a significant mixing between these components.

Fig. 2 shows SEM micrographs of the cross-sections of the Al–Ti hybrid material processed by HPT for 50 turns. The overview image in Fig. 2(a) reveals a homogeneous distribution of Ti in the Al matrix with both Ti-enriched shear bands and fine to relatively large fragments of Ti in the Al. Most of the Ti disk has undergone a severe fragmentation which permits a general mixing between Al and Ti. In this sample, the boundaries between the Al and Ti are not well defined in the mixing zone area and this indicates the possibility of the formation of intermetallic phases (Fig. 2(b)). The character of the Al/Ti interface depends on the distance from the disk centre, with a more complex lamellar structure at the area near the edge of the sample and a flatter Al/Ti interface visible around the central region. A similar structure was noted earlier in HPT-processed Al-Mg [4,9,19] and Al–Cu [2,20,21]. More intense mixing was observed in the edge area which is characterized by a laminated, multi-layered structure. This inhomogeneity is typical for HPT processing as the accumulated strain varies along the radius and reaches a minimum in the central area [22]. It was reported earlier for the Al-Cu [2,20,23] and Al–Mg [4,19] systems that intensive mixing in the edge areas of samples promotes the occurrence of solid-state reactions even at low homologous temperatures. Thus, the present samples contain mixing zones consisting of numerous areas of irregularly-shaped thin layers of Al and Ti and the boundaries between the Al and Ti are no longer distinguishable. A similar observation was reported for the Al–Mg system [19] processed by HPT.

Detailed STEM observations, presented in Fig. 3(a–c), reveal a unique, layered microstructure in which it is possible to differentiate the Al matrix with an average grain size of ~160 nm and an area of mixing, marked in Fig. 3(a and b) with an arrow, that is about 400 nm wide. Those areas of mixing consist of thin layers with very small grains having average sizes of ~20 nm, as illustrated in Fig. 3(c) where the interface between the matrix and the mixing zones is free of voids with a homogenous structure in Fig. 3(b). A significant grain refinement, to about 300 nm, is visible in the large Ti-rich particles shown in Fig. 3(d). Fig. 3(e) presents a dark-field image with the corresponding compositional maps for Al and Ti. It is apparent that the measurement area is composed of both Al and Ti and there is a Ti-rich zone in the form of bands located within the Al matrix. The occurrence of significant grain refinement, as well as the presence of both Al and Ti (Fig. 3 (d)) and the mixing zones (Fig. 3 (a,b,c)), suggests the formation of intermetallic phases from the Al–Ti system and it is important therefore to examine this possibility.

The presence of intermetallic phases was examined using XRD analysis as presented in Fig. 4 where the peaks with high intensity correspond to various crystalline planes of the face-centred cubic (FCC) Al and hexagonal close-packed (HCP) Ti. However, the pattern confirms also the formation of $Ti_{3.3}Al$ and Al_3Ti phases. The fraction of intermetallic phases in the samples after 10 and 30 revolutions was too small for detection. Those intermetallic phases are known for having low density, high hardness, good thermal and oxidation resistance and high melting temperatures and therefore they find applications in the strengthening of Al alloys for high-temperature applications [24,25]. The approach of fabricating Al–Ti metallic composites by stacking disks and using HPT processing was reported earlier but without any evidence for the formation of intermetallic phases [9]. However, the formation of Al_2Ti and Al_3Ti intermetallic phases after processing by HPT was described when processing a mixture of powders where the formation of these intermetallic phases was attributed to short circuit diffusion enhanced by the formation of many defects in the HPT-processed material [18].

Hardness testing was conducted in order to examine the influence of HPT processing and these intermetallic phases on the mechanical properties. The microhardness distributions along the radii are shown in Fig. 5 for measurements taken on the cross-sections of the disks of the Al/Ti/Al systems after processing by HPT for 30 and 50 turns; the microhardness values of the as-received and HPT-processed bulk Al-1050 and CP-Ti are also included for comparison. Thus, the hardness of the hybrid material processed for 50 turns lies between the values of ~60 Hv at the disk centre and ~300 Hv at the edge of the sample, whereas in samples processed for 30 turns the maximum hardness achieved at the edge was ~130 Hv and the hardness in the centre varied around a value of ~40 Hv. It is worth noting that for all hybrid samples, the hardness in the central regions is inhomogeneous and exhibits high standard deviations which are associated with the presence of large fragments of undeformed titanium plates. The hardness values of the

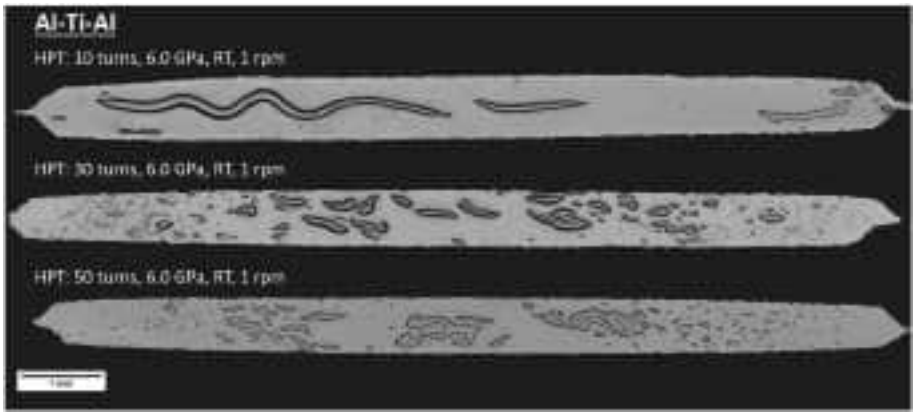

Fig. 1. Vertical cross-sections of the Al–Ti system processed by HPT under an applied pressure of 6.0 GPa for 10, 30 and 50 turns.

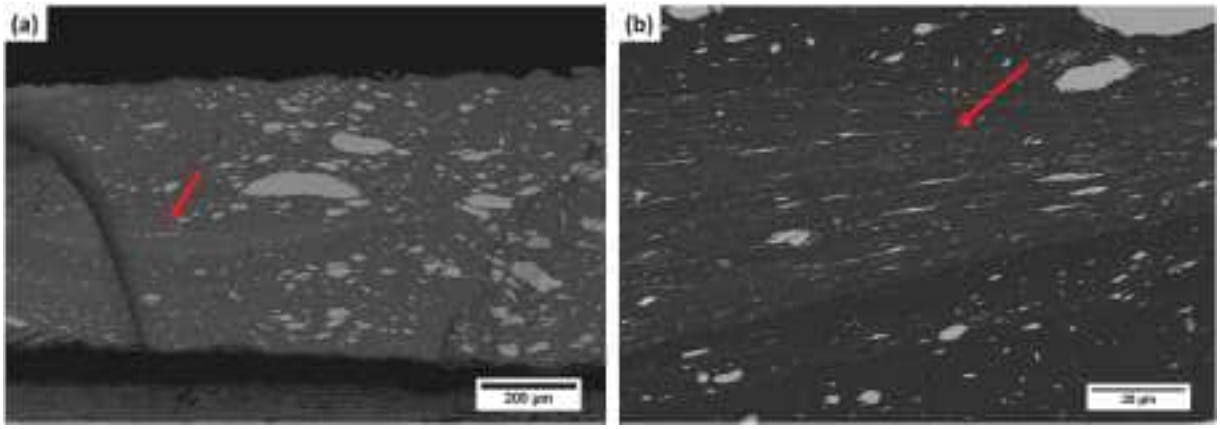

Fig. 2. SEM images of the Al–Ti system processed for 50 turns: (a) overall image of the sample, (b) magnified image of the mixing zones. The brighter contrast corresponds to the Ti-enriched regions and the darker to Al.

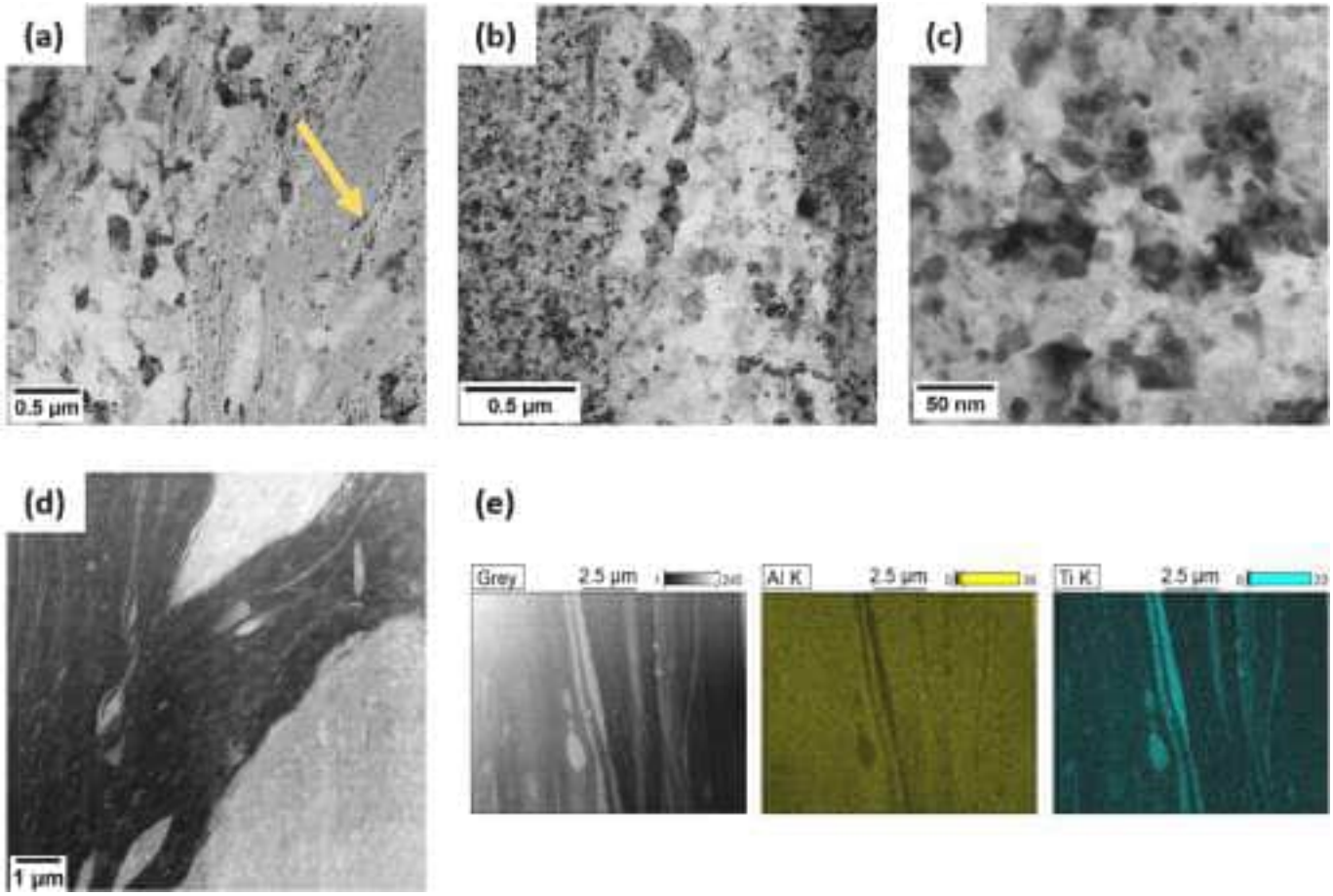

Fig. 3. (a,b) STEM images of the sample of the hybrid material processed for 50 HPT turns, (c) enlarged image of (a), (d) structure of Ti-rich blocks in the Al matrix, (e) EDX compositional maps for Al and Ti containing the mixing zone: dark-field image of the analysed area (left), compositional maps for Al and Ti, in the centre and right, respectively.

hybrid material at the edge are therefore very significantly higher than those for the as-received and HPT-processed Al-1050 and only slightly lower than those for the bulk HPT-processed Ti. It is important to note that the initial system contained 84 vol% of Al and only 16 vol% of Ti so that the hardness of the fabricated hybrid material, which consists mainly of Al, is exceptionally high. This increase in hardness is attributed to Hall-Petch strengthening by grain refinement of the Al matrix and Ti-rich particles and to precipitation hardening due to the formation of the intermetallic phases [4,19]. A similar increase in hardness was noted for the Al–Mg system where there was a hardness of ~270 Hv at the periphery of the sample after processing by HPT for 10 turns [4].

In summary, samples of an Al–Ti hybrid material were fabricated by processing a stack of Al/Ti/Al disks using high-pressure torsion at room temperature for 10, 30 and 50 turns with the application of intermediate appropriate heat treatments. Continuous and complex mixing was observed between Al and Ti after processing by HPT for 50 turns at RT,

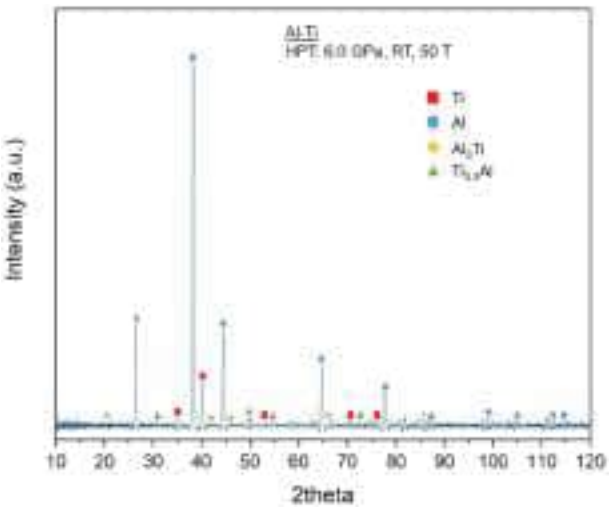

Fig. 4. XRD pattern for the hybrid Al–Ti system processed by HPT for 50 turns.

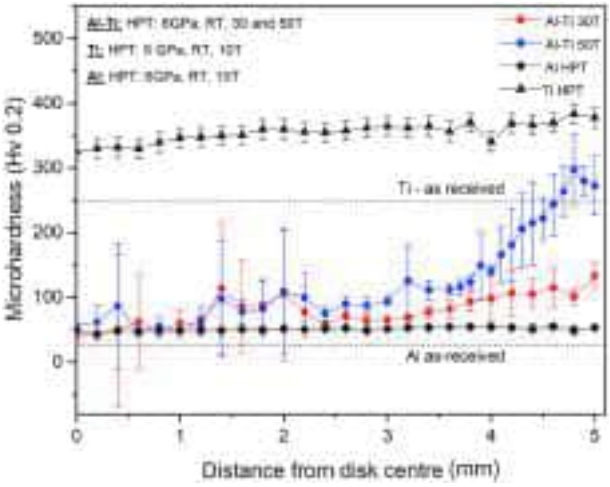

Fig. 5. Microhardness distributions of the hybrid Al–Ti systems processed by HPT for 30 and 50 turns across the half-disk: additional hardness values for the as-received and HPT-processed bulk Al 1050 and Ti are included for comparison.

indicating the potential for using this method as a processing tool for the synthesis of hybrid materials. The microstructure after processing was characterized by exceptional grain refinement, with a grain size of ~20 nm inside mixing bands and ~160 nm for the Al matrix and ~300 nm for Ti-rich blocks. Intermetallic phases from the Al–Ti system were formed during processing by HPT. These phases, together with grain refinement of the Al matrix, the presence of hard Ti-rich blocks and interfaces between the Al and Ti thin layers, lead to a significant increase in the hardness of the hybrid material compared with the hardness of the initial components.

CRediT authorship contribution statement

Aleksandra Bartkowska: SEM studies, Hv measurements. **Piotr Bazarnik:** TEM,FIB, Writing. **Yi Huang:** Visualization, Data processing. **Malgorzata Lewandowska:** Methodology, Data curation, Writing - review & editing. **Terence G. Langdon:** Conceptualization, Supervision, Reviewing and Editing.

Declaration of competing Interest

The authors declare that they have no known competing financial interests or personal relationships that could have appeared to influence the work reported in this paper.

Acknowledgements

This work was supported by the National Science Centre, Poland, within the project SONATINA 1 “Synthesis of novel hybrid materials using High-Pressure Torsion” under Grant Agreement No.2017/24/C/ST8/00145 and by the European Research Council under ERC Grant Agreement No. 267464-SPDMETALS.

References

[1] T. Miyazaki, D. Terada, Y. Miyajima, C. Suryanarayana, R. Murao, Y. Yokoyama, K. Sugiyama, M. Umemoto, Y. Todaka, N. Tsuji, Synthesis of non-equilibrium phases in immiscible metals mechanically mixed by high pressure torsion, J. Mater. Sci. 46 (2011) 4296–4301.
[2] K. Oh-ishi, K. Edalati, H.S. Kim, K. Hono, Z. Horita, High-pressure torsion for enhanced atomic diffusion and promoting solid-state reactions in the aluminum–copper system, Acta. Mater. 61 (2013) 3482–3489.
[3] O. Bouaziz, H.S. Kim, Y. Estrin, Architecturing of metal-based composites with concurrent nanostructuring: a new paradigm of materials design, Adv. Eng. Mater. 15 (2013) 336–340.
[4] B. Ahn, A.P. Zhilyaev, H.-J. Lee, M. Kawasaki, T.G. Langdon, Rapid synthesis of an extra hard metal matrix nanocomposite at ambient temperature, Mater. Sci. Eng., A 635 (2015) 109–117.
[5] B. Ahn, H.-J. Lee, I.-C. Choi, M. Kawasaki, J.-I. Jang, T.G. Langdon, Micro-mechanical behavior of an exceptionally strong metal matrix nanocomposite processed by high-pressure torsion, Adv. Eng. Mater. 18 (2016) 1001–1008.
[6] M. Kawasaki, B. Ahn, H. Lee, A.P. Zhilyaev, T.G. Langdon, Using high-pressure torsion to process an aluminum–magnesium nanocomposite through diffusion bonding, J. Mater. Res. 31 (2016) 88–99.
[7] J.-K. Han, K.-D. Liss, T.G. Langdon, M. Kawasaki, Synthesis of a bulk nanostructured metastable Al alloy with extreme supersaturation of Mg, Sci. Rprts 9 (2019) 17186.
[8] A. Korneva, B. Straumal, R. Chulist, A. Kilmametov, P. Bała, G. Cios, N. Schell, P. Zięba, Grain refinement of intermetallic compounds in the Cu–Sn system under high pressure torsion, Mater. Lett. 179 (2016) 12–15.
[9] M. Kawasaki, J.K. Han, D.H. Lee, J.I. Jang, T.G. Langdon, Fabrication of nanocomposites through diffusion bonding under high-pressure torsion, J. Mater. Res. 33 (2018) 2700–2710.
[10] J.G. Luo, V.L. Acoff, Using cold roll bonding and annealing to process Ti/Al multi-layered composites from elemental foils, Mater. Sci. Eng., A 379 (2004) 164–172.
[11] J. Peng, Z. Liu, P. Xia, M. Lin, S. Zeng, On the interface and mechanical property of Ti/Al–6%Cu–0.5%Mg–0.4%Ag bimetal composite produced by cold-roll bonding and subsequent annealing treatment, Mater. Lett. 74 (2012) 89–92.
[12] L.M. Peng, J.H. Wang, H. Li, J.H. Zhao, L.H. He, Synthesis and microstructural characterization of Ti–Al3Ti metal–intermetallic laminate (MIL) composites, Scripta Mater. 52 (2005) 243–248.
[13] M. Ma, P. Huo, W.C. Liu, G.J. Wang, D.M. Wang, Microstructure and mechanical properties of Al/Ti/Al laminated composites prepared by roll bonding, Mater. Sci. Eng., A 636 (2015) 301–310.
[14] H.P. Ng, T. Przybilla, C. Schmidt, R. Lapovok, D. Orlov, H.W. Höppel, M. Göken, Asymmetric accumulative roll bonding of aluminium–titanium composite sheets, Mater. Sci. Eng., A 576 (2013) 306–315.
[15] P.D. Motevalli, B. Eghbali, Microstructure and mechanical properties of Tri-metal Al/Ti/Mg laminated composite processed by accumulative roll bonding, Mater. Sci. Eng., A 628 (2015) 135–142.
[16] P. Qu, L. Zhou, V.L. Acoff, Deformation textures of aluminum in a multilayered Ti/Al/Nb composite severely deformed by accumulative roll bonding, Mater. Char. 107 (2015) 367–375.
[17] P. Bazarnik, B. Adamczyk-Cieślak, A. Gałka, B. Płonka, L. Snieżek, M. Cantoni, M. Lewandowska, Mechanical and microstructural characteristics of Ti6Al4V/AA2519 and Ti6Al4V/AA1050/AA2519 laminates manufactured by explosive welding, Mater. Des. 111 (2016) 146–157.
[18] Y. Sun, M. Aindow, R.J. Hebert, T.G. Langdon, E.J. Lavernia, High-pressure torsion-induced phase transformations and grain refinement in Al/Ti composites, J. Mater. Sci. 52 (2017) 12170–12184.
[19] J.-K. Han, H.-J. Lee, J. Jang, M. Kawasaki, T.G. Langdon, Micro-mechanical and tribological properties of aluminum-magnesium nanocomposites processed by high-pressure torsion, Mater. Sci. Eng., A 684 (2017) 318–327.
[20] V.N. Danilenko, G.F. Korznikova, A.P. Zhilyaev, S.N. Sergeev, G.R. Khalikova, R. K. Khisamov, K.S. Nazarov, L.U. Kiekkuzhina, R.R. Mulyukov, Effect of annealing on the structure and phase composition of Al-Cu laminated metal-matrix composites produced by shear deformation under pressure, IOP Conf. Ser. Mater. Sci. Eng. 447 (2018), 012021. Institute of Physics Publishing.
[21] G.F. Korznikova, R.R. Mulyukov, A.M. Zhilyaev, V.N. Danilenko, K.R. Khisamov, K. S. Nazarov, S.N. Sergeyev, G.R. Khalikova, R.R. Kabirov, Al-Cu layered composites

fabricated by deformation, AIP Conf. Proc. 2053 (2018), 030028. American Institute of Physics.
[22] M. Kawasaki, H.-J. Lee, B. Ahn, A.P. Zhilyaev, T.G. Langdon, Evolution of hardness in ultrafine-grained metals processed by high-pressure torsion, J. Mater. Res. Technol. 3 (2014) 311–318.
[23] V.N. Danilenko, S.N. Sergeev, J.A. Baimova, G.F. Korznikova, K.S. Nazarov, R. K. Khisamov, A.M. Glezer, R.R. Mulyukov, An approach for fabrication of Al-Cu composite by high pressure torsion, Mater. Lett. 236 (2019) 51–55.
[24] H.M. Lee, Design of high-temperature high-strength Al-Ti-V-Zr alloys, Scripta Metall. Mater. 24 (1990) 2443–2446.
[25] Y.V. Milman, D.B. Miracle, S.I. Chugunova, I.V. Voskoboinik, N.P. Korzhova, T. N. Legkaya, Y.N. Podrezov, Mechanical behaviour of Al_3Ti intermetallic and $L1_2$ phases on its basis, Intermetallics 9 (2001) 839–845.

Materials Science & Engineering A 833 (2022) 142549

Contents lists available at ScienceDirect

Materials Science & Engineering A

journal homepage: www.elsevier.com/locate/msea

Fabrication of hybrid nanocrystalline Al–Ti alloys by mechanical bonding through high-pressure torsion

Piotr Bazarnik [a,1], Aleksandra Bartkowska [b,*,1], Yi Huang [c,d], Karol Szlązak [a], Bogusława Adamczyk-Cieślak [a], Jordi Sort [b,e], Malgorzata Lewandowska [a], Terence G. Langdon [d]

[a] Warsaw University of Technology, Faculty of Materials Science and Engineering, Woloska 141, 02-507, Poland
[b] Departament de Física, Universitat Autònoma de Barcelona, 08193, Bellaterra, Spain
[c] Department of Design and Engineering, Faculty of Science and Technology, Bournemouth University, Poole, Dorset, BH12 5BB, UK
[d] Materials Research Group, Department of Mechanical Engineering, University of Southampton, Southampton, SO17 1BJ, UK
[e] Institució Catalana de Recerca i Estudis Avançats (ICREA), Passeig Ll. Companys 23, 08010, Barcelona, Spain

ARTICLE INFO

Keywords:
High-pressure torsion
Hybrid materials
Titanium
Aluminium
Ultrafine grains

ABSTRACT

This study demonstrates an approach of utilizing high-pressure torsion (HPT) to fabricate a novel hybrid material by the direct bonding of Al and Ti disks at room temperature under a compressive pressure of 6.0 GPa and with increasing numbers of HPT turns up to 50. Detailed structural observations revealed the formation of a multi-layered nanostructure in the edge regions of the disks with a grain size of ~30 nm. X-ray diffraction (XRD) and selected area electron diffraction (SAED) confirmed the presence of three intermetallic compounds, AlTi, Al_3Ti and Ti_3Al, in the layered structures. Processing by HPT led to the formation of a hybrid nanocomposite with exceptional hardness (over 300 Hv) in the edge regions of the disks. Special emphasis was placed on understanding the evolution of hardness in the hybrid material. The investigation demonstrates a significant opportunity for using HPT processing to deepen the knowledge on diffusion bonding and mechanical joining technologies as well as for fabricating new and valuable hybrid nanomaterials.

1. Introduction

High-pressure torsion (HPT) is a severe plastic deformation (SPD) technique which enables scientists to achieve truly nanometric-sized grains by a simultaneous combination of large compressive stresses (typically several GPa) and torsional forces [1–3]. In the HPT method, a sample in the form of a thin disk is placed between two solid anvils and compressed under a pressure of several GPa at room or an elevated temperature. At the same time, the sample is subjected to torsional strain initiated by the rotation of one of the anvils with respect to the other. Frictional forces prevent any sliding between the disk sample and the anvils, therefore allowing torsional deformation applied onto the disk sample.

The equivalent strain (von Mises strain) ε_{eq} imposed on the sample in the form of a disk in HPT is described by an Eq. (1) below [4]:

$$\varepsilon_{eq} = \frac{2\pi N r}{h\sqrt{3}} \quad (1)$$

where N is the number of HPT revolutions (turns), r is the radial distance from the centre of the disk and h is the final thickness of the sample. Analysis of Eq. (1) shows there is a variation in the strain value across the disk, with the maximum value on the edge and the minimum in the centre of the disk (in theory $\varepsilon_{eq} = 0$ as $r = 0$). Therefore, according to the equation HPT-processed materials will show inhomogeneous microstructures and properties. On the other hand, it is possible to fabricate materials with reasonably homogeneous microstructures as reported elsewhere [3].

The advantage of the HPT method is undoubtedly the possibility of applying very large strains through a sufficiently high number of HPT turns, where this strain is much larger than in other severe plastic deformation methods. However, there is a certain limitation regarding the minimum grain size that may be attained via SPD processing as well as any associated improvement in the mechanical properties [5,6]. Depending on the type of metal subjected to HPT processing, three main types of behaviour may be identified: strain hardening, strain softening

* Corresponding author.
E-mail address: aleksandra.bartkowska@uab.cat (A. Bartkowska).
[1] P.Bazarnik and A.Bartkowska contributed equally to this work as first authors.

https://doi.org/10.1016/j.msea.2021.142549
Received 4 October 2021; Received in revised form 21 December 2021; Accepted 22 December 2021
Available online 25 December 2021

with recovery and strain softening without recovery [5–7]. The dominant types of metals demonstrate the strain hardening type of behaviour, associated with a significant increase in mechanical properties during deformation up to some saturation level [5,6]. However, the enhanced mechanical properties are usually combined with a reduction in plasticity which significantly limits the possible application of HPT-processed materials [5,6]. On the other hand, in materials exhibiting strain softening, such as pure aluminium, it is not possible to obtain true ultrafine-grained and nanograined structure because of the recovery processes taking place during plastic deformation [6,8–10]. Nonetheless, they are showing relatively good plasticity associated with a modest increase in mechanical properties resulting from a fractional decrease in grain size which in turn tends to eliminate those materials from industrial applications.

The potential solution to overcome the limits of grain refinement and enhancement in mechanical properties lies in developing a new class of hybrid materials fabricated by HPT [11–18]. In this approach two or more dissimilar metals are joined through HPT to obtain a multilayered hybrid material with new and unique properties. Since this is a new approach, there is to date only a limited number of scientific reports focused on the fabrication of high-performance materials by bonding dissimilar bulk metals to form a new metal system through HPT. The first report demonstrated the potential for forming a spiral texture by processing of an Al–Cu hybrid material though HPT using four quarter-disks, including two of pure Cu and two of an Al-6061 alloy [19]. However, this study described only the computational calculation of the distribution of equivalent stress in the processed disk using a finite element method and there was no detailed microstructural analysis and mechanical testing of the processed disk. Later, this approach was improved and further developed by bonding of separate Al and Mg disks processed through HPT by stacking a set of two or three disks [20,21] producing multi-layered nanostructures. This same approach was used in several other investigations using stacks of three or more disks of Al-Cu [18,22–24], Cu-Ta [25], Zn-Mg [26,27], Fe–V [28], Cu-Sn [29], Zr-Nb [30].This series of research investigations proved that HPT is a good technique to create a strong bonding of the dissimilar metal disks. Moreover, for higher numbers of HPT revolutions a strong tendency for segregation was observed with the nucleation of intermetallic compounds through diffusion bonding. This led to a significant increase of hardness which was higher than may be achieved for the initial metals.

Accordingly, the present work was initiated to evaluate the microstructural changes and the mechanical properties evolution in the Al–Ti system synthesized by the HPT procedure to high numbers of turns (up to 50 revolutions). In particular, the investigation is designed to examine the extent of microstructural refinement, the formation and decomposition of composite microstructures during deformation, the formation of any intermetallic compounds and their impact on the subsequent mechanical properties.

2. Experimental materials and procedures

A bulk nanocrystalline Al–Ti hybrid material was prepared by mechanical bonding of a commercial purity aluminium Al (Al-1050 alloy) and a commercial purity titanium (CP–Ti). Both alloys were received as extruded rods with diameters of 10 mm. Those rods were cut into a series of disks with thicknesses of around 1 mm and then the disks were polished to final thicknesses of 0.3 and 0.15 mm for Al and Ti, respectively. Hybrid materials were synthesised using conventional HPT processing with the exception that the straining was applied to a stack of a few disks instead of one as described in an earlier study [31]. A stack of three Al and two Ti disks were processed through HPT at room temperature under quasi-constrained conditions [32] with a constant speed of 1 rpm and under an applied pressure of 6.0 GPa, for total numbers of revolutions N of 10, 20, 30, 40 and 50. Each anvil had a cavity depth 0.25 mm and the final thickness of the sample was about 0.8 mm. In addition, Al-1050 and Ti samples in the initial state and after HPT processing for 10 revolutions were used as reference samples.

The HPT-processed disks were initially examined by X-ray diffraction (XRD) using Bruker D8 Discover and an energy for the emitter beam of 30 kV. The filtered Co Kα X-Ray radiation was focussed to a point with a radius of 1 mm and all specimens were scanned on cross-sectional planes in the edge regions. Each sample was illuminated by high intensity hard X-rays for 5 s per step, the 2Θ angle was between 20° and 90° and the step size Δ2Θ was 0.025°.

After processing by HPT, each disk was cut vertically along a randomly selected diameter to obtain two semi-circular disks. One vertical cross-section from each disk was mounted in resin, ground and polished to obtain a mirror-like surface. Then, samples were examined using light microscopy (LM) with a Zeiss Axio Observer. Panoramic photos of the overall cross-sections were made in order to provide preliminary information on the quality of bonding between the individual components. To prepare the panoramic images, a series of photos were made and then placed together to give an overall perspective.

In order to evaluate the quality of bonding between the Al and Ti elements a scanning electron microscope (SEM) Hitachi SU8000 was used. In addition, maps of the chemical compositions were recorded for selected samples using the energy-dispersive X-ray spectroscopy (EDX) technique. SEM investigations were conducted in two modes: secondary electron mode (SE) and backscattered electron mode (BSE) on the cross-sections of disks. Microstructural observations were carried out in the peripheral regions (approximately 1.0 mm from the edge) of each disk. Specimens for SEM analysis were prepared using Hitachi IM4000 ion milling system. In practice, ion milling is a damage-less process and the polishing with an ion beam eliminates all deformation, stresses and oxide layers. Moreover, the surface quality is sufficiently good that it is possible to observe the structure of such prepared joints through the channelling contrast in an SEM.

Detailed microstructural analysis was carried out using a transmission electron microscope (TEM) JEOL JEM 1200 operating at an accelerating voltage of 120 kV and CS-corrected dedicated scanning transmission electron microscope (STEM) Hitachi HD2700, operating at 200 kV. Samples for TEM/STEM observations were prepared using a Focused Ion Beam (FIB) Hitachi NB-5000 microscope. The lamellas were cut from the cross-section of the sample in the direction parallel to the direction of rotation. STEM observations were carried out in bright-field (BF) and high-angle annular dark field (HAADF) modes. For selected samples, selected area electron diffraction (SAED) patterns were obtained.

The microstructures were evaluated quantitatively using a computer-aided image analyser. The grain sizes were described in terms of the equivalent grain diameter, d_{eq}, defined as the diameter of a circle with a surface area equal to the surface area of the grain.

Micro-computed tomography (microCT) was performed on the samples by means of a SkyScan 1172 (Bruker, USA), in order to investigate the microstructural distribution of the material constituents. For this purpose, the source voltage and source current were set to 100 kV and 100 μA, respectively. Al + Cu X-Ray filters were used. The obtained pixel sizes were 5 and 2 μm, the scanning procedures were carried out by performing a rotation of the emitted X-ray by 180°, with a step size of 0.3° and 0.2°, and an exposure time of 580 ms and 600 ms per projection for the 10 turns and 50 turns samples, respectively.

To examine the mechanical properties of the samples, microhardness and nanoindentation tests were performed. The microhardness measurements were carried out using a Zwick/Roell Z2.5 hardness testing machine with a load of 200 g. The hardness of the initial materials was measured as well as EDX linear analysis, conducted in the middle of cross-sections of the initial samples after HPT processing (Al-1050 and Ti after 10 revolutions). For the linear analysis, the distances between consecutive measurement points were 0.2 mm. Hardness maps of selected samples of the Al–Ti hybrid materials were prepared applying the distances between consecutive measurements points of 0.1 mm. Measurements were carried out on the cross-sections of selected samples

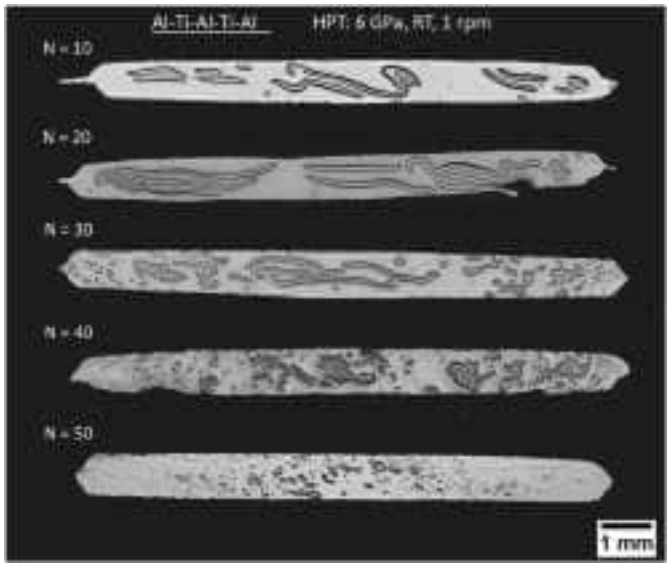

Fig. 1. LM images of Al–Ti samples after various numbers of HPT rotations.

and the microhardness data were then used to prepare colour-coded contour maps displaying the hardness distributions within each disk.

Microhardness measurements were complemented by nano-indentation studies conducted using an Anton Paar device operating in the load-control mode with a Berkovich pyramidal-shaped diamond tip. The value of the maximum applied force was chosen to be 50 mN to allow for measurements within the thin mixing layers of the hybrid material. To obtain reliable values of mechanical properties, at least 20 tests were measured per sample/condition. A series of measurements were performed in the peripheral areas for the hybrid material processed for 50 turns and HPT-processed CP-Ti as well as for Al-1050 in the as-received and HPT-processed state. The reduced Young's modulus (E_r) and hardness (H) were obtained from the load-displacement curves using the method of Oliver and Pharr [33]. The elastic and plastic energies of deformation were measured and the contribution of each in the total energy of deformation was then calculated. The elastic energy was obtained from the area enclosed between the unloading indentation segment and the displacement axis, whereas the plastic energy was assessed from the area between the loading and unloading indentation segments and the displacement axis.

3. Experimental results

3.1. Microstructures of HPT-processed hybrid materials

The LM images, prepared on cross-sections of 5-layered Al–Ti systems, are presented in Fig. 1 after deforming through various numbers of turns. In the samples after 10 and 20 turns, there are bent and fragmented Ti plates in the Al matrix without any significant mixing between the two components. There is also evidence for some delamination between the Ti and Al disks. Increasing the numbers of revolutions up to 50 gradually leads to a refinement of the two components and their mixing, and to a general elimination of any cracks and delaminations in the disks. However, even after 50 HPT turns the structure remains inhomogeneous, with visible differences between the edge and the centre of the disks. In the sample processed for 50 turns, the Ti and Al parts are indistinguishable in the edge area, which suggests the occurrence of a strong mixing between those elements. In addition, increasing the numbers of revolutions gradually leads to an expansion of the Al–Ti mixing zone in the sample, which is well observed when comparing images of samples processed from 30 to 50 turns as the area where large Ti fragments are present decreases in favour of an increase in the mixing zone of Al and Ti.

To gain a deeper understanding of the joining and mixing phenomenon which occurs in this system during HPT processing, the composites were further investigated using micro-computed X-ray tomography. This non-destructive characterization technique permits observations of new features that are generally invisible with more conventional imaging techniques such as LM or SEM analysis. The MicroCT 3D-reconstruction (in three planes: x-z, y-z and x-y-z) of the Al–Ti composites after 10 and 50 revolutions are presented on Figs. 2 and 3 respectively. Fig. 2 a and b show the scan of a quarter of the HPT disk after 10 HPT turns which corresponds to about 13.4 mm^3 of material. It is apparent that torsional straining by HPT led to a bending, necking and finally to a fragmentation of the Ti phase (marked as red) across the disk diameter. This fragmentation effect is more intense with increasing numbers of turns which is evident after 50 HPT turns (Fig. 3 a, b and c). To show more details, a smaller volume of material from a mid-section of the disk was selected for the analysis (0.52 mm^3) but the analysis itself was conducted with a higher resolution. It should be noted that this MicroCT technique is not adequate for showing elements smaller than 1–2 μm. Nevertheless, the MicroCT reconstruction of the sample after 50 turns shows intense fragmentation of the Ti phase and its uniform distribution within the Al matrix.

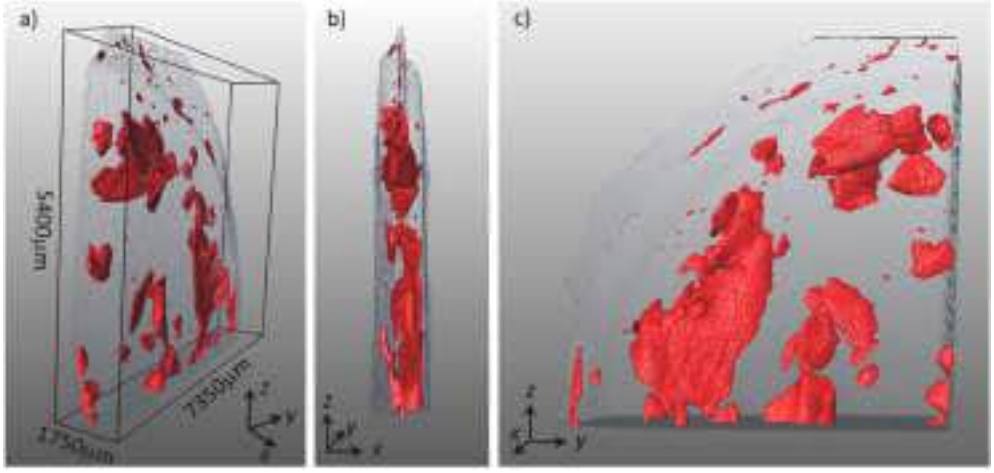

Fig. 2. MicroCT 3D-reconstruction of Al–Ti composite after 10 HPT turns. Perspective view a), cross-section view b) and disc plane view c). Scan of a quarter of HPT disk where Ti plates (marked as red) are severely bent and fragmented. (For interpretation of the references to colour in this figure legend, the reader is referred to the Web version of this article.)

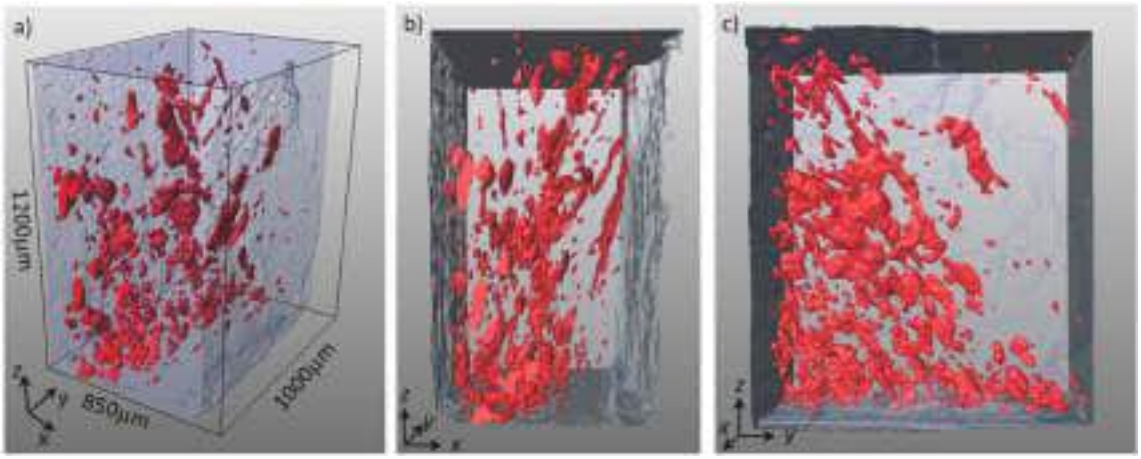

Fig. 3. MicroCT 3D-reconstruction of Al–Ti composite after 50 HPT turns. Perspective view a), cross-section view b) and disc plane view c). Scan of a small region of HPT disk, mid-section of the disk, showing strong fragmentation of Ti phase (marked as red) and its uniform distribution in the Al matrix. (For interpretation of the references to colour in this figure legend, the reader is referred to the Web version of this article.)

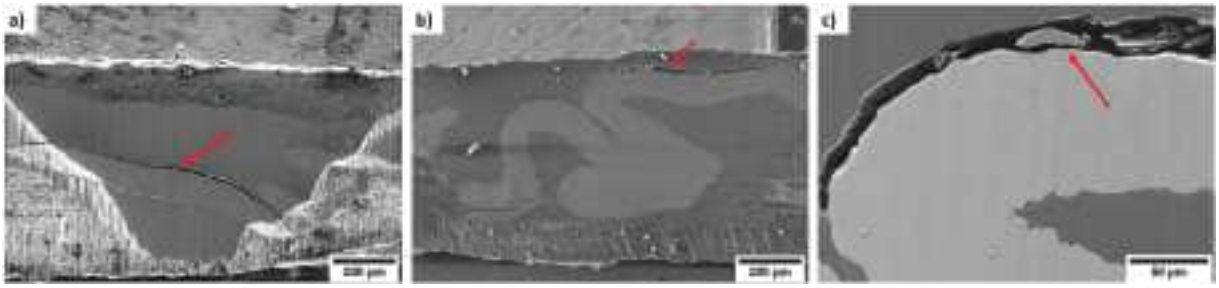

Fig. 4. Selected SEM images of the 5-layered system processed by HPT for: a) 10 turns, b and c) 20 turns. Red arrows indicate areas of delaminations and discontinuities. (For interpretation of the references to colour in this figure legend, the reader is referred to the Web version of this article.)

Detailed microstructural observations were conducted using SEM, as shown by the SEM images in Figs. 4 and 5 for the Al–Ti samples processed for 10, 20 and 50 turns where the brighter contrast represents the regions enriched in Ti and the darker contrast corresponds to the Al-rich regions. Fig. 4 shows detailed SEM images of the samples processed for 10 (a) and 20 (b,c) turns with visible delaminations and discontinuities between components as indicated by the red arrows but with no noticeable mixing between Al and Ti because the interfaces between the Al and Ti components are readily distinguishable. At the same time there is a strong bending of Ti layers inside the Al matrix and this becomes more intense with increasing numbers of turns. It is apparent that 10 and 20 rotations are not sufficient to fully bond the components and therefore further processing was applied to higher numbers of turns.

Increasing the numbers of rotations up to 50 turns produces a severe fragmentation of the disks with a more homogeneous distribution of fragments of Ti in the Al matrix at the edge regions, as illustrated in Fig. 5 showing SEM images of the Al–Ti sample processed for 50 turns. It is readily apparent that after 50 turns the dominant part of the sample consists of relatively small fragmented parts of the Ti disk in the Al matrix, as shown in Fig. 5a. Increasing the numbers of revolutions up to 50 turns therefore permits a reduction in the sizes of the areas enriched in Ti. The red arrows in Fig. 5a,c indicate regions with enhanced mixing where the BSE contrast changes, suggesting a mixing between Al and Ti and the formation of intermetallic phases. As confirmed by both LM, MicroCT and SEM observations, the numbers of large Ti fragments, with diameters above 100 μm, is smaller than in the samples processed by lower numbers of rotations, as shown in Fig. 5.

A compositional EDX analysis of the selected area was performed in the form of maps, as presented in Fig. 6. It is apparent that the analysed zone contains both Al and Ti, where Al is the matrix and Ti occurs in the form of larger fragments as well as within the mixing zones with Al.

To analyse the grain refinement and mixing processes in the sample after 50 turns, a TEM/STEM analysis was conducted. In Fig. 7 representative STEM (a,b,c) and TEM (d,e) images of the 5-layered Al–Ti system processed by HPT for 50 turns are presented. Fig. 7a and b shows overall images of the sample in BF and HAADF modes, respectively. In the HAADF image there are bands enriched in Ti (bright), an Al matrix (dark grey) and mixing zones of Al–Ti (light grey). Mixing zones, in the form of bands, form a particular layered structure with alternately occurring zones of mixing placed inside an Al matrix with a width of less than ~70 nm, as presented in Fig. 7d and e. Grains inside the mixing zone, indicated by red arrows in Fig. 7d, have a size below 30 nm, while grains in the Al matrix are around 200 nm. Grains in the Al matrix (Fig. 7c,e) are distinguished by the presence of dislocations forming a cell structure, while grains in the mixing zone are in general free of any defects. Yellow arrows are used to mark another peculiarity of the microstructure where there are very thin layers with thicknesses of around 30 nm that are rich in Ti, that vertically subdivide the layers, as was described earlier for the Al–Mg system [34]. Those layers are probably a mixture of Al and Ti, generated during processing by high-pressure torsion. By contrast, the average grain sizes in the separate Al and Ti disks were measured as ~700 and ~100 nm, respectively, after processing by HPT for 10 turns.

Linear chemical analysis, as illustrated in Fig. 8, was performed on a cross-section through the Ti-enriched bands. The point scanning and the line profile revealed that the thin layers are composed of 75–86% of Al (red line) and 14–25% of Ti (green line), thereby indicating the formation of the Al_3Ti phase.

To confirm the formation of intermetallic phases inside the mixing zones, complementary SAED pattern analyses were performed, as

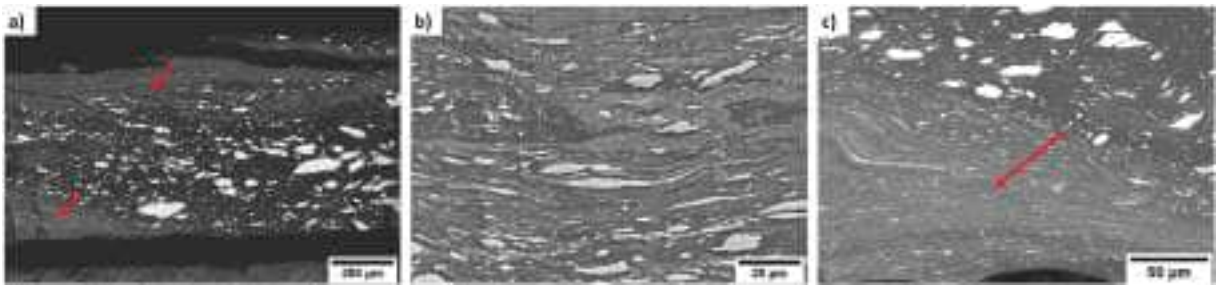

Fig. 5. SEM images of the Al–Ti sample processed for 50 turns.

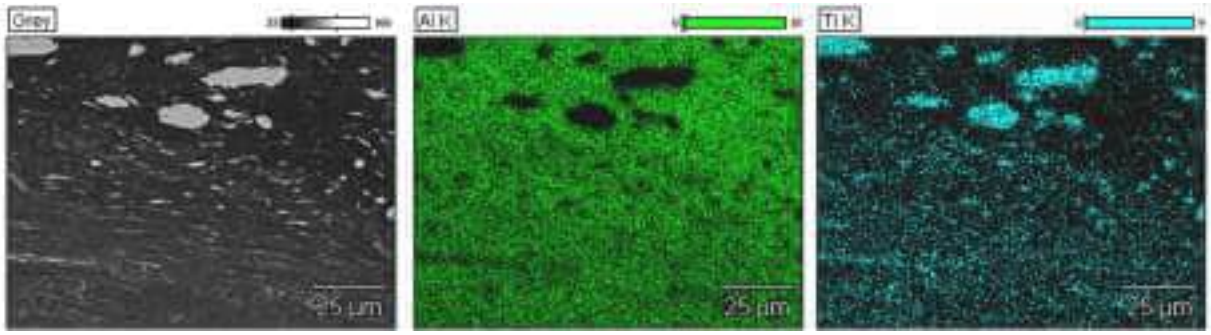

Fig. 6. EDX maps of the Al–Ti sample processed for 50 turns.

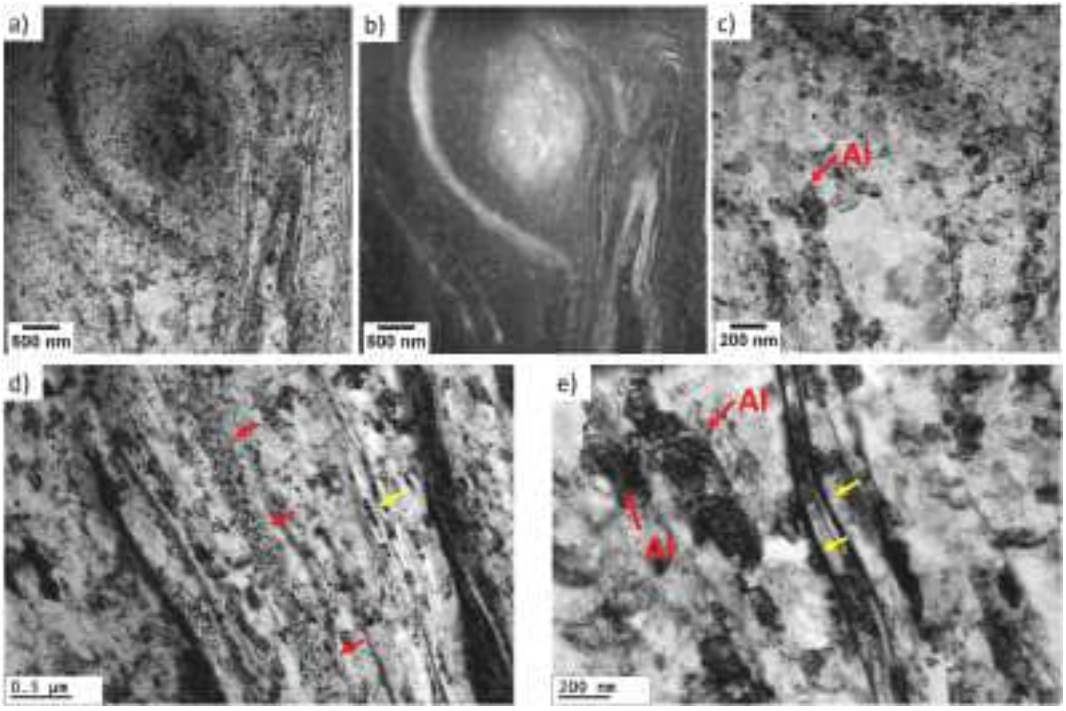

Fig. 7. Selected TEM and STEM images of the sample processed for 50 turns.

presented in Fig. 9. The electron diffraction patterns confirmed the presence of intermetallic grains randomly distributed in the matrix, such as AlTi, Al_3Ti and $AlTi_3$. Strong diffraction rings for the (001) AlTi and (101) Al_3Ti phases can be observed in the inner part of the diffractogram. It is noted that the formation of such intermetallic phases is consistent with other reports on Al–Ti systems [35–38].

The phase compositions were also complemented by XRD analysis and the pattern for the sample after 50 turns is shown in Fig. 10. These patterns reveal a significant broadening of the peaks due to the severe grain refinement. The patterns also confirm the presence of the Al and Ti phases and the formation of the AlTi, $AlTi_3$ and Al_3Ti phases with a strongest peak for the Al_3Ti phase.

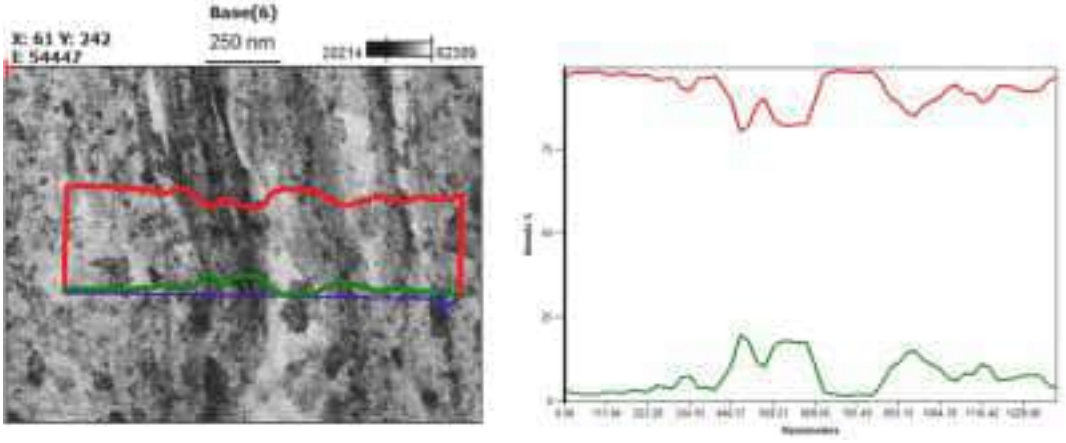

Fig. 8. EDX linear analysis through the mixing layer, where Al is represented by the red line and Ti by the green line. (For interpretation of the references to colour in this figure legend, the reader is referred to the Web version of this article.)

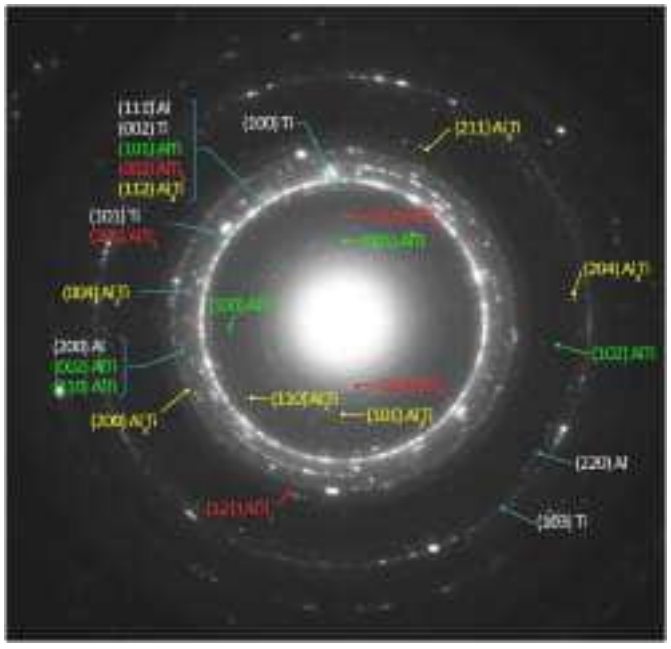

Fig. 9. SAED pattern showing presence of several intermetallic phases from the Al–Ti system.

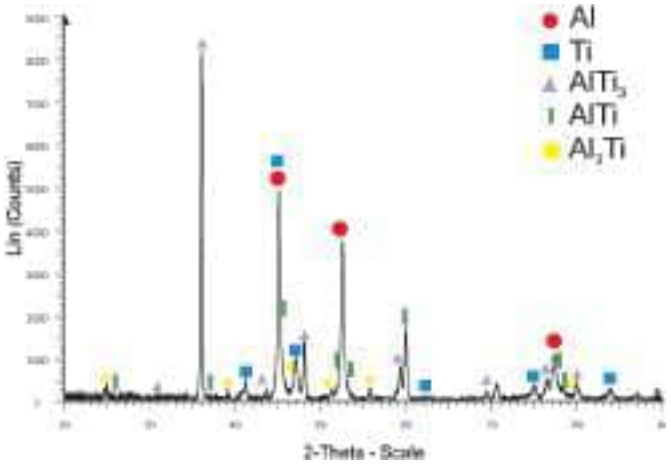

Fig. 10. XRD pattern of hybrid Al–Ti processed for 50 turns.

3.2. Evaluation of mechanical properties

3.2.1. Microhardness

Microhardness measurements were performed as a first step to evaluate the mechanical properties of the hybrid material and for a comparison with the properties of the initial materials. The hardness distribution across the disk radius is presented in Fig. 11 a. Where the hardness values in the initial state were 26 and 219 Hv for Al and Ti, respectively. After processing by HPT, the hardness in both samples underwent a significant increase with an average hardness across the disk of 51 Hv and 316 Hv for Al and Ti, respectively. In Al processed for 10 turns of HPT, the hardness across the disk was reasonably homogeneous but with slightly lower values in the central area than in the peripheral region so that an essentially saturation condition was observed. In the case of Ti, the hardness values were less homogeneous but without a strong dependence on the distance from the centre.

In all samples, the minimum hardness values were located near the disk center and the maximum in the peripheral region with a gradual

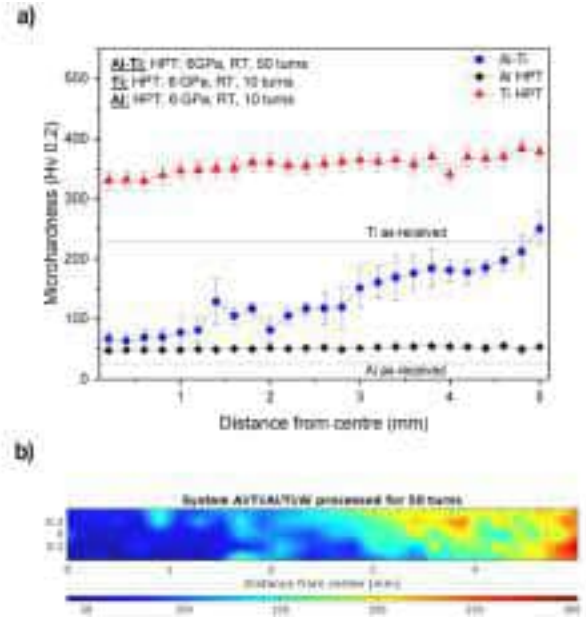

Fig. 11. a) Microhardness distribution along the sample radius, b) Microhardness distribution across the disk in the Al–Ti sample processed for 50 turns.

rise across the disks. In the Al–Ti sample processed by 50 turns, an increase in hardness was observed compared to the HPT-processed Al. The minimum hardness values in the center of the disk were close to the level of ~60 Hv for the HPT-processed Al 1050 alloy, while on the edge of a disk the values were very high and even exceeded ~250 Hv at the edge. In the peripheral region of the sample processed for 50 turns the hardness values were reasonably homogenous, indicating an efficient mixing between Al and Ti.

The hardness distribution map for the sample after 50 turns is presented in Fig. 11b and this confirms the observations made during the linear chemical analysis. It is readily apparent that the sample exhibits a gradual increase in hardness across the disk with the lowest hardness values near the centre and the highest, at close to ~300 Hv, in the peripheral region. The increase in hardness is gradual and confirms the occurrence of a gradual mixing between Al and Ti.

3.2.2. Nanoindentation

Nanoindentation was used to examine the micro/nano-mechanical response of the Al–Ti system processed by HPT. Nanoindentation tests were performed as a complementary procedure for evaluating the mechanical properties.

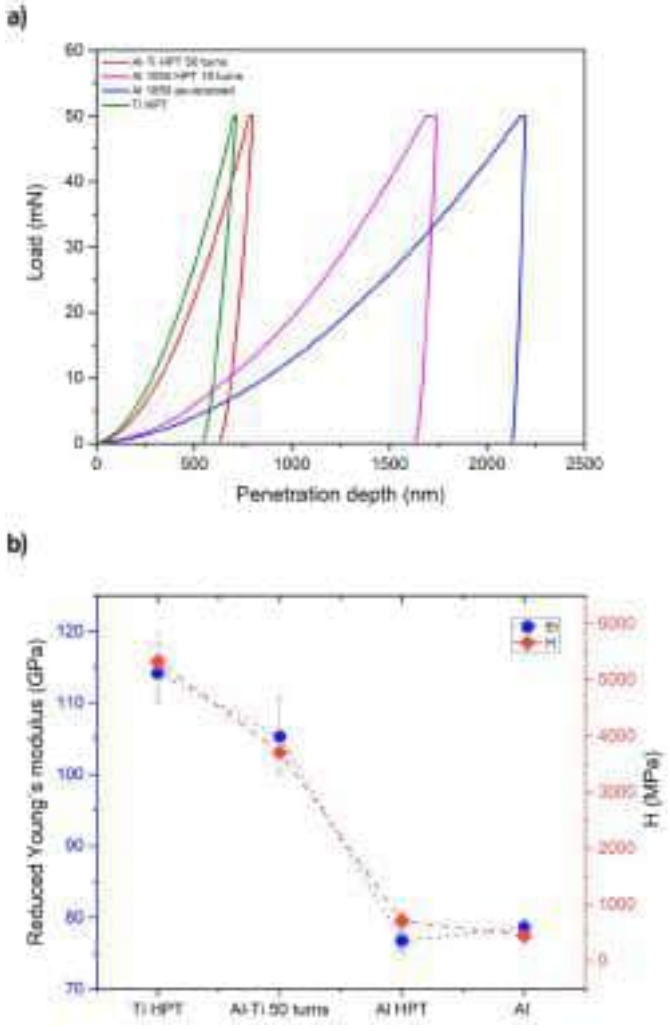

Fig. 12. a) Representative nanoindentation curves of Al–Ti hybrid material processed for 50 turns (red), Al-1050 processed for 10 turns (pink), Al 1050 in as-received state (blue) and Ti processed for 10 turns (green) and b) Reduced Young's modulus and hardness of as-received and HPT-processed materials. (For interpretation of the references to colour in this figure legend, the reader is referred to the Web version of this article.)

Table 1
Values of Young's modulus, hardness and energies of deformation.

Sample	Young's modulus (GPa)	Hardness (MPa)	H/E (wear resistance)	W_{elast}/W_{total}	W_{plast}/W_{total}
Al–Ti HPT	105 ± 5	3720 ± 346	0.035	0.23	0.77
Al 1050 HPT	81 ± 2	714 ± 12	0.009	0.06	0.94
Al 1050 as-received	79 ± 1	449 ± 15	0.006	0.03	0.97
Ti HPT	114 ± 4	5330 ± 528	0.047	0.26	0.74

Fig. 12a shows representative load-penetration depth curves measured at the edges of the Al–Ti hybrid material, the Al-1050 alloy in the HPT-processed and as-received states and the HPT-processed CP-Ti. Each curve was obtained from a series of at least 20 measurements. A significant decrease in the maximum and final penetration depths is observed between the Al–Ti hybrid material and the Al-1050 alloy thereby indicating a strengthening of the material. The indentation plot of the Al–Ti hybrid material (red) resembles that of the HPT-processed titanium which suggests that the properties of the composite became closer to that of the HPT-processed Ti. As shown in Table 1, the hardness and Young's modulus values of the Al–Ti hybrid material are significantly higher than for the as-received and HPT-processed Al, with a Young's modulus of 105 GPa (increase of 40% when compared to HPT-processed Al) and a hardness value of 3720 MPa (increase of 420% when compared to HPT-processed Al).

The ratio of H/E presented in Table 1 was measured as an indication of the wear resistance. As was shown in earlier reports [39,40], both hardness as well as the reciprocal value of elastic modulus have an influence on the wear resistance (higher H and lower E improve wear resistance). Therefore, the higher H/E ratio of the Al–Ti hybrid and HPT-processed Ti indicates a higher wear resistance than for the HPT-processed Al and as-received Al.

In Table 1 and Fig. 12b information is given on the ratio of the elastic and plastic energies versus the total energy of deformation during nanoindentation. It is demonstrated that the contribution of elastic energy is higher for the Al–Ti hybrid and the HPT-processed Ti (23% and 26%, respectively) than for the as-received and HPT-processed Al (3% and 6%, respectively). The higher contribution of elastic energy in the total energy of deformation is an indication of a higher elastic recovery and therefore of the ability of a material to regain the initial shape after deformation. On the other hand, the contribution of plastic energy in the total energy of deformation (sometimes called "plasticity index") is an indication of the overall plasticity of the material. Therefore, the HPT-processed Al and the as-received Al show higher plasticity than the HPT-processed Ti and the Al–Ti hybrid.

4. Discussion

4.1. Unique microstructure formation in the Al–Ti hybrid system

The results from this investigation demonstrate that the HPT technique has a potential for producing a bonding of dissimilar bulk metals when suitable processing parameters are applied. Earlier studies described the potential for using HPT as a technique for the synthesis of hybrid materials for systems such as Al-Mg [20,21], Al-Cu [18,22–24], Cu-Sn [41], steel-vanadium [42] and Al–Ti [31]. HPT-processed hybrid systems can be characterized by a unique layered microstructure [20,42] with significant grain refinement [21,42] and the formation of intermetallic phases [18,20] as well as enhanced mechanical properties [20,42]. However, it should be noted that the microstructure of processed Al–Ti disks is strongly influenced by the processing parameters. Depending on the numbers of HPT turns, the disks may contain a variety

of microstructural features such as bent, cracked and fragmented parts of the Ti disks or vortex-like structures and lamellar systems [43,44] which determine the potential of the hybrid materials to exhibit superior mechanical properties [45–49]. This suggests that a certain physical mechanism governs the transformation of the structural components inside the sample at the stage of transition from a wavy laminar flow to chaotic mixing of the components. For this reason it is crucial to determine the method for creating these structures.

During the HPT of laminates, the hard layers inhibit the shear in the soft layers. This leads to a strain gradient. This is confirmed by experiments showing that grain refinement with the formation of high-angle grain boundaries is more pronounced and occurs more quickly in softer alloys than in harder ones [12,50–52]. At the interface, the hard layer constrains the deformation of the soft one, which means that the soft layer is compressed and the hard one is under tension. Accordingly, buckling of their interface towards the hard layer occurs. At a certain point periodic constrictions appear in the titanium layers leading to their fragmentation. The SEM and μCT investigations (Figs. 2 and 4) confirm that in the initial stages of deformation, corresponding to low numbers of revolutions, when the shear forces exceed a critical level the harder Ti phase is refined continuously by elongation, repeated bending or necking and by a fragmentation into smaller elements [53]. Fig. 13 presents some structural images illustrating the model of further deformation of these Ti fragments. With increasing numbers of HPT turns, the overall hardness of the hybrid increases which leads to a strong shear localization. Due to this, small fragments of Ti are torn off from the Ti disk (Fig. 13a and b) and they pass into the Al matrix. Thereafter, these Ti fragments undergo further intense deformation, forming a vortex-like structure consisting of very thin Ti layers alternately arranged within the Al matrix, as shown in Fig. 13b and c. At a certain point, severely refined fragments of Ti are mixed with Al forming a lamellar structure, as illustrated in Fig. 13c. As a result, after 50 HPT turns almost a full mixing of elements is achieved in the edge regions of the disks. The final microstructure after 50 HPT turns is a composite containing an Al-rich matrix with a grain size of ~200 nm and fine Ti-rich layers with a size of about ~30 nm which are dispersed evenly within the matrix.

Moreover, it was also shown that intermetallic Al–Ti phases were generated within these lamellar structures. The formation of intermetallic phases is possible due to enhanced atomic reactions during HPT processing which are influenced by the increased density of lattice defects (vacancies, dislocations and grain boundaries) and the reduction in the atomic diffusion distance due to microstructural refinement [18,54]. As a consequence of the grain refinement, the atomic diffusion paths are shortened and this enables solid-state reactions and the formation of intermetallic phases as confirmed through the EDX mapping and SAED in Figs. 8 and 9, respectively. Such a microstructure achieved by HPT processing leads to very significant improvements in the mechanical properties. The present hybrid material exhibits extraordinary mechanical properties measured by the microhardness (Hv of 300) and nanoindentation tests (H ~3700 MPa and Young modulus of 105 GPa).

4.2. Saturation shift in the hybrid materials

Although severe plastic deformation methods are widely recognized as fabrication techniques for ultrafine-grained and even nanocrystalline materials, it is also well known that obtaining a true nanocrystalline structure, especially in pure metals, is very difficult. This is due to a saturation effect which can be explained as a certain level of accumulated strain above which it is impossible to achieve further microstructural refinement and strengthening [55,56].

To date, several techniques were implemented in order to overcome the saturation effect and thereby to obtain a more refined structure and better mechanical performances of the SPD-processed materials. One of these techniques is the use of a combination of two or more different SPD methods to activate more slip systems, such as hydrostatic extrusion followed by HPT [55] or ECAP followed by HPT [56–59]. It was demonstrated that a combination of two SPD methods provides an advantage in grain refinement when compared with processing only by HPT.

In this study, an alternative approach was proposed to overcome the saturation effect through the fabrication of hybrid materials by subjecting a set of dissimilar metal disks to HPT processing. The matrix material used in this study was a commercial purity aluminium alloy Al-1050 which exhibits a saturation effect after processing through 5 or more HPT turns at 298 K [60–62]. To study the saturation effect in the hybrid Al–Ti, the experimental microhardness points from Fig. 12 were plotted in Fig. 14 against the equivalent strain and the experimental data were supplemented with the datum points for the initial Al and Ti metals after 10 HPT turns. First of all it should be mentioned that Eq. (1) can be

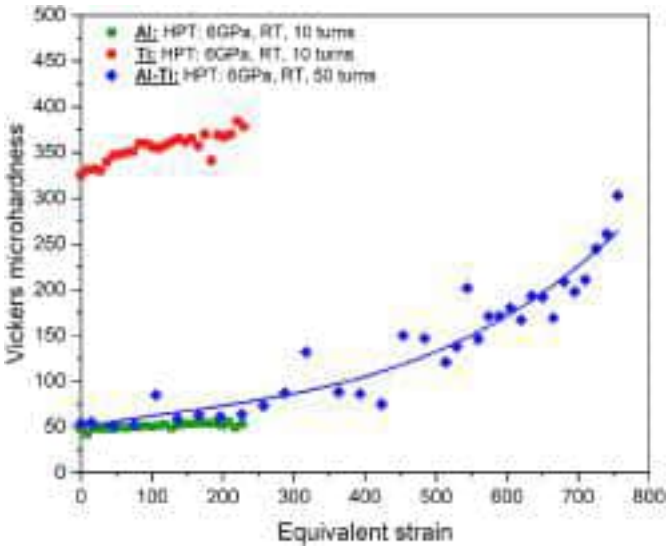

Fig. 14. Hardness as a function of accumulated strain in the Al–Ti hybrid material processed for 50 turns. HPT-processed Al-1050 and CP-Ti are added as a reference.

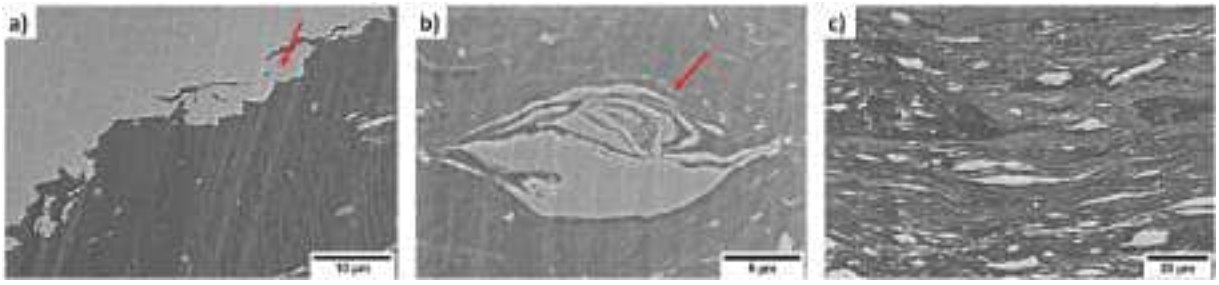

Fig. 13. Exemplary SEM images of the Al/Ti interfaces after HPT deformation.

used only to give a very rough estimate of the equivalent strain in hybrid materials. It does not take into account the stress concentration on the interfaces between the soft Al and hard Ti phases, interactions with intermetallic phases or shearing instabilities in the turbulent flow model [12]. The procedure for correctly calculating the equivalent strain of hybrid materials seems to be the next challenge for researchers.

The datum points for the initial materials are in reasonable agreement and fall around the solid line. In the early stages of HPT, the hardness values for Al and Ti rise very rapidly with the accumulating strain but ultimately there is no significant further increase at equivalent strains above ~20 and ~70 for these two materials, respectively, and thereafter the microhardness values become essentially saturated at Hv ≈ 51 and Hv ≈ 350, respectively. Nevertheless, the Al–Ti hybrid system processed under 50 HPT turns behaves differently. In the first stages of deformation (equivalent strains <300–400) the hardness values are essentially uniform (~50 Hv units) with only a few points of higher hardness values (100–150 Hv). However, a further increase in the strain produces a successive increase in hardness (above 300 Hv), without the occurrence of any saturation effect. The nanoindentation study not only confirmed the large increase of hardness, but also of the H/E ratio in the Al–Ti hybrid system, indicating much higher wear resistance when compared to the HPT-processed Al 1050. This unusual behaviour can be explained by the formation of a solid solution between the Al and Ti phases. For low strains, and in the mid-sections of the disks, there is no apparent mixing of materials (Figs. 2 and 4). This means that the only phenomenon occurring in the microstructure is grain refinement which is so intense after 50 HPT turns that it induces saturation in the Al and Ti phases. In the edge regions where the strain is higher the microhardness increases due to the mixing of the Al and Ti elements. This notable enhancement in the strain hardenability appears to be due to the combination of multiple strengthening mechanisms, including solid solution strengthening which has a strong impact on the minimum grain size and Hall-Petch strengthening [63]. However, the observed strain hardening in the present Al–Ti hybrids is mainly attributed *to in-situ* phase transformations of Al to the hard AlTi, $AlTi_3$ and Al_3Ti phases (Figs. 9 and 10) [35,36]. A similar hardening effect was also reported earlier for other hybrid systems synthesized by HPT such as the Zn–Mg system [26] where the hardness after HPT was eight times higher than for the initial material, the Al–Cu system [24] where the hardness was five times higher and the Al–Mg system [20,63] where the hardness was three times higher.

The results presented in this study on the mechanical bonding of dissimilar metals by HPT demonstrates that the fabrication of hybrid materials may be a simple and readily available solution for overcoming, or at least shifting, the saturation effect by means of the applied strain while continuing to achieve enhanced grain refinement and superior mechanical performances in the as-produced materials.

5. Conclusions

- Al–Ti hybrid materials were synthesised using quasi-constrained HPT processing under 6.0 GPa and 1 rpm for 10, 20, 30, 40 and 50 turns. The microstructures and mechanical properties evolution were investigated by SEM, TEM/STEM, SAED, MicroCT, XRD, Vickers microhardness and nano-indentation testing.
- A relatively homogeneous lamellar microstructure, consisting of an ultrafine-grained (~200 nm) Al matrix and nanoscale (~30 nm) Ti rich layers, was formed at the disk periphery after 50 HPT turns.
- After 50 turns of HPT processing, the Al–Ti hybrid material exhibited remarkably improved hardness and Young's modulus by comparison with the initial commercial purity Al and Ti. The average Vickers microhardness value was ~300 Hv and the Young's modulus measured in nanoindentation was ~105 GPa.
- HPT promotes the solid-state reaction of Al and Ti elements so that there is the formation of AlTi, Al_3Ti and $AlTi_3$ phases as well as a dissolution of Al and Ti components in each matrix.
- An investigation of the strain hardening capacity revealed that the Al–Ti hybrid system follows a two-regime behaviour during HPT processing. The first regime, up to an equivalent strain of ~400, indicates regions with no mixing of materials and limited strain hardening. The second region, above an equivalent strain of ~400, exhibits exceptional strain hardening due to intense grain refinement, solid-state reactions and the formation of intermetallic phases.
- The results demonstrate the potential for using HPT processing at room temperature to create advanced microstructures and excellent mechanical properties that are not generally achievable through other processing routes.

CRediT authorship contribution statement

Piotr Bazarnik: Conceptualization, Methodology, Investigation, Data curation, Writing – original draft, Project administration, Funding acquisition. **Aleksandra Bartkowska:** Conceptualization, Methodology, Validation, Writing – review & editing. **Yi Huang:** Processing, Investigation. **Karol Szlązak:** Investigation, Data curation, Visualization. **Bogusława Adamczyk-Cieślak:** Investigation, Data curation, Visualization. **Jordi Sort:** Validation, Writing – review & editing. **Malgorzata Lewandowska:** Conceptualization, Writing – review & editing. **Terence G. Langdon:** Conceptualization, Supervision, Writing – review & editing.

Declaration of competing interest

The authors declare that they have no known competing financial interests or personal relationships that could have appeared to influence the work reported in this paper.

Acknowledgments

This research was funded by **POB Technologie Materiałowe** of Warsaw University of Technology within the Excellence Initiative: Research University (IDUB) programme. TGL and YH were supported by the European Research Council under ERC Grant Agreement No. 267464-SPDMETALS (TGL). One of the authors acknowledges funding from the Generalitat de Catalunya (project no. 2017-SGR-0292).

References

[1] A.P. Zhilyaev, T.G. Langdon, Using high-pressure torsion for metal processing: fundamentals and applications, Progress in Materials Science 53 (2008) 893–979, https://doi.org/10.1016/j.pmatsci.2008.03.002.
[2] R.Z. Valiev, Producing bulk nanostructured metals and alloys by severe plastic deformation (SPD), in: Nanostructured Metals and Alloys, Woodhead Publishing Series in Metals and Surface Engineering, 2011, pp. 3–39, https://doi.org/10.1533/9780857091123.1.3.
[3] T.G. Langdon, Twenty-five years of ultrafine-grained materials: achieving exceptional properties through grain refinement, Acta Materialia 61 (2013) 7035–7059. https://www.sciencedirect.com/science/article/pii/S1359645413006149.
[4] R.Z. Valiev, Y.V. Ivanisenko, E.F. Rauch, B. Baudelet, Structure and deformaton behaviour of Armco iron subjected to severe plastic deformation, Acta Materialia 44 (1996) 4705–4712, https://doi.org/10.1016/S1359-6454(96)00156-5.
[5] M. Kawasaki, B. Ahn, T.G. Langdon, Significance of strain reversals in a two-phase alloy processed by high-pressure torsion, Materials Science and Engineering: A 527 (2010) 7008–7016, https://doi.org/10.1016/J.MSEA.2010.07.090.
[6] M. Kawasaki, H.J. Lee, B. Ahn, A.P. Zhilyaev, T.G. Langdon, Evolution of hardness in ultrafine-grained metals processed by high-pressure torsion, Journal of Materials Research and Technology 3 (2014) 311–318, https://doi.org/10.1016/j.jmrt.2014.06.002.
[7] M. Kawasaki, Different models of hardness evolution in ultrafine-grained materials processed by high-pressure torsion, Journal of Materials Science 49 (2013) 18–34, https://doi.org/10.1007/S10853-013-7687-9.
[8] M. Kawasaki, R.B. Figueiredo, T.G. Langdon, An investigation of hardness homogeneity throughout disks processed by high-pressure torsion, Acta Materialia 59 (2011) 308–316, https://doi.org/10.1016/j.actamat.2010.09.034.
[9] A. Loucif, R.B. Figueiredo, T. Baudin, F. Brisset, R. Chemam, T.G. Langdon, Ultrafine grains and the Hall-Petch relationship in an Al-Mg-Si alloy processed by high-pressure torsion, Materials Science and Engineering A 532 (2012) 139–145, https://doi.org/10.1016/j.msea.2011.10.074.

[10] C. Xu, Z. Horita, T.G. Langdon, The evolution of homogeneity in processing by high-pressure torsion, Acta Materialia 55 (2007) 203–212, https://doi.org/10.1016/j.actamat.2006.07.029.
[11] T. Miyazaki, D. Terada, Y. Miyajima, C. Suryanarayana, R. Murao, Y. Yokoyama, K. Sugiyama, M. Umemoto, Y. Todaka, N. Tsuji, Synthesis of non-equilibrium phases in immiscible metals mechanically mixed by high pressure torsion, Journal of Materials Science 46 (2011) 4296–4301, https://doi.org/10.1007/s10853-010-5240-7.
[12] R. Kulagin, Y. Beygelzimer, Y. Ivanisenko, A. Mazilkin, B. Straumal, H. Hahn, Instabilities of interfaces between dissimilar metals induced by high pressure torsion, Materials Letters 222 (2018) 172–175, https://doi.org/10.1016/j.matlet.2018.03.200.
[13] M.M. Castro, S. Sabbaghianrad, P.H.R. Pereira, E.M. Mazzer, A. Isaac, T. G. Langdon, R.B. Figueiredo, A magnesium-aluminium composite produced by high-pressure torsion, Journal of Alloys and Compounds 804 (2019) 421–426, https://doi.org/10.1016/j.jallcom.2019.07.007.
[14] J.K. Han, D.K. Han, G.Y. Liang, J. il Jang, T.G. Langdon, M. Kawasaki, Direct bonding of aluminum–copper metals through high-pressure torsion processing, Advanced Engineering Materials 20 (2018) 1800642, https://doi.org/10.1002/adem.201800642.
[15] J.K. Han, J. il Jang, T.G. Langdon, M. Kawasaki, Bulk-state reactions and improving the mechanical properties of metals through high-pressure torsion, Materials Transactions 60 (2019) 1131–1138, https://doi.org/10.2320/matertrans.MF201908.
[16] J.-K. Han, T. Herndon, J. Jang, T.G. Langdon, M. Kawasaki, Synthesis of hybrid nanocrystalline alloys by mechanical bonding through high-pressure torsion, Advanced Engineering Materials 22 (2020) 1901289, https://doi.org/10.1002/adem.201901289.
[17] M. Kawasaki, T.G. Langdon, Using severe plastic deformation to fabricate strong metal matrix composites, Materials Research 20 (2017) 46–52, https://doi.org/10.1590/1980-5373-MR-2017-0218.
[18] K. Oh-Ishi, K. Edalati, H.S. Kim, K. Hono, Z. Horita, High-pressure torsion for enhanced atomic diffusion and promoting solid-state reactions in the aluminum-copper system, Acta Materialia 61 (2013) 3482–3489, https://doi.org/10.1016/j.actamat.2013.02.042.
[19] O. Bouaziz, H.S. Kim, Y. Estrin, Architecturing of metal-based composites with concurrent nanostructuring: a new paradigm of materials design, Advanced Engineering Materials 15 (2013) 336–340, https://doi.org/10.1002/adem.201200261.
[20] B. Ahn, A.P. Zhilyaev, H.-J. Lee, M. Kawasaki, T.G. Langdon, Rapid synthesis of an extra hard metal matrix nanocomposite at ambient temperature, Materials Science and Engineering: A 635 (2015) 109–117, https://doi.org/10.1016/j.msea.2015.03.042.
[21] B. Ahn, H.-J. Lee, I.-C. Choi, M. Kawasaki, J.-I. Jang, T.G. Langdon, Micro-mechanical behavior of an exceptionally strong metal matrix nanocomposite processed by high-pressure torsion, Advanced Engineering Materials 18 (2016) 1001–1008, https://doi.org/10.1002/adem.201500520.
[22] V.N. Danilenko, S.N. Sergeev, J.A. Baimova, G.F. Korznikova, K.S. Nazarov, R. K. Khisamov, A.M. Glezer, R.R. Mulyukov, An approach for fabrication of Al-Cu composite by high pressure torsion, Materials Letters 236 (2019) 51–55, https://doi.org/10.1016/j.matlet.2018.09.158.
[23] G.F. Korznikova, K.S. Nazarov, R.K. Khisamov, S.N. Sergeev, R.U. Shayachmetov, G.R. Khalikova, J.A. Baimova, A.M. Glezer, R.R. Mulyukov, Intermetallic growth kinetics and microstructure evolution in Al-Cu-Al metal-matrix composite processed by high pressure torsion, Materials Letters 253 (2019) 412–415, https://doi.org/10.1016/j.matlet.2019.07.124.
[24] P. Bazarnik, A. Bartkowska, B. Romelczyk-Baishya, B. Adamczyk-Cieślak, J. Dai, Y. Huang, M. Lewandowska, T.G. Langdon, Superior strength of tri-layered Al–Cu–Al nano-composites processed by high-pressure torsion, Journal of Alloys and Compounds 846 (2020) 156380, https://doi.org/10.1016/j.jallcom.2020.156380.
[25] T. Mousavi, J. Dai, P. Bazarnik, P.H.R. Pereira, Y. Huang, M. Lewandowska, T. G. Langdon, Fabrication and characterization of nanostructured immiscible Cu–Ta alloys processed by high-pressure torsion, Journal of Alloys and Compounds 832 (2020) 155007, https://doi.org/10.1016/j.jallcom.2020.155007.
[26] D. Hernández-Escobar, J. Marcus, J.K. Han, R.R. Unocic, M. Kawasaki, C. J. Boehlert, Effect of post-deformation annealing on the microstructure and micro-mechanical behavior of Zn–Mg hybrids processed by High-Pressure Torsion, Materials Science and Engineering A 771 (2020) 138578, https://doi.org/10.1016/j.msea.2019.138578.
[27] D. Hernández-Escobar, Z.U. Rahman, H. Yilmazer, M. Kawasaki, C.J. Boehlert, Microstructural evolution and intermetallic formation in Zn-Mg hybrids processed by high-pressure torsion, Philosophical Magazine 99 (2019) 557–584, https://doi.org/10.1080/14786435.2018.1546962.
[28] S.O. Rogachev, V.M. Khatkevich, S.A. Nikulin, M. Ignateva, A.A. Gromov, High thermally stable multi-layer steel/vanadium alloy hybrid material obtained by high-pressure torsion, Materials Letters 255 (2019) 126527, https://doi.org/10.1016/j.matlet.2019.126527.
[29] A. Korneva, B. Straumal, R. Chulist, A. Kilmametov, P. Bała, G. Cios, N. Schell, P. Zięba, Grain refinement of intermetallic compounds in the Cu–Sn system under high pressure torsion, Materials Letters 179 (2016) 12–15, https://doi.org/10.1016/j.matlet.2016.05.059.
[30] D. Luo, T. Huminiuc, Y. Huang, T. Polcar, T.G. Langdon, The fabrication of high strength Zr/Nb nanocomposites using high-pressure torsion, Materials Science and Engineering A 790 (2020) 139693, https://doi.org/10.1016/j.msea.2020.139693.
[31] A. Bartkowska, P. Bazarnik, Y. Huang, M. Lewandowska, T.G. Langdon, Using high-pressure torsion to fabricate an Al–Ti hybrid system with exceptional mechanical properties, Materials Science and Engineering A 799 (2021) 140114, https://doi.org/10.1016/j.msea.2020.140114.
[32] R.B. Figueiredo, P.H.R. Pereira, M.T.P. Aguilar, P.R. Cetlin, T.G. Langdon, Using finite element modeling to examine the temperature distribution in quasi-constrained high-pressure torsion, Acta Materialia 60 (2012) 3190–3198, https://doi.org/10.1016/J.ACTAMAT.2012.02.027.
[33] W.C. Oliver, G.M. Pharr, An improved technique for determining hardness and elastic modulus using load and displacement sensing indentation experiments, Journal of Materials Research 7 (1992) 1564–1583, https://doi.org/10.1557/jmr.1992.1564.
[34] M. Kawasaki, J.K. Han, D.H. Lee, J. Il Jang, T.G. Langdon, Fabrication of nanocomposites through diffusion bonding under high-pressure torsion, Journal of Materials Research 33 (2018) 2700–2710, https://doi.org/10.1557/jmr.2018.205.
[35] Z. Lee, R. Rodriguez, R.W. Hayes, E.J. Lavernia, S.R. Nutt, Microstructural evolution and deformation of cryomilled nanocrystalline Al-Ti-Cu alloy, Metallurgical and Materials Transactions A: Physical Metallurgy and Materials Science 34 (2003) 1473–1481, https://doi.org/10.1007/s11661-003-0259-x.
[36] K. Edalati, S. Toh, H. Iwaoka, M. Watanabe, Z. Horita, D. Kashioka, K. Kishida, H. Inui, Ultrahigh strength and high plasticity in TiAl intermetallics with bimodal grain structure and nanotwins, Scripta Materialia 67 (2012) 814–817, https://doi.org/10.1016/j.scriptamat.2012.07.030.
[37] P. Bazarnik, B. Adamczyk-Cieślak, A. Gałka, B. Płonka, L. Snieżek, M. Cantoni, M. Lewandowska, Mechanical and microstructural characteristics of Ti6Al4V/AA2519 and Ti6Al4V/AA1050/AA2519 laminates manufactured by explosive welding, Materials and Design 111 (2016) 146–157, https://doi.org/10.1016/j.matdes.2016.08.088.
[38] D.M. Fronczek, R. Chulist, L. Litynska-Dobrzynska, G.A. Lopez, A. Wierzbicka-Miernik, N. Schell, Z. Szulc, J. Wojewoda-Budka, Microstructural and phase composition differences across the interfaces in Al/Ti/Al explosively welded clads, Metallurgical and Materials Transactions A: Physical Metallurgy and Materials Science 48 (2017) 4154–4165, https://doi.org/10.1007/s11661-017-4169-8.
[39] A. Leyland, A. Matthews, On the significance of the H/E ratio in wear control: a nanocomposite coating approach to optimised tribological behaviour, Wear 246 (2000) 1–11, https://doi.org/10.1016/S0043-1648(00)00488-9.
[40] E. Pellicer, S. Pané, K.M. Sivaraman, O. Ergeneman, S. Suriñach, M.D. Baró, B. J. Nelson, J. Sort, Effects of the anion in glycine-containing electrolytes on the mechanical properties of electrodeposited Co-Ni films, Materials Chemistry and Physics 130 (2011) 1380–1386, https://doi.org/10.1016/j.matchemphys.2011.09.032.
[41] A. Korneva, B. Straumal, A. Kilmametov, L. Lityńska-Dobrzyńska, G. Cios, P. Bała, P. Zięba, Effect of high pressure torsion on microstructure of Cu-Sn alloys with different content of Hume Rothery phase, Materials Characterization 118 (2016) 411–416, https://doi.org/10.1016/j.matchar.2016.06.019.
[42] S.O. Rogachev, R.V. Sundeev, V.M. Khatkevich, Evolution of the structure and strength of steel/vanadium alloy/steel hybrid material during severe plastic deformation, Materials Letters 173 (2016) 123–126, https://doi.org/10.1016/j.matlet.2016.03.044.
[43] R. Kulagin, Y. Beygelzimer, A. Bachmaier, R. Pippan, Y. Estrin, Benefits of pattern formation by severe plastic deformation, Applied Materials Today 15 (2019) 236–241, https://doi.org/10.1016/J.APMT.2019.02.007.
[44] Y. Beygelzimer, Y. Estrin, A. Mazilkin, T. Scherer, B. Baretzky, H. Hahn, R. Kulagin, Quantifying solid-state mechanical mixing by high-pressure torsion, Journal of Alloys and Compounds 878 (2021) 160419, https://doi.org/10.1016/j.jallcom.2021.160419.
[45] K. Lu, Making strong nanomaterials ductile with gradients: microstructures that increase metal crystallite size from nanoscale with surface depth are both strong and ductile, Science 345 (2014) 1455–1456, https://doi.org/10.1126/science.1255940.
[46] T.H. Fang, W.L. Li, N.R. Tao, K. Lu, Revealing extraordinary intrinsic tensile plasticity in gradient nano-grained copper, Science 331 (2011) 1587–1590, https://doi.org/10.1126/science.1200177.
[47] X. Wu, P. Jiang, L. Chen, F. Yuan, Y.T. Zhu, Extraordinary strain hardening by gradient structure, Proceedings of the National Academy of Sciences of the United States of America 111 (2014) 7197–7201, https://doi.org/10.1073/pnas.1324069111.
[48] X.L. Wu, P. Jiang, L. Chen, J.F. Zhang, F.P. Yuan, Y.T. Zhu, Synergetic strengthening by gradient structure, Materials Research Letters 2 (2014) 185–191, https://doi.org/10.1080/21663831.2014.935821.
[49] X. Wu, Y. Zhu, K. Lu, Ductility and strain hardening in gradient and lamellar structured materials, Scripta Materialia 186 (2020) 321–325, https://doi.org/10.1016/j.scriptamat.2020.05.025.
[50] D. Rahmatabadi, A. Shahmirzaloo, M. Farahani, M. Tayyebi, R. Hashemi, Characterizing the elastic and plastic properties of the multilayered Al/Brass composite produced by ARB using DIC, Materials Science and Engineering A 753 (2019) 70–78, https://doi.org/10.1016/j.msea.2019.03.002.
[51] Y. Qi, A. Kosinova, A.R. Kilmametov, B.B. Straumal, E. Rabkin, Plastic flow and microstructural instabilities during high-pressure torsion of Cu/ZnO composites, Materials Characterization 145 (2018) 389–401, https://doi.org/10.1016/j.matchar.2018.09.001.
[52] V. Tavakkoli, A. Mazilkin, T. Scherer, M. Mail, Y. Beygelzimer, B. Baretzky, Y. Estrin, R. Kulagin, Instability of a molybdenum layer under deformation of a CuMoCu laminate by high-pressure torsion, Materials Letters 302 (2021) 130378, https://doi.org/10.1016/j.matlet.2021.130378.

[53] K.S. Kormout, R. Pippan, A. Bachmaier, Deformation-induced supersaturation in immiscible material systems during high-pressure torsion, Advanced Engineering Materials 19 (2017) 1600675, https://doi.org/10.1002/adem.201600675.
[54] K. Edalati, S. Toh, M. Watanabe, Z. Horita, In situ production of bulk intermetallic-based nanocomposites and nanostructured intermetallics by high-pressure torsion, Scripta Materialia 66 (2012) 386–389, https://doi.org/10.1016/j.scriptamat.2011.11.039.
[55] P. Bazarnik, Y. Huang, M. Lewandowska, T.G. Langdon, Enhanced grain refinement and microhardness by hybrid processing using hydrostatic extrusion and high-pressure torsion, Materials Science and Engineering: A 712 (2018) 513–520, https://doi.org/10.1016/j.msea.2017.12.007.
[56] V.V. Popov, E.N. Popova, A.V. Stolbovskiy, Nanostructuring Nb by various techniques of severe plastic deformation, Materials Science and Engineering A 539 (2012) 22–29, https://doi.org/10.1016/j.msea.2011.12.082.
[57] S. Sabbaghianrad, T.G. Langdon, A critical evaluation of the processing of an aluminum 7075 alloy using a combination of ECAP and HPT, Materials Science and Engineering A 596 (2014) 52–58, https://doi.org/10.1016/j.msea.2013.12.034.
[58] S. Sabbaghianrad, T.G. Langdon, An evaluation of the saturation hardness in an ultrafine-grained aluminum 7075 alloy processed using different techniques, Journal of Materials Science 50 (2015) 4357–4365, https://doi.org/10.1007/S10853-015-8989-X.
[59] S. Sabbaghianrad, S.A. Torbati-Sarraf, T.G. Langdon, An investigation of the limits of grain refinement after processing by a combination of severe plastic deformation techniques: a comparison of Al and Mg alloys, Materials Science and Engineering A 712 (2018) 373–379, https://doi.org/10.1016/j.msea.2017.11.090.
[60] Y. Huang, P. Bazarnik, D. Wan, D. Luo, P.H.R. Pereira, M. Lewandowska, J. Yao, B. E. Hayden, T.G. Langdon, The fabrication of graphene-reinforced Al-based nanocomposites using high-pressure torsion, Acta Materialia 164 (2019) 499–511, https://doi.org/10.1016/j.actamat.2018.10.060.
[61] S.N. Alhajeri, M. Kawasaki, N. Gao, T.G. Langdon, The evolution of homogeneity during processing of aluminium alloys by HPT, Materials Science Forum 667–669 (2011) 277–282. https://doi.org/10.4028/www.scientific.net/MSF.667-669.277.
[62] M. Kawasaki, S.N. Alhajeri, C. Xu, T.G. Langdon, The development of hardness homogeneity in pure aluminum and aluminum alloy disks processed by high-pressure torsion, Materials Science and Engineering A 529 (2011) 345–351, https://doi.org/10.1016/j.msea.2011.09.039.
[63] J.-K. Han, H.-J. Lee, J. Jang, M. Kawasaki, T.G. Langdon, Micro-mechanical and tribological properties of aluminum-magnesium nanocomposites processed by high-pressure torsion, Materials Science and Engineering: A 684 (2017) 318–327, https://doi.org/10.1016/j.msea.2016.12.067.

Journal of Alloys and Compounds 846 (2020) 156380

Contents lists available at ScienceDirect

Journal of Alloys and Compounds

journal homepage: http://www.elsevier.com/locate/jalcom

Superior strength of tri-layered Al—Cu—Al nano-composites processed by high-pressure torsion

Piotr Bazarnik [a, *], Aleksandra Bartkowska [a], Barbara Romelczyk-Baishya [a], Bogusława Adamczyk-Cieślak [a], Jiaoyan Dai [b], Yi Huang [c, d], Małgorzata Lewandowska [a], Terence G. Langdon [d]

[a] Warsaw University of Technology, Faculty of Materials Science, Woloska 141, 02-507, Poland
[b] School of Materials and Chemical Engineering, Ningbo University of Technology, Ningbo, 315211, PR China
[c] Department of Design and Engineering, Faculty of Science and Technology, Bournemouth University, Poole, Dorset, BH125BB, UK
[d] Materials Research Group, Faculty of Engineering and the Environment, University of Southampton, Southampton, SO171BJ, UK

ARTICLE INFO

Article history:
Received 2 June 2020
Received in revised form
9 July 2020
Accepted 11 July 2020
Available online 23 July 2020

Keywords:
Al-Cu
High-pressure torsion
Nano-composites
Phase transformations
Ultrafine grains

ABSTRACT

This investigation demonstrates that a solid-state reaction occurs by the application of high-pressure torsion (HPT) in the production of nanostructured multilayered hybrid Al—Cu systems. Three-layered stacks of Al/Cu/Al were subjected for up to 200 revolutions of HPT under an applied pressure of 6.0 GPa. Microstructural and mechanical properties analysis were carried out after HPT using X-ray diffraction, scanning and transmission electron microscopy, energy dispersive spectrometry (EDX), microhardness measurements and tensile tests. The SEM observations revealed the formation of a multi-nano-layered structure in the whole volume of the disks. Further investigations with the use of TEM demonstrated that each nano-layer consists of nano-grains having sizes of about 20 nm. Analysis by XRD and selected area electron diffraction (SAED) confirmed the formation of intermetallic $CuAl_2$ and Cu_9Al_4 phases in the layered structures. The experiments also showed a significant improvement in microhardness (up to ~450 Hv) and tensile properties (over 900 MPa of UTS after 200 turns) when compared to both Al-1050 and 99.95%Cu alloys in the initial state and after HPT processing. The results demonstrate that HPT offers an outstanding opportunity for producing novel nanostructured Al—Cu multilayered composites having unique mechanical properties.

1. Introduction

The development of new and advanced materials is now driven by the technological demands of improved properties and wider functionalities as well as by numerous restrictions imposed by ecological considerations in various industrial applications [1]. Metals such as aluminium, copper and their alloys are now used extensively for many industrial applications and they will become principal future structural materials if their mechanical properties are sufficiently improved. In this respect, the fabrication of composites of aluminium and copper may meet the demands for higher strength and reductions in the overall weight. The Al—Cu hybrid materials appear attractive because of their low density and high thermal and electrical conductivity. They also exhibit higher strengths than other aluminium alloys.

Numerous methods are available for producing metal composites including diffusion bonding [2], powder metallurgy techniques [3] and explosive welding [4]. Nevertheless, it was shown recently that the use of severe plastic deformation (SPD) methods, including equal-channel angular pressing (ECAP) [5] and high-pressure torsion (HPT) [6], may be especially promising as fabrication techniques for the production of metal matrix nanocomposites [7—11]. These SPD techniques are attractive for the manufacturing of composite materials because they generally achieve very good bonding [12—14]. Of the various SPD methods now available, processing by HPT has the advantage of producing significant grain refinement [15,16], providing the capability of processing even hard-to-deform metals [17] or intermetallics [18] and, due to the high applied pressure and intense shear strain, producing phase transformations [19,20] or supersaturated solid solutions [21,22]. It is also well established that, by comparison with processing by

* Corresponding author.
E-mail address: Piotr.Bazarnik@pw.edu.pl (P. Bazarnik).

https://doi.org/10.1016/j.jallcom.2020.156380

ECAP, HPT produces smaller grains [23,24] and a higher fraction of grain boundaries having high angles of misorientation [25] and it has been used successfully for producing nanocomposites from metallic powders [14,26–29] and machining chips [30–33].

Recently an alternative approach was developed with HPT for the fabrication of high-performance hybrid materials by making use of the very high pressure to effectively join dissimilar bulk metals. The initial experiments were conducted using semi-circular disks of Ag-Ni [34], Nb-Zr [34], Al-Cu [35,36] and Mg–Al [37] or quarter disks of Al-Cu [38] and placing these pieces to form whole disks within the depression on the lower anvil of an HPT facility. Later, this approach was improved and further developed by stacking three whole disks of commercial Al and Mg alloys and then applying pressure and torsional straining to the stack [39]. This same approach was used in several later investigations using stacks of three or more disks of Al-Cu [40–44], Al-Fe [41,42,44], Al-Mg [21,41,42,45–50], Al-Mg-Cu-Fe-Ti [42], Al-Ti [41,42,44], Cu-Al [51], Cu-Sn [52], Cu-Ta [22,53], Cu–ZnO [54], Fe–V [55,56], V–Zr [57] and Zn–Mg [58].

Recent investigations using stacks of Al and Cu disks demonstrated the potential for fabricating Al/Cu/Al composites by HPT after processing through up to a total of 60 turns [40,43,44]. These experiments confirmed the formation of a nanocrystalline structure and intermetallic phases of Al_2Cu, AlCu and Al_4Cu_9 but nevertheless the microstructures remained relatively inhomogeneous across the disk diameters even after 60 revolutions. Thus, the presence of the initial three-layered structure was essentially retained within the central region of the disk over a diameter of ~1.5 mm and this affected the microhardness values in the disk centre which, even after the HPT processing, remained close to the initial level for the commercial purity Cu.

The present investigation was motivated by these earlier results and by the opportunity to evaluate the potential for achieving greater homogeneity by conducting the HPT processing through larger numbers of revolutions. Accordingly, tests were conducted using HPT processing for up to a maximum of 200 turns and emphasis was placed on examining the quality of bonding and the microstructural characterization in order to determine the origin of the exceptionally high strength of these hybrid materials.

2. Experimental material and procedures

The experiments were conducted using a commercial purity (CP) aluminium alloy (Al-1050, 99.95 wt% Al) and CP copper (99.95%). The samples were received in the form of rods of 10 mm diameter and these Al and Cu rods were annealed for 1 h at 370 °C and 480 °C, respectively, in order to soften both materials. The rods were then cut into disks with thicknesses of 1.1 mm and ground to a final thickness of ~0.80 mm.

The HPT processing was conducted on stacks of three disks placed in the order of Al/Cu/Al and having a total thickness of ~2.4 mm. These disks were piled in the depression on the lower anvil of the HPT facility and then subjected to an applied pressure of 6.0 GPa at room temperature and torsional straining with a rotation speed of 1 rpm under quasi-constrained conditions where there is a small outflow of material around the periphery of the disk [59]. The disks were strained through total numbers of revolutions, N, of 20, 50, 150 and 200 turns. The anvils had a high roughness to prevent the sample from slipping during deformation. In addition, and for comparative purposes, separate disks of Al and Cu were tested through 10 revolutions of HPT under the same processing conditions.

The HPT-processed disks were initially examined by X-ray diffraction (XRD) using Bruker D8 Diskover and an energy for the emitter beam of 30 kV. The Co Kα X-Ray beam was filtered to form a point with a radius of 1 mm and all specimens were scanned on cross-sectional planes in the edge regions. Each sample was illuminated by high intensity hard X-rays for 5 s per step, the 2Θ angle was between 20° and 120° and the step size Δ2Θ was 0.025°.

Each HPT disk was then cut into two halves along a diameter using a diamond wafering saw and the cross-section of each disk was examined using optical microscopy (OM) and scanning electron microscopy (SEM). Specimens for SEM observations were prepared using grinding and ion polishing with an Hitachi Ion Milling System IM-4000. The ion milling is a damage-free process and this polishing eliminates all deformation, stresses and oxide layers. Furthermore, the surface quality is sufficiently good to observe the structure using channelling contrast in an SEM microscope. Microstructural examination was carried out using an Hitachi SU-8000 SEM operated at 10 kV with a backscattered electron (BSE) detector. These microstructural observations were conducted in the central and periphery regions (approximately 1.0 mm from the edge) for each disk. Detailed microstructural observations of selected areas were performed using a CS-corrected dedicated scanning transmission electron microscope (STEM) Hitachi HD-2700 operating at an accelerating voltage of 200 kV. The STEM observations were carried out in the bright-field (BF) and high-angle annular dark field (HAADF) modes. Thin foils with a thickness of ~85 nm for STEM observations were extracted from the peripheral regions of each disk using a focused ion beam (FIB) system Hitachi NB 5000. Structural investigations were combined with advanced energy dispersive X-Ray (EDX) point and mapping analyses. The microstructures were also evaluated quantitatively using a computer-aided image analyser and the grain sizes were recorded in terms of the equivalent grain diameter, d_{eq}, defined as the diameter of a circle having a surface area equal to the surface area of the grain.

To evaluate the changes in mechanical properties due to HPT processing, microhardness tests were conducted on the cross-sections of disks using an FM-300 microhardness tester equipped with a Vickers indenter. Measurements were performed under a load of 100 g with a dwell time of 10 s and a spacing of 0.1 mm between each separate indentation. To determine the influence of HPT processing on the homogeneity of the structure, detailed microhardness measurements were performed on selected samples to permit the construction of color-coded microhardness maps.

These microhardness studies were complemented by tensile testing. Miniature tensile samples with gauge lengths of 2.5 mm were cut from off-centre positions in each disk using electro-discharge machining (EDM) [60]. The tensile tests were conducted at room temperature using a Zwick 005 universal testing machine under displacement control at an initial strain rate of 1.0×10^{-3} s^{-1}. For strain estimation, a Digital Image Correlation (DIC) was applied [61]. A charge-coupled device (CCD) camera operating at 4 fps with a Pentax lens was placed in front of the sample and the image acquisition with AVT software was synchronized with the beginning of each tensile test. The recorded images were analysed using VIC 2D software (Correlated Solutions) to create stress-strain maps. Based on the load-displacement data, the yield stress (YS), ultimate tensile stress (UTS) and elongation to failure were determined.

3. Experimental results

3.1. Microstructure and phase analysis after HPT

The OM images in Fig. 1 show the cross-sections of samples processed through 20, 50, 150 and 200 turns, respectively, where the bright regions denote the Al-rich phase and the dark regions

Fig. 1. The vertical cross-section of the Al—Cu system after HPT processing at room temperature under a pressure of 6.0 GPa for 20, 50, 150 and 200 turns.

correspond to the Cu-rich phase. Macroscopic observations confirmed that all samples were fully dense with no evidence for any macroscopic voids or delamination between the Al and Cu phases. In the disk after 20 turns the microstructure is of a gradient-type in the central section with clear evidence for the separate Al-rich and Cu-rich layers whereas in the outer regions of the disk the layered structure is fragmented due to the torsional straining and thin Cu layers or inclusions are evident within the Al phase. There is also a similar structural evolution after 50 turns but the overall size of the central layered structure is then reduced. A high degree of deformation is required to achieve a full intermixing of the Al and Cu layers throughout the disk diameter and this is achieved after 150 and 200 revolutions where there is intermixing of the Al and Cu phases over the whole diameter and the microstructures are reasonably fully homogeneous.

Detailed structural investigations were carried out using SEM and Figs. 2 and 3 show BSE images of the cross-sectional views at the disk centres and edges for the samples processed through 20 and 200 turns, respectively, where the brighter contrast corresponds to the Cu-rich regions and the darker contrast represents the Al-rich regions. The SEM images in Figs. 2 and 3 generally confirm the observations by OM. For the sample after 20 turns, a layered Al/Cu/Al structure is present in the central region in Fig. 2(a) but with no evidence for voids or delamination. There is extensive grain refinement in Fig. 2(b) and (c) with measured average grain sizes in the Al and Cu of ~650 and ~400 nm, respectively. By contrast, the average grain sizes in the separate Al and Cu disks were measured as ~700 and ~350 nm, respectively, after processing by HPT for 10 turns. In the outer parts of the disk in Fig. 2(d) and (e), the SEM observations reveal significant fragmentation and a mixing of the Al and Cu layers. The higher magnification image in Fig. 2(e) also reveals evidence for shear bands and the formation of a lamellar structure with thin Cu-rich and Al-rich bands.

It appears that this lamellar structure evolves with increasing numbers of turns and for the sample after 200 turns in Fig. 3 there is a fine nano-layered structure throughout the whole diameter of the disk although in the central region in the upper and lower parts of the disk it is apparent that the material is not fully mixed as marked in Fig. 3(a). In the outer regions of the disk there is a full mixing of Al and Cu over the entire thickness as in Fig. 3(c). Although there remains evidence for the lamellar structure in Fig. 3(d), the thicknesses of the individual Al-rich and Cu-rich bands are smaller than after 20 revolutions. In addition, some contrast changes are visible in the BSE image in Fig. 3(e) which suggests the possible formation of new phases.

A detailed structural investigation was conducted from the edge regions using STEM techniques and Figs. 4 and 5 show STEM images for the samples processed through 20 and 200 revolutions, respectively. After 20 turns the structure consists of ultra-thin Al-rich and Cu-rich layers as in Fig. 4(a) with evidence for extensive grain refinement in all layers. Measurements showed the grains in the Al layers are elongated and smaller (~230 ± 20 nm) than in the Cu bands where the grain size is strongly affected by the thickness of individual layers and reaches sizes of up to ~310 ± 70 nm. High magnification observations confirmed, as in Fig. 4(b) and (c), that the interface-affected zone on the contact surface of the Al and Cu layers is formed during HPT processing. Furthermore, there is a diffusion zone on the contact surface of nanolayers in Fig. 4(c) which was also confirmed by line EDX analysis as in Fig. 4(d). This diffusion effect was observed on almost all Al—Cu interfaces. In addition, in some places, the thinnest copper layers have transformed into nanometer-sized grains as in Fig. 4(b) with sizes of ~30 ± 20 nm.

There is a further decrease in grain size after 200 turns as in Fig. 5(a) but the lamellar structure remains as in Fig. 5(b). Measurements revealed a bimodal character of the microstructure with Al-rich grains of ~95 ± 15 nm in Fig. 5(c) and Cu-rich grains in the range of ~5—20 nm. Chemical composition analysis, as in Fig. 5(d), revealed a high concentration of Cu in these nano-sized bands although Cu was also present in the Al matrix in the form of a solid supersaturated solution. Rings in the selected area electron diffraction (SAED) patterns as in Fig. 6(a) confirmed the presence of Al and Cu as well as the formation of the Al_2Cu and Al_4Cu_9 phases where dark field imaging from the Al_2Cu (110) ring as in Fig. 6(b) confirmed that this phase occurs primarily in the Cu-rich nano-sized bands. The presence of these intermetallic phases is consistent with earlier reports [40,43]. A quantitative image correlation analysis of several dark field images after 200 turns showed that the fraction of the intermetallic Al_2Cu phase is about 9.7%. The diffraction rings from the Al_4Cu_9 phase were too weak to conduct any quantitative analysis.

The phase compositions were also examined by XRD analysis and the patterns for the initial materials and after processing from 20 to 200 turns are shown in Fig. 7. These patterns reveal a significant broadening of the peaks due to the severe grain refinement, with the broadening becoming more intense after increasing numbers of turns. The patterns confirm the presence of the Al and Cu phases and the formation of the Al_2Cu and Al_4Cu_9 phases. These latter phases are visible even after 20 turns but the peaks become more intensive with increasing numbers of turns. A semi-quantitative analysis of the XRD patterns gave estimates for the fractions of the intermetallic Al_2Cu and Al_4Cu_9 phases at 2.5%, 4.4%, 6.9% and 10.2% after 20, 50, 150 and 200 turns, respectively. It should be noted that phase calculations from XRD can be affected by many factors such as severe grain refinement, internal stresses and texture. Nevertheless, the result for the sample after 200 turns is reasonably consistent with the earlier estimate using the dark field images.

3.2. Mechanical properties

The distributions of the Vickers microhardness on one-half of the cross-sections of the disks is shown in the color-coded contour maps in Fig. 8 after processing by HPT through 20, 50, 150 and 200 turns: the values of the microhardness are given in the colour key on the right and the distributions are plotted with the centre of the disk lying along the left axis. For comparison, the reference samples

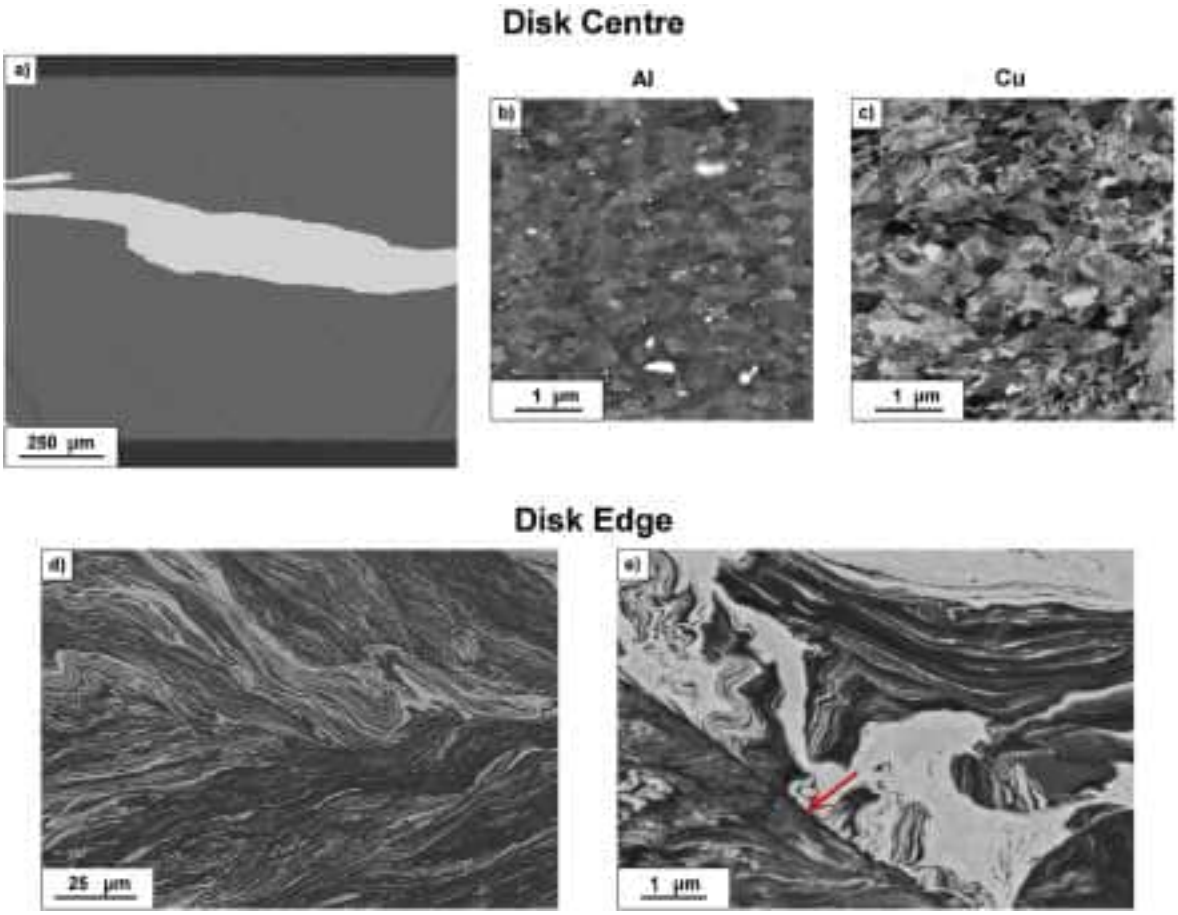

Fig. 2. SEM BSE images of the Al–Cu–Al sample after 20 turns. a) an overall image of the central region, with enlarged images of the microstructure in b) Al and c) Cu regions. Microstructure image in the edge region d) and e).

of Cu and Al showed average Vickers microhardness values of ~80 and ~25 Hv, respectively, for the as-annealed states and ~130 and ~50 Hv, respectively, after HPT for 10 turns.

Inspection of Fig. 8 shows that the microhardness of the multilayered composite increases significantly with increasing numbers of turns. The hardness values in the edge region are ~260 Hv after only 20 turns but in the central region the hardness values are in the range of ~50–130 Hv which is close to the initial values. This is consistent with earlier work on the Al/Cu/Al system where there was little or no significant increase in hardness in the central region after processing up to 60 turns [40,43]. In addition, the highest hardness values of ~110–130 Hv were recorded primarily in the Cu layers whereas the hardness was lower at ~50 Hv in the Al layers. The radius of the central zone of inhomogeneity extended through approximately 3 mm after 20 turns but this was reduced to ~2 mm after 50 turns and the hardness near the edge then increased to ~350 Hv. Further processing up to 150 turns gave an additional hardness increase up to ~400 Hv but with some small areas of lower hardness near the centre of the disk. Finally, after 200 turns the microhardness was fairly homogeneous throughout the disk with an average value of ~350 Hv but with highest hardness values of ~450 Hv near the outer edge of the disk. This hardness is exceptionally high by comparison with the initial hardness values of the pure Cu and pure Al in the as-annealed state and after HPT processing for 10 turns.

The results of tensile testing for the HPT-processed hybrid materials are illustrated in Fig. 9 where these data are complemented by including results for Cu and Al samples both in an as-annealed state and after 10 HPT revolutions. For convenience, the results are also summarized in Table 1 showing the yield strength (YS), the ultimate tensile strength (UTS) and the elongation to failure. These tensile tests demonstrate that the Al–Cu–Al composites exhibit very high strength with values for the UTS after 20 and 50 turns of ~420 ± 20 and ~460 ± 24 MPa, respectively. These results are much higher than the conventional values anticipated for Cu and Al in an as-annealed state and for Al after HPT processing but they are close to the values for Cu after HPT for 10 turns (525 ± 10 MPa). With additional HPT turns, the strength increases further and reaches extremely high strength values of ~710 and ~910 MPa for the samples processed through 150 and 200 revolutions, respectively. Nevertheless, these hybrid materials exhibit high strength but only limited elongations to failure of about 2%.

4. Discussion

The results from this investigation demonstrate the potential for fabricating aluminium-based hybrid material by using conventional quasi-constrained HPT processing with a stack of disks consisting of commercial purity Al and Cu. By HPT processing through 200 turns, which is far in excess of the 60 turns used in earlier investigations [40,43,44], it was possible to form a unique multi-layered structure which was reasonably homogeneous throughout the entire disk, both in the radial direction and on cross-sectional planes, without any visible porosity or the presence

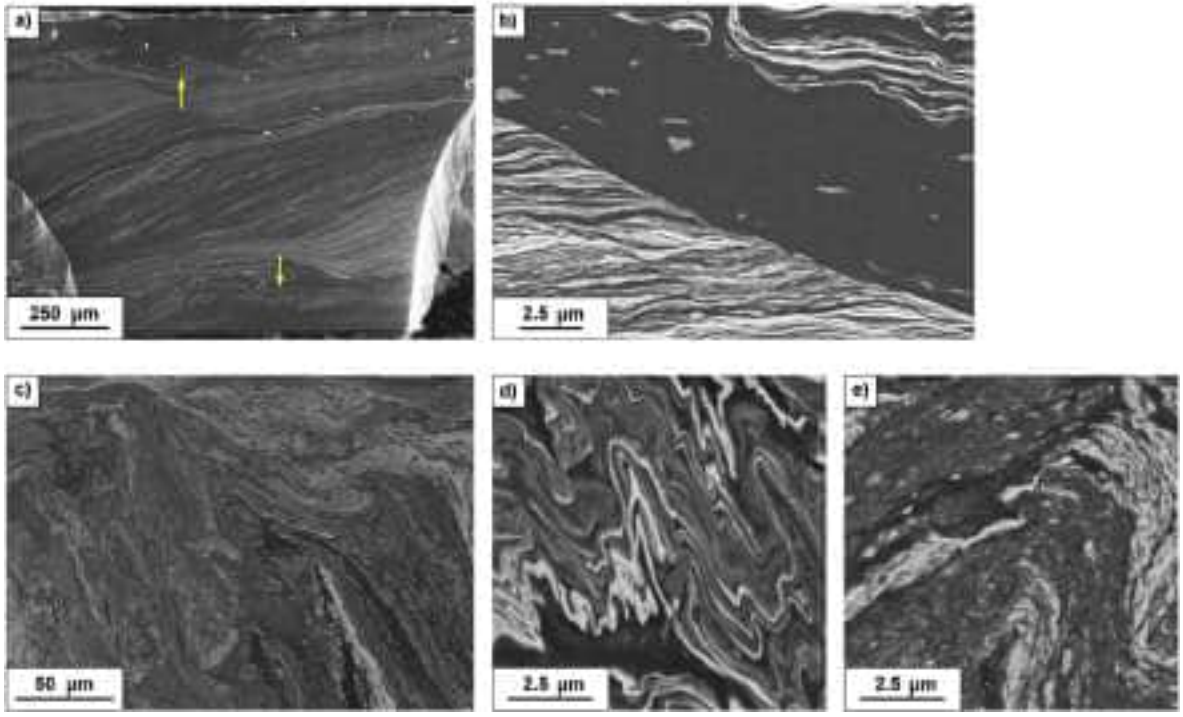

Fig. 3. SEM BSE cross-sectional images of the Al–Cu–Al sample after 200 turns. (a) an overall image of central region, showing misalignment between the upper and lower anvils (arrows mark the centres of each anvil) with enlarged images of the microstructure (b). An overall microstructure image in the edge region (c) and high magnification images showing the formation of nano-lamellar structure (d) and intermetallic phases (e).

of any delamination between the layers. The results demonstrate instead the development of a fine dispersion of Cu-rich phases within a nanostructured Al matrix and with rapid diffusion of Cu to Al and the consequent formation of intermetallic phases such as Al_2Cu and Al_4Cu_9.

Careful examination of samples suggests that the mixing effect, especially in the central part of the disks, may have been enhanced by a slight misalignment between the upper and lower anvils, as marked on Fig. 3(a), where two unmixed areas in the disk correspond to the centres of the upper and lower anvils. This proposal is reasonable because it is well established that anvil misalignments of the order of 100 or 200 μm may have significant effects on the flow properties within the HPT-processed samples [62–64]. As a result, a fully mixed structure with a thin lamellar configuration was observed in the central region after 150 revolutions and further processing up to 200 turns led to an additional reduction in the lamellar thickness. At the same time, there was a significant reduction in grain size below ~100 nm within the Al

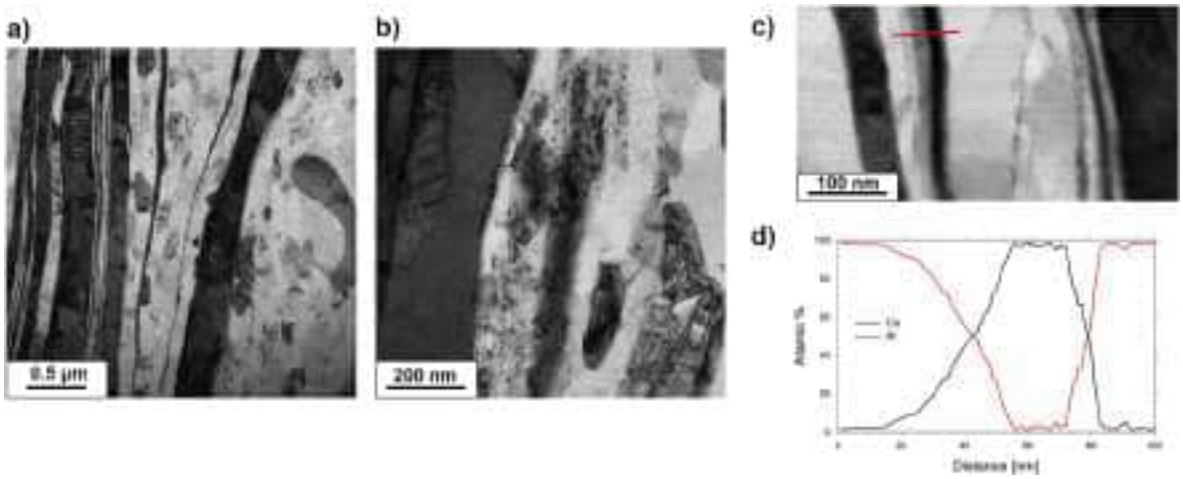

Fig. 4. STEM bright-field images of the microstructure taken at the disk edge after HPT for 20 turns (a) low magnification and (b) high magnification. (c) HAADF image of the microstructure with marked place of the line EDX scan with corresponding scanning results (d) as a plot of atomic percentage with respect to the scanning distance for Cu and Al elements.

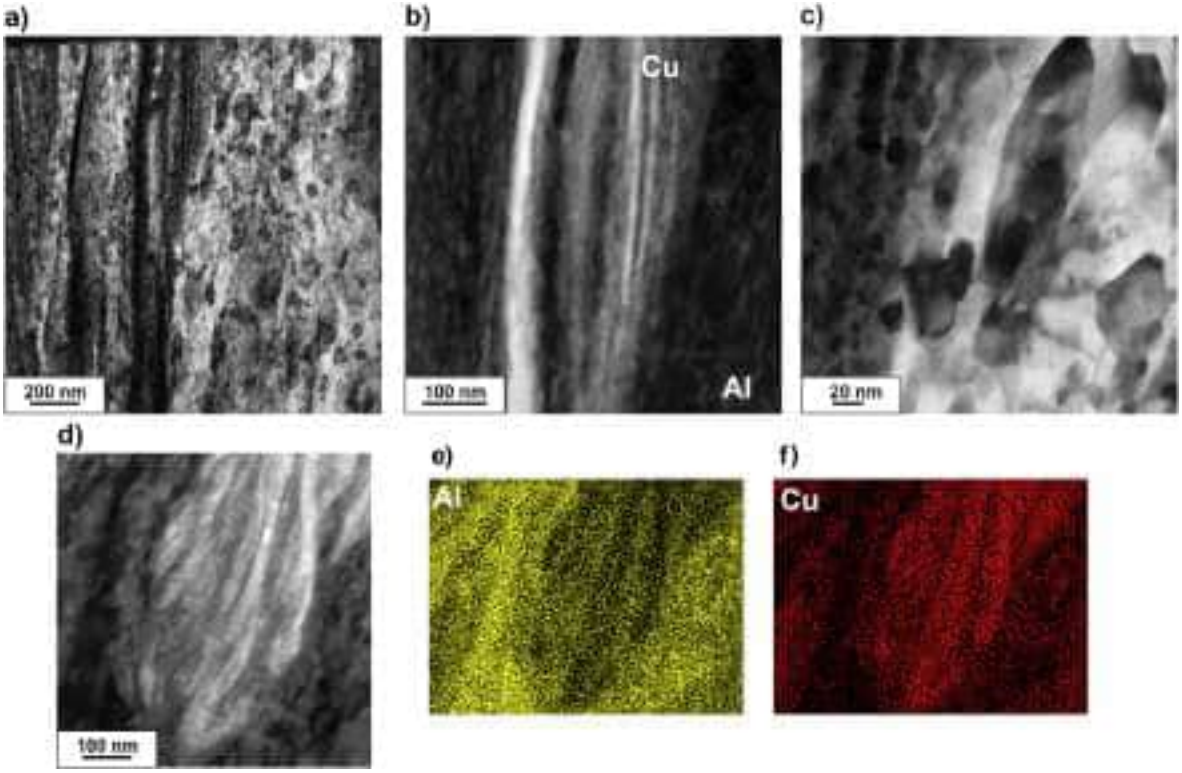

Fig. 5. STEM images taken at the disk edge after HPT for 200 turns showing (a) an overall image of lamellar structure, (b) HAADF image showing the distribution of Al and Cu elements in this lamellar structure, (c) high magnification image of a bimodal structure and (d) HAADF image and a corresponding composition maps of Al and Cu.

matrix after processing. This is a unique result especially when compared with data reported for conventional Al–Cu alloys after SPD processing [65–72]. A progressive mixing of phases with an accompanying reduction in lamellar thickness, accompanied also by significant grain size reductions, was observed also for other hybrid systems processed by HPT such as Al-Mg [45], steel-V [55], Cu-Ta [22,53], Al-Fe [44], Mg-Zn [58] and Al–Ti [44].

The initial objective of using HPT in these systems was to facilitate the formation of nano-sized intermetallic phases which will improve and strengthen the mechanical properties of the composites. An additional advantage of HPT or other SPD techniques is that the materials exhibit significantly higher diffusion coefficients due to the introduction by processing of high populations of lattice defects [35,73–75]. This effect is especially visible in the Al–Cu interfacial zones as in Fig. 4 where there was evidence for diffusion of Cu and Al elements on the surface contact of nanolayers. As a consequence, the intermetallic Al_2Cu and Al_4Cu_9 phases are formed at the interfacial zones where these phase transformations are favoured in the joining zones of the Al-rich and Cu-rich regions [35,40,51,76]. Further deformation leads to a significant increase in the fraction of intermetallic phases which are located mainly in the Cu-rich regions.

It is important to examine the kinetics of formation of these intermetallic phases. For the Al–Cu system, saturated solid solutions Al(Cu) and Cu(Al) firstly form on each side due to mutual diffusion. Since the solubility limit of Cu in Al is almost two orders of magnitude smaller than that of Al in Cu [77,78], the Al(Cu) solid solution is expected to saturate first. Moreover, the diffusion coefficient of Cu in Al is much higher than for Al in Cu ($D_{Cu} \approx 1.78 \times 10^{-15}$ m^2 s^{-1} and $D_{Al} \approx 6.54 \times 10^{-19}$ m^2 s^{-1}) [78]. Thus, the Cu atoms can diffuse to the Al side rapidly so that the Al side becomes oversaturated and subsequently Al_2Cu will form at the interfacial zone. At the same time, the Al_2Cu phase has the most negative effect of Gibbs free energy (−15.8 (J/mol)) of formation and from the thermodynamic point of view it will be the first phase formed at the Al–Cu interfacial zone [79]. By contrast the negative energy for the Al_4Cu_9 phase is −19.7 (J/mol) [79] which makes it a less-favoured phase for formation. This explains the reason for the Al_2Cu phase occurring mainly in this hybrid system (Figs. 6 and 7). It should be mentioned that the diffusion is controlled primarily by the temperature of the processing, and since in this study the HPT process was conducted at room temperature the fast diffusion on the contact surfaces was induced only by the shear deformation at the Al–Cu interfacial zones in order to maintain unity of the system. This was a direct consequence of the differences in strength and Young's modulus for the individual layers.

As shown in Figs. 8 and 9, extreme increases in hardness and strength were observed in the hybrid materials synthesized in this study. The hardness of the HPT-processed Al–Cu system approached ~450 Hv after 200 HPT turns and this is significantly higher than the hardness of nanocrystalline aluminium (~50 Hv) and copper (~130 Hv). Furthermore, a high structural homogenisation was observed across the disk diameter after 200 revolutions and this had a major impact on the values of the Vickers microhardness which were reasonably similar across the disk diameter. The UTS of the hybrid material exceeded 900 MPa which is an order of magnitude higher than for the unprocessed aluminium (~90 MPa) and more than three times higher than for the unprocessed copper (~280 MPa). Such intense hardening was also reported earlier for other hybrid systems synthesized by HPT such as the Cu–Ta system [22,53] where the hardness after HPT was four times higher than for the initial material or the Al–Mg system [42–47] where the hardness after HPT was three times higher.

Based on these results, it is reasonable to assume that in hybrid

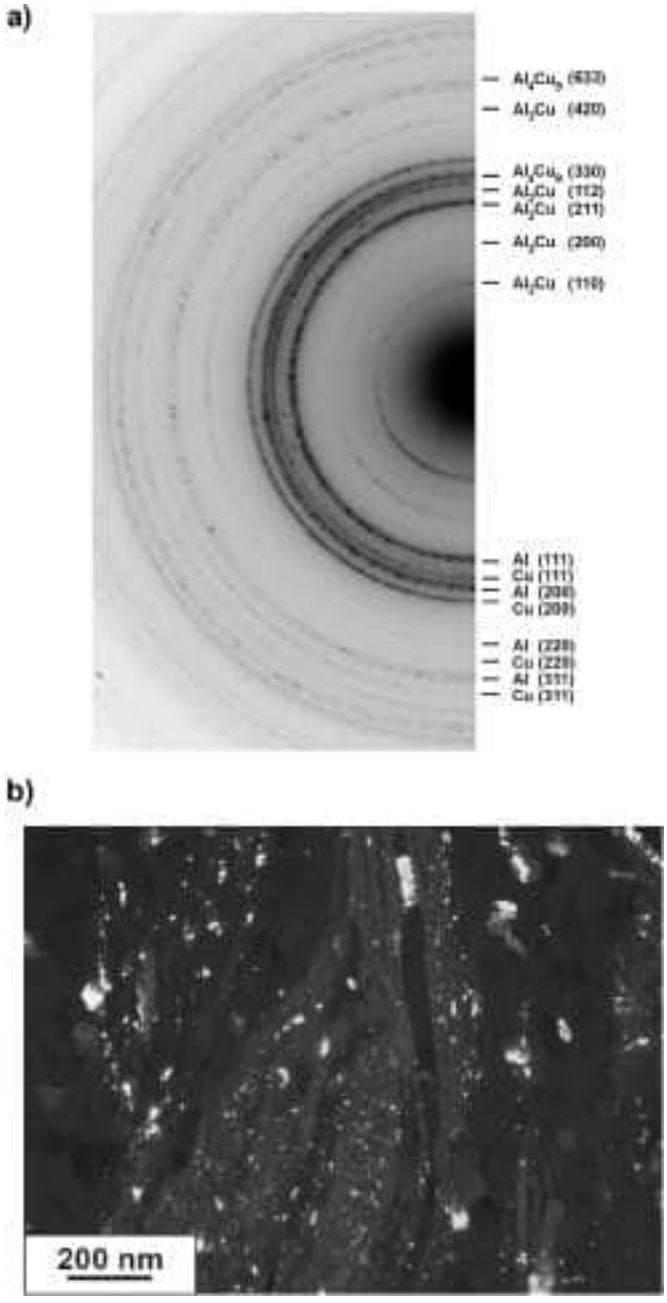

Fig. 6. (a) SAED patterns taken at the disk edge after HPT for 200 turns and (b) a dark field image from Al_2Cu (110) ring.

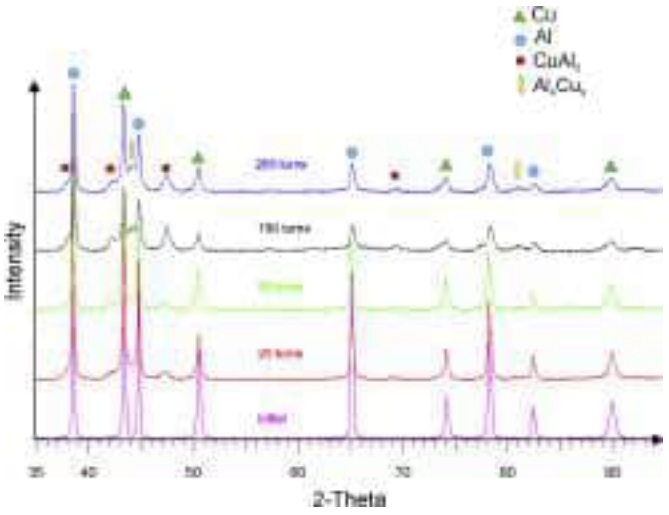

Fig. 7. XRD patterns from Al–Cu–Al system in an initial state and after HPT for 20, 50, 150 and 200 turns.

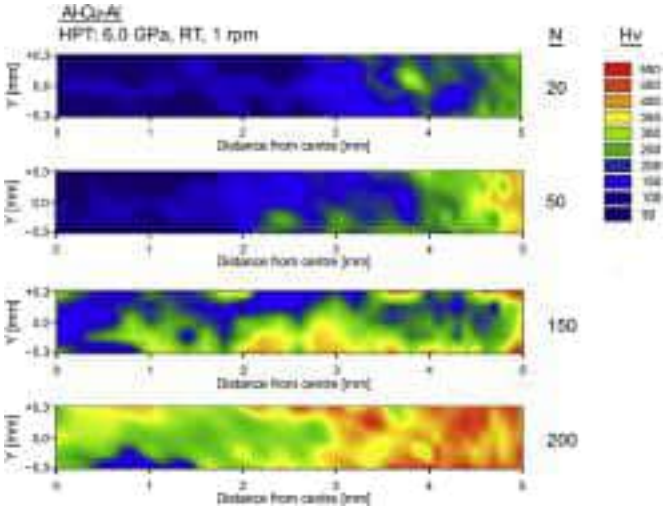

Fig. 8. Microhardness distributions maps for the Al–Cu–Al system after HPT for 20, 50, 150 and 200 turns.

systems produced by HPT processing the overall strength of the material is not governed exclusively by the grain refinement through the Hall-Petch relationship [80,81] but there is, in addition, a combination of various other strengthening mechanisms such as solid solution strengthening and precipitation hardening [82]. The value of the hardness increase based on the Hall-Petch relationship and solid solution strengthening may be expressed by the following equation [39]:

$$\Delta Hv = 1 \Big/ 3\left[H(wt.\%\ Cu) + Ho + kd^{-0.5}\right] \tag{1}$$

where H_o, H and k are material constants and d is the average grain size and, using the general relationship between yield strength (MPa) and hardness (Hv), Hv = $\sigma_y/3$ [83]. The solution strengthening from Cu in the Al matrix has a negligible effect in this case since it is only 7 MPa for each weight percent of Cu [84]. The strength from the presence of precipitates can be estimated from the Orowan model [85] which plays a significant role in the strengthening of composite materials [85,86]. Thus, the hardening effect from precipitates may be expressed by the following equation:

$$\Delta Hv_{prec} = \frac{Gb}{\pi}\left\{\frac{1}{d\left(1-\sqrt{f}\right)}\left[\frac{d\sqrt{f}}{d_{prec}}\ln\frac{d_{prec}}{r_o}+\ln d\right]-\frac{1}{d}\ln\frac{d}{r_o}\right\} \tag{2}$$

where G and b are the shear modulus (27 GPa) and the Burgers vector (0.274 nm) of the matrix element, respectively, r is the core cut-off radius in the dislocation line energy which is taken as ~1 nm, d_{prec} is the size of the reinforcing Al_2Cu and Al_4Cu_9 phases

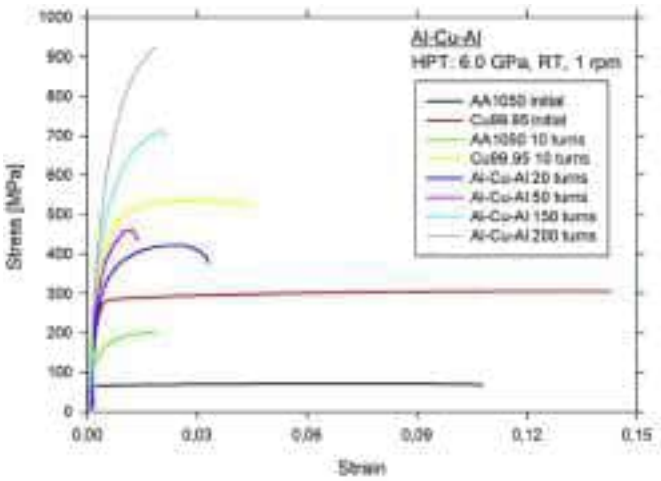

Fig. 9. Typical tensile engineering stress-strain curves for Al-1050 and 99.95Cu alloys in initial states and after HPT processing together with curves for the Al−Cu−Al system after HPT for 20, 50, 150 and 200 turns.

Table 1
The results of engineering tensile tests for initial materials and the Al−Cu−Al nanocomposites fabricated by HPT.

Sample	YS [MPa]	UTS [MPa]	Elongation [%]
Cu as-annealed	220 ± 5	280 ± 11	14 ± 4.8
Al as-annealed	70 ± 3	90 ± 5	11.5 ± 6.1
Cu HPT 10 turns	430 ± 11	525 ± 15	4 ± 2.0
Al HPT 10 turns	110 ± 7	200 ± 14	10.3 ± 3.1
Al−Cu−Al HPT 20 turns	280 ± 21	420 ± 30	3.1 ± 1.1
Al−Cu−Al HPT 50 turns	370 ± 27	460 ± 25	1.5 ± 0.6
Al−Cu−Al HPT 150 turns	540 ± 23	710 ± 34	1.7 ± 0.3
Al−Cu−Al HPT 200 turns	680 ± 22	910 ± 16	2.2 ± 0.5

and f is the fraction of these strengthening phases. In practice dislocation strengthening should also be considered as an active mechanism. However, because the structure of these materials was very complex and contained many nano elements, the dislocation density was only roughly determined and the sample after 200 revolutions revealed a large scatter of $\sigma_{ds} = 50-100$ MPa. Using data obtained in this study in equations (1) and (2) permits a direct estimate of the microhardness of the fabricated hybrid composites.

Using this approach and taking ~0.9% of Cu in the matrix as solid solution, $d \approx 240$ nm, $d_{prec} \approx 30$ nm and f ≈ 2.5%, the microhardness of the disk after 20 turns is calculated as Hv ≈ 224 ± 30. After 200 turns and taking ~5.65% of Cu in the matrix as solid solution, $d \approx 90$ nm, $d_{prec} \approx 15$ nm and f = 10.2%, the microhardness is calculated as Hv ≈ 435 ± 35. Both results are in excellent agreement with the experimental results as documented in Fig. 8. In practice, the presence of the intermetallic phases makes the largest contribution to the overall microhardness and for the sample processed through 200 turns this contribution is more than 50%.

The results presented in this study on the mechanical bonding of dissimilar metals by HPT demonstrates a very significant potential for the synthesis of nanocrystalline intermetallic-strengthened hybrid materials exhibiting extraordinary mechanical properties. It appears that the deformation-induced bonding of the Al and Cu phases gives a multi-layered structure and thereby provides a major driving force for the formation of the Al_2Cu and Al_4Cu_9 intermetallic phases. It is reasonable to anticipate the occurrence of similar effects when processing other dissimilar metal disks.

5. Summary and conclusions

- The synthesis of a new Al−Cu alloy system was demonstrated using conventional HPT processing at room temperature under 6.0 GPa at 1 rpm.
- HPT of the initial stack of Al−Cu−Al resulted in a strong joining of all layers, a fragmentation of Al and Cu layers, and their mixing and formation of a fine lamellar structure.
- HPT processing of this bimetallic system led to a strong grain refinement down to a grain size of ~10−20 nm which was accompanied by a very high microhardness and tensile results of about ~450 Hv and ~910 MPa of UTS.
- HPT promotes the solid-state reaction of Al and Cu elements so that there is the formation of Al_2Cu and Al_4Cu_9 phases as well as the dissolution of Al and Cu components in each matrix
- The major contribution to the overall strength or hardness is given by the intermetallic nanoparticles and it was estimated at about 50%.

CRediT authorship contribution statement

Piotr Bazarnik: Writing - original draft. **Aleksandra Bartkowska:** Formal analysis. **Barbara Romelczyk-Baishya:** Data curation. **Bogusława Adamczyk-Cieślak:** Formal analysis. **Jiaoyan Dai:** Methodology. **Yi Huang:** Data curation. **Małgorzata Lewandowska:** Methodology, Data curation, Writing - review & editing. **Terence G. Langdon:** Conceptualization, Supervision, Writing - review & editing.

Declaration of competing interest

The authors declare that they have no known competing financial interests or personal relationships that could have appeared to influence the work reported in this paper.

Acknowledgments

This work was carried out within a SONATINA 1 project: “Synthesis of novel hybrid materials using High-Pressure Torsion” financed by the Polish National Science Centre (Contract No. UMO-2017/24/C/ST8/00145). The work of three authors was supported by the European Research Council under ERC Grant Agreement No. 267464-SPDMETALS (YH, YH and TGL).

References

[1] K. Lu, The future of metals, Science 328 (2010) 319−320.
[2] J. Cao, J. Liu, X. Song, X. Lin, J. Feng, Diffusion bonding of TiAl inter-metallic and Ti_3AlC_2 ceramic: interfacial Microstructure and joining properties, Mater. Des. 56 (2014) 115−121.
[3] J.W. Kaczmar, K. Pietrzak, W. Włosiński, The production and application of metal matrix composite materials, J. Mater. Process. Technol. 106 (2000) 58−67.
[4] P. Bazarnik, B. Adamczyk-Cieślak, A. Gałka, B. Płonka, L. Śnieżek, M. Cantoni, M. Lewandowska, Mechanical and microstructural characteristics of Ti6Al4V/AA2519 and Ti6Al4V/AA1050/AA2519 laminates manufactured by explosive welding, Mater. Des. 111 (2016) 146−157.
[5] R.Z. Valiev, T.G. Langdon, Principles of equal-channel angular pressing as a processing tool for grain refinement, Prog. Mater. Sci. 51 (2006) 881−981.
[6] A.P. Zhilyaev, T.G. Langdon, Using high-pressure torsion for metal processing: fundamentals and applications, Prog. Mater. Sci. 53 (2008) 893−979.
[7] Y. Huang, P. Bazarnik, D. Wan, D. Luo, P.H.R. Pereira, M. Lewandowska, J. Yao, B.E. Hayden, T.G. Langdon, The fabrication of graphene-reinforced Al-based nanocomposites using high-pressure torsion, Acta Mater. 164 (2019) 499−511, https://doi.org/10.1016/j.actamat.2018.10.060.
[8] S.N. Alhajeri, K.J. Al-Fadhalah, A.I. Almazrouee, T.G. Langdon, Microstructure and microhardness of an Al-6061 metal matrix composite processed by high-pressure torsion, Mater. Char. 118 (2016) 270−278, https://doi.org/10.1016/j.matchar.2016.06.003.

[9] M. Kawasaki, Y. Huang, C. Xu, M. Furukawa, Z. Horita, T.G. Langdon, A quantitative study of cavity development in the tensile testing of an aluminum metal matrix composite processed by equal-channel angular pressing, Mater. Sci. Eng. 410–411 (2005) 402–407.

[10] Y.Z. Tian, S.D. Wu, Z.F. Zhang, R.B. Figueiredo, N. Gao, T.G. Langdon, Microstructural evolution and mechanical properties of a two-phase Cu–Ag alloy processed by high-pressure torsion to ultrahigh strains, Acta Mater. 59 (2011) 2783–2796.

[11] M.R. Akbarpour, H. Mousa Mirabad, S. Alipour, H.S. Kim, Enhanced tensile properties and electrical conductivity of Cu-CNT nanocomposites processed via the combination of flake powder metallurgy and high pressure torsion methods, Mater. Sci. Eng. 773 (2020) 138888.

[12] L. Bian, W. Liang, G. Xie, W. Zhang, J. Xue, Enhanced ductility in an Al–Mg2Si in situ composite processed by ECAP using a modified BC route, Mater. Sci. Eng. 528 (2011) 3463–3467.

[13] I. Sabirov, R. Pippan, Formation of a W–25% Cu nanocomposite during high pressure torsion, Scripta Mater. 52 (2005) 1293–1298.

[14] P. Bazarnik, S. Nosewicz, B. Romelczyk-Baishya, M. Chmielewski, A. Strojny Nędza, J. Maj, Y. Huang, M. Lewandowska, T.G. Langdon, Effect of spark plasma sintering and high-pressure torsion on the microstructural and mechanical properties of a Cu–SiC composite, Mater. Sci. Eng. 766 (2019) 138350.

[15] P. Bazarnik, Y. Huang, M. Lewandowska, T.G. Langdon, Structural impact on the Hall–Petch relationship in an Al–5Mg alloy processed by high-pressure torsion, Mater. Sci. Eng. 626 (2015) 9–15.

[16] P. Bazarnik, Y. Huang, M. Lewandowska, T.G. Langdon, Enhanced grain refinement and microhardness by hybrid processing using hydrostatic extrusion and high-pressure torsion, Mater. Sci. Eng. 712 (2018) 513–520.

[17] Y. Huang, R.B. Figueiredo, T. Baudin, F. Brisset, T.G. Langdon, Evolution of strength and homogeneity in a magnesium AZ31 alloy processed by high-pressure torsion at different temperatures, Adv. Eng. Mater. 14 (2012) 1018–1026.

[18] K. Edalati, S. Toh, M. Watanabe, Z. Horita, In situ production of bulk intermetallic-based nanocomposites and nanostructured intermetallics by high-pressure torsion, Scripta Mater. 66 (2012) 386–389.

[19] Y. Sun, M. Aindow, R.J. Hebert, T.G. Langdon, E.J. Lavernia, High-pressure torsion-induced phase transformations and grain refinement in Al/Ti composites, J. Mater. Sci. 52 (2017) 12170–12184.

[20] A. Bachmaier, R. Pippan, High-pressure torsion deformation induced phase transformations and formations: new material combinations and advanced properties, Mater. Trans. 60 (2019) 1256–1269.

[21] J. Han, K.D. Liss, T.G. Langdon, M. Kawasaki, Synthesis of a bulk nanostructured metastable Al alloy with extreme supersaturation of Mg, Sci. Rep. 9 (2019) 17186.

[22] T. Mousavi, J. Dai, P. Bazarnik, P.H.R. Pereira, Y. Huang, M. Lewandowska, T.G. Langdon, Fabrication and characterization of nanostructured immiscible Cu–Ta alloys processed by high-pressure torsion, J. Alloys Compd. 832 (2020) 155007.

[23] A.P. Zhilyaev, B.-K. Kim, G.V. Nurislamova, M.D. Baró, J.A. Szpunar, T.G. Langdon, Orientation imaging microscopy of ultrafine-grained nickel, Scripta Mater. 46 (2002) 575–580.

[24] A.P. Zhilyaev, G.V. Nurislamova, B.-K. Kim, M.D. Baró, J.A. Szpunar, T.G. Langdon, Experimental parameters influencing grain refinement and microstructural evolution during high-pressure torsion, Acta Mater. 51 (2003) 753–765.

[25] J. Wongsa-Ngam, M. Kawasaki, T.G. Langdon, A comparison of microstructures and mechanical properties in a Cu–Zr alloy processed using different SPD techniques, J. Mater. Sci. 48 (2013) 4653–4660.

[26] V.V. Stolyarov, Y.T. Zhu, T.C. Lowe, R.K. Islamgaliev, R.Z. Valiev, Processing nanocrystalline Ti and its nanocomposites from micrometer-sized Ti powder using high pressure torsion, Mater. Sci. Eng. 282 (2000) 78–85, https://doi.org/10.1016/S0921-5093(99)00764-9.

[27] R. Kulagin, A. Mazilkin, Y. Beygelzimer, D. Savvakin, I. Zverkova, D. Oryshych, H. Hahn, Influence of High Pressure Torsion on structure and properties of Zr-Ti-Nb alloy synthesized from TiH2, ZrH2 and Nb powders, Mater. Lett. 233 (2018) 31–34.

[28] A.P. Zhilyaev, G. Ringot, Y. Huang, J.M. Cabrera, T.G. Langdon, Mechanical behavior and microstructure properties of titanium powder consolidated by high-pressure torsion, Mater. Sci. Eng. 688 (2017) 498–504, https://doi.org/10.1016/j.msea.2017.02.032.

[29] C. Silva, L.A. Montoro, D.A.A. Martins, P.A. Machado, P.H.R. Pereira, B.M. Gonzalez, T.G. Langdon, R.B. Figueiredo, A. Isaac, Interface structures in Al-Nb2O5 nanocomposites processed by high-pressure torsion at room temperature, Mater. Char. 162 (2020) 110222.

[30] A.P. Zhilyaev, A.A. Gimazov, G.I. Raab, T.G. Langdon, Using high-pressure torsion for the cold-consolidation of copper chips produced by machining, Mater. Sci. Eng. 486 (2008) 123–126.

[31] M.M. Castro, A.P. Carvalho, P.H.R. Pereira, A.C.I. Neta, R.B. Figueiredo, T.G. Langdon, Consolidation of magnesium and magnesium alloy machine chips using high-pressure torsion, Mater. Sci. Forum 941 (2018) 851–856.

[32] M.M. Castro, P.H.R. Pereira, A. Isaac, R.B. Figueiredo, T.G. Langdon, Development of a magnesium-alumina composite through cold consolidation of machining chips by high-pressure torsion, J. Alloys Compd. 780 (2019) 422–427.

[33] M.M. Castro, P.H.R. Pereira, R.B. Figueiredo, T.G. Langdon, Developing magnesium-based composites through high-pressure torsion, Letters Mater 9 (2019) 541–545.

[34] T. Miyazaki, D. Terada, Y. Miyajima, C. Suryanarayana, R. Murao, Y. Yokoyama, K. Sugiyama, M. Umemoto, Y. Todaka, N. Tsuji, Synthesis of non-equilibrium phases in immiscible metals mechanically mixed by high pressure torsion, J. Mater. Sci. 46 (2011) 4296–4301.

[35] K. Oh-ishi, K. Edalati, H.S. Kim, K. Hono, Z. Horita, High-pressure torsion for enhanced atomic diffusion and promoting solid-state reactions in the aluminum–copper system, Acta Mater. 61 (2013) 3482–3489.

[36] R. Kulagin, Y. Beygelzimer, Yu Ivanisenko, A. Mazilkin, B. Straumal, H. Hahn, Instabilities of interfaces between dissimilar metals induced by high pressure torsion, Mater. Lett. 222 (2018) 172–175.

[37] M.M. Castro, S. Sabbaghianrad, P.H.R. Pereira, E.M. Mazzer, A. Isaac, T.G. Langdon, R.B. Figueiredo, A magnesium-aluminium composite produced by high-pressure torsion, J. Alloys Compd. 804 (2019) 421–426.

[38] O. Bouaziz, H.S. Kim, Y. Estrin, Architecturing of metal-based composites with concurrent nanostructuring: a new paradigm of materials design, Adv. Eng. Mater. 15 (2013) 336–340.

[39] B. Ahn, A.P. Zhilyaev, H.-J. Lee, M. Kawasaki, T.G. Langdon, Rapid synthesis of an extra hard metal matrix nanocomposite at ambient temperature, Mater. Sci. Eng. 635 (2015) 109–117.

[40] J.-K. Han, D.K. Han, G.Y. Liang, J.-I. Jang, T.G. Langdon, M. Kawasaki, Direct bonding of aluminum–copper metals through high-pressure torsion processing, Adv. Eng. Mater. 20 (2018) 1800642.

[41] J.-K. Han, J. il Jang, T.G. Langdon, M. Kawasaki, Bulk-state reactions and improving the mechanical properties of metals through high-pressure torsion, Mater. Trans. 60 (2019) 1131–1138.

[42] J.-K. Han, T. Herndon, J.-I. Jang, T.G. Langdon, M. Kawasaki, Synthesis of hybrid nanocrystalline alloys by mechanical bonding through high-pressure torsion, Adv. Eng. Mater. 22 (2020) 1901289.

[43] G.F. Korznikova, R. Kabirov, K. Nazarov, R. Khisamov, R. Shayakhmetov, E. Korznikova, G. Khalikova, R. Mulyukov, Influence of constrained high-pressure torsion on microstructure and mechanical properties of an aluminum-based metal matrix composite, JOM (2020), https://doi.org/10.1007/s11837-020-04152-1.

[44] M. Kawasaki, J.-K. Han, D.-.H. Lee, J.-I. Jang, T.G. Langdon, Fabrication of nanocomposites through diffusion bonding under high-pressure torsion, J. Mater. Res. 33 (2018) 2700–2710.

[45] M. Kawasaki, B. Ahn, H.-J. Lee, A.P. Zhilyaev, T.G. Langdon, Using high-pressure torsion to process an aluminum-magnesium nanocomposite through diffusion bonding, J. Mater. Res. 31 (2016) 88–99.

[46] B. Ahn, H.-J. Lee, I.-C. Choi, M. Kawasaki, J.-I. Jang, T.G. Langdon, Micro-mechanical behavior of an exceptionally strong metal matrix nanocomposite processed by high-pressure torsion, Adv. Eng. Mater. 18 (2016) 1001–1008.

[47] J.-K. Han, H.-J. Lee, J.-I. Jang, M. Kawasaki, T.G. Langdon, Micro-mechanical and tribological properties of aluminum-magnesium nanocomposites processed by high-pressure torsion, Mater. Sci. Eng. 684 (2017) 318.

[48] M. Kawasaki, T.G. Langdon, Using severe plastic deformation to fabricate strong metal matrix composites, Mater. Res. 20 (2017) 46–52.

[49] M. Kawasaki, T.G. Langdon, Fabrication of high strength hybrid materials through the application of high-pressure torsion, Acta Phys. Polon. A 134 (2018) 615–622.

[50] M. Kawasaki, S.-H. Jung, J.-M. Park, J. Lee, J.-I. Jang, J.-K. Han, Mechanical bonding of aluminum hybrid alloy systems through high-pressure torsion, Adv. Eng. Mater. 22 (2020) 1900483.

[51] V.N. Danilenko, S.N. Sergeev, J.A. Baimova, G.F. Korznikova, K.S. Nazarov, R. Kh Khisamov, A.M. Glezer, R.R. Mulyukov, An approach for fabrication of Al-Cu composite by high pressure torsion, Mater. Lett. 236 (2019) 51–55.

[52] A. Korneva, B. Straumal, R. Chulist, A. Kilmametov, P. Bała, G. Cios, N. Schell, P. Zięba, Grain refinement of intermetallic compounds in the Cu–Sn system under high pressure torsion, Mater. Lett. 179 (2016) 12–15.

[53] N. Ibrahim, M. Peterlechner, F. Emeis, M. Wegner, S.V. Divinski, G. Wilde, Mechanical alloying via high-pressure torsion of the immiscible Cu50Ta50 system, Mater. Sci. Eng. 685 (2017) 19–30.

[54] Y. Qi, A. Kosinova, A.R. Kilmametov, B.B. Straumal, E. Rabkin, Plastic flow and microstructural instabilities during high-pressure torsion of Cu/ZnO composites, Mater. Char. 145 (2018) 389–401.

[55] S.O. Rogachev, R.V. Sundeev, V.M. Khatkevich, Evolution of the structure and strength of steel/vanadium alloy/steel hybrid material during severe plastic deformation, Mater. Lett. 173 (2016) 123–126.

[56] S.O. Rogachev, S.A. Nikulin, A.B. Rozhnov, V.M. Khatkevich, T.A. Nechaykina, M.V. Gorshenkov, R.V. Sundeev, Multilayer “steel/vanadium alloy/steel” hybrid material obtained by high-pressure torsion at different temperatures, Metall. Mater. Trans. A 48 (2017) 6091–6101.

[57] S.O. Rogachev, R.V. Sundeev, N.Yu Tabachkova, High pressure torsion-induced amorphous phase in a multilayer V-10Ti-5Cr/Zr-2.5Nb/V-10Ti-5Cr hybrid material, Mater. Lett. 234 (2019) 220–223.

[58] D. Hernández-Escobar, Z.U. Raman, H. Yilmazer, M. Kawasaki, C.J. Boehlert, Microstructural evolution and intermetallic formation in Zn-Mg hybrids processed by high-pressure torsion, Philos. Mag. A 99 (2019) 557–584.

[59] R.B. Figueiredo, P.H.R. Pereira, M.T.P. Aguilar, P.R. Cetlin, T.G. Langdon, Using finite element modeling to examine the temperature distribution in quasi-constrained high-pressure torsion, Acta Mater. 60 (2012) 3190–3198.

[60] A. Loucif, R.B. Figueiredo, T. Baudin, F. Brisset, R. Chemam, T.G. Langdon, Effect of ageing on microstructural development in an Al-Mg-Si alloy processed by high-pressure torsion, J. Mater. Sci. 47 (2012) 7815–7820.

[61] R.M. Molak, K. Paradowski, T. Brynk, L. Ciupinski, Z. Pakiela, K.J. Kurzydlowski, Measurement of mechanical properties in a 316L stainless steel welded joint, Int. J. Pres. Ves. Pip. 86 (2009) 43–47.
[62] Y. Huang, M. Kawasaki, T.G. Langdon, Influence of anvil alignment on shearing patterns in high-pressure torsion, Adv. Eng. Mater. 15 (2013) 747–755.
[63] Y. Huang, M. Kawasaki, T.G. Langdon, An investigation of flow patterns and hardness distributions using different anvil alignments in high-pressure torsion, J. Mater. Sci. 48 (2013) 4533–4542.
[64] Y. Huang, M. Kawasaki, T.G. Langdon, An evaluation of the shearing patterns introduced by different anvil alignments in high-pressure torsion, J. Mater. Sci. 49 (2014) 3146–3157.
[65] M. Murayama, Z. Horita, K. Hono, Microstructure of two-phase Al–1.7 at% Cu alloy deformed by equal-channel angular pressing, Acta Mater. 49 (2001) 21–29.
[66] X. Xu, Q. Zhang, N. Hu, Y. Huang, T.G. Langdon, Using an Al–Cu binary alloy to compare processing by multi-axial compression and high-pressure torsion, Mater. Sci. Eng. 588 (2013) 280–287.
[67] Y.W. Ma, K.B. Yoon, Assessment of tensile strength using small punch test for transversely isotropic aluminum 2024 alloy produced by equal channel angular pressing, Mater. Sci. Eng. 527 (2010) 3630–3638.
[68] I.F. Mohamed, Y. Yonenaga, S. Lee, K. Edalati, Z. Horita, Age hardening and thermal stability of Al–Cu alloy processed by high-pressure torsion, Mater. Sci. Eng. 627 (2015) 111–118.
[69] Y.W. Ma, J.W. Choi, K.B. Yoon, Change of anisotropic tensile strength due to amount of severe plastic deformation in aluminum 2024 alloy, Mater. Sci Eng. A 529 (2011) 1–8.
[70] M. Kawasaki, J. Foissey, T.G. Langdon, Development of hardness homogeneity and superplastic behaviour in an aluminum–copper eutectic alloy processed by high-pressure torsion, Mater. Sci Eng. A 561 (2013) 118–125.
[71] X.H. An, Q.Y. Lin, S.D. Wu, Z.F. Zhang, R.B. Figueiredo, N. Gao, T.G. Langdon, The influence of stacking fault energy on the mechanical properties of nanostructured Cu and Cu–Al alloys processed by high-pressure torsion, Scripta Mater. 64 (2011) 954–957.
[72] A.K. Parimi, P.S. Robi, S.K. Dwivedy, Severe plastic deformation of copper and Al–Cu alloy using multiple channel-die compression, Mater. Des. 32 (2011) 1948–1956.
[73] T. Fujita, Z. Horita, T.G. Langdon, Using grain boundary engineering to evaluate the diffusion characteristics in ultrafine-grained Al–Mg and Al–Zn alloys, Mater. Sci. Eng. 371 (2004) 241–250.
[74] A. Alhamidi, K. Edalati, Z. Horita, S. Hirosawa, K. Matsuda, D. Terada, Softening by severe plastic deformation and hardening by annealing of aluminum–zinc alloy: significance of elemental and spinodal decompositions, Mater. Sci. Eng. 610 (2014) 17–27.
[75] S.V. Divinski, J. Ribbe, D. Baither, G. Schmitz, G. Reglitz, H. Rosner, K. Sato, Y. Estrin, G. Wilde, Nano- and micro-scale free volume in ultrafine grained Cu–1 wt.%Pb alloy deformed by equal channel angular pressing, Acta Mater. 57 (2009) 5706–5717.
[76] G.F. Korznikova, K.S. Nazarov, R.Kh Khisamov, S.N. Sergeev, R.R. Mulyukov, Intermetallic growth kinetics and microstructure evolution in Al-Cu-Al metal-matrix composite processed by high pressure torsion, Mater. Lett. 253 (2019) 412–415.
[77] C.C. Hsieh, M.S. Shi, W. Wu, Growth of intermetallic phases in Al/Cu composites at various annealing temperatures during the ARB process, Met. Mater. Int. 18 (2012) 1–6.
[78] G. Huang, W. Hou, J. Li, Y. Shen, Development of surface composite based on Al-Cu system by friction stir processing: evaluation of microstructure, formation mechanism and wear behaviour, Surf. Coating. Technol. 344 (2018) 30–42.
[79] L. Yang, B.X. Mi, L. Lin, H.J. Huang, X.P. Lin, X.G. Yuan, Formation sequence of interface intermetallic phases of cold rolling Cu/Al clad metal sheet in annealing process, Mater. Sci. Forum (2013) 600–605.
[80] E.O. Hall, The deformation and ageing of mild steel: III Discussion of results, Proc. Phys. Soc. B 64 (1951) 747–753.
[81] N.J. Petch, The cleavage strength of polycrystals, J. Iron Steel Inst. 174 (1953) 25–28.
[82] T. Shanmugasundaram, M. Heilmaier, B.S. Murty, V. Subramanya Sarma, On the Hall–Petch relationship in a nanostructured Al–Cu alloy, Mater. Sci. Eng. 527 (2010) 7821–7825.
[83] D. Tabor, The hardness of solids, Rev. Phys. Technol. 1 (1970) 145–179.
[84] ASM Metals Reference Book, ASM International, Materials Park, OH, 1984.
[85] E. Orowan, Fracture and strength of solids, Rep. Prog. Phys. 12 (1949) 185–232.
[86] S. Alexandrov, E. Lyamina, Extension of Orowan's method to analysis of rolling of three-layer sheets, Procedia Eng 207 (2017) 1391–1396.

Journal of Alloys and Compounds 832 (2020) 155007

Contents lists available at ScienceDirect

Journal of Alloys and Compounds

journal homepage: http://www.elsevier.com/locate/jalcom

Fabrication and characterization of nanostructured immiscible Cu–Ta alloys processed by high-pressure torsion

Tayebeh Mousavi [a], Jiaoyan Dai [b, **], Piotr Bazarnik [c], Pedro Henrique R. Pereira [d], Yi Huang [e, f, *], Malgorzata Lewandowska [c], Terence G. Langdon [f]

[a] Materials Department, University of Oxford, Oxford, OX1 3PH, UK
[b] School of Materials and Chemical Engineering, Ningbo University of Technology, Ningbo, 315211, PR China
[c] Faculty of Materials Science and Engineering, Warsaw University of Technology, Woloska 141, 02-507, Warsaw, Poland
[d] Department of Metallurgical and Materials Engineering, Universidade Federal de Minas Gerais, Belo Horizonte, MG, 31270-901, Brazil
[e] Department of Design and Engineering, Faculty of Science and Technology, Bournemouth University, Poole, Dorset, BH12 5BB, UK
[f] Materials Research Group, Department of Mechanical Engineering, University of Southampton, Southampton, SO17 1BJ, UK

ARTICLE INFO

Article history:
Received 15 March 2020
Accepted 31 March 2020
Available online 4 April 2020

Keywords:
Cu-Ta alloys
High-pressure torsion
Nanostructured materials
Immiscible solid solution
Severe plastic deformation

ABSTRACT

Nanostructured Cu–Ta alloys show great potential as high strength nanocrystalline materials due to their excellent mechanical properties and limited grain growth at high temperatures. This report describes the fabrication of nanostructured immiscible Cu–Ta alloys in bulk by high-pressure torsion (HPT) using a stack of Cu/Ta/Cu discs at room temperature. A microstructural study after HPT processing showed that the internal Ta layer breaks into small individual flakes which distribute uniformly over the Cu matrix through increases in the numbers of HPT turns. There is solid-state diffusion between the Cu and Ta when the HPT processing increases to 100 turns due to microstructural refinement and increasing crystalline defects. After processing through 150 turns, a composite microstructure of two phases is formed including supersaturated Cu–Ta solid solutions ($Cu_{81}Ta_{19}$ and $Ta_{78}Cu_{22}$ alloys) with a crystallite size of ~35–45 nm. This fine microstructure produces exceptional mechanical properties including a high hardness of over 350 Hv corresponding to ~3.43 GPa, a tensile strength of ~1300 MPa and a tensile elongation of about 40%.

1. Introduction

Nanostructured alloys have attracted significant interest due to their unique sets of properties which are not achievable in coarse-grained polycrystalline materials [1,2]. Non-equilibrium solid solutions have also drawn attention as they can evolve as nanoscale microstructures through processing and then form well-dispersed nanoscale composites upon annealing at elevated temperatures [3]. Both simulations and experiments indicate remarkable physical and mechanical properties for this new class of material. The Cu–Ta system is one of these immiscible systems with almost zero solubility of Cu(Ta) in Ta(Cu) at room temperature (RT) [4].

Several processing methods are available for producing nanocrystalline microstructures consisting of solid solutions having different elements. For example, processing through the introduction of severe plastic deformation (SPD) has been used successfully over the last two decades to generate non-equilibrium microstructures in a range of metals and alloys [5–7]. Potential SPD techniques, including equal-channel angular pressing (ECAP) [8,9], accumulative roll bonding (ARB) [10] and high-pressure torsion (HPT) [11–13], have the potential of not only producing nanocrystalline microstructures but also of generating alloys of immiscible systems due to the extra crystalline defects and dislocations that are introduced into the matrix through the SPD processing. This excess of defects will thereby facilitate diffusion in these systems leading to the production of non-equilibrium solid solutions.

In general, the HPT process is usually considered the most effective procedure for achieving exceptional grain refinement, typically to the nanometer range in many systems, and this has become an established processing method for studying nanocrystalline and non-equilibrium solid solutions. In HPT processing,

* Corresponding author. Department of Design and Engineering, Faculty of Science and Technology, Bournemouth University, Poole, Dorset, BH12 5BB, UK.
** Corresponding author. School of Materials and Chemical Engineering, Ningbo University of Technology, Ningbo, 315211, PR China
E-mail addresses: jydai@nbut.edu.cn (J. Dai), yhuang2@bournemouth.ac.uk (Y. Huang).

https://doi.org/10.1016/j.jallcom.2020.155007
0925-8388/

grain refinement may be achieved without cracking due to the imposed hydrostatic pressure which effectively prevents the propagation of fracture during the torsional straining [14]. Recently, FEM modelling [15–18] and experimental observations on two phase materials such as duplex stainless steel [19–24] and Cu–Ag alloys [25] demonstrated that, in addition to the in-plane shear strain, there is also mass transfer within the samples in HPT due to the development of turbulent eddy flows within the sample cross-sections during the processing [26]. It is evident that this will assist in the redistribution of metal components in an immiscible system.

The synthesis of novel nanostructured alloys formed from forced solid solutions, especially for the non-equilibrium solid solutions such as Cu and immiscible solute species, has been the focus of some recent studies [27,28]. For example, mechanical alloying has been used to generate Cu-based powders composed of immiscible alloying elements such as Ta [29] and Mo [30] where these systems have shown moderate to extraordinary high microstructural stability at elevated temperatures. There are also recent reports on the thermal stability and microstructure of high strength nanocrystalline Cu–Ta alloys [29]. For example, isothermal annealing of a Cu–10% Ta powder produced via high-energy cryogenic mechanical alloying led to a nanocrystalline, two-phase composite structure of spheroidal Ta particles and nanolamellar Ta dispersed in a Cu-rich Cu–2% Ta alloyed matrix [29]. It is important to note also that the consolidation of nanostructured powder into a bulk form is often very challenging because of limitations associated with the processing methods that are not easily scalable or due to uncontrolled grain growth of the non-equilibrium structures during processing. Despite the excellent properties achieved in these Cu–Ta alloys via mechanical alloying, there is only a limited report on the fabrication of nanostructure Cu–Ta alloys through processing a mixture of bulk Cu and bulk Ta, where the initial disc samples were a $Cu_{50}Ta_{50}$ system consisting of 19 Cu foils and 18 Ta foils assembled alternately in a single stack and successfully processed by HPT to 10, 30, 50, 100 and 150 turns under a pressure of 4.0 GPa [31]. It is noted that the HPT-processed 150 turns Cu–Ta alloy showed a superior thermal stability even after annealing at 1000 °C for 1 h [31].

The HPT processing of the $Cu_{50}Ta_{50}$ system [31] has limitations in its practical fabrication due to the difficulty and time required to prepare Cu foils and Ta foils, where the foil thickness is only ~24.3 μm, in order to make the 0.9 mm thick disc sample of stacked 19 Cu foils and 18 Ta foils before HPT processing. To improve the efficiency in materials preparation and processing, the present research was initiated to process immiscible Cu–Ta alloys using bulk Cu discs and Ta discs (thickness 0.8 mm for each Cu disc and Ta disc) which were packed in a sandwich-like structure of Cu/Ta/Cu for HPT processing. The microstructures and mechanical properties of the HPT-processed Cu–Ta alloys were subsequently investigated in detail. As will be demonstrated, the use of HPT processing produces a material having exceptionally high hardness and excellent tensile strength.

2. Experimental materials and procedures

The experiments were conducted using rods of oxygen-free Cu (99.95 wt%) and Ta (99.9 wt%). The Cu rod was first annealed for 1 h at 673 K whereas the Ta rod was received in an annealed state. Both the annealed Cu rod and the as-received Ta rod were cut into discs with diameters of 10 mm and thicknesses of 1.1 mm and this was followed by grinding to a thickness of 0.8 mm. Then a Ta disc was placed between two Cu discs in a sandwich-like configuration and the piled discs were processed by HPT at room temperature through total numbers of turns, *N*, of 0.25, 5, 10, 60, 100 and up to a maximum of 150 turns. The HPT processing was conducted using an applied pressure of 6.0 GPa and a rotation speed of 1 rpm under quasi-constrained conditions where there is a small outflow of material around the edge of the disc between the two anvils [32].

Various characterization techniques and hardness measurements were carried out on the processed discs in order to provide information on the microstructural evolution and mechanical properties achieved through the HPT processing.

The X-ray diffraction (XRD) was performed on a Rigaku SmartLab employing Cu Kα radiation (wavelength $\lambda = 0.154$ nm) at 45 kV and a tube current of 200 mA. The XRD measurements covered an angular 2θ range from 30° to 130° using a scanning step of 0.04° and a scanning speed of 2° min^{-1}. Microstructural characterization was conducted on the cross-sections of the discs using analytical scanning electron microscopy (SEM). A JEOL 5510 SEM with OI SDD detector operating at 20 kV accelerating voltage and an Hitachi SU-8000 SEM operating at 10 kV were used for microstructural examinations. The specimens were prepared by cutting the processed disc into halves along the diameter and polishing the cross-sections using an Hitachi Ion Milling System IM-4000. Since ion milling is a damageless process, this polishing eliminates all deformation and oxide layers so that the surface quality was sufficiently good for SEM analysis. High resolution microstructural analysis was carried out using a transmission electron microscope (TEM, JEOL3000F) on cross-sectional samples made by the lift-out technique in focused ion beam (FIB) milling. The polished surface of the 150 turns sample was also observed using a scanning transmission electron microscope (STEM, Hitachi HD-2700) in both bright-field (BF) and high-angle annular dark field (HAADF or Z-contrast) modes to reveal the grain structures at higher magnifications.

Measurements of the Vickers microhardness, Hv, were carried out using an FM300 microhardness tester equipped with a Vickers indenter. For these measurements, the HPT-processed discs were carefully ground with SiC papers in order to remove layers of 0.1 mm thickness from the disc surfaces. The discs were then polished with 9, 6, 3 and 1 μm diamond suspensions and polished to a mirror-like surface with 0.04 μm colloidal silica. Each hardness indentation was performed using a load of 200 gf and a dwell time of 15 s. Separate measurements were carried out at points along the disc diameter from the bottom to the top of the cross-section. The minimum distance between consecutive indentations was 150 μm in order to avoid any interference between the individual measurements. Colour-coded contour maps were constructed in which the individual hardness values were displayed using a colour scale and these values were plotted as a function of location on the cross-sections of the discs.

Tensile specimens were cut from the HPT-processed 150 turns samples. Following earlier practice [33], two tensile specimens were prepared from each disc using electro-discharge machining with these specimens arranged symmetrically on either side of the disc centre. The miniature tensile specimens had gauge lengths and widths of 1 mm. These specimens were then tested in tension at room temperature using a Zwick 30 KN Proline testing machine operating at a constant rate of cross-head displacement with an initial strain rate of 1.0×10^{-3} s^{-1}. The elongations were calculated by measuring the gauge length after tensile testing by putting the two parts of the broken tensile specimen together under an optical microscope. Three tests were repeated for each tensile curve.

3. Experimental results

3.1. Initial microstructural characteristics after HPT processing

The cross-sections of the HPT-processed samples were first observed using an optical microscope (OM) to examine the evolution of the stacked Cu–Ta–Cu layers. As shown in Fig. 1, after 0.25

HPT turn the bulk Ta layer is clearly visible between the two Cu bulk layers and there are sharp and distinct Cu–Ta interfaces. After 5 and 10 turns of HPT processing, in some areas the Cu–Ta boundaries disappear but in some regions the Cu–Ta interfaces are distinct but with significant curvature. When the HPT processing increases to 60 and 100 turns, the Cu and Ta appear to mix well in the disc edge area where there is a grey background colour which lies between the dark Ta and bright Cu and at the edge there are also no obvious Cu–Ta boundaries at the magnification used for the OM. However, in the central area after 60 and 100 HPT turns there is evidence for thin and fine Cu–Ta interfaces. After 150 turns of HPT processing, no obvious Cu–Ta boundaries are observed at any position in the OM, thereby indicating a fully-homogeneous mixing of Cu and Ta. Based on these observations from Fig. 1, it is concluded that, by increasing the numbers of HPT turns, there is a gradual increase in homogeneity as a result of mixing of the Cu and Ta and this homogeneity occurs initially in the edge regions but gradually expands to fill the disc with increasing numbers of HPT turns.

In order to evaluate the homogeneity of the 150 turns sample at a finer scale, the cross-section of the sample was observed by SEM at different positions within the central area and the edge area of the disc: Examples are shown in Fig. 2(a) and (b) where the upper image depicts the cross-section after 150 turns and marks the two positions for the subsequent SEM images. It is apparent from these images that both areas show a layered microstructure which is slightly finer within the region close to the edge. Thus, in the central region the layers are almost straight whereas in the edge region the layers are curved. This is attributed to the strain gradient imposed in the HPT processing since higher strains are attained at the edge than in the central region. Elemental maps of Cu and Ta are presented at higher magnifications in Fig. 2(c–f) for the small regions marked by squares in Fig. 2(a) and (b). As can be seen, the layered microstructure includes Cu-rich regions and Ta-rich regions at the fine scale. Furthermore, the Cu-rich regions contain Ta and similarly the Ta-rich regions contain Cu, thereby demonstrating that the Cu and Ta have dissolved into each other. The EDX line-scans across these layers shown in Fig. 2(g–h) indicate that the Cu layers contain about 18–21 at.% Ta and the Ta layers contain about 19–23 at.% Cu. Also, the Cu-rich and Ta-rich layers are within a few micrometers in both the central and edge regions. Thus, HPT processing through 150 turns leads to a fine layered microstructure and this structure uniformly covers the whole sample. It is important to note that in this condition there is no detectable pure Cu or pure Ta remaining in the microstructure and instead the immiscible Cu and Ta are visibly mixed to create Cu–Ta alloys through the HPT processing.

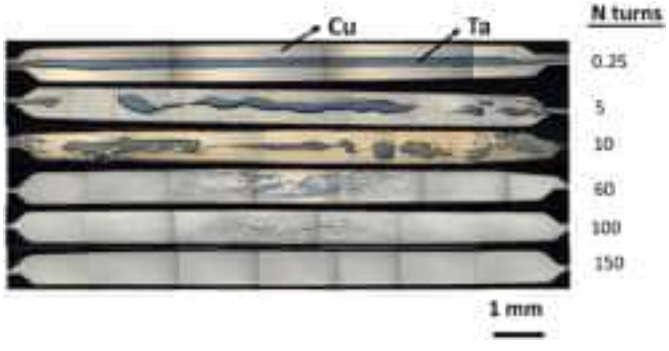

Fig. 1. Cross-sectional OM images of Cu/Ta/Cu stacks after different numbers of HPT turns: the dark regions are Ta and the bright regions are Cu.

3.2. Data from X-ray diffraction

The XRD patterns of the Cu–Ta samples processed by HPT through different numbers of turns (0.25, 5, 10, 60, 100 and 150) are shown in Fig. 3. Inspection shows that there is a systematic decrease in the relative intensities of the Cu and Ta peaks as well as a broadening of the peaks with increasing numbers of turns. The broadening of the Cu and Ta peaks is due to the effect of refinement in the crystallite size and the concomitant increase in internal strain.

The crystallite sizes and lattice distortions of the Cu and Ta were determined using the Williamson–Hall equation [34] and the results are presented in Fig. 4 as a function of the number of HPT turns: the instrumental broadening was considered in this analysis by using Si as a standard sample. Thus, the crystallite sizes of Cu and Ta decrease to less than 150 nm after 60 turns and further refinement occurs gradually up to 150 turns with final values of ~35 and ~45 nm for Cu and Ta, respectively. The lattice microstrain increases to high values of about 1.8% and 1.4% after 150 turns for Cu and Ta, respectively. Such crystallite size refinement to the nanoscale and high lattice strain accumulates within the sample as a result of the high pressure and high shear strains imposed in HPT processing. Similar reductions in grain size were reported in other systems [11,12] and they confirm the potential for using HPT to achieve grain sizes in the nanometer range.

After 100 and 150 turns in Fig. 3, the XRD data show that the Ta diffraction peaks are shifted towards higher angles and the Cu diffraction peaks are shifted towards lower angles through increasing numbers of turns. This confirms changes in the lattice parameters of Ta and Cu above about 100 turns due to the mutual dissolution of Cu and Ta. The atomic radius of Ta is larger than Cu and therefore, as a result, the Ta crystal lattice is reduced in size when Cu atoms replace some of the Ta atoms thereby causing a peak shift towards higher angles. Similarly, the Cu crystal lattice increases in size and the Cu peaks shift to lower angles due to the dissolution of the larger Ta atoms in the Cu lattice. This indicates that Cu–Ta alloys are formed by the HPT process and this is consistent with the SEM images in Fig. 2.

A further analysis of the XRD data by Materials Analysis Using Diffraction (MAUD) [35] to compute the mean lattice parameter of the metastable Cu–Ta alloy and Vegard's law [36] gave an average concentration of Cu in Ta as ~21.0 at.% and an average concentration of Ta in Cu estimated as ~18.5 at.% throughout the entire disc. It is noted that, consistent with the EDX data, these values are remarkably high when using a processing route involving a bulk-state reaction without the application of an elevated processing temperature.

3.3. Results from TEM and STEM observations

Fig. 5 shows high magnification TEM images of different cross-sectional positions for the disc processed through 150 turns where the images (a) to (c) relate to the positions shown on the upper bulk sample. In these images, the Ta-rich regions are in dark colour and it is apparent that the microstructures in all regions consist of a matrix of Cu-rich Cu–Ta alloy with a secondary Ta-rich region distributed throughout the matrix. Comparing Fig. 5(a–c), it appears that the microstructure closer to the edge is more uniform. In practice, the Ta-rich regions are well distributed over the matrix but their size and shape are different at the centre and edge of the disc. At the centre the Ta-rich regions are relatively coarse and have a layered shape ~20–200 nm in width and ~0.1–1.0 μm in length whereas at the edge these regions are individual flakes with a much

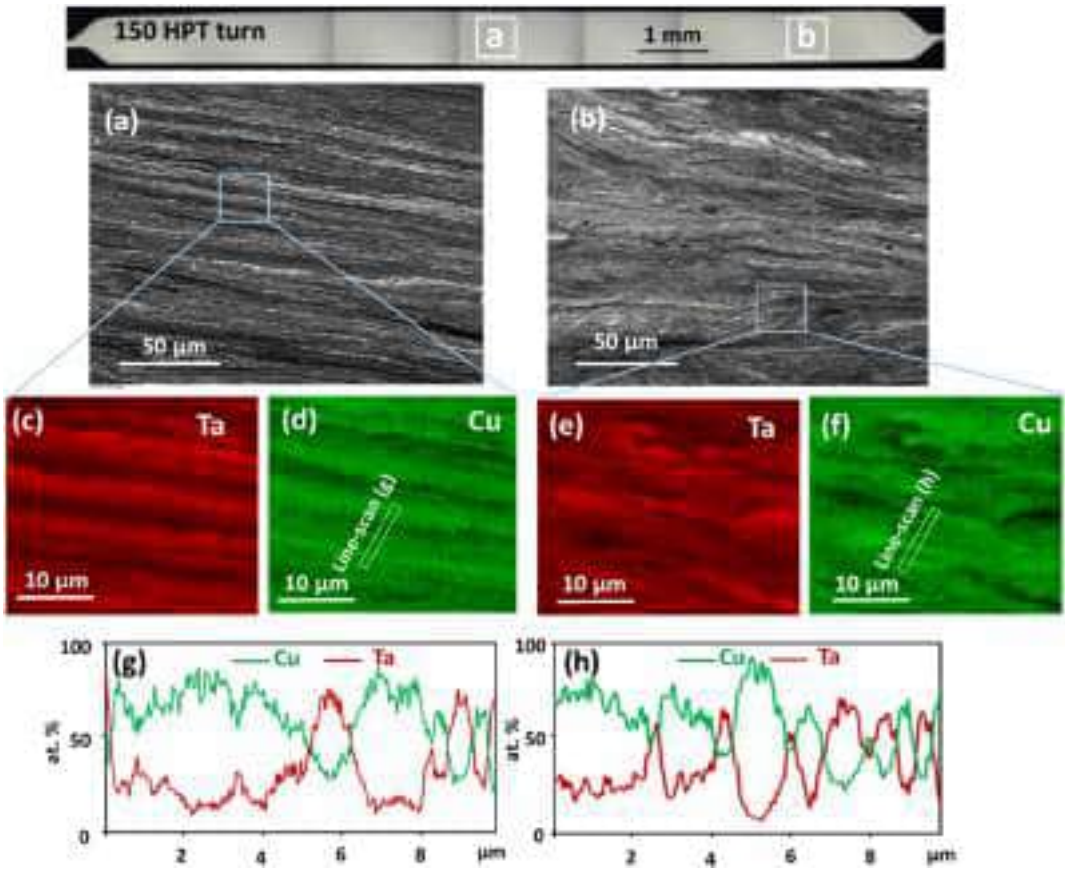

Fig. 2. Cross-sectional SEM images of the 150 turns sample at the areas marked (a) in the centre and (b) near the edge area, (c–f) elemental Cu and Ta maps of the indicated regions at higher magnifications, (g,h) EDX line scans over the regions marked in d and f.

finer size. It can be seen also that the Ta-rich regions with layered shapes present throughout the disc centre, as well as the flakes at the edge, lie essentially perpendicular to the direction of the anvils.

High magnification images from the matrix in the edge region, given in Fig. 5(d and e), show that the Cu-rich matrix contains very fine grains as well as Ta-rich clusters on a very fine scale of the order of ~5–10 nm. An atomic resolution TEM image of the interface between these nano-scale Ta-rich clusters and the Cu-rich matrix, shown in Fig. 5(f), reveals a strong atomic bonding with no evidence for any porosity and/or cracks as a result of any enhanced diffusion occurring between the Cu and Ta through the HPT processing. The *d*-spacing extracted from the high resolution TEM image shows *d*-spacing values of ~0.142 nm and ~0.205 nm for the Cu-rich matrix and the Ta-rich region, respectively, where these values correspond to (022) for Cu and (011) for Ta. Comparing these values with the theoretical values, given by d_{022} (Cu) = 0.128 nm and d_{011} (Ta) = 0.233 nm [37], it is apparent that there is a small expansion in the Cu lattice and a slight contraction in the Ta lattice due to the dissolution of large Ta atoms in Cu and small Cu atoms in

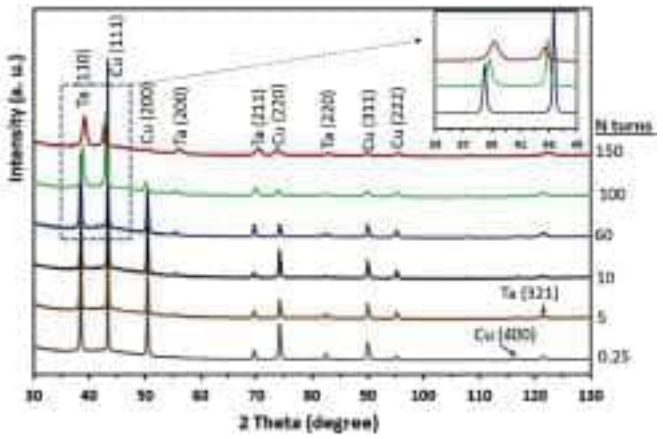

Fig. 3. The XRD patterns of the Cu–Ta discs processed by HPT at different numbers of turns (0.25, 5, 10, 60, 100 and 150). The inset shows the peak shifts for the Cu (111) and Ta (110) peaks after 100 turns.

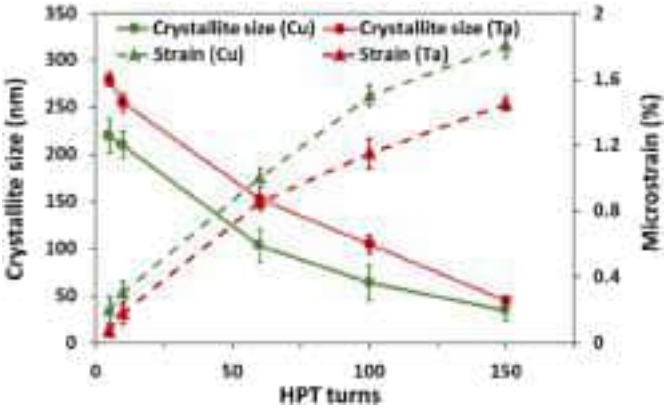

Fig. 4. Crystallite size and lattice strain in Cu and Ta at various HPT turns.

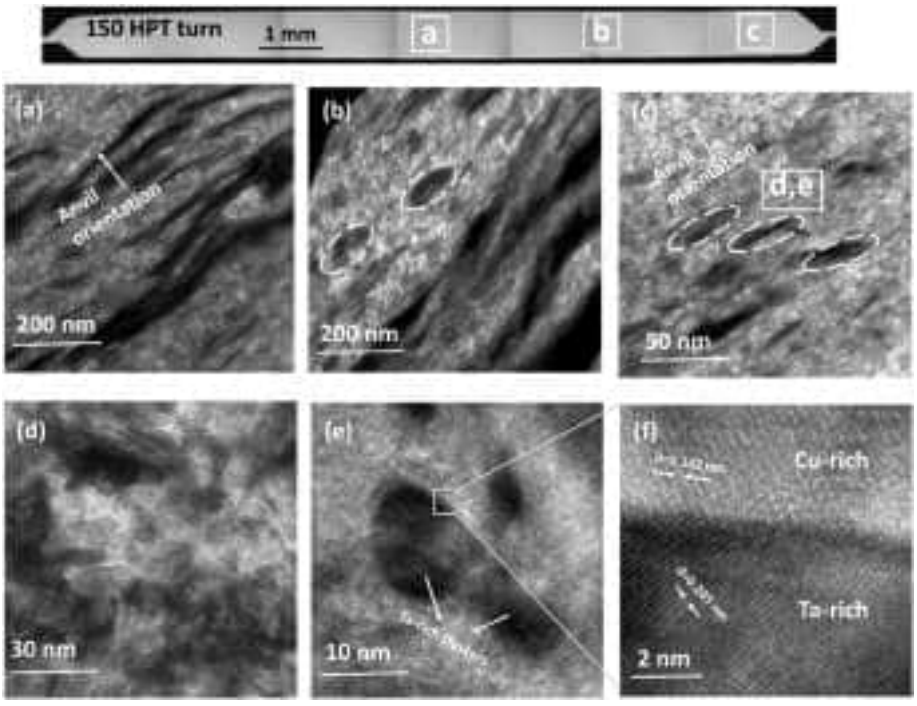

Fig. 5. (a–c) TEM images of the Cu–Ta bulk after 150 HPT turns at different positions through the disc as indicated, (d,e) high magnification image of the matrix at the edge area and (f) atomic resolution TEM image of the interface between a Ta-rich region and the Cu-rich matrix.

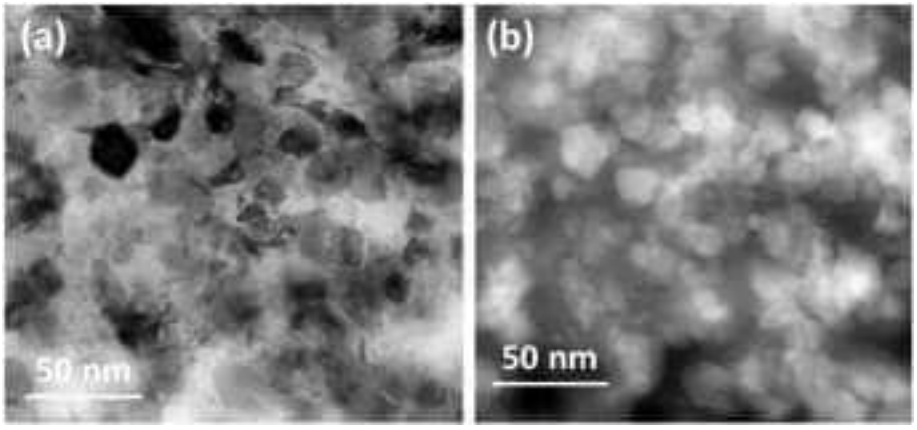

Fig. 6. (a) STEM and (b) Z-contrast HAADF images of Cu–Ta sample after 150 HPT turns.

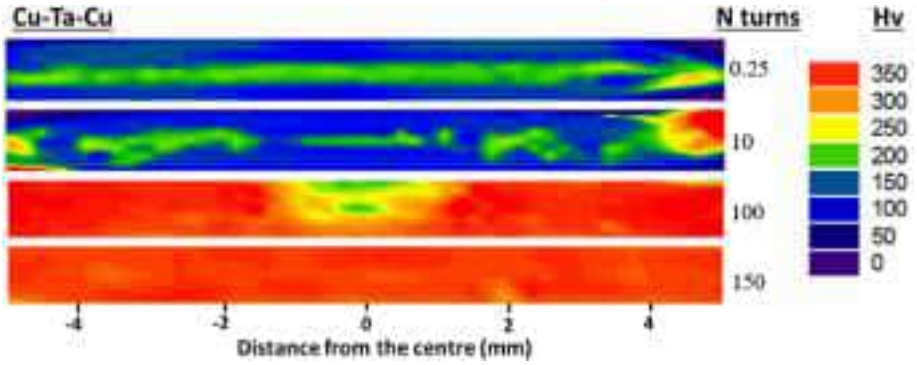

Fig. 7. Colour-coded microhardness maps of the Cu/Ta/Cu stacks after different numbers of HPT turns. (For interpretation of the references to colour in this figure legend, the reader is referred to the Web version of this article.)

Ta.

Fig. 6(a) shows an STEM image of the 150 turns disc in the half-radius area, corresponding to ~3 mm from the disc centre area, with the Ta-rich regions appearing black, and Fig. 6(b) is an HAADF image (or a Z-contrast image) of the same area. In Z-contrast images the heavy elements are bright and therefore the Ta-rich regions are now brighter. Thus, again the Ta-rich regions show good bonding with the Cu matrix with no detection of any cracks or voids after processing to 150 turns and with a size for the Ta-rich regions in the range of ~5–40 nm. These conclusions are therefore consistent with the TEM data shown in Fig. 5.

3.4. Hardness and mechanical properties of the Cu–Ta alloy after HPT processing

Fig. 7 shows colour-coded contour maps depicting the hardness values throughout cross-sections of the discs after HPT processing through different numbers of turns (0.25, 10, 100 and 150 turns). With reference to the scale for the values of Hv shown on the right, it can be seen that the microhardness increases significantly with increasing numbers of turns. Before HPT processing the annealed Cu and the as-received Ta showed average Vickers microhardness values of ~41 and ~200 Hv, respectively. After 0.25 turn the hardness was similar to the pure Cu and pure Ta but after 10 turns the hardness in the regions close to the edge of the disc increased to ~300 Hv whereas the hardness in the central section of the disc remained almost unchanged.

Further HPT deformation up to 100 turns gave an additional increase to nearly ~350 Hv across the discs except for a few small areas near the centre of the discs and an overall saturation hardness of ~350 Hv was achieved over the entire disc after 150 turns. The increase in microhardness from the centre to the edge is due to the low strain imparted in the central region during HPT processing and this trend matches results reported for many other metal systems [38,39]. Thus, after 150 turns the microhardness is reasonably homogeneous throughout the disc with an average value of ~350 Hv which is equivalent to a hardness of ~3.43 GPa. This hardness is very much higher than the initial hardness values of the pure Cu and pure Ta and the results demonstrate the remarkable hardness increases that may be achieved by processing through HPT.

Fig. 8 shows a stress-strain curve for the 150 turns sample tested at RT using an initial strain rate of 1.0×10^{-3} s^{-1}. Thus, the Cu–Ta alloy processed by HPT for 150 turns exhibits an ultimate tensile strength (UTS) of ~1300 MPa and a tensile elongation of about 40%. This very high strength is due to the microstructure achieved by the HPT processing and it is important to note that the UTS in this experiment is very much higher than the conventional values anticipated for pure copper (~150–300 MPa) and pure tantalum (~180–220 MPa) [40]). The HPT-processed Cu–Ta alloy also exhibits an acceptable elongation close to ~40%.

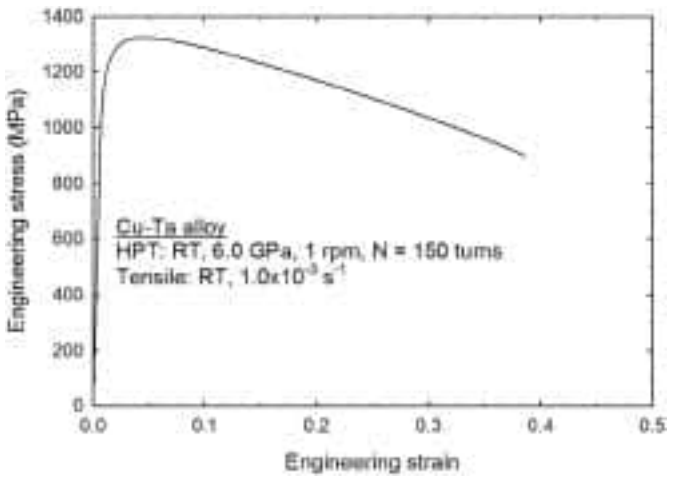

Fig. 8. Stress-strain curve for the Cu–Ta bulk sample after processing through 150 HPT turns.

4. Discussion

An evaluation of the microstructure and the phase evolution of the Cu–Ta sample through the HPT processing shows that in the early stages the Ta layer within the stack becomes thinner as a result of the HPT shear strain and then gradually these thin Ta layers are broken to form small flakes. The size of these Ta-rich flakes decreases as the HPT process continues and ultimately there is essentially a uniform dispersion of flakes throughout the Cu matrix. Since the edge area of the disc experiences a higher strain than the central region, the microstructural evolution occurs initially from the edge and then gradually extends to the centre with increasing numbers of HPT turns. As a result, the microstructure at the edge becomes more homogenous with smaller Ta-rich regions in the early stages but, by increasing the numbers of turns, most of the disc develops into a reasonably homogenous Cu–Ta alloy as a result of the accumulated strains operating through the whole disc.

This microstructural evolution is illustrated schematically in Fig. 9 where the microstructure evolves from left to right to ultimately produce a bulk Cu–Ta alloy. The microstructural features demonstrated in Fig. 9 are consistent with a Cu–Ta alloy processed by HPT from a disc with a stack of 19 Cu foils and 18 Ta foils [31] where the microstructure was a mixture of ultrafine grains corresponding to a Cu-16% Ta solid solution with embedded nano-scaled Ta-rich particles. Thus, the strategy in this research of using a disc sample with a pack of sandwich-like Cu/Ta/Cu discs for HPT processing was very effective in producing a bulk nanostructured immiscible Cu–Ta alloy. Computer modelling has confirmed the occurrence of turbulent flow in the cross-sections of HPT samples [15,16] and this may assist in the mass transfer and redistribution of metal components in the immiscible Cu–Ta system.

By increasing the numbers of HPT turns to give increased strain, there is additional grain refinement in the matrix and there are more crystalline defects thereby creating new diffusion paths for the Cu and Ta atoms. According to the XRD data, excess diffusion occurs after about 100 HPT turns. The crystallite sizes of Cu and Ta after 100 turns are ~95 and ~64 nm, respectively, and this corresponds to size reductions of ~66% and ~70% for Cu and Ta, respectively. Such large reductions in crystallite size could increase the fractions of grain boundaries which are known as effective diffusion path in this system [41]. It is therefore concluded that, after about 100 HPT turns, the numbers of grain boundaries and crystalline defects are sufficiently high to create practical diffusion paths for the Cu and Ta atoms.

In addition to the large numbers of grain boundaries and crystalline defects, the Ta-rich layers become finer with increasing HPT turns and this will also contribute to diffusion of Cu and Ta leading to the production of solid solutions in the immiscible Cu–Ta system. According to the present XRD and EDX data, after 150 HPT turns the concentration of Cu in Ta is about 22% and the concentration of Ta in Cu is about 19% generating the $Ta_{78}Cu_{22}$ and $Cu_{81}Ta_{19}$ alloys. These solubility values are remarkably high for the immiscible Cu–Ta system when it is noted that Cu and Ta have different crystalline structures (face-centred cubic and body-centred cubic, respectively) and negligible mutual solubility in the solid state [4]. It is especially notable also that such high solubility has been achieved in this

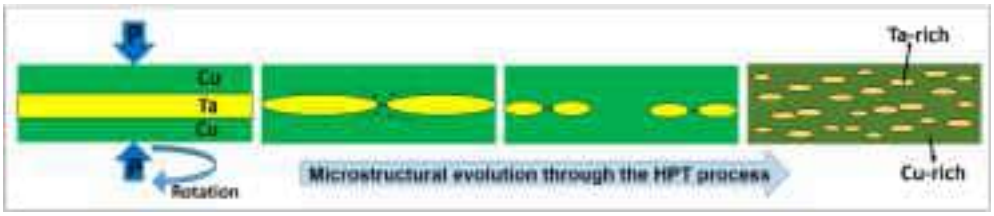

Fig. 9. Schematic image illustrating the mechanism of microstructural evolution in the Cu–Ta bulk through HPT processing.

investigation using a processing route which involves a bulk-state reaction at RT without the necessity of applying an elevated processing temperature. This indicates that the HPT process is capable of forcing a significant amount of Ta into a metastable FCC solid solution with Cu at room temperature.

The results show also that the final microstructure after 150 HPT turns is a composite containing a Cu-rich matrix with a crystallite size of ~45 nm and fine Ta-rich layers with a size of about 100–500 nm and a crystallite size of ~35 nm which is dispersed evenly within the matrix. In addition to these Ta-rich layers, Ta-rich clusters are also present and they are reasonably uniformly distributed in the microstructure but on a much finer scale of <10 nm. Such a microstructure achieved by HPT processing leads to very significant improvements in the mechanical properties.

A high UTS of ~1300 MPa with an acceptable elongation of about 40% was measured for the sample subjected to 150 turns. Measurements showed that the microhardness value was almost uniform throughout the whole disc after 150 turns with an average value of ~350 Hv which is equivalent to ~3.43 GPa. A comparison of this microhardness value with pure nanocrystalline Cu of similar grain size shows a strength increase by more than a factor of three. Thus, the hardness was reported as ~102 Hv for pure Cu with a grain size of ~35 nm [42] and this may be compared with the present hardness of ~350 Hv for the HPT-processed Cu–Ta alloy having the same grain size of ~35 nm. The final hardness value achieved in this investigation after 150 turns is also almost two times higher than the value reported for Cu–Ta alloys fabricated by magnetron sputtering [43].

Although the HPT-processed 150 turns Cu–Ta alloy has a much higher UTS (~1300 MPa) than pure Cu (~150–300 MPa) and pure tantalum (~180–220 MPa) [40] fabricated by conventional thermomechanical processing methods, it is of interest to compare the strength of HPT-processed Cu–Ta alloy with that of HPT-processed pure Cu and pure Ta. The strength of HPT-processed pure Ta and pure Cu are ~1300 MPa [44] and ~460 MPa [45] respectively. This means that the strength of the HPT-processed Cu–Ta is very close to that of the HPT-processed pure Ta. Considering the Cu–Ta alloy developed initially from Cu/Ta/Cu packed discs, the developed immiscible Cu–Ta alloy has a greater Cu component than Ta component but the minor component Ta appears to make a larger contribution to the strength of the HPT-processed Cu–Ta alloy.

In order to understand the strengthening mechanism of the HPT-processed immiscible Cu–Ta alloy, it is necessary to analyse the relationship between the microstructure and mechanical properties. As shown in Fig. 5, the microstructure of the HPT-processed Cu–Ta alloy contains Ta-rich clusters on a very fine scale of the order ~5–10 nm within the Cu-rich matrix where the Cu-rich matrix consists of a matrix of a Cu-rich Cu–Ta alloy with secondary Ta-rich flakes distributed throughout the matrix. This means that the dominant Cu-rich layers and sparsely distributed Ta-rich flakes form the matrix of the Cu–Ta alloys.

Elemental mapping by SEM in Fig. 2 and X-ray analysis in Fig. 3 confirm that a Cu–Ta solid solution formed in the Cu-rich layers and Ta–Cu solid solutions formed in the Ta-rich flakes, and significant grain refinement was achieved in both the Cu-rich and Ta-rich regions. Based on microstructural analysis, the high strength of the HPT-processed immiscible Cu–Ta alloy is attributed to a combination of several strengthening mechanisms. Thus, solid solution strengthening exists in both the Cu-rich layers and Ta-rich flakes and this will make contributions to the overall strength. In addition, the interfaces between the Cu-rich layers and the Ta-rich flakes in the matrix will provide an extra barrier to dislocation movement in addition to the grain boundaries, and the significant grain refinement due to the heavy shear strain applied during the HPT processing will also enhance the material strength. Finally, the nanoscale Ta-rich clusters will act as a dispersed hard phase in the Cu-rich matrix giving a dispersion strengthening effect.

The elongation of ~40% obtained in the 150 turns HPT-processed immiscible Cu–Ta alloy demonstrates that this new Cu–Ta alloy exhibits a good balance between high strength and reasonable ductility. Normally, the material strength and ductility are incompatible so that high strength leads to a reduced ductility. The tensile testing of HPT-processed pure Ta after 10 turns led to failure before the onset of plastic deformation [44] whereas tensile testing of HPT-processed pure Cu after 10 HPT turns gave elongations of ~4% [45]. This shows that the HPT-processed immiscible Cu–Ta alloy has a significantly improved elongation compared with either HPT-processed pure Ta or pure Cu. The reason for this reasonable elongation in the HPT-processed immiscible Cu–Ta alloy is probably related to the interfaces between the Cu-rich layers and the sparsely distributed Ta-rich flakes in the Cu-rich matrix, since this will affect the load transmission and initiation of dislocations between the interfaces and thereby permit an increased strain hardening capability and larger elongations.

5. Summary and conclusions

1. Nanostructured Cu–Ta alloys were successfully fabricated from Cu/Ta/Cu stacked discs by HPT processing at room temperature. A uniform two-phase layered microstructure was developed by increasing the numbers of HPT turns where these two phases included a Cu-rich layer with a composition of about $Cu_{81}Ta_{19}$ and a Ta-rich layer with a composition of about $Ta_{78}Cu_{22}$.
2. Significant microstructural refinement was achieved in the Cu–Ta alloy with average crystallite sizes in the range of ~35–45 nm after 150 turns of HPT processing. In addition to Cu–Ta layers, there were also Ta-rich clusters on a fine-scale of <10 nm almost uniformly embedded within the matrix.
3. After 150 turns of HPT processing, the Cu–Ta alloy exhibited remarkably improved hardness and tensile strength by comparison with commercial purity Cu and pure Ta. The average Vickers microhardness value was ~350 Hv, equivalent to ~3.43 GPa, and in tensile testing the UTS was ~1300 MPa with an elongation of about 40%.
4. The results demonstrate the potential for using HPT processing at room temperature to create advanced microstructures and

excellent mechanical properties that are not achieved through other processing routes.

Data availability

The raw/processed data required to reproduce these findings cannot be shared at this time as the data also forms part of an ongoing study.

Declaration of competing interest

The authors declare that they have no known competing financial interests or personal relationships that could have appeared to influence the work reported in this paper.

Acknowledgements

This work was supported in part by the European Research Council under grant agreement no. 267464-SPDMETALS and in part by the National Science Centre, Poland, within the project SONATINA 1 “Synthesis of novel hybrid materials using High-Pressure Torsion”, under Grant Agreement No.2017/24/C/ST8/00145. One of the authors (YH) thanks the QR fund from Bournemouth University.

References

[1] R.Z. Valiev, A.P. Zhilyaev, T.G. Langdon, Bulk Nanostructured Materials: Fundamentals and Applications, Wiley/TMS, Hoboken, NJ, USA, 2014.
[2] K.A. Darling, M. Rajagopalan, M. Komarasamy, M.A. Bhatia, B.C. Hornbuckle, R.S. Mishra, K.N. Solanki, Extreme creep resistance in a microstructurally stable nanocrystalline alloy, Nature 537 (2016) 378–381.
[3] F. Abdeljawad, P. Lu, N. Argibay, B.G. Clark, B.L. Boyce, S.M. Foiles, Grain boundary segregation in immiscible nanocrystalline alloys, Acta Mater. 126 (2017) 528–539.
[4] T.B. Massalski (Ed.), Binary Alloy Phase Diagrams, ASM, Materials Park, OH, 1986.
[5] S. Zheng, J.S. Carpenter, R.J. McCabe, I.J. Beyerlein, N.A. Mara, Engineering interface structures and thermal stabilities via SPD processing in bulk nanostructured metals, Sci. Rep. 4 (2014) 4226(1–6).
[6] J.K. Han, J.D. Liss, T.G. Langdon, M. Kawasaki, Synthesis of a bulk nanostructured metastable Al alloy with extreme supersaturation of Mg, Sci. Rep. 9 (2019) 17186(1–7).
[7] J.K. Han, T. Herndon, J.I. Jang, T.G. Langdon, M. Kawasaki, Review: synthesis of hybrid nanocrystalline alloys by mechanical bonding through high-pressure torsion, Adv. Eng. Mater. (in press) DOI: 10.1002/adem.201901289.
[8] R.Z. Valiev, T.G. Langdon, Principles of equal-channel angular pressing as a processing tool for grain refinement, Prog. Mater. Sci. 51 (2006) 881–981.
[9] H. Shahmir, T. Mousavi, J. He, Z. Lu, M. Kawasaki, T.G. Langdon, Microstructure and properties of a CoCrFeNiMn high-entropy alloy processed by equal-channel angular pressing, Mater. Sci. Eng. A 705 (2017) 411–419.
[10] L.F. Zeng, R. Gao, Q.F. Fang, X.P. Wang, Z.M. Xie, S. Miao, T. Hao, T. Zhang, High strength and thermal stability of bulk Cu/Ta nanolamellar multilayers fabricated by cross accumulative roll bonding, Acta Mater. 110 (2016) 341–351.
[11] A.P. Zhilyaev, G.V. Nurislamova, B.K. Kim, M.D. Baró, J.A. Szpunar, T.G. Langdon, Experimental parameters influencing grain refinement and microstructural evolution during high-pressure torsion, Acta Mater. 51 (2003) 753–765.
[12] A.P. Zhilyaev, T.G. Langdon, Using high-pressure torsion for metal processing: fundamentals and applications, Prog. Mater. Sci. 53 (2008) 893–979.
[13] Y. Huang, P. Bazarnik, D. Wan, D. Luo, P. Pereira, M. Lewandowska, J. Yao, B.E. Hayden, T.G. Langdon, The fabrication of graphene-reinforced Al-based nanocomposites using high-pressure torsion, Acta Mater. 164 (2019) 499–511.
[14] Y. Huang, R.B. Figueiredo, T. Baudin, F. Brisset, T.G. Langdon, Evolution of strength and homogeneity in a magnesium AZ31 alloy processed by high-pressure torsion at different temperatures, Adv. Eng. Mater. 14 (2012) 1018–1026.
[15] R. Kulagin, Y. Beygelzimer, Y. Ivanisenko, A. Mazilkin, H. Hahn, High pressure torsion: from laminar flow to turbulence, IOP Conf. Ser. Mater. Sci. Eng. 194 (2017) 1–6, 012045.
[16] R. Kulagin, Y. Beygelzimer, Y. Ivanisenko, A. Mazilkin, B. Straumal, H. Hahn, Instabilities of interfaces between dissimilar metals induced by high pressure torsion, Mater. Lett. 222 (2018) 172–175.
[17] M. Pouryazdan, B.J.P. Kaus, A. Rack, A. Ershov, H. Hahn, Mixing instabilities during shearing of metals, Nat. Commun. 8 (2017) 1611(1–7).
[18] P.H.R. Pereira, R.B. Figueiredo, Finite element modelling of high-pressure torsion: an overview, Mater. Trans. 60 (2019) 1139–1150.
[19] Y. Cao, Y.B. Wang, S.N. Alhajeri, X.Z. Liao, W.L. Zheng, S.P. Ringer, T.G. Langdon, Y.T. Zhu, A visualization of shear strain in processing by high-pressure torsion, J. Mater. Sci. 45 (2010) 765–770.
[20] Y. Cao, M. Kawasaki, Y.B. Wang, S.N. Alhajeri, X.Z. Liao, W.L. Zheng, S.P. Ringer, Y.T. Zhu, T.G. Langdon, Unusual macroscopic shearing patterns observed in metals processed by high-pressure torsion, J. Mater. Sci. 45 (2010) 4545–4553.
[21] Y. Cao, Y.B. Wang, R.B. Figueiredo, L. Chang, X.Z. Liao, M. Kawasaki, W.L. Zheng, S.P. Ringer, T.G. Langdon, Y.T. Zhu, Three-dimensional shear-strain patterns induced by high-pressure torsion and their impact on hardness evolution, Acta Mater. 59 (2011) 3903–3914.
[22] Y. Huang, M. Kawasaki, T.G. Langdon, Influence of anvil alignment on shearing patterns in high-pressure torsion, Adv. Eng. Mater. 15 (2013), 747-655.
[23] Y. Huang, M. Kawasaki, T.G. Langdon, An investigation of flow pattern and hardness distribution using different anvil alignments in high-pressure torsion, J. Mater. Sci. 48 (2013) 4533–4542.
[24] W. Jiang, X.H. An, S.D. Wu, Z.F. Zhang, R.B. Figueiredo, N. Gao, T.G. Langdon, Y. Zhu, On the heterogeneity of local shear strain induced by high-pressure torsion, Adv. Eng. Mater. 22 (2020) 1900477(1–8).
[25] Y.Z. Tian, X.H. An, S.D. Wu, Z.F. Zhang, R.B. Figueiredo, N. Gao, T.G. Langdon, Direct observations of microstructural evolution in a two-phase Cu-Ag alloy processed by high-pressure torsion, Scripta Mater. 63 (2010) 65–68.
[26] R. Kulagin, Y. Beygelzimer, A. Bachmaier, R. Pippan, Y. Estrin, Benefits of pattern formation by severe plastic deformation, Appl. Mater. Today 15 (2019) 236–241.
[27] A. Bachmaier, G.B. Rathmayr, M. Bartosik, D. Apel, Z. Zhang, R. Pippan, New insights on the formation of supersaturated solid solutions in CuCr system deformed by high-pressure torsion, Acta Mater. 69 (2014) 301–313.
[28] S. Sabooni, T. Mousavi, F. Karimzadeh, Fabrication and characterization of nanostructured Cu-15wt% Mo compound by mechanical alloying, Int. J. Mod. Phys. 5 (2012) 456–463.
[29] K.A. Darling, E.L. Huskins, B.E. Schuster, Q. Wei, L.J. Kecskes, Mechanical properties of a high strength Cu–Ta composite at elevated temperature, Mater. Sci. Eng. A 638 (2015) 322–328.
[30] S. Sabooni, T. Mousavi, F. Karimzadeh, Thermodynamic analysis and characterization of nanostructured Cu(Mo) compounds prepared by mechanical alloying and subsequent sintering, Powder Metall. 55 (3) (2012) 222–227.
[31] N. Ibrahim, M. Peterlechner, F. Emeis, M. Wegner, S.V. Divinski, G. Wilde, Mechanical alloying via high-pressure torsion of the immiscible $Cu_{50}Ta_{50}$ system, Mater. Sci. Eng. A 685 (2017) 19–30.
[32] R.B. Figueiredo, P.H.R. Pereira, M.T.P. Aguilar, P.R. Cetlin, T.G. Langdon, Using finite element modeling to examine the temperature distribution in quasi-constrained high-pressure torsion, Acta Mater. 60 (2012) 3190–3198.
[33] A. Loucif, R.B. Figueiredo, M. Kawasaki, T. Baudin, F. Brisset, R. Chemam, T.G. Langdon, Effect of aging on microstructural development in an Al–Mg–Si alloy processed by high-pressure torsion, J. Mater. Sci. 47 (2012) 7815–7820.
[34] C. Suryanarayana, M.G. Norton, X-Ray Diffraction: A Practical Approach, Plenum Press, New York, 1998, p. 207.
[35] L. Lutterotti, S. Matthiers, H.R. Wenk, MAUD (Material Analysis Using Diffraction): a user friendly Java program for Rietveld texture analysis and more, in: Proceedings of the 12th International Conference on Textures of Materials (ICOTOM-12), NRC Research Press, Ottawa, Canada, 1999, pp. 1599–1604.
[36] A. Denton, N.W. Ashcroft, Vegard’s law, Phys. Rev. A 43 (1991) 3161–3164.
[37] B.D. Cullity, Elements of X-Ray Diffraction, Addison-Wesley, Reading, MA, USA, 1956.
[38] J. Wongsa-Ngam, M. Kawasaki, T.G. Langdon, Achieving homogeneity in a Cu-Zr alloy processed by high-pressure torsion, J. Mater. Sci. 47 (2012) 7782–7788.
[39] S. Sabbaghianrad, M. Kawasaki, T.G. Langdon, Microstructural evolution and the mechanical properties of an aluminum alloy processed by high-pressure torsion, J. Mater. Sci. 47 (2012) 7789–7795.
[40] Materials Data Handbook, Cambridge University Engineering Department, Cambridge, UK, 2003.
[41] R.K. Koju, K.A. Darling, K.N. Solanki, Y. Mishin, Atomistic modeling of capillary-driven grain boundary motion in Cu-Ta alloys, Acta Mater. 148 (2018) 311–319.
[42] J. Chen, L. Lu, K. Lu, Hardness and strain rate sensitivity of nanocrystalline Cu, Scripta Mater. 54 (2006) 1913–1918.
[43] W. Qin, L. Fu, T. Xie, J. Zhu, W. Yang, D. Li, L. Zhou, Abnormal hardness behavior of Cu-Ta films prepared by magnetron sputtering, J. Alloys Compd. 708 (2017) 1033–1037.
[44] N. Maury, N.X. Zhang, Y. Huang, A.P. Zhilyaev, T.G. Langdon, A Critical examination of pure tantalum processed by high-pressure torsion, Mater. Sci. Eng. A 638 (2015) 174–182.
[45] M.Y. Alawadhi, S. Sabbaghianrad, Y. Huang, T.G. Langdon, Direct influence of recovery behaviour on mechanical properties in oxygen-free copper processed using different SPD techniques: HPT and ECAP, J. Mater, Res, Technol. 6 (4) (2017) 369–377.

Statement

Publication title, journal, year, doi:

The fabrication of graphene-reinforced Al-based nanocomposites using high-pressure torsion, Acta Materialia 164 (2019) 499-511. 10.1016/j.actamat.2018.10.060.

Names and surnames of publication authors:

*Huang Yi, **Bazarnik Piotr**, Wan Diqing, Luo Dan, Pereira Pedro Henrique R., Lewandowska Malgorzata, Yao Jin, Hayden Brian E., Langdon Terence G.,*

Statement on the substantive contribution of the work to the above-mentioned publication and consent to submit it for habilitation

No.	Author	Contribution	Signature
1	***Piotr Bazarnik***	In this article I was responsible for: - conceptualization of microstructural research, - methodology selection for structural analysis, - performing all microstructural observations using transmission electron microscopy, analysing obtained microstructures, - writing structural section and discussion on structural evolution in the original draft of the paper, reviewing and editing. This publication is a result of the SONATINA project, 'Synthesis of Novel Hybrid Materials Using High-Pressure Torsion' (UMO-2017/24/C/ST8/00145), in which I have been a leader (PI)	
Co-authors' contribution:			
2	*Yi Huang*	Conceptualization of work, Sample production, Writing and editing the final version of the article, Performing static tensile test, Funding support	
3	*Wan Diqing*	HPT processing of Al-GNP samples	Brak kontaktu
4	*Luo Dan*	Data menagment of tensile tests results. Editing the final version of the article	Brak kontaktu
5	*Pereira Pedro Henrique R.*	Performing microhardness measurements and analysing results, Editing the final version of the article	
6	*Lewandowska Malgorzata*	Editing the final version of the article	

7	*Yao Jin*	Electrical conduction measurements	Brak kontaktu
8	*Hayden Brian E.*	Data analysis, Editing the final version of the article	Brak kontaktu
9	*Langdon Terence G.*	Editing the final version of the article	

Statement

Publication title, journal, year, doi:

The fabrication of graphene-reinforced Al-based nanocomposites using high-pressure torsion, Acta Materialia 164 (2019) 499-511. 10.1016/j.actamat.2018.10.060.

Names and surnames of publication authors:

Huang Yi, ***Bazarnik Piotr****, Wan Diqing, Luo Dan, Pereira Pedro Henrique R., Lewandowska Malgorzata, Yao Jin, Hayden Brian E., Langdon Terence G.,*

Statement on the substantive contribution of the work to the above-mentioned publication and consent to submit it for habilitation

No.	Author	Contribution	Signature
1	***Piotr Bazarnik***	In this article I was responsible for: - conceptualization of microstructural research, - methodology selection for structural analysis, - performing all microstructural observations using transmission electron microscopy, analysing obtained microstructures, - writing structural section and discussion on structural evolution in the original draft of the paper, reviewing and editing. This publication is a result of the SONATINA project, 'Synthesis of Novel Hybrid Materials Using High-Pressure Torsion' (UMO-2017/24/C/ST8/00145), in which I have been a leader (PI)	
Co-authors' contribution:			
2	*Yi Huang*	Conceptualization of work, Sample production, Writing and editing the final version of the article, Performing static tensile test, Funding support	
3	*Wan Diqing*	HPT processing of Al-GNP samples	
4	*Luo Dan*	Data menagment of tensile tests results. Editing the final version of the article	
5	*Pereira Pedro Henrique R.*	Performing microhardness measurements and analysing results, Editing the final version of the article	PHRereira
6	*Lewandowska Malgorzata*	Editing the final version of the article	

7	*Yao Jin*	Electrical conduction measurements	
8	*Hayden Brian E.*	Data analysis, Editing the final version of the article	
9	*Langdon Terence G.*	Editing the final version of the article	

Statement

Publication title, journal, year, doi:

The fabrication of graphene-reinforced Al-based nanocomposites using high-pressure torsion, Acta Materialia 164 (2019) 499-511. 10.1016/j.actamat.2018.10.060.

Names and surnames of publication authors:

*Huang Yi, **Bazarnik Piotr**, Wan Diqing, Luo Dan, Pereira Pedro Henrique R., Lewandowska Malgorzata, Yao Jin, Hayden Brian E., Langdon Terence G.,*

Statement on the substantive contribution of the work to the above-mentioned publication and consent to submit it for habilitation

No.	Author	Contribution	Signature
1	***Piotr Bazarnik***	In this article I was responsible for: - conceptualization of microstructural research, - methodology selection for structural analysis, - performing all microstructural observations using transmission electron microscopy, analysing obtained microstructures, - writing structural section and discussion on structural evolution in the original draft of the paper, reviewing and editing. This publication is a result of the SONATINA project, 'Synthesis of Novel Hybrid Materials Using High-Pressure Torsion' (UMO-2017/24/C/ST8/00145), in which I have been a leader (PI)	
Co-authors' contribution:			
2	*Yi Huang*	Conceptualization of work, Sample production, Writing and editing the final version of the article, Performing static tensile test, Funding support	
3	*Wan Diqing*	HPT processing of Al-GNP samples	
4	*Luo Dan*	Data menagment of tensile tests results. Editing the final version of the article	

5	*Pereira Pedro Henrique R.*	Performing microhardness measurements and analysing results, Editing the final version of the article	
6	*Lewandowska Malgorzata*	Editing the final version of the article	
7	*Yao Jin*	Electrical conduction measurements	
8	*Hayden Brian E.*	Data analysis, Editing the final version of the article	
9	*Langdon Terence G.*	Editing the final version of the article	

Statement

Publication title, journal, year, doi:

The fabrication of graphene-reinforced Al-based nanocomposites using high-pressure torsion, Acta Materialia 164 (2019) 499-511. 10.1016/j.actamat.2018.10.060.

Names and surnames of publication authors:

*Huang Yi, **Bazarnik Piotr**, Wan Diqing, Luo Dan, Pereira Pedro Henrique R., Lewandowska Malgorzata, Yao Jin, Hayden Brian E., Langdon Terence G.,*

Statement on the substantive contribution of the work to the above-mentioned publication and consent to submit it for habilitation

No.	Author	Contribution	Signature
1	***Piotr Bazarnik***	In this article I was responsible for: - conceptualization of microstructural research, - methodology selection for structural analysis, - performing all microstructural observations using transmission electron microscopy, analysing obtained microstructures, - writing structural section and discussion on structural evolution in the original draft of the paper, reviewing and editing. This publication is a result of the SONATINA project, 'Synthesis of Novel Hybrid Materials Using High-Pressure Torsion' (UMO-2017/24/C/ST8/00145), in which I have been a leader (PI)	
Co-authors' contribution:			
2	*Yi Huang*	Conceptualization of work, Sample production, Writing and editing the final version of the article, Performing static tensile test, Funding support	
3	*Wan Diqing*	HPT processing of Al-GNP samples	
4	*Luo Dan*	Data menagment of tensile tests results. Editing the final version of the article	
5	*Pereira Pedro Henrique R.*	Performing microhardness measurements and analysing results, Editing the final version of the article	
6	*Lewandowska Malgorzata*	Editing the final version of the article	

7	*Yao Jin*	Electrical conduction measurements	
8	*Hayden Brian E.*	Data analysis, Editing the final version of the article	
9	*Langdon Terence G.*	Editing the final version of the article	

Statement

Publication title, journal, year, doi:

Using direct high-pressure torsion synthesis to produce aluminium matrix nanocomposites reinforced with carbon nanotubes, Journal of Alloys and Compounds 968 (2023). 10.1016/j.jallcom.2023.171928. Correndum in Journal of Alloys and Compounds 977 (2024) 173067

Names and surnames of publication authors:

Bazarnik Piotr, *Emerla Maria, Aleksandra Bartkowska, Huang Yi, Lewandowska Małgorzata, Langdon Terence G.,*

Statement on the substantive contribution of the work to the above-mentioned publication and consent to submit it for habilitation

No.	Author	Contribution	Signature
1	***Piotr Bazarnik***	In this article I was responsible for: - conceptualization of all performed research, results analysis - methodology selection, - HPT processing of Al-CNT samples during research stay at Southampton University - Funding and project management - performing all microstructural observations using transmission electron microscopy, analysing obtained microstructures, - Creating figures regarding structural analysis - writing the original draft of the paper ,reviewing and editing. This publication is a result of the OPUS project, "Metal matrix composites fabricated by high-pressure torsion and reinforced with 2D and 3D nano-particles" (UMO-2020/37/B/ST5/01837), in which I have been a leader (PI)	
Co-authors' contribution:			
2	*Emerla Maria*	Writing the original draft of the paper, Performing annealing of samples and SEM observations after annealing. Microhardness measurements after annealing, creating figures regarding microhardness tests and saturation effect	
3	*Aleksandra Bartkowska*	Performing SEM observations and microhardness tests of initial samples	

4	*Huang Yi*	Literature review and background research, Editing the final version of the article, selection of parameters for the HPT process	
5	*Lewandowska Małgorzata*	Discussion of the results obtained, Hall-Petch relationship studies based on literature data	
6	*Langdon Terence G.*	Proofreading and language editing, Discussion on the results obtained, Validation and verification, Editing the final version of the article	

Statement

Publication title, journal, year, doi:

Using direct high-pressure torsion synthesis to produce aluminium matrix nanocomposites reinforced with carbon nanotubes, Journal of Alloys and Compounds 968 (2023). 10.1016/j.jallcom.2023.171928. Correndum in Journal of Alloys and Compounds 977 (2024) 173067

Names and surnames of publication authors:

Bazarnik Piotr, *Emerla Maria, Aleksandra Bartkowska, Huang Yi, Lewandowska Małgorzata, Langdon Terence G.,*

Statement on the substantive contribution of the work to the above-mentioned publication and consent to submit it for habilitation

No.	Author	Contribution	Signature
1	***Piotr Bazarnik***	In this article I was responsible for: - conceptualization of all performed research, results analysis - methodology selection, - HPT processing of Al-CNT samples during research stay at Southampton University - Funding and project management - performing all microstructural observations using transmission electron microscopy, analysing obtained microstructures, - Creating figures regarding structural analysis - writing the original draft of the paper ,reviewing and editing. This publication is a result of the OPUS project, "Metal matrix composites fabricated by high-pressure torsion and reinforced with 2D and 3D nano-particles" (UMO-2020/37/B/ST5/01837), in which I have been a leader (PI)	
Co-authors' contribution:			
2	*Emerla Maria*	Writing the original draft of the paper, Performing annealing of samples and SEM observations after annealing. Microhardness measurements after annealing, creating figures regarding microhardness tests and saturation effect	
3	*Aleksandra Bartkowska*	Performing SEM observations and microhardness tests of initial samples	Aleksandra Bartkowska

4	*Huang Yi*	Literature review and background research, Editing the final version of the article, selection of parameters for the HPT process	
5	*Lewandowska Małgorzata*	Discussion of the results obtained, Hall-Petch relationship studies based on literature data	
6	*Langdon Terence G.*	Proofreading and language editing, Discussion on the results obtained, Validation and verification, Editing the final version of the article	

Statement

Publication title, journal, year, doi:

Using direct high-pressure torsion synthesis to produce aluminium matrix nanocomposites reinforced with carbon nanotubes, Journal of Alloys and Compounds 968 (2023). 10.1016/j.jallcom.2023.171928. Correndum in Journal of Alloys and Compounds 977 (2024) 173067

Names and surnames of publication authors:

Bazarnik Piotr, *Emerla Maria, Aleksandra Bartkowska, Huang Yi, Lewandowska Małgorzata, Langdon Terence G.,*

Statement on the substantive contribution of the work to the above-mentioned publication and consent to submit it for habilitation

No.	Author	Contribution	Signature
1	***Piotr Bazarnik***	In this article I was responsible for: - conceptualization of all performed research, results analysis - methodology selection, - HPT processing of Al-CNT samples during research stay at Southampton University - Funding and project management - performing all microstructural observations using transmission electron microscopy, analysing obtained microstructures, - Creating figures regarding structural analysis - writing the original draft of the paper ,reviewing and editing. This publication is a result of the OPUS project, "Metal matrix composites fabricated by high-pressure torsion and reinforced with 2D and 3D nano-particles" (UMO-2020/37/B/ST5/01837), in which I have been a leader (PI)	
Co-authors' contribution:			
2	*Emerla Maria*	Writing the original draft of the paper, Performing annealing of samples and SEM observations after annealing. Microhardness measurements after annealing, creating figures regarding microhardness tests and saturation effect	
3	*Aleksandra Bartkowska*	Performing SEM observations and microhardness tests of initial samples	

4	*Huang Yi*	Literature review and background research, Editing the final version of the article, selection of parameters for the HPT process	
5	*Lewandowska Małgorzata*	Discussion of the results obtained, Hall-Petch relationship studies based on literature data	
6	*Langdon Terence G.*	Proofreading and language editing, Discussion on the results obtained, Validation and verification, Editing the final version of the article	

Statement

Publication title, journal, year, doi:

Using direct high-pressure torsion synthesis to produce aluminium matrix nanocomposites reinforced with carbon nanotubes, Journal of Alloys and Compounds 968 (2023). 10.1016/j.jallcom.2023.171928. Correndum in Journal of Alloys and Compounds 977 (2024) 173067

Names and surnames of publication authors:

Bazarnik Piotr, *Emerla Maria, Aleksandra Bartkowska, Huang Yi, Lewandowska Małgorzata, Langdon Terence G.,*

Statement on the substantive contribution of the work to the above-mentioned publication and consent to submit it for habilitation

No.	Author	Contribution	Signature
1	***Piotr Bazarnik***	In this article I was responsible for: - conceptualization of all performed research, results analysis - methodology selection, - HPT processing of Al-CNT samples during research stay at Southampton University - Funding and project management - performing all microstructural observations using transmission electron microscopy, analysing obtained microstructures, - Creating figures regarding structural analysis - writing the original draft of the paper ,reviewing and editing. This publication is a result of the OPUS project, "Metal matrix composites fabricated by high-pressure torsion and reinforced with 2D and 3D nano-particles" (UMO-2020/37/B/ST5/01837), in which I have been a leader (PI)	
Co-authors' contribution:			
2	*Emerla Maria*	Writing the original draft of the paper, Performing annealing of samples and SEM observations after annealing. Microhardness measurements after annealing, creating figures regarding microhardness tests and saturation effect	
3	*Aleksandra Bartkowska*	Performing SEM observations and microhardness tests of initial samples	

4	*Huang Yi*	Literature review and background research, Editing the final version of the article, selection of parameters for the HPT process	
5	*Lewandowska Małgorzata*	Discussion of the results obtained, Hall-Petch relationship studies based on literature data	
6	*Langdon Terence G.*	Proofreading and language editing, Discussion on the results obtained, Validation and verification, Editing the final version of the article	

Statement

Publication title, journal, year, doi:

Effect of spark plasma sintering and high-pressure torsion on the microstructural and mechanical properties of a Cu–SiC composite, Materials Science and Engineering A 766 (2019) 138350 https://doi.org/10.1016/j.msea.2019.138350.

Names and surnames of publication authors:

***Bazarnik Piotr**, Nosewicz Szymon, Romelczyk-Baishya Barbara, Chmielewski Marcin, Strojny Nędza Agata, Maj Justyna, Huang Yi, Lewandowska Małgorzata, Langdon Terence G.*

Statement on the substantive contribution of the work to the above-mentioned publication and consent to submit it for habilitation

No.	Author	Contribution	Signature
1	***Piotr Bazarnik***	In this article I was responsible for: - conceptualization of all performed research, - methodology selection, - performing microhardness measurements and analysing results, - Funding and project management - performing all microstructural observations using transmission electron microscopy, analysing obtained microstructures, - results analysis - writing the original draft of the paper, reviewing and editing. This publication is a result of the SONATINA project, 'Synthesis of Novel Hybrid Materials Using High-Pressure Torsion' (UMO-2017/24/C/ST8/00145), in which I have been a leader (PI)	
Co-authors' contribution:			
2	*Nosewicz Szymon*	Synthesis od Cu-SiC composites, Analysis of the obtained results , Editing the final version of the article	
3	*Romelczyk-Baishya Barbara*	Performing static tensile test	
4	*Chmielewski Marcin*	Selection of sintering parameters	

5	*Strojny Nędza Agata*	Thermal conduction measurements	Strojny-Nędza
6	*Maj Justyna*	Thermal conduction data analysis	Brak kontaktu
7	*Huang Yi*	HPT processing of Cu-SiC samples. Editing the final version of the article, Examination of the results	
8	*Lewandowska Małgorzata*	Editing the final version of the article, analysis of the results	Lewandowska
9	*Langdon Terence G.*	Editing the final version of the article, Discussion of the results obtained, Proofreading and language editing	

Statement

Publication title, journal, year, doi:

Effect of spark plasma sintering and high-pressure torsion on the microstructural and mechanical properties of a Cu–SiC composite, Materials Science and Engineering A 766 (2019) 138350 https://doi.org/10.1016/j.msea.2019.138350.

Names and surnames of publication authors:

***Bazarnik Piotr**, Nosewicz Szymon, Romelczyk-Baishya Barbara, Chmielewski Marcin, Strojny Nędza Agata, Maj Justyna, Huang Yi, Lewandowska Małgorzata, Langdon Terence G.*

Statement on the substantive contribution of the work to the above-mentioned publication and consent to submit it for habilitation

No.	Author	Contribution	Signature
1	***Piotr Bazarnik***	In this article I was responsible for: - conceptualization of all performed research, - methodology selection, - performing microhardness measurements and analysing results, - Funding and project management - performing all microstructural observations using transmission electron microscopy, analysing obtained microstructures, - results analysis - writing the original draft of the paper, reviewing and editing. This publication is a result of the SONATINA project, 'Synthesis of Novel Hybrid Materials Using High-Pressure Torsion' (UMO-2017/24/C/ST8/00145), in which I have been a leader (PI)	
Co-authors' contribution:			
2	*Nosewicz Szymon*	Synthesis of Cu-SiC composites, Analysis of the obtained results , Editing the final version of the article	
3	*Romelczyk-Baishya Barbara*	Performing static tensile test	
4	*Chmielewski Marcin*	Selection of sintering parameters	

5	*Strojny Nędza Agata*	Thermal conduction measurements	
6	*Maj Justyna*	Thermal conduction data analysis	
7	*Huang Yi*	HPT processing of Cu-SiC samples. Editing the final version of the article, Examination of the results	
8	*Lewandowska Małgorzata*	Editing the final version of the article, analysis of the results	
9	*Langdon Terence G.*	Editing the final version of the article, Discussion of the results obtained, Proofreading and language editing	

Statement

Publication title, journal, year, doi:

Effect of spark plasma sintering and high-pressure torsion on the microstructural and mechanical properties of a Cu–SiC composite, Materials Science and Engineering A 766 (2019) 138350 https://doi.org/10.1016/j.msea.2019.138350.

Names and surnames of publication authors:

***Bazarnik Piotr**, Nosewicz Szymon, Romelczyk-Baishya Barbara, Chmielewski Marcin, Strojny Nędza Agata, Maj Justyna, Huang Yi, Lewandowska Małgorzata, Langdon Terence G.*

Statement on the substantive contribution of the work to the above-mentioned publication and consent to submit it for habilitation

No.	Author	Contribution	Signature
1	***Piotr Bazarnik***	In this article I was responsible for: - conceptualization of all performed research, - methodology selection, - performing microhardness measurements and analysing results, - Funding and project management - performing all microstructural observations using transmission electron microscopy, analysing obtained microstructures, - results analysis - writing the original draft of the paper, reviewing and editing. This publication is a result of the SONATINA project, 'Synthesis of Novel Hybrid Materials Using High-Pressure Torsion' (UMO-2017/24/C/ST8/00145), in which I have been a leader (PI)	
Co-authors' contribution:			
2	*Nosewicz Szymon*	Synthesis od Cu-SiC composites, Analysis of the obtained results , Editing the final version of the article	
3	*Romelczyk-Baishya Barbara*	Performing static tensile test	
4	*Chmielewski Marcin*	Selection of sintering parameters	

5	*Strojny Nędza Agata*	Thermal conduction measurements	
6	*Maj Justyna*	Thermal conduction data analysis	
7	*Huang Yi*	HPT processing of Cu-SiC samples. Editing the final version of the article, Examination of the results	
8	*Lewandowska Małgorzata*	Editing the final version of the article, analysis of the results	
9	*Langdon Terence G.*	Editing the final version of the article, Discussion of the results obtained, Proofreading and language editing	

Statement

Publication title, journal, year, doi:

The influence of graphene oxide on the microstructure and properties of ultrafine-grained copper processed by high-pressure torsion. Journal of Alloys and Compounds, 1005 (2024), 176208. https://doi.org/10.1016/j.jallcom.2024.176208

Names and surnames of publication authors:

Emerla Maria, **Bazarnik Piotr**, Yi Huang, Wojciechowska Anita, Ciemiorek Marta, Pura Jarosław, Wieczorek-Czarnocka Monika, Kenichi Purbayanto Muhammad Abiyyu, Jastrzębska Agnieszka, Lewandowska Małgorzata, Langdon Terence G.,

Statement on the substantive contribution of the work to the above-mentioned publication and consent to submit it for habilitation

No.	Author	Contribution	Signature
1	***Piotr Bazarnik***	In this article I was responsible for: - conceptualization of all performed research, - methodology selection, - data analysis - funding and project management - performing all microstructural observations using transmission electron microscopy and scanning electron microscopy, analysing obtained microstructures, EDX analysis which were used to create table 2 - creating figures regarding structural analysis (Fig. 2, 10 and 11) - writing parts in the original draft of the paper (including the discussion part), reviewing and editing - submission of paper This publication is a result of the OPUS project, "Metal matrix composites fabricated by high-pressure torsion and reinforced with 2D and 3D nano-particles" (UMO-2020/37/B/ST5/01837), in which I have been a leader (PI)	
Co-authors' contribution:			
2	*Emerla Maria*	HPT processing of Cu composite samples during research stay at Southampton University, Performing annealing experiments, SEM observations annealed samples, Data analysis, SEM observations after wear tests, writing the original draft of the paper (including the discussion part), reviewing and editing	

3	*Yi Huang*	Selection of parameters for the HPT process, Editing the final version of the article, Discussion on the results obtained	
4	*Wojciechowska Anita*	Synthesis of GO nanoparticles	brak kontaktu
5	*Ciemiorek Marta*	Conducting tensile tests	
6	*Pura Jarosław*	Conducting wear tests	
7	Wieczorek-Czarnocka Monika	Conducting tensile tests	
8	Purbayanto Muhammad Abiyyu Kenichi	Performing electrical conductivity tests	
9	Jastrzębsta Agnieszka	Performing microhardness tests and their analysis, Discussion of the results obtained,	
10	Lewandowska Małgorzata	Discussion of the results obtained, Editing the final version of the article	
11	*Langdon Terence G.*	Proofreading and language editing, Validation and verification, Editing the final version of the article, conceptualization	

Statement

Publication title, journal, year, doi:

The influence of graphene oxide on the microstructure and properties of ultrafine-grained copper processed by high-pressure torsion, Journal of Alloys and Compounds, 1005 (2024), 176208. https://doi.org/10.1016/j.jallcom.2024.176208

Names and surnames of publication authors:

Emerla Maria, **Bazarnik Piotr**, Yi Huang, Wojciechowska Anita, Ciemiorek Marta, Pura Jarosław, Wieczorek-Czarnocka Monika, Kenichi Purbayanto Muhammad Abiyyu, Jastrzębsta Agnieszka, Lewandowska Małgorzata, Langdon Terence G.,

Statement on the substantive contribution of the work to the above-mentioned publication and consent to submit it for habilitation

No.	Author	Contribution	Signature
1	***Piotr Bazarnik***	In this article I was responsible for: - conceptualization of all performed research, - methodology selection, - data analysis - funding and project management - performing all microstructural observations using transmission electron microscopy and scanning electron microscopy, analysing obtained microstructures, EDX analysis which were used to create table 2 - creating figures regarding structural analysis (Fig. 2, 10 and 11) - writing parts in the original draft of the paper (including the discussion part), reviewing and editing - submission of paper This publication is a result of the OPUS project, "Metal matrix composites fabricated by high-pressure torsion and reinforced with 2D and 3D nano-particles" (UMO-2020/37/B/ST5/01837), in which I have been a leader (PI)	
Co-authors' contribution:			
2	*Emerla Maria*	HPT processing of Cu composite samples during research stay at Southampton University, Performing annealing experiments, SEM observations annealed samples, Data analysis, SEM observations	

		after wear tests, writing the original draft of the paper (including the discussion part), reviewing and editing	
3	*Yi Huang*	Selection of parameters for the HPT process, Editing the final version of the article, Discussion on the results obtained	
4	*Wojciechowska Anita*	Synthesis of GO nanoparticles	
5	*Ciemiorek Marta*	Conducting tensile tests	
6	*Pura Jarosław*	Conducting wear tests	
7	Wieczorek-Czarnocka Monika	Conducting tensile tests	
8	Purbayanto Muhammad Abiyyu Kenichi	Performing electrical conductivity tests	
9	Jastrzębsta Agnieszka	Performing microhardness tests and their analysis, Discussion of the results obtained,	
10	Lewandowska Małgorzata	Discussion of the results obtained, Editing the final version of the article	
11	*Langdon Terence G.*	Proofreading and language editing, Validation and verification, Editing the final version of the article, conceptualization	

Statement

Publication title, journal, year, doi:

The influence of graphene oxide on the microstructure and properties of ultrafine-grained copper processed by high-pressure torsion, Journal of Alloys and Compounds, 1005 (2024), 176208. https://doi.org/10.1016/j.jallcom.2024.176208

Names and surnames of publication authors:

Emerla Maria, **Bazarnik Piotr**, Yi Huang, Wojciechowska Anita, Ciemiorek Marta, Pura Jarosław, Wieczorek-Czarnocka Monika, Kenichi Purbayanto Muhammad Abiyyu, Jastrzębsta Agnieszka, Lewandowska Małgorzata, Langdon Terence G.,

Statement on the substantive contribution of the work to the above-mentioned publication and consent to submit it for habilitation

No.	Author	Contribution	Signature
1	***Piotr Bazarnik***	In this article I was responsible for: - conceptualization of all performed research, - methodology selection, - data analysis - funding and project management - performing all microstructural observations using transmission electron microscopy and scanning electron microscopy, analysing obtained microstructures, EDX analysis which were used to create table 2 - creating figures regarding structural analysis (Fig. 2, 10 and 11) - writing parts in the original draft of the paper (including the discussion part), reviewing and editing - submission of paper This publication is a result of the OPUS project, "Metal matrix composites fabricated by high-pressure torsion and reinforced with 2D and 3D nano-particles" (UMO-2020/37/B/ST5/01837), in which I have been a leader (PI)	
Co-authors' contribution:			
2	*Emerla Maria*	HPT processing of Cu composite samples during research stay at Southampton University, Performing annealing experiments, SEM observations annealed samples, Data analysis, SEM observations after wear tests, writing the original draft of the paper (including the discussion part), reviewing and editing	

3	*Yi Huang*	Selection of parameters for the HPT process, Editing the final version of the article, Discussion on the results obtained	
4	*Wojciechowska Anita*	Synthesis of GO nanoparticles	
5	*Ciemiorek Marta*	Conducting tensile tests	
6	*Pura Jarosław*	Conducting wear tests	
7	Wieczorek-Czarnocka Monika	Conducting tensile tests	
8	Purbayanto Muhammad Abiyyu Kenichi	Performing electrical conductivity tests	
9	Jastrzębsta Agnieszka	Performing microhardness tests and their analysis, Discussion of the results obtained,	
10	Lewandowska Małgorzata	Discussion of the results obtained, Editing the final version of the article	
11	*Langdon Terence G.*	Proofreading and language editing, Validation and verification, Editing the final version of the article, conceptualization	

Statement

Publication title, journal, year, doi:

Enhanced thermal stability of nanocrystalline Cu composites processed by high-pressure torsion: The pinning effect of Al_2O_3, GO, and rGO/Al_2O_3 nanoparticles, Journal of Alloys and Compounds, 1033 (2025), 181283. https://doi.org/10.1016/j.jallcom.2025.181283

Names and surnames of publication authors:

Bazarnik Piotr, Emerla Maria, Huang Yi, Wojciechowska Anita, Ciemiorek Marta, Bednarczyk Wiktor, Jastrzębska Agnieszka, Lewandowska Małgorzata, Langdon Terence G.,

Statement on the substantive contribution of the work to the above-mentioned publication and consent to submit it for habilitation

No.	Author	Contribution	Signature
1	***Piotr Bazarnik***	In this article I was responsible for: - conceptualization of all performed research, - methodology selection, - data analysis - funding and project management - performing all microstructural observations using transmission electron microscopy, analysing obtained microstructures, EDX analysis which were used to create table 1 - creating figures regarding structural analysis (Fig. 2, 3, 4 and 9) - writing the original draft of the paper (including the discussion part), reviewing and editing This publication is a result of the OPUS project, "Metal matrix composites fabricated by high-pressure torsion and reinforced with 2D and 3D nano-particles" (UMO-2020/37/B/ST5/01837), in which I have been a leader (PI)	
Co-authors' contribution:			
2	*Emerla Maria*	HPT processing of Cu composite samples during research stay at Southampton University, Performing annealing experiments, SEM observations annealed samples, Data analysis, SEM observations after wear tests, writing the original draft of the paper	
3	*Yi Huang*	Selection of parameters for the HPT process, Editing the final version of the article, Discussion on the results obtained	
4	*Wojciechowska Anita*	Synthesis of GO, Al_2O_3 and rGO/Al_2O_3 nanoparticles	

5	*Ciemiorek Marta*	Conducting tensile tests	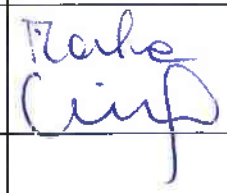
6	*Bednarczyk Wiktor*	EBSD analysis	
7	Jastrzębska Agnieszka	Discussion of the results obtained	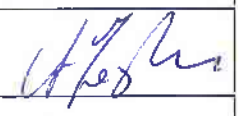
8	Lewandowska Małgorzata	Discussion of the results obtained, Editing the final version of the article	
9	*Langdon Terence G.*	Proofreading and language editing, Validation and verification, Editing the final version of the article, conceptualization	

Statement

Publication title, journal, year, doi:

Enhanced thermal stability of nanocrystalline Cu composites processed by high-pressure torsion: The pinning effect of Al_2O_3, GO, and rGO/Al_2O_3 nanoparticles, Journal of Alloys and Compounds, 1033 (2025), 181283. https://doi.org/10.1016/j.jallcom.2025.181283

Names and surnames of publication authors:

Bazarnik Piotr, Emerla Maria, Huang Yi, Wojciechowska Anita, Ciemiorek Marta, Bednarczyk Wiktor, Jastrzębska Agnieszka, Lewandowska Małgorzata, Langdon Terence G.,

Statement on the substantive contribution of the work to the above-mentioned publication and consent to submit it for habilitation

No.	Author	Contribution	Signature
1	***Piotr Bazarnik***	In this article I was responsible for: - conceptualization of all performed research, - methodology selection, - data analysis - funding and project management - performing all microstructural observations using transmission electron microscopy, analysing obtained microstructures, EDX analysis which were used to create table 1 - creating figures regarding structural analysis (Fig. 2, 3, 4 and 9) - writing the original draft of the paper (including the discussion part), reviewing and editing This publication is a result of the OPUS project, "Metal matrix composites fabricated by high-pressure torsion and reinforced with 2D and 3D nano-particles" (UMO-2020/37/B/ST5/01837), in which I have been a leader (PI)	
Co-authors' contribution:			
2	*Emerla Maria*	HPT processing of Cu composite samples during research stay at Southampton University, Performing annealing experiments, SEM observations annealed samples, Data analysis, SEM observations after wear tests, writing the original draft of the paper	

3	*Yi Huang*	Selection of parameters for the HPT process, Editing the final version of the article, Discussion on the results obtained	
4	*Wojciechowska Anita*	Synthesis of GO, Al_2O_3 and rGO/Al_2O_3 nanoparticles	
5	*Ciemiorek Marta*	Conducting tensile tests	
6	*Bednarczyk Wiktor*	EBSD analysis	
7	Jastrzębska Agnieszka	Discussion of the results obtained	
8	Lewandowska Małgorzata	Discussion of the results obtained, Editing the final version of the article	
9	*Langdon Terence G.*	Proofreading and language editing, Validation and verification, Editing the final version of the article, conceptualization	

Statement

Publication title, journal, year, doi:

Enhanced thermal stability of nanocrystalline Cu composites processed by high-pressure torsion: The pinning effect of Al_2O_3, GO, and rGO/Al_2O_3 nanoparticles, Journal of Alloys and Compounds, 1033 (2025), 181283. https://doi.org/10.1016/j.jallcom.2025.181283

Names and surnames of publication authors:

Bazarnik Piotr, Emerla Maria, Huang Yi, Wojciechowska Anita, Ciemiorek Marta, Bednarczyk Wiktor, Jastrzębska Agnieszka, Lewandowska Małgorzata, Langdon Terence G.,

Statement on the substantive contribution of the work to the above-mentioned publication and consent to submit it for habilitation

No.	Author	Contribution	Signature
1	***Piotr Bazarnik***	In this article I was responsible for: - conceptualization of all performed research, - methodology selection, - data analysis - funding and project management - performing all microstructural observations using transmission electron microscopy, analysing obtained microstructures, EDX analysis which were used to create table 1 - creating figures regarding structural analysis (Fig. 2, 3, 4 and 9) - writing the original draft of the paper (including the discussion part), reviewing and editing This publication is a result of the OPUS project, "Metal matrix composites fabricated by high-pressure torsion and reinforced with 2D and 3D nano-particles" (UMO-2020/37/B/ST5/01837), in which I have been a leader (PI)	
Co-authors' contribution:			
2	*Emerla Maria*	HPT processing of Cu composite samples during research stay at Southampton University, Performing annealing experiments, SEM observations annealed samples, Data analysis, SEM observations after wear tests, writing the original draft of the paper	
3	*Yi Huang*	Selection of parameters for the HPT process, Editing the final version of the article, Discussion on the results obtained	

4	*Wojciechowska Anita*	Synthesis of GO, Al_2O_3 and rGO/Al_2O_3 nanoparticles	
5	*Ciemiorek Marta*	Conducting tensile tests	
6	*Bednarczyk Wiktor*	EBSD analysis	
7	Jastrzębska Agnieszka	Discussion of the results obtained	
8	Lewandowska Małgorzata	Discussion of the results obtained, Editing the final version of the article	
9	*Langdon Terence G.*	Proofreading and language editing, Validation and verification, Editing the final version of the article, conceptualization	

Statement

Publication title, journal, year, doi:

Enhanced thermal stability of nanocrystalline Cu composites processed by high-pressure torsion: The pinning effect of Al_2O_3, GO, and rGO/Al_2O_3 nanoparticles, Journal of Alloys and Compounds, 1033 (2025), 181283. https://doi.org/10.1016/j.jallcom.2025.181283

Names and surnames of publication authors:

Bazarnik Piotr, Emerla Maria, Huang Yi, Wojciechowska Anita, Ciemiorek Marta, Bednarczyk Wiktor, Jastrzębska Agnieszka, Lewandowska Małgorzata, Langdon Terence G.,

Statement on the substantive contribution of the work to the above-mentioned publication and consent to submit it for habilitation

No.	Author	Contribution	Signature
1	***Piotr Bazarnik***	In this article I was responsible for: - conceptualization of all performed research, - methodology selection, - data analysis - funding and project management - performing all microstructural observations using transmission electron microscopy, analysing obtained microstructures, EDX analysis which were used to create table 1 - creating figures regarding structural analysis (Fig. 2, 3, 4 and 9) - writing the original draft of the paper (including the discussion part), reviewing and editing This publication is a result of the OPUS project, "Metal matrix composites fabricated by high-pressure torsion and reinforced with 2D and 3D nano-particles" (UMO-2020/37/B/ST5/01837), in which I have been a leader (PI)	
Co-authors' contribution:			
2	*Emerla Maria*	HPT processing of Cu composite samples during research stay at Southampton University, Performing annealing experiments, SEM observations annealed samples, Data analysis, SEM observations after wear tests, writing the original draft of the paper	
3	*Yi Huang*	Selection of parameters for the HPT process, Editing the final version of the article, Discussion on the results obtained	
4	*Wojciechowska Anita*	Synthesis of GO, Al_2O_3 and rGO/Al_2O_3 nanoparticles	

5	*Ciemiorek Marta*	Conducting tensile tests	
6	*Bednarczyk Wiktor*	EBSD analysis	
7	Jastrzębska Agnieszka	Discussion of the results obtained	
8	Lewandowska Małgorzata	Discussion of the results obtained, Editing the final version of the article	
9	*Langdon Terence G.*	Proofreading and language editing, Validation and verification, Editing the final version of the article, conceptualization	

Statement

Publication title, journal, year, doi:

Using high-pressure torsion to fabricate an Al–Ti hybrid system with exceptional mechanical properties, Materials Science and Engineering A 799 (2021) 140114 https://doi.org/10.1016/j.msea.2020.140114.

Names and surnames of publication authors:

*Bartkowska Aleksandra, **Bazarnik Piotr**, Huang Yi, Lewandowska Małgorzata, Langdon Terence G.*

Statement on the substantive contribution of the work to the above-mentioned publication and consent to submit it for habilitation

No.	Author	Contribution	Signature
1	***Piotr Bazarnik***	In this article I was responsible for: - conceptualization of all performed research, - HPT processing of samples during research stay at Southampton University - methodology selection, results analysis - funding and project management - performing all microstructural observations using transmission electron microscopy, performing EDX analysis - analysing obtained microstructures, creating Fig. 3 - writing parts of the original draft of the paper (including the discussion part), reviewing and editing. - Submission of paper This publication is a result of the SONATINA project, 'Synthesis of Novel Hybrid Materials Using High-Pressure Torsion' (UMO-2017/24/C/ST8/00145), in which I have been a leader (PI)	
Co-authors' contribution:			
2	*Bartkowska Aleksandra*	Writing and editing the final version of the article, Analysis of XRD spectra, Performing of microhardness measurements and their analysis.	
3	*Huang Yi*	Literature review and background research, Conceptualization of HPT experiments, Editing the final version of the article,	
4	*Lewandowska Małgorzata*	Discussion of the results obtained, Editing the final version of the article, Conceptualization of work	

5	*Langdon Terence G.*	Editing the final version of the article, Proofreading and language editing, funding support	

Statement

Publication title, journal, year, doi:

Using high-pressure torsion to fabricate an Al–Ti hybrid system with exceptional mechanical properties, Materials Science and Engineering A 799 (2021) 140114 https://doi.org/10.1016/j.msea.2020.140114.

Names and surnames of publication authors:

*Bartkowska Aleksandra, **Bazarnik Piotr**, Huang Yi, Lewandowska Malgorzata, Langdon Terence G.*

Statement on the substantive contribution of the work to the above-mentioned publication and consent to submit it for habilitation

No.	Author	Contribution	Signature
1	***Piotr Bazarnik***	In this article I was responsible for: - conceptualization of all performed research, - HPT processing of samples during research stay at Southampton University - methodology selection, results analysis - funding and project management - performing all microstructural observations using transmission electron microscopy, performing EDX analysis - analysing obtained microstructures, creating Fig. 3 - writing parts of the original draft of the paper (including the discussion part), reviewing and editing. - Submission of paper This publication is a result of the SONATINA project, 'Synthesis of Novel Hybrid Materials Using High-Pressure Torsion' (UMO-2017/24/C/ST8/00145), in which I have been a leader (PI)	
Co-authors' contribution:			
2	*Bartkowska Aleksandra*	Writing and editing the final version of the article, Analysis of XRD spectra, Performing of microhardness measurements and their analysis, metallographic observations of the samples	Aleksandra Bartkowska
3	*Huang Yi*	Literature review and background research, Conceptualization of HPT experiments, Editing the final version of the article,	
4	*Lewandowska Małgorzata*	Discussion of the results obtained, Editing the final version of the article, Conceptualization of work	

5	*Langdon Terence G.*	Editing the final version of the article, Proofreading and language editing, funding support	

Statement

Publication title, journal, year, doi:

Using high-pressure torsion to fabricate an Al–Ti hybrid system with exceptional mechanical properties, Materials Science and Engineering A 799 (2021) 140114 https://doi.org/10.1016/j.msea.2020.140114.

Names and surnames of publication authors:

*Bartkowska Aleksandra, **Bazarnik Piotr**, Huang Yi, Lewandowska Malgorzata, Langdon Terence G.*

Statement on the substantive contribution of the work to the above-mentioned publication and consent to submit it for habilitation

No.	Author	Contribution	Signature
1	***Piotr Bazarnik***	In this article I was responsible for: - conceptualization of all performed research, - HPT processing of samples during research stay at Southampton University - methodology selection, results analysis - funding and project management - performing all microstructural observations using transmission electron microscopy, performing EDX analysis - analysing obtained microstructures, creating Fig. 3 - writing parts of the original draft of the paper (including the discussion part), reviewing and editing. - Submission of paper This publication is a result of the SONATINA project, 'Synthesis of Novel Hybrid Materials Using High-Pressure Torsion' (UMO-2017/24/C/ST8/00145), in which I have been a leader (PI)	
Co-authors' contribution:			
2	*Bartkowska Aleksandra*	Writing and editing the final version of the article, Analysis of XRD spectra, Performing of microhardness measurements and their analysis.	
3	*Huang Yi*	Literature review and background research, Conceptualization of HPT experiments, Editing the final version of the article,	

4	*Lewandowska Małgorzata*	Discussion of the results obtained, Editing the final version of the article, Conceptualization of work	
5	*Langdon Terence G.*	Editing the final version of the article, Proofreading and language editing, funding support	

Statement

Publication title, journal, year, doi:

Using high-pressure torsion to fabricate an Al–Ti hybrid system with exceptional mechanical properties, Materials Science and Engineering A 799 (2021) 140114 https://doi.org/10.1016/j.msea.2020.140114.

Names and surnames of publication authors:

*Bartkowska Aleksandra, **Bazarnik Piotr**, Huang Yi, Lewandowska Malgorzata, Langdon Terence G.*

Statement on the substantive contribution of the work to the above-mentioned publication and consent to submit it for habilitation

No.	Author	Contribution	Signature
1	***Piotr Bazarnik***	In this article I was responsible for: - conceptualization of all performed research, - HPT processing of samples during research stay at Southampton University - methodology selection, results analysis - funding and project management - performing all microstructural observations using transmission electron microscopy, performing EDX analysis - analysing obtained microstructures, creating Fig. 3 - writing parts of the original draft of the paper (including the discussion part), reviewing and editing. - Submission of paper This publication is a result of the SONATINA project, 'Synthesis of Novel Hybrid Materials Using High-Pressure Torsion' (UMO-2017/24/C/ST8/00145), in which I have been a leader (PI)	
Co-authors' contribution:			
2	*Bartkowska Aleksandra*	Writing and editing the final version of the article, Analysis of XRD spectra, Performing of microhardness measurements and their analysis.	
3	*Huang Yi*	Literature review and background research, Conceptualization of HPT experiments, Editing the final version of the article,	
4	*Lewandowska Małgorzata*	Discussion of the results obtained, Editing the final version of the article, Conceptualization of work	

5	*Langdon Terence G.*	Editing the final version of the article, Proofreading and language editing, funding support	

Statement

Publication title, journal, year, doi:

Fabrication of hybrid nanocrystalline Al–Ti alloys by mechanical bonding through high-pressure torsion, Materials Science and Engineering A 833 (2022) 142549. https://doi.org/10.1016/j.msea.2021.142549

Names and surnames of publication authors:

Bazarnik Piotr, *Bartkowska Aleksandra, Huang Yi, Szlązak Karol, Adamczyk-Cieślak Bogusława, Sort Jordi, Lewandowska Małgorzata, Langdon Terence G.*

Statement on the substantive contribution of the work to the above-mentioned publication and consent to submit it for habilitation

No.	Author	Contribution	Signature
1	***Piotr Bazarnik***	In this article I was responsible for: - conceptualization of all performed research, - HPT processing of samples during research stay at Southampton University - methodology selection, - funding and project management - performing all microstructural observations using transmission electron microscopy, SAED, performing EDX analysis - analysing obtained microstructures, - writing original draft of the paper This publication is a result of the IDUB project, ' Thermal Stability and Deformation Mechanisms of Hybrid Nanocrystalline Materials Produced by High Pressure Torsion (HPT) Techniques' (504/04496/1090), in which I have been a leader (PI)	
Co-authors' contribution:			
2	*Bartkowska Aleksandra*	Editing the final version of the article, Conceptualization, Performing of microhardness measurements and their analysis. SEM analysis of fabricated samples, Submission of paper	
3	*Huang Yi*	Conceptualization of HPT experiments, Editing the final version of the article,	
4	*Szlązak Karol*	Performing of microanalysis tests	
5	*Adamczyk-Cieślak Bogusława*	XRD analysis	

6	*Sort Jordi*	Editing the final version of the article	
7	*Lewandowska Małgorzata*	Discussion of the results obtained, Editing the final version of the article, Conceptualization of work	
8	*Langdon Terence G.*	Editing the final version of the article, Discussion of the results obtained Proofreading and language editing, funding support	

Statement

Publication title, journal, year, doi:

Fabrication of hybrid nanocrystalline Al–Ti alloys by mechanical bonding through high-pressure torsion, Materials Science and Engineering A 833 (2022) 142549. https://doi.org/10.1016/j.msea.2021.142549

Names and surnames of publication authors:

Bazarnik Piotr, *Bartkowska Aleksandra, Huang Yi, Szlązak Karol, Adamczyk-Cieślak Bogusława, Sort Jordi, Lewandowska Malgorzata, Langdon Terence G.*

Statement on the substantive contribution of the work to the above-mentioned publication and consent to submit it for habilitation

No.	Author	Contribution	Signature
1	***Piotr Bazarnik***	In this article I was responsible for: - conceptualization of all performed research, - HPT processing of samples during research stay at Southampton University - methodology selection, - funding and project management - performing all microstructural observations using transmission electron microscopy, SAED, performing EDX analysis - analysing obtained microstructures, - writing original draft of the paper This publication is a result of the IDUB project, ' Thermal Stability and Deformation Mechanisms of Hybrid Nanocrystalline Materials Produced by High Pressure Torsion (HPT) Techniques' (504/04496/1090), in which I have been a leader (PI)	
Co-authors' contribution:			
2	*Bartkowska Aleksandra*	Editing the final version of the article, Conceptualization, Performing of microhardness and nanoindentation measurements and their analysis. SEM analysis of fabricated samples, Submission of paper	Aleksandra Bartkowska
3	*Huang Yi*	Conceptualization of HPT experiments, Editing the final version of the article,	
4	*Szlązak Karol*	Performing of microanalysis tests	

5	*Adamczyk-Cieślak Bogusława*	XRD analysis	
6	*Sort Jordi*	Editing the final version of the article, conceptualization of nanoindentation test.	JORDI SORT VIÑAS - DNI 45480838V Firmado digitalmente por JORDI SORT VIÑAS - DNI 45480838V Nombre de reconocimiento (DN): c=ES, sn=SORT VIÑAS, givenName=JORDI, serialNumber=IDCES-45480838V, cn=JORDI SORT VIÑAS - DNI 45480838V Fecha: 2025.03.19 09:38:17 +01'00'
7	*Lewandowska Małgorzata*	Discussion of the results obtained, Editing the final version of the article, Conceptualization of work	
8	*Langdon Terence G.*	Editing the final version of the article, Discussion of the results obtained Proofreading and language editing, funding support	

Statement

Publication title, journal, year, doi:

Fabrication of hybrid nanocrystalline Al–Ti alloys by mechanical bonding through high-pressure torsion, Materials Science and Engineering A 833 (2022) 142549. https://doi.org/10.1016/j.msea.2021.142549

Names and surnames of publication authors:

Bazarnik Piotr, *Bartkowska Aleksandra, Huang Yi, Szlązak Karol, Adamczyk-Cieślak Bogusława, Sort Jordi, Lewandowska Malgorzata, Langdon Terence G.*

Statement on the substantive contribution of the work to the above-mentioned publication and consent to submit it for habilitation

No.	Author	Contribution	Signature
1	***Piotr Bazarnik***	In this article I was responsible for: - conceptualization of all performed research, - HPT processing of samples during research stay at Southampton University - methodology selection, - funding and project management - performing all microstructural observations using transmission electron microscopy, SAED, performing EDX analysis - analysing obtained microstructures, - writing original draft of the paper This publication is a result of the IDUB project, ' Thermal Stability and Deformation Mechanisms of Hybrid Nanocrystalline Materials Produced by High Pressure Torsion (HPT) Techniques' (504/04496/1090), in which I have been a leader (PI)	
Co-authors' contribution:			
2	*Bartkowska Aleksandra*	Editing the final version of the article, Conceptualization, Performing of microhardness measurements and their analysis. SEM analysis of fabricated samples, Submission of paper	
3	*Huang Yi*	Conceptualization of HPT experiments, Editing the final version of the article,	
4	*Szlązak Karol*	Performing of microanalysis tests	

5	*Adamczyk-Cieślak Bogusława*	XRD analysis	
6	*Sort Jordi*	Editing the final version of the article	
7	*Lewandowska Małgorzata*	Discussion of the results obtained, Editing the final version of the article, Conceptualization of work	
8	*Langdon Terence G.*	Editing the final version of the article, Discussion of the results obtained Proofreading and language editing, funding support	

Statement

Publication title, journal, year, doi:

Fabrication of hybrid nanocrystalline Al–Ti alloys by mechanical bonding through high-pressure torsion, Materials Science and Engineering A 833 (2022) 142549. https://doi.org/10.1016/j.msea.2021.142549

Names and surnames of publication authors:

Bazarnik Piotr, *Bartkowska Aleksandra, Huang Yi, Szlązak Karol, Adamczyk-Cieślak Bogusława, Sort Jordi, Lewandowska Malgorzata, Langdon Terence G.*

Statement on the substantive contribution of the work to the above-mentioned publication and consent to submit it for habilitation

No.	Author	Contribution	Signature
1	***Piotr Bazarnik***	In this article I was responsible for: - conceptualization of all performed research, - HPT processing of samples during research stay at Southampton University - methodology selection, - funding and project management - performing all microstructural observations using transmission electron microscopy, SAED, performing EDX analysis - analysing obtained microstructures, - writing original draft of the paper This publication is a result of the IDUB project, ' Thermal Stability and Deformation Mechanisms of Hybrid Nanocrystalline Materials Produced by High Pressure Torsion (HPT) Techniques' (504/04496/1090), in which I have been a leader (PI)	
Co-authors' contribution:			
2	*Bartkowska Aleksandra*	Editing the final version of the article, Conceptualization, Performing of microhardness measurements and their analysis. SEM analysis of fabricated samples, Submission of paper	
3	*Huang Yi*	Conceptualization of HPT experiments, Editing the final version of the article,	
4	*Szlązak Karol*	Performing of microanalysis tests	
5	*Adamczyk-Cieślak Bogusława*	XRD analysis	

6	*Sort Jordi*	Editing the final version of the article	
7	*Lewandowska Małgorzata*	Discussion of the results obtained, Editing the final version of the article, Conceptualization of work	
8	*Langdon Terence G.*	Editing the final version of the article, Discussion of the results obtained Proofreading and language editing, funding support	

Statement

Publication title, journal, year, doi:

Superior strength of tri-layered Al–Cu–Al nano-composites processed by high-pressure torsion, Journal of Alloys and Compounds 846 (2020), 156380. https://doi.org/10.1016/j.jallcom.2020.156380.

Names and surnames of publication authors:

Bazarnik Piotr, *Bartkowska Aleksandra, Romelczyk-Baishya Barbara, Adamczyk-Cieślak Bogusława, Dai Jiaoyan, Huang Yi, Lewandowska Małgorzata, Langdon Terence G.*

Statement on the substantive contribution of the work to the above-mentioned publication and consent to submit it for habilitation

No.	Author	Contribution	Signature
1	***Piotr Bazarnik***	In this article I was responsible for: - conceptualization of all performed research, - methodology selection, - funding and project management - performing all microstructural observations using transmission electron microscopes and scanning electron microscopy, SAED analysis, dark field and EDX analysis - analysing of obtained microstructural and mechanical results - writing the original draft of the paper, reviewing and editing. - Creating of all figures - Submission of paper This publication is a result of the SONATINA project, 'Synthesis of Novel Hybrid Materials Using High-Pressure Torsion' (UMO-2017/24/C/ST8/00145), in which I have been a leader (PI)	
Co-authors' contribution:			
2	*Bartkowska Aleksandra*	Editing the final version of the article, Performing of microhardness measurements.	
3	*Romelczyk-Baishya Barbara*	Performing tensile test	
4	*Adamczyk-Cieślak Bogusława*	Performing XRD analysis	

5	*Dai, Jiaoyan*	HPT processing of Al-Cu samples	
6	*Huang Yi*	Conceptualization of HPT experiments, Editing the final version of the article, HPT processing	
7	*Lewandowska Małgorzata*	Discussion of the results obtained, Editing the final version of the article	
8	*Langdon Terence G.*	Editing the final version of the article, Proofreading and language editing,	

Statement

Publication title, journal, year, doi:

Superior strength of tri-layered Al–Cu–Al nano-composites processed by high-pressure torsion, Journal of Alloys and Compounds 846 (2020), 156380. https://doi.org/10.1016/j.jallcom.2020.156380.

Names and surnames of publication authors:

Bazarnik Piotr, *Bartkowska Aleksandra, Romelczyk-Baishya Barbara, Adamczyk-Cieślak Bogusława, Dai Jiaoyan, Huang Yi, Lewandowska Małgorzata, Langdon Terence G.*

Statement on the substantive contribution of the work to the above-mentioned publication and consent to submit it for habilitation

No.	Author	Contribution	Signature
1	***Piotr Bazarnik***	In this article I was responsible for: - conceptualization of all performed research, - methodology selection, - funding and project management - performing all microstructural observations using transmission electron microscopes and scanning electron microscopy, SAED analysis, dark field and EDX analysis - analysing of obtained microstructural and mechanical results - writing the original draft of the paper, reviewing and editing. - Creating of all figures - Submission of paper This publication is a result of the SONATINA project, 'Synthesis of Novel Hybrid Materials Using High-Pressure Torsion' (UMO-2017/24/C/ST8/00145), in which I have been a leader (PI)	
Co-authors' contribution:			
2	*Bartkowska Aleksandra*	Editing the final version of the article, Performing of microhardness measurements.	
3	*Romelczyk-Baishya Barbara*	Performing tensile test	
4	*Adamczyk-Cieślak Bogusława*	Performing XRD analysis	

5	*Dai, Jiaoyan*	HPT processing of Al-Cu samples	Jiaoyan Dai
6	*Huang Yi*	Conceptualization of HPT experiments, Editing the final version of the article, HPT processing	
7	*Lewandowska Małgorzata*	Discussion of the results obtained, Editing the final version of the article	
8	*Langdon Terence G.*	Editing the final version of the article, Proofreading and language editing,	

Statement

Publication title, journal, year, doi:

Superior strength of tri-layered Al–Cu–Al nano-composites processed by high-pressure torsion, Journal of Alloys and Compounds 846 (2020), 156380. https://doi.org/10.1016/j.jallcom.2020.156380.

Names and surnames of publication authors:

Bazarnik Piotr, *Bartkowska Aleksandra, Romelczyk-Baishya Barbara, Adamczyk-Cieślak Bogusława, Dai Jiaoyan, Huang Yi, Lewandowska Małgorzata, Langdon Terence G.*

Statement on the substantive contribution of the work to the above-mentioned publication and consent to submit it for habilitation

No.	Author	Contribution	Signature
1	***Piotr Bazarnik***	In this article I was responsible for: - conceptualization of all performed research, - methodology selection, - funding and project management - performing all microstructural observations using transmission electron microscopes and scanning electron microscopy, SAED analysis, dark field and EDX analysis - analysing of obtained microstructural and mechanical results - writing the original draft of the paper, reviewing and editing. - Creating of all figures - Submission of paper This publication is a result of the SONATINA project, 'Synthesis of Novel Hybrid Materials Using High-Pressure Torsion' (UMO-2017/24/C/ST8/00145), in which I have been a leader (PI)	
Co-authors' contribution:			
2	*Bartkowska Aleksandra*	Editing the final version of the article, Performing of microhardness measurements and data analysis.	Aleksandra Bartkowska
3	*Romelczyk-Baishya Barbara*	Performing tensile test	
4	*Adamczyk-Cieślak Bogusława*	Performing XRD analysis	

5	*Dai, Jiaoyan*	HPT processing of Al-Cu samples	
6	*Huang Yi*	Conceptualization of HPT experiments, Editing the final version of the article, HPT processing	
7	*Lewandowska Małgorzata*	Discussion of the results obtained, Editing the final version of the article	
8	*Langdon Terence G.*	Editing the final version of the article, Proofreading and language editing,	

Statement

Publication title, journal, year, doi:

Superior strength of tri-layered Al–Cu–Al nano-composites processed by high-pressure torsion, Journal of Alloys and Compounds 846 (2020), 156380. https://doi.org/10.1016/j.jallcom.2020.156380.

Names and surnames of publication authors:

Bazarnik Piotr, *Bartkowska Aleksandra, Romelczyk-Baishya Barbara, Adamczyk-Cieślak Bogusława, Dai Jiaoyan, Huang Yi, Lewandowska Małgorzata, Langdon Terence G.*

Statement on the substantive contribution of the work to the above-mentioned publication and consent to submit it for habilitation

No.	Author	Contribution	Signature
1	***Piotr Bazarnik***	In this article I was responsible for: - conceptualization of all performed research, - methodology selection, - funding and project management - performing all microstructural observations using transmission electron microscopes and scanning electron microscopy, SAED analysis, dark field and EDX analysis - analysing of obtained microstructural and mechanical results - writing the original draft of the paper, reviewing and editing. - Creating of all figures - Submission of paper This publication is a result of the SONATINA project, 'Synthesis of Novel Hybrid Materials Using High-Pressure Torsion' (UMO-2017/24/C/ST8/00145), in which I have been a leader (PI)	
Co-authors' contribution:			
2	*Bartkowska Aleksandra*	Editing the final version of the article, Performing of microhardness measurements.	
3	*Romelczyk-Baishya Barbara*	Performing tensile test	

4	*Adamczyk-Cieślak Bogusława*	Performing XRD analysis	
5	*Dai, Jiaoyan*	HPT processing of Al-Cu samples	
6	*Huang Yi*	Conceptualization of HPT experiments, Editing the final version of the article, HPT processing	
7	*Lewandowska Małgorzata*	Discussion of the results obtained, Editing the final version of the article	
8	*Langdon Terence G.*	Editing the final version of the article, Proofreading and language editing,	

Statement

Publication title, journal, year, doi:

Superior strength of tri-layered Al–Cu–Al nano-composites processed by high-pressure torsion, Journal of Alloys and Compounds 846 (2020), 156380. https://doi.org/10.1016/j.jallcom.2020.156380.

Names and surnames of publication authors:

Bazarnik Piotr, *Bartkowska Aleksandra, Romelczyk-Baishya Barbara, Adamczyk-Cieślak Bogusława, Dai Jiaoyan, Huang Yi, Lewandowska Małgorzata, Langdon Terence G.*

Statement on the substantive contribution of the work to the above-mentioned publication and consent to submit it for habilitation

No.	Author	Contribution	Signature
1	***Piotr Bazarnik***	In this article I was responsible for: - conceptualization of all performed research, - methodology selection, - funding and project management - performing all microstructural observations using transmission electron microscopes and scanning electron microscopy, SAED analysis, dark field and EDX analysis - analysing of obtained microstructural and mechanical results - writing the original draft of the paper, reviewing and editing. - Creating of all figures - Submission of paper This publication is a result of the SONATINA project, 'Synthesis of Novel Hybrid Materials Using High-Pressure Torsion' (UMO-2017/24/C/ST8/00145), in which I have been a leader (PI)	
Co-authors' contribution:			
2	*Bartkowska Aleksandra*	Editing the final version of the article, Performing of microhardness measurements.	
3	*Romelczyk-Baishya Barbara*	Performing tensile test	
4	*Adamczyk-Cieślak Bogusława*	Performing XRD analysis	

5	*Dai, Jiaoyan*	HPT processing of Al-Cu samples	
6	*Huang Yi*	Conceptualization of HPT experiments, Editing the final version of the article, HPT processing	
7	*Lewandowska Małgorzata*	Discussion of the results obtained, Editing the final version of the article	
8	*Langdon Terence G.*	Editing the final version of the article, Proofreading and language editing,	

Statement

Publication title, journal, year, doi:

Fabrication and characterization of nanostructured immiscible Cu–Ta alloys processed by high-pressure torsion. Journal of Alloys and Compounds 832 (2020) 155007. https://doi.org/10.1016/j.jallcom.2020.155007.

Names and surnames of publication authors:

*Mousavi Tayebeh, Dai, Jiaoyan, **Bazarnik Piotr**, Pereira Pedro Henrique R., Huang Yi, Lewandowska Małgorzata, Langdon Terence G.*

Statement on the substantive contribution of the work to the above-mentioned publication and consent to submit it for habilitation

No.	Author	Contribution	Signature
1	***Piotr Bazarnik***	In this article I was responsible for: - performing microstructural observations using transmission electron microscopy, analysing obtained microstructures, - writing part of the original draft of the paper, reviewing and editing. - Results analysis - Funding This publication is a result of the SONATINA project, 'Synthesis of Novel Hybrid Materials Using High-Pressure Torsion' (UMO-2017/24/C/ST8/00145), in which I have been a leader (PI)	
Co-authors' contribution:			
2	*Mousavi Tayebeh*	Editing the final version of the article, Conceptualization, SEM and EDX analysis	
3	*Dai, Jiaoyan*	Writing original draft of the paper, XRD analysis, Methodology selection,	
4	*Pereira Pedro Henrique R.*	Mechanical properties measurements	
5	*Huang Yi*	HPT processing, funding support	
6	*Lewandowska Małgorzata*	Editing the final version of the article	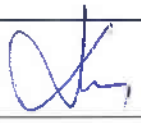

7	*Langdon Terence G.*	Editing the final version of the article, Discussion of the results obtained Proofreading and language editing, funding support	

Statement

Publication title, journal, year, doi:

Fabrication and characterization of nanostructured immiscible Cu–Ta alloys processed by high-pressure torsion. Journal of Alloys and Compounds 832 (2020) 155007. https://doi.org/10.1016/j.jallcom.2020.155007.

Names and surnames of publication authors:

*Mousavi Tayebeh, Dai, Jiaoyan, **Bazarnik Piotr**, Pereira Pedro Henrique R., Huang Yi, Lewandowska Malgorzata, Langdon Terence G.*

Statement on the substantive contribution of the work to the above-mentioned publication and consent to submit it for habilitation

No.	Author	Contribution	Signature
1	***Piotr Bazarnik***	In this article I was responsible for: - performing microstructural observations using transmission electron microscopy, analysing obtained microstructures, - writing part of the original draft of the paper, reviewing and editing. - Results analysis - Funding This publication is a result of the SONATINA project, 'Synthesis of Novel Hybrid Materials Using High-Pressure Torsion' (UMO-2017/24/C/ST8/00145), in which I have been a leader (PI)	
Co-authors' contribution:			
2	*Mousavi Tayebeh*	Editing the final version of the article, Conceptualization, SEM and EDX analysis	
3	*Dai, Jiaoyan*	Writing original draft of the paper, XRD analysis, Methodology selection,	Jiaoyan Dai
4	*Pereira Pedro Henrique R.*	Mechanical properties measurements	
5	*Huang Yi*	HPT processing, funding support	
6	*Lewandowska Małgorzata*	Editing the final version of the article	

7	*Langdon Terence G.*	Editing the final version of the article, Discussion of the results obtained Proofreading and language editing, funding support	

Statement

Publication title, journal, year, doi:

Fabrication and characterization of nanostructured immiscible Cu–Ta alloys processed by high-pressure torsion. Journal of Alloys and Compounds 832 (2020) 155007. https://doi.org/10.1016/j.jallcom.2020.155007.

Names and surnames of publication authors:

Mousavi Tayebeh, Dai, Jiaoyan, ***Bazarnik Piotr****, Pereira Pedro Henrique R., Huang Yi, Lewandowska Malgorzata, Langdon Terence G.*

Statement on the substantive contribution of the work to the above-mentioned publication and consent to submit it for habilitation

No.	Author	Contribution	Signature
1	***Piotr Bazarnik***	In this article I was responsible for: - performing microstructural observations using transmission electron microscopy, analysing obtained microstructures, - writing part of the original draft of the paper, reviewing and editing. - Results analysis - Funding This publication is a result of the SONATINA project, 'Synthesis of Novel Hybrid Materials Using High-Pressure Torsion' (UMO-2017/24/C/ST8/00145), in which I have been a leader (PI)	
Co-authors' contribution:			
2	*Mousavi Tayebeh*	Editing the final version of the article, Conceptualization, SEM and EDX analysis	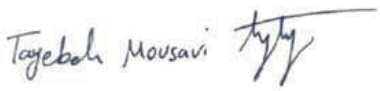 18/03/2025
3	*Dai, Jiaoyan*	Writing original draft of the paper, XRD analysis, Methodology selection,	
4	*Pereira Pedro Henrique R.*	Mechanical properties measurements	

5	*Huang Yi*	HPT processing, funding support	
6	*Lewandowska Małgorzata*	Editing the final version of the article	
7	*Langdon Terence G.*	Editing the final version of the article, Discussion of the results obtained Proofreading and language editing, funding support	

Statement

Publication title, journal, year, doi:

Fabrication and characterization of nanostructured immiscible Cu–Ta alloys processed by high-pressure torsion. Journal of Alloys and Compounds 832 (2020) 155007. https://doi.org/10.1016/j.jallcom.2020.155007.

Names and surnames of publication authors:

Mousavi Tayebeh, Dai, Jiaoyan, ***Bazarnik Piotr****, Pereira Pedro Henrique R., Huang Yi, Lewandowska Malgorzata, Langdon Terence G.*

Statement on the substantive contribution of the work to the above-mentioned publication and consent to submit it for habilitation

No.	Author	Contribution	Signature
1	***Piotr Bazarnik***	In this article I was responsible for: - performing microstructural observations using transmission electron microscopy, analysing obtained microstructures, - writing part of the original draft of the paper, reviewing and editing. - Results analysis - Funding This publication is a result of the SONATINA project, 'Synthesis of Novel Hybrid Materials Using High-Pressure Torsion' (UMO-2017/24/C/ST8/00145), in which I have been a leader (PI)	
Co-authors' contribution:			
2	*Mousavi Tayebeh*	Editing the final version of the article, Conceptualization, SEM and EDX analysis	
3	*Dai, Jiaoyan*	Writing original draft of the paper, XRD analysis, Methodology selection,	
4	*Pereira Pedro Henrique R.*	Mechanical properties measurements	
5	*Huang Yi*	HPT processing, funding support	
6	*Lewandowska Malgorzata*	Editing the final version of the article	

7	*Langdon Terence G.*	Editing the final version of the article, Discussion of the results obtained Proofreading and language editing, funding support	

Statement

Publication title, journal, year, doi:

Fabrication and characterization of nanostructured immiscible Cu–Ta alloys processed by high-pressure torsion. Journal of Alloys and Compounds 832 (2020) 155007. https://doi.org/10.1016/j.jallcom.2020.155007.

Names and surnames of publication authors:

*Mousavi Tayebeh, Dai, Jiaoyan, **Bazarnik Piotr**, Pereira Pedro Henrique R., Huang Yi, Lewandowska Malgorzata, Langdon Terence G.*

Statement on the substantive contribution of the work to the above-mentioned publication and consent to submit it for habilitation

No.	Author	Contribution	Signature
1	***Piotr Bazarnik***	In this article I was responsible for: - performing microstructural observations using transmission electron microscopy, analysing obtained microstructures, - writing part of the original draft of the paper, reviewing and editing. - Results analysis - Funding This publication is a result of the SONATINA project, 'Synthesis of Novel Hybrid Materials Using High-Pressure Torsion' (UMO-2017/24/C/ST8/00145), in which I have been a leader (PI)	
Co-authors' contribution:			
2	*Mousavi Tayebeh*	Editing the final version of the article, Conceptualization, SEM and EDX analysis	
3	*Dai, Jiaoyan*	Writing original draft of the paper, XRD analysis, Methodology selection,	
4	*Pereira Pedro Henrique R.*	Mechanical properties measurements	
5	*Huang Yi*	HPT processing, funding support	

6	*Lewandowska Małgorzata*	Editing the final version of the article	
7	*Langdon Terence G.*	Editing the final version of the article, Discussion of the results obtained Proofreading and language editing, funding support	

Statement

Publication title, journal, year, doi:

Fabrication and characterization of nanostructured immiscible Cu–Ta alloys processed by high-pressure torsion. Journal of Alloys and Compounds 832 (2020) 155007. https://doi.org/10.1016/j.jallcom.2020.155007.

Names and surnames of publication authors:

*Mousavi Tayebeh, Dai, Jiaoyan, **Bazarnik Piotr**, Pereira Pedro Henrique R., Huang Yi, Lewandowska Malgorzata, Langdon Terence G.*

Statement on the substantive contribution of the work to the above-mentioned publication and consent to submit it for habilitation

No.	Author	Contribution	Signature
1	***Piotr Bazarnik***	In this article I was responsible for: - performing microstructural observations using transmission electron microscopy, analysing obtained microstructures, - writing part of the original draft of the paper, reviewing and editing. - Results analysis - Funding This publication is a result of the SONATINA project, 'Synthesis of Novel Hybrid Materials Using High-Pressure Torsion' (UMO-2017/24/C/ST8/00145), in which I have been a leader (PI)	
Co-authors' contribution:			
2	*Mousavi Tayebeh*	Editing the final version of the article, Conceptualization, SEM and EDX analysis	
3	*Dai, Jiaoyan*	Writing original draft of the paper, XRD analysis, Methodology selection,	
4	*Pereira Pedro Henrique R.*	Mechanical properties measurements	
5	*Huang Yi*	HPT processing, funding support	
6	*Lewandowska Małgorzata*	Editing the final version of the article	

7	*Langdon Terence G.*	Editing the final version of the article, Discussion of the results obtained Proofreading and language editing, funding support	

I. WYKAZ OSIĄGNIĘĆ NAUKOWYCH ALBO ARTYSTYCZNYCH, O KTÓRYCH MOWA W ART. 219 UST. 1. PKT 2 USTAWY

1. **Monografie naukowe, zgodnie z art. 219 ust. 1. pkt 2a ustawy**
   brak
2. **Cykl powiązanych tematycznie artykułów naukowych, zgodnie z art. 219 ust. 1. pkt 2b ustawy;**

Tytuł: „Nowoczesne nanomateriały o podwyższonej wytrzymałości kształtowane techniką skręcenia pod wysokim ciśnieniem (HPT- high pressure torsion)”

A.1 Huang Yi, **Bazarnik Piotr**, Wan Diqing, Luo Dan, Pereira Pedro Henrique R., Lewandowska Malgorzata, Yao Jin, Hayden Brian E., Langdon Terence G., The fabrication of graphene-reinforced Al-based nanocomposites using high-pressure torsion, Acta Materialia, 2019, 164, 499 – 511 (*IF$_{2019}$* 7.656, *punkty MEiN* - 200) (**załącznik 5**)

A.2 Bazarnik Piotr, Emerla Maria, Aleksandra Bartkowska, Huang Yi, Lewandowska Małgorzata, Langdon Terence G., Using direct high-pressure torsion synthesis to produce aluminium matrix nanocomposites reinforced with carbon nanotubes, Journal of Alloys and Compounds, 2023, 968, 171928 (IF2023 6.371, punkty MEiN - 140) (**załącznik 5**)

A.3 Bazarnik Piotr, Nosewicz Szymon, Romelczyk-Baishya Barbara, Chmielewski Marcin, Strojny Nędza Agata, Maj Justyna, Huang Yi, Lewandowska Małgorzata, Langdon Terence G., Effect of spark plasma sintering and high-pressure torsion on the microstructural and mechanical properties of a Cu–SiC composite, Materials Science and Engineering A, 2019, 766 , 138350 (*IF$_{2019}$* 4.652, *punkty MEiN* - 140) (**załącznik 5**)

A.4 Emerla Maria, **Bazarnik Piotr,** Yi Huang, Wojciechowska Anita, Ciemiorek Marta, Pura Jarosław, Wieczorek-Czarnocka Monika, Kenichi Purbayanto Muhammad Abiyyu, Jastrzębsta Agnieszka, Lewandowska Małgorzata, Langdon Terence G., The influence of graphene oxide on the microstructure and properties of ultrafine-grained copper processed by high-pressure torsion, Journal of Alloys and Compounds, 2024, 1005, 176208 (*IF$_{2024}$* 5.8 *punkty MEiN* - 100) (**załącznik 5**)

A.5 Bazarnik Piotr, Emerla Maria, Yi Huang, Wojciechowska Anita, Ciemiorek Marta, Bednarczyk Wiktor, Jastrzębsta Agnieszka, Lewandowska Małgorzata, Langdon Terence G; „Enhanced thermal stability of nanocrystalline Cu composites processed by high-pressure torsion: The pinning effect of Al_2O_3, GO, and rGO/Al_2O_3 nanoparticles" Journal of Alloys and Compounds, 2025, 1033, 181283 (*IF*$_{2025}$ 6.3 , *punkty MEiN* - 100) (**załącznik 5**)

A.6 Bartkowska Aleksandra, **Bazarnik Piotr**, Huang Yi, Lewandowska Malgorzata, Langdon Terence G., Using high-pressure torsion to fabricate an Al–Ti hybrid system with exceptional mechanical properties, Materials Science and Engineering A, 2021, 799 140114 (*IF*$_{2021}$ 5.96, *punkty MEiN* - 140) (**załącznik 5**)

A.7 Bazarnik Piotr, Bartkowska Aleksandra, Huang Yi, Szlązak Karol, Adamczyk-Cieślak Bogusława, Sort Jordi, Lewandowska Malgorzata, Langdon Terence G., Fabrication of hybrid nanocrystalline Al–Ti alloys by mechanical bonding through high-pressure torsion, Materials Science and Engineering A, 2022, 833, 142549 (IF2022 7.328, punkty MEiN - 140) (**załącznik 5**)

A.8 Bazarnik Piotr, Bartkowska Aleksandra, Romelczyk-Baishya Barbara, Adamczyk-Cieślak Bogusława, Dai, Jiaoyan, Huang Yi, Lewandowska Małgorzata, Langdon Terence G., Superior strength of tri-layered Al–Cu–Al nano-composites processed by high-pressure torsion, Journal of Alloys and Compounds, 2020, 846, 156380 (*IF*$_{2020}$ 5.316, *punkty MEiN* - 100) (**załącznik 5**)

A.9 Mousavi Tayebeh, Dai, Jiaoyan, **Bazarnik Piotr**, Pereira Pedro Henrique R., Huang Yi, Lewandowska Malgorzata, Langdon Terence G., Fabrication and characterization of nanostructured immiscible Cu–Ta alloys proc essed by high-pressure torsion, Journal of Alloys and Compounds, 2020, 832, 155007 (IF2020 5.316, punkty MEiN - 100) (**załącznik 5**)

Oświadczenia potwierdzające mój merytoryczny wkład w powstanie powyższych prac zostały przedstawione w Załączniku 6 (A1–A9). Ze względu na współpracę z wieloma zagranicznymi naukowcami reprezentującymi różne jednostki naukowe, nie było możliwe zebranie wszystkich podpisów na jednym formularzu dla każdego artykułu. W związku z

tym, oświadczenia dotyczące poszczególnych publikacji składają się z kilku stron, z których każda zawiera podpis jednego z współautorów.

3. Zrealizowane oryginalne osiągnięcia projektowe, konstrukcyjne, technologiczne lub artystyczne, zgodnie z art. 219 ust. 1. pkt 2c ustawy

brak

4. Inne, niż wymienione w pkt. I.1-3, osiągnięcia naukowe lub artystyczne

Wykaz opublikowanych artykułów **przed uzyskaniem stopnia doktora**:

4A-1 **Bazarnik Piotr**, Lewandowska Małgorzata, Kurzydłowski Krzysztof, Mechanical behaviour of ultrafine grained Al-Mg alloys obtained by different processing routes, Archives of Metallurgy and Materials, 2012, 57, 869-876 (*IF*$_{2012}$ 0,431, *punkty MEiN* - 20)

4A-2 **Bazarnik Piotr**, Lewandowska Małgorzata, Andrzejczuk Mariusz, Kurzydłowski Krzysztof, The strength and thermal stability of Al–5Mg alloys nano-engineered using methods of metal forming, Materials Science and Engineering A 2012, 556, 134-139. (*IF*$_{2012}$ 2,108, *punkty MEiN* - 30)

4A-3 Kulczyk Mariusz, Skiba Jacek, Przybysz Sylwia, **Bazarnik Piotr**, Lewandowska Małgorzata, High strength silicon bronze (C65500) obtained by hydrostatic extrusion, Archives of Metallurgy and Materials 2012, 57.859-862. (*IF*$_{2012}$ 0,431, *punkty MEiN* - 20)

4A-4 Kulczyk M., **Bazarnik Piotr**, Pachla Wacław Skiba Jacek, Lewandowska Małgorzata, Kurzydłowski Krzysztof, Combination of equal channel angular pressing and hydrostatic extrusion as a method for effective grain refinement of Cu and Cu-alloy, Inżynieria Materiałowa 2013, 34, 314-316 (*IF*$_{2013}$ ---- *punkty MEiN* - 3)

4A-5 Łubkowska Katarzyna, **Bazarnik Piotr**, Onyszczuk Tomasz Lewandowska Małgorzata, Microstructure of a traditional scythe blade using a SEM, the FIB technique and a TEM, Inżynieria Materiałowa 2013, 34, 176-179 (*IF*$_{2013}$ ---- *punkty MEiN* - 3)

4A-6 **Bazarnik Piotr**, Huang Y, Lewandowska Małgorzata, Langdon Terence G., Structural impact on the Hall-Petch relationship in an Al-5Mg alloy processed by high-pressure torsion, Materials Science and Engineering A, 2015, 626, 9-15 (*IF*$_{2015}$ 2,647 *punkty MEiN* - 35)

4A-7 Lipińska Marta, Olejnik Lech, Pietras Adam, Rosochowski Andrzej, **Bazarnik Piotr**, Goliński Jacek, Brynk Tomasz, Lewandowska Małgorzata, Microstructure and mechanical properties of friction stir welded joints made from ultrafine grained aluminium 1050, Materials & Design 2015, 88, 22-31 (*IF*$_{2015}$ 3,997 *punkty MEiN* - 35)

4A-8 Sharman Katarzyna, **Bazarnik Piotr**, Brynk Tomasz, Gunay-Bulutsuz Asli, Lewandowska Małgorzata, Enhancement in mechanical properties of a β-titanium alloy by high-pressure torsion, Journal of Materials Research and Technology, 2015, vol. 4, nr 1, s.79-83 (*IF*$_{2015}$ 2,359 *punkty MEiN* - 5)

4A-9 Alsubaie Saad A., **Bazarnik Piotr**, Lewandowska Małgorzata Huang Yi, Langdon Terence G., Evolution of microstructure and hardness in an AZ80 magnesium alloy processed by high-pressure torsion, Journal of Materials Research and Technology 2016, 5, 152-158 (*IF*$_{2016}$ 2,359 *punkty MEiN* - 5)

4A-10 **Bazarnik Piotr**, Romelczyk Barbara, Yi Huang, Lewandowska Małgorzata, Langdon Terence G., Effect of applied pressure on microstructure development and homogeneity in an aluminium alloy processed by high-pressure torsion, Journal of Alloys and Compounds 2016, 688, 736-745. (*IF*$_{2016}$ 3,133 *punkty MEiN* - 35)

4A-11 **Bazarnik Piotr**, Adamczyk-Cieślak Bogusława, Gałka Aleksander, Płonka Bartosz, Śnieżek Lucjan, Marco Cantoni, Lewandowska Małgorzata Mechanical and microstructural characteristics of Ti6Al4V/AA2519 and Ti6Al4V/AA1050/AA2519 laminates manufactured by explosive welding, Materials & Design 2016, 111, 5, 146-157 (*IF*$_{2016}$ 4,364 *punkty MEiN* - 35)

4A-12 Chmielewski Marcin, Nosewicz Szymon, Jakubowska Dorota, Lewandowska Małgorzata, Mizera Jarosław, Rojek J., **Bazarnik Piotr**, The influence of sintering time on the microstructural properties of chromium-rhenium matrix composites, International Journal of Refractory Metals & Hard Materials 2016, 59, 78-86 (*IF*$_{2016}$ 2,155 *punkty MEiN* - 35)

4A-13 Ciecierska Ewelina, Jurczyk-Kowalska Magdalena, **Bazarnik Piotr**, Gloc Michał, Kulesza Michał, Kowalski Maciej, Krauze Sławomir, Lewandowska Małgorzata, Flammability, mechanical properties and structure of rigid polyurethane foams with different types of carbon reinforcing materials, Composite Structures 2016, 160, 67-76 (*IF*$_{2016}$ 3,858 *punkty MEiN* - 40)

4A-14 Ciecierska Ewelina, Jurczyk-Kowalska Magdalena, **Bazarnik Piotr**, Kowalski Maciej, Krauze Sławomir, Lewandowska Małgorzata, The influence of carbon fillers on the

thermal properties of polyurethane foam, Journal of Thermal Analysis and Calorimetry 2016, 126.283-291 (IF_{2016} 1,953 *punkty MEiN* - 25)

4A-15 Lipińska Marta, **Bazarnik Piotr**, Lewandowska Małgorzata, The influence of severe plastic deformation processes on electrical conductivity of commercially pure aluminium and 5483 aluminium alloy, Archives of Civil and Mechanical Engineering 2016, 16, 717-723 (IF_{2016} 2,216 *punkty MEiN* – 30

Wykaz opublikowanych artykułów **po uzyskaniu stopnia doktora** - publikacje naukowe w czasopismach znajdujących się w bazie Journal Citation Reports (JRC). Pozycje z listy A zgodnie z wykazem czasopism punktowanych w latach 2008-2018 oraz komunikatem Ministra Nauki i Szkolnictwa Wyższego z dnia 31 lipca 2019 r. w sprawie wykazu czasopism naukowych i recenzowanych materiałów z konferencji międzynarodowych wraz z przypisaną liczbą punktów w latach 2019 i kolejnych niewymienione w pkt. I.2

4B-1 Łada Paula, Miazga Aleksandra, **Bazarnik Piotr**, Konopka Katarzyna: Microstructure Characterization of Composite from ZrO2 – Ti System, Archives of Metallurgy and Materials, 2017, 62, 2045-2049 (IF_{2017} 0.381 *punkty MEiN* – 20)

4B-2 Chmielewski Marcin, Pietrzak Katarzyna, Strojny-Nędza Agata, Kaszyca Kamil, Zybała Rafał, **Bazarnik Piotr**, Lewandowska Małgorzata, Nosewicz Szymon: Microstructure and Thermal Properties of Cu-SiC Composite Materials Depending on the Sintering Technique, Science of Sintering, 2017, 49, 11-22 (IF_{2017} 0.667 *punkty MEiN* – 30)

4B-3 Chmielewski Marcin, Pietrzak Katarzyna, Teodorczyk Marian, Nosewicz Szymon, Jarząbek Dariusz, Zybała Rafał, **Bazarnik Piotr**, Lewandowska Małgorzata, Strojny-Nędza Agata: Effect of metallic coating on the properties of copper-silicon carbide composites, Applied Surface Science, 2017, 421, 159-169 (IF_{2017} 4,439 *punkty MEiN* – 35)

4B-4 Bartosewicz Bartosz, Bujno Kamil, Liszewska Malwina, Budner Bogusław, **Bazarnik Piotr**, Płociński Tomasz, Jankiewicz Bartłomiej J.: Effect of citrate substitution by various α-hydroxycarboxylate anions on properties of gold nanoparticles synthesized by Turkevich method, Colloids and Surfaces A-Physicochemical and Engineering Aspects, 2018, 549, 25-33 (IF_{20178} 3,131 *punkty MEiN* – 30)

4B-5 Łada Paula, Miazga Aleksandra, **Bazarnik Piotr**, Konopka Katarzyna, Szafran Mikołaj: Zirconia–Titanium Interface in Ceramic Based Composite, Powder Metallurgy and Metal Ceramics, 2018, 57, 458-464 (IF_{2018} 0.381 *punkty MEiN* – 20)

4B-6 **Bazarnik Piotr**, Huang Yi, Lewandowska Małgorzata, Langdon T.G.: Enhanced grain refinement and microhardness by hybrid processing using hydrostatic extrusion and high-pressure torsion, Materials Science and Engineering A 2018, 712, 513-520, (IF_{2018} 4,081 *punkty MEiN* – 35)

4B-7 Guziewicz Marek, Taube Andrzej, Ekielski Marek, Gołaszewska Krystyna, Zdunek Joanna, **Bazarnik Piotr**, Adamczyk-Cieślak Bogusława, Szerling Anna: Structural and electrical studies on Ti/Al-based Au-free ohmic contact metallization for AlGaN/GaN HEMTs, Materials Science in Semiconductor Processing, 2019, 96, 153-160, (IF_{2019} 3,085 *punkty MEiN* – 70)

4B-8 Kowalska-Mori Agata, Mamiya Hiroaki, Ohnuma Masato, Ilavsky Jan, Gilbert Elliot P., **Bazarnik Piotr**, Kitazawa Hideaki, Lewandowska Małgorzata, Effect of post annealing on microstructure and mechanical properties in Ni-free N-containing ODS steel, Materials Characterization 2019, 153, 339-347 (IF_{2019} 3,562 *punkty MEiN* – 100)

4B-9 Chmielewski Marcin, Nosewicz Szymon, Wyszkowska Edyta, Kurpaska Łukasz, Strojny-Nędza Agata, Piątkowska Anna, **Bazarnik Piotr**, Pietrzak Katarzyna, Analysis of the micromechanical properties of copper-silicon carbide composites using nanoindentation measurements, Ceramics International 2019, 45, 9164-9173 (IF_{2019} 3,83 *punkty MEiN* – 100)

4B-10 Nosewicz Szymon, Romelczyk-Baishya Barbara, Lumelskyj Dmytro, Chmielewski Marcin, **Bazarnik Piotr**, Jarząbek Dariusz, Pietrzak Katarzyna, Kaszyca Kamil, Pakieła Zbigniew: Experimental and numerical studies of micro- and macromechanical properties of modified copper–silicon carbide composites, International Journal of Solids and Structures 2019, 160, 187-200 (IF_{2019} 3,213 *punkty MEiN* – 140)

4B-11 Chromiński Witold, Ciupiński Łukasz, **Bazarnik Piotr**, Markelj Sabina, Schwarz-Selinger Thomas: TEM investigation of the influence of dose rate on radiation damage and deuterium retention in tungsten, Materials Characterization, 2019, 154, 1-6, (IF_{2019} 3,562 *punkty MEiN* – 100)

4B-12 Mościcki Tomasz, Psiuk Rafal, Słomińska Hanna, Levintant-Zayonts Neonila, Garbiec Dariusz, Pisarek Marcin, **Bazarnik Piotr**, Nosewicz Szymon, Chrzanowska-Giżyńska Justyna: Influence of overstoichiometric boron and titanium addition on the properties

of RF magnetron sputtered tungsten borides, Surface and Coatings Technology, 2020, 390, 125689 (*IF*$_{2020}$ 4,158 *punkty MEiN* – 100)

4B-13 Jarząbek Dariusz, Milczarek Michał, Nosewicz Szymon, **Bazarnik Piotr**, Schift Helmut: Size Effects of Hardness and Strain Rate Sensitivity in Amorphous Silicon Measured by Nanoindentation, Metallurgical and Materials Transactions A-Physical Metallurgy and Materials Science, 2020, 51, 1625-1633 (*IF*$_{2020}$ 2,556 *punkty MEiN* – 200)

4B-14 Chromiński Witold, Ciupiński Łukasz, **Bazarnik Piotr**, Markelj Sabina, Schwarz-Selinger Thomas: Microstructure evolution in helium implanted self-irradiated tungsten annealed at 1700 K studied by TEM, Materials Characterization, 2021, 174, 110991 (*IF*$_{2021}$ 4,342 *punkty MEiN* – 100)

4B-15 Chausov Mykola, Brezinova Janette, Zasimchuk Elena, Maruschak Pavlo, Khyzhun Oleg, Pylypenko Andrii, **Bazarnik Piotr**, Brezina Jakub: Effect of Structure Self-Organization of Aluminum Alloy D16ChATW under Impact-Oscillatory Loading on Its Fatigue Life, Journal of Materials Engineering and Performance, 2021, 30, 6235-6242, (*IF*$_{2021}$ 1,819 *punkty MEiN* – 70)

4B-16 Psiuk Rafał, Milczarek Michał, Jenczyk Piotr, Denis Piotr, Jarząbek Dariusz, **Bazarnik Piotr**, Pisarek Marcin, Mościcki Tomasz: Improved mechanical properties of W-Zr-B coatings deposited by hybrid RF magnetron – PLD method, Applied Surface Science, 2021, 570, 151239 (*IF*$_{2021}$ 6,707 *punkty MEiN* – 140)

4B-17 Jaroszewicz Jakub, **Bazarnik Piotr**, Osiecka-Iwan Anna, Hyc Anna, Choińska Emilia, Chlanda Adrian, Święszkowski Wojciech, Moskalewski Stanisław: From Matrix Vesicles to Miniature Rocks: Evolution of Calcium Deposits in Calf Costochondral Junctions, Cartilage, 2021, 13, 326-335 (*IF*$_{2021}$ 4,634 *punkty MEiN* – 70)

4B-18 Majchrowicz Anna, Roguska Agata, Majchrowicz Kamil, Pisarek Marcin, Hołdyński Marcin, **Bazarnik Piotr**, Lewandowska Małgorzata: Influence of microstructural features on the growth of nanotubular oxide layers on β-phase Ti-24Nb-4Zr-8Sn and α + β-phase Ti-13Nb-13Zr alloys, Surface and Coatings Technology 2021, 425, 127695 (*IF*$_{2021}$ 4,158 *punkty MEiN* – 100)

4B-19 Sitek Ryszard, Molak Rafał, Zdunek Joanna, **Bazarnik Piotr**, Wiśniewski Paweł, Kubiak K., Mizera Jarosław: Influence of an aluminizing process on the microstructure and tensile strength of the nickel superalloy IN 718 produced by the Selective Laser Melting, Vacuum, 2021, 186, 110041 (*IF*$_{2021}$ 3,627 *punkty MEiN* – 70)

4B-20 Dobkowska Anna, Sotniczuk Agata, **Bazarnik Piotr**, Mizera Jarosław, Garbacz Halina: Corrosion Behavior of Cold-Formed AA5754 Alloy Sheets, Materials, 2021, 14, 1-14 (*IF_{2021}* 2,972 *punkty MEiN* – 140)

4B-21 Zgłobicka Izabela, Gluch Jürgen, Liao Zhongquan, Werner Stephan, Guttmann Peter, Li Qiong, **Bazarnik Piotr**, Płociński Tomasz, Witkowski Andrzej, Kurzydłowski Krzysztof: Insight into diatom frustule structures using various imaging techniques, Scientific Reports 2021, 1, 14555 (*IF_{2021}* 0.381 *punkty MEiN* – 20)

4B-22 Bojarska Zuzanna, Kopytowski Janusz, Mazurkiewicz-Pawlicka Marta, **Bazarnik Piotr**, Gierlotka Stanisław, Rożeń Antoni, Makowski Łukasz: Molybdenum disulfide-based hybrid materials as new types of oil additives with enhanced tribological and rheological properties, Tribology International, 2021, 160, 106999 (*IF_{2021}* 4,38 *punkty MEiN* – 140)

4B-23 Mykola Chausov, Janette Brezinova, Elena Zasimchuk, Pavlo Maruschak, Oleg Khyzhun, Andrii Pylypenko, **Piotr Bazarnik**, Jakub Brezina; Effect of Structure Self-Organization of Aluminum Alloy D16ChATW under Impact-Oscillatory Loading on Its Fatigue Life, Journal of Materials Engineering and Performance, 2021, 30, 6235 – 6242 August 2021 (*IF_{2021}* 1.819 *punkty MEiN* – 70)

4B-24 Anna Majchrowicz, Agata Roguska, Kamil Majchrowicz, Marcin Pisarek, Marcin Hołdyński, **Piotr Bazarnik**, Małgorzata Lewandowska; Influence of microstructural features on the growth of nanotubular oxide layers on β-phase Ti-24Nb-4Zr-8Sn and α + β-phase Ti-13Nb-13Zr alloys, Surface and Coatings Technology, 2021, 425, 127695 (*IF_{2021} 4.865 punkty MEiN* – 100)

4B-25 Jakub Jaroszewicz, **Piotr Bazarnik**, Anna Osiecka-Iwan, Anna Hyc, Emilia Choinska, Adrian Chlanda, Wojciech Swieszkowski, Stanisław Moskalewski; From Matrix Vesicles to Miniature Rocks: Evolution of Calcium Deposits in Calf Costochondral Junctions, Cartilage, 2021, 13, 326S - 335S (*IF_{2021} 1.519 punkty MEiN* – 70)

4B-26 Izabela Zgłobicka, Jürgen Gluch, Zhongquan Liao, Stephan Werner, Peter Guttmann, Qiong Li, **Piotr Bazarnik**, Tomasz Plocinski, Andrzej Witkowski, Krzysztof J. Kurzydlowski; Insight into diatom frustule structures using various imaging techniques, Scientific Reports, 2021, 11, 14555 (*IF_{2021} 4.996 punkty MEiN* – 140)

4B-27 Rafał Psiuk, Michał Milczarek, Piotr Jenczyk, Piotr Denis, Dariusz Jarząbek, **Piotr Ba zarnik**, Marcin Pisarek, Tomasz Mościcki; Improved mechanical properties of W-Zr-B coatings deposited by hybrid RF magnetron – PLD method, Applied Surface Science, 2021 570, 151239 (*IF_{2021} 7.392 punkty MEiN* – 140)

4B-28 Hsuan-Kai Lin, Y. Cheng, Guan-Yuan Li, Ying-Chi Chen, **Piotr Bazarnik**, Jessica Muzy, Yi Huang, Terence G. Langdon; Study on the Surface Modification of Nanostructured Ti Alloys and Coarse-Grained Ti Alloys, Metals, 2022, 12, 948 (*IF_{2022} 2.695 punkty MEiN* – 70)

4B-29 Saad A. Alsubaie, **Piotr Bazarnik**, Yi Huang, Malgorzata Lewandowska, Terence G. Langdon; Achieving Superplastic Elongations in an AZ80 Magnesium Alloy Processed by High-Pressure Torsion, Advanced Engineering Materials, 2022, 24, 2200620 (*IF_{2022} 3.6 punkty MEiN* – 100)

4B-30 Ewa Ura-Bińczyk, Anna Dobkowska, **Piotr Bazarnik**, Jakub Ciftci, Agnieszka Krawczyńska, Witold Chromiński, Tomasz Wejrzanowski, Rafał Molak, Ryszard Sitek, Tomasz Płociński, Jakub Jaroszewicz, Jarosław Mizera; Effect of annealing on the mechanical and corrosion properties of 316L stainless steel manufactured by laser powder bed fusion, Materials Science and Engineering: A, 2022, 860, 144263 (*IF_{2022} 6.4 punkty MEiN* – 140)

4B-31 Donata Kuczyńska-Zemła, Piotr Kwaśniak, Agata Sotniczuk, Torben Boll, Delphine Chassaing, **Piotr Bazarnik**, Piotr Wieciński, Marcin Pisarek, Roman Ostrowski, Halina Garbacz; Effect of interference laser treatment on the surface region homogeneity of a biomedical β-Ti alloy, Applied Surface Science, 2023, 614, 156211 (*IF_{2023} 6.3 punkty MEiN* – 140)

4B-32 Wiktor Bednarczyk, Maria Wątroba, Manish Jain, Krzysztof Mech, **Piotr Bazarnik**, Piotr Bała, Johann Michler, Krzysztof Wieczerzak; Determination of critical resolved shear stresses associated with <a> slips in pure Zn and Zn-Ag alloys via micro-pillar compression, Materials and Design, 2023, 229, 111897 (*IF_{2023} 7.6 punkty MEiN* – 140)

4B-33 Marcin Chmielewski, Rafał Zybała, Agata Strojny-Nędza, Anna Piątkowska, Artur Dobrowolski, Jakub Jagiełło, Ryszard Diduszko, **Piotr Bazarnik**, Szymon Nosewicz; Microstructural Evolution of Ni-SiC Composites Manufactured by Spark Plasma Sintering, Metallurgical and Materials Transactions A: Physical Metallurgy and Materials Science, 2023, 54, 2191 - 2207 (*IF_{2023} 2.2 punkty MEiN* – 200)

4B-34 Pedro Henrique R. Pereira, **Piotr Bazarnik**, Yi Huang, Małgorzata Lewandowska, Terence G. Langdon; Flow behaviour and microstructural stability in an Al–3Mg-0.2Sc alloy processed by high-pressure torsion at different temperatures, Materials Science and Engineering: A, 2023, 887, 145766 (*IF_{2023} 6.4 punkty MEiN* – 140)

4B-35 Szymon Nosewicz, Piotr Jenczyk,Barbara Romelczyk-Baishya, **Piotr Bazarnik**, Dariusz Jarząbek, Kamil Majchrowicz, Zbigniew Pakieła, Krystian Kowiorski, Marcin Chmielewski; The influence of spark plasma sintering on multiscale mechanical properties, Materials Science and Engineering: A, 2024, 891, 146001 (*IF_{2024} 6.4 punkty MEiN* – 140)

4B-36 Asli Gunay Bulutsuz, Witold Chrominski, **Piotr Bazarnik**, Enrico Bruder; Development of Fe-10% (HA/β-Tricalcium Phosphate) Composite via Solid-State Manufacturing Route and Investigation of Material Properties for Biodegradable Implant Applications, Advanced Engineering Materials, 2024, 26, 2301858 (*IF_{2024} 3.4 punkty MEiN* – 100)

4B-37 Ould Mohamed Ouarda, **Bazarnik Piotr**, Huang Yi, Azzeddine Hiba, Baudin Thierry, Brisset François, Langdon Terence G., A Comparative Study Between AZ31 and Mg-Gd Alloys After High-Pressure Torsion, Journal of Materials Engineering and Performancee 2024, 33, 2860–2874 (*IF_{2023}* 2.036, *punkty MEiN* - 70)

4B-38 Ould Mohamed Ouarda, Azzeddine Hiba, Huang Yi, Baudin Thierry, **Bazarnik Piotr**, Brisset François, Kawasaki Megumi, Langdon Terence G., Investigation of Microstructure and Texture Evolution in an AZ31/Mg–Gd Alloy Hybrid Metal Fabricated by High-Pressure Torsion, Advanced Engineering Materials, 2023, 25(11), 2201794 (*IF_{2023}* 3.6 , *punkty MEiN* - 100)

4B-39 Ould Mohamed Ouarda, **Bazarnik Piotr**, Huang Yi, Azzeddine Hiba, Baudin Thierry, Brisset François, Kawasaki Megumi, Langdon Terence G.; "Primary recrystallization of a magnesium hybrid material fabricated by high-pressure torsion", Materials Today Communications, 38 (2024) 108305 (*IF_{2024}* 1.859 , *punkty MEiN* - 70)

4B-40 Azzeddine Hiba, Avettand-Fènoël Marie-Noëlle, **Bazarnik Piotr**, Baudin Thierry, Huang Yi, Langdon Terence G.; "Recrystallization and grain growth activation energies in a hybrid magnesium material fabricated by high-pressure torsion", Thermochimica Acta, 738 (2024) 179805, (*IF_{2024}* 3.1 , *punkty MEiN* - 100)

4B-41 Asli Gunay Bulutsuz, Witold Chrominski, **Piotr Bazarnik**, Enrico Bruder: "Development of Fe-10% (HA/β-Tricalcium Phosphate) Composite via Solid-State Manufacturing Route and Investigation of Material Properties for Biodegradable Implant Applications" Advanced Engineering Materials 26, 2024, 2301858 (*IF_{2024}* 3.4 , *punkty MEiN* - 100)

4B-42 Hsuan-Kai Lin, Tsai-Hsuan Hsieh, Yi-Hong Cheng, **Piotr Bazarnik**, Chuan Ting Wang, Yi Huang, Jing Ye, Amor Abdelkader, Terence G. Langdon; "Improving the

strength and surface properties of TNTZ alloy through a combination of high-pressure torsion and laser surface treatment", International Journal of Advanced Manufacturing Technology 134, 2024, pp. 2693–2704 (*IF*$_{2024}$ 2.9 , *punkty MEiN* - 100)

4B-43 Pedro Henrique R. Pereira, , Piotr Bazarnik, Yi Huang, Malgorzata Lewandowska,Terence G. Langdon; "The role of processing temperature for achieving superplastic properties in an Al-3Mg-0.2Sc alloy processed by high-pressure torsion", Materials Science and Engineering A 916, 2024, 147320, (*IF*$_{2024}$ 6.1 , *punkty MEiN* - 140)

4B-44 Abdelkader Khalfallah, Sid Ahmed Amzert, Fahd Arbaoui, Nacereddine Titouche, Noureddine Selmi, **Piotr Bazarnik**, Hiba Azzeddine, Thierry Baudin, François Brisset, Yi Huang, Terence G. Langdon; "Corrosion performance of Al-6061 alloy after high-pressure torsion processing", Materials Characterization 220, 2025, 114714 (*IF*$_{2025}$ 4.8 , *punkty MEiN* - 100)

Wykaz artykułów opublikowanych w materiałach konferencyjnych

4C-1 **Bazarnik Piotr**, Romelczyk Barbara, Kulczyk M. Lewandowska Małgorzata, Tailoring Microstructure and Mechanical Properties of 6063 Aluminium Alloy for Lightweight Structural Parts, Materials Science Forum, 2013, vol. 765, s.423-428. DOI:10.4028/www.scientific.net/MSF.765.388

4C-2 **Bazarnik Piotr**, Romelczyk-Baishya Barbara, Kulczyk Mariusz, Lewandowska MałgorzataThe strength and ductility of 5483 aluminium alloy processed by various SPD methods, W: Materials Science Forum, Materials Science Forum, 2013, s.423-428, ISBN 9783037857663. DOI:10.4028/www.scientific.net/MSF.765.423

4C-3 Ciecierska Ewelina, Jurczyk-Kowalska Magdalena, **Bazarnik Piotr**, Małgorzata Lewandowska, Kowalski Marcin, Influence of carbon nanotubes on mechanical properties and structure of rigid polyurethane foam, IOP Conference Series: Materials Science and Engineering 2014, 64, 1-3.

4C-4 Lipińska Małgorzata, **Bazarnik Piotr**, Lewandowska Małgorzata: The electrical conductivity of CuCrZr alloy after SPD processing, IOP Conference Series: Materials Science and Engineering 2014, 63, 012119

II. WYKAZ AKTYWNOŚCI NAUKOWEJ ALBO ARTYSTYCZNEJ

1. Wykaz członkostwa w redakcjach naukowych monografii.

2. Wykaz wystąpień na krajowych lub międzynarodowych konferencjach naukowych lub artystycznych, z wyszczególnieniem przedstawionych wykładów na zaproszenie i wykładów plenarnych.

Po uzyskaniu stopnia doktora:

- The XVIth International Conference on Electron Microscopy 2017 wykład: *Grain boundaries and related phenomena in ultrafine grained Al-Mg alloy processed by high-pressure torsion*, Warsaw, Polska
- Advanced Materials and Technologies Conference 2019, wykład; *"Superior strength of tri-layered Al/Cu/Al nano-composites processed by high-pressure torsion",* Bukowina Tatrzańska, Polska
- EUROMAT 2019, wykład: "*Synthesis of an aluminium–copper nanocomposite by high-pressure torsion",* Stockholm, Szwecja
- FMC 2019, poster*: Sample preparation techniques and TEM/STEM observations of tungsten samples subjected to work under severe reactor conditions*, Eindhoven, Holand
- The XVIIth International Conference on Electron Microscopy poster: *Advanced hybrid materials fabricated by high pressure torsion*, 2020, Kraków, Polska
- TMS Annual Meeting wykład: *"Mechanical properties and microstructure evolution of multilayered Al-Cu hybrid materials produced by high-pressure torsion",* February 2020, San Diego, USA
- EUROMAT 2021, wykład: "The effect of processing parameters on the synthesis of an aluminium–titanium nanocomposite by high-pressure torsion" online conference
- Advanced Materials and Technologies Conference 2023, wykład: "Thermal stability of Cu GO-Al2O3 metal matrix nanocomposites fabricated by High-Pressure Torsion" Wisła, Polska
- NanoSPD8 - 8th International Conference on Nanomaterials by Severe Plastic Deformation, 2023 wykład: *Effects of aluminium purity and addition of carbon*

nanotubes on the hardness and thermal stability of CNT reinforced aluminum nanocomposites processed by the high-pressure torsion technique July Bangalore, Indie

- Yucomat 2024 wykład: *Advanced composite nanomaterials fabricated by high-pressure torsion technique ,* Herceg Novi
- XVIIIth International Conference on Electron Microscopy (EM 2024) – poster: Structural investigations on advanced composite materials fabricated by high-pressure torsion, Zakopane, Polska

3. Wykaz udziału w komitetach organizacyjnych i naukowych konferencji krajowych lub międzynarodowych, z podaniem pełnionej funkcji.

- XVI International Conference on Electron Microscopy 10-13 Września 2017, Politechnika Warszawska, Jachranka, Polska, członek komitetu organizacyjnego.
- Międzynarodowa konferencja E-MRS Fall-Meeting, od 2015 członek komitetu organizacyjnego.
- XVII International Conference on Electron Microscopy - Co-chair w sesji dla młodych naukowców.

4. **Wykaz uczestnictwa w pracach zespołów badawczych realizujących projekty finansowane w drodze konkursów krajowych lub zagranicznych, z podziałem na projekty zrealizowane i będące w toku realizacji, oraz z uwzględnieniem informacji o pełnionej funkcji w ramach prac zespołów.**

Okres po uzyskaniu stopnia doktora

Załącznik 9 zawiera dokumenty potwierdzające przyznanie mi opisanych projektów badawczych

Projekty w trakcie realizacji

4.1. ***Kierownik projektu***:

UMO-2020/37/B/ST5/01837 **OPUS**, Narodowe Centrum Nauki, tytuł: „Synteza metodą skręcania pod wysokim ciśnieniem niemieszalnych układów wykazujących unikalne właściwości fizyczne i mechaniczne”
okres realizacji: 2025-2028, budżet 1 690 900 zł

Projekty zrealizowane

4.2. ***Kierownik projektu***:

UMO-2024/53/B/ST11/00531 **OPUS**, Narodowe Centrum Nauki, tytuł: „Kompozyty na osnowie metalicznej wzmacniane nano-cząstkami 2D i 3D wytwarzane techniką skręcania pod wysokim ciśnieniem”
okres realizacji: 2021-2024, budżet 1 003 920 zł

4.3. ***Kierownik projektu***:

UMO-2017/24/C/ST8/00145 **SONATINA**, Narodowe Centrum Nauki, tytuł: „Synteza nowych materiałów hybrydowych metodą skręcania pod wysokim ciśnieniem”
okres realizacji: 2017-2021, budżet 651 673 zł

4.4. Wykonawca w projekcie: Wysokowytrzymałe wielomateriałowe rozwiązania do zastosowań w konstrukcjach lekkich TECHMATSTRATEG. Prowadziłem badania strukturalne

4.5. Wykonawca w projekcie: Opracowanie nisko-odpadowej technologii platerowania wybuchowego oraz technologii przetwarzania wielowarstwowych,

wysokowytrzymałościowych materiałów lekkich i superlekkich z warstwami reaktywnymi i funkcjonalnymi oraz blach platerowanych wybuchowo metalami reaktywnymi i ich stopami. TECHMATSTRATEG II. Prowadziłem badania strukturalne

4.6. Wykonawca w projekcie: Nowe powłoki zwiększające trwałość narzędzi w procesach kucia i wyciskania TECHMATSTRATEG III, Prowadziłem badania strukturalne

4.7. Wykonawca w projekcie EUROFUSION nr.633053 Implementation of activities described in the Roadmap to Fusion during Horizon 2020 through a joint programe of the member of the EUROfusion consortium. Prowadziłem badania strukturalne

Okres przed uzyskaniem stopnia doktora

4.8. ***Kierownik projektu***: **ETIUDA**, Rola granic ziaren w kształtowaniu właściwości mechanicznych stopu Al 5483 otrzymywanego metodami dużego odkształcenia plastycznego, UMO/015/16/T/ST8/00160, 2015-2016, 71 292 zł

4.9. ***Kierownik projektu***: P**RELUDIUM**, Mikrostrukturalne uwarunkowania właściwości ultra drobnoziarnistego stopu aluminium 5483 UMO/2014/13/N/ST8/01661, 2015-2017, 99 840 zł

4.10. Wykonawca w projekcie PBS3/A6/27/2015, Model obiektu wodnego typu "stelth" o innowacyjnych rozwiązaniach w zakresie kształtu, konstrukcji i materiałów decydujących o jego trudno wykrywalności. PBS 3, NCBiR

4.11. Wykonawca w projekcie STRATEGMED 1/248644/7/NCBR/2014, Zintegrowany system urządzeń do diagnostyki i telerehabilitacji schorzeń narządów zmysłu (słuchu, wzroku, mowy, równowagi, powonienia) STRATEGMED, NCBiR

4.12. Wykonawca w projekcie PBS3/B5/37/2015 Innowacyjna technologia laserowego napawania, hartowania i ablacyjnego strukturyzowania w procesach wytwarzania elementów funkcjonalnych podzespołów parowych turbin energetycznych PBS 3, NCBiR

4.13. Wykonawca w projekcie PBS2/A5/35/2013 Nowe, zaawansowane materiały warstwowe Al-Ti o podwyższonej odporności balistycznej na konstrukcje lotnicze i kosmiczne PBS 2, NCBiR

4.14. Wykonawca w projekcie PBS1/A5/27/2012 Nowe polimerowe ogniwa fotowoltaiczne: Badanie wpływu budowy polimeru, architektury ogniwa oraz rodzaju domieszki na sprawność polimerowych ogniw słonecznych opartych na poliazometinach i politiofenach PBS 1, NCBiR

4.15. Wykonawca w projekcie PBS1/A1/4/2012 Badania i rozwój nowoczesnych technologii polimerowych baterii litowo-jonowych o podwyższonym bezpieczeństwie eksploatacji PBS 1, NCBiR

4.16. Wykonawca w projekcie ELECTROMOBILITY+/3/NCBR/2012 Nowe Materiały i Technologie do Wytwarzania Ultralekkich Elementów Konstrukcji Pojazdów Elektrycznych ELECTROMOBILITY+, NCBiR

4.17. Wykonawca w projekcie DEC-2013/11/B/ST8/00309. Kompozyty ceramika-metal w układzie ZrO2-Ti OPUS 6, NCN

4.18. Wykonawca w projekcie POIG.01.03.01-00-015/08 NANOMET - Nowe materiały metaliczne o strukturze nanometrycznej do zastosowań w nowoczesnych gałęziach gospodarki POIG, NCBiR

4.19. Wykonawca w projekcie EUROFUSION nr.633053 Implementation of activities described in the Roadmap to Fusion during Horizon 2020 through a joint programme of the member of the EUROfusion consortium Euratom - Adhoc-2014-20, fundusze europejskie

5. Wykaz członkostwa w międzynarodowych lub krajowych organizacjach i towarzystwach naukowych wraz z informacją o pełnionych funkcjach.

Od 2022 jestem członkiem Polskiego Towarzystwa Mikroskopii

6. Wykaz staży w instytucjach naukowych lub artystycznych, w tym zagranicznych, z podaniem miejsca, terminu, czasu trwania stażu i jego charakteru.

W ***załączniku 10*** zebrano dokumenty potwierdzające odbyte staże zagraniczne.

Okres po uzyskaniu stopnia doktora:

- Luty - Marzec 2018: dwumiesięczny staż naukowy na Uniwersytecie Southampton (Anglia). Współpracowałem z prof. Terence G. Langdonem przy syntezie nowej generacji nanokrystalicznych hybrydowych materiałów warstwowych o wysokiej wytrzymałości i jednocześnie dobrej plastyczności. Wyjazd realizowałem w ramach mojego projektu SONATINA
- Sierpień 2019 - miesięczny pobyt naukowy w Southampton University (Anglia). Koncentrował się na optymalizacji parametrów przetwarzania HPT do syntezy systemów hybrydowych z układów Al-Ti, Cu-Ta, Al-Cu. Wyjazd realizowałem w ramach mojego projektu SONATINA

okres przed uzyskaniem stopnie doktora

- Marzec - Maj 2016: trzymiesięczny staż naukowy w Interdisciplinary Center for Electron Microscopy (CIME) na Politechnice w Lausanne (Szwajcaria). Staż obejmował szkolenia na zaawansowanych mikroskopach elektronowych: FEI Tecnai OSIRIS, FEI TALOS i JEOL 2200FS wyposażony w system ASTAR służący do orientacji ziarna i mapowania faz o rozdzielczości przestrzennej 2-3 nm. Urządzenia te były wykorzystywane do prowadzenia badań własnych na próbkach po procesach dużego odkształcenia plastycznego oraz badań składu chemicznego granic ziaren w silnie odkształconych stopach aluminium.
- Wrzesień - Listopad 2014: trzymiesięczny staż naukowy na Uniwersytecie Southampton (Anglia). Współpraca z grupą prof. Terence G. Langdona, twórcą technik dużego odkształcania plastycznego (SPD) stosowanych do produkcji litych próbek metalicznych o strukturze nanokrystalicznej. Podczas tego stażu przeprowadzałem eksperymenty z wykorzystaniem skręcania wysokociśnieniowego (HPT) i przeciskania przez kanał kątowy (ECAP) do wytworzenie różnych nanokrystalicznych stopów metali. Charakteryzowałem również ich właściwości mechaniczne.

7. **Wykaz członkostwa w komitetach redakcyjnych i radach naukowych czasopism wraz z informacją o pełnionych funkcjach (np. redaktora naczelnego, przewodniczącego rady naukowej, itp.).**

   Brak

8. **Wykaz recenzowanych prac naukowych lub artystycznych, w szczególności publikowanych w czasopismach międzynarodowych.**

   Recenzent artykułów naumowych dla chasopism z listy Filadelfijskiej:

   - Materials Science and Engineering A – 5 rezenzowanych artykułów
   - Journal of Alloys and Compound - 8 rezenzowanych artykułów
   - Acta Materialia - 1 rezenzowany artykuł

9. **Wykaz uczestnictwa w programach europejskich lub innych programach międzynarodowych.**

   Praca w projekcie EUROfusion, Komisja Europejska, 2017-2023, European Consortium for the Development of Fusion Energy, manages and funds European fusion research activities on behalf of Euratom, realizacja badań struktury materiałów do konstrukcji reactora termojądrowego

10. **Wykaz udziału w zespołach badawczych, realizujących projekty inne niż określone w pkt. II.4.**

    10.1. ***Kierownik projektu***:

    Technologie Materiałowe-1 – POB PW Inicjatywa Doskonałości Uczelnia Badawcza , tytuł: „Stabilność termiczna i mechanizmy odkształcania hybrydowych materiałów nanokrystalicznych wytwarzanych technikami skręcania pod wysokim ciśnieniem (HPT)”
    okres realizacji: 2010-2022, budżet 191 300 zł

10.2. ***Kierownik projektu***:

Grant wewnętrzny wspierający prowadzenie działalności naukowej dla młodych naukowców w dyscyplinie inżynieria materiałowa, tytuł: „Wpływ obróbki cieplnej na mikrostrukturę, właściwości mechaniczne i odporność na korozję wżerową stali 316L wytworzonej technologią selektywnego stapiania wiązką lasera (SLM)"
Okres realizacji: 2021, budżet: 34 920 zł

11. Wykaz uczestnictwa w zespołach oceniających wnioski o finansowanie badań, wnioski o przyznanie nagród naukowych, wnioski w innych konkursach mających charakter naukowy lub dydaktyczny

Recenzent Narodowego Centrum Nauki w konkursie Miniatura (11 wniosków ocenionych)

III. WSPÓŁPRACA Z OTOCZENIEM SPOŁECZNYM I GOSPODARCZYM

1. **Wykaz dorobku technologicznego**.
   Brak
2. **Współpraca z sektorem gospodarczym.**
   Brak
3. **Wykaz uzyskanych praw własności przemysłowej, w tym uzyskanych patentów krajowych lub międzynarodowych.**
   Brak
4. **Wykaz wdrożonych technologii.**
   Brak
5. **Wykaz wykonanych ekspertyz lub innych opracowań wykonanych na zamówienie instytucji publicznych lub przedsiębiorców.**
   Prowadziłem prace badawcze struktury materiałów wytworzonych przez prywatne firmy: VIGO Photonics S.A., EXPLOMET, TAPS – Maciej Kowalski.
6. **Wykaz udziału w zespołach eksperckich lub konkursowych.**
   Brak
7. **Wykaz projektów artystycznych realizowanych ze środowiskami pozaartystycznymi**.
   Brak

IV. DANE NAUKOMETRYCZNE

Dane pobrano z bazy SCOPUS i Web of Knowledge, stan na dzień: 03.08.2025

1. Impact Factor (w dziedzinach i dyscyplinach, w których parametr ten jest powszechnie używany jako wskaźnik naukometryczny).

Okres	Sumaryczny IF publikacji (współczynnik IF z roku opublikowania)
do 2017 roku (przed uzyskaniem stopnia doktora)	29,958
od 2017 roku (po uzyskaniu stopnia doktora)	217,969
Łącznie	247,927

2. Liczba cytowań publikacji wnioskodawcy, z oddzielnym uwzględnieniem autocytowań.

Baza	Liczba cytowani Całkowita (bez autocytowań habilitanta)
Scopus	1474 (1391)
Web of Science	1368 (1283)

3. Indeks Hirscha i liczba punktów MNSW

- Web of Science (WoS): 22
- Scopus: 22
- sumaryczna liczba punktów wg. **MNSW** = 5721

……..…….

(podpis wnioskodawcy)

JMEPEG (2024) 33:2860–2874
https://doi.org/10.1007/s11665-023-08856-8

1059-9495/$19.00

ORIGINAL RESEARCH ARTICLE

A Comparative Study Between AZ31 and Mg-Gd Alloys After High-Pressure Torsion

Ouarda Ould Mohamed, Piotr Bazarnik, Yi Huang, Hiba Azzeddine, Thierry Baudin, François Brisset, and Terence G. Langdon

Submitted: 22 July 2023 / Revised: 29 September 2023 / Accepted: 5 October 2023 / Published online: 19 October 2023

The evolution of microstructure, texture, and mechanical properties of AZ31 (Mg-3Al-1Zn, wt.%) and Mg-0.6Gd (wt.%) alloys was investigated and compared after high-pressure torsion at room temperature through the equivalent strain range of $\varepsilon_{eq} = 0.6 - 287.5$. The results demonstrated that the grain refinement behavior is different for these two alloys. For the AZ31 alloy, dynamic recrystallization (DRX) was restricted leading to a gradual and continuous formation of ultrafine grains with a mean grain size of ~ 0.3 μm through the entire strain range and the development of deviated B, C_1, and C_2 texture fibers. For the Mg-0.6Gd alloy, the DRX was very fast and a rapid ultrafine grain microstructure with a mean grain size of ~ 0.7 μm was developed at a strain range of $\varepsilon_{eq} = 0.6 - 5.7$ and this remained stable with a relatively stable B-fiber over the strain range $\varepsilon_{eq} = 5.7 - 287.5$. The evolution of microhardness in the AZ31 alloy indicated a strain hardening without recovery while that of the Mg-0.6Gd alloy showed a strain hardening with recovery. The differences between the AZ31 and Mg-0.6Gd alloys are discussed based on a comprehensive characterization of twinning, dislocation density, the initial microstructure and the presence of second phases.

Keywords dynamic recrystallization, high-pressure torsion, magnesium, microstructure, rare-earth, texture

1. Introduction

Magnesium (Mg) and its alloys have great potential to be used in diverse industries including transportation, electronic and biomedical owing to their attractive physical and chemical properties such as low density, high strength, recyclability, and biocompatibility (Ref 1-4). However, the formability of Mg-based alloys is very limited at room temperature (RT) because of the lack of sufficient active slip systems and the development of sharp basal texture which is due to the hexagonal close-packed structure of Mg (Ref 5). The deformation at low temperatures is accommodated by the basal $<a>$ slip system and the mechanical twinning generally known as $\{10\text{-}11\}$ $<10\text{-}12>$ contraction and $\{10\text{-}12\}$ $<10\text{-}11>$ extension twins owing to their low critical resolved shear stress (CRSS) values (Ref 6, 7). The activation of non-basal slip systems like $<c + a>$ pyramidal slip which can accommodate strain along the c-axis is hard due to its high CRSS value which is ~80 times larger than that of $<a>$ basal slip in pure Mg (Ref 8). The promotion of $<c + a>$ pyramidal slip system by decreasing the CRSS value may be achieved by changing the alloying elements (Ref 9) or increasing the deformation temperature (Ref 10).

It follows therefore that the mechanical properties of Mg-based alloys can be tailored by chemical composition and by processing technologies (Ref 11). The improvement of mechanical properties of Mg alloyed with rare-earth (RE) elements is usually related to solute strengthening, fine-grain strengthening and precipitation strengthening (Ref 12). In addition, one of the benefic effects of adding RE elements is the modification of texture which leads to a weakening of the basal texture by comparison to the traditional AZ-based alloys which has a direct effect on improving the ductility and decreasing the anisotropy of the Mg-RE alloys (Ref 13-17).

Conventional thermomechanical processing, which is a combination of deformation and heat treatment, is an excellent tool for controlling the microstructures and mechanical properties of Mg-based alloys. In such conditions, the mechanical improvement is related to grain refinement owing to the activation of non-basal slip systems and the occurrence of dynamic recrystallization (DRX) (Ref 18-25). According to the nature of the recrystallization process, discontinuous DRX (DDRX) and continuous DRX (CDRX) are the main mechanisms responsible for DRX in Mg-based alloys (Ref 26). DDRX mechanism is characterized by nucleation and a growth process and usually the formation of recrystallized grains occurring along the grain boundaries (Ref 26). In the CDRX mechanism, the formation of recrystallized new grains is due to the continuous absorption of dislocations in sub-grain bound-

Ouarda Ould Mohamed and **Hiba Azzeddine**, Laboratory of Materials and Renewable Energy, Faculty of Sciences, Mohamed Boudiaf University, 28000, M'sila, Algeria; **Piotr Bazarnik**, Faculty of Materials Science and Engineering, Warsaw University of Technology, Woloska 141, 02-507 Warsaw, Poland; **Yi Huang**, Materials Research Group, Department of Mechanical Engineering, University of Southampton, Southampton SO17 1BJ, UK; and Department of Design and Engineering, Faculty of Science and Technology, Bournemouth University, Poole BH12 5BB Dorset, UK; **Thierry Baudin** and **François Brisset**, Institut de chimie moléculaire et des matériaux d'Orsay, Université Paris-Saclay, CNRS, 91405 Orsay, France; and **Terence G. Langdon**, Materials Research Group, Department of Mechanical Engineering, University of Southampton, Southampton SO17 1BJ, UK. Contact e-mail: hiba.azzeddine@univ-msila.dz.

aries which progressively transform into low-angle grain boundaries (LAGBs) and then into high-angle grain boundaries (HAGBs) (Ref 26). The CDRX mechanism dominates when the initial material exhibits coarse grains, while DDRX dominates in deformed material with initial fine grains (Ref 27, 28). It is reported that the CDRX mechanism is characterized by slow kinetics and requires larger strains than the DDRX mechanism (Ref 29).

Among the new severe plastic deformation (SPD) techniques, high-pressure torsion (HPT) has become an established processing procedure that is used extensively for achieving remarkable grain refinement and superior properties in a range of different metals (Ref 30, 31). Furthermore, the HPT process is at present the only SPD technique that allows Mg-based metals to be deformed conveniently at room temperature (RT) (Ref 32-36). Indeed, HPT processing was successfully applied at RT to fabricate a novel hybrid material from separate disks of the AZ31 (Mg-3Al-1Zn, wt.%) and Mg-0.6Gd (wt.%) alloys (Ref 37). It is recognized that grain refinement is governed by the CDRX mechanism in SPD-processed materials at RT or warm temperatures (Ref 29, 38).

Several reports show that the DRX in Mg-RE alloys is retarded or restricted due to the easy activation of non-basal slip systems so that DRX is not required to accommodate the deformation (Ref 23-25). By contrast, it was reported that the improvement in formability of Mg-Gd alloys is related to a change in the recrystallization behavior and the resulting texture rather than the activation of supplementary slip systems (Ref 39). There has been significant research focusing on highlighting the differences in deformation behavior, microstructure, and texture evolution under conventional thermomechanical processing between pure Mg or the traditional AZ31 alloy and Mg-RE alloys (Ref 39-44). For example, the stored energy was lower for AZ31 than the Mg-1.5Gd (wt.%) alloy under hot plane strain compression for a true strain of 0.7 (Ref 40). Consequently, the static recrystallization kinetics of the Mg-1.5Gd alloy was notably faster than the AZ31 alloy (Ref 41).

It is important to note that similar comparison studies are not yet available for HPT-processed Mg-based alloys. Therefore, the present work was designed specifically to compare the evolution of the microstructure, texture and microhardness of AZ31 and Mg-0.6Gd (wt. %) alloys separately processed by HPT at RT for an equivalent strain range of $\varepsilon_{eq} = 0.6 - 287.5$.

2. Experimental Materials and Procedures

Sheets of a hot-rolled AZ31 alloy and an as-cast Mg-0.6Gd alloy were provided by the Magnesium Innovations Center (MagIC, Germany) and the Institute of Physical Metallurgy and Materials Physics (RWTH-Aachen University, Germany), respectively. The Mg-0.6Gd alloy was fabricated by induction melting and casting under a protective gas of Ar/CO_2 using preheated copper mold. Then, the as-cast alloy was subjected to heat treatment for 20 h at 420 °C.

The HPT processing was performed on disks with diameters of 10 mm and thicknesses of 0.85 mm at room temperature for $N = 1/2$, 5, 10 and 20 turns under quasi-constrained conditions (Ref 45). The disk samples were processed under a pressure of 6.0 GPa with a rotational speed of 1 rpm. In quasi-constrained HPT processing, the two anvils are separated so that there is always a minor outflow of material around the periphery of the disk during processing and this causes a decrease in the thickness of the disk which was from 0.85 to 0.63 mm in the present experiments.

The microstructure and texture analyses were taken on the cross-sectional (CD-RD) planes of the HPT disks where the shear reference frame is defined as the radial direction (RD), compression direction (CD) and shear direction (SD) (Ref 46).

The EBSD measurements were performed near the center ($r \sim 0.2$ mm) and at the mid-radius position ($r \sim 2.5$ mm) of the mid-thickness plane of the HPT-processed disks using a TSL-EDAX-Hikari system mounted on a scanning electron microscope (FEG-SEM Zeiss Supra 55 VP) operating at 20 kV.

The equivalent strain, ε_{eq}, imposed during HPT can be calculated from the following equation (Ref 47):

$$\varepsilon_{eq} = \frac{2\pi Nr}{\sqrt{3}h} \quad \text{(Eq 1)}$$

where r is the radial distance from the center of the disk and h is the thickness of the disk after HPT. Accordingly, Table 1 summarizes the values of ε_{eq} in each HPT-processed disk.

The scanned areas for the AZ31 disks were 40 × 40 μm^2 with a step size of 0.1 μm for $N = 0$, 1/2, 5 and 10 turns and for the AZ31 disk processed for $N = 20$ turns the scanned area was 5 × 5 μm^2 with a step size of 20 nm. The scanned area for the initial state ($N = 0$) of the Mg-0.6Gd alloy was 700 × 2500 μm^2 with a step size of 1 μm, whereas the scanned areas for the HPT-processed Mg-0.6Gd disks ($N = 1/2$, 5, 10 and 20 turns) were 40 × 40 μm^2 with a step size of 50 nm. The EBSD data were analyzed by the Orientation Imaging Microscopy OIM™ software.

The dynamically recrystallized grains were identified using the grain orientation spread (GOS) approach implemented in the OIM™ software, where grains with GOS < 2° are considered fully recrystallized (Ref 48).

The texture was analyzed using toolbox MTEX by calculating the orientation distribution function (ODF) using the harmonic method ($L = 22$) and a Gaussian function with a half-width of 5° to model each orientation (Ref 49).

Detailed microstructural observations at the mid-radius positions of disks processed for i = 5 turns were performed using a CS-corrected dedicated Thermo Fisher Scientific Spectra scanning transmission electron microscope (STEM) operating at an accelerating voltage of 200 kV. The STEM observations were carried out in the bright-field (BF) and high-angle annular dark field (HAADF) modes. Structural investi-

Table 1 Values of the imposed equivalent strain ε_{eq} in different positions (near center and mid-radius) of HPT-processed disks

N	*r*, mm	ε_{eq}
1/2	0.2	0.6
	2.5	7.2
5	0.2	5.7
	2.5	71.9
10	0.2	11.5
	2.5	143.7
20	0.2	23.0
	2.5	287.5

gations were combined with advanced energy-dispersive x-ray (EDX) point and mapping analyses. Thin foils for observations were prepared using a focused ion beam (FIB) Hitachi NB-5000 microscope.

The microhardness of the samples was measured using a Vickers microhardness tester (SHIMADZU type HMV-2 tester) with a load of 100 g ($Hv_{0.1}$) and a dwell time of 10 s. At least 5 Hv measurements were recorded to obtain the average value for each sample.

3. Results

Figure 1 and 2 presents the evolution of the microstructure of AZ31 and Mg-0.6Gd alloys in terms of an inverse pole figure (SD-IPF) map as a function of equivalent strain: (a) $\varepsilon_{eq} = 0$, (b) $\varepsilon_{eq} = 0.6$, (c) $\varepsilon_{eq} = 7.2$, (d) $\varepsilon_{eq} = 71.9$, (e) $\varepsilon_{eq} = 143.7$ and (f) $\varepsilon_{eq} = 287.5$, respectively. The grain boundaries with high misorientations ($\theta > 15°$) are highlighted by a black line. It should be noted that the SD-IPF map of the HPT-processed AZ31 sample at $\varepsilon_{eq} = 287.5$ (Fig. 1f) is presented with a different scale bar. The initial microstructures of the AZ31 and Mg-0.6Gd alloys are different and related directly to the processing history. The microstructure of the as-received AZ31 alloy is characterized by deformed grains with a mean grain size of ~ 12.5 μm and the presence of twins identified as {10-11} contraction twins.

The rectangular box indicates the occurrence of the twin-induced dynamic recrystallization (TDRX) mechanism which is characterized by the formation of recrystallized grains inside the twins (Ref 50). By contrast, the microstructure of the as-received Mg-0.6Gd alloy contains coarse grains with a mean grain size of about ~ 670 μm which is typical of an as-cast condition.

The microstructure of the as-cast Mg-0.6Gd alloy contains also massive twins identified as {10-12} extension twins in the form of steps and it is reasonable to assume that their presence is due to the mechanical preparation of the sample. The SD-IPF maps indicate that the twins remain present during HPT processing and they are more visible in the AZ31 alloy through strains from 0.6 to 7.2 as shown by the black arrows. However, the fraction of twins decreases with increasing equivalent strain due to the grain refinement. Indeed, the deformation microstructure of both alloys transformed gradually to equiaxed fine grains with increasing equivalent strain. It is interesting to note that the deformation microstructure of the Mg-0.6Gd alloy became more homogeneously distributed (at $\varepsilon_{eq} = 7.2$) than for the AZ31 alloy (at $\varepsilon_{eq} = 143.7$). The evolutions of mean grain size, DRX fraction and HAGBs fraction as a function of equivalent strain in the AZ31 and Mg-0.6Gd alloys are shown in Fig. 3.

The HPT processing at a strain of 0.6 causes a decrease in grain size to 3.6 μm for the AZ31 alloy. Thereafter, the mean grain size of the HPT-processed AZ31 alloy decreases gradually with increasing equivalent strain to 0.55 μm at $\varepsilon_{eq} = 23$ and then decreases slowly to 0.3 μm at $\varepsilon_{eq} = 287.5$. The mean grain size of the Mg-0.6Gd alloy rapidly deceases from 670 to 2.6 μm after a strain of $\varepsilon_{eq} = 0.6$, then to 0.71 μm at $\varepsilon_{eq} = 5.7$ where it appears to reach a saturation value.

It is apparent from Fig. 3(b) that the fraction of DRX in the Mg-0.6Gd alloy is higher than in the AZ31 alloy. The fraction of DRX was relatively similar in both alloys during low straining ($\varepsilon_{eq} = 0.6 - 5.7$) but DRX occurred rapidly in the Mg-0.6Gd alloy and reached a high value of 85 % at a strain of $\varepsilon_{eq} = 7.2$ which was a saturated condition. For the AZ31 alloy, the DRX fraction increased slowly but continuously with increasing strain and the microstructure became essentially fully recrystallized (about 80 %) at a strain $\varepsilon_{eq} = 287.5$. Consequently, the fraction of HAGBs increases with increasing equivalent strain for both alloys, as demonstrated in Fig. 3(c). However, it is obvious that the fraction of HAGBs is higher in the Mg-0.6Gd alloy than in the AZ31 alloy, especially during an equivalent strain range of $\varepsilon_{eq} = 5.4 - 143.7$.

Figure 4 and 5 shows STEM images in (a) BF and (b) HAADF at low magnification after processing for $N = 5$ turns ($\varepsilon_{eq} = 71.9$) near the mid-radius of the AZ31 and Mg-0.6Gd disk, respectively. In addition, Fig. 4(c) shows a high magnification of the yellow box of the HPT-processed AZ31 alloy showing the EDS mapping for the Mg, Al, and Mn elements and the EDS analysis of particles present at point 1.

Observations by STEM confirmed extensive grain refinement in both alloys although, the images (BF mode) indicate that the AZ31 alloy exhibits a more homogeneous microstructure in terms of grain refinement when compared with the Mg-0.6Gd alloy (Fig. 4a and 5a). The grain size calculated for the AZ31 and Mg-0.6Gd alloys was 260 ± 30 nm and 650 ± 68 nm, respectively. The HAADF images (Fig. 4b and 5b) demonstrate a net difference in the presence of second phase particles. No particles are visible in the HAADF images of the Mg-0.6Gd sample indicating the fragmentation and dissolution of the metastable Mg_5Gd particles which were present in the as-cast state, where this is consistent with an earlier report (Ref 37). High-magnification observations of the AZ31 sample showed a high concentration of small spherical nanoparticles having sizes from 10-45 nm. The EDS analysis (Fig. 4c) indicates that these particles consist mainly of Al and Mn and the atomic and weight percentages shown in Fig. 4(d) demonstrate that these Mn-containing particles are stable Al_8Mn_5 (Ref 51). It must be noted that the fraction of the Mg element (present only in the matrix) was excluded in order to show Al/Mn proportions.

Figure 6 and 7 shows the recalculated {0002} pole figures and ODF sections at $\varphi_2 = 0$ and 30° of the HPT processed AZ31 and Mg-0.6Gd alloys for (a) $\varepsilon = 0$, (b) $\varepsilon = 0.6$, (c) $\varepsilon = 7.2$, (d) i = 71.9, (e) $\varepsilon = 143.7$, and (f) $\varepsilon = 287.5$, respectively. The ideal shear texture component positions on the RD-CD plane for materials with HCP structure (Ref 46) are also present in both figures (Fig. 6g and 7g) and their description in the form of the Euler angles (φ_1, Φ, φ_2) is given in Table 2. The initial texture of the AZ31 alloy shows the presence of a basal texture (B-fiber) which is a typical texture formed during the rolling of Mg-based alloys (Ref 52, 53).

The HPT processing at a strain of 0.6 (Fig. 6b) led to the development of the C_2-fiber. As can be seen from Fig. 6(c), the C_1-fiber is developed with a weak B-fiber at a strain of 7.2.

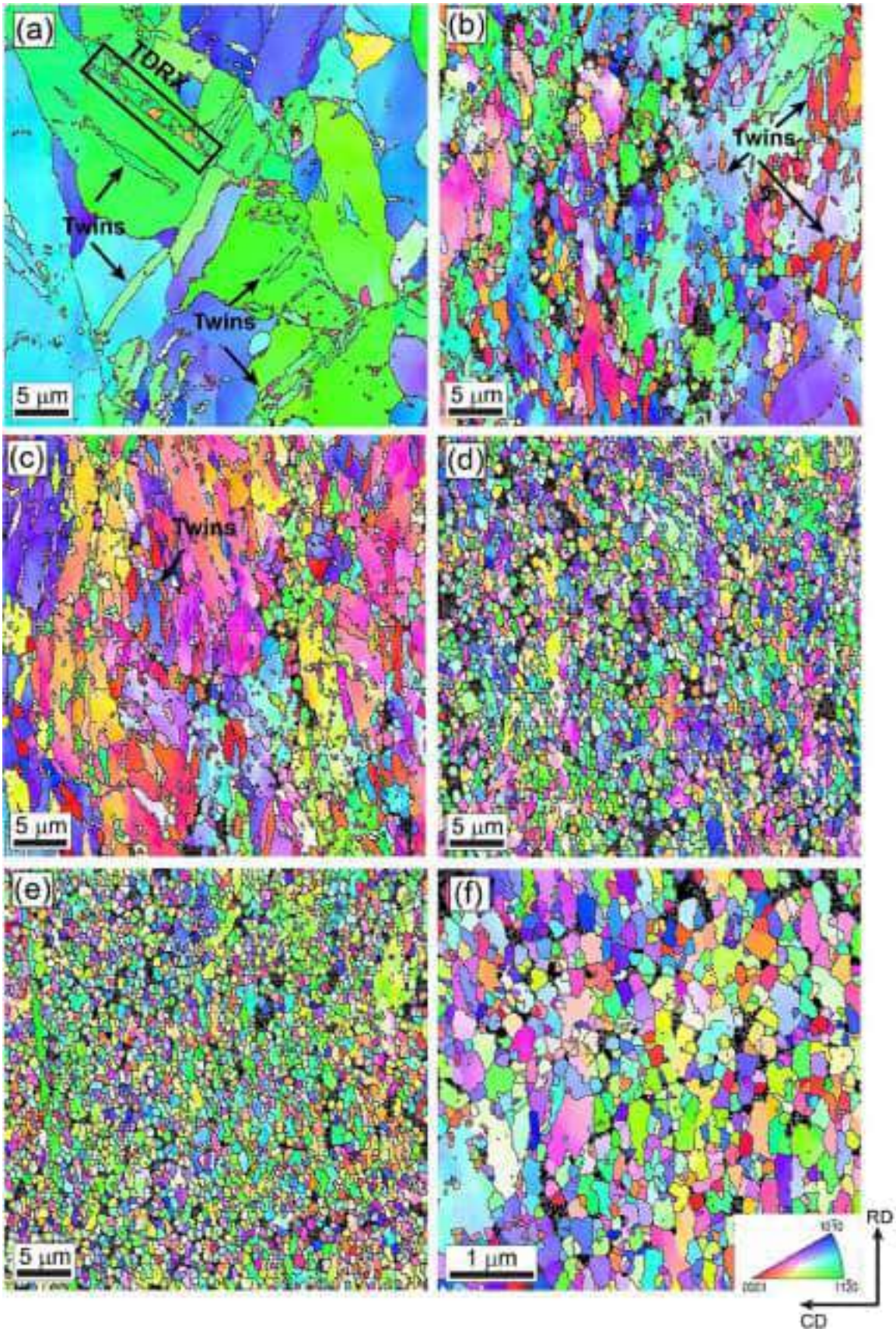

Fig. 1 SD-IPF maps of AZ31 alloy HPT processed for (a) $\varepsilon_{eq} = 0$ (initial state), (b) $\varepsilon_{eq} = 0.6$ (center of $N = 1/2$ turn), (c) $\varepsilon_{eq} = 7.2$ (middle of N = 1/2 turn), (d) $\varepsilon_{eq} = 71.9$ (middle of $N = 5$ turns), (e) $\varepsilon_{eq} = 143.7$ (middle of $N = 10$ turns) and (f) $\varepsilon_{eq} = 287.5$ (middle of $N = 20$ turns). Note that Fig. 1f is presented with different scale bar

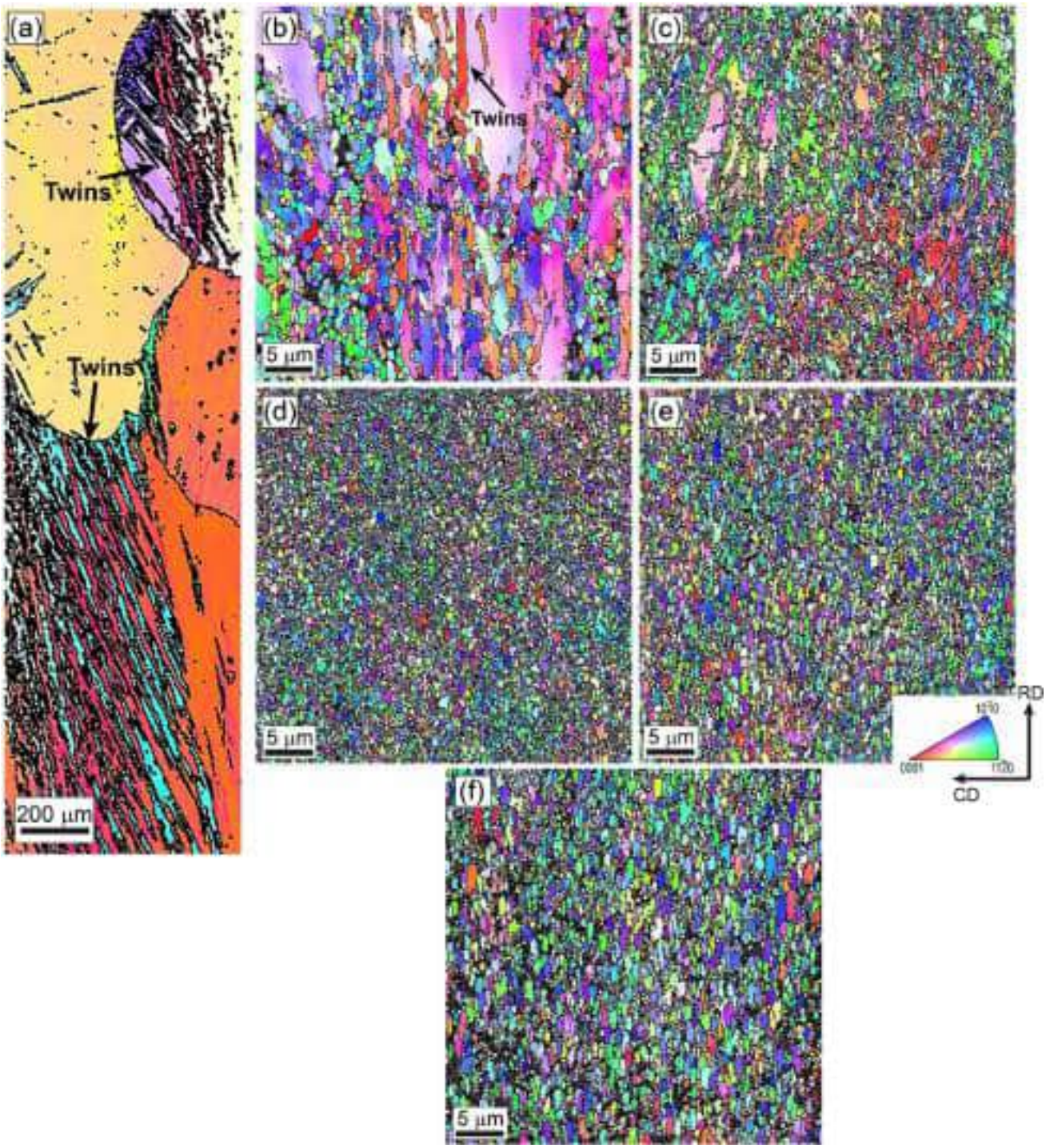

Fig. 2 SD-IPF maps of Mg-0.6Gd alloy HPT processed for (a) $\varepsilon_{eq} = 0$ (initial state), (b) $\varepsilon_{eq} = 0.6$ (center of $N = 1/2$ turn), (c) $\varepsilon_{eq} = 7.2$ (middle of $N = 1/2$ turn), (d) $\varepsilon_{eq} = 71.9$ (middle of $N = 5$ turns), (e) $\varepsilon_{eq} = 143.7$ (middle of $N = 10$ turns) and (f) $\varepsilon_{eq} = 287.5$ (middle of $N = 20$ turns)

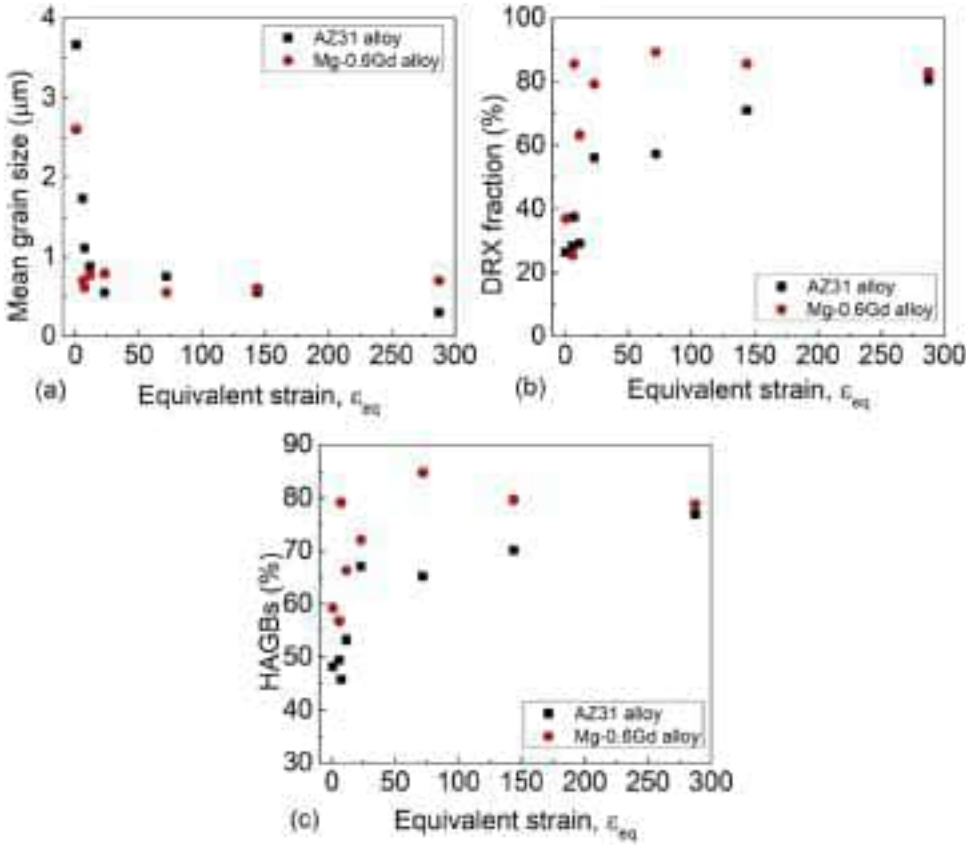

Fig. 3 Evolution of (a) mean grain size, (b) DRX fraction, and (c) HAGBs fraction in AZ31 and Mg-0.6Gd alloy as a function of equivalent strain

Again, the C_2 and basal fibers appeared at a strain of 71.9 with significant deviation from their ideal positions as can be observed with further increasing strain at ε_{eq} = 143.7 (about 20° toward RD) and 287.5 (about 30° toward RD). It is evident from the {0002} pole figure (Fig. 6f) that there is the presence of a deviated C_1-fiber at a strain of 287.5.

The identification of texture type (see Fig. 7a) of the as-cast Mg-0.6Gd sample was not possible since the sample exhibits limited grain numbers as revealed in Fig. 2(a). However, the B-fiber and C_2-fiber formed rapidly after HPT processing at ε_{eq} = 0.6. The C_2-fiber disappears with increasing strain at ε = 71.9 leading to a dominant basal texture through the entire strain. It can be noticed that there is a small deviation of basal fiber from its ideal position with increasing strain from ε_{eq} = 143.7 (about 10° toward RD) to ε_{eq} = 287.5 (about 15° toward RD).

Figure 8(a) and (b) presents the evolution of microhardness as a function of the equivalent strain for the AZ31 and Mg-0.6Gd alloys, respectively. The microhardness of the initial states of the AZ31 and Mg-0.6Gd alloys were 72 and 24 Hv, respectively. The microhardness of the AZ31 alloy increased with increasing strain to reach a value of 108 Hv at a strain of ε_{eq} = 7.2 and slightly decreased to reach a saturated value of 102.6 Hv. In the case of the Mg-0.6Gd alloy, the microhardness goes through three stages. First, the microhardness increases with increasing equivalent strain to a maximum value of 53.1Hv at ε_{eq} = 3.6. Second, it decreases with increasing strain to 39.5 Hv at ε_{eq} = 71.9, and then finally, it saturates at this value up to a strain of ε_{eq} = 287.5.

4. Discussion

The evolution of the microstructural parameters such as mean grain size, DRX and HAGBs fractions in the AZ31 and Mg-0.6Gd alloys through HPT processing shown in Fig. 1, 2 and 3 demonstrates that the grain refinement of both alloys is obtained by the CDRX process. Nevertheless, the DRX kinetics and consequently the grain refinement behavior were different between the two alloys. In general, the grain refinement of both alloys can be separated into two stages. For the AZ31 alloy,

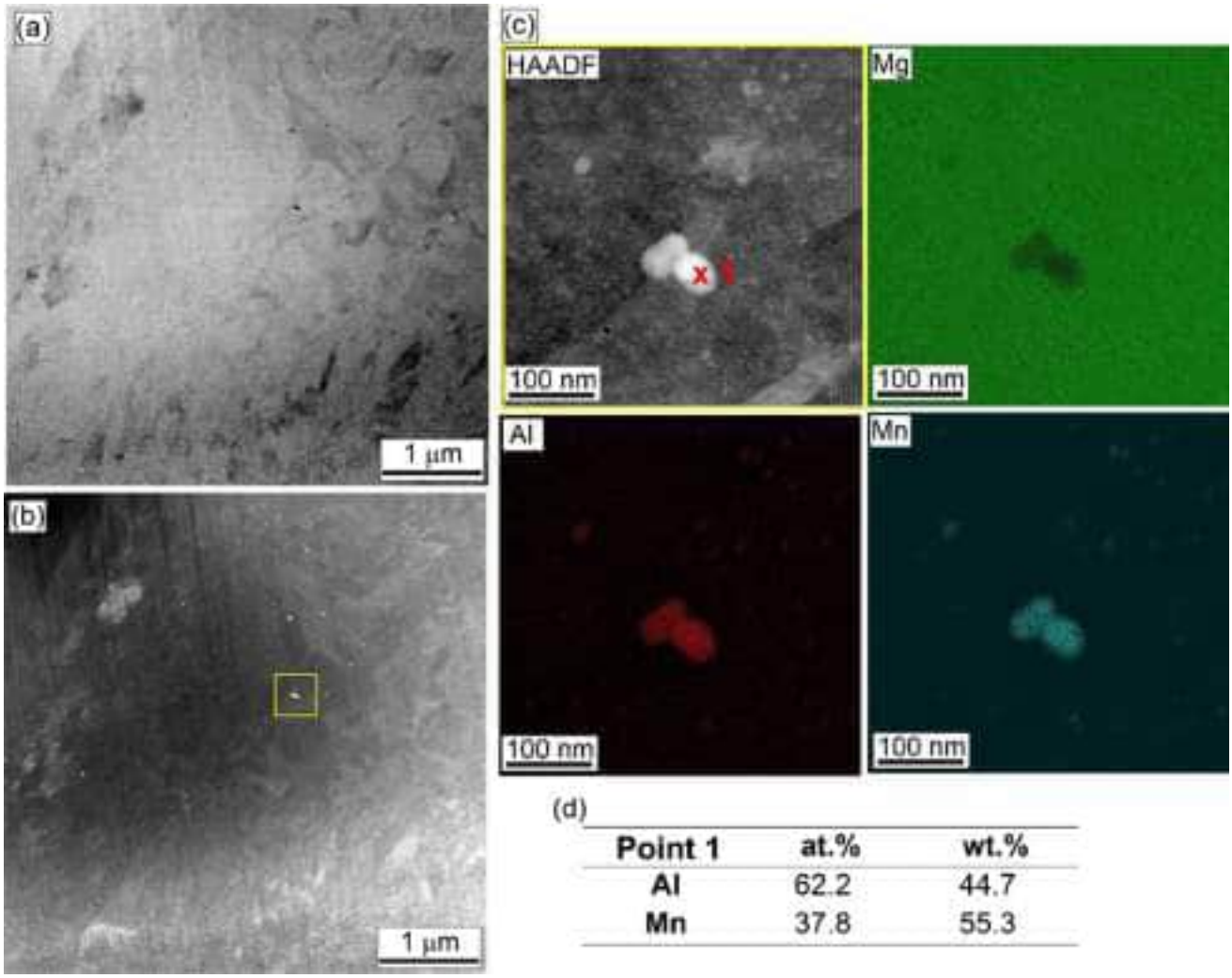

Point 1	at.%	wt.%
Al	62.2	44.7
Mn	37.8	55.3

Fig. 4 STEM images in (a) BF and (b) HAADF at low magnification near the mid-radius of the AZ31 disk processed for $N = 5$ turns ($\varepsilon_{eq} = 71.9$), and (c) high magnification of yellow box showing the EDS mapping for Mg, Al and Mn elements and (d) EDS analysis of particles present at point 1 (Color figure online)

stage I occurred during $\varepsilon_{eq} = 0.6 - 11.5$ where the DRX and HAGBs fractions increase and the mean grain size decreases gradually from 25 to 1.1 μm and in stage II ($\varepsilon_{eq} = 11.5 - 287.5$) the DRX and HAGBs fractions continue to increase and the grain size decreases slowly by comparison with stage I to reach a value of 0.3 μm at a strain of 287.5. For the Mg-0.6Gd alloy, the DRX and HAGBs fractions increase quickly during stage I ($\varepsilon_{eq} = 0.6 - 5.7$) leading to the formation of an equiaxed microstructure with a mean grain size of 0.7 μm and then stage II ($\varepsilon_{eq} = 5.7 - 287.5$) shows the saturations of the mean grain size and the HAGBs and DRX fractions. Such behavior is consistent with the evolution of microhardness shown in Fig. 8. The evolution of microhardness of the AZ31 alloy indicated a strain hardening without recovery (Ref 54, 55), while that of the Mg-0.6Gd alloy shows a strain hardening with recovery and dynamic recrystallization (Ref 54, 55).

It must be noted that the present results show that the AZ31 and Mg-0.6Gd alloys exhibit an inverse behavior compared with that reported for the AZ31 and Mg-1.5Gd alloys under conventional processing (Ref 40). The enhancement of DRX is mainly attributed to the stored energy during deformation processing. At RT and low strains, the deformation of Mg-based alloys is accommodated by twinning and dislocations generated mainly from the activation of $<a>$ basal slip. Hence, to further analyze the DRX behavior, the presence of twins and an estimate of the dislocation densities at a low strain, $\varepsilon_{eq} = 0.6$, are compared for both alloys as in Fig. 9 and 10.

Figure 9(a) and (b) presents the Image Quality (IQ) maps highlighted by the common twinning mode found in Mg-based

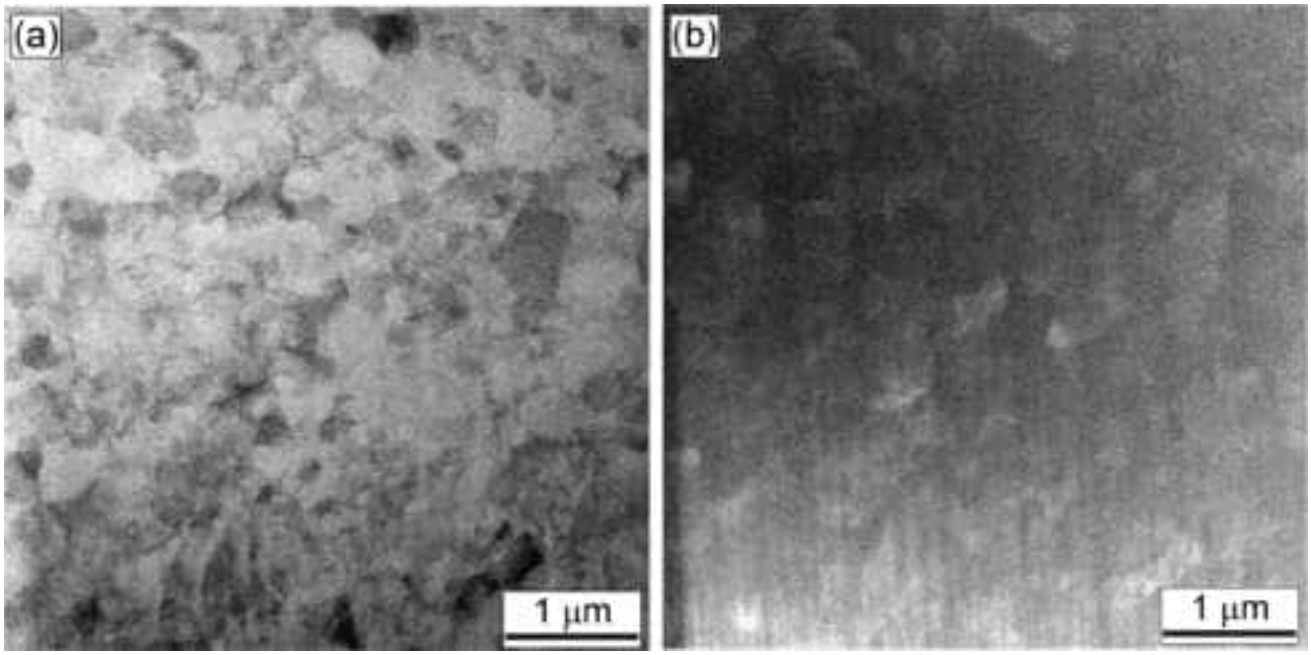

Fig. 5 STEM images in (a) BF and (b) HAADF at low magnification near the mid-radius of the Mg-0.6Gd disk processed for $N = 5$ turns ($\varepsilon_{eq} = 71.9$)

alloy: {10-11}-contraction twinning (56° <11-20>) and {10-12}-extension twinning (86° <11-20>). The {10-11}-contraction and {10-12}-extension twins are identified with an error angle of 10° and labeled by blue and green colors, respectively. The fractions of twins are shown in the upper IQ maps (Fig. 9a and b) and seem similar in both samples except that there is a higher fraction of {10-12}-extension twins in the AZ31 alloy (11.8 % vs. 8.0%). The magnification of the yellow box shown in Fig. 9(c) and (g) demonstrates that the twins have different shapes depending on the alloy. Figure 9(c) shows that the extension twins in the AZ31 alloy have lenticular shape structures. It is interesting to note that the extension twins are responsible for the development of the C_2-fiber as indicated by the SD-IPF map and the corresponding {0002} pole figure (Fig. 9d and f).

By contrast, Fig. 9(g) and (i) shows that the extension and contraction twins present in the Mg-0.6Gd alloy are mostly boundaries for the dynamically recrystallized grains. The SD-IPF map and the corresponding {0002} pole figure shown in Fig. 9(h) and (j) confirm that the development of the C_2-fiber comes from the activation of contraction and extension twins.

Despite the fact that the AZ31 and Mg-0.6Gd alloys exhibit different initial textures (Fig. 6a and 7a), similar textures composed of basal and C_2-fiber formed in both alloys at a low strain ($\varepsilon_{eq} = 0.6$). In fact, most hexagonal materials develop the B-fiber during HPT processing and exactly during the compression stage (Ref 46, 56) due to the easy activation of the <a> -basal slip system which orients the basal planes parallel to the shear plane producing a typical basal texture (Ref 46, 57). It is well known that twinning has more effect on texture modification than grain refinement due to the creation of a high misorientation angle between twins and their parent grains (Ref 24). It is also worth noting that the development of the C_1-fiber in the HPT-processed AZ31 sample at $\varepsilon_{eq} = 7.2$ (Fig. 6c) is due to the activation of twins as can be seen from Fig. 1(c). The C_1 and C_2 fibers are considered as pairs since they are defined as *c*-fiber where the *c*-axis is first rotated 90° in the shear direction, then ± 30° in the shear plane direction (Ref 57).

The evolutions of texture show that the C_1 and C_2 fibers remain present in the AZ31 alloy (Fig. 6) but with a significant deviation from their ideal position with increasing strain. First, the lenticular extension twins can propagate and grow rapidly with further strain due to their high mobility (Ref 58) and eventually consume the parent grain which can explain the persistence of the C_1 and C_2 fibers. Second, the deviation of the texture at higher stains is attributed to the torsional straining imposed by the rotation of the anvil during HPT processing (Ref 46). However, the C_2-fiber completely disappeared in the Mg-0.6Gd alloy (Fig. 7) with increasing strain and this indicates that the effect of twins on the texture evolution of the Mg-0.6Gd alloy is not permanent. In practice, the twin boundaries can strongly block the dislocation motion which contributes to their accumulation and the formation of LAGBs (Ref 59). As can be seen in Fig. 9(e) and (i), the GOS maps indicate that within the contraction twins and near the twin boundaries there are LAGBs which will transform into HAGBs and eventually into newly refined grains with further strain. These new grains may have similar orientations to the twin (Ref

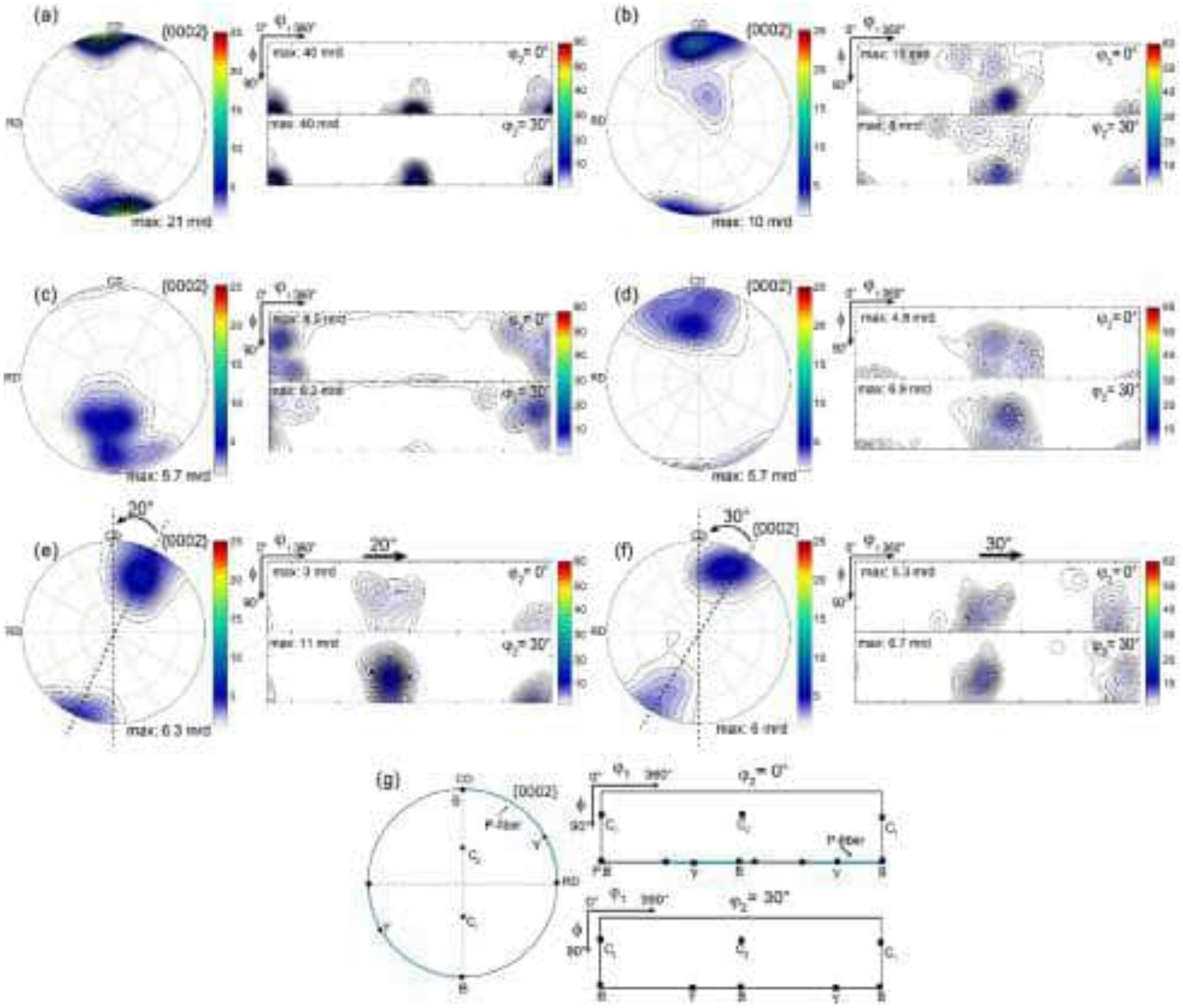

Fig. 6 Recalculated {0002} pole figures and ODF sections at $\varphi_2 = 0$ and 30° of AZ31 alloy HPT processed for (a) $\varepsilon_{eq} = 0$ (initial state), (b) $\varepsilon_{eq} = 0.6$ (center of $N = 1/2$ turn), (c) $\varepsilon_{eq} = 7.2$ (middle of $N = 1/2$ turn), (d) $\varepsilon_{eq} = 71.9$ (middle of $N = 5$ turns), (e) $\varepsilon_{eq} = 143.7$ (middle of $N = 10$ turns), (f) $\varepsilon_{eq} = 287.5$ (middle of $N = 20$ turns) and (g) the ideal shear texture components positions on CD-RD plane for materials with HCP structure (Ref 46)

24, 60) or they may develop different orientations (Ref 61). Unlike the extension twins, contraction twins have a very low mobility (Ref 62) so that the recrystallized grains within them will not grow and hence they will be devoured by the neighboring grains with further strain.

To estimate the dislocation density, ρ, especially the geometrically necessary dislocations, a Kernel Average Misorientation (KAM) method was applied following the expression (Ref 63):

$$\rho = \frac{\theta_{KAM}}{db} \qquad \text{(Eq 2)}$$

where b is the Burgers vector, d is the scan step size, and θ_{KAM} is the average misorientation angle.

It should be mentioned that an accurate determination of the dislocation density depends strongly on the choice of various EBSD parameters such as the size of the kernel, the EBSD step size and the threshold angle. Since the absolute dislocation density values were not pursued in this investigation, the θ_{KAM} was calculated from the mean misorientation angle between the point and its 3rd neighbors and by excluding misorientations of $\theta > 5°$. These chosen parameters are compatible with the average grain size even for the highest strains (about 0.3 μm for the AZ31 alloy).

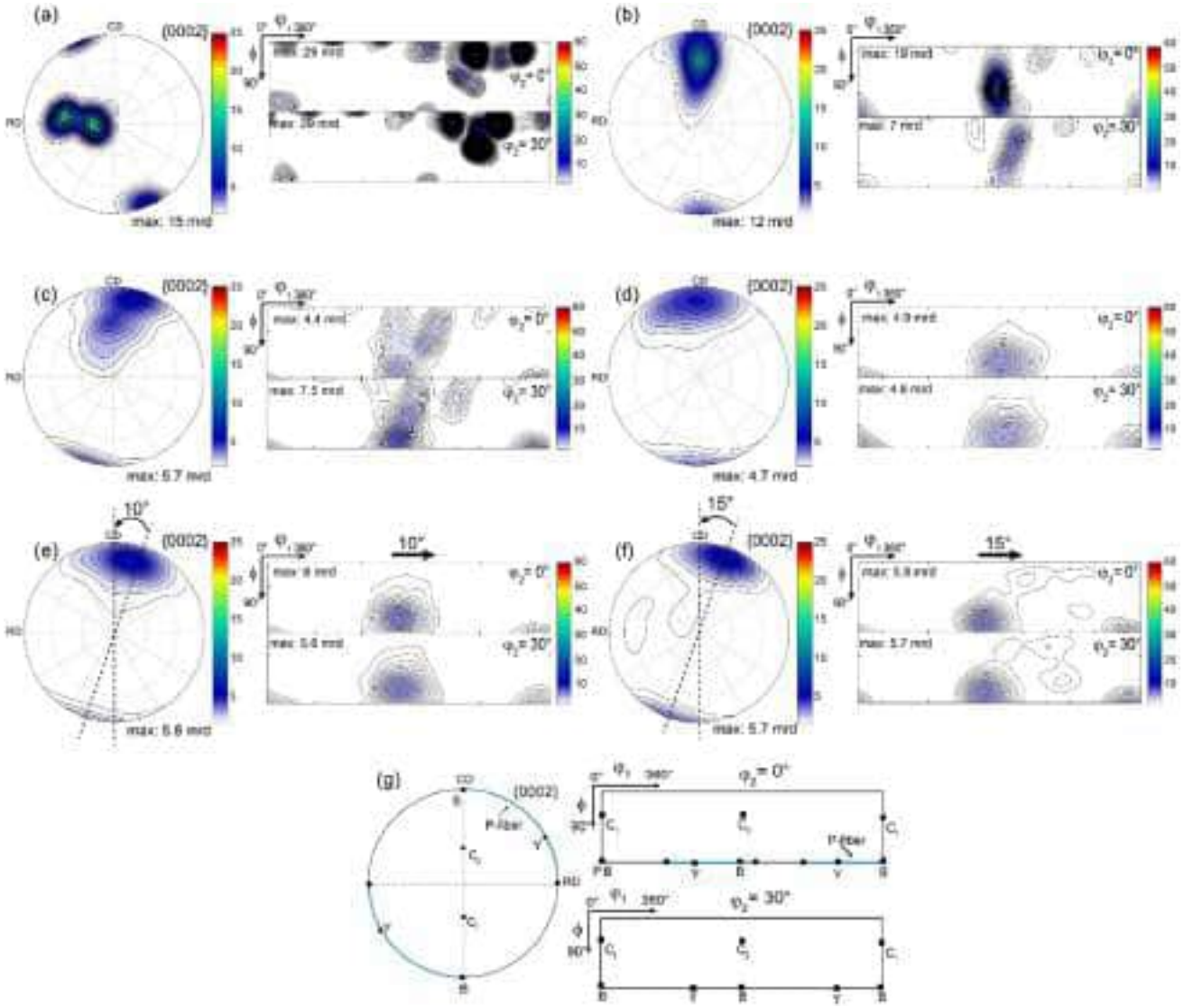

Fig. 7 Recalculated {0002} pole figures and ODF sections at $\varphi_2 = 0$ and 30° of Mg-0.6Gd alloy HPT processed for (a) $\varepsilon_{eq} = 0$ (initial state), (b) $\varepsilon_{eq} = 0.6$ (center of $N = 1/2$ turn), (c) $\varepsilon_{eq} = 7.2$ (middle of $N = 1/2$ turn), (d) $\varepsilon_{eq} = 71.9$ (middle of $N = 5$ turns), (e) $\varepsilon_{eq} = 143.7$ (middle of $N = 10$ turns), (f) $\varepsilon_{eq} = 287.5$ (middle of $N = 20$ turns) and (g) the ideal shear texture components positions on CD-RD plane for materials with HCP structure (Ref 46)

Table 2 Position of ideal shear texture components for HCP materials and alloys projected in the CD-RD plane (Ref 46)

Notation	B-fiber	P-fiber	Y-fiber	C_1-fiber	C_2-fiber
(φ_1, Φ, φ_2)	(360, 90, 0-60)	(90-180, 90, 0)	(300, 90, 0-60)	(0, 30, 0-60)	(180, 30, 0-60)

Figure 10(a) and (b) presents the KAM maps at $\varepsilon_{eq} = 0.6$ for the HPT-processed AZ31 and Mg-0.6Gd alloys, respectively. The θ_{KAM} and ρ values are shown in the upper KAM maps. The results indicate that the AZ31 alloy ($\rho = 8.3 \times 10^{14}$ m^{-2}) stored more energy than the Mg-0.6Gd alloy ($\rho = 7.1 \times 10^{14}$ m^{-2}). The evolution of dislocation density as a function of equivalent strain for both alloys is presented in Fig. 10(c). As can be seen, the dislocation density of the AZ31 alloy increases with increasing strain at 11.5 and then starts to decrease indicating the occurrence of DRX and the formation of new

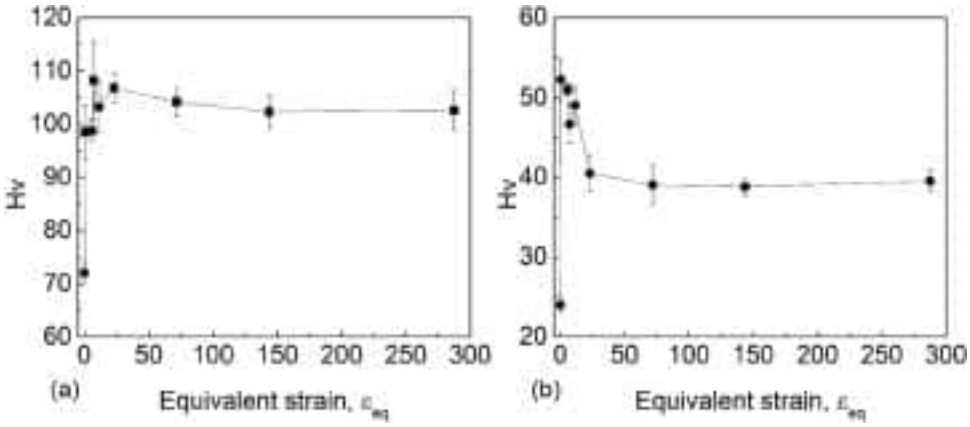

Fig. 8 Evolution of microhardness as a function of equivalent strain of: (a) AZ31, and (b) Mg-0.6Gd alloys

grains. By contrast, the dislocation density of the Mg-0.6Gd alloy is stable around 7×10^{14} m^{-2} through the entire strain which demonstrates that an equilibrium is reached between the generation of dislocations and the formation of new grains. This may explain the saturation of the grain refinement at 0.7 μm with increasing strain ($\varepsilon_{eq} = 5.7 - 287.5$). In this case, the new dislocations prevent the HAGBs of the dynamically recrystallized grains from migration and thereby they limit the grain growth. It is known that a high stored energy will increase the rate of recrystallization (Ref 26). Figure 10 shows that the stored energy is higher in the AZ31 alloy but the DRX was restricted by comparison with the Mg-0.6Gd alloy which shows a lower stored energy and a fast DRX.

The presence of nano-size particles of Al_8Mn_5 (shown in Fig. 4) may be one of the reasons for the retardation of DRX in the AZ31 alloy. On the one hand, it is recognized that the pinning effect of large second particles ($> 1\mu$m) on the dislocation motion will increase the stored energy around them and promote DRX via the particle-stimulated nucleation mechanism (Ref 26, 64). The morphology, size, quantity and distribution of second particles are important parameters affecting the DRX process (Ref 26, 59, 65, 66). On the other hand, it was found that DRX is restricted when the small second phase particles pinned the dislocations and sub-grain boundaries resulting from the DRX process and inhibited their transformation to HAGBs (Ref 59, 66) which is mostly the case in the present AZ31 alloy. The second reason to consider for the DRX kinetics is the nature and concentration of the alloying element. It is expected that the effect of 3% Al and 1% Zn in the AZ31 alloy on segregation to grain boundaries and the limitation of their mobility in solute drag will be greater than the low concentration of 0.6% Gd in the Mg-0.6Gd alloy.

The difference in the initial microstructure is also another reason for the difference in the DRX kinetics. As shown in Fig. 1(a) and 2(a), the AZ31 alloy contains more grain boundaries than the Mg-0.6Gd alloy and these eventually act as pinning points delaying further dislocation propagation (Ref 67) and causing grain boundary strengthening for the AZ31 alloy. The latter proposal is supported by the high dislocation density shown in Fig. 10(c) and the evolution of the microhardness presented in Fig. 8.

The present results demonstrate that HPT processing has the ability to change the deformation behavior and the DRX kinetics of Mg-based alloys by comparison with conventional thermomechanical processing. This suggests that in future it will be interesting to compare the static recrystallization of HPT-processed AZ31 and Mg-0.6Gd alloys.

5. Summary and Conclusions

Alloys of AZ31 and Mg-0.6Gd were processed by HPT at RT through $\varepsilon_{eq} = 0.6 - 287.5$ and their microstructure, texture and microhardness evolutions were reported and compared. The main findings can be summarized as follows:

- The EBSD, STEM and microhardness results show that the grain refinement of each alloy was different and it was the opposite of that generally reported under conventional deformation.
- The AZ31 alloy exhibits a gradual and continuous formation of ultrafine grains with a mean grain size of ~ 0.3 μm through the entire strain due to the retardation of DRX. By contrast, DRX was fast in the Mg-0.6Gd alloy leading to a rapid ultrafine grain microstructure over a strain range of $\varepsilon_{eq} = 0.6 - 5.7$ with a mean grain size of 0.7 μm and remaining stable at a strain range of $\varepsilon_{eq} = 5.7 - 287.5$.
- The restriction of DRX in the AZ31 alloy was explained by the presence of stable Al_8Mn_5 particles, solute drag and grain boundary strengthening.
- The evolution of microhardness in the AZ31 alloy showed a strain hardening without recovery, whereas the Mg-0.6Gd alloy displayed a strain hardening with recovery.
- The AZ31 alloy was characterized by the development of deviated B, C_1, and C_2 fibers. By contrast, the Mg-0.6Gd

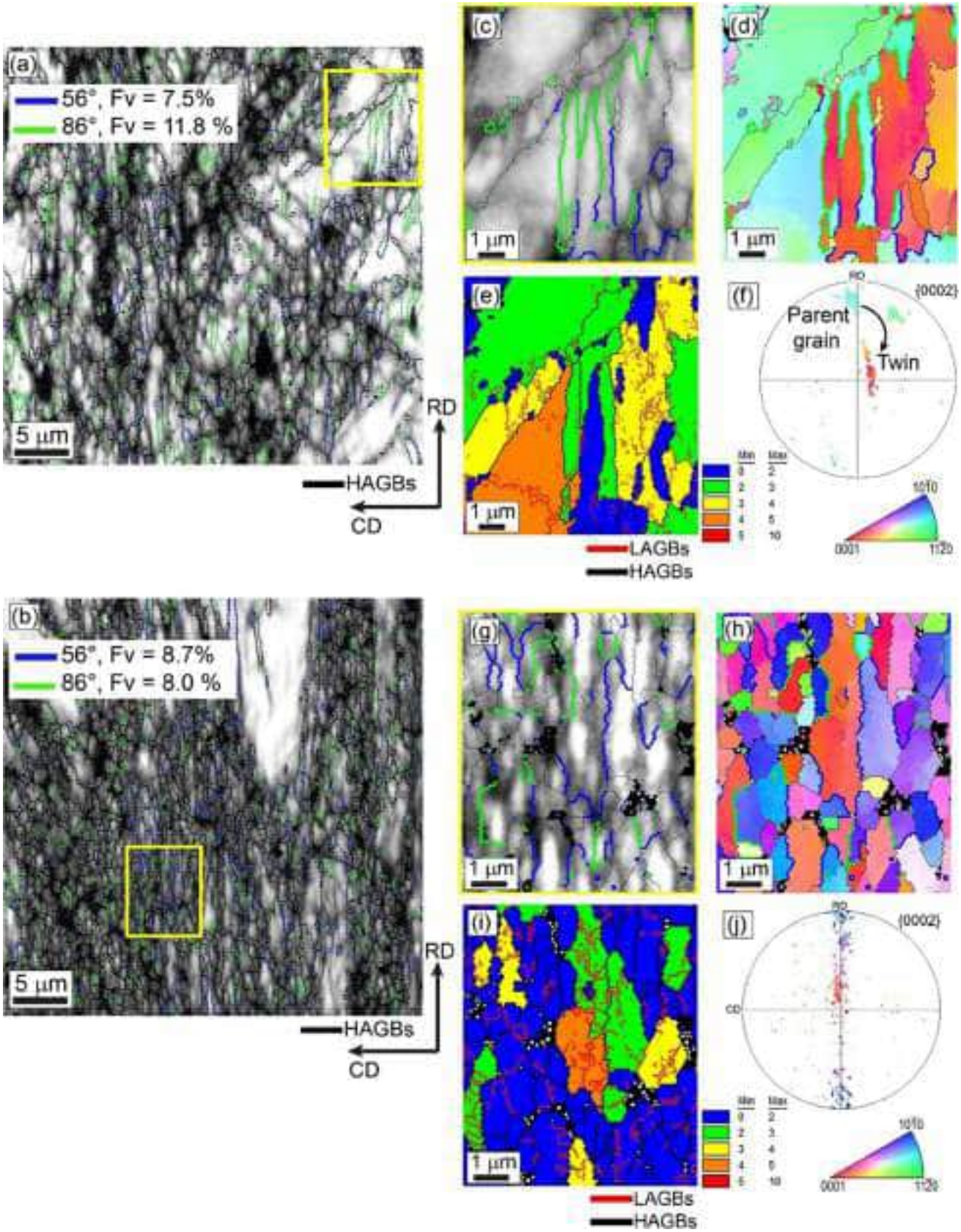

Fig. 9 (a, b) Image Quality (IQ) map highlighted by contraction twin (blue color) and extension twin (green color) in HPT-processed AZ31 and Mg-0.6Gd alloys at $\varepsilon_{eq} = 0.6$, respectively. (c, d, e, f) and (g, h, i, j) IQ, SD-IPF, GOS maps and {0002} corresponding pole figure of yellow box of HPT-processed AZ31 and Mg-0.6Gd samples, respectively (Color figure online)

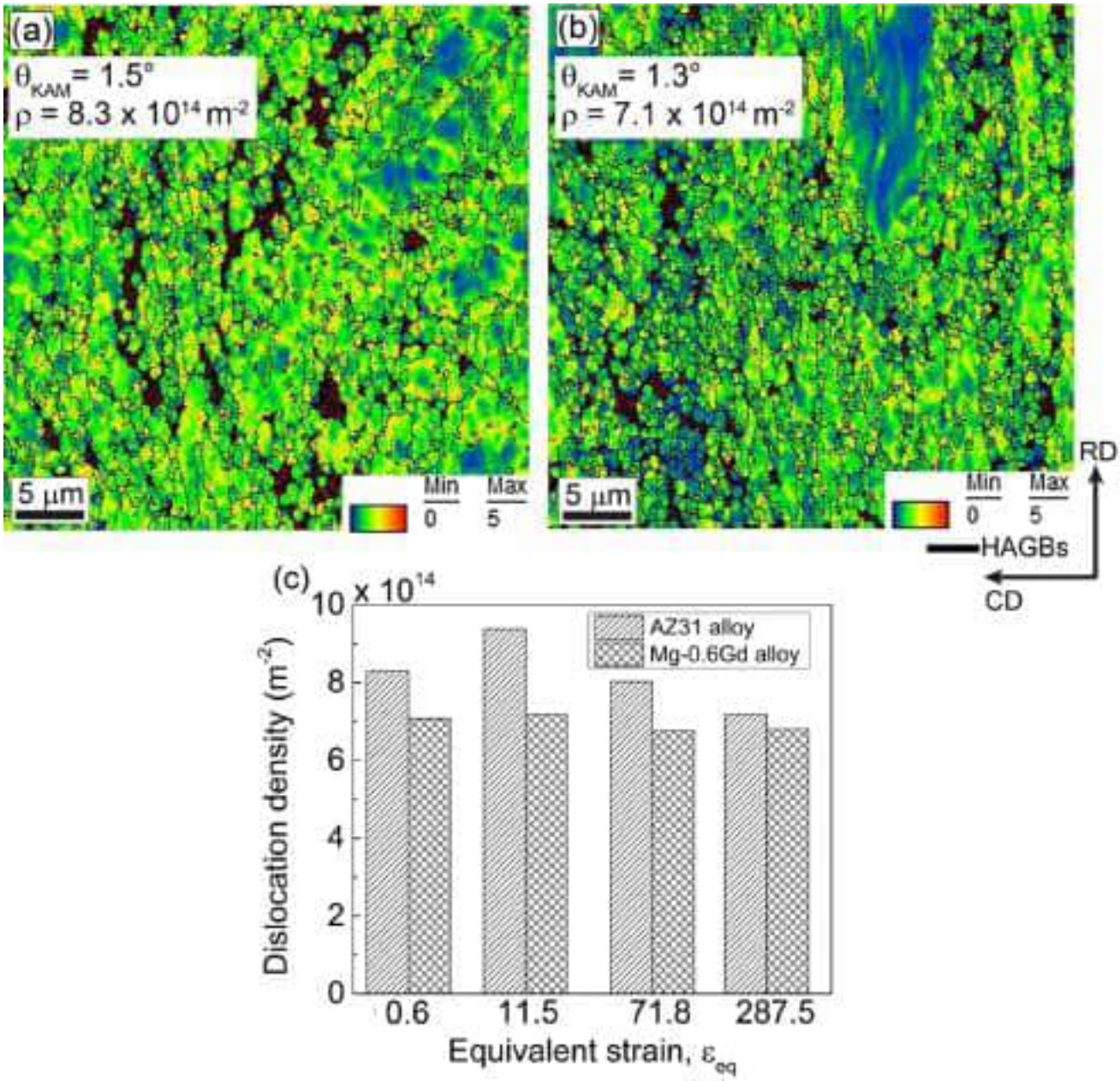

Fig. 10 KAM map of (a) AZ31, (b) Mg-0.6Gd alloys HPT processed at ε_{eq} = 0.6 and (c) evolution of dislocation density as a function of equivalent strain for both alloys

alloy exhibited a relatively stable B-fiber. The formation and disappearance of C_1 and C_2 fibers were due to the activation and evolution of mechanical twinning.

Acknowledgments

Dr-Ing. N. Hort and Dr. D. Letzig (MagIC, Germany) and Dr-Ing. Talal Al-Samman (RWTH-Aachen University, Germany) are gratefully acknowledged for providing the AZ31 and Mg-0.6Gd alloys, respectively. Two of the authors were supported by the European Research Council under Grant Agreement No. 267464-SPDMETALS (YH and TGL).

Data Availability

The raw/processed data required to reproduce these findings cannot be shared at this time as the data also forms part of an ongoing study.

References

1. R. Radha and D. Sreekanth, Insight of Magnesium Alloys and Composites for Orthopedic Implant Applications–A Review, *J. Magnes Alloys*, 2017, **5**(3), p 286–312
2. J. Song, J. She, D. Chen, and F. Pan, Latest Research Advances on Magnesium and Magnesium Alloys Worldwide, *J. Magnes. Alloys*, 2020, **8**(1), p 1–41

3. G. Wu, C. Wang, M. Sun, and W. Ding, Recent Developments and Applications on High-Performance Cast Magnesium Rare-Earth Alloys, *J. Magnes. Alloys*, 2021, **9**(1), p 1–20
4. M.P. Medeiros, D.R. Lopes, M. Kawasaki, T.G. Langdon, and R.B. Figueiredo, An Overview on the Effect of Severe Plastic Deformation on the Performance of Magnesium for Biomedical Applications, *Materials*, 2023, **16**, p 2401
5. M.H. Yoo, Slip, Twinning, and Fracture in Hexagonal Close-Packed Metals, *Metall. Trans. A*, 1981, **12**(3), p 409–418
6. G. Han, H.-K. Park, H.-K. Kim, and T.-S. Jun, Local and Global Deformation Behaviour in Rolled Pure Magnesium Sheets at Room Temperature under Different Strain Rates, *Mater. Sci. Eng. A*, 2019, **762**, p 138110
7. J. Wu, L. Jin, J. Dong, F. Wang, and S. Dong, The Texture and its Optimization in Magnesium Alloy, *J. Mater. Sci. Technol.*, 2020, **42**, p 175–189
8. R.E. Reed-Hill and W.D. Robertson, Deformation of Magnesium Single Crystals by Nonbasal Slip, *JOM*, 1957, **9**(4), p 496–502
9. Z. Wu, R. Ahmad, B. Yin, S. Sandlöbes, and W.A. Curtin, Mechanistic Origin and Prediction of Enhanced Ductility in Magnesium Alloys, *Science*, 2018, **359**(6374), p 447–452
10. A. Chapuis and J.H. Driver, Temperature Dependency of Slip and Twinning in Plane Strain Compressed Magnesium Single Crystals, *Acta Mater.*, 2011, **59**(5), p 1986–1994
11. J. Hirsch and T. Al-Samman, Superior Light Metals by Texture Engineering: Optimized Aluminum and Magnesium Alloys for Automotive Applications, *Acta Mater.*, 2013, **61**(3), p 818–843
12. J. Xie, J. Zhang, Z. You, S. Liu, K. Guan, R. Wu, J. Wang, and J. Feng, Towards Developing Mg Alloys with Simultaneously Improved Strength and Corrosion Resistance via RE Alloying, *J. Magnes. Alloys*, 2021, **9**(1), p 41–56
13. E.A. Ball and P.B. Prangnell, Tensile-compressive Yield Asymmetries in High Strength Wrought Magnesium Alloys, *Scr. Metall. Mater.*, 1994, **31**(2), p 111–116
14. K. Hantzsche, J. Bohlen, J. Wendt, K.U. Kainer, S.B. Yi, and D. Letzig, Effect of Rare Earth Additions on Microstructure and Texture Development of Magnesium Alloy Sheets, *Scripta Mater.*, 2010, **63**(7), p 725–730
15. T. Al-Samman and X. Li, Sheet Texture Modification in Magnesium-Based Alloys by Selective Rare Earth Alloying, *Mater. Sci. Eng. A*, 2011, **528**(10), p 3809–3822
16. A. Imandoust, C.D. Barrett, T. Al-Samman, K.A. Inal, and H. El Kadiri, A reviw on the effet of rar-earth elemnts on textre evoution during procesing of magnesiu alloy, *J. Mater. Sci.*, 2017, **52**(1), p 1–29
17. R.K. Sabat, A.P. Brahme, R.K. Mishra, K. Inal, and S. Suwas, Ductility Enhancement in Mg-0.2%Ce Alloys, *Acta Mater.*, 2018, **161**, p 246–257
18. M.R. Barnett, Influence of Deformation Conditions and Texture on the High Temperature Flow Stress of Magnesium AZ31, *J. Light. Met.*, 2001, **1**(3), p 167–177
19. T. Al-Samman and G. Gottstein, Dynamic Recrystallization during High Temperature Deformation of Magnesium, *Mater. Sci. Eng. A*, 2008, **490**(1), p 411–420
20. H. Azzeddine and D. Bradai, Texture and Microstructure of WE54 Alloy after Hot Rolling and Annealing, *Mater. Sci. Forum*, 2012, **702–703**, p 453–456
21. H. Azzeddine and D. Bradai, On the Texture and Grain Growth in Hot-Deformed and Annealed WE54 Alloy, *Int. J. Mater. Res.*, 2012, **103**(11), p 1351–1360
22. S.K. Mishra, S.M. Tiwari, J.T. Carter, and A. Tewari, Texture Evolution during Annealing of AZ31 Mg Alloy Rolled Sheet and its Effect on Ductility, *Mater. Sci. Eng. A*, 2014, **599**, p 1–8
23. D. Elfiad, Y.I. Bourezg, H. Azzeddine, and D. Bradai, Investigation of Texture, Microstructure, and Mechanical Properties of a Magnesium–Lanthanum Alloy After Thermo-Mechanical Processing, *Int. J. Mater. Res.*, 2016, **107**(4), p 315–323
24. F. Guerza-Soualah, H. Azzeddine, T. Baudin, A.-L. Helbert, F. Brisset, and D. Bradai, Microstructural and Textural Investigation of an Mg–Dy Alloy after Hot Plane Strain Compression, *J. Magnes. Alloys*, 2020, **8**(4), p 1198–1207
25. F. Guerza-Soualah, A. Hanna, H. Azzeddine, A.-L. Helbert, F. Brisset, T. Baudin, and D. Bradai, The Deformation and Recrystallization Behaviour of an Mg-Dy Alloy Processed by Plane Strain Compression, *Mater. Today Commun.*, 2020, **24**, p 101239
26. F.J. Humphreys and M. Hatherly, *Recrystallization and related annealing phenomena*, 2nd ed. Elsevier, Oxford, 2004
27. J. Zhao, Y. Deng, F. Xu, and J. Zhang, Effects of Initial Grain Size of Al-Zn-Mg-Cu Alloy on the Recrystallization Behavior and Recrystallization Mechanism in Isothermal Compression, *Metals*, 2019, **9**(2), p 110
28. X.Y. Yang, H. Miura, and T. Sakai, Initial Grain Size Effect of Dynamic Recrystallization of Magnesium Alloy AZ31, *Mater. Sci. Forum*, 2003, **426–432**, p 611–616
29. T. Sakai, A. Belyakov, R. Kaibyshev, H. Miura, and J.J. Jonas, Dynamic and Post-dynamic Recrystallization under Hot, Cold and Severe Plastic Deformation Conditions, *Prog. Mater. Sci.*, 2014, **60**, p 130–207
30. A.P. Zhilyaev and T.G. Langdon, Using High-pressure Torsion for Metal Processing: Fundamentals and Applications, *Prog. Mater. Sci.*, 2008, **53**(6), p 893–979
31. K. Edalati, A. Bachmaier, V.A. Beloshenko, Y. Beygelzimer, V.D. Blank, W.J. Botta, K. Bryła, J. Čížek, S. Divinski, N.A. Enikeev, Y. Estrin, G. Faraji, R.B. Figueiredo, M. Fuji, T. Furuta, T. Grosdidier, J. Gubicza, A. Hohenwarter, Z. Horita, J. Huot, Y. Ikoma, M. Janeček, M. Kawasaki, P. Král, S. Kuramoto, T.G. Langdon, D.R. Leiva, V.I. Levitas, A. Mazilkin, M. Mito, H. Miyamoto, T. Nishizaki, R. Pippan, V.V. Popov, E.N. Popova, G. Purcek, O. Renk, Á. Révész, X. Sauvage, V. Sklenicka, W. Skrotzki, B.B. Straumal, S. Suwas, L.S. Toth, N. Tsuji, R.Z. Valiev, G. Wilde, M.J. Zehetbauer, and X. Zhu, Nanomaterials by Severe Plastic Deformation: Review of Historical Developments and Recent Advances, *Mater. Res. Lett.*, 2022, **10**(4), p 163–256
32. Y. Huang, R.B. Figueiredo, T. Baudin, F. Brisset, and T.G. Langdon, Evolution of Strength and Homogeneity in a Magnesium AZ31 Alloy Processed by High-Pressure Torsion at Different Temperatures, *Adv. Eng. Mater.*, 2012, **14**(11), p 1018–1026
33. F. Meng, J.M. Rosalie, A. Singh, H. Somekawa, and K. Tsuchiya, Ultrafine Grain Formation in Mg–Zn Alloy by in situ Precipitation during High-Pressure Torsion, *Scripta Mater.*, 2014, **78–79**, p 57–60
34. K. Bryła, J. Morgiel, M. Faryna, K. Edalati, and Z. Horita, Effect of High-pressure Torsion on Grain Refinement, Strength Enhancement and Uniform Ductility of EZ Magnesium Alloy, *Mater. Lett.*, 2018, **212**, p 323–326
35. A. Hanna, H. Azzeddine, R. Lachhab, T. Baudin, A.-L. Helbert, F. Brisset, Y. Huang, D. Bradai, and T.G. Langdon, Evaluating the Textural and Mechanical Properties of an Mg-Dy alloy Processed by High-pressure Torsion, *J. Alloy. Compd.*, 2019, **778**, p 61–71
36. R.B. Figueiredo and T.G. Langdon, Using High-Pressure Torsion to Achieve Superplasticity in an AZ91 Magnesium Alloy, *Metals*, 2020, **10**(5), p 681
37. O. Ould Mohamed, H. Azzeddine, Y. Huang, T. Baudin, P. Bazarnik, F. Brisset, M. Kawasaki, and T.G. Langdon, Investigation of Microstructure and Texture Evolution in an AZ31/Mg–Gd Alloy Hybrid Metal Fabricated by High-Pressure Torsion, Advanced Engineering Materials n/a(n/a) (2023) 2201794
38. R.Z. Valiev, Y.V. Ivanisenko, E.F. Rauch, and B. Baudelet, Structure and Deformaton Behaviour of Armco Iron Subjected to Severe Plastic Deformation, *Acta Mater.*, 1996, **44**(12), p 4705–4712
39. K.D. Molodov, T. Al-Samman, and D.A. Molodov, Effect of Gadolinium on the Deformation and Recrystallization Behavior of Magnesium Crystals, *Acta Mater.*, 2022, **240**, p 118312
40. N. Stanford, M.D. Callaghan, and B. de Jong, The Effect of Rare Earth Elements on the Behaviour of Magnesium-based Alloys: Part 1—Hot Deformation Behaviour, *Mater. Sci. Eng. A*, 2013, **565**, p 459–468
41. N. Stanford, The Effect of Rare Earth Elements on the Behaviour of Magnesium-based Alloys: Part 2 – Recrystallisation and Texture Development, *Mater. Sci. Eng. A*, 2013, **565**, p 469–475
42. I. Basu and T. Al-Samman, Competitive Twinning Behavior in Magnesium and its Impact on Recrystallization and Texture Formation, *Mater. Sci. Eng. A*, 2017, **707**, p 232–244
43. J.-F. Deng, J. Tian, Y. Zhou, Y. Chang, W. Liang, and J. Ma, Plastic Deformation and Fracture Mechanisms of Rolled Mg-8Gd-4Y-Zn and AZ31 Magnesium Alloys, *Mater. Des.*, 2022, **223**, p 111179
44. C. He, J. Zhou, Y. Yang, B. Jiang, M. Yuan, Z. Dong, Y. Chai, W. He, G. Huang, D. Zhang, and F. Pan, In-situ Investigation on the Microstructure Evolution of Mg-2Gd Alloys during the V-bending Tests, *J. Mater. Sci. Technol.*, 2022, **131**, p 167–176

45. R.B. Figueiredo, P.R. Cetlin, and T.G. Langdon, Using Finite Element Modeling to Examine the Flow Processes in Quasi-constrained High-pressure Torsion, *Mater. Sci. Eng. A*, 2011, **528**(28), p 8198–8204
46. H. Azzeddine, D. Bradai, T. Baudin, and T.G. Langdon, Texture Evolution in High-pressure Torsion Processing, *Prog. Mater. Sci.*, 2022, **125**, p 100886
47. F. Wetscher, A. Vorhauer, R. Stock, and R. Pippan, Structural Refinement of Low Alloyed Steels During Severe Plastic Deformation, *Mater. Sci. Eng. A*, 2004, **387–389**, p 809–816
48. J.-H. Cho, A.D. Rollett, and K.H. Oh, Determination of a Mean Orientation in Electron Backscatter Diffraction Measurements, *Metall. Mater. Trans. A*, 2005, **36**(12), p 3427–3438
49. R. Hielscher and H. Schaeben, A Novel Pole Figure Inversion Method: Specification of the MTEX Algorithm, *J. Appl. Cryst.*, 2008, **41**(6), p 1024–1037
50. O. Sitdikov, R. Kaibyshev, and T. Sakai, Dynamic Recrystallization Based on Twinning in Coarse-Grained Mg, *Mater. Sci. Forum*, 2003, **419–422**, p 521–526
51. H.Z. Ye and X.Y. Liu, In situ Formation Behaviors of Al8Mn5 Particles in Mg–Al Alloys, *J. Alloy. Compd.*, 2006, **419**(1), p 54–60
52. J.F. Nie, K.S. Shin, and Z.R. Zeng, Microstructure, Deformation, and Property of Wrought Magnesium Alloys, *Metall. and Mater. Trans. A.*, 2020, **51**(12), p 6045–6109
53. M. Nienaber, G. Kurz, D. Letzig, K.U. Kainer, and J. Bohlen, Effect of Process Temperature on the Texture Evolution and Mechanical Properties of Rolled and Extruded AZ31 Flat Products, *Crystals*, 2022, **12**(9), p 1307
54. M. Kawasaki, Different Models of Hardness Evolution in Ultrafine-Grained Materials Processed by High-pressure Torsion, *J. Mater. Sci.*, 2014, **49**(1), p 18–34
55. M. Kawasaki, R.B. Figueiredo, Y. Huang, and T.G. Langdon, Interpretation of Hardness Evolution in Metals Processed by High-Pressure Torsion, *J. Mater. Sci.*, 2014, **49**(19), p 6586–6596
56. H.-J. Lee, S.K. Lee, K.H. Jung, G.A. Lee, B. Ahn, M. Kawasaki, and T.G. Langdon, Evolution in Hardness and Texture of a ZK60A Magnesium Alloy Processed by High-Pressure Torsion, *Mater. Sci. Eng. A*, 2015, **630**, p 90–98
57. B. Beausir, L.S. Tóth, and K.W. Neale, Ideal Orientations and Persistence Characteristics of Hexagonal Close Packed Crystals in Simple Shear, *Acta Mater.*, 2007, **55**(8), p 2695–2705
58. K.E. Prasad and K.T. Ramesh, In-situ Observations and Quantification of Twin Boundary Mobility in Polycrystalline Magnesium, *Mater. Sci. Eng. A*, 2014, **617**, p 121–126
59. Z.Y. Zhao, R.G. Guan, Y.F. Shen, and P.K. Bai, Grain Refinement Mechanism of Mg-3Sn-1Mn-1La Alloy during Accumulative Hot Rolling, *J. Mater. Sci. Technol.*, 2021, **91**, p 251–261
60. T. Al-Samman, K.D. Molodov, D.A. Molodov, G. Gottstein, and S. Suwas, Softening and Dynamic Recrystallization in Magnesium Single Crystals during c-axis Compression, *Acta Mater.*, 2012, **60**(2), p 537–545
61. K.D. Molodov, T. Al-Samman, D.A. Molodov, and G. Gottstein, Mechanisms of Exceptional Ductility of Magnesium Single Crystal during Deformation at Room Temperature: Multiple Twinning and Dynamic Recrystallization, *Acta Mater.*, 2014, **76**, p 314–330
62. D. Guan, W.M. Rainforth, L. Ma, B. Wynne, and J. Gao, Twin Recrystallization Mechanisms and Exceptional Contribution to Texture Evolution during Annealing in a Magnesium Alloy, *Acta Mater.*, 2017, **126**, p 132–144
63. H. Azzeddine, Y.I. Bourezg, A.Y. Khereddine, T. Baudin, A.-L. Helbert, F. Brisset, M. Kawasaki, D. Bradai, and T.G. Langdon, An Investigation of the Stored Energy and Thermal Stability in a Cu-Ni-Si Alloy Processed by High-Pressure Torsion, *Phil. Mag.*, 2020, **100**(6), p 688–712
64. J.D. Robson, D.T. Henry, and B. Davis, Particle Effects on Recrystallization in Magnesium–Manganese Alloys: Particle-Stimulated Nucleation, *Acta Mater.*, 2009, **57**(9), p 2739–2747
65. Y. Meng, J. Yu, K. Liu, H. Yu, F. Zhang, Y. Wu, Z. Zhang, N. Luo, and H. Wang, The Evolution of Long-period Stacking Ordered Phase and its Effect on Dynamic Recrystallization in Mg-Gd-Y-Zn-Zr Alloy Processed by Repetitive Upsetting-Extrusion, *J. Alloy. Compd.*, 2020, **828**, p 154454
66. Q. Wu, H. Yan, J. Chen, W. Xia, M. Song, and B. Su, The Interactions Between Dynamic Precipitates and Dynamic Recrystallization in Mg-5Zn-1Mn Alloys during Hot Compression, *Mater Charact*, 2020, **160**, p 110131
67. J. Kacher, B.P. Eftink, B. Cui, and I.M. Robertson, Dislocation Interactions with Grain Boundaries, *Curr. Opin. Solid State Mater. Sci.*, 2014, **18**(4), p 227–243

ADVANCED ENGINEERING MATERIALS
www.aem-journal.com

Investigation of Microstructure and Texture Evolution in an AZ31/Mg–Gd Alloy Hybrid Metal Fabricated by High-Pressure Torsion

Ouarda Ould Mohamed, Hiba Azzeddine, Yi Huang, Thierry Baudin, Piotr Bazarnik, François Brisset, Megumi Kawasaki, and Terence G. Langdon*

High-pressure torsion (HPT) processing is successfully applied to fabricate a novel hybrid material from separate discs of AZ31 (Mg–3Al–1Zn, wt%) and Mg–0.6Gd (wt%) alloys by straining through numbers of rotations, *N*, of 1/4, 1/2, 5, 10, and 20 turns at room temperature. The microstructure and texture are investigated near the bonding interface through the disc diameter using electron backscatter diffraction (EBSD), scanning electron microscopy (SEM), and transmission electron microscopy (TEM). The microstructure exhibits two grain refinement regimes with the first occurring during an equivalent strain range, ε_{eq}, of ≈0.3–72 and the second during ε_{eq} from ≈72 to 517. The general texture changes from B-fiber to Y-fiber and C_2-fiber through the HPT processing. The resultant microstructures and textures of this hybrid alloy are examined separately for the AZ31 and Mg-0.6Gd alloys and found controlled by the presence of twinning, slip systems, and second phases and the occurrence of different dynamic recrystallization mechanisms.

1. Introduction

It is now well recognized that high-pressure torsion (HPT) is one of the most efficient techniques of severe plastic deformation (SPD) that can produce materials with excellent grain refinement and outstanding mechanical properties at room temperature (RT).[1] Moreover, HPT processing allows materials having low crystal symmetry, such as magnesium-based alloys having hexagonal close-packed (HCP) structures, to be deformed at RT.[2–8] Significant grain refinement, to the range of ≈110–250 nm, was reported using HPT processing in several Mg-based alloys.[4,5,8–12]

The mechanism responsible for grain refinement in these Mg-based alloys is dynamic recrystallization (DRX) due to the lack of a sufficient number of active slip systems.[13] Specifically, it is a discontinuous DRX process in which an array of new fine grains form along the original grain boundaries in a necklace-like structure in the process known as a strain-induced boundary migration (SIBM) mechanism.[13,14] In this mechanism, the bulging of the grain boundaries is caused directly by the difference in the dislocation density on either side of the boundary. The misorientations between the bulges and the deformed grains then increase with increasing strain and this leads to the formation of sub-grain boundaries which ultimately transform to new fine grains having high-angle grain boundaries (HAGBs). These new grains gradually consume the deformed grains leading to an ultrafine-grained microstructure.[13,14] Consequently, the

O. Ould Mohamed, H. Azzeddine
Laboratory of Materials and Renewable Energy
Faculty of Sciences
Mohamed Boudiaf University
M'sila 28000, Algeria
E-mail: hiba.azzeddine@univ-msila.dz

Y. Huang, T. G. Langdon
Materials Research Group
Department of Mechanical Engineering
University of Southampton
Southampton SO17 1BJ, UK

Y. Huang
Department of Design and Engineering
Faculty of Science and Technology
Bournemouth University
Poole, Dorset BH12 5BB, UK

T. Baudin, F. Brisset
Université Paris-Saclay
CNRS
Institut de Chimie Moléculaire et des Matériaux d'Orsay
91405 Orsay, France

P. Bazarnik
Faculty of Materials Science and Engineering
Warsaw University of Technology
Woloska 141, 02-507 Poland, Poland

M. Kawasaki
School of Mechanical
Industrial and Manufacturing Engineering
Oregon State University
Corvallis, OR 97331, USA

The ORCID identification number(s) for the author(s) of this article can be found under https://doi.org/10.1002/adem.202201794.

DOI: 10.1002/adem.202201794

distribution of the misorientations in the grain boundaries is not altered through the deformation and grain refinement.[7,15] The majority of HCP materials processed by HPT develop a basal texture (B-fiber), where the basal {0002} planes of the lattices in the grains become parallel to the normal shear plane.[16] Nevertheless, the presence of alloying elements such as rare-earth (RE) elements in Mg-based alloys, and the distribution of second phases, cause deviations in the basal texture from its ideal position.[7,16,17]

Recent reports have demonstrated the feasibility of using HPT processing at RT to synthesize new hybrid alloys such as the Cu–Ni,[18] Ag–Cu,[19] Al–Cu,[20] Al–Mg,[21,22] Al–Ti,[23] V–Zr[24] and Zn–Mg[25] systems which are formed through solid-state reactions. An earlier report summarized the formation of unique alloy systems from separate bulk metals through the application of HPT[26] and it is evident that, well below the application of ultra-SPD,[27] a heterogeneous microstructure is formed with ultrafine multilayered structures in the central areas of HPT disc samples and with nano-layered intermetallic phases embedded within mixed zones near the edges of the sample.

The homogeneity developed in these hybrid systems is controlled by the HPT-processing conditions including the amount of the imposed strain, the processing temperature, and any post-deformation heat treatment.[18,23,24,28–30] To date, the scientific investigations have focused primarily on exploring the mechanical properties, as in tensile testing and the Vickers microhardness, together with the corrosion and tribological properties of the fabricated hybrid systems. The results confirm that HPT processing is a promising technique for bonding dissimilar materials at RT and for fabricating new materials for different structural applications.

Currently, most published data are based on characterizing the microstructures of the mixed layers and the formation of the intermetallic phases during HPT processing of dissimilar materials.[20,23–25,30–33]

Following a comprehensive examination of these earlier results, the present work was undertaken specifically to explore the potential for bonding two alloys having similar Mg matrices, namely AZ31 (Mg–3Al–1Zn, wt%) and Mg–0.6Gd (wt%) alloys, through the application of HPT processing.

Lightweight Mg–Al based alloys such as AZ31 alloy are very promising candidates to be used for weight reduction in transportations (aerospace and automotive) and the electronics industries and also as potential biodegradable implant materials in biomedical applications due to their low density, high specific strength, and biodegradability.[34–39] However, Mg–Al based alloys usually suffer from poor ductility and a rapid corrosion rate which significantly limits their industrial applications.[34,39,40] Mg alloyed with RE elements is now considered as an efficient route for improving the ductility of Mg-based alloys without compromising their strength.[41–43] Hence, the fabricates of a new generation of Mg hybrid materials with similar Mg matrices using HPT processing could be a new strategy to achieve the desired combinations of properties and enhance the lightweight characteristics to extend the use of Mg-based alloys in different structural applications. It is important to note that, to date, there are no similar investigations describing the joining of dissimilar Mg-based alloys using HPT processing. Accordingly, the present research was initiated to examine the microstructure and texture development near the bonding interface in AZ31 and Mg–0.6Gd alloys using electron backscatter diffraction (EBSD) and transmission electron microscopy (TEM). The results are discussed with reference to the initial conditions and the separate microstructural and textural changes produced in the AZ31 and Mg–0.6Gd alloys.

2. Experimental Section

Sheets of hot-rolled AZ31 and an as-cast Mg–0.6Gd alloy were supplied by the Magnesium Innovations Center (MagIC, Germany) and the Institute of Physical Metallurgy and Materials Physics (RWTH-Aachen University, Germany), respectively. The microstructure of the as-received alloys was revealed using optical microscopy after grinding with progressively finer SiC papers followed by electropolishing with 5:3-part ethanol and phosphoric acid for 30 min under a 3 V applied voltage and etching at RT in an acetic-nital solution (5% HNO_3, 15% acetic acid, 20% distilled water, and 60% ethanol) for 3 s.

Discs with diameters of 10 mm and thicknesses of 0.85 mm were machined and prepared from both alloys. The AZ31 disc was placed on the lower anvil in the HPT facility and then the Mg–0.6Gd disc was placed on top as illustrated in **Figure 1**a and the two disks were processed together by HPT at RT for numbers of HPT turns, N, of 1/4, 1/2, 5, 10, and 20 under quasi-constrained conditions.[44,45] The HPT discs were processed under a pressure of 6.0 GPa with a rotational speed of 1 rpm and care was taken to ensure there was no significant slippage during the HPT processing.[46] The equivalent strain, ε_{eq}, imposed during HPT was given by the relationship[47]

$$\varepsilon_{eq} = \frac{2\pi N r}{\sqrt{3}h} \tag{1}$$

where r is the radial distance from the center of the disc and h is the thickness of the disc.

All microstructural observations and texture and microhardness measurements were undertaken on the cross-sectional (shear direction compression direction [CD–SD]) planes of the HPT discs where the shear reference frame is defined as the shear direction (SD), rotational direction (RD), and compression direction (CD). Following the HPT processing, the discs were cut into two halves along their mid-plane.

The EBSD measurements were performed near the center ($r \approx 0.2$ mm), at the mid-radius position ($r \approx 2.5$ mm) and at the edge ($r \approx 4.5$ mm) of the mid-thickness plane of the HPT-processed discs as illustrated in Figure 1 using a TSL-EDAX-Hikari system mounted on a field-emission gun scanning electron microscope (FEG-SEM ZEISS Supra 55 VP) operating at 20 kV. Data collected from scanned areas of $40 \times 40\ \mu m^2$ with a 0.1 μm step size were managed by the Orientation Imaging Microscopy OIM™ software. Grain size data were obtained using a grain tolerance angle of 5° and a minimum grain size of 5 pixels. All datum points with a confidence index (CI) <0.05 were excluded from the quantitative analyses.[48] In addition, spurious boundaries with misorientation angles $\theta < 2°$ were excluded from the EBSD maps to avoid any orientation noise. The mean grain size was measured using the equivalent diameter approach.

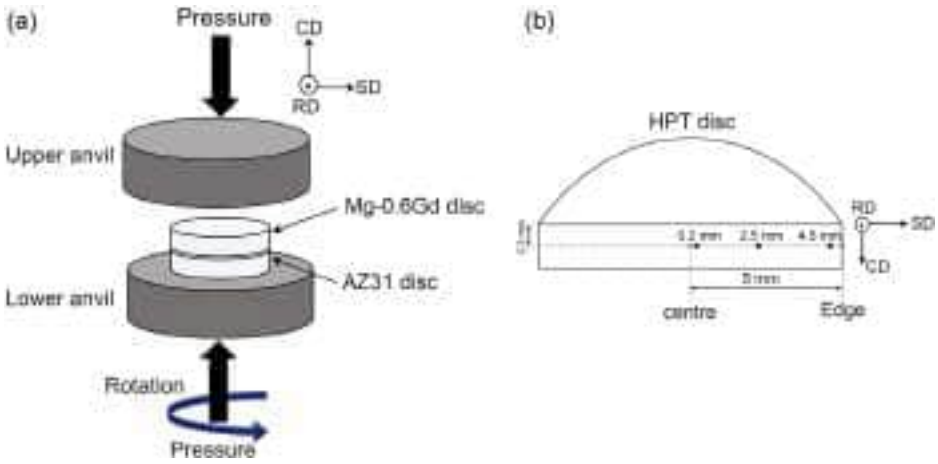

Figure 1. An illustration showing the following: a) high-pressure torsion (HPT) processing and b) the position for the electron backscatter diffraction (EBSD) on the vertical cross section of the HPT disc. Shear direction (SD), compression direction (CD), and rotational direction (RD) are the coordinate systems.

The grain orientation spread (GOS) approach in the OIM software was used for the identification of dynamic recrystallized grains. The GOS is defined as the average deviation between the orientation of each point in the grain and the average orientation of the grain, where grains with GOS $< 1°$ are considered as fully recrystallized.[49]

MTEX software was used to analyze the evolution of texture by calculating the orientation distribution function (ODF) using the harmonic method ($L = 22$) and a Gaussian function with a half-width of 5° to model each orientation.[50]

A FEG–SEM, Zeiss Gemini equipped with an energy-dispersive spectrometry (EDS) system in backscattering electrons (BSE) mode operating at 15 kV was used for the microstructural investigation and to obtain the chemical element mapping of samples processed for $N = 1/4$ turn. Another SEM (Hitachi SU8000) was used to analyze the microstructures at the bonding interfaces between the AZ31 and Mg–0.6Gd regions near the edges ($r \approx 4$ mm) of the HPT-processed discs for $N = 1/2$, 10, and 20 turns in the two modes of secondary electron (SE) mode and BSE. Samples for SEM analysis were prepared using an Hitachi IM4000 ion milling system to eliminate all deformation, stresses, and oxide layers.

A detailed microstructural analysis for the sample processed to $N = 20$ turns was carried out using a TEM (TEM-JEOL JEM 1200) operating at an accelerating voltage of 120 kV and a spherical aberration (Cs)-corrected dedicated scanning transmission electron microscope (STEM-Hitachi HD2700) operating at 200 kV. The TEM/STEM observations were prepared using a focused-ion beam (FIB) Hitachi NB-5000 microscope. Lamellas were cut from the cross sections of samples in the direction parallel to RD and the STEM observations were carried out in bright-field (BF) and high-angle annular dark field (HAADF) modes. For some samples, selected area electron diffraction (SAED) patterns were also obtained.

Vickers microhardness measurements were taken using a Mitutoyo HM-200 with a load of 50 gf and a dwell time of 10 s. The disc samples were cut vertically across the disk diameters and the cross sections were polished to mirror-like surfaces. A series of hardness values were recorded on these vertical cross sections, measuring $8000 \times 450\ \mu m^2$, where a rectilinear grid pattern, having 150 μm separation between adjacent points, was applied for the automated measurement procedure. The recorded hardness values gave a total of 248 points and these points were used for construction of color-coded contour maps.

3. Experimental Results

3.1. Initial Microstructures before HPT Processing

Figure 2 shows the initial microstructures of a,c) AZ31 and b,d) the Mg–0.6Gd alloys taken by optical microscopy (upper row) and SEM in BSE mode (lower row).

In the initial state, the AZ31 alloy exhibited a typical deformation microstructure having a mixture of elongated deformed grains and small recrystallized grains (Figure 2a) with a mean grain size of $\approx 16 \pm 2.5$ μm and the presence of a high fraction of twins. Figure 2c shows that the AZ31 alloy contained massive nano-sized particles that were homogenously distributed within the microstructure. By contrast, the Mg–0.6Gd alloy exhibited a typical as-cast microstructure with coarse grains (Figure 2b) and with the presence of metastable large particles that were distributed reasonably homogenously (Figure 2d).

3.2. Microstructure Characterization Using SEM and TEM after HPT Processing

Figure 3 shows SEM images (upper row) of the AZ31/Mg–0.6Gd hybrid material after HPT processing for $N = 1/4$ turn near the center, mid-radius, and edge of the disc, where the estimated equivalent strains by Equation (1) are ≈0.3, ≈3.6, and ≈6.5, respectively. The elemental compositions of the magnified zone from the mid-radius area (red frame) are determined through Mg, Al, Zn, and Gd EDS elemental mapping (lower row). In addition, the chemical compositions of points marked 1–3 in this mid-radius area are given in **Table 1**. The total initial disc height of 1.7 mm decreased to ≈0.63 mm after HPT processing and the

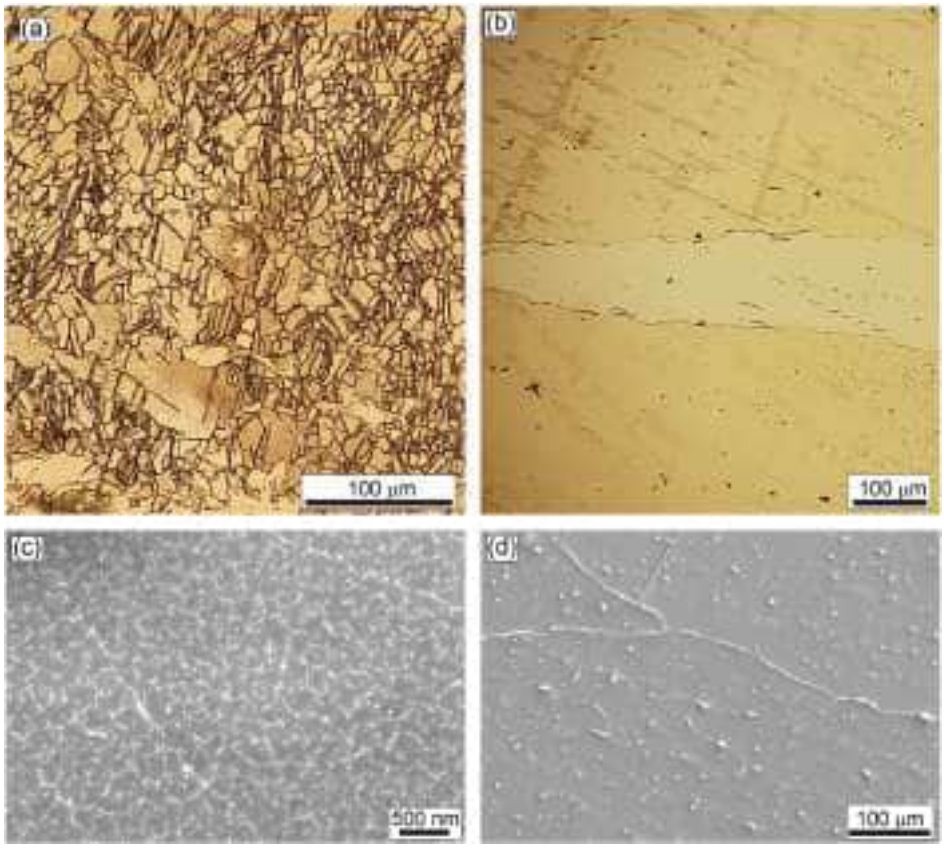

Figure 2. Initial microstructures of AZ31 on left and the Mg-0.6Gd alloy on right: a,b) by optical microscopy and c,d) by scanning electron microscope (SEM) in backscattering (BSE) mode.

AZ31 and Mg–0.6Gd alloys bonded successfully as shown in the center of the disc.

A fragmentation of the AZ31 alloy into layers occurred in the mid-radius area and the numbers of AZ31 layers increased near the edge of the sample. Such variations in morphology of the AZ31 layers are caused by the different strains introduced across the disc by the HPT processing since, as shown in Equation (1), the imposed strain varies from zero at the disc center to a maximum at the edge. Table 1 indicates that the atomic percentage of Mg (89.5%) and Gd (10.5%) at point 3 suggests that this particle should be Mg_5Gd (83% of Mg and 17% of Gd, in at%) second phase which is in good agreement with the binary Mg–Gd phase diagram[42] and reports in the literature.[51–53]

Figure 4 presents SEM micrographs with different magnifications near the center of the sample processed for $N = 1/4$ turn and at the edges for the samples processed for $N = 1/2$ and 10 turns where the equivalent strains for these three conditions are ≈0.3, ≈11.5, and ≈230, respectively. The disc processed for $N = 1/4$ turn reveals an interesting microstructural evolution of the Mg–0.6Gd alloy. Thus, the microstructure is heterogenous through the thickness but near the interface, at about 26 μm of thickness, the microstructure is very refined. Far from the interface there are elongated large grains containing twins that are marked by arrows in the magnification of the red frame area. Shear bands are also present in this zone as indicated by the dashed white lines. Although the microstructure of the AZ31 region appears homogenous through the thickness, the magnification within the yellow frame in AZ31 shows that the microstructure is formed principally of a mixture of refined grains and deformed grains containing twins.

The microstructure of the Mg–0.6Gd alloy is homogenous through the thickness with increasing numbers of HPT turns as demonstrated at the edge of the disc processed for $N = 1/2$ turn. An EDS analysis was performed for this sample at four different positions labeled 1–4 and the recorded elemental compositions are listed in **Table 2**.

In addition to the presence of Mg_5Gd second phase particles at point 3 in the Mg–0.6Gd region, new particles were detected at point 4 containing an exceptionally high fraction of Gd (93.1%, wt%) and these are probably associated with fragmentation of the initial Mg_5Gd second phase particles. The presence of Si element in point 3 is probably due to grinding with SiC papers during the sample preparation. A bending of the interfaces and the formation of multilayers is visible in the sample after 10 turns as indicated by the yellow arrows and the magnified region in the blue frame. Nevertheless, there was no evidence for any delamination between the layers and the two alloys bonded perfectly as shown by the magnified region in the blue frame.

A series of observations by TEM in BF and STEM in BF and HAADF modes are shown in **Figures 5** and **6** with different

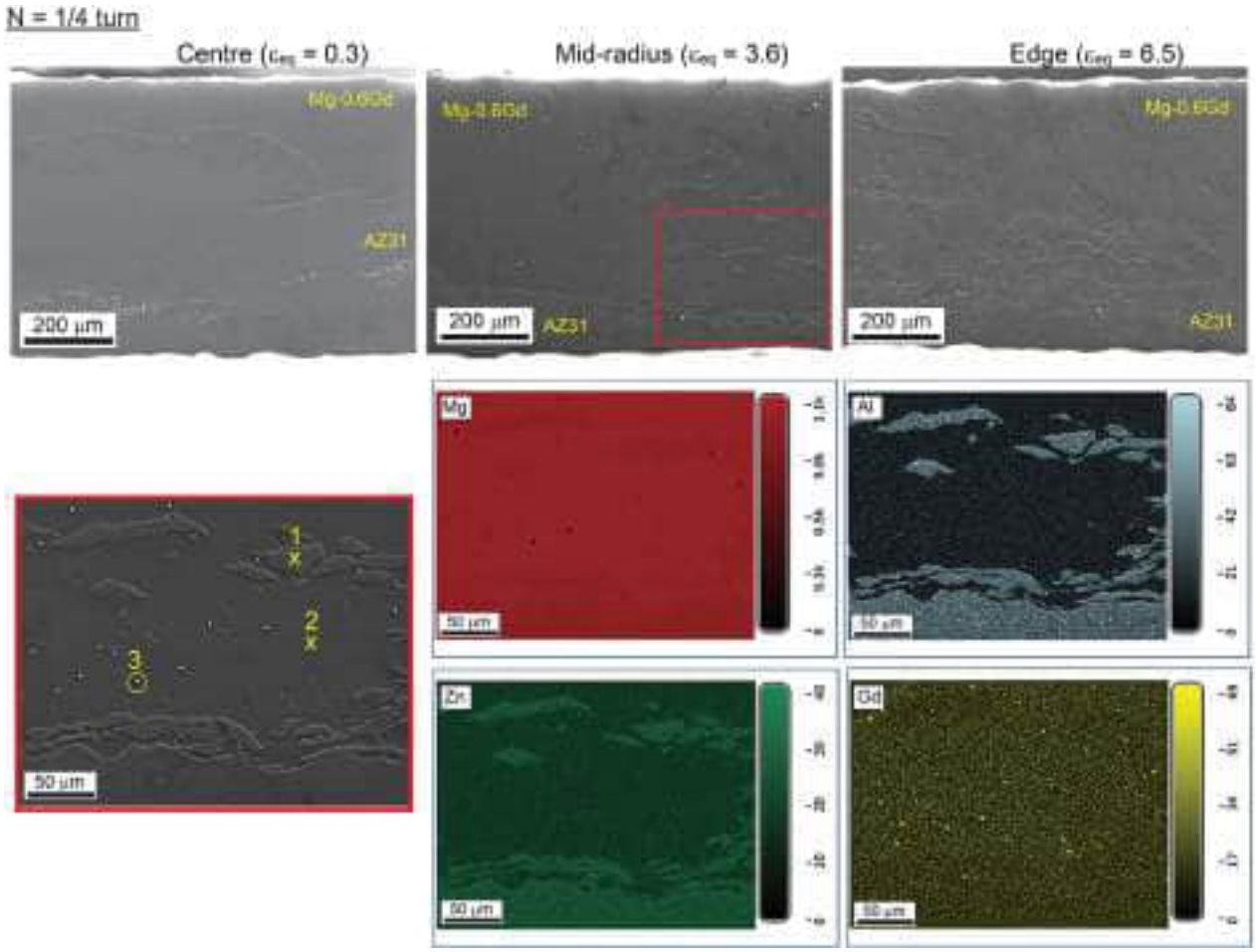

Figure 3. SEM images (upper row) of the AZ31/Mg-0.6Gd hybrid material after HPT processing for $N = 1/4$ turn near the center, mid-radius, and edge of the disk. Energy-dispersive spectrometry (EDS) maps (lower rows) for the Mg, Al, Zn, and Gd elements in the selected zone from the mid-radius region denoted by the red frame.

Table 1. Chemical composition at different locations on the sample processed for $N = 1/4$ turn as shown in Figure 3.

	Point 1		Point 2		Point 3	
	wt%	at%	wt%	at%	wt%	at%
Mg	96.2	97.1	99.1	99.9	56.9	89.5
Gd	–	–	0.9	0.1	43.1	10.5
Al	2.7	2.5	–	–	–	–
Zn	0.6	0.2	–	–	–	–
Mn	0.5	0.2	–	–	–	–

magnifications for the AZ31/Mg–0.6Gd interface near the edge of the disc processed for $N = 20$ turns where the equivalent strain is ≈460.

The microstructure shown in the low-magnification TEM image and the continuous rings in the SAED pattern provide clear evidence for grain refinement with the development of HAGBs in the hybrid AZ31/Mg–0.6Gd system. A region near the formed interface between the AZ31 and Mg–0.6Gd alloy is shown in Figure 5b representing an enlargement of the area within the yellow frame in Figure 5a.

Figure 6a,b shows another interface region in STEM–BF and HAADF modes, respectively, and the AZ31 regions at high magnification are shown in Figure 6c,d, respectively. These images demonstrate that the AZ31 alloy underwent greater grain refinement than the Mg–0.6Gd alloy. Thus, the AZ31 region shows reasonably equiaxed grains with a small average size of $\approx 0.11 \pm 0.06$ µm whereas the Mg–0.6Gd region exhibits an equiaxed microstructure with a larger average grain size of $\approx 0.40 \pm 0.03$ µm. The STEM–HAADF image shown in Figure 6b reveals a weak fraction of an Mg_5Gd phase marked by an arrow in the Mg–0.6Gd region and this contrasts with the presence of spherical particles with diameters in the range of ≈10–24 nm homogenously distributed in the AZ31 region as can be seen in the STEM–HAADF image shown in Figure 6d. A table of EDS results included in Figure 6e identifies these particles as the $Mg_{17}Al_{12}$ phase and some of these particles also contain Zn. There is no evidence for the formation of any

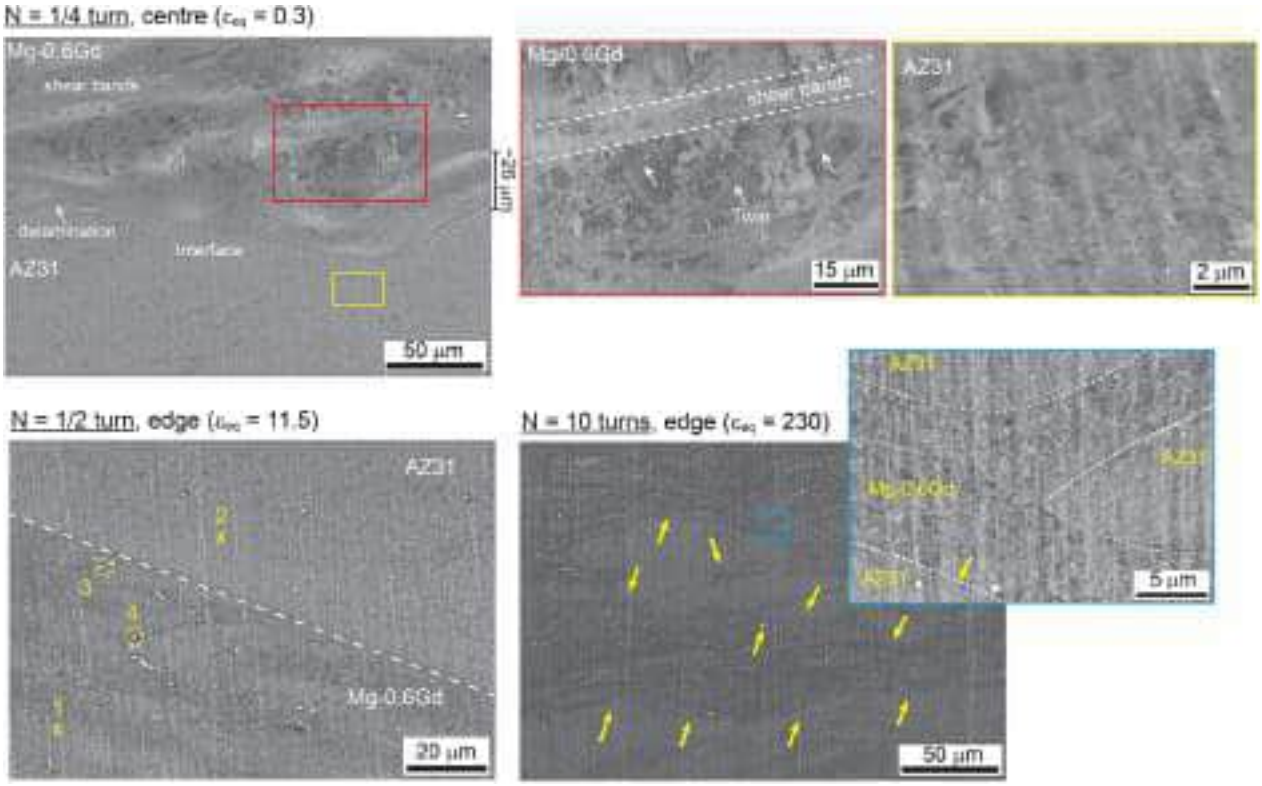

Figure 4. SEM micrographs with different magnifications near the center of a sample processed for $N = 1/4$ turn and at the edge of samples processed for $N = 1/2$ and 10 turns, respectively. Red and yellow frames show magnifications of Mg-0.6Gd and AZ31 regions of sample processed for $N = 1/4$ turn, respectively. White arrows show the presence of a twin in Mg-0.6Gd region of sample processed for $N = 1/4$ turn. The dashed line shown in the sample processed for $N = 1/2$ turn presents the interface between the AZ31 and Mg-0.6Gd regions. Yellow arrows and the blue frame indicate the bending of the interfaces and the formation of multilayers in the sample processed for $N = 10$ turns.

Table 2. Chemical compositions at different locations on the sample processed to $N = 1/2$ turn as shown in Figure 4.

	Point 1		Point 2		Point 3		Point 4	
	wt%	at%	wt%	at%	wt%	at%	wt%	at%
Mg	100	100	95.2	96.1	54.5	85.2	6.9	32.5
Al	–	–	4.0	3.6	–	–	–	–
Zn	–	–	0.8	0.3	–	–	–	–
Gd	–	–	–	–	42.1	10.2	93.1	67.5
Si	–	–	–	–	3.4	4.6	–	–

new intermetallic phases within the examined regions of this hybrid AZ31–Mg–0.6Gd system.

3.3. Microstructure and Texture Evolution from EBSD

3.3.1. Microstructure Evolution near the Interfaces after HPT Processing

Figures 7 and **8** show the orientation imaging micrographs (OIM) in RD inverse pole figure (RD–IPF) maps and grain size distributions, respectively, at the AZ31/Mg–0.6Gd interfaces near the centers, mid-radii, and edges of samples processed for a) 1/4, b) 1/2, c) 5, d) 10, and e) 20 turns.

The AZ31 and Mg–0.6Gd regions are indicated in the RD–IPF maps and the interface in each area is marked by a dashed black line in Figure 7 where RD is perpendicular in each OIM. The mean grain sizes at the interfaces in each measurement are depicted in the grain size distribution plots in Figure 8.

The RD–IPF maps in Figure 7 show the presence of black zones especially in the AZ31 region where these are due to the high amounts of deformation in the sample. The grain size distributions appear bimodal at the lower numbers of HPT rotations in the range of ≈1/4–5 turns where a group of grains of <1 μm is present with another group of grains having an average size of ≈3 μm or larger. With further HPT processing, the distribution of grain sizes becomes more uniform with an average value of less than 1 μm throughout the disc diameter.

These quantitative measurements show there is excellent grain refinement to an average of $\approx 0.80 \pm 0.05$ μm near the center of the sample after 1/4 turn and thereafter the mean grain size appears to saturate at $\approx 0.67 \pm 0.02$ μm after 10 turns. There is a net decrease to about $\approx 0.36 \pm 0.02$ μm at the edge of the sample after 10 turns and a similar grain size is evident at the mid-radius position after 20 turns.

The evolution of the mean grain size corresponding to the AZ31 and Mg–0.6Gd regions is shown in Figure 8f as a function

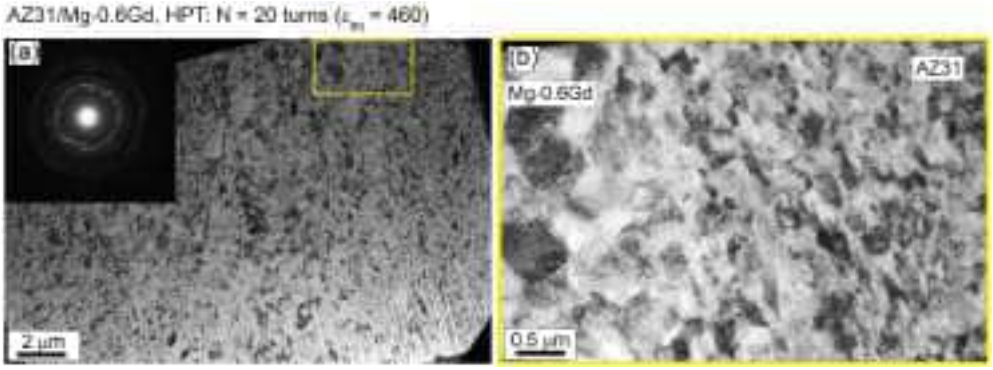

Figure 5. Transmission electron microscope with bright-field (TEM-BF) image near the edge of the disc processed for $N = 20$ turns at a) low magnification with the corresponding selected area electron diffraction (SAED) pattern and b) in an enlargement of the area within the yellow frame shown in 5a.

of the numbers of HPT turns. These curves indicate that the average grain sizes of both alloys decrease slowly near the centers of the discs and more rapidly near the mid-radius and edge positions due to the larger imposed strains. At higher numbers of HPT turns, the average grain size in the AZ31 region is slightly lower than in the Mg–0.6Gd region and the final values after 20 turns at the edges of the discs are $\approx 0.30 \pm 0.02$ and $\approx 0.34 \pm 0.02$ μm, respectively.

Figure 9 shows the fractions of separate grain boundary types for very low-angle grain boundaries (VLAGBs) with misorientations of $2° < \theta < 5°$, low-angle grain boundaries (LAGBs) with $5° < \theta < 15°$, and HAGBs with misorientations $\theta > 15°$ at the interfaces near the center, mid-radius, and edge of samples processed for a) 1/4, b) 1/2, c) 5, d) 10, and e) 20 turns. In addition, the evolution of the HAGBs fraction of the AZ31 and Mg–0.6Gd regions is shown in Figure 9f as a function of the numbers of HPT turns. In general, the fractions of VLAGBs, LAGBs, and HAGBs are similar through the distance from the center of each disc. It is apparent that the fraction of VLAGBs decreases with increasing numbers of HPT turns up to 5 turns and then saturates at ≈18% whereas the fraction of HAGBs increases due to the occurrence of DRX and reaches a value of ≈75% after 20 turns. There are low fractions of LAGBs of the order of ≈10% after any number of HPT turns.

Figure 9f shows that the fraction of HAGBs increases with increasing numbers of HPT turns up to 5 turns for both alloys and then saturates at each position. In addition, the HAGBs fraction for the Mg–0.6Gd region is higher at ≈80% than for the AZ31 region at ≈65% and this confirms the occurrence of a higher fraction of DRX in the Mg–0.6Gd alloy.

Noticeable microstructural features were extracted from the RD–IPF maps near the centers of the discs after a) 1/2 turn and b) 5 turns in **Figure 10**. In practice, the AZ31 and Mg–0.6Gd alloys exhibit different deformation features and mechanisms. As observed in Figure 10a, the GOS map shows that 28% of the Mg–0.6Gd grains are dynamically recrystallized and ultrafine equiaxed grains are formed at the interface after $\varepsilon_{eq} = 0.6$ where this microstructural feature is readily visible within the marked oval in the RD–IPF map. Typical elongated deformed grains develop in the AZ31 region and the DRX is limited to only ≈10% by comparison with the Mg–0.6Gd region. A magnification of the area within the red frame in the AZ31 region after 1/2 turn shows that these grains host different twin types.

The misorientation profiles at the distances of AB, CD, and EF gives evidence for the presence of double twins 22°<11–20>, extension twins 86°<11–20>, and contraction twins 56°<11–20>, respectively. These twins contain LAGBs which suggest the possibility of the formation of new finer grains with further deformation. This mechanism corresponds to the traditional twin-induced dynamic recrystallization (TDRX).[54]

There is also another DRX mechanism within the AZ31 grains in the same magnified RD–IPF map where fine grains are formed within the deformed grain, as marked by black arrows, by the sub-grain development (SGD) mechanism.[55] In this mechanism, high densities of dislocations within the deformed grains lead to the development of sub-grains boundaries which transform to LAGBs and ultimately to new refined grains with HAGBs. In addition, the RD–IPF and GOS maps of the AZ31 region in the center of the disc processed for 5 turns, as shown in Figure 10b, reveal the formation of dynamically recrystallized grains marked with blue arrows along the grain boundaries and this indicates the occurrence of the SIBM mechanism.[14]

3.3.2. Texture Evolution at the Interfaces

The texture evolution at the interface near the center, mid-radius, and edge of the samples processed for 1/4, 1/2, 5, 10, and 20 turns is given in **Figure 11** using recalculated {0002} pole figures. The positions of the ideal shear texture components in the {0002} pole figures projected in the SD–RD plane for materials with an HCP structure are shown for comparison in Figure 11 and their description in the form of the Euler angles (φ_1, Φ, φ_2) is given in **Table 3**.

It is apparent that the texture is heterogeneously distributed through the diameters of all of the examined discs. At the centers of the discs, a typical basal texture (B-fiber) is developed through 10 turns and then Y-fibers with B-fibers are formed in the centers of samples processed for 20 turns. At the mid-radius of the discs, the B-fiber rapidly transforms to B with Y-fibers after processing for 1/2 turn and then changes to a new fiber where the B-fiber deviates by about 20° toward RD after 10 turns. Thereafter, it

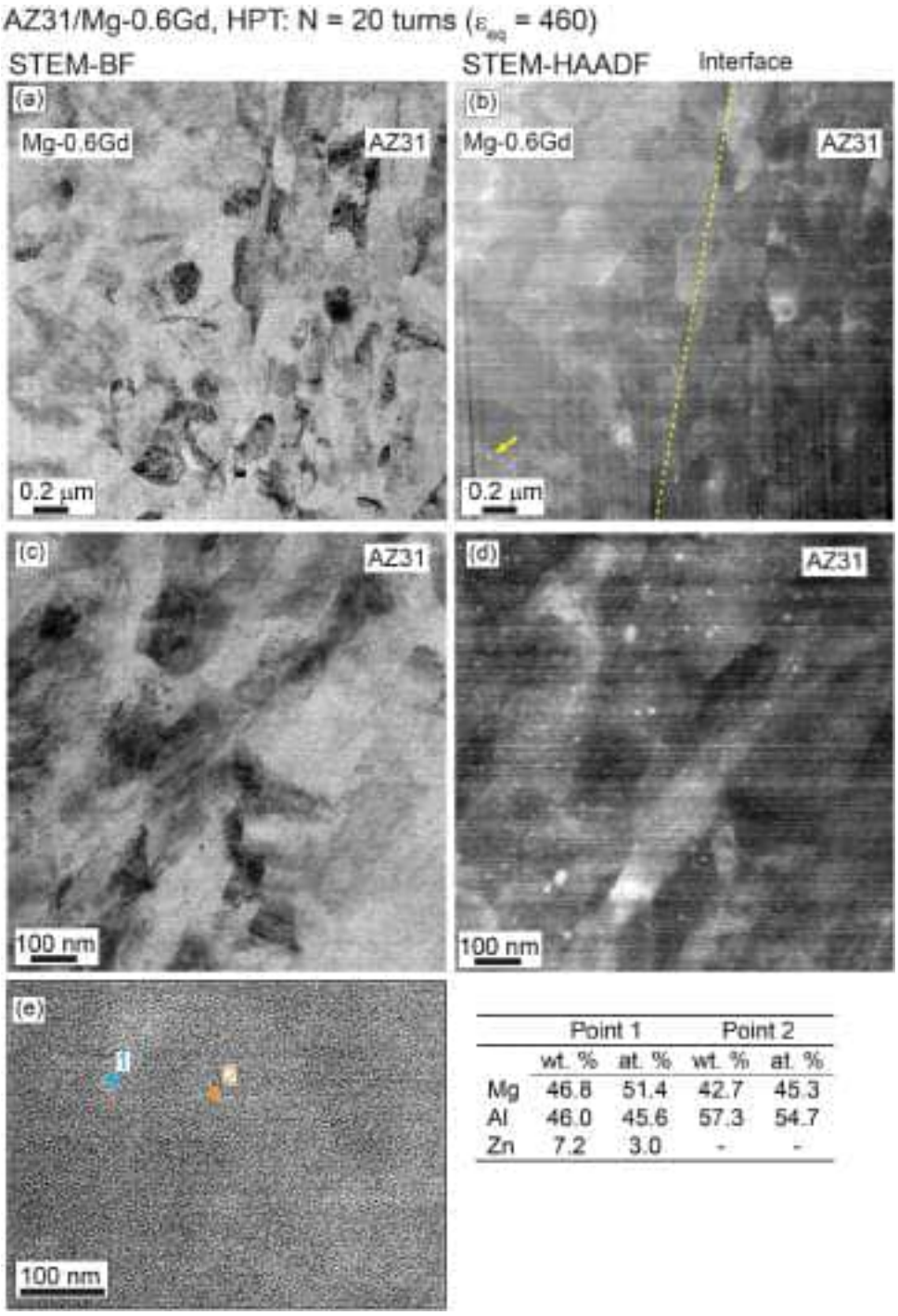

	Point 1		Point 2	
	wt. %	at. %	wt. %	at. %
Mg	46.8	51.4	42.7	45.3
Al	46.0	45.6	57.3	54.7
Zn	7.2	3.0	-	-

Figure 6. Scanning transmission electron microscope (STEM) images in a) BF and b) high-angle annular dark field (HAADF) at low magnification near the edge of the disc processed for $N = 20$ turns, high-magnification STEM images in c) BF and d) HAADF showing AZ31 regions and e) EDS analysis of particles present at points 1 and 2 in the AZ31 region. Yellow dashed line in 6b shows the interface between the AZ31 and Mg-0.6Gd regions.

changes again to a C_2-fiber through 20 turns. At the edges of the discs, the B and Y fibers are formed rapidly after processing for 1/4 turn and this changes to a deviated B-fiber after processing through 5 turns and thereafter gradually changes to a C_2-fiber through 20 turns. Consequently, the texture formation evolves through 4 stages as a function of the equivalent strain. These stages may be designated as stage 1 ($0.3 < \varepsilon_{eq} < 6.5$) with the presence of a basal texture; stage 2 ($6.5 < \varepsilon_{eq} < 72$) where a Y-fiber is formed with a B-fiber; stage 3 ($129 < \varepsilon_{eq} < 259$) where the Y-fiber disappears and the B-fiber deviates by about 20° toward RD; and stage 4 ($259 < \varepsilon_{eq} < 517$) where the C_2-fiber develops.

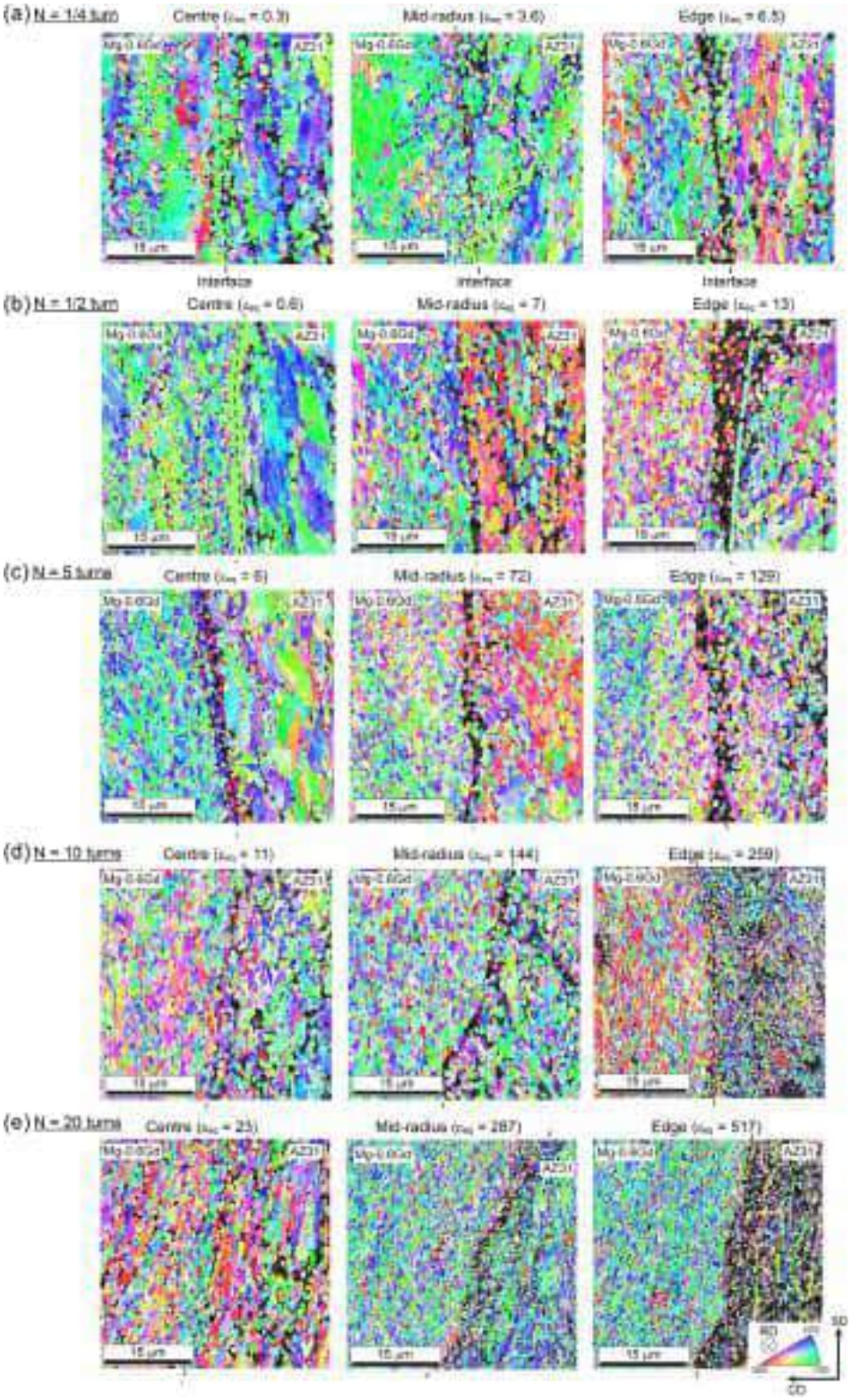

Figure 7. RD inverse pole figure (RD–IPF) maps at the interface near the center, mid-radius, and edge of samples processed for a) 1/4, b) 1/2, c) 5, d) 10, and e) 20 turns. The interface between the AZ31 ang Mg-0.6Gd regions is marked by a dashed black line in each RD–IPF map.

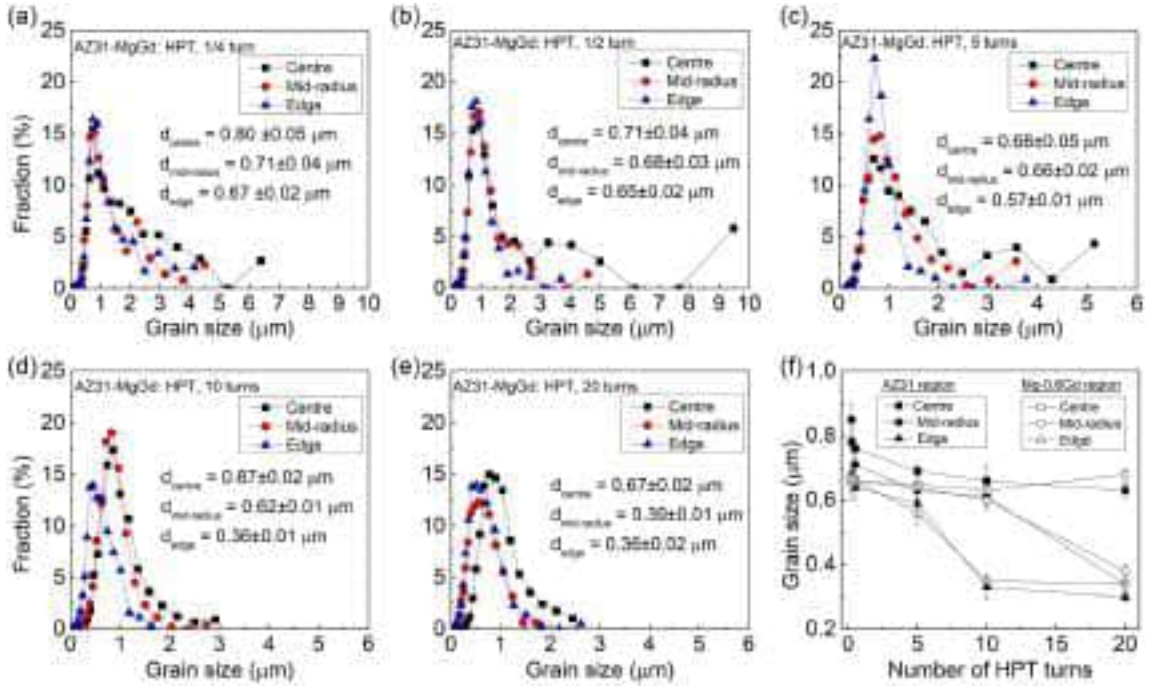

Figure 8. Grain size distributions at the interface near the center, mid-radius, and edge of samples processed for a) 1/4, b) 1/2, c) 5, d) 10, and e) 20 turns, and f) evolution of the mean grain size in the AZ31 and Mg-0.6Gd regions as a function of numbers of HPT turns.

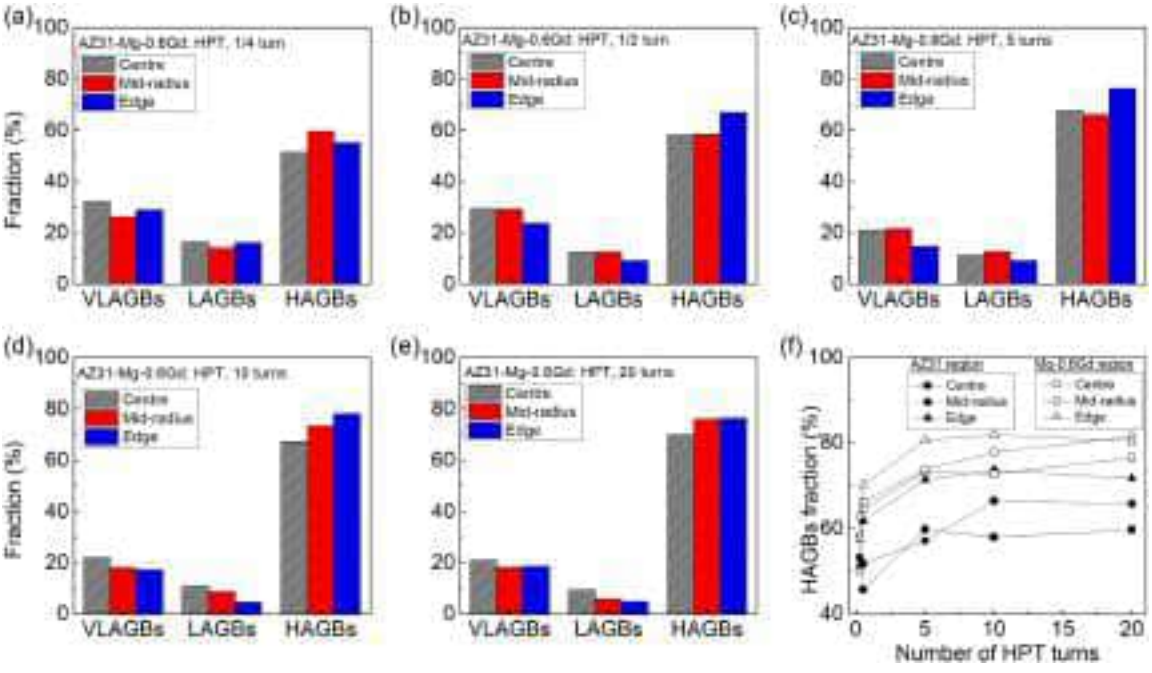

Figure 9. Fraction of very low-angle grain boundaries (VLAGBs), low-angle grain boundaries (LAGBs), and high-angle grain boundaries (HAGBs) at the interface near the center, mid-radius, and edge of samples processed for a) 1/4, b) 1/2, c) 5, d) 10, and e) 20 turns, and f) evolution of the HAGB fraction of the AZ31 and Mg-0.6Gd regions as a function of numbers of HPT turns.

Figure 12 presents the separate texture evolution in the AZ31 and Mg–0.6Gd regions in terms of the recalculated {0002} pole figures through the 4 stages of texture evolution. It is important to note that the as-received AZ31 alloy exhibited a typical basal texture (B-fiber) as described in an earlier report[56] while the initial texture of the as-cast Mg–0.6Gd alloy was not measured since the alloy contained limited grain numbers and multiple coarse grains as shown in Figure 2. The texture of the AZ31 alloy

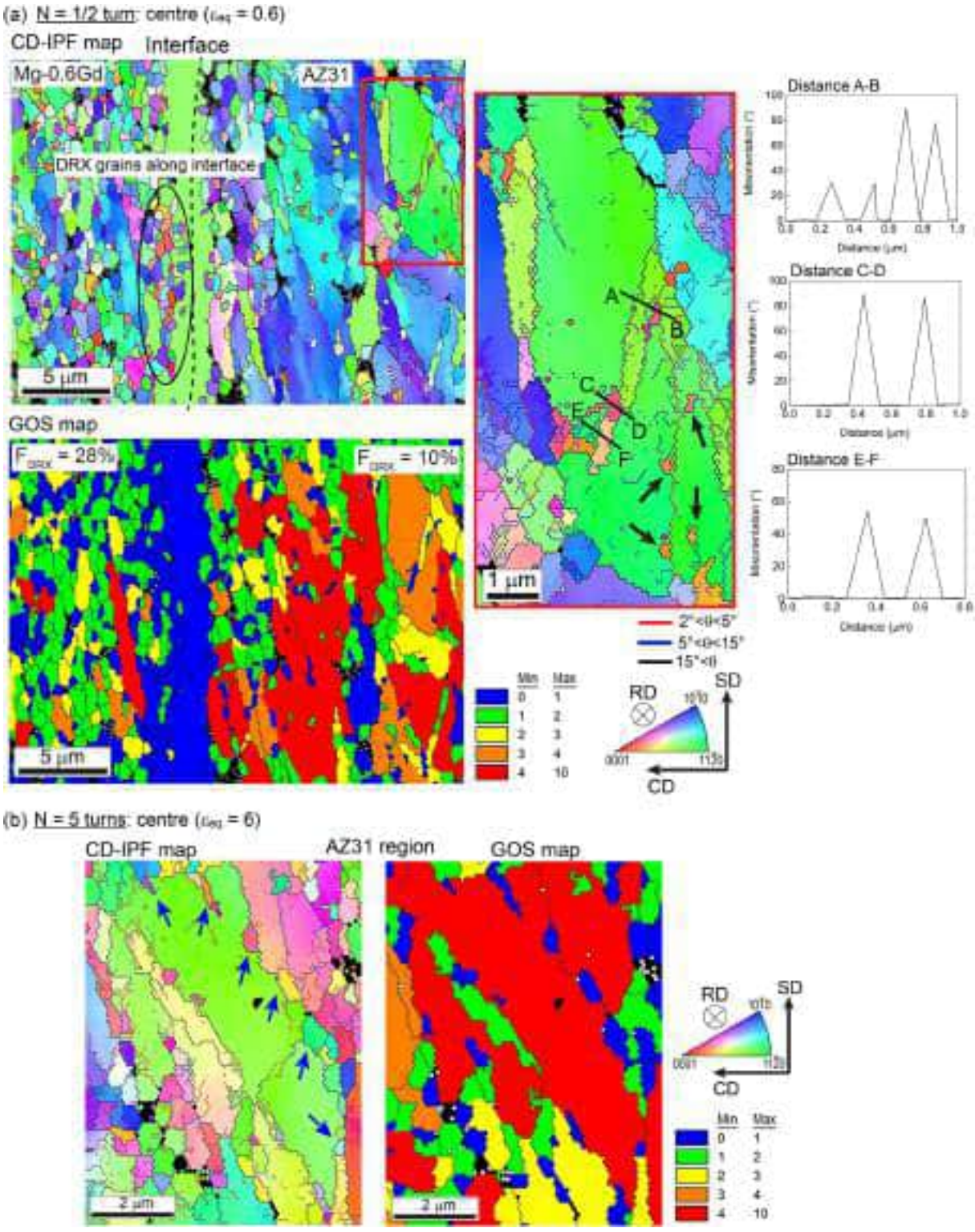

Figure 10. a) RD–IPF and grain orientation spread (GOS) maps and misorientation profiles corresponding to the lines A–B, C–D, and E–F in the red frame near the center of the disc processed for 1/2 turn and b) RD–IPF and GOS maps showing the occurrence of the strain-induced boundary migration (SIBM) mechanism in the AZ31 region in the center of the disc processed for 5 turns. The black circle in the Mg-0.6Gd region of the sample processed for 1/2 turn indicates the formation of dynamic recrystallization (DRX) grains along the interface. The magnified red frame in the AZ31 region after 1/2 turn shows the presence of different twin types. The black arrows in the red frame show the occurrence of the sub-grain development (SGD) mechanism. The blue arrows indicate the occurrence of the SIBM mechanism.

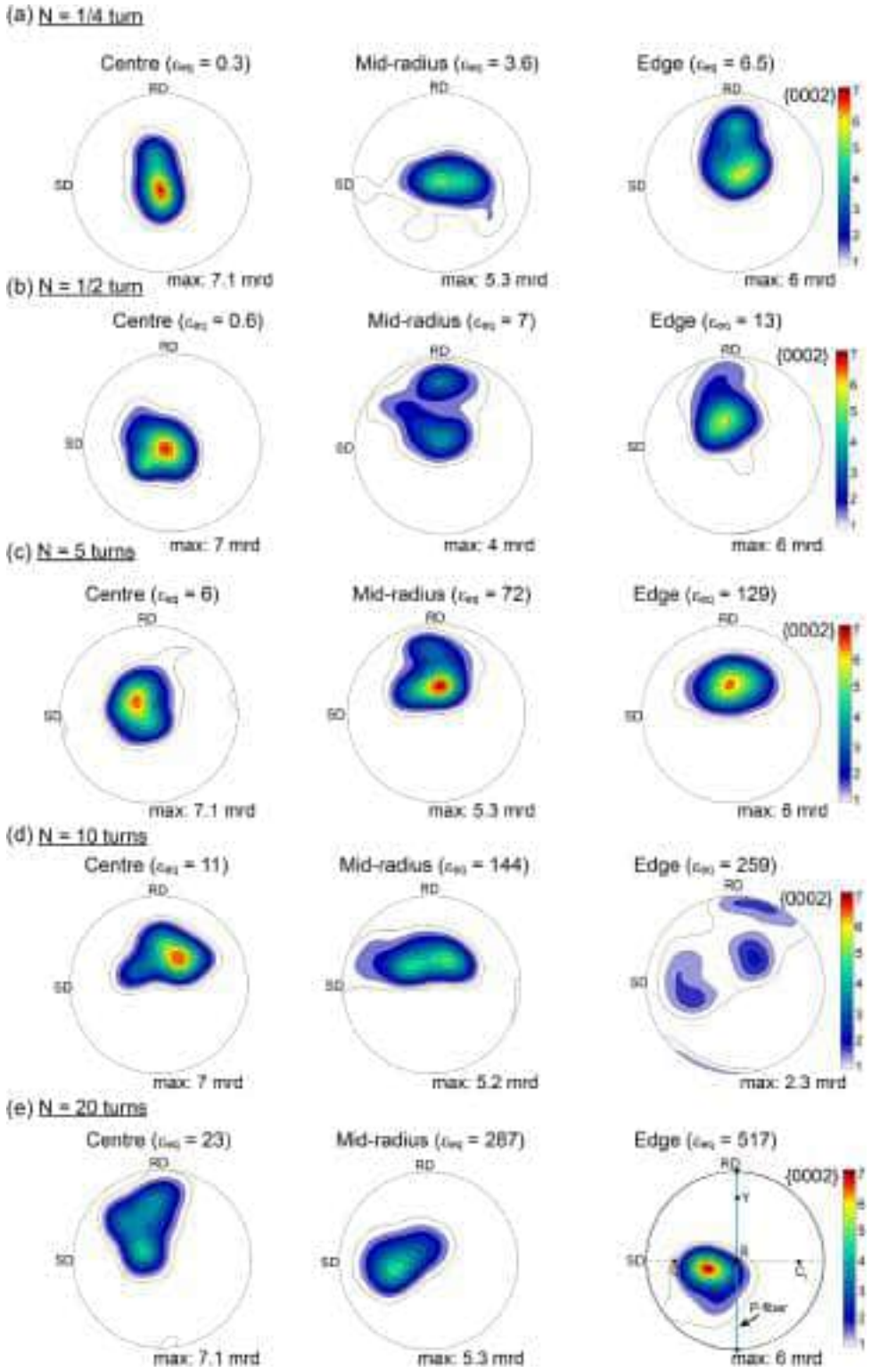

Figure 11. Recalculated {0002} pole figures at the interface near the center, mid-radius, and edge of samples processed for a) 1/4, b) 1/2, c) 5, d) 10, and e) 20 turns.

changes significantly through these four stages similar to the behavior of the texture around the interfaces as shown in Figure 11. The B-fiber changes to a B-fiber with Y-fiber during stages 1 and 2, the texture changes continuously through stage 3 and finally a C_2-fiber with a weak C_1-fiber develops in stage 4. By contrast, the basal texture formed in the Mg–0.6Gd alloy at stage

Table 3. Position of ideal shear texture components for HCP materials and alloys projected in the SD–RD planes.[16]

Notation	B fiber	P fiber	Y fiber	C_1 fiber	C_2 fiber
(φ_1, Φ, φ_2)	(0–60, 0, 0)	(180, 0–90, 30)	(180, 60, 0–60)	(90, 60, 0–60)	(270, 60, 0–60)

1 seems quite stable through the 4 stages except for a deviation from its ideal position.

3.4. Microhardness Evolution after HPT Processing

Figure 13 shows the color-coded maps depicting the distributions of microhardness over the radial cross sections of the HPT-processed hybrid system for 1/4, 1/2, 5, 10, and 20 turns. The initial microhardness values of the as-received AZ31 and Mg–0.6Gd alloys were ≈72.5 and ≈24.5 Hv, respectively. The evolution of microhardness as a function of numbers of HPT turns was reported earlier for AZ31 alloys to lie in the range of Hv ≈ 60–120.[4,10] There are no reports of the microhardness of the Mg–0.6Gd alloy after HPT processing but it is reasonable to anticipate the Hv range is probably close to ≈30–50 as reported for an HPT-processed Mg–0.4Dy (wt%) alloy[7] and ≈35–65 as reported for a Mg–0.6Ce (wt%) alloy processed by equal-channel angular pressing (ECAP).[57]

It is readily apparent from Figure 13 that the values of the microhardness increase with increasing numbers of HPT turns. The interface between the AZ31 and Mg–0.6Gd alloys are reasonably flat along the disc diameters 1/4 and 1/2 turn but after 10 turns there is a heterogeneously distributed microhardness demonstrating a bending of the interface and the consequent formation of multilayers as observed in the SEM image. Thereafter, the microhardness distributions tend to saturate at values of ≈40 and ≈125 Hv for the Mg–0.6Gd and AZ31 alloys, respectively.

The shifting of the bonding interfaces and the development of multilayers of the AZ31/Mg–0.6Gd hybrid material can be easily highlighted by plotting the evolution of microhardness along the diameter in the mid-thickness of the HPT-processed disc as shown in **Figure 14**. The average microhardness of the Mg–0.6Gd alloy increases from ≈24.5 Hv in the as-received condition to ≈54.5 Hv after 1/4 turn and then decreases and saturates at ≈44.5 Hv after 5 turns. Up to 5 turns, the microhardness shows values above 80 Hv in various positions along the disc diameter and this is attributed to the AZ31 alloy. Hence, it appears that within the mid-thickness there are discrete AZ31 layers in which the microhardness of the AZ31 alloy evolves from the as-received condition of ≈72.5 Hv to values close to ≈125 Hv after 10 and 20 turns.

4. Discussion

This report describes the first characterization of a dissimilar Mg-based hybrid material fabricated by HPT processing at RT using initial discs of two different Mg alloys where detailed microstructural observations of the AZ31/Mg–0.6Gd hybrid material provide confirmation that HPT processing is an effective technique for the bonding of Mg-based alloys. The mechanism of the grain refinement and the nature of the texture development in the AZ31/Mg–0.6Gd hybrid material are now discussed.

4.1. Grain Refinement Mechanisms

Figure 15 shows a) the evolution of the mean grain sizes and the HAGBs fractions at the interfaces, b) the mean grain sizes, c) the fractions of HAGBs in the separate AZ31 and Mg–0.6Gd regions recorded from the EBSD measurements, and d) the microhardness values taken at the mid-thickness of the discs replotted as a function of the equivalent strain. The evolution of mean grain size and HAGBs at the interfaces and for the AZ31 region are readily separated into four separate stages which match the texture evolution described in Section 3.3.2. In stage 1 at $0.3 < \varepsilon_{eq} < 6.5$, the grain size decreases and the fraction of HAGBs increases slowly; in stage 2 at $6.5 < \varepsilon_{eq} < 72$, the grain size and fraction of HAGBs are stable; in stage 3 at $72 < \varepsilon_{eq} < 259$, the grain size deceases and the fraction of HAGBs increases rapidly; and then in stage 4 at $259 < \varepsilon_{eq} < 517$, the grain size and the fraction of HAGBs appear reasonably stable based on the limited available data. Figure 15b shows that the mean grain size of the Mg–0.6Gd region was stable during the first and second stages and then decreases and stabilizes during the third and fourth stages, respectively. By contrast, the mean grain size of the AZ31 region was higher than for the Mg–0.6Gd region during the first stage, it was essentially equal to the Mg–0.6Gd region in stages 2 and 3 and then was slightly lower than for the Mg–0.6Gd alloy in stage 4. It is apparent from inspection of Figure 15c that the evolutions of the HAGBs fractions are generally similar for both the Mg–0.6Gd and AZ31 regions.

The stabilization of a mean grain size and the evolution of microhardness in stages 1 and 2 is evidence for a rapid softening with recovery behavior in the Mg–0.6Gd alloy. Such behavior was reported for a Mg–0.4Dy (wt%) alloy during HPT processing.[7] The high microhardness values in stage 3 as in Figure 15d demonstrate the presence of the AZ31 alloy in the mid-thickness of the disc in the form of multilayers which coincide with the decrease in the mean grain size in Figure 15b.

This result demonstrates that the effective strain must be larger than that predicted by Equation (1) when the multilayers are developed which leads to extra grain refinement and texture modification in stages 3 and 4. Hence, it is concluded that the occurrence of the first grain refinement in stages 1 and 2 ($\varepsilon_{eq} \approx 0.3$–72) is due to the strain induced by HPT processing and the second grain refinement in stages 3 and 4 ($\varepsilon_{eq} \approx 72$–517) is due to the development of multilayers as evident from the SEM images at the edge of the disc processed for 10 turns in Figure 4.

It is interesting to note that the formation of multilayers is still not homogenously distributed through the cross section of the disc even after a high number of HPT turns such as 20 turns (ε_{eq} up to 517) as demonstrated by the non-homogenous

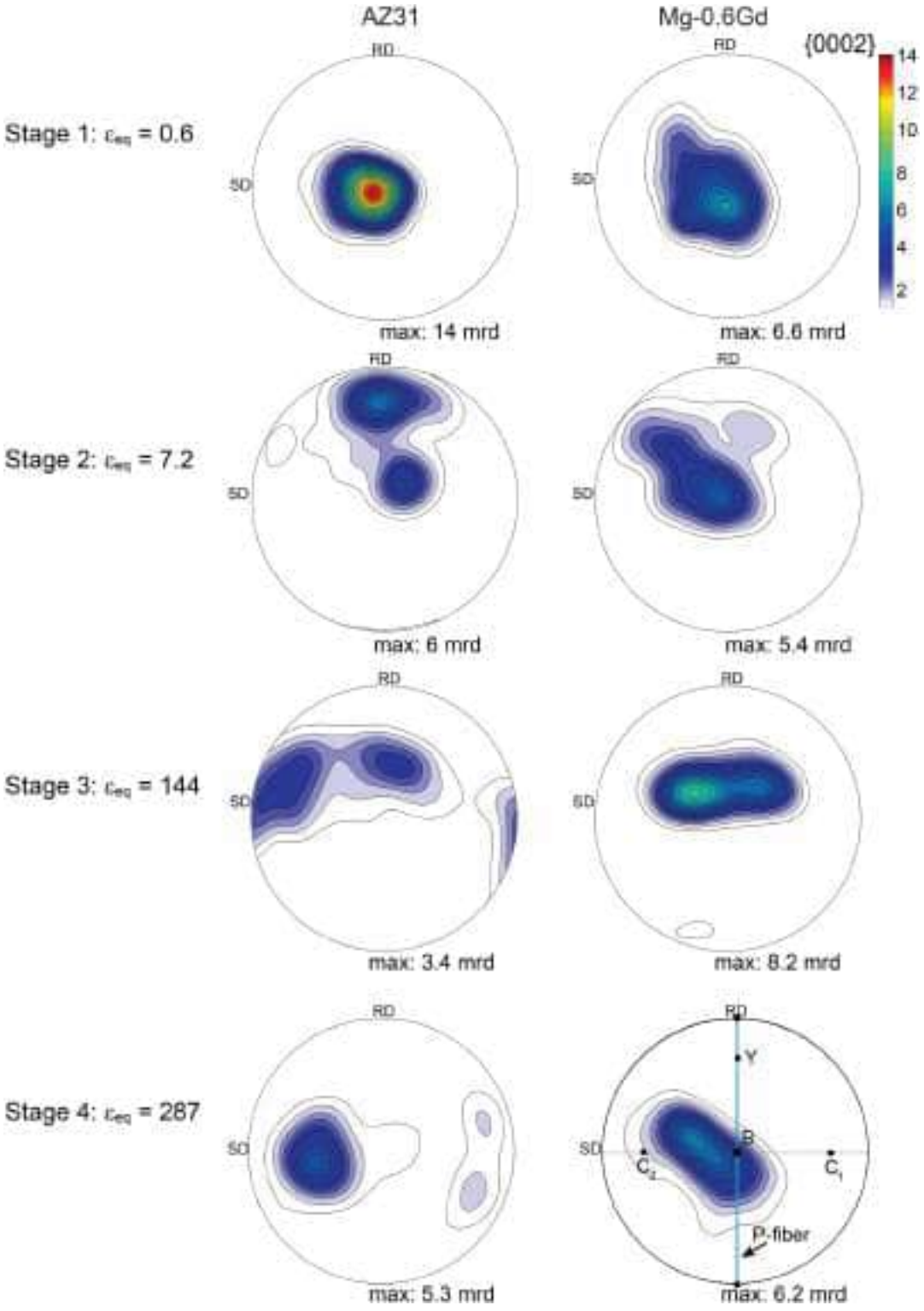

Figure 12. Evolution of recalculated {0002} pole figures corresponding to the AZ31 and Mg-0.6Gd regions in stages 1 ($\varepsilon_{eq} = 0.6$), 2 ($\varepsilon_{eq} = 7.2$), 3 ($\varepsilon_{eq} = 144$), and 4 ($\varepsilon_{eq} = 287$).

distribution of microhardness shown in Figure 13. This observation indicates that more strain is probably needed for the fragmentation of AZ31 and Mg–0.6Gd alloys into thinner layers.

The microstructural observations obtained from EBSD, SEM, and TEM indicate that the AZ31 and Mg–0.6Gd alloys have different grain refinement mechanisms. Thus, the mean grain size

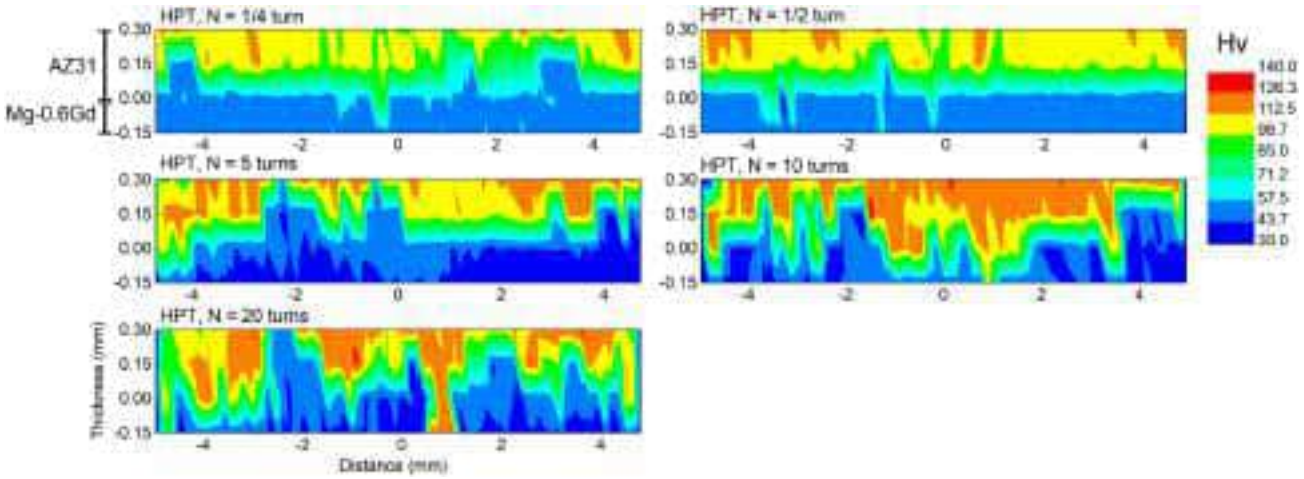

Figure 13. Color-coded microhardness maps of the hybrid AZ31/Mg-0.6Gd material processed by HPT for 1/4, 1/2, 5, 10, and 20 turns.

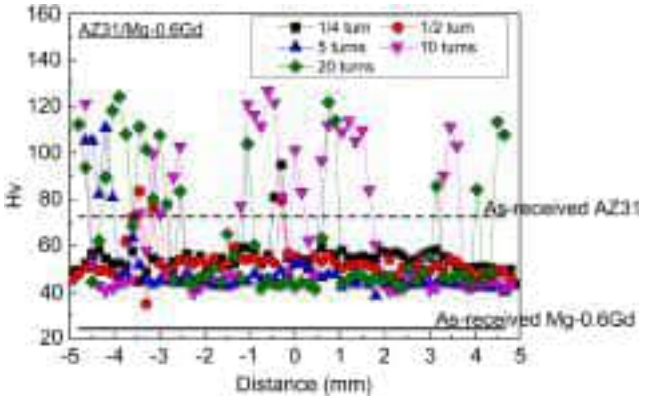

Figure 14. Evolution of microhardness along the diameter in the mid-thickness of the AZ31/Mg-0.6Gd discs after HPT processing for 1/4, 1/2, 5, 10, and 20 turns. The continued and dashed black lines indicate the initial microhardness values of Mg–0.6Gd and AZ31 alloys, respectively.

of $\approx 0.11 \pm 0.06$ μm obtained by TEM and STEM observations of the AZ31 alloy after HPT processing for 20 turns is smaller than the mean grain size of $\approx 0.4 \pm 0.03$ μm for the Mg–0.6Gd alloy. It follows from Figure 15c that the second grain refinement in stage 3 is stronger in the AZ31 alloy and this difference may be associated with the role of the alloying elements in the two materials (Al and Zn versus Gd) and the initial conditions of both alloys.

Figure 10 shows a clear example where the AZ31 and Mg–0.6Gd alloys behave differently at the interfaces during low strains. The TDRX and SGD mechanisms were detected in the AZ31 region after processing for $\varepsilon_{eq} = 0.3$. In addition, the SIBM mechanism was evident in the AZ31 region for a sample processed for $\varepsilon_{eq} = 6$ as shown in Figure 10b. Up to this strain, the microstructures of the AZ31 and Mg–0.6Gd regions were similar with the formation of equiaxed fine grains. However, even with the initial coarse grains of the Mg–0.6Gd alloy, it was not feasible to identify the grain refinement mechanisms near the interfaces since a homogenous ultrafine microstructure was rapidly developed at $\varepsilon_{eq} = 0.3$ as shown in Figure 7.

Nevertheless, Figure 4 reveals that the microstructure of the Mg–0.6Gd alloy far from the interface contains a combination of both twins and shear bands. These shear bands are reasonably homogeneously distributed within the microstructure where this is known as a characteristic of SPD Mg-RE alloys due to the effect of the RE elements and the easy activation of the <c + a> pyramidal slip system.[58–60] Consequently, it is concluded that the grain refinement mechanisms in the Mg–0.6Gd alloy are also controlled by twinning and slip deformation.

It is important to note that the Mg–0.6Gd alloy was more sensitive to the formation of ultrafine grain at the interface than the AZ31 alloy. This difference is attributed to the initial grain sizes of both alloys. As shown in Figure 2, the AZ31 alloy exhibits a microstructure with very small grains compared to the coarser grains that are initially present in the Mg–0.6Gd alloy. This is consistent with a proposed model where there is a critical initial grain size that is sufficiently small to ensure a homogeneous microstructure during deformation processing.[13]

Although the grain refinement was rapid for the Mg–0.6Gd alloy near the interface, the AZ31 alloy exhibits an overall finer mean grain size after HPT processing as shown by TEM and STEM observations in Figures 5 and 6 and this is probably associated with the presence of second phase particles in the AZ31 alloy. Thus, the $Mg_{17}Al_{12}$ phase is present in the as-received alloy and this phase remains qualitatively present throughout the HPT processing. By contrast, HPT processing leads to a dissolution of the metastable phases present in the as-cast Mg–0.6Gd alloy and in this case the $Mg_{17}Al_{12}$ phase produces a strong pinning effect on grain boundary migration which delays the occurrence of DRX by suppressing the growth of the DRX grains.

Except only for the presence of the $Mg_{17}Al_{12}$ phase in the AZ31 alloy and the dissolution of the metastable phases in the Mg–0.6Gd alloy, there is no evidence for the formation of any new second phases in the AZ31/Mg–0.6Gd hybrid during HPT processing. An absence of formation of any intermetallic phases was reported earlier in a Mg/Al composite fabricated by HPT processing at RT while an additional heat treatment

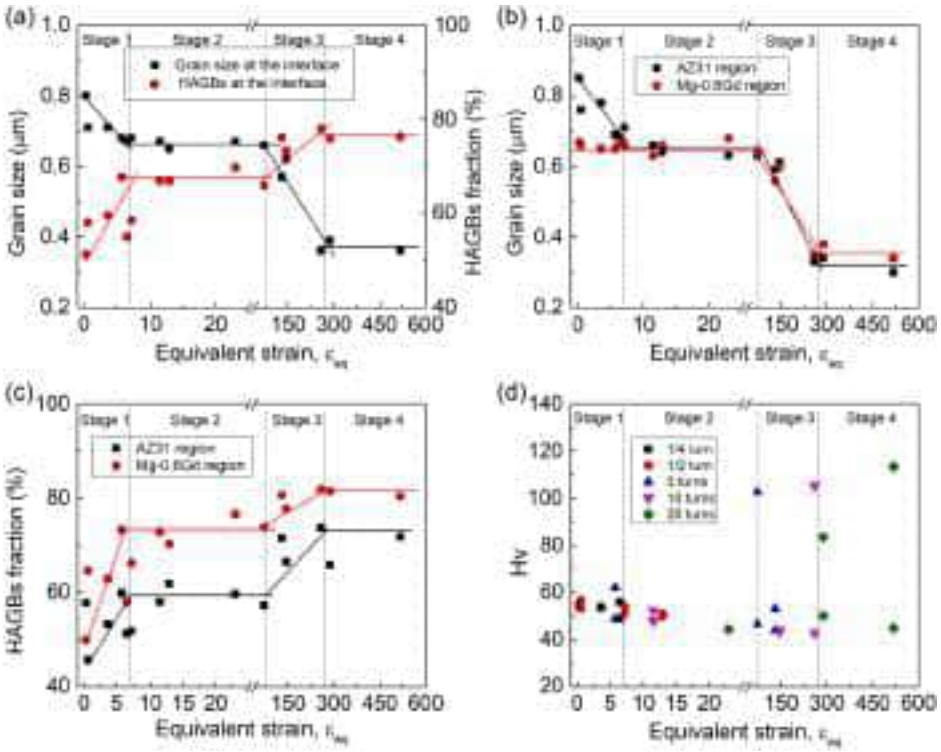

Figure 15. Evolution of a) mean grain size and HAGBs fraction at the interfaces, b) mean grain size, and c) HAGBs fractions of the AZ31 and Mg–0.6Gd regions obtained from EBSD measurements and d) microhardness values taken from the mid-thickness of the HPT-processed discs as a function of the equivalent strain. Stage 1: $0.3 < \varepsilon_{eq} < 6.5$, stage 2: $6.5 < \varepsilon_{eq} < 72$, stage 3: $72 < \varepsilon_{eq} < 259$, and stage 4: $259 < \varepsilon_{eq} < 517$.

at 573 K for 1 h led to the formation of Al_3Mg_2 and $Al_{12}Mg_{17}$ phases since, it was suggested, processing at RT hinders the nucleation and growth of any second phase.[61] This suggests that it would be beneficial to investigate the microstructural evolution of the AZ31/Mg–0.6Gd hybrid material after a heat treatment.

4.2. Texture Evolution during HPT Processing

The basal texture (B-fiber) in HCP materials is often formed in the earlier stage of HPT processing and is maintained throughout the entire deformation processing.[16] The formation of the B-fiber causes a low formability of the material and hence it generally restricts the potential structural applications. The present results show that the texture evolution of the AZ31/Mg–0.6Gd hybrid material changes in Figure 11 as a function of equivalent strain and this provides an opportunity to design a new generation of Mg-based alloys having superior formability. This change in the texture evolution is connected directly with the change in grain refinement and deformation mechanisms[16] since the AZ31 and Mg–0.6Gd alloys undergo different grain refinement mechanisms and this affects the texture evolution of each alloy as shown in Figure 12.

Inspection of Figure 12 shows that the texture of the AZ31 alloy changes through the four stages whereas the basal texture of the Mg–0.6Gd alloy is retained through these stages except only for the deviation from its ideal position. The deviation of the B-fiber and its saturation through HPT processing was reported earlier in Mg-RE binary alloys.[7,62] In accordance with the microstructural evolution of the AZ31 alloy, and by comparison with the Mg–0.6Gd alloy, the formation of the Y-fiber in the AZ31 alloy may be due to the presence of twins in the AZ31 sample after processing for 1/2 and 5 turns, and this is especially associated with the contraction and extension twins which produce a rotation of about 56° and 86° of the initial basal texture, respectively. A similar texture of B- and Y-fibers was reported for the AZ31 alloy after processing by HPT at RT for 1 and 5 turns[63] and it was also reported that the development of the C_2-fiber is due to an activation of the pyramidal $<c + a>$ slip system.[64] It is reasonable to conclude that the extra strain introduced by the bending and development of multilayers in the hybrid material facilitates the activation of the pyramidal $<c + a>$ slip system in the AZ31 alloy. Nevertheless, further investigations are now needed to more fully explore the effect of the resultant texture on the formability of this new AZ31/Mg–0.6Gd hybrid material.

The present report demonstrates the possibility of joining dissimilar Mg-based alloys with HPT processing. Much research and investigation are now needed to explore the anisotropy of the mechanical properties across the disc and the thermal stability of the hybrid material. The results obtained will be useful for finding potential applications for this new hybrid material.

5. Summary and Conclusions

1) HPT processing at RT was successfully used to fabricate a dissimilar magnesium AZ31/Mg–0.6Gd hybrid material. 2) The fabricated hybrid alloy exhibited two stages of grain

refinements. The first grain refinement occurred during $\varepsilon_{eq} \approx 0.3$–72 due to the strain introduced by HPT processing and the second grain refinement was observed during $\varepsilon_{eq} \approx 72$–517 due to the extra strain induced from bending and the development of multilayers. 3) The microstructure exhibited excellent grain refinement after 20 turns but the AZ31 region gave a greater grain size reduction ($\approx 0.11 \pm 0.06$ μm) than the Mg–0.6Gd region ($\approx 0.40 \pm 0.03$ μm). 4) The grain refinement and DRX mechanisms in the AZ31 alloy were controlled by twinning, slip systems, and the $Mg_{17}Al_{12}$ precipitates. The Mg–0.6Gd alloy showed rapid grain refinement but twinning and slip were the main mechanisms responsible for DRX. 5) The texture of the AZ31 alloy changed from B-fiber to Y-fiber and C_2-fiber through HPT processing together with the formation of multilayers. The basal texture of the Mg–0.6Gd alloy was stable through the HPT processing except for a deviation from its ideal position.

Acknowledgements

Dr-Ing. N. Hort and Dr. D. Letzig (MagIC, Germany) and Dr-Ing. Talal Al-Samman (RWTH-Aachen University, Germany) are gratefully acknowledged for providing the AZ31 and Mg-0.6Gd alloys, respectively. Two of the authors were supported by the European Research Council under Grant Agreement No. 267464-SPDMETALS (YH and TGL).

Conflict of Interest

The authors declare no conflict of interest.

Data Availability Statement

The data that support the findings of this study are available from the corresponding author upon reasonable request.

Keywords

high-pressure torsion, hybrid metal, magnesium, microstructure, rare-earth, texture

Received: December 10, 2022
Revised: January 23, 2023
Published online: February 3, 2023

[1] K. Edalati, A. Bachmaier, V. A. Beloshenko, Y. Beygelzimer, V. D. Blank, W. J. Botta, K. Bryła, J. Čížek, S. Divinski, N. A. Enikeev, Y. Estrin, G. Faraji, R. B. Figueiredo, M. Fuji, T. Furuta, T. Grosdidier, J. Gubicza, A. Hohenwarter, Z. Horita, J. Huot, Y. Ikoma, M. Janeček, M. Kawasaki, P. Král, S. Kuramoto, T. G. Langdon, D. R. Leiva, V. I. Levitas, A. Mazilkin, M. Mito, et al., *Mater. Res. Lett.* **2022**, *10*, 163.
[2] Y. Huang, R. B. Figueiredo, T. Baudin, F. Brisset, T. G. Langdon, *Adv. Eng. Mater.* **2012**, *14*, 1018.
[3] A. Al-Zubaydi, R. B. Figueiredo, Y. Huang, T. G. Langdon, *J. Mater. Sci.* **2013**, *48*, 4661.
[4] J. Xu, X. Wang, M. Shirooyeh, G. Xing, D. Shan, B. Guo, T. G. Langdon, *J. Mater. Sci.* **2015**, *50*, 7424.
[5] A. S. J. Al-Zubaydi, A. P. Zhilyaev, S. C. Wang, P. Kucita, P. A. S. Reed, *J. Mater. Sci.* **2016**, *51*, 3380.
[6] R. B. Figueiredo, T. G. Langdon, *Adv. Eng. Mater.* **2019**, *21*, 1801039.
[7] A. Hanna, H. Azzeddine, R. Lachhab, T. Baudin, A.-L. Helbert, F. Brisset, Y. Huang, D. Bradai, T. G. Langdon, *J. Alloys Compd.* **2019**, *778*, 61.
[8] A. A. Khaleghi, F. Akbaripanah, M. Sabbaghian, K. Máthis, P. Minárik, J. Veselý, M. El-Tahawy, J. Gubicza, *Mater. Sci. Eng., A* **2021**, *799*, 140158.
[9] F. Meng, J. M. Rosalie, A. Singh, H. Somekawa, K. Tsuchiya, *Scr. Mater.* **2014**, *78–79*, 57.
[10] J. Stráská, M. Janeček, J. Gubicza, T. Krajňák, E. Y. Yoon, H. S. Kim, *Mater. Sci. Eng., A* **2015**, *625*, 98.
[11] E. A. Lukyanova, N. S. Martynenko, V. N. Serebryany, A. N. Belyakov, L. L. Rokhlin, S. V. Dobatkin, Y. Z. Estrin, *Russ. Metall.* **2017**, *2017*, 912.
[12] K. Bryła, J. Morgiel, M. Faryna, K. Edalati, Z. Horita, *Mater. Lett.* **2018**, *212*, 323.
[13] R. B. Figueiredo, T. G. Langdon, *J. Mater. Sci.* **2010**, *45*, 4827.
[14] T. Sakai, A. Belyakov, R. Kaibyshev, H. Miura, J. J. Jonas, *Prog. Mater. Sci.* **2014**, *60*, 130.
[15] R. B. Figueiredo, S. Sabbaghianrad, T. G. Langdon, *IOP Conf. Ser.: Mater. Sci. Eng.* **2017**, *194*, 012039.
[16] H. Azzeddine, D. Bradai, T. Baudin, T. G. Langdon, *Prog. Mater. Sci.* **2022**, *125*, 100886.
[17] S. Tighiouaret, R. Lachhab, A. Hanna, H. Azzeddine, Y. Huang, T. Baudin, A.-L. Helbert, F. Brisset, D. Bradai, T. G. Langdon, *Adv. Eng. Mater.* **2019**, *21*, 1900801.
[18] Y. F. Sun, H. Fujii, T. Nakamura, N. Tsuji, D. Todaka, M. Umemoto, *Scr. Mater.* **2011**, *65*, 489.
[19] M. Pouryazdan, B. J. P. Kaus, A. Rack, A. Ershov, H. Hahn, *Nat. Commun.* **2017**, *8*, 1611.
[20] K. Oh-ishi, K. Edalati, H. S. Kim, K. Hono, Z. Horita, *Acta Mater.* **2013**, *61*, 3482.
[21] J.-K. Han, K.-D. Liss, T. G. Langdon, M. Kawasaki, *Sci. Rep.* **2019**, *9*, 17186.
[22] J.-K. Han, K. Sugimoto, M. Kawasaki, K.-D. Liss, *Mater. Lett.* **2022**, *321*, 132414.
[23] P. Bazarnik, A. Bartkowska, Y. Huang, K. Szlązak, B. Adamczyk-Cieślak, J. Sort, M. Lewandowska, T. G. Langdon, *Mater. Sci. Eng., A* **2022**, *833*, 142549.
[24] S. O. Rogachev, S. A. Nikulin, V. M. Khatkevich, N. Y. Tabachkova, R. V. Sundeev, *Russ. Metall.* **2018**, *2018*, 372.
[25] D. Hernández-Escobar, Z. U. Rahman, H. Yilmazer, M. Kawasaki, C. J. Boehlert, *Philos. Mag.* **2019**, *99*, 557.
[26] J.-K. Han, T. Herndon, J.-I. Jang, T. G. Langdon, M. Kawasaki, *Adv. Eng. Mater.* **2020**, *22*, 1901289.
[27] K. Edalati, R. Uehiro, K. Fujiwara, Y. Ikeda, H.-W. Li, X. Sauvage, R. Z. Valiev, E. Akiba, I. Tanaka, Z. Horita, *Mater. Sci. Eng., A* **2017**, *701*, 158.
[28] D. Hernández-Escobar, R. R. Unocic, M. Kawasaki, C. J. Boehlert, *J. Alloys Compd.* **2020**, *831*, 154891.
[29] S. O. Rogachev, S. A. Nikulin, A. B. Rozhnov, V. M. Khatkevich, T. A. Nechaykina, M. V. Gorshenkov, R. V. Sundeev, *Metall. Mater. Trans. A* **2017**, *48*, 6091.
[30] Y. Sun, M. Aindow, R. J. Hebert, T. G. Langdon, E. J. Lavernia, *J. Mater. Sci.* **2017**, *52*, 12170.
[31] B. Ahn, A. P. Zhilyaev, H.-J. Lee, M. Kawasaki, T. G. Langdon, *Mater. Sci. Eng., A* **2015**, *635*, 109.
[32] S. O. Rogachev, R. V. Sundeev, V. M. Khatkevich, *Mater. Lett.* **2016**, *173*, 123.
[33] S. O. Rogachev, S. A. Nikulin, V. M. Khatkevich, R. V. Sundeev, A. Komissarov, *Metall. Mater. Trans. A* **2020**, *51*, 1781.

[34] B. L. Mordike, T. Ebert, *Mater. Sci. Eng., A* **2001**, *302*, 37.
[35] J. Hirsch, T. Al-Samman, *Acta Mater.* **2013**, *61*, 818.
[36] X. Li, X. Liu, S. Wu, K. W. K. Yeung, Y. Zheng, P. K. Chu, *Acta Biomater.* **2016**, *45*, 2.
[37] A. Atrens, S. Johnston, Z. Shi, M. S. Dargusch, *Scr. Mater.* **2018**, *154*, 92.
[38] B. Elambharathi, S. D. Kumar, V. U. Dhanoop, S. Dinakar, S. Rajumar, S. Sharma, V. Kumar, C. Li, E. M. T. Eldin, S. Wojciechowski, *Heliyon* **2022**, *8*, e11712.
[39] J. Song, J. Chen, X. Xiong, X. Peng, D. Chen, F. Pan, *J. Magnesium Alloys* **2022**, *10*, 863.
[40] A. Atrens, G.-L. Song, M. Liu, Z. Shi, F. Cao, M. S. Dargusch, *Adv. Eng. Mater.* **2015**, *17*, 400.
[41] G. Wu, C. Wang, M. Sun, W. Ding, *J. Magnesium Alloys* **2021**, *9*, 1.
[42] L. L. Rokhlin, *Magnesium Alloys Containing Rare Earth Metals: Structure and Properties*, CRC Press, London **2003**.
[43] A. Imandoust, C. D. Barrett, T. Al-Samman, K. A. Inal, H. El Kadiri, *J. Mater. Sci.* **2017**, *52*, 1.
[44] R. B. Figueiredo, P. R. Cetlin, T. G. Langdon, *Mater. Sci. Eng., A* **2011**, *528*, 8198.
[45] R. B. Figueiredo, P. H. R. Pereira, M. T. P. Aguilar, P. R. Cetlin, T. G. Langdon, *Acta Mater.* **2012**, *60*, 3190.
[46] K. Edalati, Z. Horita, T. G. Langdon, *Scr. Mater.* **2009**, *60*, 9.
[47] F. Wetscher, A. Vorhauer, R. Stock, R. Pippan, *Mater. Sci. Eng., A* **2004**, *387–389*, 809.
[48] Y. Mikami, K. Oda, M. Kamaya, M. Mochizuki, *Mater. Sci. Eng., A* **2015**, *647*, 256.
[49] J.-H. Cho, A. D. Rollett, K. H. Oh, *Metall. Mater. Trans. A* **2005**, *36*, 3427.
[50] R. Hielscher, H. Schaeben, *J. Appl. Cryst.* **2008**, *41*, 1024.
[51] N. Bayat Tork, S. H. Razavi, H. Saghafian, R. Mahmudi, *Adv. Eng. Mater.* **2016**, *18*, 156.
[52] N. Azizi, R. Mahmudi, *Mater. Sci. Eng., A* **2021**, *817*, 141385.
[53] Y. Lu, Y. Huang, J. Bode, C. Vogt, R. Willumeit-Römer, K. U. Kainer, N. Hort, *Adv. Eng. Mater.* **2022**, *24*, 2200966.
[54] O. Sitdikov, R. Kaibyshev, T. Sakai, *Mater. Sci. Forum* **2003**, *419–422*, 521.
[55] C. Xie, J. M. He, B. W. Zhu, X. Liu, J. Zhang, X. F. Wang, X. D. Shu, Q. H. Fang, *Int. J. Plast.* **2018**, *111*, 211.
[56] S. Tighiouaret, A. Hanna, H. Azzeddine, L. Rabahi, A. Dakhouche, F. Brisset, A.-L. Helbert, T. Baudin, D. Bradai, *Mater. Chem. Phys.* **2021**, *267*, 124598.
[57] S. Sadi, A. Hanna, H. Azzeddine, C. Casas, T. Baudin, A.-L. Helbert, F. Brisset, J. M. Cabrera, *Mater. Charact.* **2021**, *181*, 111454.
[58] F. Guerza-Soualah, A. Hanna, H. Azzeddine, A.-L. Helbert, F. Brisset, T. Baudin, D. Bradai, *Mater. Today Commun.* **2020**, *24*, 101239.
[59] S. Sandlöbes, I. Schestakow, S. B. Yi, S. Zaefferer, J. Q. Chen, M. Friák, J. Neugebauer, D. Raabe, *Mater. Sci. Forum* **2011**, *690*, 202.
[60] M. R. Barnett, M. D. Nave, C. J. Bettles, *Mater. Sci. Eng., A* **2004**, *386*, 205.
[61] M. M. Castro, S. Sabbaghianrad, P. H. R. Pereira, E. M. Mazzer, A. Isaac, T. G. Langdon, R. B. Figueiredo, *J. Alloys Compd.* **2019**, *804*, 421.
[62] Y. I. Bourezg, H. Azzeddine, T. Baudin, A.-L. Helbert, Y. Huang, D. Bradai, T. G. Langdon, *Mater. Sci. Eng., A* **2018**, *724*, 477.
[63] Y. Huang, R. Figueiredo, T. Baudin, A.-L. Helbert, F. Brisset, T. G. Langdon, *Mater. Res.* **2013**, *16*, 577.
[64] R. Kocich, L. Kunčická, P. Král, T. C. Lowe, *Mater. Des.* **2016**, *90*, 1092.

Materials Today Communications 38 (2024) 108305

Contents lists available at ScienceDirect

Materials Today Communications

journal homepage: www.elsevier.com/locate/mtcomm

Primary recrystallization of a magnesium hybrid material fabricated by high-pressure torsion

Ouarda Ould Mohamed [a], Piotr Bazarnik [b], Yi Huang [c,d], Hiba Azzeddine [a,*], Thierry Baudin [e], François Brisset [e], Megumi Kawasaki [f], Terence G. Langdon [c]

[a] Laboratory of Materials and Renewable Energy, Faculty of Sciences, Mohamed Boudiaf University, 28000 M'sila, Algeria
[b] Warsaw University of Technology, Faculty of Materials Science and Engineering, Woloska 141, 02-507, Poland
[c] Materials Research Group, Department of Mechanical Engineering, University of Southampton, Southampton SO17 1BJ, UK
[d] Department of Design and Engineering, Faculty of Science and Technology, Bournemouth University, Poole, Dorset BH12 5BB, UK
[e] Université Paris-Saclay, CNRS, Institut de Chimie Moléculaire et des Matériaux d'Orsay, 91405 Orsay, France
[f] School of Mechanical, Industrial and Manufacturing Engineering, Oregon State University, Corvallis, OR 97331, USA

ARTICLE INFO

Keywords:
High-pressure torsion
Hybrid metal
Magnesium
Precipitation
Recrystallization

ABSTRACT

The static recrystallization and grain growth of a hybrid AZ31/Mg-0.6Gd (wt%) material fabricated by high-pressure torsion (HPT) through 20 turns were explored after isochronal annealing at 150, 250, 350 and 450 °C for 1 h using electron backscatter diffraction, transmission electron microscopy and Vickers microhardness measurements. The results reveal heterogeneity in the grain size distributions of the AZ31 and Mg-0.6Gd regions after annealing at the lower temperatures of 150 and 250 °C leading to a clear AZ31/Mg-0.6Gd interfacial border. At the higher temperatures of 350 and 450 °C the AZ31/Mg-0.6Gd interfaces were not well-defined owing to the occurrence of grain growth. It is shown that grain growth is restricted in the AZ31 and Mg-0.6Gd regions due to the presence of stable nano-size Al_8Mn_5 particles and the precipitation of $Mg_{17}Al_{12}$ and $Mg_{12}Zn$ at 250 °C and of Mg_5Gd and $Mg_{12}Gd$ phases at 350 and 450 °C. The distribution of the basal texture in both regions was strongly controlled by dynamic recrystallization, precipitation and grain growth. The values of the microhardness over the radial cross-sections of the hybrid discs decrease and become more uniform, in the range of ~35–66 Hv, with increasing annealing temperature.

1. Introduction

The fabrication of hybrid metals by solid-state bonding is an effective concept for creating a new generation of functional materials with exceptional mechanical and structural properties which meet industrial requirements [1]. These hybrid metals can be fabricated using different techniques such as mechanical alloying [2], friction stir processing [3] and severe plastic deformation (SPD) [4].

During the last decade, the use of the high-pressure torsion (HPT) technique became not only well established for achieving significant grain refinement but also became a powerful method for synthesizing new hybrid metals [5,6]. Moreover, HPT processing has the ability to change the deformation behaviour and the dynamic recrystallization kinetics of Mg-based alloys by comparison with conventional thermo-mechanical processing [7,8].

Recently, a novel hybrid material was successfully fabricated from separate discs of dissimilar Mg-based alloys (AZ31 and Mg-Gd) using HPT processing at room temperature [9]. It was found that the grain refinement in the hybrid material occurs through two stages due to the strain induced by HPT processing and an additional strain from the formation of interface bonding [9]. Furthermore, the hybrid AZ31/Mg-0.6Gd material exhibited a different texture than the undesirable strong basal texture that is usually formed in conventionally deformed Mg-based alloys and causes subsequent poor formability. The hybrid AZ31/Mg-0.6Gd material has a strong chance of replacing the conventional AZ31 alloy often used as lightweight structural material in the transportation industries, as well as a possible biodegradable implant material in biomedical applications [10,11].

Numerous investigations are now available exploring the properties of hybrid materials related to the bonding and grain refinement and the formation of intermetallic phases during post deformation [5,6,9,12,13]. However, less attention has been given to the effect of heating on

* Corresponding author.
E-mail address: hiba.azzeddine@univ-msila.dz (H. Azzeddine).

https://doi.org/10.1016/j.mtcomm.2024.108305
Received 17 November 2023; Received in revised form 21 January 2024; Accepted 2 February 2024
Available online 5 February 2024

the evolution of properties and the thermal stability of hybrid metals [14] and in practice post-deformation annealing treatments are necessary to release the stored energy into a recrystallized microstructure with optimized grain size and modified texture. Accordingly, the purpose of the present study was to fully characterize the microstructure and mechanical properties of an AZ31/Mg-0.6Gd (wt%) hybrid material fabricated by HPT processing after an isochronal annealing treatment.

2. Experimental material and procedures

The details of the AZ31 and Mg-0.6Gd alloys and the HPT processing conditions were given earlier [9]. In brief, AZ31 and Mg-0.6Gd discs with diameters of 10 mm and thicknesses of 0.85 mm were placed on the lower and the top anvil of the HPT facility, respectively. Then these two discs were processed by HPT at room temperature for 20 HPT turns under a pressure of 6.0 GPa with a rotational speed of 1 rpm and using quasi-constrained conditions [9]. The HPT-processed discs were subjected to isochronal annealing in a radiation furnace at 150, 250, 350 and 450 °C for 1 h.

The microstructure, texture and Vickers microhardness (Hv) measurements were undertaken on the cross-sectional (CD-SD) planes of the annealed discs as illustrated in Fig. 1 where the shear reference frame is defined as the shear direction (SD), rotational direction (RD) and compression direction (CD), respectively.

Structural observations of the fabricated materials were collected using a scanning electron microscope (SEM) Hitachi Su8000 operating in back-scattered electron (BSE) mode. Observations were carried out on cross-sectional planes approximately 1 mm from the edges of the discs. Samples for the SEM investigations were prepared using a Hitachi IM4000 ion milling system. This procedure gives high-quality surfaces for observation due to ion beam polishing which eliminates any deformation stresses and/or the formation of oxide layers. The surface quality after the ion milling permitted the structure to be observed in so-called channel contrast showing the grain boundaries in the material. These SEM observations were complemented by electron back-scattered diffraction (EBSD) measurements performed near the mid-radius positions of the mid-thickness planes of the annealed discs (see Fig. 1) using a TSL-EDAX-Hikari system mounted on a scanning electron microscope (FEG-SEM ZEISS Supra 55 VP) operating at 20 kV. The scanned areas for the discs annealed at 150 and 250 °C were 40 × 40 μm^2 with a 50 nm step size. The scanned area for the disc annealed at 350 °C was 100 × 100 μm^2 with a step size of 0.1 μm and the scanned area for the disc annealed at 450 °C was 200 × 200 μm^2 with a step size of 0.1 μm. The EBSD data were analysed by the Orientation Imaging Microscopy OIM™ software by considering a grain tolerance angle of 5° and a minimum grain size of 5 pixels.

The texture was analysed using MTEX software by calculating the orientation distribution function (ODF) using the harmonic method (L = 22) and a Gaussian function with a half-width of 5° to model each orientation [15].

Detailed microstructural observations of selected areas were performed using a CS-corrected dedicated scanning transmission electron (STEM) Thermo Fisher Scientific Spectra microscope operating at an accelerating voltage of 200 kV. The STEM observations were carried out in the bright-field (BF) and high-angle annular dark field (HAADF) modes. Structural investigations were combined with advanced energy dispersive X-Ray (EDX) point and mapping analyses. Thin foils for observations were prepared using a Focused Ion Beam (FIB) Hitachi NB-5000 microscope.

Color-coded contour Vickers microhardness maps were constructed over the cross-sections of the annealed discs (see Fig. 1) by using a Mitutoyo HM-200 facility with a load of 50 gf and a dwell time of 10 s

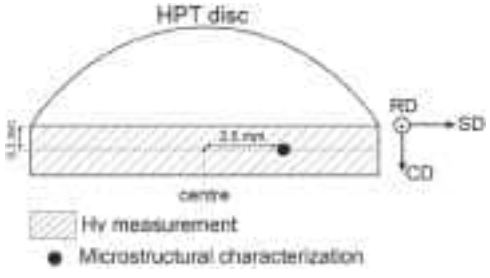

Fig. 1. Schematic illustration showing the positions for the microstructure and microhardness measurements on the vertical cross-section of the HPT disc: SD, CD, and RD are the coordinate system.

3. Experimental results

Fig. 2 shows the inverse pole figure (RD-IPF) maps near the AZ31/Mg-0.6Gd interface of the discs annealed at (a) 150, (b) 250, (c) 350 and (d) 450 °C, respectively. The grain boundaries with high misorientations (HAGBs, θ > 15°) are highlighted by a black line. In addition, the AZ31 and Mg-0.6Gd regions are indicated in each map. It should be noted that the RD-IPF map of the disc annealed at 450 °C (Fig. 2d) is shown with a different scale bar. Fig. 3 displays the evolution of the mean grain size of the AZ31 and Mg-0.6Gd regions as a function of annealing temperature.

The microstructures are heterogeneous in the discs annealed at 150 and 250 °C where the AZ31 and Mg-0.6Gd regions are easily identified. The AZ31 region of the annealed disc at 150 °C, as shown in Fig. 2a, is characterized by a black zone referring to the non-index area which is a consequence of the large amounts of deformation. This may suggest that annealing at 150 °C for 1 h is not sufficient for the occurrence of static recrystallization of the AZ31 region. A net difference in the grain size distribution is apparent between the AZ31 and Mg-0.6Gd regions in the disc annealed at 250 °C, as shown in Fig. 2b. Thus, the microstructure becomes more homogeneous in discs annealed at 350 and 450 °C in which the AZ31/Mg-0.6Gd interfaces are hardly recognized. Some coarse grains are visible in the Mg-0.6Gd region after annealing at 350 °C (Fig. 2(c)) and these grains are further coarsened at 450 °C. In addition, the white arrows in Fig. 2d indicate the presence of annealing twins in the AZ31 and Mg-0.6Gd regions of the disc annealed at 450 °C. The formation of annealing twins is often observed in various annealed Mg-based alloys [16–19]. The mean grain size evolution shown in Fig. 3 demonstrates that the mean grain size of the Mg-0.6Gd region continuously increases from 0.8 ± 0.2 μm at 150 °C to a value of 6.5 ± 0.8 μm at 450 °C.

For the record, it should be noted that the grain sizes of the AZ31 and Mg-06Gd regions after HPT processing for 20 turns was reported earlier as 0.1 and 0.4 μm, respectively [9]. The mean grain size of the AZ31 region also increases with increasing annealing temperature except that the mean grain size is lower at 250 °C (0.6 ± 0.3 μm) than at 150 °C (1.7 ± 0.5 μm). The AZ31 region exhibits a smaller grain size than the Mg-0.6Gd region through the annealing temperature range of 250–450 °C.

Fig. 4 displays histograms of the grain boundary misorientation distributions for the AZ31 and Mg-0.6Gd regions as a function of annealing temperature. The grain boundary misorientation distribution for randomly oriented material with an hexagonal structure is added for comparison [20]. In addition, the fraction of HAGBs in each region is also shown in the plots. It is apparent that the AZ31 and Mg-0.6Gd regions do not show any random distribution under the isochronal annealing. Indeed, the grain boundary distribution shows a peak around 30° indicating a 30° < 0001 > grain boundary resulting from the formation of a basal texture [21]. This peak tends to disappear in the AZ31 and Mg-0.6Gd regions annealed at 350 and 450 °C, respectively. Fig. 3d shows a peak around 86° for both regions indicating the presence of an extension twin (86°<11–20 >). The fraction of HAGBs increases with increasing annealing temperature in both AZ31 and Mg-0.6Gd regions due to the formation of recrystallized grains.

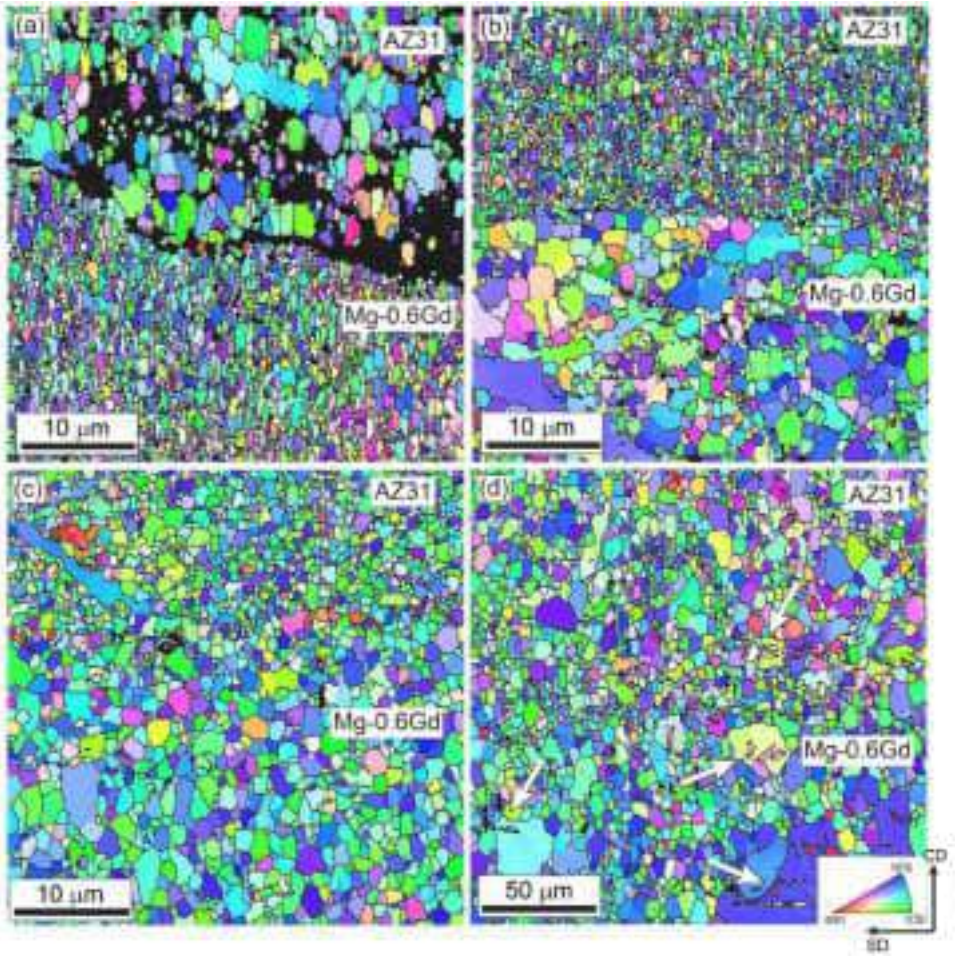

Fig. 2. RD-IPF maps near the AZ31/Mg-0.6Gd interfaces of the hybrid material after isochronal annealing for 1 h at: (a) 150, (b) 250, (c) 350, and (d) 450 °C.

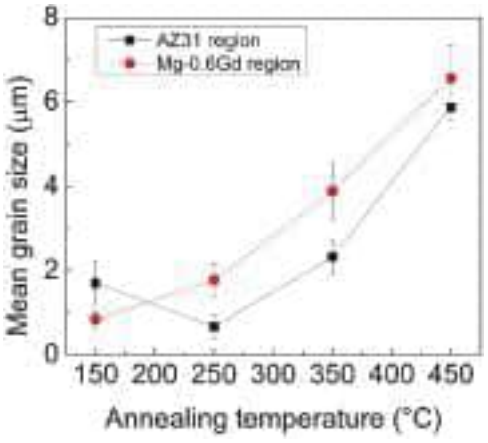

Fig. 3. Evolution of the mean grain size of the AZ31 and Mg-0.6Gd regions as a function of annealing temperature.

The SEM micrographs with different magnifications near the AZ31/Mg-0.6Gd interfaces of the isochronal annealed discs are presented in Fig. 5. It was found that the AZ31 region under the HPT processing condition contained nano-sized Al_8Mn_5 (~10–45 nm) and nano-sized $Mg_{17}Al_{12}$ (~10–24 nm) particles [8,9]. Moreover, the HPT processing caused the fragmentation of the Mg_5Gd phase initially present in the as-cast condition of the Mg-0.6Gd region [8,9]. The SEM micrograph of the disc annealed at 150 °C (Fig. 5a) shows an equiaxed microstructure of the hybrid material except that the mean grain size of the Mg-0.6Gd region is obviously smaller than for the AZ31 region which is in accordance with the EBSD measurements (Figs. 2a and 3). Fig. 5b indicates that there is a large number of precipitates in the AZ31 region at an annealing temperature of 250 °C whereas these precipitations are absent in the AZ31 regions in the discs annealed at 350 and 450 °C as shown in Figs. 5c and 5d. The precipitation occurs also in the Mg-0.6Gd region during annealing at 350 and 450 °C as observed in Figs. 5c and 5d. However, the precipitation in the Mg-0.6Gd region at a temperature of 450 °C tends to be less pronounced than in the Mg-0.6Gd region at a temperature of 350 °C thereby indicating the dissolution of precipitates.

HAADF-STEM and EDS mapping for the Mg, Al, Zn, Mn and Gd elements shown in Fig. 6 was used to identify the precipitates observed in the annealed AZ31 region at 250 °C and the annealed Mg-0.6Gd region at 350 °C, respectively. The EDS analysis of different particles (points 1–5) is summarized in the Table shown also in Fig. 6. The annealed AZ31 region at 250 °C contains three types of second phases with different chemical compositions. First, nano-sized particles of Al_8Mn_5 (point 1) with a size of 10 nm are distributed homogeneously in the entire AZ31 region. Second, large $Mg_{17}Al_{12}$ precipitates (point 2) with lengths of 50–90 nm are localized preferably along grain boundaries in the region and, in addition, spherical $Mg_{17}Al_{12}$ particles with diameters of ~10–40 nm are homogeneously distributed in the AZ31 region which are similar to those reported under the deformation condition [9]. Third, particles with a diameter of 40 nm are present within the grains containing only Mg and Zn elements as indicated by point 3 which was identified as the $Mg_{12}Zn$ phase. A close examination of Zn element mapping of the AZ31 region annealed at 250 °C indicates the

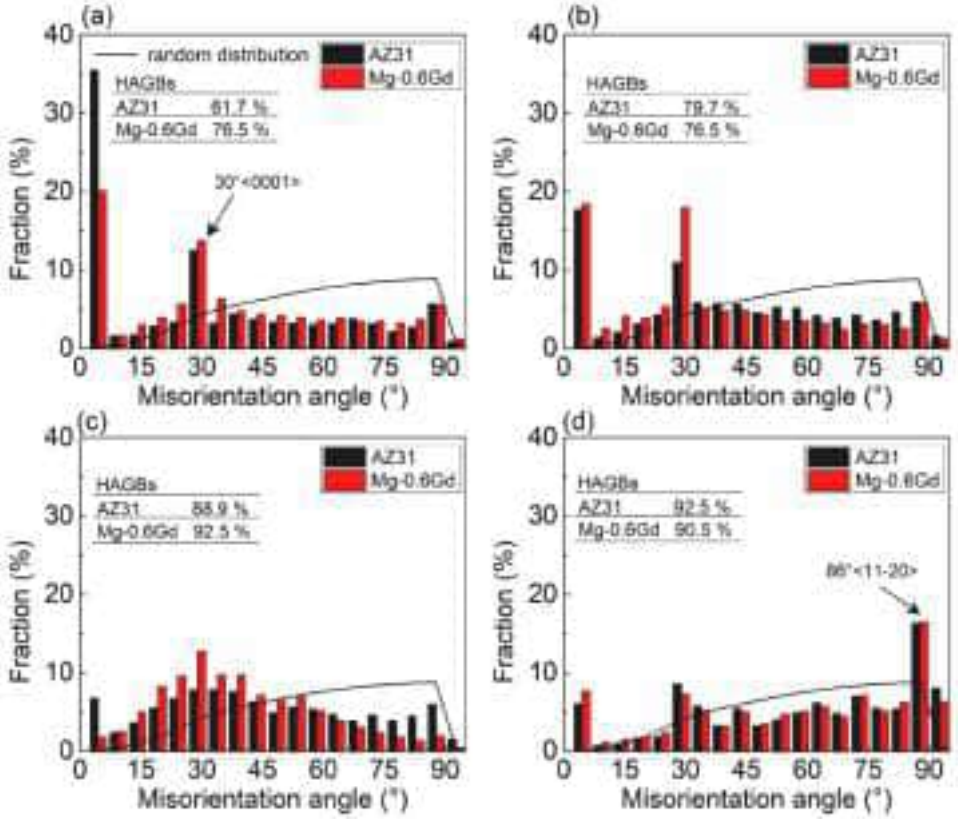

Fig. 4. Histograms of the grain boundary misorientation distributions in the AZ31 and Mg-0.6Gd regions as a function of annealing temperature: (a) 150, (b) 250, (c) 350 and (d) 450 °C.

segregation of Zn elements at the grain boundaries. By contrast, the Mg-0.6Gd region annealed at 350 °C shows the presence of two types of second-phase particles, corresponding to precipitation of an Mg_5Gd phase (point 4) at the grain boundaries and nano-sized particles of $Mg_{12}Gd$ (point 5) with a diameter of 17 nm distributed reasonably homogenously within the microstructure.

Fig. 7 presents the recalculated {0002} pole figures, from left, near the AZ31/Mg-0.6Gd interface of the hybrid material, AZ31, and Mg-0.6Gd regions after annealing at (a) 150, (b) 250, (c) 350 and (d) 450 °C, respectively. It is noted that the texture near the mid-radius of the hybrid disc processed for 20 turns was characterized by a deviated basal texture [9]. As is apparent from Fig. 7, a typical basal texture developed in the hybrid material during annealing at 150 through 350 °C and a net scattering of the basal pole from CD towards SD is visible for the hybrid disc annealed at 450 °C. It was reported earlier that the AZ31 region of the hybrid material fabricated by HPT at 20 turns developed a C_2-fiber with a weak C_1-fiber texture, while a deviated basal texture was formed in the Mg-0.6Gd region [9]. The texture evolutions of the AZ31 and Mg-0.6Gd regions are quite similar as a function of annealing temperature. In practice, both regions exhibit a basal texture where the basal {0002} planes of the grains are preferentially oriented parallel to the shear (SD-RD) plane but their distribution around CD changed during annealing at different temperatures. The scattering of the basal pole at an annealing temperature of 450 °C is more pronounced in the AZ31 region. By contrast, the texture of the Mg-0.6Gd region exhibits a spread of the basal texture from CD towards SD with a high intensity around the orientation of (180°, 35°, 0 °) as indicated by arrows in Fig. 7d.

Fig. 8 presents microhardness maps taken over the cross-sections of the hybrid AZ31/Mg-0.6Gd material after isochronal annealing. Usually, the Vickers microhardness values of the deformed and recrystallized AZ31 alloy are in the range of 60–120 Hv [8,9,22,23]. In the case of Mg-0.6Gd alloy, the Vickers microhardness value was found in the range of 24–53 Hv [8,9]. Consequently, it appears that the AZ31 and Mg-0.6Gd regions are in the upper and lower parts of the discs, respectively. The highest microhardness values in the range of 98– 130 Hv are located in the upper periphery of the disc annealed at 150 °C (Fig. 8a). Then the microhardness values decrease with increasing annealing temperature due to recrystallization and grain growth. In addition, the microhardness variations became less across the AZ31 and Mg-0.6Gd regions when annealing at higher temperatures. For example, microhardness values were recorded in the range of 35–66 Hv after annealing at 450 °C (see Fig. 8d).

The inhomogeneity factor (IF) [24] was used to evaluate the microstructural inhomogeneity of the hybrid discs as a function of annealing temperature and the estimated IF values are presented in Table 1. The equation for computing IF is given by:

$$IF = \frac{\sqrt{\sum_{i=1}^{n} (Hv_i - Hv_{ave})^2 \Big/ n-1}}{Hv_{ave}} \times 100 \quad (1)$$

where Hv_{ave} and Hv_i are the average microhardness value and the microhardness value of the i^{th} measurement, respectively, and n is the number of microhardness measurements on each disc.

Thus, a microstructure with less variation in the microhardness values exhibits a low IF value [24] and hence the discs annealed at 150 and 250 °C exhibit the highest (36.3%) and the lowest IF (13.8%) values, respectively. The IF value increases slightly to 17% during annealing at 350 and 450 °C indicating a minor increase in hardness variations across the regions.

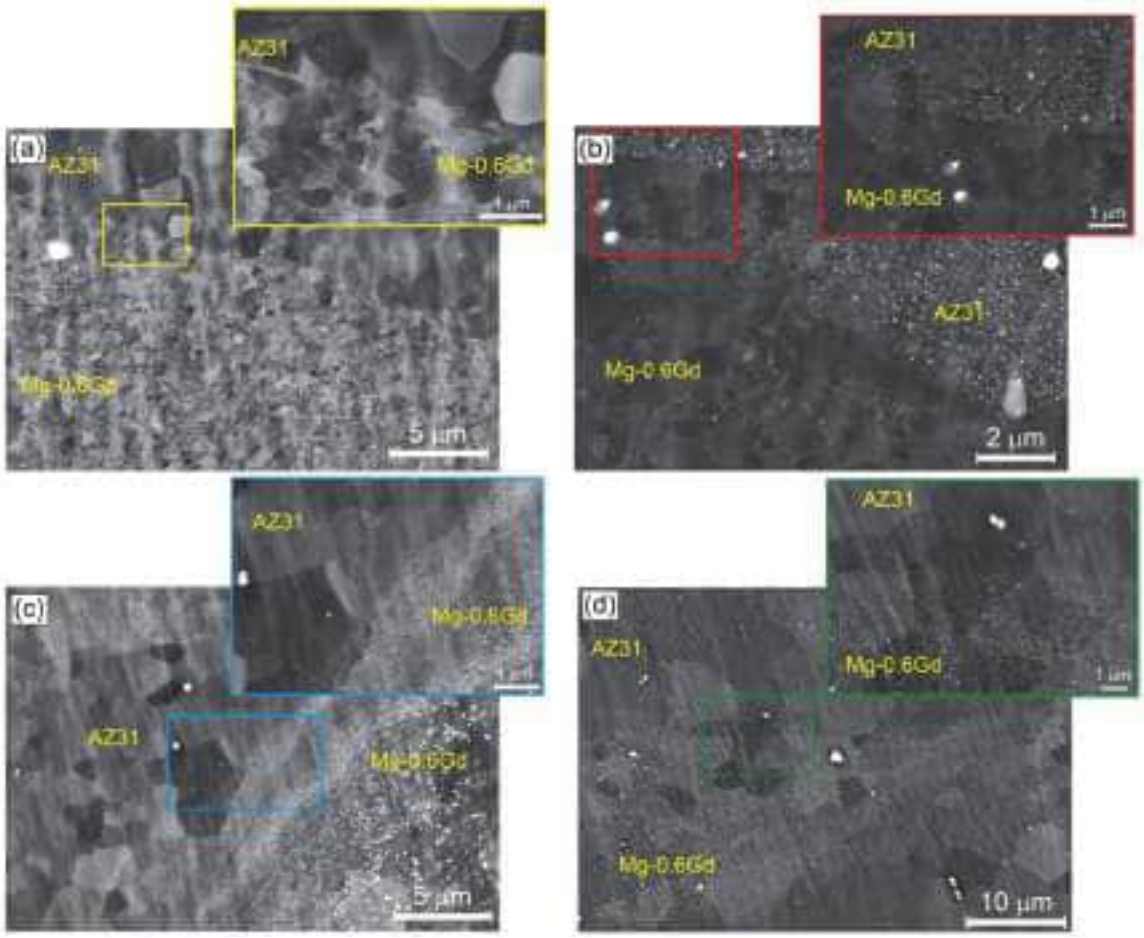

Fig. 5. SEM micrographs with different magnifications near the AZ31/Mg-0.6Gd interfaces after annealing for 1 h at: (a) 150, (b) 250, (c) 350, and (d) 450 °C.

4. Discussion

The present results demonstrate that the microstructure near the interfaces and the microhardness distributions through the disc surfaces become homogeneous over the vertical cross-sections of the hybrid AZ31/Mg-0.6Gd material after HPT followed by annealing with increasing annealing temperature. Nevertheless, the evolution of grain size and texture as a function of annealing temperature is slightly different between the AZ31 and Mg-0.6Gd regions and these separate regions, which form the hybrid alloy, undergo different static recrystallization and grain growth behaviors.

4.1. Microstructure evolution in the annealed AZ31 and Mg-0.6Gd regions

The distinctive outcome from the present investigation is the observation and identification of a large number of precipitates of $Mg_{17}Al_{12}$ and $Mg_{12}Zn$ in the AZ31 region at an annealing temperature of 250 °C and Mg_5Gd and $Mg_{12}Gd$ in the Mg-0.6Gd region at annealing temperatures of 350 and 450 °C. It is well known that the $Mg_{17}Al_{12}$ compound is the only precipitate phase that can develop in Mg-Al alloy even with low Al content such as the AZ31 alloy [25,26]. However, precipitation of the $Mg_{12}Zn$ phase was not reported earlier in the AZ31 alloys under other thermomechanical processing. For the Mg-0.6Gd region, the precipitate phases were not expected after annealing since the alloy contained a very low Gd content (0.6%). According to the Mg-Gd binary phase diagram [27], the precipitation of the Mg_5Gd phase dissolves in the temperature range of 200–500 °C when the Gd content is < 0.6 wt%. Thus, the precipitation sequence in Mg-Gd alloy is usually investigated with Gd concentrations in the range of 10–15 Gd wt% [28–31] and Mg alloys containing Gd concentrations around 1% are investigated in order to avoid the effect of second particles [32,33].

It is known that HPT processing enhances precipitation due to the introduction of a large number of defects, such as dislocations and vacancies, that are preferential sites for precipitate nucleation [34]. However, it is noted that no precipitation was reported in the same Mg-0.6Gd alloy processed by HPT through 5 turns and annealed at 450 °C for 1 h [35]. This led to the conclusion that the strain induced by HPT processing was not sufficient to produce non-equilibrium phases such as Mg_5Gd, $Mg_{12}Gd$ and $Mg_{12}Zn$. In addition to the high strain induced by HPT processing, it was demonstrated that the formation of interface bonding in the HPT-hybrid material by solid diffusion also induced strain that caused a second grain refinement regime [9]. Based on these earlier results, it may be anticipated that not only the accumulation of the high strain for grain refinement during HPT processing but also the formation of bonding of different phases produces a high number of defects, such as vacancies, and this produces an unbalanced segregation of solute atoms and dislocations which act as preferential sites for precipitation nucleation during the annealing treatment. Usually, the precipitation causes an age hardening which could be detected by an increase in the microhardness values. However, it is considered that the $Mg_{17}Al_{12}$ compound plays only a minor role in the strengthening of the AZ31 alloy during conventional deformation due to its low volume fraction [25]. Unfortunately, it was not possible to confirm whether the precipitation of non-equilibrium Mg_5Gd, $Mg_{12}Gd$ and $Mg_{12}Zn$ phases caused an age hardening using the Hv map shown in Fig. 8 since the AZ31 and Mg-0.6Gd regions were not easily identified and their Hv values could not be separated. Nevertheless, Table 1 shows

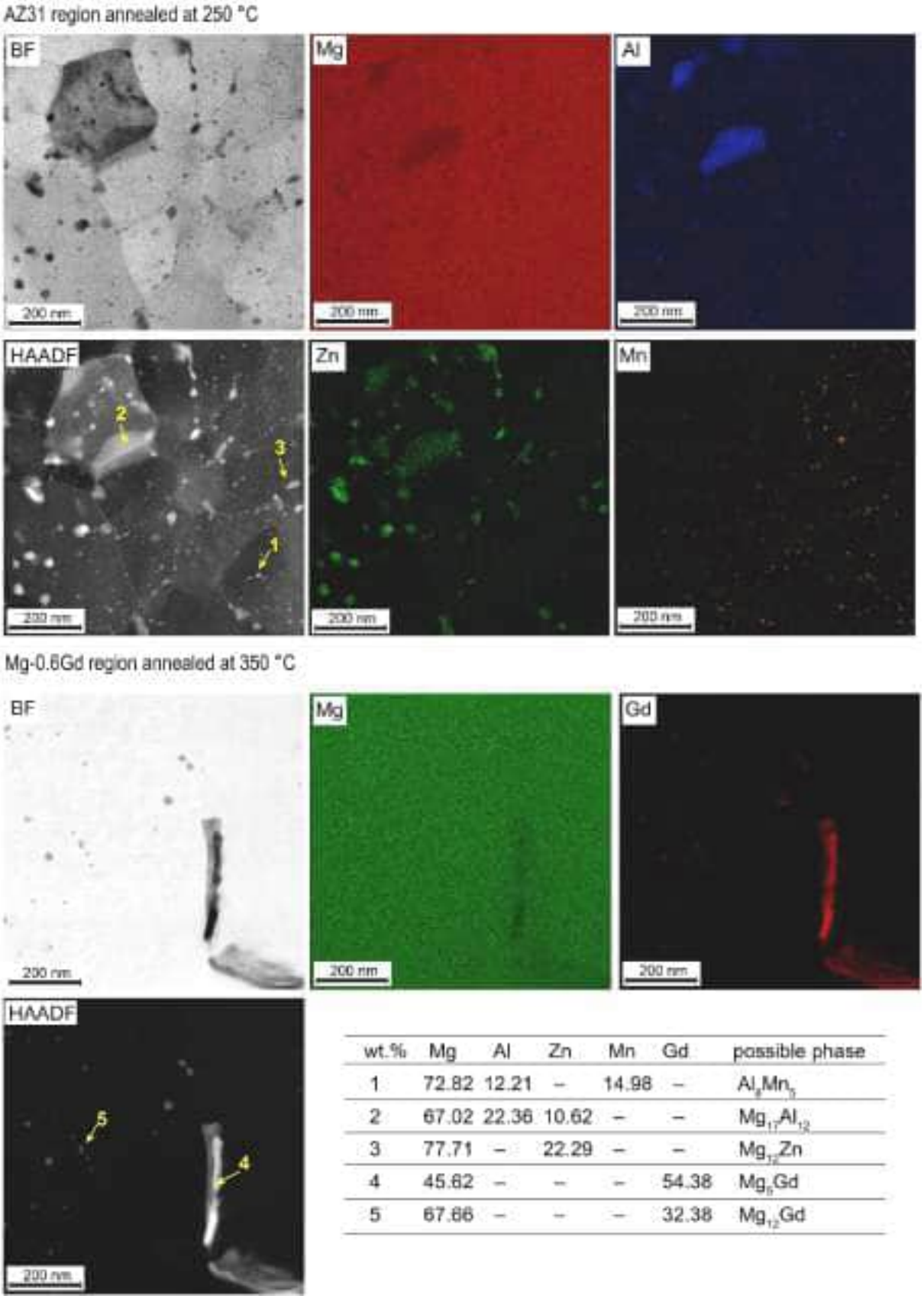

wt.%	Mg	Al	Zn	Mn	Gd	possible phase
1	72.82	12.21	–	14.98	–	Al_8Mn_5
2	67.02	22.36	10.62	–	–	$Mg_{17}Al_{12}$
3	77.71	–	22.29	–	–	$Mg_{12}Zn$
4	45.62	–	–	–	54.38	Mg_5Gd
5	67.66	–	–	–	32.38	$Mg_{12}Gd$

Fig. 6. STEM images in BF and HAADF modes and EDS mapping for Mg, Al, Zn, Mn and Gd elements and EDS analysis of particles present at points 1–5 of the AZ31 region annealed at 250 °C and the Mg-0.6Gd region annealed at 350 °C.

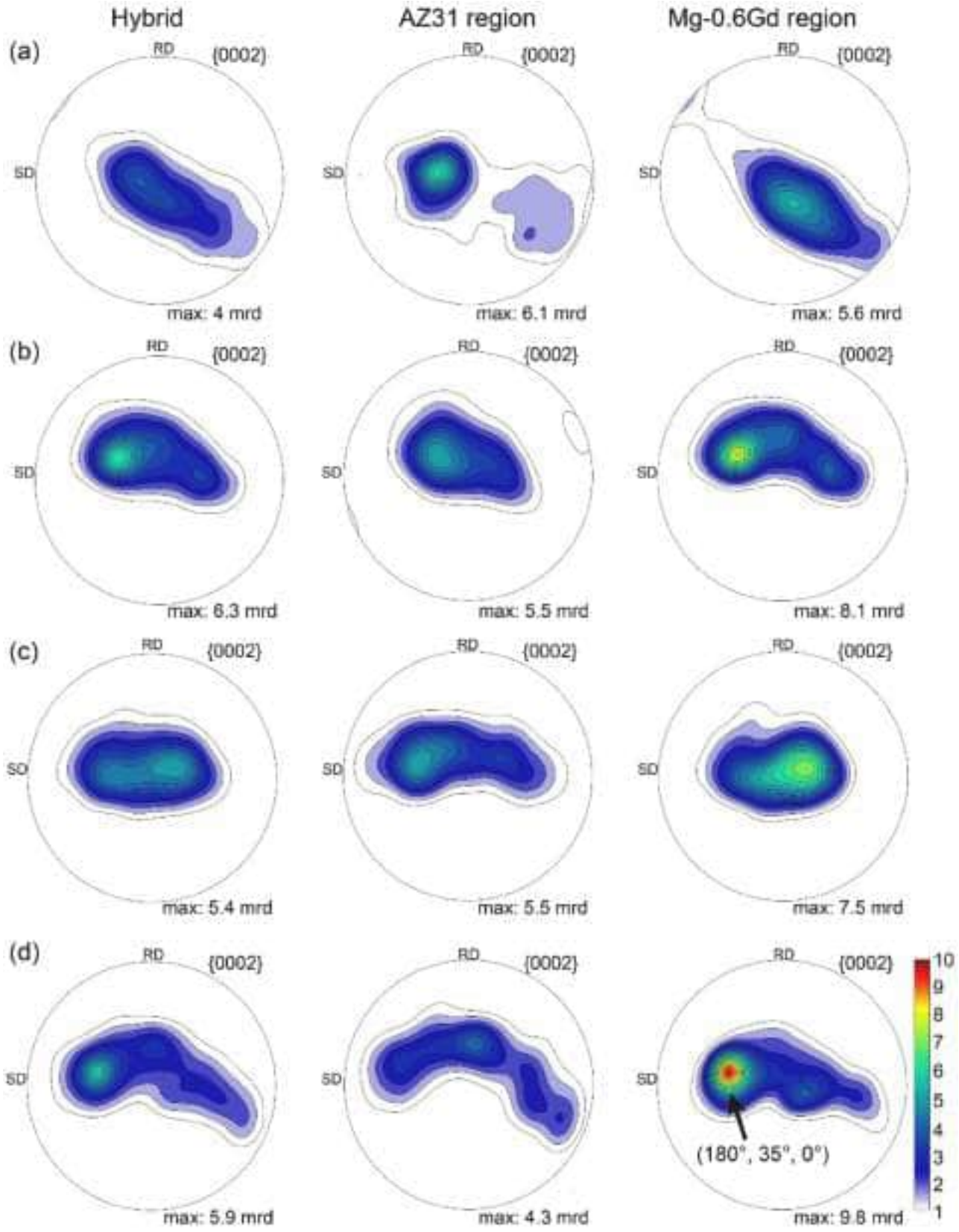

Fig. 7. Recalculated {0002} pole figures of the hybrid AZ31/Mg-0.6Gd material, the AZ31 and the Mg-0.6Gd regions after annealing at: (a) 150, (b) 250, (c) 350, and (d) 450 °C.

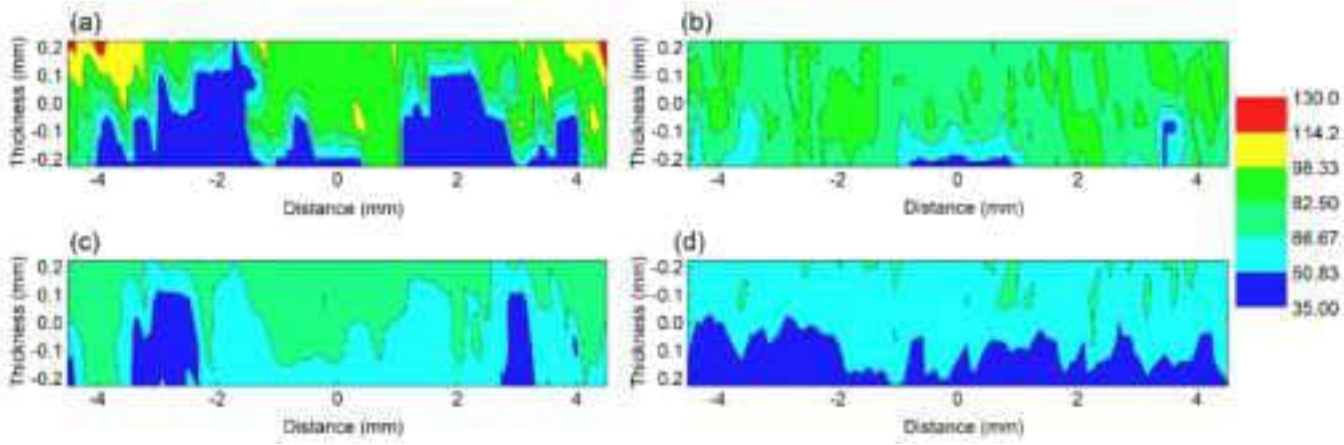

Fig. 8. Color-coded microhardness maps of the hybrid AZ31/Mg-0.6Gd material after annealing for 1 h at: (a) 150, (b) 250, (c) 350, and (d) 450 °C.

Table 1
IF values as a function of annealing temperature.

Temperature (°C)	150	250	350	450
IF (%)	36.3	13.8	17.4	16.9

that the IF of the microhardness distribution increases after annealing at 350 and 450 °C which may be explained by the strengthening of the Mg-0.6Gd region due to precipitation of the Mg_5Gd and $Mg_{12}Gd$ phases.

Precipitation in the AZ31 and Mg-0.6Gd regions plays the main role in controlling the evolution of grain size in both regions and throughout the hybrid material as well. The restricted grain growth noticed at the annealing temperature of 250 °C for the AZ31 region by comparison with the AZ31 region annealed at 150 °C (see Fig. 3) which is mainly attributed to the precipitation of $Mg_{17}Al_{12}$ and $Mg_{12}Zn$ phases. Also, the segregation of Zn element to the grain boundaries as shown in Fig. 6 produces a strong drag effect on grain boundary migration. It is believed that the presence of stable $Mg_{17}Al_{12}$ and Al_8Mn_5 phases are responsible for the small grain size during annealing temperatures superior to 250 °C. As shown in Fig. 6, the majority of the precipitates and the stable phases are nano-sized which prevents the migration of recrystallized grain boundaries and thereby slows the grain growth rate of the recrystallized grains.

A further factor which produces a slow grain growth in the AZ31 region compared with the Mg-0.6Gd region (Fig. 3) is the high content of solute elements in the AZ31 alloy (3% of Al and 1% of Zn). This leads to a significant reduction in the stacking fault energy through the solute–dislocation interaction and produces smaller grain sizes under HPT processing and annealing treatments. Indeed, it was demonstrated that the mean grain size decreases with decreasing stacking fault energy in the deformed material [36].

The presence of Mg_5Gd and $Mg_{12}Gd$ precipitates along the grain boundaries and within the recrystallized grains (Fig. 6) suggests that the precipitation takes place after the static recrystallization. Hence, it is anticipated that the driving force of recrystallization is the stored energy during HPT which plays a major role in the Mg-0.6Gd region where the grain boundaries are only partially pinned by the precipitates. The mean grain size of the Mg-0.6Gd region increases with increasing annealing temperature even with the precipitation of Mg_5Gd and $Mg_{12}Gd$ phases at annealing temperatures of 350 and 450 °C but the mean grain size values remain much smaller (6.5 μm) than those reported for the same alloy under similar HPT processing and annealing conditions without precipitation (~20.1 μm) [35]. It is interesting to note that the AZ31 and Mg-0.6Gd regions have mean gain sizes smaller than 10 μm which suggests the hybrid material is a good candidate for achieving superplasticity [23].

4.2. Texture evolution in the annealed AZ31 and Mg-0.6Gd regions

The AZ31 and Mg-Gd alloys exhibit a retained deformation texture during recrystallization and grain growth phenomena [22,35,37,38]. The present results show that the recrystallization textures of the AZ31 and Mg-0.6Gd regions are different from the deformation texture [9] and also they can be modified with appropriate annealing treatments.

The development of texture in the AZ31 and Mg-0.6Gd regions during isochronal annealing is a consequence of the contributions of dynamic recrystallization (DRX) [19,38–40], precipitation [19,35] and grain growth [41–43]. It was found earlier that the DRX fractions of the AZ31 and Mg-0.6Gd regions near the mid-radii of the hybrid discs processed for 20 HPT turns were 55% and 80%, respectively [9]. This explained the change of the deformation texture from C_1 and C_2 fibres to a deviated basal texture at 150 °C in the case of the AZ31 region while the Mg-0.6Gd region annealed at 150 °C displays a retained deformation texture or deviated basal texture.

In the present study, the precipitation and grain growth in the AZ31 and Mg-0.6Gd regions occurred simultaneously and this made it difficult to separately evaluate their contributions to the texture evolution. Nevertheless, it is believed that the precipitated phases ($Mg_{17}Al_{12}$, $Mg_{12}Zn$, Mg_5Gd and $Mg_{12}Gd$) are the main reasons for the formation of a typical basal texture in the AZ31 region at 250 °C and in the Mg-0.6Gd region at 350 °C (Fig. 7b and c), respectively. The precipitates drag the mobility of different grain boundaries except those of grains with a basal orientation that can preferentially grow during the annealing treatment and this leads to the domination of a basal texture. Indeed, the domination of the basal texture during an annealing treatment was attributed earlier to the high mobility of the grain boundaries of grains with a basal orientation [44]. Thus, the basal texture became more spread along SD with increasing annealing temperature for the AZ31 region, especially at 450 °C, due to the absence of second phase particles and the occurrence of grain growth that allowed the formation of recrystallized grains with different orientations. Annealing at high temperatures such as 450 °C provides the necessary energy for migration of the random high-angle grain boundaries, leading to uniform growth of recrystallized grains with different orientations rather than the basal orientation. In addition, the fraction of sub-grain boundaries decreases significantly during high annealing temperatures, as shown in Fig. 4(d). The sub-grain boundaries have low mobility energy and hence high temperature such as 450 °C gives these boundaries the opportunity to gradually transform into high-angle grain boundaries and form new grains. This process is known as continuous static recrystallization with the formed grains usually exhibiting different orientations [45]. The spread of basal texture for the Mg-0.6Gd region at 450 °C is less intense than in the AZ31 region due to the concurrent effects of precipitation and grain growth.

The present findings provide a clear demonstration that the

application of various annealing temperatures produces unique microstructural pathways for these hybrid Mg alloys from well-defined phase boundaries to homogeneous microstructures with texture modifications. Thus, this study provides a critical initiative for using thermal treatments in the design and manufacture of Mg alloys and hybrids for different applications and opportunities.

5. Summary and conclusions

The evolution of microstructure, texture and Vickers microhardness in a hybrid AZ31/Mg-0.6Gd material fabricated by HPT through 20 turns was successfully characterized after isochronal annealing at 150, 250, 350 and 450 °C for 1 h. The main finding are as follows:

- The AZ31/Mg-0.6Gd interface disappeared during annealing temperatures higher than 350 °C where significant grain growth took place. In addition, the distributions of microhardness through the cross-sections of the discs became more homogeneous.
- The strain induced by HPT processing and interface bonding enhanced solute diffusion and caused the development of precipitation in the AZ31 and Mg-0.6Gd regions.
- Nano-sized stable particles of Al_8Mn_5 and precipitation of $Mg_{17}Al_{12}$ and $Mg_{12}Zn$ in the AZ31 region and precipitations of Mg_5Gd and $Mg_{12}Gd$ phases in the Mg-0.6Gd region contribute to a slowing in grain growth in the hybrid material.
- The distributions of basal texture in the AZ31 and Mg-0.6Gd regions throughout the annealing treatment of both regions was controlled by DRX, precipitation and grain growth.

CRediT authorship contribution statement

Huang Yi: Methodology. **Bazarnik Piotr:** Software, Methodology, Investigation. **Baudin Thierry:** Visualization, Methodology, Conceptualization. **Azzeddine Hiba:** Writing – review & editing, Writing – original draft, Conceptualization. **Kawasaki Megumi:** Software, Methodology. **Brisset François:** Software, Methodology. **Langdon Terence G.:** Writing – review & editing, Supervision. **Ould Mohamed Ouarda:** Investigation.

Declaration of Competing Interest

The authors declare that they have no known competing financial interests or personal relationships that could have appeared to influence the work reported in this paper.

Data Availability

Data will be made available on request.

Acknowledgements

Dr-Ing. N. Hort and Dr. D. Letzig (MagIC, Germany) and Dr-Ing. Talal Al-Samman (RWTH-Aachen University, Germany) are gratefully acknowledged for providing the AZ31 and Mg-0.6Gd alloys, respectively. YH and TGL were supported by the European Research Council under Grant Agreement No. 267464-SPDMETALS. MK was supported by the National Science Foundation of the United States under Grant No. CMMI-2051205.

References

[1] V. Rana, H. Kumar, A. Kumar, Fabrication of hybrid metal matrix composites (HMMCs) – A review of comprehensive research studies, Mater. Today.: Proc. 56 (2022) 3102–3107.
[2] C. Suryanarayana, Mechanical alloying: a critical review, Mater. Res. Lett. 10 (10) (2022) 619–647.
[3] R.S. Mishra, Z.Y. Ma, I. Charit, Friction stir processing: a novel technique for fabrication of surface composite, Mater. Sci. Eng.: A 341 (1) (2003) 307–310.
[4] M. Kawasaki, J.-K. Han, D.-H. Lee, J.-i Jang, T.G. Langdon, Fabrication of nanocomposites through diffusion bonding under high-pressure torsion, J. Mater. Res. 33 (18) (2018) 2700–2710.
[5] J.-K. Han, T. Herndon, J.-i Jang, T.G. Langdon, M. Kawasaki, Synthesis of hybrid nanocrystalline alloys by mechanical bonding through high-pressure torsion, Adv. Eng. Mater. 22 (4) (2020) 1901289.
[6] D. Hernández-Escobar, M. Kawasaki, C.J. Boehlert, Metal hybrids processed by high-pressure torsion: synthesis, microstructure, mechanical properties and developing trends, Int. Mater. Rev. 67 (3) (2022) 231–265.
[7] N. Stanford, M.D. Callaghan, B. de Jong, The effect of rare earth elements on the behaviour of magnesium-based alloys: Part 1—Hot deformation behaviour, Mater. Sci. Eng.: A 565 (2013) 459–468.
[8] O.Ould Mohamed, P. Bazarnik, Y. Huang, H. Azzeddine, T. Baudin, F. Brisset, T. G. Langdon, A comparative study between AZ31 and Mg-Gd alloys after high-pressure torsion, J. Mater. Eng. Perform. (2023).
[9] O. Ould Mohamed, H. Azzeddine, Y. Huang, T. Baudin, P. Bazarnik, F. Brisset, M. Kawasaki, T.G. Langdon, Investigation of microstructure and texture evolution in an AZ31/Mg–Gd alloy hybrid metal fabricated by high-pressure torsion, Adv. Eng. Mater. 25 (11) (2023) 2201794.
[10] J. Song, J. She, D. Chen, F. Pan, Latest research advances on magnesium and magnesium alloys worldwide, J. Magnes. Alloy. 8 (1) (2020) 1–41.
[11] M.P. Medeiros, D.R. Lopes, M. Kawasaki, T.G. Langdon, R.B. Figueiredo, An overview on the effect of severe plastic deformation on the performance of magnesium for biomedical applications, Materials 16 (6) (2023) 2401.
[12] P. Bazarnik, A. Bartkowska, Y. Huang, K. Szlązak, B. Adamczyk-Cieślak, J. Sort, M. Lewandowska, T.G. Langdon, Fabrication of hybrid nanocrystalline Al–Ti alloys by mechanical bonding through high-pressure torsion, Mater. Sci. Eng.: A 833 (2022) 142549.
[13] S.O. Rogachev, R.V. Sundeev, V.M. Khatkevich, Evolution of the structure and strength of steel/vanadium alloy/steel hybrid material during severe plastic deformation, Mater. Lett. 173 (2016) 123–126.
[14] D. Hernández-Escobar, R.R. Unocic, M. Kawasaki, C.J. Boehlert, High-pressure torsion processing of Zn–3Mg alloy and its hybrid counterpart: a comparative study, J. Alloy. Compd. 831 (2020) 154891.
[15] R. Hielscher, H. Schaeben, A novel pole figure inversion method: specification of the MTEX algorithm, J. Appl. Crystallogr. 41 (6) (2008) 1024–1037.
[16] J. Stráská, M. Janeček, J. Čížek, J. Stráský, B. Hadzima, Microstructure stability of ultra-fine grained magnesium alloy AZ31 processed by extrusion and equal-channel angular pressing (EX–ECAP), Mater. Charact. 94 (2014) 69–79.
[17] R.L. Doiphode, S.V.S.N. Murty, N. Prabhu, B.P. Kashyap, Grain growth in calibre rolled Mg–3Al–1Zn alloy and its effect on hardness, J. Magnes. Alloy. 3 (4) (2015) 322–329.
[18] M. Roostaei, M. Shirdel, M.H. Parsa, R. Mahmudi, H. Mirzadeh, Microstructural evolution and grain growth kinetics of GZ31 magnesium alloy, Mater. Charact. 118 (2016) 584–592.
[19] S. Tighiouaret, R. Lachhab, A. Hanna, H. Azzeddine, Y. Huang, T. Baudin, A.-L. Helbert, F. Brisset, D. Bradai, T.G. Langdon, Thermal stability of an Mg–Nd alloy processed by high-pressure torsion, Adv. Eng. Mater. 21 (12) (2019) 1900801.
[20] A. Morawiec, Misorientation-angle distribution of randomly oriented symmetric objects, J. Appl. Crystallogr. 28 (3) (1995) 289–293.
[21] J.A. del Valle, M.T. Pérez-Prado, O.A. Ruano, The distribution of disorientation angles in a rolled AZ31 Mg alloy, Rev. De. Metal. 38 (5) (2002) 353–357.
[22] S. Sadi, A. Hanna, T. Baudin, A.-L. Helbert, F. Brisset, D. Bradai, H. Azzeddine, Evaluation of static recrystallization and grain growth kinetics of hot-rolled AZ31 alloy, J. Met., Mater. Miner. 32 (1) (2022) 12–26.
[23] L.R.C. Malheiros, R.B. Figueiredo, T.G. Langdon, Grain size and microhardness evolution during annealing of a magnesium alloy processed by high-pressure torsion, J. Mater. Res. Technol. 4 (1) (2015) 14–17.
[24] S. Sadi, A. Hanna, H. Azzeddine, C. Casas, T. Baudin, A.-L. Helbert, F. Brisset, J. M. Cabrera, Characterization of microstructure and texture of binary Mg-Ce alloy processed by equal channel angular pressing, Mater. Charact. 181 (2021) 111454.
[25] X. Li, F. Jiao, T. Al-Samman, S. Ghosh Chowdhury, Influence of second-phase precipitates on the texture evolution of Mg–Al–Zn alloys during hot deformation, Scr. Mater. 66 (3) (2012) 159–162.
[26] E. Dogan, S. Wang, M.W. Vaughan, I. Karaman, Dynamic precipitation in Mg-3Al-1Zn alloy during different plastic deformation modes, Acta Mater. 116 (2016) 1–13.
[27] L.L. Rokhlin. Magnesium Alloys Containing Rare Earth Metals: Structure and Properties, First ed., CRC Press, London, 2003.
[28] X. Gao, S.M. He, X.Q. Zeng, L.M. Peng, W.J. Ding, J.F. Nie, Microstructure evolution in a Mg–15Gd–0.5Zr (wt%) alloy during isothermal aging at 250°C, Mater. Sci. Eng.: A 431 (1) (2006) 322–327.
[29] H. Zhou, W.Z. Xu, W.W. Jian, G.M. Cheng, X.L. Ma, W. Guo, S.N. Mathaudhu, Q. D. Wang, Y.T. Zhu, A new metastable precipitate phase in Mg–Gd–Y–Zr alloy, Philos. Mag. 94 (21) (2014) 2403–2409.
[30] J.K. Zheng, R. Luo, X. Zeng, B. Chen, Nano-scale precipitation and phase growth in Mg-Gd binary alloy: An atomic-scale investigation using HAADF-STEM, Mater. Des. 137 (2018) 316–324.
[31] Y. Zhang, W. Rong, Y. Wu, L. Peng, J.-F. Nie, N. Birbilis, A detailed HAADF-STEM study of precipitate evolution in Mg–Gd alloy, J. Alloy. Compd. 777 (2019) 531–543.
[32] N. Stanford, D. Atwell, M.R. Barnett, The effect of Gd on the recrystallisation, texture and deformation behaviour of magnesium-based alloys, Acta Mater. 58 (20) (2010) 6773–6783.

[33] W.X. Wu, L. Jin, F.H. Wang, J. Sun, Z.Y. Zhang, W.J. Ding, J. Dong, Microstructure and texture evolution during hot rolling and subsequent annealing of Mg–1Gd alloy, Mater. Sci. Eng.: A 582 (2013) 194–202.
[34] H. Azzeddine, B. Mehdi, L. Hennet, D. Thiaudière, B. Alili, M. Kawasaki, D. Bradai, T.G. Langdon, An in situ synchrotron X-ray diffraction study of precipitation kinetics in a severely deformed Cu–Ni–Si alloy, Mater. Sci. Eng.: A 597 (2014) 288–294.
[35] H. Azzeddine, A. Hanna, A. Dakhouche, T. Baudin, F. Brisset, Y. Huang, T. G. Langdon, Evaluation of thermal stability and its effect on the corrosion behaviour of Mg-RE alloys processed by high-pressure torsion, Crystals 13 (4) (2023) 662.
[36] Y.H. Zhao, X.Z. Liao, Y.T. Zhu, Z. Horita, T.G. Langdon, Influence of stacking fault energy on nanostructure formation under high pressure torsion, Mater. Sci. Eng.: A 411 (2005) 188–193, 410.
[37] N. Stanford, The effect of rare earth elements on the behaviour of magnesium-based alloys: Part 2 – recrystallisation and texture development, Mater. Sci. Eng.: A 565 (2013) 469–475.
[38] S. Tighiouaret, A. Hanna, H. Azzeddine, L. Rabahi, A. Dakhouche, F. Brisset, A.-L. Helbert, T. Baudin, D. Bradai, On the evolution of microstructure, texture and corrosion behavior of a hot-rolled and annealed AZ31 alloy, Mater. Chem. Phys. 267 (2021) 124598.
[39] H. Azzeddine, D. Bradai, T. Baudin, T.G. Langdon, Texture evolution in high-pressure torsion processing, Prog. Mater. Sci. 125 (2022) 100886.
[40] S. Sadi, A. Hanna, T. Baudin, F. Brisset, J.M. Cabrera, H. Azzeddine, Microstructure and texture evolution of ECAP-processed Mg-Ce alloy during isothermal annealing, Mater. Today Commun. 32 (2022) 103920.
[41] J.J. Bhattacharyya, B. Radhakrishnan, G. Muralidharan, S.R. Agnew, Texture Evolution During Grain Growth of Magnesium Alloy AZ31B, in: M. Alderman, M. V. Manuel, N. Hort, N.R. Neelameggham (Eds.), Magnesium Technology 2014, Springer International Publishing, Cham, 2016, pp. 233–238.
[42] D. Panda, R.K. Sabat, S. Suwas, V.D. Hiwarkar, S.K. Sahoo, Texture weakening in pure magnesium during grain growth, Philos. Mag. 99 (11) (2019) 1362–1385.
[43] L.Y. Zhao, H. Yan, R.S. Chen, E.-H. Han, The preferential growth and related textural evolution during static recrystallization in a cold-rolled Mg–Zn–Gd alloy, J. Magnes. Alloy. 9 (3) (2021) 818–828.
[44] F. Guo, R. Pei, L. Jiang, D. Zhang, S. Korte-Kerzel, T. Al-Samman, The role of recrystallization and grain growth in optimizing the sheet texture of magnesium alloys with calcium addition during annealing, J. Magnes. Alloy. 8 (1) (2020) 252–268.
[45] X. Yang, Y. Okabe, H. Miura, T. Sakai, Annealing of a magnesium alloy AZ31 after interrupted cold deformation, Mater. Des. 36 (2012) 626–632 (1980-2015).

Thermochimica Acta 738 (2024) 179805

Contents lists available at ScienceDirect

Thermochimica Acta

journal homepage: www.elsevier.com/locate/tca

Recrystallization and grain growth activation energies in a hybrid magnesium material fabricated by high-pressure torsion

Hiba Azzeddine [a,*], Marie-Noëlle Avettand-Fènoël [b], Piotr Bazarnik [c], Thierry Baudin [d], Yi Huang [e,f], Terence G. Langdon [e]

[a] Laboratory of Materials and Renewable Energy, Faculty of Sciences, Mohamed Boudiaf University, M'sila 28000, Algeria
[b] UMET - Unité Matériaux Et Transformations, Universite Lille, CNRS, INRAE, Centrale Lille, UMR 8207, Lille F-59000, France
[c] Faculty of Materials Science and Engineering, Warsaw University of Technology, Woloska 141, 02-507, Poland
[d] Université Paris-Saclay, CNRS, Institut de chimie moléculaire et des matériaux d'Orsay, Orsay 91405, France
[e] Materials Research Group, Department of Mechanical Engineering, University of Southampton, Southampton SO17 1BJ, UK
[f] Department of Design and Engineering, Faculty of Science and Technology, Bournemouth University, Poole, Dorset BH12 5BB, UK

ARTICLE INFO

Keywords:
Activation energy
Grain growth
High-pressure torsion
Magnesium
Recrystallization

ABSTRACT

The recrystallization and grain growth activation energies of the hybrid AZ31/Mg-0.6Gd (wt.%) alloy were calculated using differential scanning calorimetry analyses and scanning electron microscopy, respectively, after fabricating by high-pressure torsion up to 20 turns and then subjecting to an isochronal annealing treatment from 423 to 723 K for 1 h. The DSC results show one exothermic peak belonging to the static recrystallization of the AZ31 region with an activation energy of 112 ± 10 kJ/mol. The grain growth kinetics for the AZ31 and Mg-0.6Gd regions were described by the Arrhenius equation. The calculation with a grain growth exponent equal to 4 gave values for the activation energies in both the AZ31 (146.2 ± 8.4 kJ/mol) and Mg-0.6Gd (90.9 ± 13.5 kJ/mol) regions. The present results reveal the heterogeneity of the thermal stability of the AZ31/Mg-0.6Gd hybrid material.

1. Introduction

At the present time the use of metal-matrix composites is gradually increasing in various industries such as transportation and construction owing to their superior properties compared to the use of single materials [1]. From an economic and environmental point of view, magnesium (Mg) based composites attract much attention from both the academic and industrial communities due to their combination of high strength and lightweight structure [2]. Moreover, the biocompatibility and biodegradable characteristics of Mg-based alloys make them excellent potential candidate materials for use in biological applications such as temporary implants [3–5].

Severe plastic deformation (SPD) techniques, particularly processing by high-pressure torsion (HPT), is now considered one of the most effective production routes for fabricating metal-matrix composites at room temperature (RT) [6]. In the production of bulk ultrafine-grained materials, the high hydrostatic compressive stress combined with high shear deformation under HPT processing permit the successful bonding of particles through a solid state reaction without any sample cracking. For example, dense bulk Mg-Al_2O_3 and Mg-hydroxyapatite composites were produced with better mechanical properties and corrosion resistance than pure Mg by applying HPT processing through 5 turns at a pressure of 6 GPa [7–9] and the production of dense AZ91-Al_2O_3 composite bulk discs needed 20 turns of HPT processing at the same pressure of 6 GPa [10]. By contrast, HPT processing through 50 turns failed to consolidate an AZ91-bioactive glass composite due to sliding between the particles and strain localization [8].

Processing by HPT is important also for producing Mg hybrid materials by stacking different discs together including Al/Mg [11–14], Zn/Mg [15–18] and the AZ31(Mg-3Al-1 Zn, wt.%)/Mg-0.6Gd (wt.%) [19-21] systems. Diffusion bonding induced by HPT processing is capable of improving the mechanical properties of the hybrid systems by a combination of grain refinement and the creation of microstructural heterogeneities such as a segregation of alloying elements at defects, precipitation and the formation of unexpected intermetallic phases at RT [15,16,20].

Despite the numerous reports describing the fabrication of new generations of Mg-based composites [7-21], neither the deformation and

* Corresponding author.
E-mail address: hiba.azzeddine@univ-msila.dz (H. Azzeddine).

https://doi.org/10.1016/j.tca.2024.179805
Received 17 May 2024; Received in revised form 17 June 2024; Accepted 18 June 2024
Available online 19 June 2024

the thermal stability behaviour nor the corresponding mechanisms controlling the microstructural evolution and mechanical properties of these composites are fully understood. This is a significant limitation since the recrystallization and grain growth kinetics of composite materials is a key factor for controlling their mechanical properties in order to meet the requirements for industrial applications. Accordingly, the present research was initiated to contribute towards this understanding by determining the activation energies for recrystallization and grain growth in a hybrid AZ31-Mg-0.6Gd (wt.%) material by fabricating using HPT processing for 20 turns under a pressure of 6.0 GPa.

2. Experimental material and procedures

AZ31 and Mg-0.6Gd discs of 10 mm diameter and 0.85 mm thickness were processed together by HPT at RT for a total of 20 turns under an applied pressure of 6.0 GPa using a rotational speed of 1 rpm and quasi-constrained conditions [22]. The HPT-processed discs were then exposed to isochronal annealing for 1 h at 423, 523, 623 and 723 K in a radiation furnace. More details on the AZ31 and Mg-0.6Gd alloys, and specifically the microstructural evolution and mechanical properties of the hybrid material under HPT processing and annealing conditions, were given in earlier reports [19–21].

Microstructural observations near the AZ31 and Mg-0.6Gd interface of the annealed samples were performed using a scanning electron microscope (SEM) Hitachi Su8000, Hitachi High-Tech corporation, Tokyo, Japan, operating in back-scattered electron (BSE) mode. Complementary microstructural observations on the AZ31 and Mg-0.6Gd regions of the annealed samples at 523 and 623 K were performed in bright-field (BF) and high-angle annular dark field (HAADF) modes using a scanning transmission electron microscope (STEM) Spectra 200, Thermo Fisher Scientific, Massachusetts, U.S., operating at an accelerating voltage of 200 kV. Structural investigations were combined with advanced energy dispersive X-Ray (EDX) point and mapping analyses. More details on the sample preparations for SEM and STEM characterization are given elsewhere [20].

The DSC analyses were performed using alumina crucibles in a DSC 404 calorimeter Netzsch GmbH, Dardilly, France, under an Argon atmosphere and over a temperature range between 298 and 623 K. The DSC analyses of the processed hybrid material with a mass of 15.5 mg were conducted with constant heating rates of 5, 10 and 15 K/min. For comparison, DSC scans under a heating rate of 10 K/min were performed for the AZ31 (18.6 mg) and Mg-0.6Gd (12.6 mg) alloys processed by HPT separately for 20 turns.

3. Experimental results and discussion

3.1. Recrystallization activation energy

Fig. 1a shows the DSC curves of the hybrid material at heating rates of 5, 10 and 15 K/min. All curves display one exothermic (heat-releasing) peak (named 1) corresponding to the recrystallization process and one endothermic (heat-absorbing) peak (named 2) indicating the dissolution of precipitates. Fig. 1b shows the DSC curves at a heating rate of 10 K/min for the AZ31 and Mg-0.6Gd alloys after HPT processing separately. As can be seen, the DSC curve of the HPT-processed AZ31 alloy shows the presence of one exothermic peak and a small endothermic peak is evident in the enlarged curve between 593 and 423 K shown in Fig. 1b. In this case, the exothermic peak is attributed to a static recrystallization process and the endothermic peak corresponds to the dissolution of the $Mg_{17}Al_{12}$ phase. The peak temperature for the

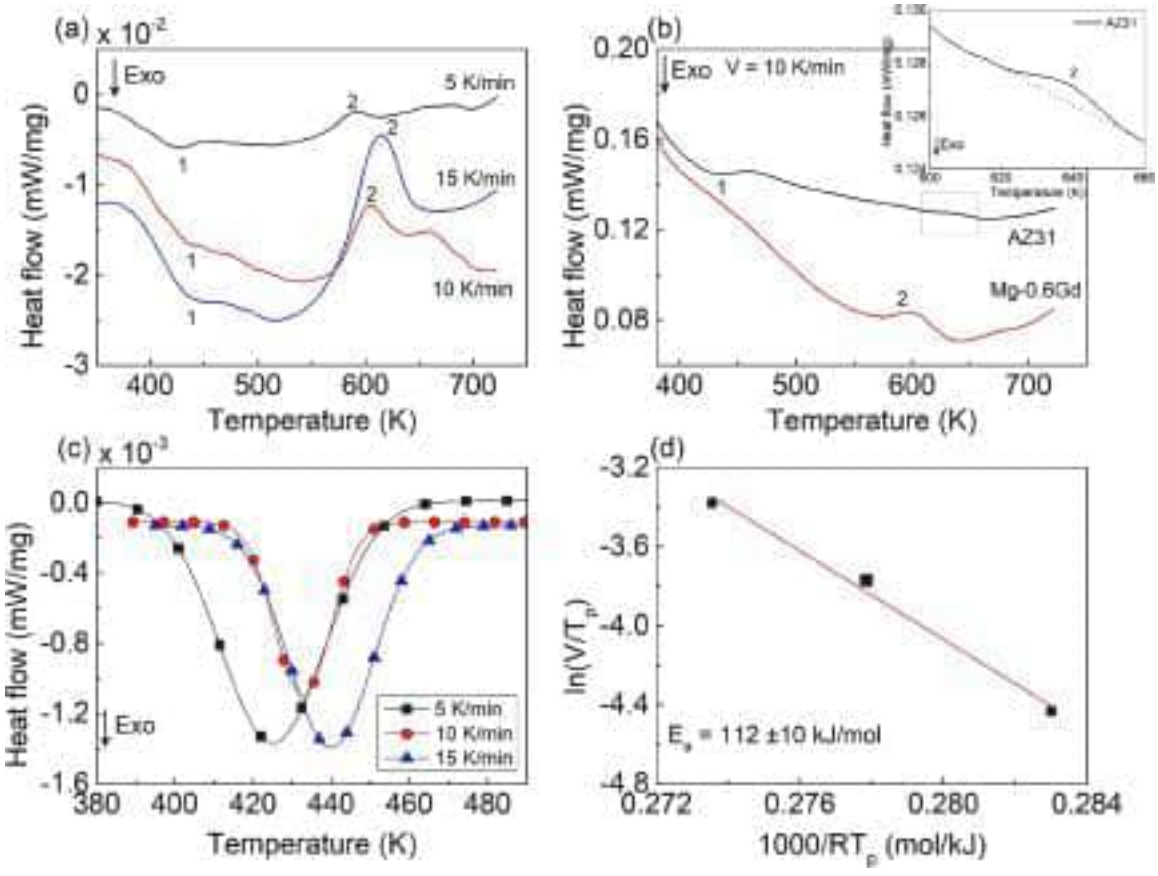

Fig. 1. (a) DSC curves of hybrid material measured at heating rates of 5, 10 and 15 K/min, (b) DSC curves measured at a rate of 10 K/min for separate HPT-processed AZ31 and Mg-0.6Gd alloys, (c) recrystallization peak with baseline subtraction of the hybrid material at heating rates of 5, 10 and 15 K/min and (d) determination of the activation energy for recrystallization of the hybrid material.

dissolution of this phase is around 639 K which is lower than the usual report of 684 K for the AZ31 alloy [23]. This reduction in the dissolution temperature is mainly attributed to the effect of the severe plastic deformation. Indeed, the large numbers of grain boundaries resulting from the grain refinement and the high density of dislocations and vacancies induced by the SPD processing strongly disturbs the mobility of the solute atoms and therefore affects the sequence and precipitation kinetics [24–26]. By contrast, the DSC curve of the HPT-processed Mg-0.6Gd alloy in Fig. 1b indicates the presence of only one endothermic peak which is consistent with the dissolution of phases. Based on the equilibrium phase diagram of the Mg-Gd system, these could be the Mg_5Gd and $Mg_{12}Gd$ phases [27]. The absence of an exothermic peak for the Mg-0.6Gd alloy, even if the alloy undergoes HPT processing, is explained since the grains were already recrystallized during deformation due to the occurrence of extensive dynamic recrystallization (DRX). Indeed, it was reported earlier that DRX was enhanced in the Mg-0.6Gd alloy (80 %) by comparison with the AZ31 alloy (58 %) under HPT processing [19,28]. It must be mentioned that, unlike the traditional AZ31 alloy, the DRX process is usually retarded in RE-containing Mg alloys during thermomechanical processing such as extrusion [29], hot-rolling [30,31] and plane strain compression [32–34]. It is believed that the RE elements play a key role by pinning the grain boundary mobility and reducing the stacking fault energy of the alloy which changes significantly the recovery process [30,35]. However, the reversal deformation behavior between AZ31 and Mg-0.6Gd alloys during HPT processing was related to the manner in which the alloys stored the energy induced by the high strain, the amount and the distribution of second phases (stable nano-sized $Mg_{17}Al_{12}$ and Al_8Mn_5 phases vs. the fragmentation of Mg_5Gd phase) and the concentration of alloying elements (3 % Al and 1% Zn vs. 0.6 % Gd element) [28].

Thus, it is concluded that the exothermic peak shown in the hybrid material in Fig. 1a is essentially due to the recrystallization of the AZ31 region while the endothermic peak is due to a combined precipitate dissolution of the $Mg_{17}Al_{12}$ and Mg_5Gd/$Mg_{12}Gd$ phases in both the AZ31 and Mg-0.6Gd regions, respectively. In the following, therefore, only the recrystallization peak is taken into account and the dissolution of the precipitate phases remains a subject for future investigation.

Fig. 1c presents the recrystallization peak after baseline subtraction of the hybrid material at heating rates of 5, 10 and 15 K/min. The corresponding values of the maximum temperature of the recrystallization peak, T_p, increases with increasing heating rate in the sequence of 150, 433 and 440 K at 5, 10 and 15 K/min, respectively. The shifting of the recrystallization peak towards higher temperatures with increasing heating rate means that the recrystallization phenomenon is a thermally-activated process. It is important to note that comparable findings were also reported for deformed Mg-based alloys such as the hot-rolled Mg-1.3La (wt.%) [31], HPT-processed Mg-1.4Nd (wt.%) [36] and Mg-0.4Dy (wt.%) [37] alloys.

The Boswell-Kissinger method was used to evaluate the activation energy for recrystallization according to the following equation [38]:

$$ln\left(\frac{V}{T_p}\right) = C - \frac{E_a}{RT_p} \quad (1)$$

where V is the heating rate, C is a constant, R is the universal gas constant and E_a is the activation energy for recrystallization. It follows that the value of E_a corresponds to the slope of $\ln(V/T_p)$ plotted as a function of $1000/RT_p$ of the recrystallization peak of the hybrid material, as shown in Fig. 1d.

The activation energy for recrystallization of the hybrid material was estimated as 112 ± 10 kJ/mol which falls between the activation energy for boundary self-diffusion in Mg (~92 kJ/mol) [39] and the activation energy for lattice self-diffusion in Mg (~135 kJ/mol) [39]. Based on the reported results, the activation energy for recrystallization in the AZ31 alloy under conventional deformation such as hot-rolling and cold-drawing is in the range of 69–88 kJ/mol [40–42]. It is interesting to note the activation energies for recrystallization in these earlier reports [40–42] were obtained by means of the Johnson-Mehl-Avrami-Kolmogorov model where isothermal annealing treatments were performed. For example, an activation energy of 85.9 kJ/mol was estimated for the cold-drawn AZ31 alloy at annealing temperatures ranging from 483 to 573 K and holding times ranging from 30 min to 8 h [40].

It was demonstrated earlier that the presence of nano-sized Al_8Mn_5 (~10 nm) and $Mg_{17}Al_{12}$ (~10–40 nm) phases in the microstructure of the HPT-processed AZ31 alloy inhibited the grain boundary motion during the annealing treatments leading to a delay for the static recrystallization process [20]. It is believed that the relative high activation energy obtained for the static recrystallization process is a consequence of the presence of second phases and is indicative of the good thermal stability of the hybrid material.

The activation energy for recrystallization in HPT-processed Mg-1.4Ce (wt.%) alloy calculated by DSC analysis was found to decrease with increasing numbers of HPT turns and the values range from 87.48 to 72.33 kJ/mol for N = 1/2 and 10 turns, respectively [43]. The decrease in activation energy was attributed to the increase in stored energy and the number of recrystallization nucleation sites, such as grain boundaries and dislocations, with increasing numbers of HPT turns [36,43]. A similar observation was reported for the hot-rolled Mg-1.3La (wt.%) alloy, where the activation energy decreased slightly from 112 to 97 kJ/mol after 20 and 50 % of thickness reduction, respectively [31].

3.2. Grain growth activation energy

Fig. 2 shows SEM images near the AZ31 and Mg-0.6Gd interfaces of the hybrid material after isochronal annealing for 1 h at 423, 523, 623 and 723 K. The interface between the AZ31 and Mg-0.6Gd regions are identified by dashed yellow lines in each SEM micrograph. The corresponding mean grain size in the annealed AZ31 and Mg-0.6Gd regions is displayed in Fig. 2e where the linear intercept method was used to determine these mean grain sizes.

In addition, EDS mapping for Al, Zn and Mn elements of selected areas in the AZ31 region annealed at 523 K (Fig. 2b) shows the $Mg_{17}Al_{12}$, Mg_2Zn and Al_8Mn_5 phases and the STEM image in the HAADF mode of the selected area in the Mg-0.6Gd region annealed at 623 K shows $Mg_{12}Gd$ and Mg_5Gd phases (Fig. 2c).

The mean grain sizes based on the SEM micrographs of the AZ31 and Mg-06Gd regions after HPT processing was reported earlier as 0.30 ± 0.03 and 0.34 ± 0.02 μm, respectively [19]. As can be seen from Fig. 2a and e, the grain size of the AZ31 region increased after annealing at 423 K to ~1.1 ± 0.5 μm and then decreased after annealing at 523 K to ~0.35 ± 0.6 μm because of the precipitation of a large $Mg_{17}Al_{12}$ phase (~ 50–90 nm) and a small (~40 nm) phase as evident in the EDS map shown in Fig. 2b. As mentioned above, the deformation microstructure of the AZ31 region exhibited already nano-sized Al_8Mn_5 and $Mg_{17}Al_{12}$ particles [19,28]. In practice, the presence of these nano-sized particles was the main reason for restricting the DRX in the HPT-processed AZ31 alloy [19,28]. Fig. 2c and the results reported previously [20] show that precipitation does not develop in the AZ31 region after annealing at 623 and 723 K and this leads to grain growth.

In the case of the Mg-0.6Gd region, the grain size increased slowly from ~0.41 ± 0.2 to ~0.75 ± 0.2 μm after annealing at 423 and 523 K, respectively. Subsequently, the microstructure exhibits a notable grain growth at higher temperatures. The mean grain size increases significantly at an annealing temperature of 623 K to ~2.10 ± 0.7 μm even with extensive precipitation of the Mg_5Gd and $Mg_{12}Gd$ phases as shown in Fig. 2c and the HAADF image within the red frame. Based on the HAADF image, the Mg_5Gd phase is located along the grain boundaries while $Mg_{12}Gd$ particles with an approximately spherical shape and a diameter of ~20 nm are distributed within the grains. This precipitation does not restrict the grain boundary mobility as observed in the AZ31

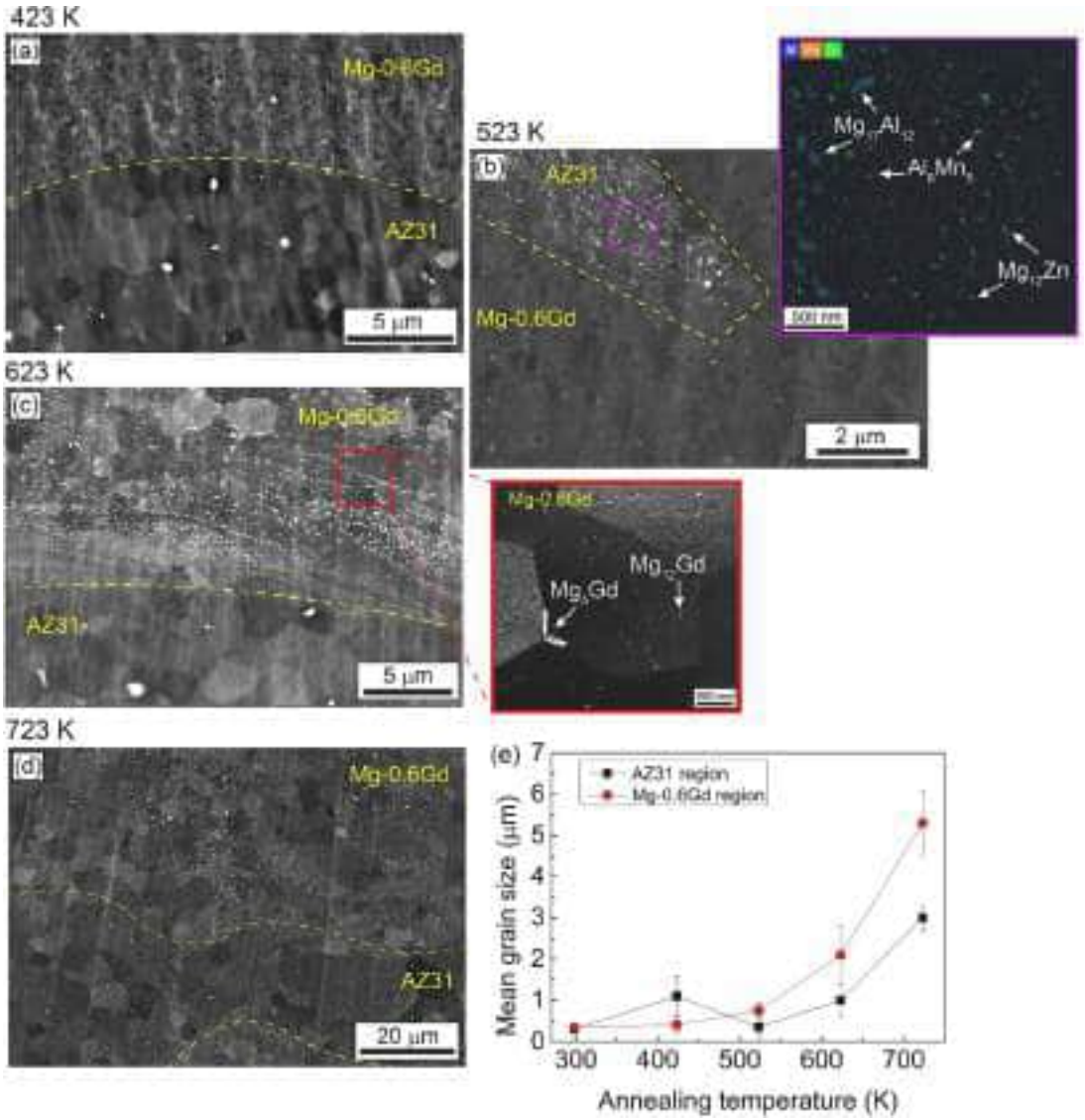

Fig. 2. SEM micrographs near the AZ31/Mg-0.6Gd interfaces after annealing for 1 h at (a) 423, (b) 523, (c) 623, and (d) 723 K, (e) evolution of the mean grain size of the AZ31 and Mg-0.6Gd regions as a function of annealing temperature for the hybrid material. In addition, EDS mapping for Al, Zn and Mn elements of the selected area in the AZ31 region annealed at 523 K (Fig. 2b) shows the $Mg_{17}Al_{12}$, Mg_2Zn and Al_8Mn_5 phases and the STEM image in HAADF mode of the selected area in the Mg-0.6Gd region annealed at 623 K shows the $Mg_{12}Gd$ and Mg_5Gd phases (Fig. 2c).

region which suggests that the Mg_5Gd and $Mg_{12}Gd$ phases probably precipitated after completing the recrystallization and grain growth processes.

Based on the Mg-Gd phase diagram [27], the Mg_5Gd and $Mg_{12}Gd$ phases are not expected to precipitate in an Mg-Gd alloy containing 0.6 % of Gd element. Furthermore, the development of the Mg_2Zn phase was never reported in the AZ31 alloy. It was suggested that the combination of the high strain induced by HPT processing and the formation of the interface bonding by solid diffusion is the origin of the unexpected precipitations in both the AZ31 and Mg-0.6Gd regions [20]. Indeed, the fabrication of the hybrid AZ31/Mg-0.6Gd material by HPT processing allows both the AZ31 and Mg-0.6Gd regions to store high energies in the form of high dislocation densities, vacancies or grain boundaries which can promote solute diffusion and provide nucleation sites for precipitate phases. The enhancement of precipitation phenomena by HPT processing is widely reported in Mg-based alloys [18,44–47].

The microstructure of the hybrid material became more homogeneous after annealing at 723 K (Fig. 2d) where the interface bonding is less visible and the precipitates dissolved in the Mg-0.6Gd region [20]. The average mean grain of the AZ31 and Mg-0.6Gd regions at 723 K reached values of 3.0 ± 0.3 and 5.3 ± 0.8 μm, respectively.

The mean grain size of the AZ31 and Mg-0.6Gd regions in the hybrid material can be used to examine the grain growth kinetics using the following equation [48]:

$$\frac{d^n - d_0^n}{t} = Aexp\left(\frac{-E_g}{RT}\right) \quad (2)$$

where d is the mean grain size at the annealing time of $t = 1$ h, d_0 is the initial mean grain size at $t = 0$ h corresponding to the deformation condition (taken as 0.30 ± 0.03 μm for the AZ31 region and 0.34 ± 0.02 μm for the Mg-0.6Gd region), n is the grain growth exponent which is related to the mobility and energy of the grain boundaries [49], A is the grain growth rate constant and E_g is the activation energy for grain growth that corresponds to the slope of a plot of $ln\left(d^n - d_0^n\right)$ against $1000/RT_p$.

The grain growth exponent n is determined by analysing the slope of the curve of $\ln(dd/dt)$ as a function of $\ln(d)$ where, for the material without defects, n should be equal to 2. Unfortunately, an experimental determination of n was not possible for these results because isothermal

annealing was not performed. Based on previous investigations, the grain growth exponent for various deformed Mg-based alloys is often in the range of 2–4 [40,50–55] although some investigations reported much higher values such as $n = 8$ [42,56]. The presence of microstructural heterogeneities including the presence of solute drag, dislocation substructure and the grain orientation is responsible for the deviation of n from the ideal value [42,57].

Hence, the activation energy for the present results was calculated by separately assuming $n = 2$, 4 and 8. Fig. 3 shows the evolution of $ln(d^n - d_0^n)$ as a function of $1000/RT_p$ with these different grain growth exponents for the AZ31 and Mg-0.6Gd regions of the hybrid material, respectively. It is evident that the plot of the AZ31 region can be separated into two stages which may be identified as the low-temperature and high-temperature stages. The precipitation of the $Mg_{17}Al_{12}$ and Mg_2Zn phases hindered grain growth in the low-temperature stage and therefore the activation energy in this stage was not considered since it has no physical meaning. An AZ31 alloy processed by equal-channel angular pressing [58] and HPT-processed Mg-1.4Nd (wt.%) alloy [59] were also shown to have two distinct ranges of grain growth activation energy. By contrast, the plot for the Mg-0.6Gd region (Fig. 3b) can be well fitted by a single line and this confirms that the precipitation of the Mg_5Gd and $Mg_{12}Gd$ phases does not affect the grain growth process. This result demonstrates that the nature of both the second phase and the solute element play a key role in controlling the grain growth process in Mg composite materials.

Table 1 summarizes the values of the activation energy for grain growth with different n values for the AZ31 and Mg-0.6Gd regions of the hybrid material. Using $n = 2$ gives values for the activation energy for both the AZ31 (88.2 ± 1.3 kJ/mol) and Mg-0.6Gd (52.7 ± 5.1 kJ/mol) regions that are lower than the activation energy for grain boundary diffusion in pure Mg (~92 kJ/mol). It is reasonable to anticipate that the value of $n = 2$ underestimates the real activation energy since, as already noted, n is equal to 2 for materials with no defects. However, the evolution of the microstructures of both the AZ31 and the Mg-0.6Gd regions shown in Fig. 2 and the former reports [19-21,28] demonstrate that the alloys are far removed from a material without defects and microstructural heterogeneity.

When $n = 4$, the activation energy in the AZ31 region of 146.2 ± 8.4 kJ/mol is close to the activation energy for lattice self-diffusion in pure Mg (~135 kJ/mol). For the Mg-0.6Gd region, the activation energy of 90.9 ± 13.5 kJ/mol corresponds to the activation energy for grain boundary diffusion in pure Mg (~92 kJ/mol). The activation energies when $n = 8$ are equal to 272.7 ± 25.6 and 173.1 ± 30.6 kJ/mol in the AZ31 and Mg-0.6Gd regions, respectively, and these values are significantly higher than the activation energy for lattice self-diffusion in pure Mg which suggests that a value of $n = 8$ overestimates the real activation energy.

Table 1
Activation energy for grain growth of hybrid AZ31/Mg-0.6Gd material using different grain growth exponents ($n = 2$, 4 and 8).

E_g (kJ/mol)	$n = 2$	$n = 4$	$n = 8$
AZ31 region	88.2 ± 1.3	146.2 ± 8.4	272.7 ± 25.6
Mg-0.6Gd region	52.7 ± 5.1	90.9 ± 13.5	173.1 ± 30.6

Usually, the activation energy for grain growth of the AZ31 alloy is in the range of 92–115 kJ/mol [42,50,55] and the high activation energy in the present analysis appears to be associated with the precipitates ($Mg_{17}Al_{12}$ and Mg_2Zn) and the segregation of the Zn element at the grain boundaries [20]. This precipitation was also the origin of the high grain growth activation energy of ~147 kJ/mol in the temperature range of 523–723 K for an HPT-processed Mg-1.4Nd (wt.%) alloy [59]. The lower activation energy for the Mg-0.6Gd region is reasonable because the grain growth process occurred in a microstructure which was already dynamically recrystallized and contained a low dislocation density [58].

The difference in the recrystallization and grain growth mechanisms found for the AZ31 and Mg-0.6Gd regions confirms the heterogeneous thermal stability of this hybrid AZ31/Mg-0.6Gd material. Thus, these results provide useful information for tailoring and appropriately adjusting the processing of new Mg-based composites.

4. Summary and conclusions

The activation energy for recrystallization of the hybrid AZ31/Mg-0.6Gd material fabricated by HPT processing through 20 turns was calculated using DSC analyses. In addition, the activation energies for grain growth were estimated using microstructural observations after isochronal annealing at 423, 523, 623 and 723 K for 1 h. The key conclusions are as follows:

- The exothermic peak in the hybrid material is attributed to the recrystallization of the AZ31 region. The activation energy of recrystallization was estimated as 112 ± 10 kJ/mol which falls between the activation energies for bulk and grain boundary diffusion.
- The precipitation of $Mg_{17}Al_{12}$ and Mg_2Zn phases in the AZ31 region significantly obstructs the grain growth process in the low-temperature range of 423–523 K. By contrast, the impact of precipitation of Mg_5Gd and $Mg_{12}Gd$ phases on grain growth of the Mg-0.6Gd region is less evident due to their development after complete recrystallization and grain growth.
- The activation energies for grain growth in the AZ31 and Mg-0.6Gd regions with grain growth exponent of $n = 4$ were found equal to 146.2 ± 8.4 and 90.9 ± 13.5 kJ/mol, respectively.

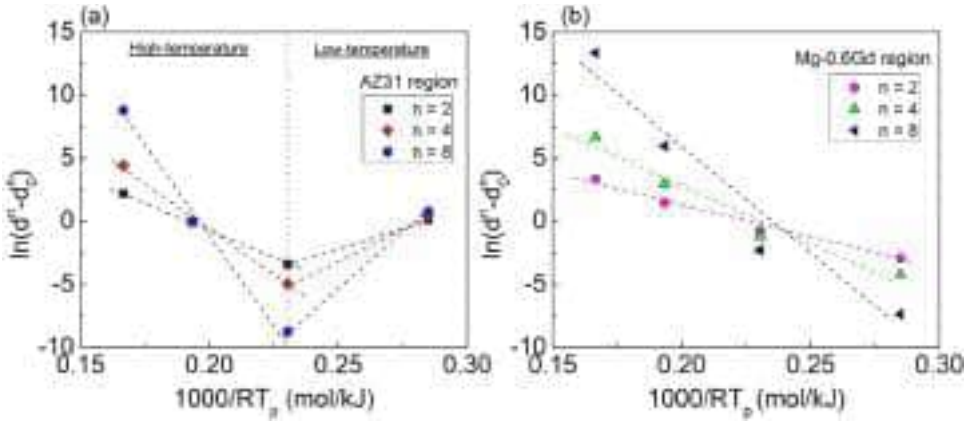

Fig. 3. Evolution of $ln(d^n - d_0^n)$ as a function of $1000/RT_p$ with different grain growth exponents ($n = 2$, 4 and 8) for (a) AZ31 and (b) Mg-0.6Gd regions of the hybrid material.

CRediT authorship contribution statement

Hiba Azzeddine: Writing – original draft, Investigation, Conceptualization. **Marie-Noëlle Avettand-Fènoël:** Writing – review & editing, Software, Conceptualization. **Piotr Bazarnik:** Software, Investigation. **Thierry Baudin:** Writing – original draft, Validation. **Yi Huang:** Investigation, Conceptualization. **Terence G. Langdon:** Writing – review & editing, Validation.

Declaration of competing interest

The authors declare that they have no known competing financial interests or personal relationships that could have appeared to influence the work reported in this paper.

Data availability

Data will be made available on request.

Acknowledgments

The authors sincerely thank Drs. N. Hort and D. Letzig (MagIC, Germany) and Dr. T. Al-Samman (RWTH-Aachen University, Germany) for supplying the AZ31 and Mg-0.6Gd alloys, respectively. The European Research Council provided funding for YH and TGL under Grant Agreement No. 267464-SPDMETALS. PB was supported by the National Science Centre Poland under Grant Agreement No. 2020/37/B/ST5/01837.

References

[1] I.M. Alarifi, R. Asmatulu, I.M. Alarifi, R. Asmatulu, 4 - Matrix hybrid composite materials. Advanced Hybrid Composite Materials and Their Applications, Woodhead Publishing, Cambridge, U.K, 2023, pp. 67–88.
[2] S.K. Khatkar, Hybrid magnesium matrix composites: a review of reinforcement philosophies, mechanical and tribological characteristics, RAMS 62 (2023) 20220294.
[3] Y. Chen, Z. Xu, C. Smith, J. Sankar, Recent advances on the development of magnesium alloys for biodegradable implants, Acta Biomater. 10 (2014) 4561–4573.
[4] M.M. Zerankeshi, R. Alizadeh, E. Gerashi, M. Asadollahi, T.G. Langdon, Effects of heat treatment on the corrosion behavior and mechanical properties of biodegradable Mg alloys, J. Magnes. Alloy 10 (2022) 1737–1785.
[5] R.Z. Valiev, Y. Zheng, K. Edalati, Review: nanoSPD-produced metallic materials for advanced medical devices, J. Mater. Sci. 59 (2024) 5681–5697.
[6] R.Z. Valiev, I.V. Alexandrov, M. Kawasaki, T.G. Langdon, Ultrafine-Grained Materials, Springer International Publishing, Cham, Switzerland, 2024.
[7] M.M. Castro, P.H.R. Pereira, A. Isaac, R.B. Figueiredo, T.G. Langdon, Development of a magnesium-alumina composite through cold consolidation of machining chips by high-pressure torsion, J. Alloys Compd. 780 (2019) 422–427.
[8] M.M. Castro, D.R. Lopes, R.B. Soares, D.M.M. dos Santos, E.H.M. Nunes, V.F. C. Lins, P.H.R. Pereira, A. Isaac, T.G. Langdon, R.B. Figueiredo, Magnesium-based bioactive composites processed at room temperature, Mater 12 (2019) 2609.
[9] D. Lopes, R.B. Soares, M.M. Castro, R.B. Figueiredo, T.G. Langdon, V.F.C. Lins, Corrosion behavior in hank's solution of a magnesium–hydroxyapatite composite processed by high-pressure torsion, Adv. Eng. Mater. 22 (2020) 2000765.
[10] M.M. Castro, P.H.R. Pereira, A. Isaac, T.G. Langdon, R.B. Figueiredo, Inverse Hall–petch behaviour in an AZ91 alloy and in an AZ91–Al2O3 composite consolidated by high-pressure torsion, Adv. Eng. Mater. 22 (2020) 1900894.
[11] B. Ahn, A.P. Zhilyaev, H.J. Lee, M. Kawasaki, T.G. Langdon, Rapid synthesis of an extra hard metal matrix nanocomposite at ambient temperature, Mater. Sci. Eng. A 635 (2015) 109–117.
[12] M. Kawasaki, B. Ahn, H. Lee, A.P. Zhilyaev, T.G. Langdon, Using high-pressure torsion to process an aluminum–magnesium nanocomposite through diffusion bonding, J. Mater. Res. 31 (2016) 88–99.
[13] J.K. Han, K.D. Liss, T.G. Langdon, M. Kawasaki, Synthesis of a bulk nanostructured metastable Al alloy with extreme supersaturation of Mg, Sci. Rep. 9 (2019) 17186.
[14] J.K. Han, K. Sugimoto, M. Kawasaki, K.D. Liss, Strain-dependent phase transformation mapping of diffusion-bonded nanocrystalline aluminum-magnesium by high-energy synchrotron X-rays, Mater. Lett. 321 (2022) 132414.
[15] D. Hernández-Escobar, Z.U. Rahman, H. Yilmazer, M. Kawasaki, C.J. Boehlert, Microstructural evolution and intermetallic formation in Zn-Mg hybrids processed by high-pressure torsion, Philos. Mag. 99 (2019) 557–584.
[16] M.M. Castro, L.A. Montoro, A. Isaac, M. Kawasaki, R.B. Figueiredo, Mechanical mixing of Mg and Zn using high-pressure torsion, J. Alloys Compd. 869 (2021) 159302.
[17] D. Hernández-Escobar, J. Marcus, J.K. Han, R.R. Unocic, M. Kawasaki, C. J. Boehlert, Effect of post-deformation annealing on the microstructure and micro-mechanical behavior of Zn–Mg hybrids processed by high-pressure torsion, Mater. Sci. Eng. A 771 (2020) 138578.
[18] D. Hernández-Escobar, R.R. Unocic, M. Kawasaki, C.J. Boehlert, High-pressure torsion processing of Zn–3Mg alloy and its hybrid counterpart: a comparative study, J. Alloys Compd. 831 (2020) 154891.
[19] O. Ould Mohamed, H. Azzeddine, Y. Huang, T. Baudin, P. Bazarnik, F. Brisset, M. Kawasaki, T.G. Langdon, Investigation of microstructure and texture evolution in an AZ31/Mg–Gd alloy hybrid metal fabricated by high-pressure torsion, Adv. Eng. Mater. 25 (2023) 2201794.
[20] O. Ould Mohamed, P. Bazarnik, Y. Huang, H. Azzeddine, T. Baudin, F. Brisset, M. Kawasaki, T.G. Langdon, Primary recrystallization of a magnesium hybrid material fabricated by high-pressure torsion, Mater. Today Commun. 38 (2024) 108305.
[21] T. Baudin, H. Azzeddine, F. Brisset, Y. Huang, T.G. Langdon, Estimating dislocation density from electron backscatter diffraction data for an AZ31/Mg-0.6Gd hybrid alloy fabricated by high-pressure torsion, Philos. Mag. 104 (2024) 389–405.
[22] R.B. Figueiredo, P.R. Cetlin, T.G. Langdon, Using finite element modeling to examine the flow processes in quasi-constrained high-pressure torsion, Mater. Sci. Eng. A 528 (2011) 8198–8204.
[23] A. Sheikhani, R. Roumina, R. Mahmudi, Texture softening in a rare earth elements-containing AZ31 magnesium alloy during hot compression deformation, J. Mater. Res. Technol. 18 (2022) 4089–4098.
[24] Z. Horita, K. Ohashi, T. Fujita, K. Kaneko, T.G. Langdon, Achieving high strength and high ductility in precipitation-hardened alloys, Adv. Mater. 17 (2005) 1599–1602.
[25] G. Sha, Y.B. Wang, X.Z. Liao, Z.C. Duan, S.P. Ringer, T.G. Langdon, Influence of equal-channel angular pressing on precipitation in an Al–Zn–Mg–Cu alloy, Acta Mater. 57 (2009) 3123–3132.
[26] H. Azzeddine, B. Mehdi, L. Hennet, D. Thiaudière, B. Alili, M. Kawasaki, D. Bradai, T.G. Langdon, An in situ synchrotron X-ray diffraction study of precipitation kinetics in a severely deformed Cu–Ni–Si alloy, Mater. Sci. Eng. A 597 (2014) 288–294.
[27] L.L. Rokhlin, Magnesium Alloys Containing Rare Earth metals: Structure and Properties, 1st ed., Crc Press, London, 2003.
[28] O. Ould Mohamed, P. Bazarnik, Y. Huang, H. Azzeddine, T. Baudin, F. Brisset, T. G. Langdon, A comparative study between AZ31 and Mg-Gd alloys after high-pressure torsion, J. Mater. Eng. Perform. 33 (2024) 2860–2874.
[29] J. Zhang, W. Li, Z. Guo, Static recrystallization and grain growth during annealing of an extruded Mg–Zn–Zr–Er magnesium alloy, J. Magnes. Alloy 1 (2013) 31–38.
[30] I. Basu, K.G. Pradeep, C. Mießen, L.A. Barrales-Mora, T. Al-Samman, The role of atomic scale segregation in designing highly ductile magnesium alloys, Acta Mater. 116 (2016) 77–94.
[31] Y.I. Bourezg, D. Elfiad, H. Azzeddine, D. Bradai, Investigation of recrystallization kinetics in hot-rolled Mg-La alloy using differential scanning calorimetry technique, Thermochim. Acta 690 (2020) 178688.
[32] F. Guerza-Soualah, A. Hanna, H. Azzeddine, A.L. Helbert, F. Brisset, T. Baudin, D. Bradai, The deformation and recrystallization behaviour of an Mg-Dy alloy processed by plane strain compression, Mater. Today Commun. 24 (2020) 101239.
[33] F. Guerza-Soualah, H. Azzeddine, T. Baudin, A.L. Helbert, F. Brisset, D. Bradai, Microstructural and textural investigation of an Mg–Dy alloy after hot plane strain compression, J. Magnes. Alloy 8 (2020) 1198–1207.
[34] N. Stanford, M.D. Callaghan, B. de Jong, The effect of rare earth elements on the behaviour of magnesium-based alloys: part 1—Hot deformation behaviour, Mater. Sci. Eng. A 565 (2013) 459–468.
[35] S. Sandlöbes, M. Friák, S. Zaefferer, A. Dick, S. Yi, D. Letzig, Z. Pei, L.F. Zhu, J. Neugebauer, D. Raabe, The relation between ductility and stacking fault energies in Mg and Mg–Y alloys, Acta Mater. 60 (2012) 3011–3021.
[36] Y.I. Bourezg, H. Azzeddine, K. Abib, Y. Huang, D. Bradai, T.G. Langdon, Recrystallization in an Mg-Nd alloy processed by high-pressure torsion: a calorimetric analysis, J. Mater. Res. Technol. 9 (2020) 3047–3054.
[37] A. Hanna, H. Azzeddine, Y. Huang, D. Bradai, J.M. Cabrera, T.G. Langdon, An investigation of the thermal stability of an MgDy alloy after processing by high-pressure torsion, Mater. Charact. 151 (2019) 519–529.
[38] P.G. Boswell, On the calculation of activation energies using a modified Kissinger method, J. Therm. Anal. 18 (1980) 353–358.
[39] H.J. Frost, M.F. Ashby, Deformation-mechanism Maps: The Plasticity and Creep of Metals and Ceramics, 1st ed., Pergamon Press, Oxford, New York, 1982.
[40] H.Y. Chao, H.F. Sun, W.Z. Chen, E.D. Wang, Static recrystallization kinetics of a heavily cold drawn AZ31 magnesium alloy under annealing treatment, Mater. Charact. 62 (2011) 312–320.
[41] H. Zhao, P.J. Li, L.J. He, Kinetics of recrystallization for twin-roll casting AZ31 magnesium alloy during homogenization, Int. J. Min. Met. Mater. 18 (2011) 570–575.
[42] S. Sadi, A. Hanna, T. Baudin, A.L. Helbert, F. Brisset, D. Bradai, H. Azzeddine, Evaluation of static recrystallization and grain growth kinetics of hot-rolled AZ31 alloy, J. Met. Mater. Miner. 32 (2022) 12–26.
[43] Y.I. Bourezg, H. Azzeddine, Y. Huang, D. Bradai, T. Langdon, Investigation of recrystallization kinetics by DSC analysis of Mg-Ce alloy after severe plastic deformation, in: Proceedings of the 26th International Conference on Metallurgy and Materials (Metal 2017), Brno, Czech Republic, Tanger Ltd, 2017, pp. 1524–1530. EU.

[44] J. Čížek, I. Procházka, B. Smola, I. Stulíková, V. Očenášek, R.K. Islamgaliev, O. B. Kulyasova, The enhanced kinetics of precipitation effects in ultra fine grained Mg alloys prepared by high pressure torsion, Defect Diffus. Forum 273-276 (2008) 75–80.
[45] O. Melikhova, J. Čížek, P. Hruška, M. Vlček, I. Procházka, M. Vlach, I. Stulíková, B. Smola, N. Žaludová, R.K. Islamgaliev, Influence of deformation on precipitation kinetics in Mg-Tb alloy, Defect Diffus. Forum 322 (2012) 151–162.
[46] Y.I. Bourezg, H. Azzeddine, L. Hennet, D. Thiaudière, Y. Huang, D. Bradai, T. G. Langdon, The sequence and kinetics of pre-precipitation in Mg-Nd alloys after HPT processing: a synchrotron and DSC study, J. Alloys Compd. 719 (2017) 236–241.
[47] X. Liu, Y. Li, Y. Man, J. Wang, R. Xu, Precipitation and recrystallization of HPT-processed Mg-Sm-Ca alloy at low temperatures, Mater. Lett. 277 (2020) 128252.
[48] J.E. Burke, D. Turnbull, Recrystallization and grain growth, Prog. Phys. Met. 3 (1952) 220–292.
[49] A. Kazaryan, Y. Wang, S.A. Dregia, B.R. Patton, Grain growth in anisotropic systems: comparison of effects of energy and mobility, Acta Mater. 50 (2002) 2491–2502.
[50] C.W. Su, L. Lu, M.O. Lai, Mechanical behaviour and texture of annealed AZ31 Mg alloy deformed by ECAP, Mater. Sci. Technol. 23 (2007) 290–296.
[51] C.W. Su, L. Lu, M.O. Lai, Recrystallization and grain growth of deformed magnesium alloy, Philos. Mag. 88 (2008) 181–200.
[52] M. Roostaei, M. Shirdel, M.H. Parsa, R. Mahmudi, H. Mirzadeh, Microstructural evolution and grain growth kinetics of GZ31 magnesium alloy, Mater. Charact. 118 (2016) 584–592.
[53] Z. Jin, D. Yu, X. Wu, K. Yin, K. Yan, Drag effects of solute and second phase distributions on the grain growth kinetics of pre-extruded Mg-6Zn alloy, J. Mater. Sci. Technol. 32 (2016) 1260–1266.
[54] C.J. Silva, A. Kula, R.K. Mishra, M. Niewczas, Grain growth kinetics and annealed texture characteristics of Mg-*Sc* binary alloys, J. Alloys Compd. 687 (2016) 548–561.
[55] Q. Wang, B. Jiang, A. Tang, J. Fu, Z. Jiang, H. Sheng, D. Zhang, G. Huang, F. Pan, Unveiling annealing texture formation and static recrystallization kinetics of hot-rolled Mg-Al-Zn-Mn-Ca alloy, J. Mater. Sci. Technol. 43 (2020) 104–118.
[56] M.A. Thein, L. Lu, M.O. Lai, Kinetics of grain growth in nanocrystalline magnesium-based metal–metal composite synthesized by mechanical alloying, Compos. Sci. Technol. 66 (2006) 531–537.
[57] G.T. Higgins, Grain-boundary migration and grain growth, Met. Sci. 8 (1974) 143–150.
[58] H.K. Kim, Activation energies for the grain growth of an AZ31 Mg alloy after equal channel angular pressing, J. Mater. Sci. 39 (2004) 7107–7109.
[59] S. Tighiouaret, R. Lachhab, A. Hanna, H. Azzeddine, Y. Huang, T. Baudin, A. L. Helbert, F. Brisset, D. Bradai, T.G. Langdon, Thermal stability of an Mg–Nd alloy processed by high-pressure torsion, Adv. Eng. Mater. 21 (2019) 1900801.

Materials Science & Engineering A 916 (2024) 147320

Contents lists available at ScienceDirect

Materials Science & Engineering A

journal homepage: www.elsevier.com/locate/msea

The role of processing temperature for achieving superplastic properties in an Al-3Mg-0.2Sc alloy processed by high-pressure torsion

Pedro Henrique R. Pereira [a,*], Piotr Bazarnik [b], Yi Huang [c,d], Malgorzata Lewandowska [b], Terence G. Langdon [c]

[a] Department of Metallurgical and Materials Engineering, Universidade Federal de Minas Gerais, Belo Horizonte, 31270-901, MG, Brazil
[b] Faculty of Materials Science and Engineering, Warsaw University of Technology, Woloska 141, 02-507, Warsaw, Poland
[c] Materials Research Group, Department of Mechanical Engineering, University of Southampton, Southampton, SO17 1BJ, UK
[d] Department of Design and Engineering, Faculty of Science and Technology, Bournemouth University, Poole, Dorset, BH12 5BB, UK

ARTICLE INFO

Keywords:
Aluminium alloys
Grain boundary sliding
High-pressure torsion
Superplasticity
Ultrafine grains

ABSTRACT

Experiments were conducted to systematically assess the superplastic properties and the microstructural changes of an Al-3Mg-0.2Sc alloy processed by 10 HPT revolutions at room temperature (RT ≈ 300 K) or at 450 K after subsequent tensile testing at temperatures from 473 to 723 K over a wide range of strain rates. The HPT processing at RT led to the development of elongated grains with an average size of ~140 nm whereas the grain structures were equiaxed and slightly larger (~150 nm) after HPT at 450 K. After HPT processing at RT, the Al-Mg-Sc alloy exhibited true superplastic flow at low homologous temperatures and attained a maximum elongation of ~850 % at 523 K. Nevertheless, the elongations decreased at temperatures $T \geq 623$ K and an elongation higher than 400 % was only achieved at 673 K for a strain rate of $\dot{\varepsilon} = 4.5 \times 10^{-3}$ s^{-1}. The material processed by HPT at 450 K displayed superior microstructural stability and substantially higher superplastic ductilities. Elongations of >1100 % were attained at 673 K for strain rates from 3.3×10^{-4} to 1.0×10^{-1} s^{-1} and a record elongation of ~1880 % for an HPT-processed metal was achieved at 1.5×10^{-2} s^{-1} at 673 K. High strain rate superplasticity was also reached for an extended range of temperatures and strain rates. Analysis of the data confirms a stress exponent of ~2 which is consistent with superplastic flow by grain boundary sliding accommodated by dislocation glide and climb.

1. Introduction

The processing of alloys through severe plastic deformation (SPD) procedures has been extensively evaluated over the last three decades in order to fabricate metals with ultrafine grain sizes [1–4]. These materials usually exhibit improved mechanical strength and superplastic properties by comparison with their counterparts prepared using conventional metal-working procedures this due to the exceptional levels of grain refinement introduced during SPD processing [3]. Although various SPD processes are now available, major focus has been devoted to the procedures of equal-channel angular pressing (ECAP) [5] and high-pressure torsion (HPT) [6,7] using anvils having quasi-constrained configurations [8,9]. Both techniques require relatively simple apparatus and they permit the processing of difficult-to-work materials by controlling the imposed pressure and the temperature in the work-pieces [10–12]. In practice, HPT processing is more effective than ECAP because it leads to both smaller grain sizes [13,14] and larger fractions of grain boundaries having high angles of misorientation [15].

As the strain rate in superplasticity is inversely proportional to the square of the grain size [16], SPD processing produces nanostructured metals that may be used for superplastic forming at faster production rates [17–20]. In this context, the Al-Mg-Sc alloys have attracted significant attention due to their enhanced microstructural stability [21–25] which is promoted by the precipitation of nanosized Al_3Sc particles [26–29]. This could potentially permit the application of this alloy as aircraft components exposed to temperatures up to ~573 K for short periods to replace traditional Al-Li alloys or heavier materials such as titanium alloys [27]. It has been recently demonstrated that Al-Mg-Sc alloys reach yield stresses >600 MPa after HPT [25,30]. It was also revealed that even after exposure to temperatures up to 623 K for 1 h the yield strength remains higher than 300 MPa [25]. Accordingly, the Al-Mg-Sc alloys consistently achieve high strength at low temperatures

* Corresponding author.
E-mail address: ppereira@demet.ufmg.br (P.H.R. Pereira).

https://doi.org/10.1016/j.msea.2024.147320
Received 16 July 2024; Received in revised form 5 September 2024; Accepted 25 September 2024
Available online 26 September 2024

[25,30] and excellent superplastic ductilities after SPD [31].

Although numerous studies have highlighted the excellent mechanical properties of Al-Mg-Sc alloys, their widespread commercial use remains limited due to the relatively high cost of scandium (Sc) additions. For this reason, these Sc-containing aluminium alloys are predominantly utilized in specialized applications where performance outweighs material cost considerations, such as in aerospace components and in the automotive industry [27,32].

The superplastic properties of Al-Mg-Sc alloys have been extensively examined after ECAP [21,33–37]. For example, an Al-3Mg-0.2Sc alloy processed by 8 ECAP passes at room temperature (RT) attained an elongation of ~2580 % after tensile testing at 3.3×10^{-3} s^{-1} at 723 K [33]. Similarly, an Al-Mg-Sc-Zr alloy displayed an even higher ductility after processing by ECAP at the high temperature of ~600 K with a maximum elongation of ~4100 % in tensile deformation at 723 K [36]. Although these results demonstrate that the processing of Al-Mg-Sc alloys through ECAP at high temperatures permits the achievement of superior superplastic ductilities, the reasons for this behaviour are not fully understood.

It has been shown that finer grain structures are produced in Al-Mg-Sc alloys by HPT processing than by ECAP [38–40] but, nevertheless, this is not supported by higher elongations in tensile testing at high temperatures [38,41]. The lower tensile elongations recorded in samples processed by HPT are generally attributed to the utilisation of miniature specimens or at least to specimens cut from discs having relatively small thicknesses [38,40,42,43]. Furthermore, the microstructures developed during HPT at RT are less thermally stable than after ECAP [21,25,44], and grain coarsening can potentially reduce the superplastic properties at high temperatures and low strain rates.

These observations motivated the current research to provide a more comprehensive understanding of the superplastic behaviour of Al-Mg-Sc alloys after processing by HPT. It is important to note that higher superplastic elongations were reported for the Mg–9Al [45] and AZ61 [46] alloys after processing by HPT at elevated temperatures and recent investigations revealed a remarkable enhancement in the thermal stability of the Al-3Mg-0.2Sc alloy after undertaking the HPT processing at ~450 K [24,25,47]. Thus, it appears that this strategy has the potential of enhancing the superplastic properties of Al-Mg-Sc alloys after HPT processing.

Accordingly, the present research was conducted to evaluate the flow properties and microstructural changes of an Al-3Mg-0.2Sc alloy after processing through 10 turns of HPT at 300 or 450 K and subsequently testing in tension at temperatures from 473 to 723 K. The overall objective was to determine the range of strain rates and temperatures in which this alloy exhibits true superplastic flow and to identify the optimum deformation conditions for attaining tensile elongations that are adequate for achieving reasonably rapid superplastic forming.

2. Experimental material and procedures

An Al-3% Mg-0.2 % Sc (in wt. %) alloy was used in this research. This material was supplied by China Rare Metal Material Corporation (Jiangxi Province, China) as forged billets with diameters of ~10 mm. The billets were solution treated at 880 ± 2 K for 1 h and then quenched in water to maximise the Sc content in solid solution and thereby produce a uniform array of grains with an average size of ~300 μm. Thereafter, the bars were cut in the form of discs and then ground to thicknesses of ~0.8 mm.

These Al-3Mg-0.2Sc discs were processed by HPT either at RT ≈ 300 K (HPT-RT) or at ~450 ± 5 K (HPT-HT) where this corresponds to homologous temperatures (T_H) of ~0.3 and ~0.5, respectively. As documented in earlier studies [25,45,47,48], a processing temperature of ~450 K was attained by using a heating element encircling the massive anvils. The temperature was controlled by inserting a thermocouple within a specially designed hole in the upper anvil such that the tip of the temperature sensor was positioned at a distance of ~10 mm from the upper surface of the HPT disc. The HPT samples were initially compressed within the depression of the quasi-constrained anvils [49–51] until a nominal pressure of 6 GPa was achieved. They were then subjected to torsional straining up to 10 HPT turns using a rotation rate of ~1 rpm.

The HPT-processed discs were ground to the mid-thickness positions and finally they were polished using 0.06 μm silica colloidal. Vickers hardness measurements were recorded along the entire surfaces of the polished samples using an FM300 microhardness tester under a load of ~200 gf and a dwell time of 15 s. As in an earlier study [52], the measurements followed a rectilinear grid with indentations separated by 0.3 mm and the individual hardness values were then used to construct colour-coded contour maps.

As reported earlier [25,48,53–55], two off-centre miniature tensile specimens, having widths and gauge lengths of ~1.0 and 1.1 mm, respectively, were machined from each HPT-processed disc using electrical discharge wire cutting. After processing, the surfaces of the discs became curved due to the elastic distortion of the anvils [56]. Therefore, in order to remove any irregularities, the surfaces of the HPT-processed samples were ground and polished to a thickness of ~0.6 mm. Tensile tests were conducted using a Zwick Z030 testing machine over wide ranges of strain rates ($\dot{\varepsilon}$) and temperatures (T) varying from 3.3×10^{-4} to 1.0 s^{-1} and 473–723 K, respectively. The procedure involved clamping the miniature specimens within specially designed grips and then assembling the grips and specimen in the testing machine equipped with a tubular furnace. The miniature specimens were held in a hot chamber for ~10 min to permit temperature stabilisation and thereafter pulled to failure at a constant rate of cross-head displacement with the temperature held constant to within ±2 K during testing. The tensile tests were conducted at least in duplicate for each individual temperature and strain rate condition to ensure the reproducibility of the results. A M420 stereoscope was used to obtain images of the fractured specimens and to measure the final lengths in the gauge sections of the samples.

Following tensile testing, observations of the surfaces of the fractured specimens were undertaken using a JSM6500F thermal field emission scanning electron microscope (SEM) operating at 15 kV. The secondary electron (SE) images were used to measure the average grain boundary spacing ($\bar{L}$) in the gauge sections of the tested specimens using the linear intercept method. The microstructures of the Al-3Mg-0.2Sc alloy tensile tested at selected strain rates at 673 K were also examined using transmission electron microscopy (TEM) with a JEOL 1200EX microscope operating at 200 kV and through orientation imaging microscopy using electron backscattered diffraction (EBSD). The EBSD scans were conducted at the grip and within the gauge areas of the fractured specimens with a minimum step size of 0.09 μm whereas the TEM examinations were performed on lamellas extracted by focused ion beam along the gauge sections. The EBSD mappings were conducted at an operating voltage of 15 kV using tilt angles and working distances of 60° and ~15 mm, respectively. Orientation maps were generated from each EBSD scan, and these results were used to analyse the distributions of the correlated misorientation angles and the grain diameters measured using the equivalent circle method.

The microstructures of the HPT-processed discs were investigated through scanning transmission electron microscopy (STEM) using a Hitachi 5500 microscope operating at 30 kV. Discs of ~3 mm diameter were punched at distances of ~3.5 mm from the centres of the HPT discs and then twin-jet electropolished with 70 % CH_3OH and 30 % HNO_3 at ~250 K using a Struers Tenupol-5 system.

3. Experimental results

3.1. Vickers microhardness and microstructure after HPT

Fig. 1 shows colour-coded contour maps for the distributions of the

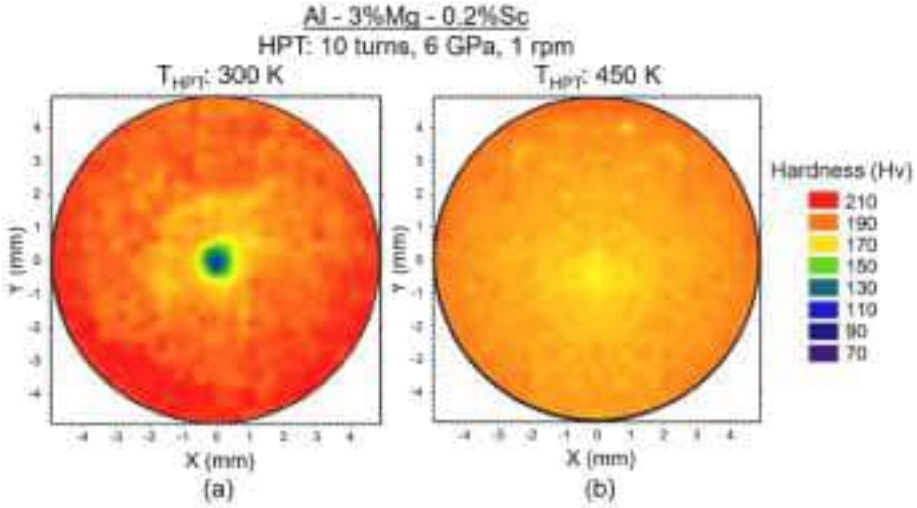

Fig. 1. Colour-coded contour maps revealing the distributions of the Vickers microhardness over the surfaces of Al-Mg-Sc discs processed by 10 HPT revolutions at (a) 300 and (b) 450 K. (For interpretation of the references to colour in this figure legend, the reader is referred to the Web version of this article.)

Vickers hardness over the surfaces of Al-Mg-Sc discs processed by 10 HPT turns at RT and 450 K. As noted earlier [47,57], the unprocessed Al-3Mg-0.2Sc alloy displayed a fairly uniform hardness distribution with an average value of ~60 Hv. After 10 HPT revolutions at RT the microhardness distribution in Fig. 1 is a doughnut-like pattern containing an outer ring of higher hardness values in the range of ~190–210 Hv whereas the central area shows lower hardness values within the interval of ~110–150 Hv.

It is readily apparent from Fig. 1 that the microhardness distribution is more homogenous after processing at 450 K although the hardness values are lower and mostly lie within the range of ~170–190 Hv. These results are consistent with recent results demonstrating that the same Al-Mg-Sc alloy exhibits yield strengths of ~600 and 550 MPa after HPT at 300 and 450 K, respectively [25]. Thus, the local mechanical strength after HPT at different temperatures, as represented by the Vickers hardness values, shows similar percentage differences compared with the yield strengths measured after tensile testing using miniature specimens.

The dislocation and grain structures of representative Al-Mg-Sc microstructures obtained after processing through 10 HPT revolutions are depicted in the STEM images presented in Fig. 2. Average grain sizes of ~140 and ~150 nm were calculated for the Al-3Mg-0.2Sc alloy after HPT at RT and 450 K, respectively, although the grain structures appeared more elongated after processing at RT. A more thorough examination of Fig. 2 reveals the presence of sparse dislocations within some of the grains which are mostly isolated as shown in detail in Fig. 2

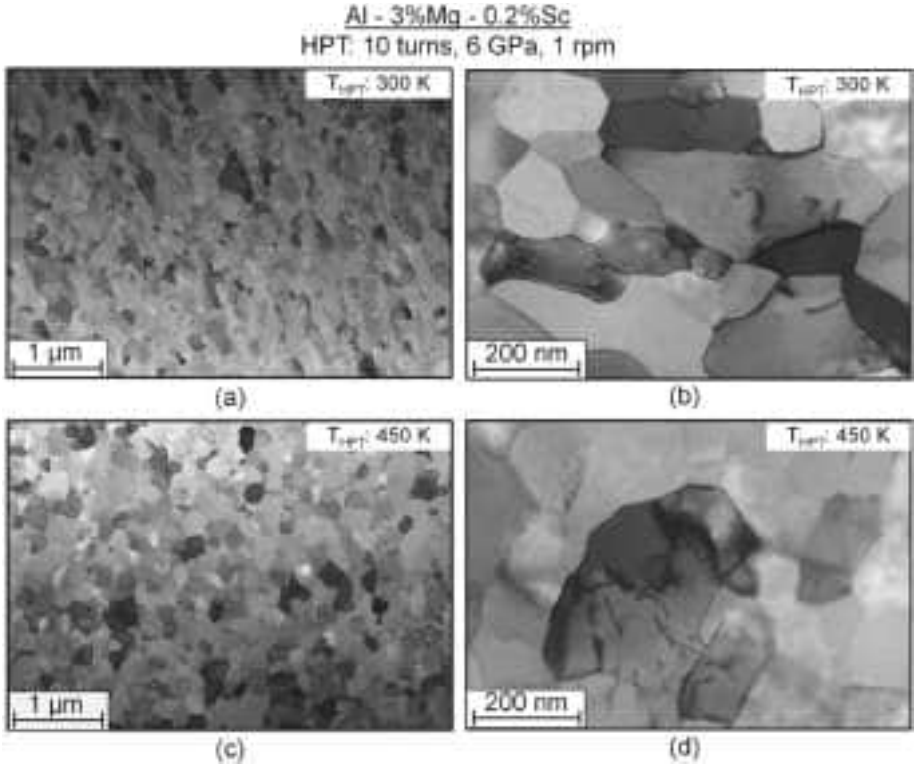

Fig. 2. STEM images showing dislocation and grain structures in the Al-3Mg-0.2Sc alloy processed through 10 turns of HPT at (a and b) RT and (c and d) 450 K.

(b) and (d).

These findings are consistent with both the TEM and the EBSD results documented in a recent report [25]. For example, it was demonstrated that there is no precipitation of nano-sized Al_3Sc particles in the solution-treated Al-3Mg-0.2Sc alloy when HPT processing up to 10 turns. Furthermore, the dislocation density estimated through Rietveld refinement of X-Ray diffraction profiles of the alloy processed by up to 10 HPT revolutions at 300 K was ~5 × higher than after processing at 450 K.

3.2. Tensile properties at high temperatures

Fig. 3 shows representative plots of true stress *vs* true strain for the Al-3Mg-0.2Sc alloy processed through 10 HPT turns at either 300 or 450 K and subsequently tested in tension at 523 or 673 K using strain rates from 3.3×10^{-4} to 1.4 s^{-1}. As in recent studies [48,58], the plots were obtained by converting the load and displacement data into true stress and true strain by considering uniform deformation along the gauge sections of the miniature specimens. Accordingly, although the values of true stress at strains beyond the maximum load do not reflect the precise flow behaviour, the maximum true stress obtained in each test probably provides a better estimate of the load bearing capacity of the microstructures developed at the later stages of testing as further documented in the discussion section.

The results in Fig. 3 demonstrate that the HPT-HT material consistently exhibits lower flow stresses and higher elongations than the same alloy processed by HPT at RT for tensile tests carried out at comparable temperatures and strain rates. For both processing temperatures, it is also emphasized that the flow behaviour of the HPT-processed alloy at high temperatures strongly depends upon the strain rates. For tests conducted at 523 K, it is apparent that the material processed at 450 K reaches lower flow stresses and higher maximum strains than the HPT-RT metal for $\dot{\varepsilon} \geq 10^{-2}$ s^{-1}. Nonetheless, specimens tested at 523 K using lower strain rates display very similar ductilities although the latter

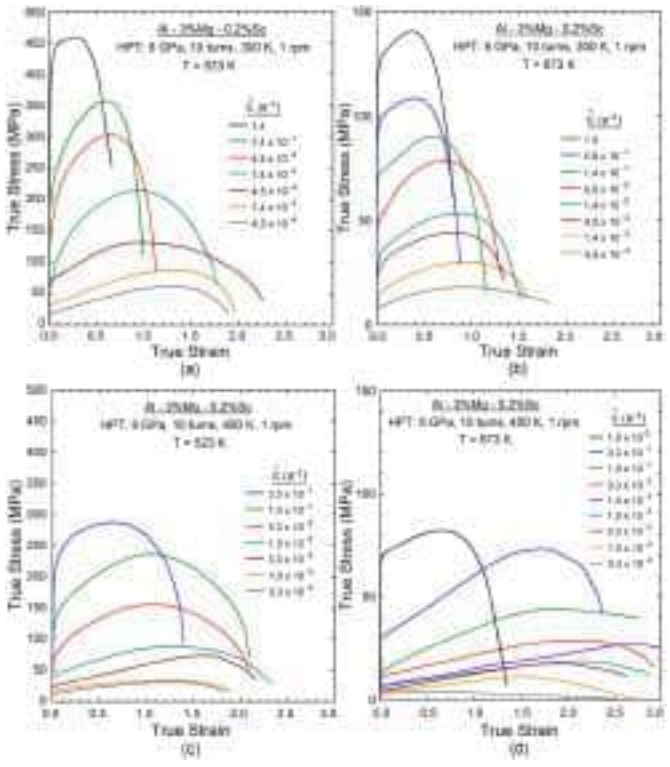

Fig. 3. True stress vs true strain curves for the Al-3Mg-0.2Sc alloy processed through 10 HPT turns at either 300 or 450 K and then tensile tested at (a, c) 523 and (b, d) 673 K using strain rates from 3.3×10^{-4} to 1.4 s^{-1}.

require higher yield stresses.

Inspection of Fig. 3 reveals that increasing the testing temperature from 523 to 673 K promotes a marked decrease in the flow stresses regardless of the HPT temperature. There is a significant increase in the ductility for the alloy processed at 450 K as follows from the attainment of $\varepsilon > 2.5$ for strain rates from 3.3×10^{-4} to 10^{-1} s^{-1}. Conversely, it is shown that the specimens of the HPT-RT material fail at similar or even lower strains at 673 K compared with the testing temperature of 523 K. It is important to emphasize that the alloy processed by HPT at 450 K reaches a maximum strain of ~2.4 when tested at 673 K with a strain rate of 3.3×10^{-1} s^{-1} and this was not achieved for the HPT-RT specimens under any testing condition in Fig. 3(a) and (b). Furthermore, the HPT-HT material exhibits a more significant work hardening during testing at 673 K than the alloy processed by HPT at 300 K.

Fig. 4 displays the appearance of the deformed specimens of the Al-3Mg-0.2Sc alloy after tensile testing and pulling to failure for the same conditions presented in Fig. 3. The values of the elongations to failure ($\Delta l/l_0$) are shown on the right-hand side of the fractured samples where Δl and l_0 are the change in length and the initial gauge length, respectively. Examination of Fig. 4 demonstrates that the HPT-RT samples tested in tension at 523 K achieved elongations >400 % for $\dot{\varepsilon} \leq 1.4 \times 10^{-2}$ s^{-1} revealing the occurrence of both superplastic flow which requires an elongation of at least 400 % [59] and the advent of high strain rate superplasticity which occurs at strain rates at and above 10^{-2} s^{-1} [60]. Furthermore, the general lack of any visible incipient necking within the gauge lengths of the specimens processed by HPT at 450 K confirms the occurrence of quasi-stable plastic flow and true superplasticity [61].

Nevertheless, it is noted that an increase in the testing temperature to 673 K consistently leads to a reduction in the tensile ductility such that for the material processed by HPT at RT there is an elongation of $\Delta l/l_0 >$ 400 % only at $\dot{\varepsilon} \approx 4.5 \times 10^{-4}$ s^{-1}. A more detailed inspection of the fractured specimens in Fig. 4 (a) shows that the HPT-RT specimens develop very diffuse necking during testing at 673 K for $\dot{\varepsilon} \leq 4.5 \times 10^{-3}$ s^{-1} as the widths of the samples are reasonable constant along the entire gauge lengths. By contrast, there is a sharper width gradient for the HPT-RT samples tested at 523 K even though the material then reaches higher elongations.

The results in Fig. 4 (b) demonstrate reliably that the Al-Mg-Sc alloy processed by HPT at 450 K exhibits greater ductility than after processing by HPT at 300 K. High strain rate superplasticity is achieved during testing at 523 K for strain rates as high as 1.0×10^{-1} s^{-1}. Additionally, the HPT-HT alloy achieves extraordinarily high elongations for all testing strain rates at 673 K with a maximum elongation of 1880 % when testing with a strain rate of 1.5×10^{-2} s^{-1}. This represents the highest elongation achieved to date in conventional Al alloys subjected to HPT processing [31,62,63] and it exceeds the earlier record-breaking elongation of 1600 % reported for the same alloy processed by HPT for 2 revolutions at RT when samples of ~1 mm in thickness were subjected to tensile testing at 573 K using a strain rate of 3.3×10^{-3} s^{-1} [40]. It should be noted also that elongations ≥980 % were recorded for the HPT-HT specimens when testing at 673 K at all strain rates over the range from 3.3×10^{-4} to 3.3×10^{-1} s^{-1}.

To better visualize the variation of the tensile elongations with the strain rate and temperature, Fig. 5 shows plots of the $\Delta l/l_0$ values *vs* strain rate for the Al-3Mg-0.2Sc alloy processed by 10 HPT turns at (a) RT and (b) 450 K for tensile tests conducted at temperatures from 473 to 723 K. Fig. 5 (a) shows that the HPT-RT material achieves an elongation of ~560 % when pulled to failure at 473 K for $\dot{\varepsilon} = 1.4 \times 10^{-3}$ s^{-1} but increasing the temperature to 573 K leads to a general enhancement of ductility. Nevertheless, the tensile elongations decrease significantly when increasing the temperature to 673 K.

The plots in Fig. 5 (b) demonstrate that the alloy processed by HPT at 450 K exhibits superior superplastic properties such that elongations >400 % were achieved for tests performed at 473 K with $\dot{\varepsilon} \leq 3.3 \times 10^{-2}$ s^{-1}. The elongations tend to increase with increasing temperatures with

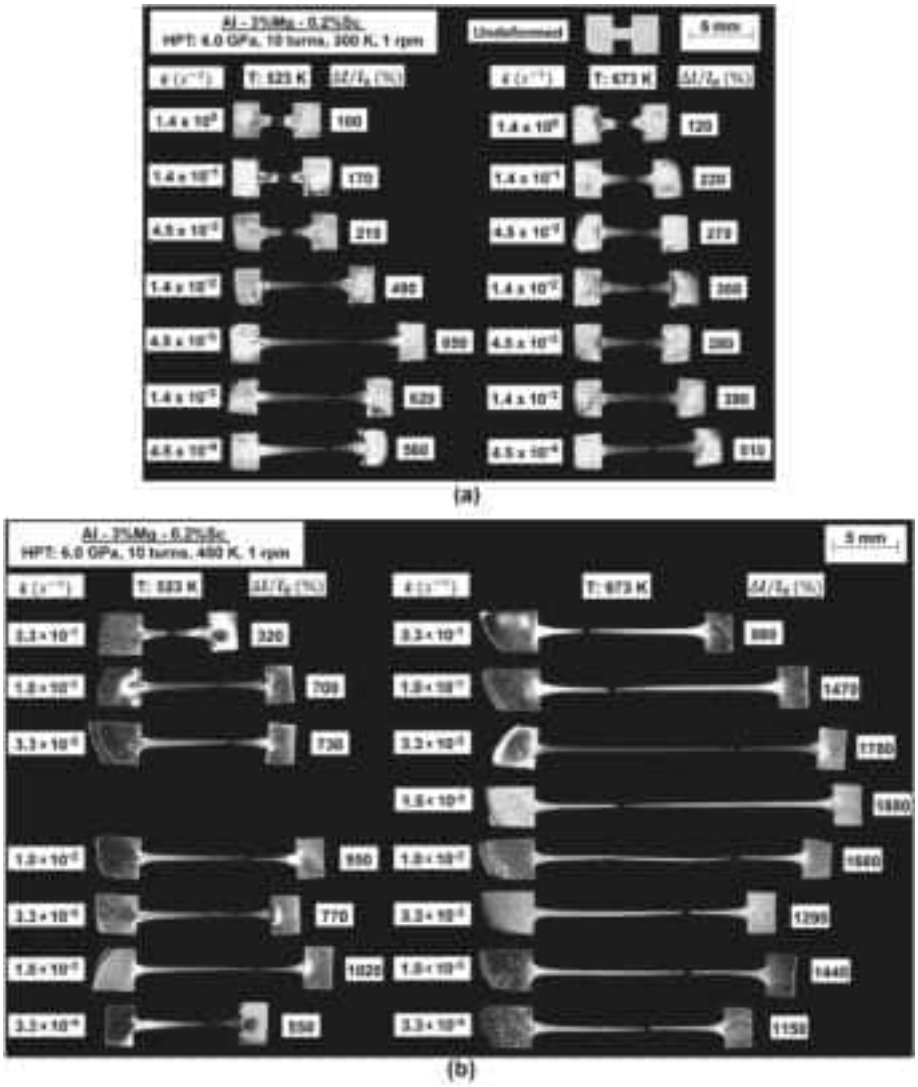

Fig. 4. Fractured specimens of the Al-3Mg-0.2Sc alloy processed by 10 HPT turns at (a) 300 K and (b) 450 K and then pulled to failure at 523 and 673 K.

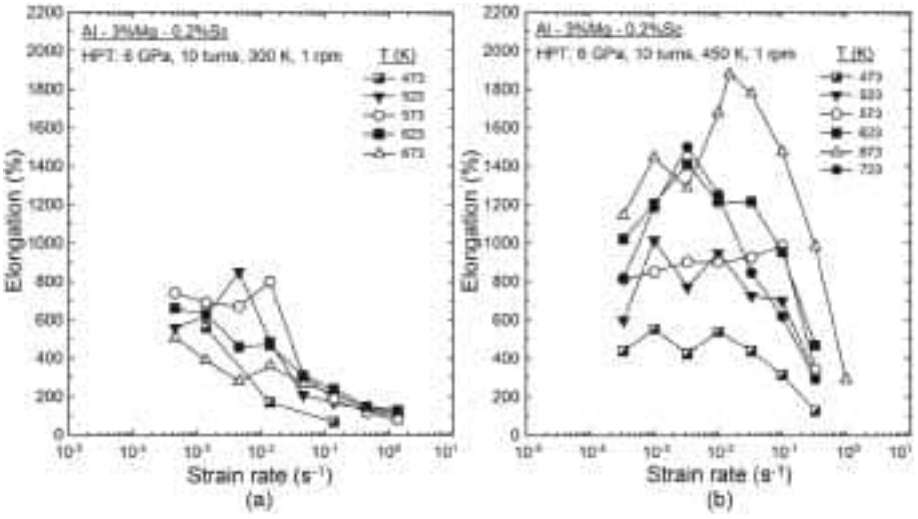

Fig. 5. Elongation vs strain rate for the Al-3Mg-0.2Sc alloy processed by 10 HPT revolutions at (a) 300 and (b) 450 K and tensile tested using various strain rates at temperatures from 473 to 723 K.

maximum values at 673 K and slightly lower elongations at 723 K. It is important to note that elongations higher than 600 % were consistently obtained for all tests conducted at strain rates ranging from 3.3×10^{-4} to 10^{-2} s^{-1}.

Fig. 6 shows plots of the variation of the flow stress at $\varepsilon = 0.3$ with the strain rate for the alloy processed by 10 HPT turns at two different temperatures and tested in tension using various strain rates at temperatures from 473 to 723 K. The experimental data were plotted using logarithmic scales for both the stress and the strain rate so that the local slopes of these curves represent the apparent strain rate sensitivity, m.

It is apparent from Fig. 6 (a) that the plots of the HPT-RT alloy indicate two separate slopes depending on the strain rate and temperature. For tests at 473 K there is a value of $m \approx 0.5$ for $\dot{\varepsilon} < 10^{-2}$ s^{-1} and a slope of ~0.22 at faster strain rates. Furthermore, the range of strain rates with $m \approx 0.5$ expands towards faster strain rates (~4.5×10^{-2} s^{-1}) with increasing temperatures up to $T \approx 623$ K.

A comparison of Fig. 6 (a) and (b) shows that the alloy processed at 450 K displays markedly lower flow stresses at $\varepsilon = 0.3$ than after HPT at RT. The curves of the HPT-HT metal at 473 and 523 K exhibit a sigmoidal profile with a slope of ~0.5 at intermediate strain rates. The curves in Fig. 6 (b) show $m \geq 0.5$ for $T \geq 573$ K considering $\dot{\varepsilon} \geq 10^{-2}$ s^{-1}. However, these slopes decrease at lower strain rates and the HPT-HT alloy exhibits m values of ~0.2–0.3 at temperatures from 573 to 673 K and $\dot{\varepsilon} < 10^{-2}$ s^{-1}. It should be noted that the HPT-HT alloy achieves higher flow stresses during deformation at 723 K than at 673 K for $\dot{\varepsilon} \geq 10^{-2}$ s^{-1}.

3.3. Microstructures after deformation at high temperatures

Fig. 7 shows typical orientation maps and the corresponding {111} pole figures taken along (a) the undeformed area and (b) the gauge section of the specimens processed by HPT at RT and tested in tension at 673 K with a strain rate of 4.5×10^{-2} s^{-1}. Examination of Fig. 7 (a) reveals the onset of abnormal coarsening at the grip area of the miniature specimen during heating at 673 K for the period of ~660 s when considering the total time the sample was held within the tensile testing apparatus. This is consistent with a recent study where the same alloy underwent secondary recrystallisation and extensive grain growth after heating at either 623 or 673 K for 1 h [25]. This microstructure displays fine grains together with a population of grains having sizes of tens of micrometres with the {100} planes nearly parallel to the thickness direction.

By contrast, the grains in the gauge section are predominantly oriented with the {110} planes parallel to the thickness direction. It should be noted that these grains are elongated towards the tensile axis and contain a substantial fraction of low-angle grain boundaries (LAGBs) with misorientation angles ranging from 2 to 15° and which are often organised in the form of subgrains. The grain structures in the gauge area of the specimen are slightly finer than in the undeformed section and measurements for each orientation map gave values of the average grain size, $\overline{L}$, of ~2.2 and ~2.5 μm in the undeformed and gauge section, respectively.

Histograms detailing the distributions of grain diameters and the fraction of correlated boundaries as a function of the misorientation angles are presented in Fig. 1A of the Supplementary Material. They reveal that the gauge section of the specimen has a narrower distribution of grain diameters although there is evidence of bimodal distributions of grain diameters for both areas. The histograms of the misorientation angles for the HPT-RT alloy are noticeably different from the Mackenzie distribution shown by the solid line in Fig. 1A (b) [64] and this may be attributed to the development of a preferential texture and substructures. The deformed and the undeformed areas of the samples have fractions of LAGBs of ~26 and 22 %, respectively, and these values are higher than the fraction measured after HPT at RT [25].

Fig. 8 shows orientation maps and the corresponding {111} pole figures taken at the undeformed areas and the gauge sections of the fractured specimens of the alloy originally processed by HPT at 450 K and then tested in tension at 673 K using various strain rates. The lines coloured in white denote Σ3 60° <111> twin boundaries. Inspection shows that abnormal coarsening gradually evolves in the undeformed areas of the HPT-HT alloy as specimens are tested at slower strain rates and the consequent exposure to the testing temperature for longer periods of time leads to larger grain sizes. In contrast with the HPT-RT material, the deformed areas of the fractured specimens have grains with larger sizes than their undeformed counterparts and the microstructures display very few LAGBs.

The gauge section of the material tested at 1.0 s^{-1} in Fig. 8 (b) shows a weaker texture than the undeformed area but there is an increase in the fraction of grains with a texture component around {110}. There is also evidence for the development of an essentially random texture during testing at 3.3×10^{-2} s^{-1} for the alloy in Fig. 8 (d) processed by HPT at 450 K. Furthermore, after tensile testing at 3.3×10^{-4} s^{-1} in Fig. 8 (f) the grains in the HPT-HT sample exhibit higher aspect ratios than after deformation at faster strain rates and there is some evidence for twinning activity and the onset of abnormal grain growth. Similar histograms were constructed for the HPT-RT metal tested at 673 K and

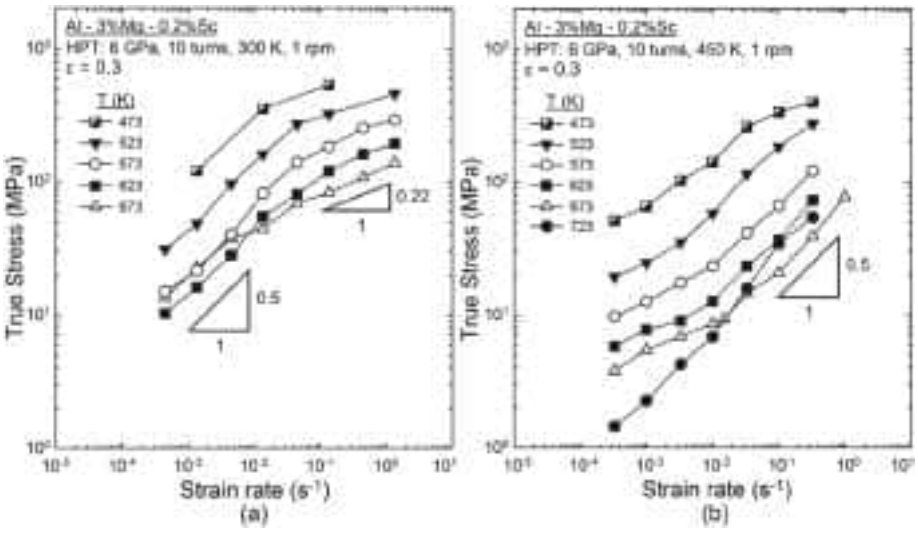

Fig. 6. True stress at $\varepsilon = 0.3$ vs strain rate for the Al-3Mg-0.2Sc alloy processed by 10 HPT revolutions at (a) 300 and (b) 450 K and tensile tested using various strain rates at temperatures from 473 to 723 K.

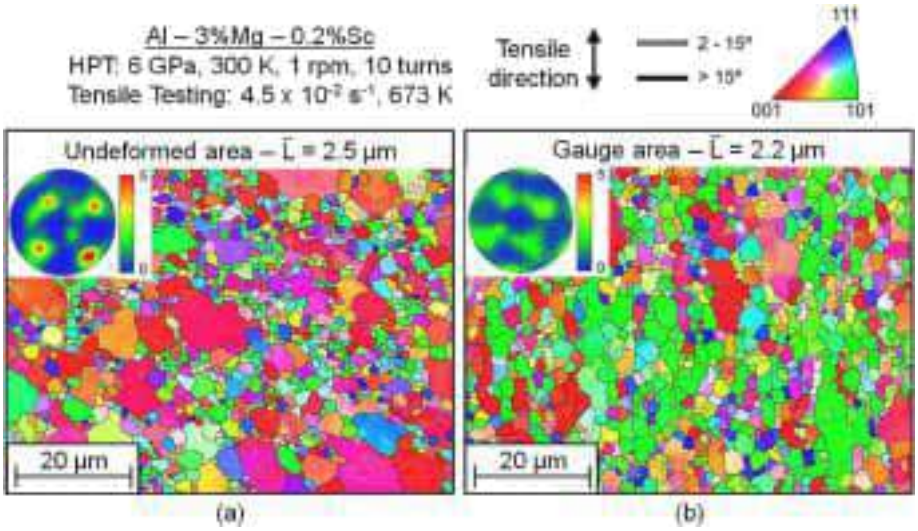

Fig. 7. Orientation maps and corresponding {111} pole figures taken along (a) the undeformed and (b) the gauge area of the fractured specimens of the Al-3Mg-0.2Sc alloy subjected to 10 HPT turns at 300 K and tested in tension at 673 K.

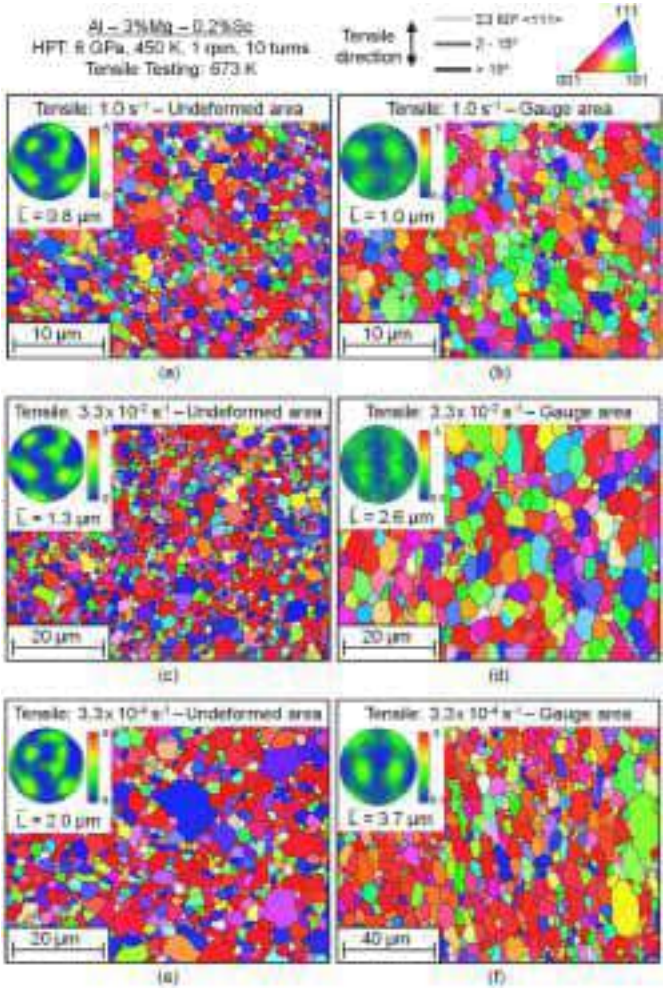

Fig. 8. Orientation maps and corresponding {111} pole figures taken along (a, c, e) the undeformed and (b, d, f) the gauge area of the fractured specimens of the Al-3Mg-0.2Sc alloy subjected to 10 HPT revolutions at 450 K and tested in tension at 673 K at strain rates of (a, b) 1.0, (c, d) 3.3×10^{-2} and (e, f) 3.3×10^{-4} s^{-1}.

they are presented in Fig. 2A of the Supplementary Material corresponding to the orientation maps shown in Fig. 8.

It is well established that, due to the occurrence of grain boundary sliding, the grains become elevated above the surfaces of specimens during straining under superplastic conditions [48,65,66]. For this reason, a thorough examination of the surface topography of the fractured samples permits measurement of the grain sizes in the HPT-processed alloy after tensile testing. Several SE images were taken along the deformed areas of the fractured specimens and examples are shown in Fig. 3A of the Supplementary Material for the samples tested at 673 K after processing at (a) 300 and (b) 450 K. These images were used to estimate the grain sizes after tensile testing and to thereby analyse the grain growth kinetics under dynamic conditions. The results are presented in Fig. 9 as plots of grain size *vs* time at testing temperature for the Al-3Mg-0.2Sc alloy processed by HPT at RT or 450 K and tested in tension at temperatures from 473 to 723 K.

It is readily apparent from Fig. 9 that the material processed by HPT at RT displays faster kinetics of grain coarsening than the material processed by HPT at 450 K under comparable conditions of tensile testing. After straining at 473 K, all specimens continue to exhibit ultrafine-grained (UFG) structures even after prolonged exposure times of ~4 h. There is a substantial increase in grain size after raising the temperature from 473 to 523 K although the grain sizes in the HPT-HT alloy are smaller. Further increases in temperature produce minor coarsening for the material processed by HPT at 450 K but the grain sizes increase markedly for the HPT-RT material deformed at $T \geq 573$ K.

To investigate whether high temperature straining leads to the development of second phases in the HPT-processed alloy, TEM observations were undertaken along the gauge sections of the miniature specimens of the Al-3Mg-0.2Sc alloy originally subjected to 10 HPT revolutions at either 300 or 450 K and then tested at 673 K using similar strain rates. Typical results are shown in Fig. 10 in which the TEM images on the left were obtained using transfer electron (TE) contrast but the micrographs on the right were from atomic number (Z) contrast.

For both processing temperatures, it is readily apparent that there is a profuse distribution of second phase particles in the vicinity of the grain boundaries of the HPT-processed alloy. These second phases were identified as Al_3Sc precipitates using electron dispersive spectroscopy and the electron diffraction patterns (see Fig. 4A and 5A in the Supplementary Material). These phases appear to display smaller sizes and cover large amounts of the grain boundaries in the HPT-HT material compared with the alloy processed by HPT at 300 K. Furthermore, the Al_3Sc particles appear to be in a later stage of coalescence in the latter

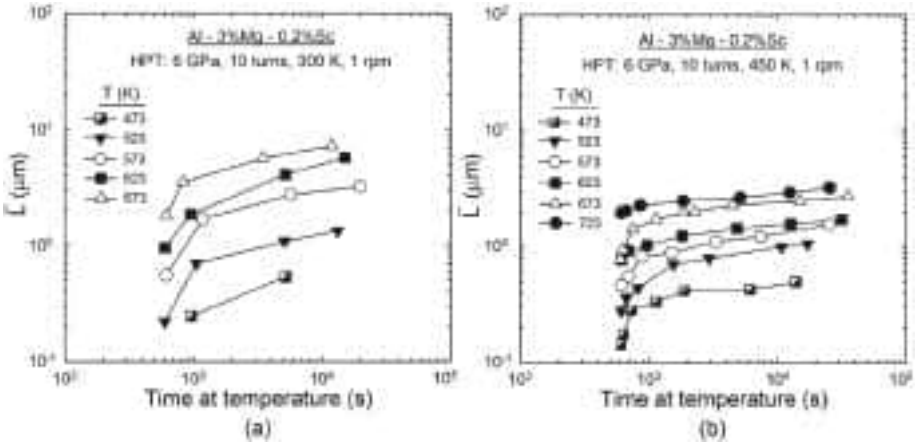

Fig. 9. Average grain size ($\bar{L}$) vs total time at the testing temperature for miniature specimens of the Al-3Mg-0.2Sc alloy subjected to 10 HPT turns at (a) 300 and (b) 450 K and tested in tension at temperatures from 473 to 723 K using strain rates ranging from 3.3×10^{-4} to 1.0 s^{-1}.

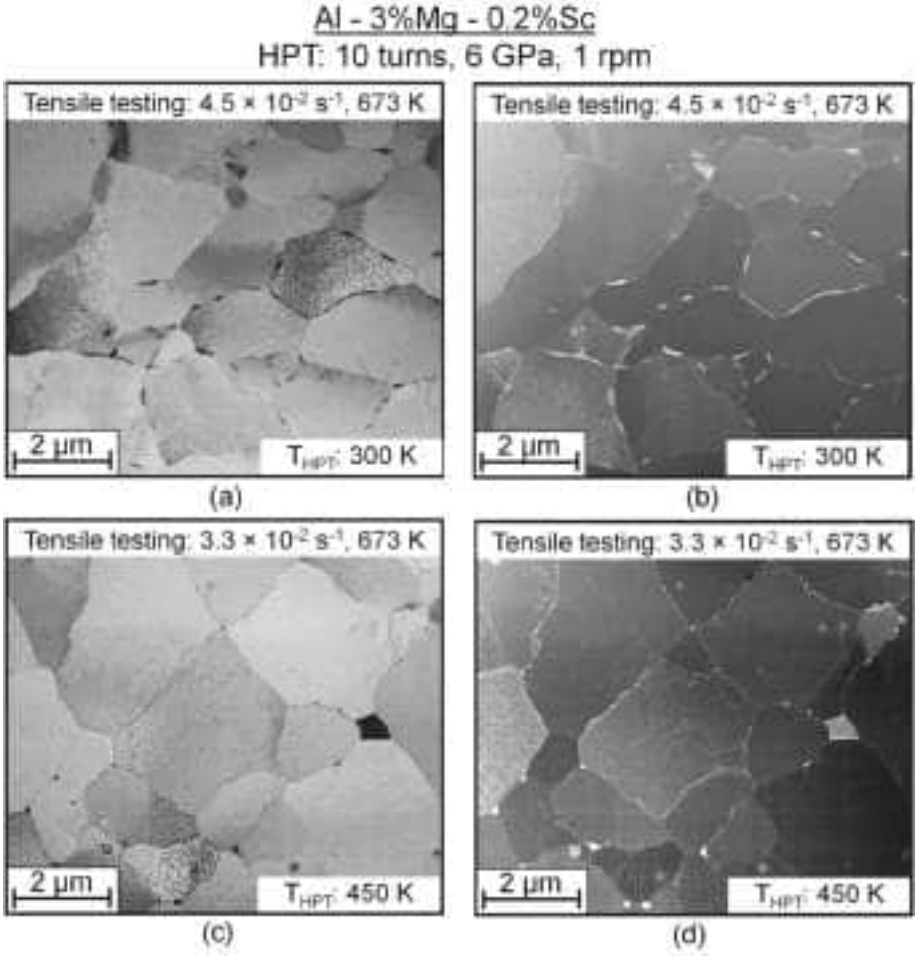

Fig. 10. TEM images taken along the gauge areas of the fractured specimens of the Al-3Mg-0.2Sc alloy subjected to 10 HPT turns at (a, b) 300 and (c, d) 450 K and tested in tension at 673 K using similar strain rates.

material and they form relatively thick films along the grain boundaries of the grains having sizes of ~1–2 μm.

4. Discussion

4.1. Superplastic characteristics after HPT

Fig. 11 shows colour-coded maps that were constructed using the data from Fig. 5 to plot the variations in elongation with temperature and strain rate where the broken lines added to these plots delineate the

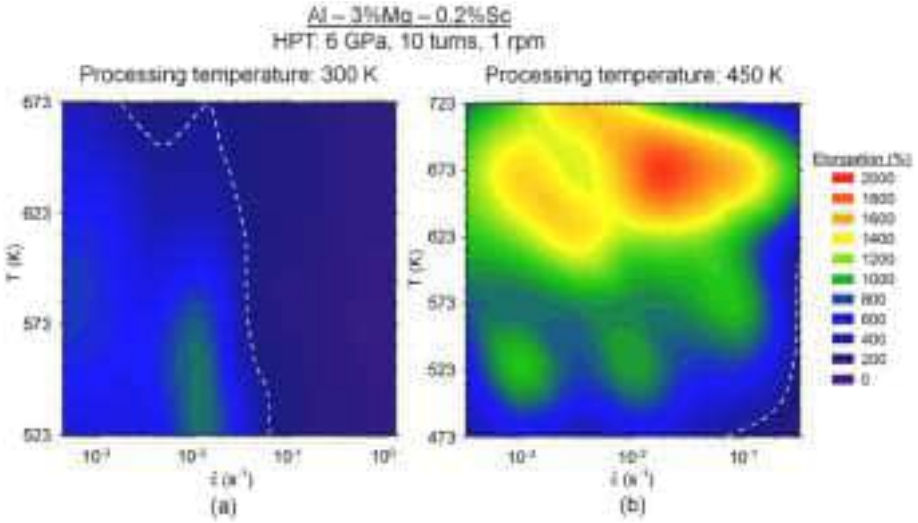

Fig. 11. Colour-coded contour maps showing the tensile elongations achieved in miniature specimens of the Al-3Mg-0.2Sc alloy processed through 10 HPT turns at (a) 300 and (b) 450 K and tested in tension at temperatures from 473 to 723 K using strain rates ranging from 3.3×10^{-4} to 1.0 s^{-1}. (For interpretation of the references to colour in this figure legend, the reader is referred to the Web version of this article.)

contours where there is an elongation of at least 400 %. Following the earlier definition of superplastic flow [59], these broken lines therefore represent the onset of true superplasticity at the slower strain rates. The maps of temperature *vs* strain rate in Fig. 11 provide a new procedure for depicting the superplastic data and careful analysis shows the trends are generally consistent with the reported results for many other superplastic ultrafine-grained materials [67]. It follows from Fig. 11 that the alloy processed through 10 HPT revolutions at 473 K displays remarkable ductility compared with the samples processed by HPT at RT. The HPT-HT material reached high elongations for all testing conditions examined in this research and exhibited true superplastic ductilities over an extended range of temperatures and strain rates. In general, the elongation values for the HPT-HT alloy increase with increasing temperature up to $T \approx 673$ K where elongations higher than 1000 % were achieved for tests conducted at $\sim 3.3 \times 10^{-4} \leq \dot{\varepsilon} \leq 3.3 \times 10^{-1}$ s^{-1}. There is also consistent evidence that the superplastic properties of the alloy processed by HPT at RT deteriorate at $T \geq 623$ K.

In superplastic materials the variation of elongation with strain rate shows a peak at intermediate strain rates [68–70]. The true stress *vs* true strain curves at superplastic conditions often show a sigmoidal shape which allows the classification of three distinct deformation regimes. At extremely high strain rates (region III), the contribution of grain boundary sliding (GBS) to the total straining decreases and intragranular dislocation processes are more prominent. This leads to a reduction in the strain rate sensitivity and thus the achievement of lower elongations at faster strain rates. By contrast, the decrease in strain rate occurs concurrently with more intense grain coarsening at very low strain rates (region I). The increase in grain size and the formation of subgrain structures are detrimental for GBS and favours the onset of internal cavities at the grain boundaries which ultimately leads to premature failure during tensile testing.

At an intermediate range of strain rates (region II), there is an optimum condition in which the material achieves enhanced superplastic properties. Within this deformation regime, the material is capable of retaining ultrafine-grained structures and the recovery kinetics are sufficiently fast to efficiently accommodate GBS by dislocation climb into the opposite grain boundaries. As a consequence, it exhibits higher m values and thus superior ductility. Also, the strain rate sensitivity tends to increase with temperature concurrently with the recovery kinetics and the superplastic ductility. Nonetheless, this effect is counteracted by grain coarsening and the formation of subgrains which adversely affect the action of GBS and may lead to premature failure. Accordingly, in the current study the optimum condition for superplasticity was achieved for the Al-Mg-Sc alloy processed by HPT at 450 K for tests carried out at 673 K and at 1.5×10^{-2} s^{-1}.

The superplastic behaviour observed in this alloy processed by HPT at 450 K is intrinsically associated with its improved thermal stability compared with the HPT-RT material. It is demonstrated in Fig. 9 that the HPT-HT material is capable of retaining fine grain structures for prolonged times during tensile testing at high temperatures. This is consistent with the coarsening kinetics during static annealing as reported in earlier studies [25,47,57]. Also, the presence of precipitates influences superplastic behaviour, as the Zener pinning effect more effectively hinders grain boundary migration when the particles are smaller and more uniformly distributed [71,72].

The results in Fig. 10 reveal that the Al_3Sc particles are substantially smaller and more dispersed in the Al-Mg-Sc alloy processed by HPT at 450 K even though the total time at the testing temperature was ~1430 s, whereas the Al alloy processed by HPT at RT was exposed to the testing temperature of 673 K for only ~540 s. Accordingly, superplastic flow will occur at faster rates in the material processed by HPT at 450 K as it preserves the smaller grains and thereby exhibits a higher density of HAGBs which are then available to undergo GBS during deformation at high temperatures [16,62,67].

It is worth noting that the material processed by HPT at RT was reported to have a large fraction of grains with $\bar{L} > 10$ μm after heating at 623 and 673 K [25]. These structures have a large fraction of LAGBs as shown in Fig. 7. In addition, even though the HPT-RT specimens continue exhibiting fine grain structures capable of deforming by GBS, this mechanism may not be operative in the abnormally coarse grains which will probably deform by dislocation glide and climb in the tensile tests performed at faster strain rates. For this reason, the decrease in the elongations in the HPT-RT material tested at $\dot{\varepsilon} \geq 4.5 \times 10^{-2}$ s^{-1} and at $T \geq 623$ K is attributed directly to the reduced contributions from GBS in the overall straining.

This conclusion is supported by the orientation maps corresponding to the gauge section of the HPT-RT alloy deformed at 673 K as it shows many grains having the {110} planes parallel to the thickness direction which is a common feature for FCC metals strained under non-superplastic conditions [73]. Furthermore, these grains are elongated along the tensile direction and this is not consistent with the occurrence of straining by Rachinger GBS [74,75] which is the fundamental mechanism of superplastic flow [16]. Finally, the plots in Fig. 6 (a) demonstrate that the range of strain rates with $m \approx 0.22$ increases for T

$\geq$ 623 K and this suggests that dislocation climb becomes predominant at these testing conditions in accordance with the results presented in an earlier study for a coarse-grained Al-Mg-Sc alloy tested over many orders of magnitude of strain rate [44].

It follows from Fig. 6 that the HPT-HT alloy exhibits lower flow stresses than the HPT-RT alloy. However, it is noted that the apparent strain rate sensitivity tends to be < 0.5 in these samples for tests conducted at $\dot{\varepsilon} \leq 10^{-2}$ s^{-1} although the specimens consistently attained superplastic elongations. It should be noted, however, that these values need to be evaluated with caution as for each corresponding testing temperature grain coarsening tends to be more prominent at slower deformation rates and thus prolonged testing times [76,77]. For this reason, the grain sizes of the Al-Mg-Sc alloy at the same testing temperature are essentially different for the datum points recorded at the equivalent strain of 0.3 for each individual strain rate. Accordingly, the following section proposes a more adequate model to describe the superplastic flow in the HPT-processed Al alloy.

4.2. The mechanism of flow under superplastic conditions

The strain rate under steady-state conditions during superplastic flow at high temperatures is given by the following expression [16]:

$$\dot{\varepsilon} = \frac{AD_{gb}Gb}{kT}\left(\frac{b}{d}\right)^2\left(\frac{\sigma}{G}\right)^2 \quad (1)$$

where A is a dimensionless constant having a value of ~10 for conventional metals, D_{gb} is the grain boundary diffusion coefficient, G is the shear modulus, **b** is the Burgers vector, k is Boltzmann's constant, d is the spatial grain size given by $d = 1.74\,\bar{L}$ [78] and

$$D_{gb} = D_{o,gb}\, e^{\left(-\frac{Q_{gb}}{kT}\right)} \quad (2)$$

where D o, gb is a frequency factor and Q_{gb}, is the activation energy for grain boundary diffusion.

To identify whether the rate-controlling flow process in all HPT samples displaying elongations of $\Delta l/l_0 \geq 400$ % is GBS, the temperature and grain size compensated strain rate $(\dot{\varepsilon}KT/D_{gb}GB)(d/b)^2$ was plotted against the normalized stress (σ/G) in Fig. 12. These plots were constructed considering σ as the maximum flow stress and d as the spatial grain size in the fractured metal. As in earlier studies [48,62,67,79,80], the calculations used values of $D_{o,gb} = 1.86 \times 10^{-4}$ m^{2}s^{-1}, $Q_{gb} = 86$ kJ mol^{-1}, G (MPa) = (3.022×10^4) - $16T$ [81] and $\mathbf{b} = 2.86 \times 10^{-10}$ m [81]. The solid line labelled $\dot{\varepsilon}_{sp}$ shows the theoretical prediction for superplasticity controlled by grain boundary sliding accommodated by dislocation glide within the grains and subsequent climb into the opposite grain boundaries [16]. Also, additional data were included in Fig. 12 for various superplastic Al-Mg-Sc alloy processed by HPT [38,41,42].

It is readily apparent from Fig. 12 that the experimental values from both the current research and the earlier studies [38,41,42] are consistent with the predictions from the theoretical model for GBS in superplasticity although many of these values tend to lie slightly above $\dot{\varepsilon}_{sp}$. Nevertheless, as indicated in Fig. 12 and from results plotted in a recent review for this Al-Mg-Sc alloy [31], experimental datum points for the alloy processed by ECAP and HPT at RT generally lie below $\dot{\varepsilon}_{sp}$. This is a direct consequence of the thermally unstable Al-Mg-Sc microstructures developed after processing at RT since the grain sizes were taken from measurements performed immediately after the SPD processing.

It is important to note that the results obtained after conventional metal-working processes are generally more consistent with the theoretical predictions because these materials display less pronounced grain coarsening during superplastic straining. In the present research, the calculations considered the maximum flow stress and the spatial grain size along the gauge area of the fractured specimens. This means that, although grain growth occurred concurrently with pronounced work hardening during the tensile testing, the present procedure gave a more accurate assessment of the rate-controlling mechanism during superplasticity.

4.3. The influence of subgrain formation on the accommodation process during GBS

There are increases in the fractions of LAGBs organised as subgrains in the HPT-RT metal during deformation at 673 K. Accordingly, in addition to the effect of grain coarsening, there are slower accommodation rates during GBS due to a hindrance in dislocation glide by the subgrain boundaries [82] and this may also contribute to the reduction in ductility observed in the HPT-RT alloy at $T \geq 623$ K. To analyse if there is any correlation between the presence of subgrains and the elongations achieved in this study, Fig. 13 shows the variation of the values of $\bar{L}$ with the normalized stress, σ/G, for the alloy tested in tension after processing by HPT for 10 turns at (a) 300 and (b) 450 K, respectively, where the solid line represents the prediction for the equilibrium subgrain size, λ, in Al-Mg alloys estimated as $\lambda = 20\,\mathbf{b}\,(\sigma/G)^{-1}$ [44,83,84].

Examination of Fig. 13 shows that, as anticipated based on the theoretical analysis [16], for all samples giving superplastic elongations there is a value of $\bar{L} < \lambda$. This is consistent with the orientation maps in Fig. 8 as subgrains are nearly absent in the HPT-HT alloy after testing at 673 K for $\dot{\varepsilon} \leq 3.3 \times 10^{-2}$ s^{-1}. Thus, GBS is easily accommodated by dislocation glide under these conditions and this permits the

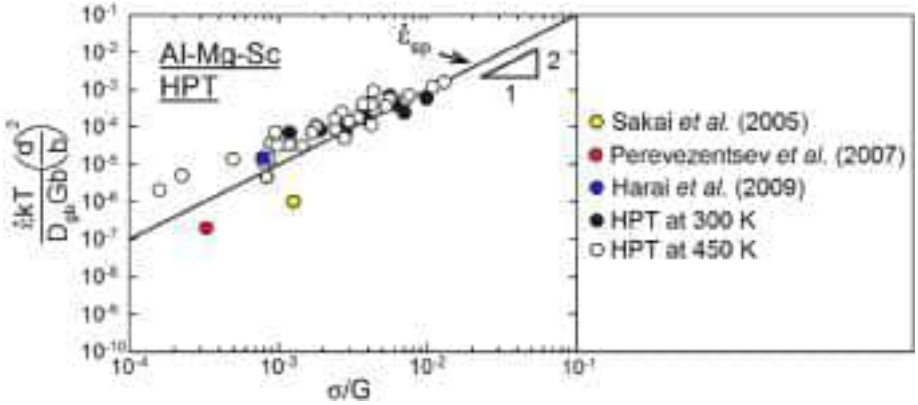

Fig. 12. Temperature and grain size compensated strain rate as a function of normalized stress for Al-3Mg-0.2Sc specimens exhibiting superplastic elongations after 10 turns of HPT processing at 300 or 450 K and tensile tested at temperatures from 473 to 723 K: additional data are also included for various superplastic Al-Mg-Sc alloys processed by HPT [38,41,42] and the solid line shows the theoretical prediction for superplastic flow, $\dot{\varepsilon}_{sp}$ [16].

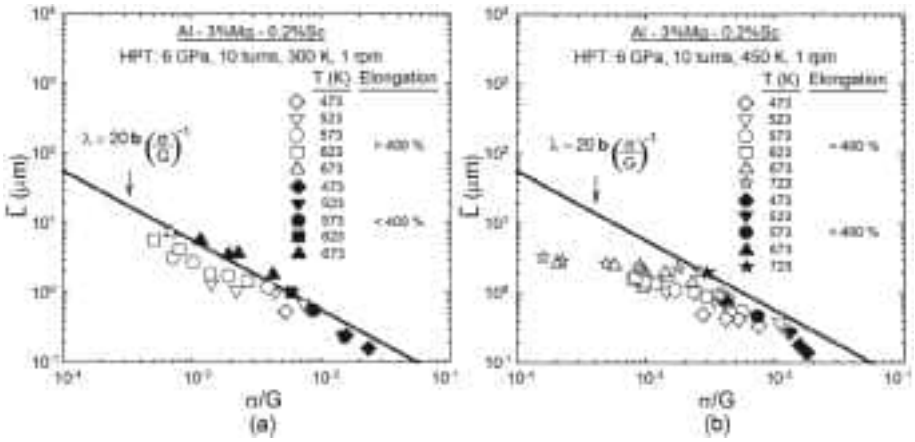

Fig. 13. Plots of grain size *vs* normalized stress for the Al-3Mg-0.2Sc alloy processed by 10 HPT turns at (a) 300 and (b) 450 K and tested in tension at temperatures from 473 to 723 K using various strain rates: the solid line represents the theoretical prediction for the equilibrium subgrain size, λ [44,83,84].

achievement of extensive superplastic ductilities. By contrast, $\overline{L} > \lambda$ for the HPT-RT alloy tested in tension at 673 K for $\dot{\varepsilon} > 4.5 \times 10^{-4}\ s^{-1}$, as confirmed in Fig. 7 (b) for $\dot{\varepsilon} = 4.5 \times 10^{-2}\ s^{-1}$, and accordingly the accommodating intragranular slip occurs at slower rates and this ultimately promotes premature failure during tensile testing due to the occurrence of internal cavitation [82]. This failure mode is more likely to occur during deformation at slower strain rates which is consistent with the nearly uniform widths of the fractured specimens deformed at 673 K for $\dot{\varepsilon} \leq 4.5 \times 10^{-3}\ s^{-1}$ as shown in Fig. 4 (a).

It also follows from Figs. 11 and 13 that elongations >400 % were not always achieved in the HPT-processed alloy at testing conditions where $\overline{L} < \lambda$ and this is because GBS is thermally-activated so that the sliding rates of adjacent HAGBs increase with increasing temperatures. Although the lack of subgrains facilitates the advent of accommodation during superplasticity, GBS requires exceptionally small grain sizes to operate during deformation at fast strain rates and low temperature [85,86]. In addition, the existence of second phase particles along the grain boundaries makes sliding more difficult and these particles appear to have larger sizes for the HPT-RT alloy deformed at 673 K as shown in Fig. 10.

4.4. An examination of the total elongations achieved in tensile testing

It is important to emphasize that the Al-3Mg-0.2Sc alloy used in this research achieved exceptionally high elongations for an HPT-processed material during deformation at 673 K with an elongation of ~1880 % at this temperature for a strain rate of $\dot{\varepsilon} = 1.5 \times 10^{-2}\ s^{-1}$ as shown in Fig. 4 (b). This is the highest elongation reported for any material after conventional HPT processing when tensile tests were conducted using miniature samples cut from the discs with initial thicknesses of ~0.6 mm. Nevertheless, in comparing the tensile elongations achieved using different processing techniques, it is important to note that earlier experiments showed conclusively that the measured elongations in tensile testing were dependent upon the initial overall dimensions of the specimens. Specifically, it was established that higher elongations may be achieved by using specimens having reduced gauge lengths and larger thicknesses [87,88].

In order to demonstrate and understand the reasons underlying the relatively lower ductilities encountered in Al-Mg-Sc alloys after HPT when compared with processing by ECAP, miniature tensile specimens having the same dimensions utilized in the current research were subjected to tensile testing at 523 K and at a strain rate of $\sim 10^{-3}\ s^{-1}$ [24,31]. The results consistently revealed that the elongations attained after HPT at 450 K were ~2 × higher than after ECAP. It has been shown that the Al alloy processed by HPT at 450 K exhibits smaller grain sizes and lower hardness after tensile testing than the ECAP-processed alloy. This confirms that HPT processing at 450 K permits the achievement of superior superplasticity at this temperature range due to its enhanced stability.

Also, this set of experiments with miniature tensile specimens was carried out over a wider range of temperatures and strain rates [44]. Although superplastic elongations of ~1880 % were achieved using conventional tensile specimens for the same alloy after ECAP at RT followed by tensile testing at 673 K and at $3.3 \times 10^{-2}\ s^{-1}$ [33], the maximum elongation reached in a miniature specimen under comparable processing and testing conditions was ~980 %. Conversely, an elongation to failure of ~1780 % was achieved in the current study for a miniature specimen of the Al-3Mg-0.2c alloy after HPT at 450 K and subsequent tensile testing at 673 K and at $3.3 \times 10^{-2}\ s^{-1}$. This confirms the intrinsic influence of sample size on the elongations achieved under superplastic conditions. It should be further noted that the comparably lower flow stress values at 673 K are consistent with the enhanced ductility encountered after HPT at 450 K compared with after HPT at RT or even ECAP at RT.

Earlier experiments on an $Al_9(CoCrFeMnNi)_{91}$ high-entropy alloy processed by HPT showed that it was possible to achieve an elongation of 2000 % at 1073 K using a strain rate of $5 \times 10^{-2}\ s^{-1}$ [89] but the specimen thickness was 0.7 mm which is larger than in the present investigation. There are also reports of high elongations of 2580 % in an Al-3Mg-0.2Sc alloy [33] and 4100 % in an Al-5Mg-0.2Sc alloy [36] but these samples were processed by ECAP where the tensile samples have thicknesses of 2 mm or larger. Finally, it is noted that an elongation to failure of 2320 % was reported at a temperature of 298 K for a Bi-43Sn alloy [90] where the sample was processed using the new procedure of tube high-pressure shearing (t-HPS) [91] and the experiments were undertaken using tensile specimens having thicknesses of ~2 mm [92]. Based on this analysis, it is apparent that the maximum elongation of 1880 % achieved in the present study is exceptionally large when considering the very thin gauge thickness of ~0.6 mm which severely limits the number of grains available in the specimen cross-section.

4.5. The role of processing temperature on the microstructural evolution during HPT

The Al-3Mg-0.2Sc alloy processed by HPT at RT exhibits slightly elongated grain structures with an average size of ~140 nm. It also displays a dislocation density of $\sim 3.6 \times 10^{13}\ m^{-2}$ as reported in a recent study [25]. These microstructural features are consistent with earlier experiments performed using Al-Mg-Sc alloys processed by SPD at low homologous temperatures [38,42,93,94]. At this range of temperature and strain rate, the restoration mechanism during severe plastic deformation is mechanically-driven which gives rise to grains having higher

aspect ratios [95–97].

After HPT at ~450 K, the same Al alloy displays a homogenous array of equiaxed grains with a mean size of ~150 nm, but a considerably lower dislocation density of $\sim 0.7 \times 10^{13}$ m^{-2} [25]. It is thus apparent that the restoration mechanism which permits the achievement of a steady state grain size in the Al-3Mg-0.2Sc alloy during HPT processing at ~450 K is prominently assisted by dynamic recovery. This is consistent with its relative low density of dislocations and the nearly equiaxed grain structures, as obtained in a recent study performed with an Al-Mg-Sc-Zr alloy processed by HPT at 473 K [30].

It should be noted also that the material processed by 10 HPT turns at RT exhibits a broader distribution of grain sizes and sharper gradients in the distributions of extrinsic dislocations throughout the Al microstructure. As demonstrated in detail in an earlier investigation [25], these microstructural features provide conditions for grain boundary migration at faster rates in the material processed by HPT at RT which also shows a more intense susceptibility for abnormal grain coarsening.

The excellent superplastic behaviour achieved in the current investigation is attributed to the enhanced microstructural stability which was promoted by undertaking the HPT processing at 473 K [25]. Thus, this permitted the preservation of an extremely small grain size in the Al-Mg-Sc microstructure and these grains co-existed with a larger proportion of HAGBs and more dispersed Al_3Sc precipitates compared with the material processed by HPT at RT.

5. Summary and conclusions

1 An Al-3Mg-0.2Sc alloy was processed through 10 turns of HPT at RT $\approx$ 300 K and at 450 K to produce a homogeneous array of grains with average sizes of ~140 and 150 nm, respectively. The HPT-processed material was then subjected to tensile testing over a wide range of strain rates and temperatures.

2 Superplastic elongations >400 % were achieved in the alloy processed by HPT at 300 K during deformation at temperatures up to 573 K and a maximum elongation of ~850 % was achieved at 523 K with a strain rate of $\dot{\varepsilon} = 4.5 \times 10^{-3}$ s^{-1}. Nevertheless, the tensile elongations decreased for tests conducted at $T \geq 623$ K due to extensive grain coarsening.

3 The alloy processed by HPT at 450 K showed enhanced low temperature superplasticity with elongations >900 % for tests conducted at 573 K for $3.3 \times 10^{-3} \leq \dot{\varepsilon} \leq 1.0 \times 10^{-1}$ s^{-1}. High strain rate superplasticity was attained over an extended range of strain rates. These results are due to the exceptionally small grain sizes and the low fractions of LAGBs in the alloy during deformation at low temperatures.

4 The material processed by HPT at 473 K exhibited optimum superplastic ductilities at 673 K and a record elongation of ~1880 % was achieved at this temperature at $\dot{\varepsilon} = 1.5 \times 10^{-2}$ s^{-1} for an Al-based alloy processed by HPT. Superplastic elongations ≥980 % were attained at 673 K for $\dot{\varepsilon} \leq 3.3 \times 10^{-1}$ s^{-1}. This enhanced superplasticity originated from a combination of the high diffusion rates at 673 K and the retention of microstructures with very fine grains having larger proportions of HAGBs.

5 Analysis of the data confirms a stress exponent of ~2 for the HPT-processed material during superplastic flow demonstrating that flow occurs by GBS accommodated by dislocation glide and climb. The high elongations occur when the grain size remains smaller than the equilibrium subgrain size. The absence of subgrains under these conditions was confirmed by orientation maps and this facilitates accommodation by intragranular slip during GBS.

Data availability

The raw/processed data required to reproduce these findings can be shared upon request.

CRediT authorship contribution statement

Pedro Henrique R. Pereira: Writing – original draft, Visualization, Validation, Investigation, Formal analysis, Data curation, Conceptualization. **Piotr Bazarnik:** Writing – review & editing, Methodology, Investigation. **Yi Huang:** Writing – review & editing, Supervision, Resources, Methodology. **Malgorzata Lewandowska:** Funding acquisition, Methodology, Resources, Writing – review & editing. **Terence G. Langdon:** Conceptualization, Funding acquisition, Methodology, Project administration, Resources, Supervision, Validation.

Declaration of competing interest

The authors declare that they have no known competing financial interests or personal relationships that could have appeared to influence the work reported in this paper.

Data availability

Data will be made available on request.

Acknowledgements

This research was supported by FAPEMIG under Grant APQ-01342–21 (PHRP), the European Research Council under ERC Grant Agreement No. 267464-SPDMETALS (TGL and YH) and CNPq under Grant No. 443736/2018–9 (PHRP).

Appendix A. Supplementary data

Supplementary data to this article can be found online at https://doi.org/10.1016/j.msea.2024.147320.

References

[1] R.Z. Valiev, R.K. Islamgaliev, I.V. Alexandrov, Bulk nanostructured materials from severe plastic deformation, Prog. Mater. Sci. 45 (2000) 103–189, https://doi.org/10.1016/S0079-6425(99)00007-9.

[2] T.G. Langdon, Twenty-five years of ultrafine-grained materials: achieving exceptional properties through grain refinement, Acta Mater. 61 (2013) 7035–7059, https://doi.org/10.1016/j.actamat.2013.08.018.

[3] K. Edalati, A. Bachmaier, V.A. Beloshenko, Y. Beygelzimer, V.D. Blank, W.J. Botta, K. Bryła, J. Čížek, S. Divinski, N.A. Enikeev, Y. Estrin, G. Faraji, R.B. Figueiredo, M. Fuji, T. Furuta, T. Grosdidier, J. Gubicza, A. Hohenwarter, Z. Horita, J. Huot, Y. Ikoma, M. Janeček, M. Kawasaki, P. Král, S. Kuramoto, T.G. Langdon, D. R. Leiva, V.I. Levitas, A. Mazilkin, M. Mito, H. Miyamoto, T. Nishizaki, R. Pippan, V.V. Popov, E.N. Popova, G. Purcek, O. Renk, Á. Révész, X. Sauvage, V. Sklenicka, W. Skrotzki, B.B. Straumal, S. Suwas, L.S. Toth, N. Tsuji, R.Z. Valiev, G. Wilde, M. J. Zehetbauer, X. Zhu, Nanomaterials by severe plastic deformation: review of historical developments and recent advances, Mater Res Lett 10 (2022) 163–256, https://doi.org/10.1080/21663831.2022.2029779.

[4] R.Z. Valiev, I.V. Alexandrov, M. Kawasaki, T.G. Langdon, Ultrafine-Grained Materials, TMS/Springer Nature, Cham, Switzerland, 2024, https://doi.org/10.1007/978-3-031-31729-3.

[5] R.Z. Valiev, T.G. Langdon, Principles of equal-channel angular pressing as a processing tool for grain refinement, Prog. Mater. Sci. 51 (2006) 881–981, https://doi.org/10.1016/J.PMATSCI.2006.02.003.

[6] A.P. Zhilyaev, T.G. Langdon, Using high-pressure torsion for metal processing: fundamentals and applications, Prog. Mater. Sci. 53 (2008) 893–979, https://doi.org/10.1016/j.pmatsci.2008.03.002.

[7] K. Edalati, Z. Horita, A review on high-pressure torsion (HPT) from 1935 to 1988, Mater. Sci. Eng. 652 (2016) 325–352, https://doi.org/10.1016/j.msea.2015.11.074.

[8] A. Hohenwarter, A. Bachmaier, B. Gludovatz, S. Scheriau, R. Pippan, Technical parameters affecting grain refinement by high pressure torsion, Int. J. Mater. Res. 100 (2009) 1653–1661, https://doi.org/10.3139/146.110224.

[9] P.H.R. Pereira, R.B. Figueiredo, Finite element modelling of high-pressure torsion: an overview, Mater. Trans. 60 (2019) 1139–1150, https://doi.org/10.2320/matertrans.MF201906.

[10] R.B. Figueiredo, P.R. Cetlin, T.G. Langdon, The processing of difficult-to-work alloys by ECAP with an emphasis on magnesium alloys, Acta Mater. 55 (2007) 4769–4779, https://doi.org/10.1016/j.actamat.2007.04.043.

[11] P.H.R. Pereira, R.B. Figueiredo, Y. Huang, P.R. Cetlin, T.G. Langdon, Modeling the temperature rise in high-pressure torsion, Mater. Sci. Eng. 593 (2014) 185–188, https://doi.org/10.1016/j.msea.2013.11.015.

[12] K. Edalati, Y. Hashiguchi, P.H.R. Pereira, Z. Horita, T.G. Langdon, Effect of temperature rise on microstructural evolution during high-pressure torsion, Mater. Sci. Eng. 714 (2018) 167–171, https://doi.org/10.1016/j.msea.2017.12.095.
[13] A.P. Zhilyaev, B.K. Kim, G.V. Nurislamova, M.D. Baró, J.A. Szpunar, T.G. Langdon, Orientation imaging microscopy of ultrafine-grained nickel, Scripta Mater. 46 (2002) 575–580, https://doi.org/10.1016/S1359-6462(02)00018-0.
[14] A.P. Zhilyaev, G.V. Nurislamova, B.K. Kim, M.D. Baró, J.A. Szpunar, T.G. Langdon, Experimental parameters influencing grain refinement and microstructural evolution during high-pressure torsion, Acta Mater. 51 (2003) 753–765, https://doi.org/10.1016/S1359-6454(02)00466-4.
[15] J. Wongsa-Ngam, M. Kawasaki, T.G. Langdon, A comparison of microstructures and mechanical properties in a Cu–Zr alloy processed using different SPD techniques, J. Mater. Sci. 48 (2013) 4653–4660, https://doi.org/10.1007/s10853-012-7072-0.
[16] T.G. Langdon, A unified approach to grain boundary sliding in creep and superplasticity, Acta Metall. Mater. 42 (1994) 2437–2443, https://doi.org/10.1016/0956-7151(94)90322-0.
[17] R.Z. Valiev, D.A. Salimonenko, N.K. Tsenev, P.B. Berbon, T.G. Langdon, Observations of high strain rate superplasticity in commercial aluminum alloys with ultrafine grain sizes, Scripta Mater. 37 (1997) 1945–1950, https://doi.org/10.1016/S1359-6462(97)00387-4.
[18] Z. Horita, M. Furukawa, M. Nemoto, A.J. Barnes, T.G. Langdon, Superplastic forming at high strain rates after severe plastic deformation, Acta Mater. 48 (2000) 3633–3640, https://doi.org/10.1016/S1359-6454(00)00182-8.
[19] A.J. Barnes, Superplastic forming 40 Years and still growing, J. Mater. Eng. Perform. 16 (2007) 440–454, https://doi.org/10.1007/s11665-007-9076-5.
[20] J. Wongsa-Ngam, T.G. Langdon, Advances in superplasticity from a laboratory curiosity to the development of a superplastic forming industry, Metals 12 (2022) 1921, https://doi.org/10.3390/MET12111921.
[21] S. Lee, A. Utsunomiya, H. Akamatsu, K. Neishi, M. Furukawa, Z. Horita, T. G. Langdon, Influence of scandium and zirconium on grain stability and superplastic ductilities in ultrafine-grained Al-Mg alloys, Acta Mater. 50 (2002) 553–564, https://doi.org/10.1016/S1359-6454(01)00368-8.
[22] D.G. Morris, M.A. Muñoz-Morris, Microstructure of severely deformed Al-3Mg and its evolution during annealing, Acta Mater. 50 (2002) 4047–4060, https://doi.org/10.1016/S1359-6454(02)00203-3.
[23] Y.L. Duan, G.F. Xu, X.Y. Peng, Y. Deng, Z. Li, Z.M. Yin, Effect of Sc and Zr additions on grain stability and superplasticity of the simple thermal–mechanical processed Al–Zn–Mg alloy sheet, Mater. Sci. Eng., A 648 (2015) 80–91, https://doi.org/10.1016/j.msea.2015.09.049.
[24] P.H.R. Pereira, Y. Huang, T.G. Langdon, Thermal stability and superplastic behaviour of an Al-Mg-Sc alloy processed by ECAP and HPT at different temperatures, IOP Conf. Ser. Mater. Sci. Eng. 194 (2017) 012013, https://doi.org/10.1088/1757-899X/194/1/012013.
[25] P.H.R. Pereira, P. Bazarnik, Y. Huang, M. Lewandowska, T.G. Langdon, Flow behaviour and microstructural stability in an Al-3Mg-0.2Sc alloy processed by high-pressure torsion at different temperatures, Mater. Sci. Eng., A 887 (2023) 145766, https://doi.org/10.1016/j.msea.2023.145766.
[26] E.A. Marquis, D.N. Seidman, Nanoscale structural evolution of Al3Sc precipitates in Al(Sc) alloys, Acta Mater. 49 (2001) 1909–1919, https://doi.org/10.1016/S1359-6454(01)00116-1.
[27] J. Røyset, N. Ryum, Scandium in aluminium alloys, Int. Mater. Rev. 50 (2005) 19–44, https://doi.org/10.1179/174328005X14311.
[28] J. Røyset, N. Ryum, Kinetics and mechanisms of precipitation in an Al-0.2wt.% Sc alloy, Mater. Sci. Eng. 396 (2005) 409–422, https://doi.org/10.1016/j.msea.2005.02.015.
[29] E.A. Marquis, D.N. Seidman, M. Asta, C. Woodward, Composition evolution of nanoscale Al3Sc precipitates in an Al-Mg-Sc alloy: experiments and computations, Acta Mater. 54 (2006) 119–130, https://doi.org/10.1016/j.actamat.2005.08.035.
[30] R.T. Mathew, S. Singam, P. Ghosh, S.K. Masa, M.J.N.V. Prasad, The defining role of initial microstructure and processing temperature on microstructural evolution, hardness and tensile response of Al-Mg-Sc-Zr (AA5024) alloy processed by high pressure torsion, J. Alloys Compd. 901 (2022) 163548, https://doi.org/10.1016/j.jallcom.2021.163548.
[31] P.H.R. Pereira, Y. Huang, M. Kawasaki, T.G. Langdon, An examination of the superplastic characteristics of Al–Mg–Sc alloys after processing, J. Mater. Res. 32 (2017) 4541–4553, https://doi.org/10.1557/jmr.2017.286.
[32] Y.A. Filatov, V.I. Yelagin, V. V Zakharov, New Al–Mg–Sc alloys, Mater. Sci. Eng., A 280 (2000) 97–101, https://doi.org/10.1016/S0921-5093(99)00673-5.
[33] S. Komura, Z. Horita, M. Furukawa, M. Nemoto, T.G. Langdon, An evaluation of the flow behavior during high strain rate superplasticity in an Al-Mg-Sc alloy, Metall Mater Trans A Phys Metall Mater Sci 32 (2001) 707–716, https://doi.org/10.1007/s11661-001-1006-9.
[34] F. Musin, R. Kaibyshev, Y. Motohashi, G. Itoh, Superplastic behavior and microstructure evolution in a commercial Al-Mg-Sc alloy subjected to intense plastic straining, Metall. Mater. Trans. 35 (2004) 2383–2392, https://doi.org/10.1007/s11661-006-0218-4.
[35] R. Kaibyshev, E. Avtokratova, A. Apollonov, R. Davies, High strain rate superplasticity in an Al-Mg-Sc-Zr alloy subjected to simple thermomechanical processing, Scripta Mater. 54 (2006) 2119–2124, https://doi.org/10.1016/j.scriptamat.2006.03.020.
[36] E. Avtokratova, O. Sitdikov, M. Markushev, R. Mulyukov, Extraordinary high-strain rate superplasticity of severely deformed Al–Mg–Sc–Zr alloy, Mater. Sci. Eng., A 538 (2012) 386–390, https://doi.org/10.1016/j.msea.2012.01.041.
[37] D. Yuzbekova, A. Mogucheva, R. Kaibyshev, Superplasticity of ultrafine-grained Al–Mg–Sc–Zr alloy, Mater. Sci. Eng. 675 (2016) 228–242, https://doi.org/10.1016/j.msea.2016.08.074.
[38] G. Sakai, Z. Horita, T.G. Langdon, Grain refinement and superplasticity in an aluminum alloy processed by high-pressure torsion, Mater. Sci. Eng., A 393 (2005) 344–351, https://doi.org/10.1016/j.msea.2004.11.007.
[39] S.V. Dobatkin, V.V. Zakharov, A.Yu Vinogradov, K. Kitagawa, N.A. Krasil'nikov, T. D. Rostova, E.N. Bastarash, Nanocrystalline Structure Formation in Al-Mg-Sc Alloys during Severe Plastic Deformation, vol. 2006, Russian Metallurgy (Metally), 2006, pp. 533–540, https://doi.org/10.1134/S0036029506060115.
[40] Z. Horita, T.G. Langdon, Achieving exceptional superplasticity in a bulk aluminum alloy processed by high-pressure torsion, Scripta Mater. 58 (2008) 1029–1032, https://doi.org/10.1016/j.scriptamat.2008.01.043.
[41] V.N. Perevezentsev, M.Yu Shcherban, M.Yu Murashkin, R.Z. Valiev, High-strain-rate superplasticity of nanocrystalline aluminum alloy 1570, Tech. Phys. Lett. 33 (2007) 648–650, https://doi.org/10.1134/S106378500708007X.
[42] Y. Harai, K. Edalati, Z. Horita, T.G. Langdon, Using ring samples to evaluate the processing characteristics in high-pressure torsion, Acta Mater. 57 (2009) 1147–1153, https://doi.org/10.1016/j.actamat.2008.10.046.
[43] M. El-Tahawy, P.H.R. Pereira, Y. Huang, H. Park, H. Choe, T.G. Langdon, J. Gubicza, Exceptionally high strength and good ductility in an ultrafine-grained 316L steel processed by severe plastic deformation and subsequent annealing, Mater. Lett. 214 (2018) 240–242, https://doi.org/10.1016/j.matlet.2017.12.040.
[44] P.H.R. Pereira, Y.C. Wang, Y. Huang, T.G. Langdon, Influence of grain size on the flow properties of an Al-Mg-Sc alloy over seven orders of magnitude of strain rate, Mater. Sci. Eng. 685 (2017) 367–376, https://doi.org/10.1016/j.msea.2017.01.020.
[45] M. Kai, Z. Horita, T.G. Langdon, Developing grain refinement and superplasticity in a magnesium alloy processed by high-pressure torsion, Mater. Sci. Eng. 488 (2008) 117–124, https://doi.org/10.1016/j.msea.2007.12.046.
[46] Y. Harai, M. Kai, K. Kaneko, Z. Horita, T.G. Langdon, Microstructural and mechanical characteristics of AZ61 magnesium alloy processed by high-pressure torsion, Mater. Trans. 49 (2008) 76–83, https://doi.org/10.2320/matertrans.ME200718.
[47] P.H.R. Pereira, Y. Huang, T.G. Langdon, Examining the microhardness evolution and thermal stability of an Al–Mg–Sc alloy processed by high-pressure torsion at a high temperature, J. Mater. Res. Technol. 6 (2017) 348–354, https://doi.org/10.1016/j.jmrt.2017.05.008.
[48] D.C. Machado, P.C. Alves Flausino, Y. Huang, P.R. Cetlin, T.G. Langdon, P.H. R. Pereira, Influence of processing temperature on microhardness evolution, microstructure and superplastic behaviour in an Al–Mg alloy processed by high-pressure torsion, J. Mater. Res. Technol. 24 (2023) 2850–2867, https://doi.org/10.1016/J.JMRT.2023.03.167.
[49] R.B. Figueiredo, P.R. Cetlin, T.G. Langdon, Using finite element modeling to examine the flow processes in quasi-constrained high-pressure torsion, Mater. Sci. Eng. 528 (2011) 8198–8204, https://doi.org/10.1016/j.msea.2011.07.040.
[50] P.H.R. Pereira, R.B. Figueiredo, P.R. Cetlin, T.G. Langdon, Using finite element modelling to examine the flow process and temperature evolution in HPT under different constraining conditions, IOP Conf. Ser. Mater. Sci. Eng. 63 (2014) 012041, https://doi.org/10.1088/1757-899X/63/1/012041.
[51] R.B. Figueiredo, P.H.R. Pereira, M.T.P. Aguilar, P.R. Cetlin, T.G. Langdon, Using finite element modeling to examine the temperature distribution in quasi-constrained high-pressure torsion, Acta Mater. 60 (2012) 3190–3198, https://doi.org/10.1016/j.actamat.2012.02.027.
[52] M. Kawasaki, T.G. Langdon, The significance of strain reversals during processing by high-pressure torsion, Mater. Sci. Eng. 498 (2008) 341–348, https://doi.org/10.1016/j.msea.2008.08.021.
[53] A. Loucif, R.B. Figueiredo, M. Kawasaki, T. Baudin, F. Brisset, R. Chemam, T. G. Langdon, Effect of aging on microstructural development in an Al-Mg-Si alloy processed by high-pressure torsion, J. Mater. Sci. 47 (2012) 7815, https://doi.org/10.1007/s10853-012-6400-8, 1820.
[54] H. Shahmir, P.H.R. Pereira, Y. Huang, T.G. Langdon, Mechanical properties and microstructural evolution of nanocrystalline titanium at elevated temperatures, Mater. Sci. Eng., A 669 (2016) 358–366, https://doi.org/10.1016/j.msea.2016.05.105.
[55] Y. Huang, M. Lemang, N.X. Zhang, P.H.R. Pereira, T.G. Langdon, Achieving superior grain refinement and mechanical properties in vanadium through high-pressure torsion and subsequent short-term annealing, Mater. Sci. Eng. 655 (2016) 60–69, https://doi.org/10.1016/j.msea.2015.12.086.
[56] P.H.R. Pereira, R.B. Figueiredo, P.R. Cetlin, T.G. Langdon, An examination of the elastic distortions of anvils in high-pressure torsion, Mater. Sci. Eng. 631 (2015) 201–208, https://doi.org/10.1016/j.msea.2015.02.052.
[57] P.H.R. Pereira, Y. Huang, T.G. Langdon, Examining the thermal stability of an Al-Mg-Sc alloy processed by high-pressure torsion, Mater. Res. 20 (2017) 39–45, https://doi.org/10.1590/1980-5373-MR-2017-0207.
[58] Y. Huang, P. Bazarnik, D. Wan, D. Luo, P.H.R. Pereira, M. Lewandowska, J. Yao, B. E. Hayden, T.G. Langdon, The fabrication of graphene-reinforced Al-based nanocomposites using high-pressure torsion, Acta Mater. 164 (2019) 499–511, https://doi.org/10.1016/j.actamat.2018.10.060.
[59] T.G. Langdon, Seventy-five years of superplasticity: historic developments and new opportunities, J. Mater. Sci. 44 (2009) 5998–6010, https://doi.org/10.1007/s10853-009-3780-5.
[60] K. Higashi, M. Mabuchi, T.G. Langdon, High-strain-rate superplasticity in metallic materials and the potential for ceramic materials, ISIJ Int. 36 (1996) 1423–1438, https://doi.org/10.2355/isijinternational.36.1423.

[61] T.G. Langdon, Fracture processes in superplastic flow, Met. Sci. 16 (1982) 175–183, https://doi.org/10.1179/030634582790427208.
[62] M. Kawasaki, T.G. Langdon, Review: achieving superplasticity in metals processed by high-pressure torsion, J. Mater. Sci. 49 (2014) 6487–6496, https://doi.org/10.1007/s10853-014-8204-5.
[63] M. Kawasaki, T.G. Langdon, Developing superplasticity and a deformation mechanism map for the Zn-Al eutectoid alloy processed by high-pressure torsion, Mater. Sci. Eng. 528 (2011) 6140–6145, https://doi.org/10.1016/j.msea.2011.04.053.
[64] J.K. Mackenzie, Second paper on statistics associated with the random disorientation of cubes, Biometrika 45 (1958) 229–240, https://doi.org/10.2307/2333059.
[65] T.G. Langdon, An evaluation of the strain contributed by grain boundary sliding in superplasticity, Mater. Sci. Eng. A 174 (1994) 225–230, https://doi.org/10.1016/0921-5093(94)91092-8.
[66] R.B. Figueiredo, P.H.R. Pereira, T.G. Langdon, Effect of numbers of turns of high-pressure torsion on the development of exceptional ductility in pure magnesium, Adv. Eng. Mater. 22 (2020) 1900565, https://doi.org/10.1002/adem.201900565.
[67] M. Kawasaki, T.G. Langdon, Principles of superplasticity in ultrafine-grained materials, J. Mater. Sci. 42 (2007) 1782–1796, https://doi.org/10.1007/s10853-006-0954-2.
[68] F.A. Mohamed, Creep and superplasticity: evolution and rationalization, Adv. Eng. Mater. 22 (2020) 1900532, https://doi.org/10.1002/ADEM.201900532.
[69] F.A. Mohamed, M.M.I. Ahmed, T.G. Langdon, Factors influencing ductility in the superplastic Zn-22 Pct Al eutectoid, Metall. Trans. A 8 (1977) 933–938, https://doi.org/10.1007/BF02661575.
[70] H. Ishikawa, F.A. Mohamed, T.G. Langdon, The influence of strain rate on ductility in the superplastic Zn–22% Al eutectoid, Phil. Mag. 32 (1975) 1269–1271, https://doi.org/10.1080/14786437508228105.
[71] F.J. Humphreys, M. Hatherly, Recrystallization and Related Annealing Phenomena, second ed., Pergamon Press, Oxford, 2004 https://doi.org/10.1016/B978-0-08-044164-1.X5000-2.
[72] F.J. Humphreys, A unified theory of recovery, recrystallization and grain growth, based on the stability and growth of cellular microstructures - II. The effect of second-phase particles, Acta Mater. 45 (1997) 5031–5039, https://doi.org/10.1016/S1359-6454(97)00173-0.
[73] C.A. Bronkhorst, S.R. Kalidindi, L. Anand, Polycrystalline plasticity and the evolution of crystallographic texture in FCC metals, Philosophical Transactions of the Royal Society A 341 (1992) 443–477, https://doi.org/10.1098/rsta.1992.0111.
[74] W.A. Rachinger, Relative grain translations in the plastic flow of aluminium, J. Inst. Met. 81 (1952) 33–41.
[75] T.G. Langdon, Identifying creep mechanisms in plastic flow, Z. Metallkd. 96 (2005) 522–531, https://doi.org/10.3139/146.101066.
[76] G. Rai, N.J. Grant, On the measurements of superplasticity in an Al-Cu alloy, Metall. Trans. A 6 (1975) 385–390, https://doi.org/10.1007/BF02667294.
[77] T.G. Langdon, The mechanical properties of superplastic materials, Metall. Trans. A 13 (1982) 689–701, https://doi.org/10.1007/BF02642383.
[78] F.A. Mohamed, T.G. Langdon, Creep at low stress levels in the superplastic Zn-22% Al eutectoid, Acta Metall. 23 (1975) 117–124, https://doi.org/10.1016/0001-6160(75)90076-0.
[79] M. Kawasaki, N. Balasubramanian, T.G. Langdon, Flow mechanisms in ultrafine-grained metals with an emphasis on superplasticity, Mater. Sci. Eng., A 528 (2011) 6624–6629, https://doi.org/10.1016/j.msea.2011.05.005.
[80] M. Kawasaki, T.G. Langdon, Review: achieving superplastic properties in ultrafine-grained materials at high temperatures, J. Mater. Sci. 51 (2016) 19–32, https://doi.org/10.1007/s10853-015-9176-9.
[81] F.A. Mohamed, T.G. Langdon, Deformation mechanism maps based on grain size, Metall. Trans. A 5 (1974) 2339–2345, https://doi.org/10.1007/BF02644014.
[82] R.B. Figueiredo, S. Terzi, T.G. Langdon, Using X-ray microtomography to evaluate cavity formation in a superplastic magnesium alloy processed by equal-channel angular pressing, Acta Mater. 58 (2010) 5737–5748, https://doi.org/10.1016/j.actamat.2010.06.049.
[83] Bird, Mukherjee, Dorn, In: Brandon, Rosen, Quantitative Relation between Properties and Microstructure, Israel Universities Press, Jerusalem, Israel, 1969, pp. 255–342.
[84] R. Kapoor, J.B. Singh, J.K. Chakravartty, High strain rate behavior of ultrafine-grained Al-1.5 Mg, Mater. Sci. Eng. 496 (2008) 308–315, https://doi.org/10.1016/j.msea.2008.05.043.
[85] R.B. Figueiredo, M. Kawasaki, T.G. Langdon, Seventy years of Hall-Petch, ninety years of superplasticity and a generalized approach to the effect of grain size on flow stress, Prog. Mater. Sci. 137 (2023) 101131, https://doi.org/10.1016/J.PMATSCI.2023.101131.
[86] R.B. Figueiredo, T.G. Langdon, Deformation mechanisms in ultrafine-grained metals with an emphasis on the Hall-Petch relationship and strain rate sensitivity, J. Mater. Res. Technol. 14 (2021) 137, https://doi.org/10.1016/j.jmrt.2021.06.016.
[87] Y.H. Zhao, Y.Z. Guo, Q. Wei, A.M. Dangelewicz, C. Xu, Y.T. Zhu, T.G. Langdon, Y. Z. Zhou, E.J. Lavernia, Influence of specimen dimensions on the tensile behavior of ultrafine-grained Cu, Scripta Mater. 59 (2008) 627–630, https://doi.org/10.1016/j.scriptamat.2008.05.031.
[88] Y.H. Zhao, Y.Z. Guo, Q. Wei, T.D. Topping, A.M. Dangelewicz, Y.T. Zhu, T. G. Langdon, E.J. Lavernia, Influence of specimen dimensions and strain measurement methods on tensile stress–strain curves, Mater. Sci. Eng., A 525 (2009) 68–77, https://doi.org/10.1016/j.msea.2009.06.031.
[89] N.T.C. Nguyen, P. Asghari-Rad, P. Sathiyamoorthi, A. Zargaran, C.S. Lee, H.S. Kim, Ultrahigh high-strain-rate superplasticity in a nanostructured high-entropy alloy, Nat. Commun. 11 (2020) 2736, https://doi.org/10.1038/s41467-020-16601-1.
[90] C.T. Wang, Z. Li, J.T. Wang, T.G. Langdon, New developments in the processing of metallic alloys for achieving exceptional superplastic properties, Materials Research Proceedings 32 (2023) 3–14, https://doi.org/10.21741/9781644902561 5-1.
[91] C.T. Wang, Z. Li, Y. He, J.T. Wang, T.G. Langdon, Microstructural evolution and tensile testing of a Bi–Sn (57/43) alloy processed by tube high-pressure shearing, Crystals 11 (2021) 1229, https://doi.org/10.3390/cryst11101229.
[92] J.T. Wang, Z. Li, J. Wang, T.G. Langdon, Principles of severe plastic deformation using tube high-pressure shearing, Scripta Mater. 67 (2012) 810–813, https://doi.org/10.1016/j.scriptamat.2012.07.028.
[93] G. Sakai, K. Nakamura, Z. Horita, T.G. Langdon, Developing high-pressure torsion for use with bulk samples, Mater. Sci. Eng. 406 (2005) 268–273, https://doi.org/10.1016/j.msea.2005.06.049.
[94] S. Komura, M. Furukawa, Z. Horita, M. Nemoto, T.G. Langdon, Optimizing the procedure of equal-channel angular pressing for maximum superplasticity, Mater. Sci. Eng. 297 (2001) 111–118, https://doi.org/10.1016/S0921-5093(00)01255-7.
[95] P. Ghosh, O. Renk, R. Pippan, Microtexture analysis of restoration mechanisms during high pressure torsion of pure nickel, Mater. Sci. Eng. 684 (2017) 101–109, https://doi.org/10.1016/j.msea.2016.12.032.
[96] O. Renk, R. Pippan, Transition from thermally assisted to mechanically driven boundary migration and related apparent activation energies, Scripta Mater. 154 (2018) 212–215, https://doi.org/10.1016/j.scriptamat.2018.05.052.
[97] O. Renk, R. Pippan, Saturation of grain refinement during severe plastic deformation of single phase materials: reconsiderations, current status and open questions, Mater. Trans. 60 (2019) 1270–1282, https://doi.org/10.2320/matertrans.MF201918.

Materials Science & Engineering A 887 (2023) 145766

Contents lists available at ScienceDirect

Materials Science & Engineering A

journal homepage: www.elsevier.com/locate/msea

Flow behaviour and microstructural stability in an Al–3Mg-0.2Sc alloy processed by high-pressure torsion at different temperatures

Pedro Henrique R. Pereira [a,*], Piotr Bazarnik [b], Yi Huang [c,d], Malgorzata Lewandowska [b], Terence G. Langdon [c]

[a] Department of Metallurgical and Materials Engineering, Universidade Federal de Minas Gerais, Belo Horizonte, 31270-901, MG, Brazil
[b] Faculty of Materials Science and Engineering, Warsaw University of Technology, Woloska 141, 02-507, Warsaw, Poland
[c] Materials Research Group, Department of Mechanical Engineering, University of Southampton, Southampton, SO17 1BJ, UK
[d] Department of Design and Engineering, Faculty of Science and Technology, Bournemouth University, Poole, Dorset, BH12 5BB, UK

ARTICLE INFO

Keywords:
Aluminium alloys
Grain refinement
Flow properties
High-pressure torsion
Microstructural stability
Portevin-le chatelier effect

ABSTRACT

Experiments were performed to examine the flow behaviour at room temperature (RT ≈ 300 K) and the microstructural stability of a solution-treated Al–3Mg-0.2Sc alloy processed through 10 turns of high-pressure torsion (HPT) at either RT or 450 K and further annealed for 1 h at temperatures (T) up to 773 K. The results revealed that the Al–3Mg-0.2Sc alloy achieved yield strengths of ~590 and 540 MPa after HPT at RT and 450 K, respectively. This followed from the higher dislocation densities achieved after processing at RT since both microstructures had average grain diameters of ~320 nm. After annealing at $T \geq 523$ K, there was evidence for the onset of dynamic strain ageing (DSA) during tensile testing at RT and this occurred concurrently with increases in the elongations to failure. The grain structures developed during HPT at 450 K exhibited superior microstructural stability than after HPT at RT for comparable heating conditions. A model derived for materials having second-phase particles was applied to understand the microstructural evolution observed during heating. It is shown that the values calculated for the driving and restraining pressures for boundary migration and the boundary stability factors are consistent with the experimental results.

1. Introduction

The need for more fuel-efficient transports has driven the tailoring of novel aluminium alloys with high load bearing capacities and low densities [1–4]. Some applications such as aircraft also demand resistance against incipient recrystallisation after exposure at high temperatures for short periods of time. This can be achieved by the addition of dispersoid-forming elements such as Zr, Ce, and Sc in the Al alloys [5–7]. Al–Mg-Sc alloys with up to 0.3 wt% Sc are capable of significantly delaying recrystallisation due to the formation of nano-sized Al_3Sc dispersoids [7–10]. These precipitates hinder grain boundary migration due to the Zenner pinning effect which enhances the microstructural stability by comparison with alloys having no second phases [11–13].

The superior thermal stability of Al–Mg-Sc alloys is especially appealing considering the possibility of retaining ultrafine-grained (UFG) structures produced by severe plastic deformation (SPD) procedures [14,15], such as equal-channel angular pressing (ECAP) [16] and high-pressure torsion (HPT) [17,18], after heating for prolonged times. As recently reported [19,20], the presence of Al_3Sc makes it possible to achieve extremely high elongations to failure in SPD-processed Al–Mg-Sc alloys due to deformation through grain boundary sliding [21–23]. It is noted, however, that the Al–3Mg-0.2Sc alloy has finer grain sizes after HPT [24–26] but it exhibits lower superplastic ductilities than after ECAP due to the occurrence of grain coarsening during deformation at high homologous temperatures (T_H) [19,24,27,28].

These results have motivated several investigations which were designed to evaluate procedures for further improving the thermal stability of nanostructured materials. Some of these strategies include inducing the formation of nanosized particles and/or solute segregation at grain boundaries by applying the SPD procedure in alloys having second phase particles prior to processing [29–34] and the processing of alloys at higher temperatures [26,35–37]. It was shown that the Al–3Mg-0.2Sc alloy achieves an elongation to failure of ~1020% during testing at 523 K and at 10^{-3} s^{-1} after HPT at 450 K [26]. On the other hand, the same metal after HPT at RT reaches an elongation of ~620%

* Corresponding author.
E-mail address: ppereira@demet.ufmg.br (P.H.R. Pereira).

https://doi.org/10.1016/j.msea.2023.145766
Received 18 August 2023; Received in revised form 27 September 2023; Accepted 28 September 2023
Available online 29 September 2023

when tested under an equivalent condition. These differing results demonstrate the need for conducting a more thorough investigation to model the microstructural changes in HPT-processed Al–Mg-Sc alloys during heating at various temperatures.

Although different studies have examined the flow behaviour of Al–Mg-Sc alloys after processing by ECAP or other conventional metal-working techniques [38–40], there is a lack of data on the flow properties at room temperature (RT) for this alloy after processing by HPT. In addition, if annealing is undertaken after processing, the onset of different solid-state reactions such as static recovery and precipitation could offer conditions for the achievement of an adequate combination between material strength and ductility and thereby provide important insight on the tailoring of the mechanical properties of this alloy.

Accordingly, the current research was designed to study the effect of HPT processing at different temperatures on the flow behaviour at ambient temperature and the microstructural stability of an Al–3Mg-0.2Sc alloy processed by HPT at either RT or 450 K and with subsequent annealing for 1 h at temperatures up to 773 K. A theoretical model was used to provide further understanding on the microstructural changes observed in the HPT-processed alloy during heating.

2. Experimental material and procedures

This investigation was undertaken using Al-3% Mg-0.2% Sc (% in weight) billets of ~10 mm diameter provided by the China Rare Metal Material Corporation in the as-forged state. First, the as-received Al–Mg-Sc billets were solution-treated at 880 ± 2 K for 1 h and thereafter quenched in iced water to homogenise the grain structures and maximise the Sc content in the Al matrix. The solubilised bars were cut in the form of discs having thicknesses of ~1 mm and thereafter were ground down to ~0.8 mm.

The solution-treated Al–Mg-Sc discs were processed through quasi-constrained HPT [41,42] at either room temperature (~300 K) or at 450 ± 5 K. The high temperature was achieved by using a resistive heating element positioned around the anvils as described in earlier investigations [29,35,43]. First, the discs were compressed within the shallow depression of the anvils [44] using a nominal pressure of 6 GPa. For processing at ~450 K the pressure was held constant without any rotation of the lower anvil for ~10 min to permit a more accurate temperature control and thereafter the discs were subjected to 10 revolutions at a rotation speed of ~1 rpm.

Afterwards, the HPT-processed discs were annealed for 1 h at selected temperatures from 423 to 773 K. For each procedure, the furnace was heated to the annealing temperature and then the HPT-processed discs were rapidly inserted into the hot chamber to give a nearly isothermal heating condition.

The flow behaviours of the Al–3Mg-0.2Sc alloy processed by up to 10 turns of HPT followed by annealing at different conditions were assessed through tensile testing using miniature specimens with gauge lengths and widths of ~1.1 and 1.0 mm, respectively. As in earlier reports [29, 45–47], two off-centre specimens were cut from each processed disc using electrical discharge machining. The surfaces of the tensile specimens were carefully flattened through grinding and polishing down to ~0.6 mm to remove any irregularities impressed by the anvils during processing. Tensile tests were carried out at RT using a Zwick Z030 universal testing machine at a constant rate of crosshead displacement to give an initial strain rate of 1.0×10^{-3} s^{-1}.

The microstructures of the HPT-processed and subsequently annealed Al–Mg-Sc discs were examined through orientation imaging microscopy using electron backscattered diffraction (EBSD). Sample preparation involved grinding using abrasive papers and final polishing using 0.06 μm silica colloidal. EBSD scans were conducted at positions located at ~3 mm from the disc centres using a JSM6500F thermal field emission microscope with a minimum step size of 30 nm. Orientation maps were generated from each EBSD scan and these results were used to calculate the area-weighted grain diameters and assess the distributions of the correlated misorientation angles and the grain diameters.

The Al–3Mg-0.2Sc alloy was also examined through transmission electron microscopy (TEM) using a JEOL 1200EX facility. Discs of ~3 mm in diameter were punched at positions located at ~3.5 mm from the centre of both the HPT-processed discs and the discs subjected to post-HPT annealing for 1 h at 673 K. The punched discs were electro-polished using a Struers Tenupol-5 system using an electrolytic solution of 30% HNO_3 and 70% CH_3OH at ~250 K.

The surfaces of the HPT-processed discs were analysed by means of X-Ray diffraction (XRD) using a Bruker D2 Phaser X-ray diffractometer with Cu Kα radiation. The XRD profiles were recorded through θ-2θ scans undertaken with a step size of 0.02° and using a scanning angle interval from 30 to 110°. The mean crystallite size (D_c) and the micro-strain ($\langle\varepsilon^2\rangle^{1/2}$) were estimated from Maud software and these parameters were used to estimate the density of dislocations (ρ) from the following expression [48,49]:

$$\rho = \frac{2\sqrt{3}\langle\varepsilon^2\rangle^{1/2}}{D_c\,\mathbf{b}} \tag{1}$$

where **b** is the modulus of the Burgers vector.

3. Experimental results

3.1. Tensile properties

Fig. 1 shows engineering stress vs engineering strain curves obtained at RT for the Al–3Mg-0.2Sc alloy after 10 turns of HPT at either 300 or 450 K and subsequently annealed for 1 h at temperatures ranging from 423 to 773 K. It is readily apparent that the material exhibits extremely high flow stresses, exceeding 650 MPa, immediately after HPT at RT. Nevertheless, it displays very limited ductility such that the material fails without any noticeable necking.

After annealing at increasing temperatures, the stress-strain curves of the alloy processed at RT show a clear trend of increasing ductility and a reduction in the flow stresses during tensile testing. Additionally, the curves start to exhibit a serrated flow for HPT-processed samples annealed at $T \geq 523$ K. This flow behaviour was documented earlier for different Al–Mg-Sc alloys having UFG structures [20,38,40] and suggests the occurrence of dynamic strain ageing (DSA). It should be noted that the uniform elongation continues at very low values and strain hardening becomes more prominent when the HPT-processed metal undergoes annealing at $T \geq 623$ K.

A comparison of Fig. 1 (a) and (b) shows that the material processed by HPT at RT exhibits higher flow stresses immediately after processing and after annealing up to $T = 523$ K than the same alloy processed at 450 K and annealed at similar conditions. This trend is more readily visible in Fig. 2 that depicts the yield stress (σ_y), tensile strength (σ_u) and elongation to failure ($\Delta L/L_0$, where ΔL and L_0 are the increase in length and the initial length, respectively) as a function of annealing temperature for the curves presented in Fig. 1. The datum points in Fig. 1 (a) and (b) follow the same tendency of the plots of microhardness vs annealing temperature displayed in earlier reports [35,50]. In practice, annealing up to $T = 423$ K leads to a slight reduction in the yield strength of the HPT-processed samples. Conversely, the decrease in the σ_y values with increasing temperatures becomes more significant when the annealing is performed at 473 K $\leq T \leq$ 623 K. For $T \geq 623$ K, σ_y continues to decrease with increasing annealing temperatures but at a much lower rate.

The variation of the tensile strength as a function of annealing temperature is very similar to the trend already described for the yield stress. Nevertheless, annealing at 423 K promoted a more sizable reduction in the σ_u values when compared with the material processed by 10 HPT revolutions at RT. It follows from Fig. 2 (c) that the elongations achieved in the HPT-processed alloy increase with increasing

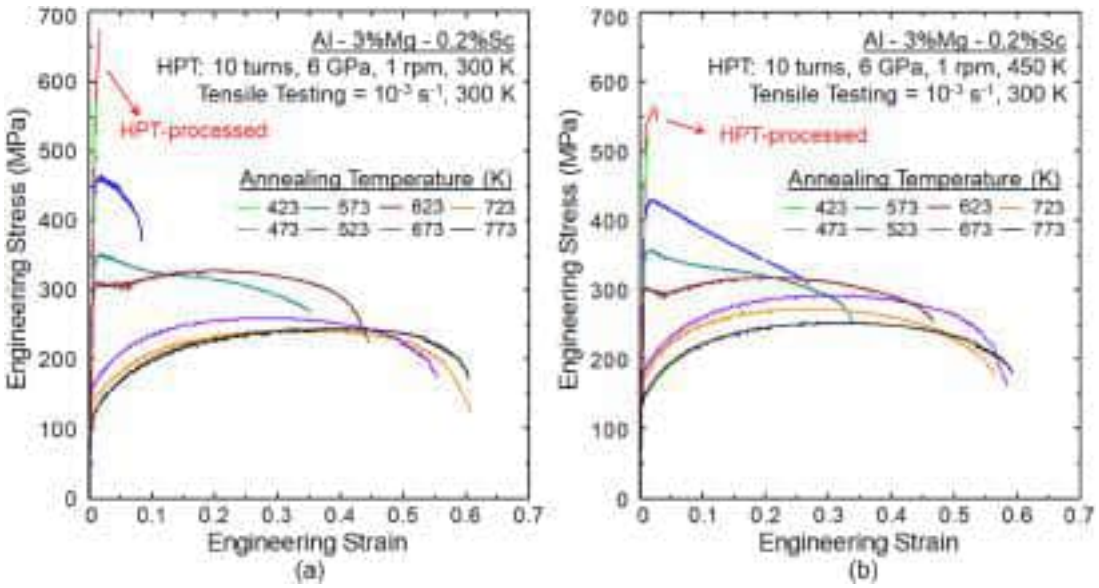

Fig. 1. Stress *vs* strain curves obtained at RT for the Al–3Mg-0.2Sc alloy processed by HPT at (a) 300 or (b) 450 K and annealed for 1 h at temperatures from 423 to 773 K.

annealing temperatures and the plots exhibit a general sigmoidal shape. It is important to note that annealing at 523–573 K leads to very sharp increases in the $\Delta L/L_0$ values and this is especially evident for the alloy processed by HPT at 450 K and further annealed at 523 K.

3.2. Microstructures after HPT

Table 1 summarizes the values calculated using the XRD profiles shown Fig. 1A of the Supplementary Material in Maud software for the crystallite size, the microstrain and the density of dislocations after processing through 10 HPT turns at 300 and 450 K, respectively. It is apparent that processing at 450 K led to a slightly larger crystallite size (~190 nm) than HPT at RT (~160 nm). However, both the microstrain and the dislocation density are significantly lower in the material processed at the higher temperature. This is attributed to the faster recovery kinetics at a homologous temperature of ~0.5 when compared with processing at RT ($T_H \approx 0.3$).

Fig. 3 shows typical orientation maps obtained at positions located at ~3 mm from the centre of the Al–3Mg-0.2Sc discs subjected to 10 HPT revolutions at either 300 or 450 K. The low-angle grain boundaries (LAGBs) with misorientation angles between 2 and 15° are coloured in gray whereas the high-angle grain boundaries (HAGBs) correspond to black lines. The results in Fig. 3 demonstrate that the grain structures in the Al–Mg-Sc alloy processed at different temperatures exhibit similar sizes but are slightly elongated in the material processed by HPT at RT. Additionally, there appears to exist a larger area of grains whose {110} planes are parallel to the thickness direction in the alloy processed at RT. By contrast, HPT at 450 K gives a microtexture with a more prominent participation of grains having {111} planes parallel to the disc thickness.

The data collected in the EBSD scans is presented in Fig. 4 as histograms showing (a) the variation in the area fraction of grain diameters measured using the circle equivalent method and (b) the fraction of correlated boundaries as a function of the misorientation angle. It is readily seen that the distributions of grain diameters show a close resemblance for both HPT temperatures although it is somewhat broader after HPT at *RT*. The area-weighted grain size (*d*) calculated for both HPT conditions is ~0.32 μm.

Inspection of in Fig. 4 (b) reveals that the misorientation distributions marginally deviate from the theoretical Mackenzie distribution (black contours) for a random array of grain structures [51]. This is due to the presence of a small number of LAGBs which corresponds to ~20% of the correlated boundaries used to construct the histogram for the material processed by HPT at 300 K.

Fig. 5 gives representative bright field (BF) TEM micrographs and their corresponding SAED patterns showing the dislocation and grain structures in the alloy processed by HPT at RT and 450 K. It is evident that the grain structures in the material processed at 300 K exhibit higher aspect ratios than after HPT at 450 K. This suggests the occurrence of a mechanically-driven process of boundary migration during HPT at RT as documented for other materials processed at low T_H [33, 52]. On the other hand, the alloy deformed at 450 K exhibits a uniform array of equiaxed grains which usually follows from thermally-assisted boundary migration [52].

The SAED patterns in both microstructures exhibit annular shapes which are consistent with the EBSD results and indicate that the grains are separated mainly by HAGBs. It is important to highlight that Al_3Sc particles were not detected in the microstructures of the solution-treated alloy after 10 HPT revolutions at either 300 or 450 K. Furthermore, some of the grains display a few internal dislocations and they are not arranged in the form of cells at this stage of processing.

The linear intercept method was used to estimate the average grain boundary spacing ($\bar{L}$) using several TEM micrographs and the orientation maps shown in Fig. 3. The calculations based on the TEM images gave grain boundary spacings of ~140 and 150 nm for the alloy processed by HPT at *RT* and 450 K, respectively, whereas $\bar{L}$ was estimated as ~170 nm from the EBSD maps for both HPT temperatures. These results are consistent with earlier investigations in which a grain size of ~150 nm was measured for Al–3Mg [25,29] and Al–3Mg-0.2Sc [25] alloys after 5–10 HPT turns at RT.

3.3. Microstructures after annealing

Fig. 6 presents typical orientation maps for the Al–3Mg-0.2Sc alloy processed through 10 HPT revolutions at 300 K and subsequently annealed for 1 h at various temperatures. Inspection of Fig. 6 (a) and (b) reveals that after heating at 523 and 573 K the microstructures of the alloy have very few LAGBs and are mainly constituted by equiaxed arrays of submicrometre grains with mean diameters of ~0.56 and 0.67 μm for these two temperatures, respectively.

An increase in the annealing temperature to the range of 623–673 K leads to the development of a bimodal distribution of grain sizes as is evident in Fig. 6 (c) and (d) and this is shown in more detail in the form

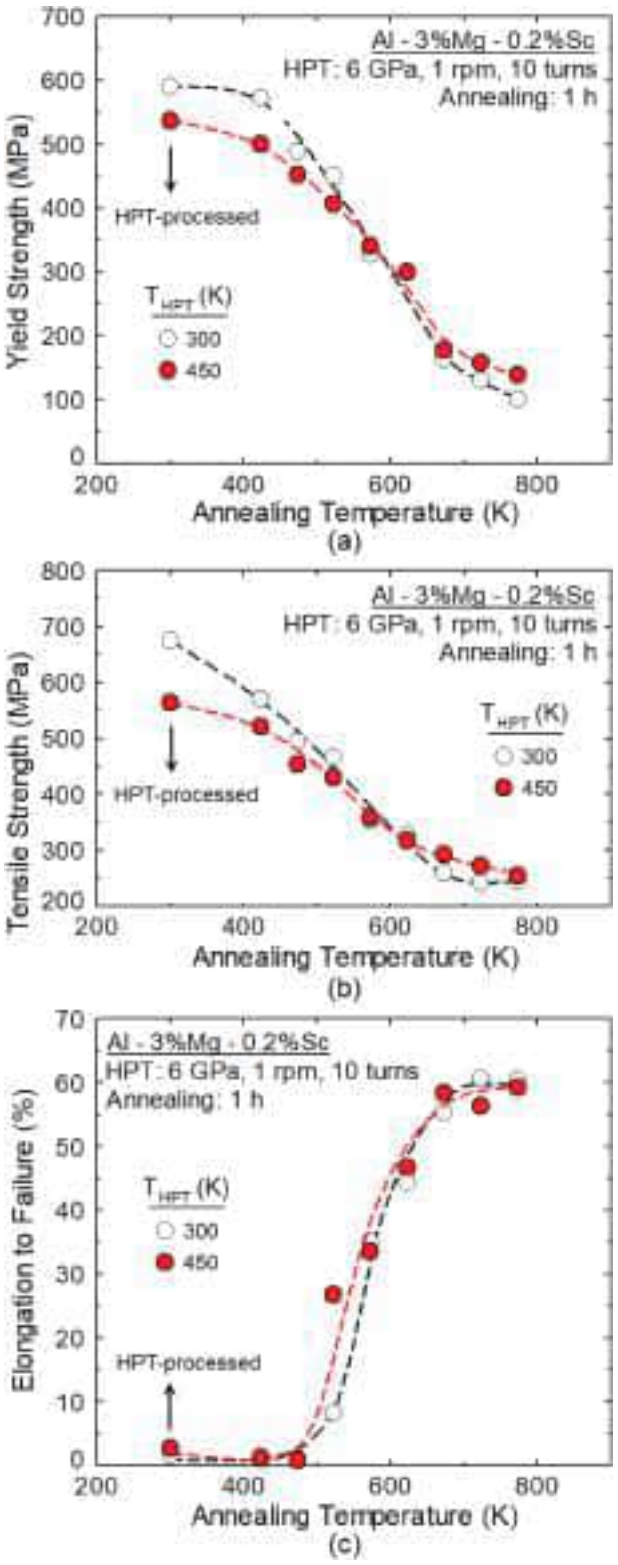

Fig. 2. (a) Yield stress, (b) tensile strength and (c) elongation to failure as function of annealing temperature for the Al–3Mg-0.2Sc alloy processed by HPT at (a) 300 or (b) 450 K, annealed for 1 h and further tested in tension at RT.

of histograms in Fig. 2A of the Supplementary Material. There remain existing UFG structures but nevertheless they correspond to an area fraction of <30% after heating at 673 K. Conversely, the remaining microstructure exhibits grains with sizes of the order of tens of micrometres and they appear preferably oriented with the {110} and {100} planes parallel to the disc thickness. Additional increases in the annealing temperature to the interval of 723–773 K promotes the formation of a uniform distribution of grains having a similar microtexture when compared with the abnormally larger grains developed during annealing at 623–673 K.

Table 1
Crystallite size, microstrain and dislocation density for the Al–3Mg-0.2Sc alloy processed through 10 HPT revolutions at 300 or 450 K.

Processing condition	Crystallite size (nm)	Microstrain (%)	Dislocation density ($m^{-2} \times 10^{13}$)
HPT: 300 K, 10 turns	160 ± 2	0.048 ± 0.004	3.6 ± 0.4
HPT: 450 K, 10 turns	190 ± 2	0.012 ± 0.002	0.7 ± 0.1

The microstructural evolution after annealing of the alloy processed by HPT at 450 K is presented in the orientation maps in Fig. 7. As with the material processed by HPT at RT, annealing at temperatures ranging from 523 to 573 K promotes the formation of equiaxed grain structures in the material processed originally at 450 K. However, these grains achieve smaller sizes after annealing as follows from plots of the mean grain diameter as a function of temperature in Fig. 8.

Similarly, annealing at 623–673 K promotes the onset of a duplex distribution of grain sizes. Nevertheless, the grains with sizes in the submicrometre range constitute a much larger fraction of the microstructure and exceeding an area fraction of 70% after annealing at 673 K. The group of larger grains also attains markedly smaller sizes. It should be further noted that the grain structures at this temperature range display grains with {110} and {111} planes lying parallel to the thickness direction.

A homogenous array of grain structures with average diameters up to ~5 μm developed in the alloy processed by HPT at 450 K after heat treatments at 723–773 K. By contrast with the alloy processed by HPT at ~300 K, a minor population of grains displays {110} planes oriented towards the thickness direction but the microtexture is mostly formed by {100} and {111} planes parallel to this direction. It is therefore evident from Fig. 8 that HPT at 450 K leads to a slower kinetics of grain growth and this is especially noted for annealing temperatures between 623 and 673 K.

Histograms showing the distributions of correlated boundaries as a function of misorientation angles after annealing are displayed in Fig. 3A of the Supplementary Material. They demonstrate there are no sizable differences between the distributions obtained at comparable temperatures, except at $T = 623$ and 673 K where the alloy originally processed at RT exhibits a significantly larger fraction of LAGBs.

To provide information concerning the nature, size, and distribution of second phase particles in the Al–3Mg-0.2Sc alloy after annealing for 1 h at 673 K, TEM and High-Resolution TEM (HRTEM) micrographs are shown in Figs. 9 and 10 for the samples processed by HPT at either 300 or 450 K, respectively. The TEM micrographs reveal the occurrence of extensive precipitation of Al_3Sc particles during heating at 673 K for HPT discs initially processed at either temperature. Examination of the dispersoid morphology suggests that most of these phases exhibit a coffee-bean-like appearance, suggesting a coherency with the Al matrix even after 1 h of annealing. In the lower region of Fig. 9 (c), there is evidence for the presence of nano-sized dispersoids in the metal processed by HPT at RT. These dispersoids exhibit radii of less than ~5 nm and are closely spaced and partially coherent with the Al matrix, as suggested from their characteristic coffee-bean-like contrast and confirmed in the HRTEM images in Fig. 9 (e) and (f).

Nevertheless, Al_3Sc particles with diameters exceeding ~25 nm become incoherent with the Al matrix, as shown clearly in the HRTEM image in Fig. 9 (d). It should be noted, however, that there are a few Al_3Sc precipitates having notably larger sizes in the range of hundreds of nanometres. These particles probably correspond to Al_3Sc precipitates

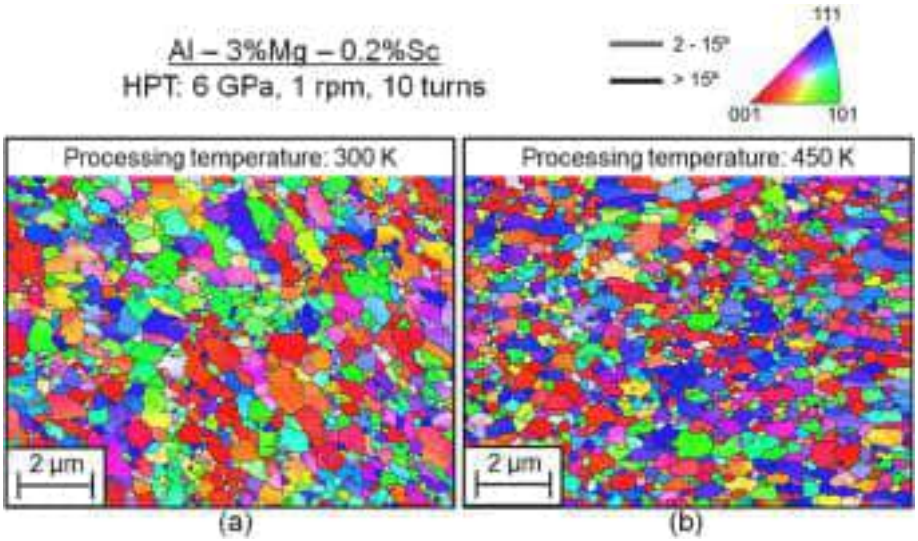

Fig. 3. Orientation maps of the Al–3Mg-0.2Sc alloy subjected to 10 turns of HPT at either (a) 300 or (b) 450 K.

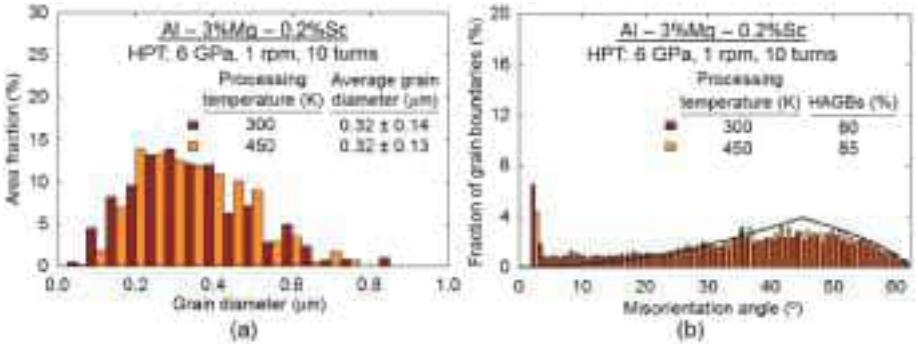

Fig. 4. Histograms of (a) the area fraction of grain diameters and (b) the misorientation angles of the Al–3Mg-0.2Sc alloy processed through 10 HPT turns at 300 or 450 K.

that were not fully dissolved during the initial solution treatment and remain stable ever after HPT processing followed by annealing at 673 K. Furthermore, the interspacing distance between precipitates is significantly larger near the coarse particles, which is apparent in the micrographs in Figs. 9 and 10. It should be noted that the bi-dimensional TEM images are direct projections of 3D volumes. Consequently, Al_3Sc precipitates may misleadingly overlap and thereby give a deceptive impression of larger phases, as follows from Fig. 9 (e) and (f) for the alloy initially processed by HPT at RT.

It is also evident in Fig. 10 that a few of the grain boundaries are pinned by Al_3Sc precipitates and these boundaries exhibit clear bulges suggesting the occurrence of strain-induced grain boundary migration delayed by the Zener pinning effect. Fig. 11 displays histograms showing the size distributions of the Al_3Sc nanoparticles for the Al–Mg-Sc discs subjected to 10 HPT revolutions at either RT or 450 K followed by annealing at 673 K. These plots were generated by measuring the radii of precipitates (r) using the circle equivalent method in Image J software with representative TEM micrographs having high magnifications as in Fig.. 9 (c) and 10 (e). In these calculations, totals of 153 and 192 particles were recorded for discs initially processed by HPT at RT or 450 K, respectively.

The histograms presented in Fig. 11 demonstrate that the HPT discs exhibit similar size distributions after annealing, even though it is apparent that Al_3Sc phases with lower radii are detected for the alloy subjected to HPT at 450 K. After annealing at 673 K, the mean radius of the nanoparticles was estimated as ~3.2 and 3.3 nm for the Al–Mg-Sc alloy processed by 10 HPT turns at RT or 450 K, respectively. These values show reasonable agreement with earlier experiments undertaken on an Al-0.25Sc alloy [53] where an average precipitate radius of ~3.5 nm was recorded after heating under similar conditions.

4. Discussion

4.1. Flow properties after HPT at different temperatures and further annealing

The results of this research reveal that the application of 10 HPT revolutions at 300 and 450 K to the solution-treated Al–3Mg-0.2Sc alloy successfully promotes the development of a uniform array of submicrometre grains with average diameters of ~320 nm. It should be noted, however, that an increased contribution of dynamic recovery during 450 K HPT at $T_H \approx 0.5$ promotes both the formation of more equiaxed grain structures and the partial annihilation of dislocations and this leads to much lower ρ values by comparison with the same alloy after HPT at RT (see Table 1). These microstructural features allow the achievement of values of $\sigma_y \approx 550$ and 600 MPa immediately after processing at 450 K and RT, respectively, as shown in Fig. 1.

After annealing for 1 h at 423 K, the tensile strength of the alloy subjected to HPT at RT decreases from ~680 to 580 MPa whereas there is only a minor reduction in σ_u for the alloy processed at 450 K. These differences are associated with the occurrence of static recovery which has a more prominent effect in the material originally processed at RT as it displays a higher density of dislocations prior to annealing. The results in Figs. 6–8 reveal that grain coarsening becomes evident after

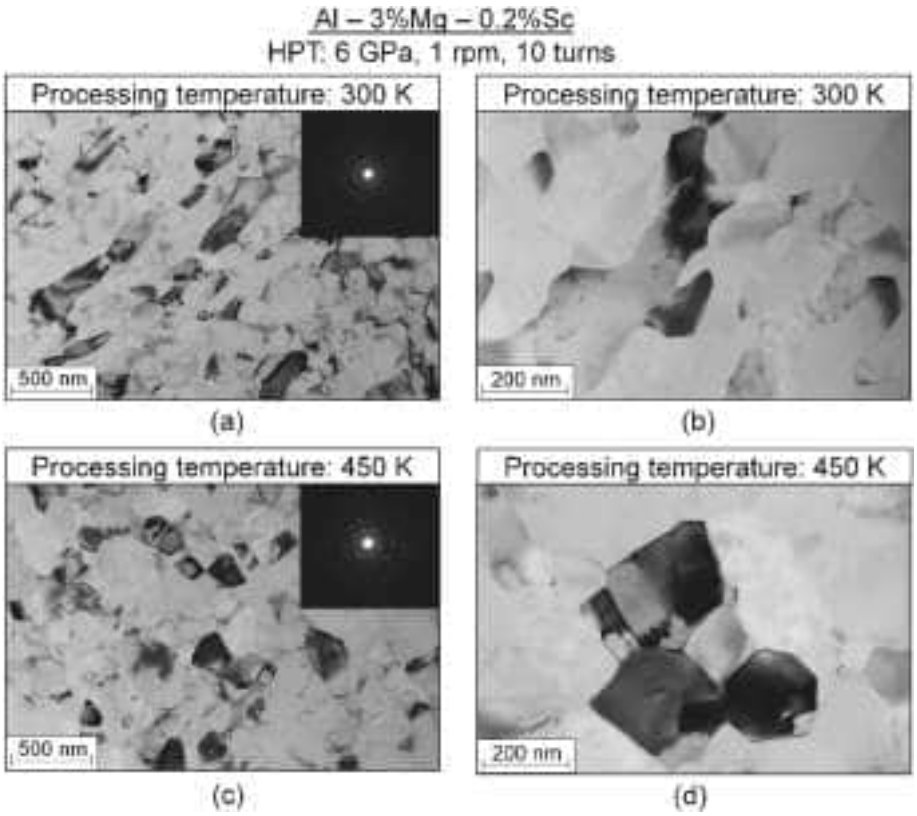

Fig. 5. TEM micrographs and corresponding SAED patterns revealing grains and dislocation structures in the Al–3Mg-0.2Sc alloy processed through 10 HPT turns at either (a, b) 300 or (c, d) 450 K.

annealing at $T \geq 523$ K. This is consistent with the drops in the values of σ_y and σ_u shown in Fig. 2.

Nevertheless, it is important to emphasize that the grains structures in the HPT-processed material continue to exhibit average sizes <1 μm after heating at temperatures of 523–573 K. Also, there is evidence of further grain growth, the formation of a duplex structure and precipitation of Al_3Sc particles at temperatures ranging from 623 to 673 K. It is well-known that the Hall-Petch relationship [54–56] may be used to predict the effect of grain boundary strengthening at RT in Al alloys as shown in the following equation:

$$\sigma_y = \sigma_0 + kd^{-0.5} \quad (2)$$

where σ_0 and k are alloy constants. To better understand the microstructural changes associated with material strength during annealing, Fig. 12 shows plots of σ_y *vs* $d^{-0.5}$ and σ_u *vs* $\Delta L/L_0$ for the alloy processed by HPT at either 300 or 450 K and further annealed for 1 h at temperatures within the interval of 423–773 K.

It is readily apparent in Fig. 12 (a) that the values of σ_y and $d^{-0.5}$ do not lie in a single line as expected if the Hall-Petch equation was uniquely sufficient to predict the flow behaviour. On the contrary, the datum points can be divided into three regions based on the observed trends. For the region with $d^{-0.5} > 1400$ m$^{-0.5}$, there is an increasing strength with decreasing grain size and the data belonging to this interval correspond to material in the HPT-processed state and after annealing at 523 and 573 K. The HPT-processed alloy reaches σ_y values > 500 MPa and there is a consistent reduction in σ_y after heating at 523 and 573 K.

Regardless of the HPT processing temperature, the Al–Mg-Sc alloy annealed at 523–573 K exhibited grain coarsening and probably a decrease in the density of dislocations by comparison with the HPT-processed states. This is consistent with the increases in the fractions of HAGBs in the orientation maps as shown in Fig. 3A in the Supplementary Material and the higher elongations achieved during tensile testing as highlighted with a blue oval in Fig. 12 (b). There is also evidence that deformation is controlled by dynamic strain ageing due to the onset of type B Portevin-Le Chatelier (PLC) serrations in the stress-strain curves in Fig. 1 which contribute to the increased ductility during tensile testing, where this matches results for a UFG Al–6Mg-0.2Sc alloy deformed under comparable conditions [38,57].

It should be noted that the time exposure during annealing at 523 K (1 h) was probably not sufficient to promote the precipitation of Al_3Sc particles in the supersaturated alloy but the formation of coherent dispersoids in supersaturated Al–Sc alloys has been documented after 8 passes of ECAP at $T = 573$ K [58] and after ageing at 573 K for shorter times [8]. Accordingly, the most prominent strengthening mechanisms in the Al–Mg-Sc alloy heat treated up to $T = 523$ K are probably grain boundary, dislocation and solid solution strengthening whereas the contribution from the precipitation becomes relevant only for $T \geq 573$ K.

It is surprisingly revealed in Fig. 12 (a) that, although an increase in the annealing temperature from 573 to 623 K promotes a marked reduction in the grain sizes, in practice the HPT discs processed at RT or 450 K exhibit very similar yield strengths. This follows from the analogous ageing kinetics for the Al–Mg-Sc alloy at 573 and 623 K which generate homogeneous arrays of coherent particles with radii below 2 nm after heating at comparable conditions [8,9,59]. It has been shown that Al–Sc alloys achieve a peak ageing condition for Al_3Sc particles having r values ranging from ~1 to 2 nm and this led to an increment in σ_y up to ~180–210 MPa by comparison with the supersaturated alloy [59]. For this reason, the yield strength in the Al–3Mg-0.3Sc alloy after annealing at 573–673 K is insensitive to the grain size since the mean free path for dislocation motion is determined instead by the particle interspacing. Furthermore, DSA together with shearing of coherent dispersoids are almost certainly the prevalent deformation mechanisms [59].

Finally, it is interesting to note that there is an abrupt decrease in the

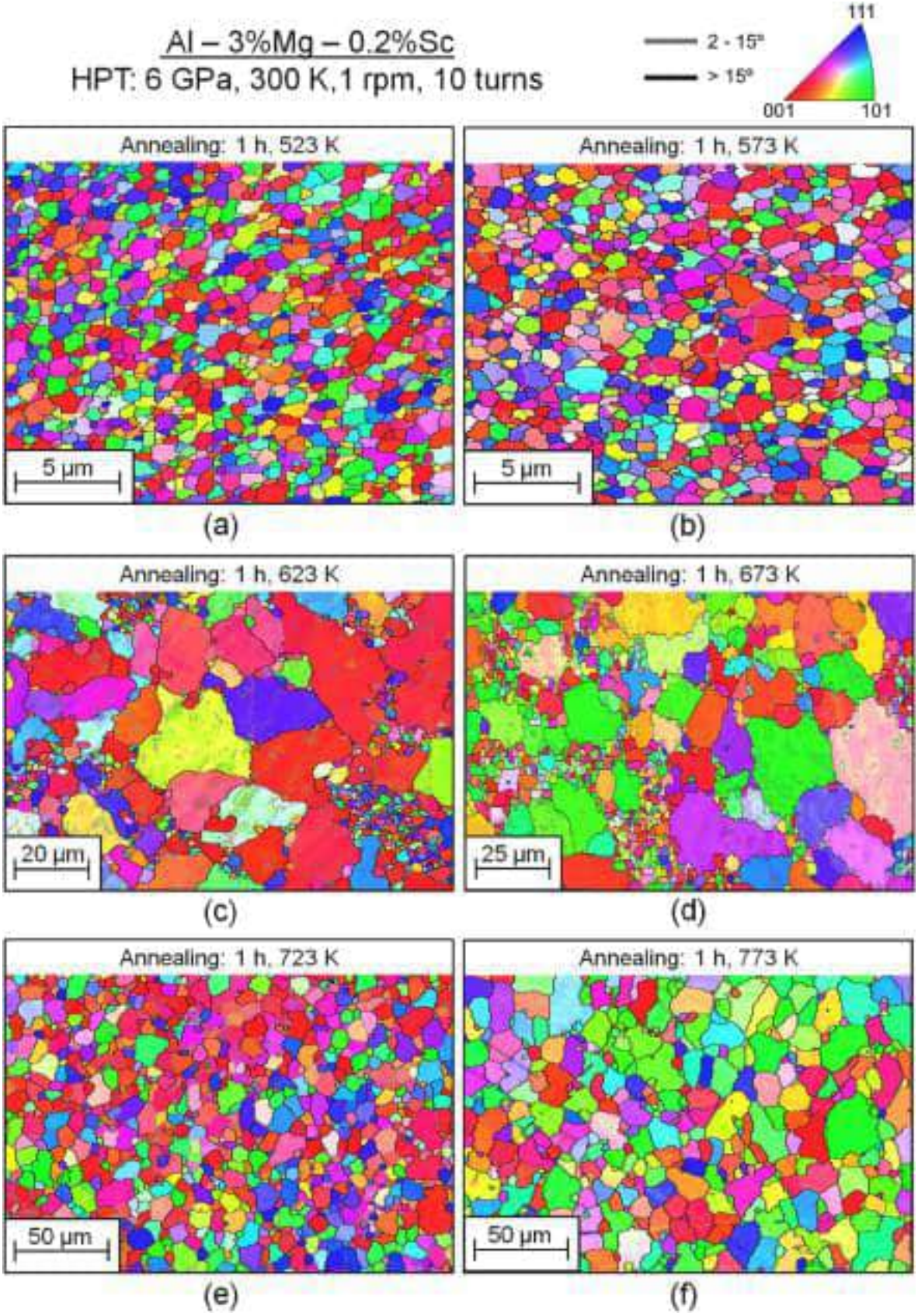

Fig. 6. Orientation maps of the Al–3Mg-0.2Sc alloy subjected to 10 HPT turns at RT and subsequently annealed for 1 h at temperatures from 523 to 773 K.

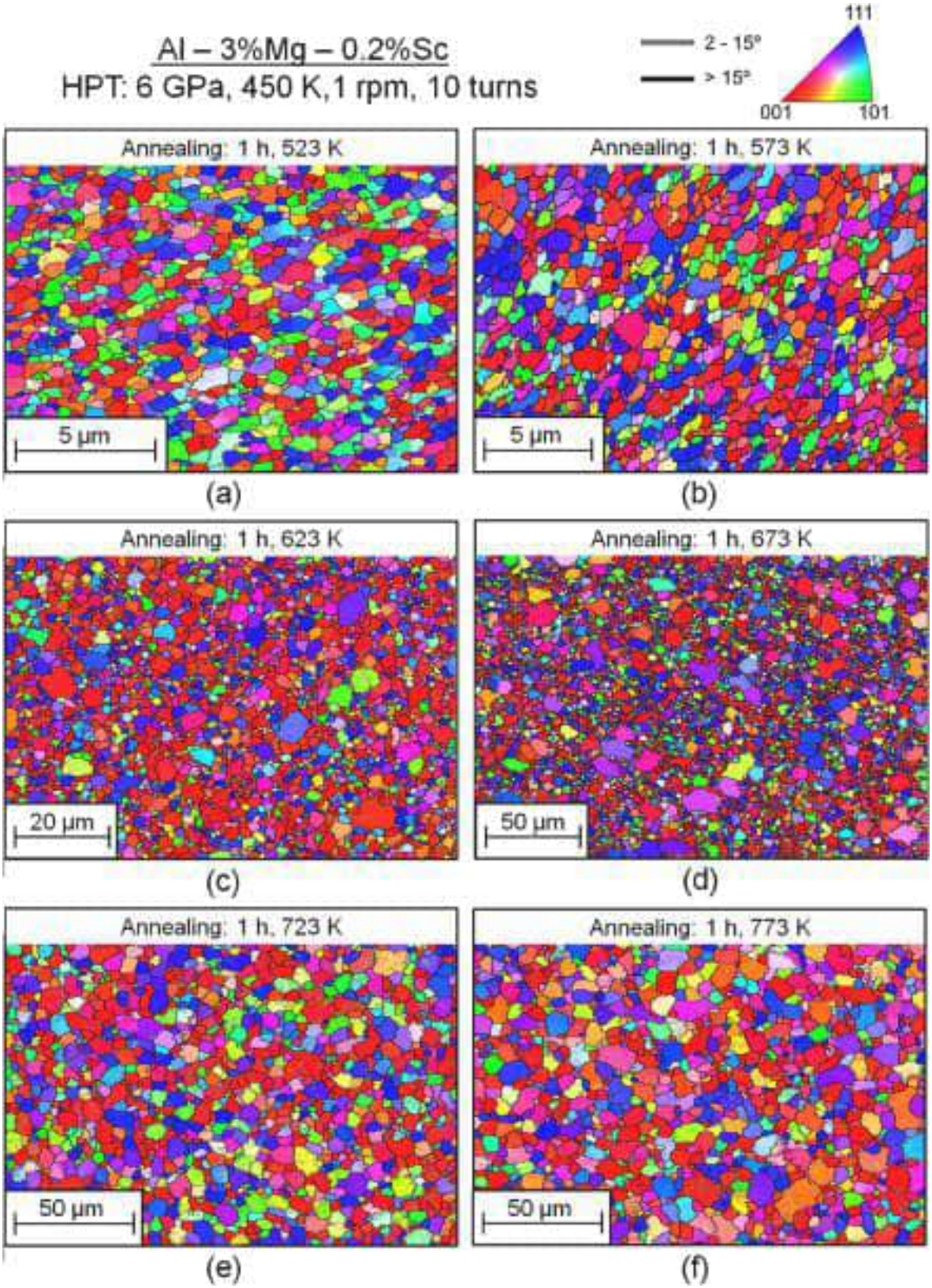

Fig. 7. Orientation maps of the Al–3Mg-0.2Sc alloy subjected to 10 HPT turns at 450 K and subsequently annealed for 1 h at temperatures from 523 to 773 K.

σ_y values when annealing is conducted at $T \geq 673$ K. This change in the flow behaviour is attributed to the onset of discontinuous precipitation of the Al_3Sc dispersoids as also documented for other Al–Sc alloys at $T \geq$ 643 K [8]. In this temperature range, the precipitates preferably nucleate at dislocations and grain boundaries and they become progressively larger with increasing temperature [60]. Also, the Al_3Sc particles eventually lose their coherency with the Al matrix as is apparent from the TEM observations.

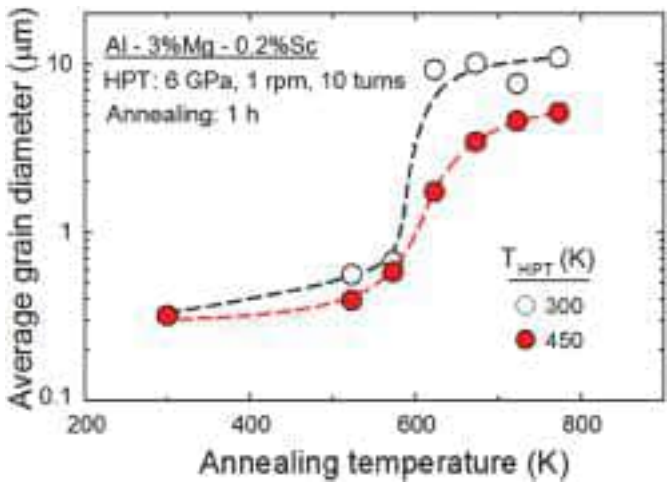

Fig. 8. Average grain diameter as a function of annealing temperature for the Al–3Mg-0.2Sc alloy processed through 10 turns of HPT at 300 either or 450 K.

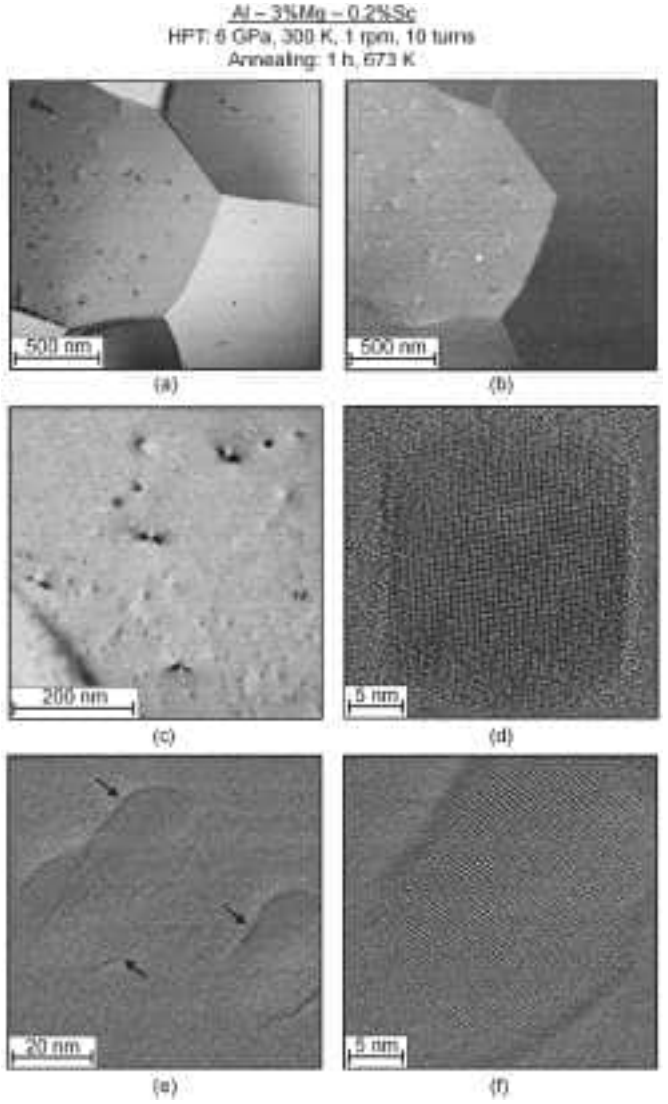

Fig. 9. (a, c) Bright and (b) dark field TEM and HRTEM images showing details of the (d) incoherent and (e, f) semi-coherent Al_3Sc precipitates of the Al–3Mg-0.2Sc alloy processed by up to 10 turns of HPT at RT and further annealed at 673 K for 1 h.

This phenomenon is consistent with the mechanical behaviour and microstructural features of the Al–3Mg-0.2Sc alloy annealed at 673 K as the occurrence of heterogenous precipitation renders areas having depleted fractions of dispersoids. These regions correspond to abnormally grown grains whose interiors exhibit larger free paths for dislocation motion and are thus softer than the remaining areas encompassing UFGs and more closely spaced particles. Consequently, plastic straining is probably first triggered within the areas having larger grains and fewer Al_3Sc particles and this is consistent with the decreasing yield strength with increasing annealing temperature.

It should be noted that, although σ_y appears to decrease with increasing grain sizes for annealing at $T \geq 673$ K, it is unlikely that grain boundary strengthening becomes again predominant because the mean free path is consistently determined by the precipitate interspacing. There may also occur a gradual change in the deformation mechanism from precipitate shearing to Orowan looping due to the increasing presence of nonshearable particles as reported for other Al–Sc alloys [59,61]. This is consistent with the occurrence of considerable work-hardening in the HPT-processed alloy deformed at RT after annealing at $T \geq 673$ K. It also explains the increased elongations attained during tensile testing [38,62]. Furthermore, DSA remains prevalent during deformation at RT as follows from the presence of oscillations in the stress-strain curves. Nevertheless, the PLC serrations are now from types B + C which are consistent with the increase in grain size with increasing temperature [38,39,57].

4.2. Microstructural stability after HPT at different temperatures

This research demonstrates that the microstructural stability of Al–Mg alloys with Sc additions is markedly improved by conducting HPT at 450 K as the Al–3Mg-0.2Sc alloy displays a more homogenous array of grain structures with lower sizes after annealing for the same duration and temperature. The reasons underlying this conclusion can be evaluated through a calculation of the restraining pressure due to the Zenner pinning effect (P_z) and the driving pressures for boundary migration associated with the release of the internal energy due to stored dislocations (P_d) and the grain boundary energy (P_g) as expressed in the following equations [63]:

$$P_z = k\frac{f\gamma}{r} \tag{3}$$

where k is a shape factor equal to 1.5 for spherical precipitates, γ is the energy associated with HAGBs and f and r are the volume fraction and the mean precipitate radius,

$$P_d = 0.5\, G\, \mathbf{b}\, \rho^{1/2} \tag{4}$$

where G is the shear modulus and

$$P_g = \frac{3\gamma}{d} \tag{5}$$

Table 2 displays the values estimated for f considering equilibrium conditions for the Al–Sc phase diagram [7] together with the precipitate radii obtained in this research and in other studies for solubilised Al–Sc alloys having similar compositions [9,53] after heat treatment at temperatures from 573 to 773 K. The values calculated for P_z using eq. (3) are also tabulated. The results reveal that the high fraction of Al_3Sc precipitates with radii below 2 nm leads to pinning pressures >1.0 MPa as predicted for the Al–3Mg-0.2Sc alloy after annealing for 1 h at 573–623 K. Conversely, the P_z values are drastically reduced at higher temperatures and are lower than 0.1 MPa after heating at 773 K. It should be further noted that the r values measured in this research show excellent agreement with the values reported for an Al-0.25Sc alloy annealed for ~1 h [53].

The driving pressures for the HPT-processed Al–3Mg-0.2Sc alloy were calculated using eqs. (4) and (5) with $G = 25.42$ GPa, $\mathbf{b} = 2.86 \times$

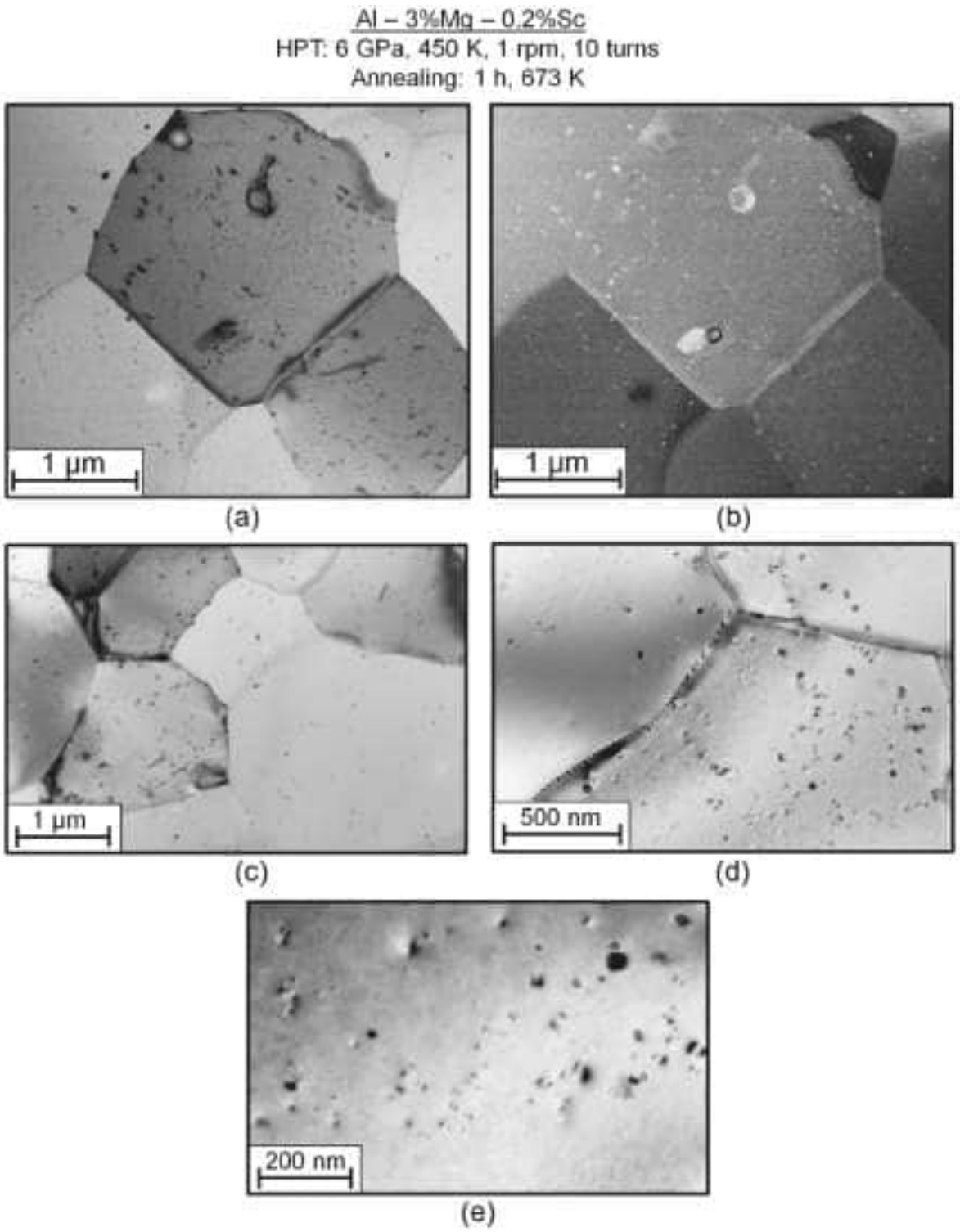

Fig. 10. (a, c, d and e) Bright and (b) dark field TEM images showing details of the Al_3Sc precipitates of the Al–3Mg-0.2Sc alloy processed by up to 10 turns of HPT at 450 K and further annealed at 673 K for 1 h.

10^{-10} m [64] and $\gamma = 0.324$ Jm^{-2} [65]. The estimated values of P_d and P_g are shown in Table 3 together with the sum of the driving and restraining pressures ($\Sigma P = P_g + P_d - P_z$) for migration of HAGBs. It follows from Table 3 that the pressure due to stored dislocations appears to play a minor role by comparison with P_g regarding the potential for recrystallisation. The interfacial energy due to the presence of grain diameters of ~320 nm is three orders of magnitude higher than P_d, considering the dislocation densities predicted using the XRD profiles. Nevertheless, $\Sigma P > 0$ for all annealing temperatures in Table 3 and this suggests that grain coarsening may occur if the grain boundary mobilities are sufficiently high [63,66].

A thorough comparison of the ΣP values in Table 3 reveals, surprisingly, that there is no significant difference in the net pressure for boundary migration in the material processed by HPT at either 300 or 450 K for heat treatments conducted at similar conditions. Therefore, in order to fully understand the reasons for the superior microstructural

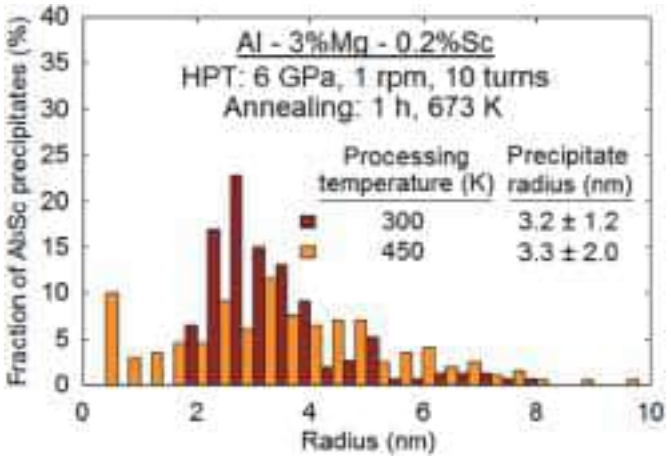

Fig. 11. Histograms revealing the size distributions for the Al_3Sc precipitates in the Al–3Mg-0.2Sc alloy processed by up to 10 turns of HPT at either 300 or 450 K and further annealed at 673 K for 1 h.

stability after HPT at 450 K it is first necessary to consider that the velocity of the moving boundary (v) is expressed as follows [63,66]:

$$v = M\,\Sigma P \tag{6}$$

where M is the grain boundary mobility.

The grain boundary mobility increases with increasing temperature and may decrease due to segregation of solute atoms at grain boundaries [33,63,66]. Furthermore, the M values depend upon the boundary orientation to their neighbouring grains such that, in general, more closely-packed grain contours display lower mobilities [63]. Also, some orientation relationships may exhibit extremely high mobilities as reported in Al alloys for <111> tilt boundaries with misorientation angles of ~40° [66,67].

However, in this investigation, there is no evidence for the occurrence of solute segregation in the Al–3Mg-0.2Sc alloy after 10 HPT revolutions for both processing temperatures. Additionally, the orientation maps after annealing are not conclusive in revealing a particular orientation relationship having consistently faster growth rates. Thus, the enhanced thermal stability in the Al–Mg-Sc alloy processed by HPT at 450 K may be associated with a more homogenous microstructure than after processing by HPT at RT.

The Al–Mg-Sc alloy processed at 300 K exhibits a notably higher density of dislocations which are heterogeneously distributed throughout the HPT disc. It also displays grains with higher aspect ratios and a broader size distribution. Therefore, these local gradients may provide conditions for either triggering the discontinuous precipitation of Al_3Sc particles or they may promote boundary motion at faster rates during heating if this latter phenomenon precedes the precipitation of large numbers of nanosized Al_3Sc particles. Nevertheless, further studies

Table 2
Volume fraction of Al_3Sc particles (f), mean precipitate radius (r) and estimated Zener pinning pressure, P_z, for an Al–Mg-Sc alloy after heating at temperatures from 423 to 773 K for 1 h.

T (K)	f (%)[a]	r (nm)	P_z (MPa)[e]
573	0.50	1.0[b]	2.43
623	0.48	1.8[b]	1.29
673	0.46	3.2–3.3[c]	0.70–0.68
		3.5[d]	0.64
723	0.43	9.5[d]	0.26
773	0.33	21.5[d]	0.08

[a] Calculated from the Al–Sc phase diagram assuming equilibrium conditions at temperature of annealing [7].
[b] Average radius of Al_3Sc precipitates in an Al-0.3Sc alloy aged for ~1 h [9].
[c] Values measured in the Al–3Mg-0.2Sc alloy in this research.
[d] Mean radius of Al_3Sc particles in an Al-0.25Sc alloy annealed for ~1 h [53].
[e] Calculated using Eq. (4) using $\gamma = 0.324$ Jm^{-2} [65].

Table 3
Sum of the driving (P_d and P_g) and restraining (P_z) pressures for boundary migration (ΣP) and factor for boundary stability (ψ) for the Al–3Mg-0.2Sc alloy processed through 10 HPT turns at 300 or 450 K after annealing for 1 h at temperatures from 423 to 773 K.

Processing condition	T (K)	P_d (MPa)	P_g (MPa)	ΣP (MPa)	ψ
HPT: 300 K, 10 turns	573	0.04	3.04	0.65	1.20
	623			1.79	0.64
	673			2.37	0.35
	723			2.86	0.11
	773			3.00	0.04
HPT: 450 K, 10 turns	573	0.01	3.04	0.62	1.20
	623			1.76	0.64
	673			2.36	0.34
	723			2.83	0.11
	773			2.97	0.04

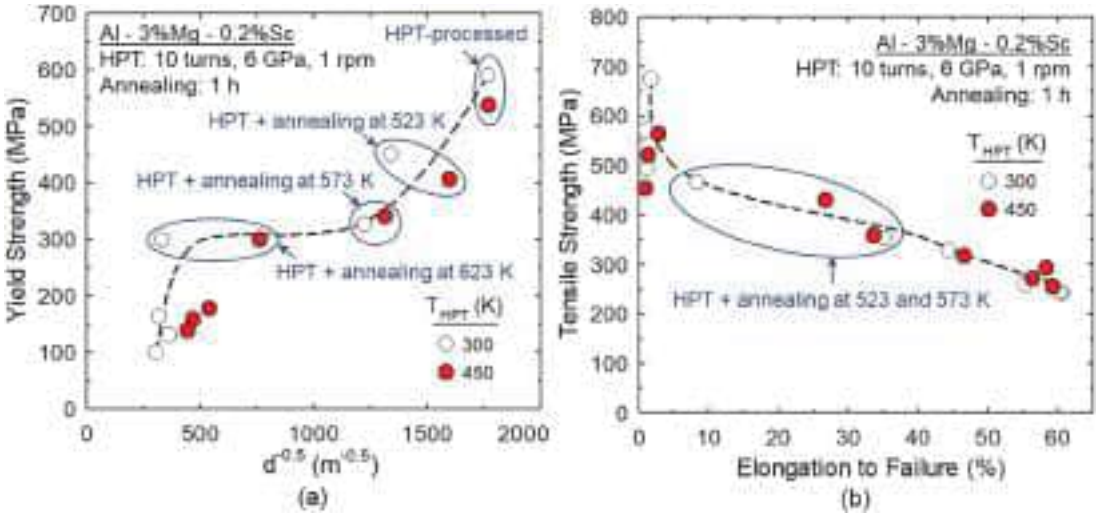

Fig. 12. Plots of (a) yield strength as a function of $d^{-0.5}$ and (b) tensile strength as a function of elongation to failure for the Al–3Mg-0.2Sc alloy processed by HPT and further annealed for 1 h at temperatures ranging from 423 to 773 K.

are now needed to more fully elucidate the reasons for the superior thermal stability encountered after HPT at 450 K.

The susceptibility for abnormal grain growth in alloys with second phases can be analysed by calculating a boundary stability factor (ψ) defined as follows [68]:

$$\psi = \frac{k f d}{2r} \tag{7}$$

The application of Eq. (7) assumes a broadening in the distribution of grain sizes which can be expressed as the ratio between the diameter of a single grain and the mean grain size [68]. According to this model, abnormal coarsening occurs when $0.25 < \psi < 1$ and this may arise concurrently with normal grain growth for $0.1 < \psi < 0.25$. For $\psi < 0.1$, the distribution of grain sizes may show some dispersion and grain growth should not be detected for $\psi > 1$. The various ψ values estimated in this study are given in Table 3.

The boundary stability factor is estimated as ~1.20 MPa in the Al–Mg-Sc alloy after heat treatment at 573 K. At first sight, this apparently contradicts the model used to derive Eq. (7) but nevertheless the calculations of ψ considered the mean precipitate radii achieved at the end of annealing. It is possible, therefore, that boundary motion started before precipitation and the HAGBs were effectively hindered only after the formation of a critical number of nanosized particles. The ψ values for the Al–3Mg-0.2Sc alloy range from 0.64 to 0.35 after annealing at 623 and 673 K and this is consistent with the current results as abnormal grain coarsening was detected at these temperatures. After annealing at $T \geq 723$ K, the distribution of grain sizes in the Al–Mg-Sc alloy is reasonably uniform and this also agrees with the model as follows from the ψ values shown in Table 3.

For convenience, Fig. 13 shows schematically the most relevant microstructural changes occurring during heating for the Al–3Mg-0.2Sc alloy processed through 10 HPT turns at different temperatures. These illustrations demonstrate that after HPT at 300 or 450 K there is no precipitation of Al_3Sc dispersoids and the microstructures are composed of a homogenous array of ultrafine grains having similar overall sizes. Nevertheless, the grains are less elongated after processing at a high homologous temperature and there are then fewer free dislocations. Annealing at T_H up to ~0.60 leads to a minor increase in the overall size of the grains and a reduction in the fraction of LAGBs. These combined factors produce a decrease in the yield and tensile strengths and permit the achievement of higher elongations during tensile testing at RT.

An increase in the homologous temperature to ~0.65–0.75 produces abnormal grain coarsening in the Al microstructure and this occurs concurrently with the heterogeneous nucleation of Al_3Sc dispersoids [69]. Conversely, the Al–3Mg-0.2Sc alloy displays a uniform array of grains having larger sizes after heating at $T_H > 0.75$. This follows from the higher boundary mobilities at these temperatures which permit the fast migration of grain boundaries prior to the precipitation of a large number of nano-sized particles [60]. The ageing kinetics are also accelerated at high homologous temperatures and this leads to particle coarsening and the achievement of larger equilibrium grain sizes.

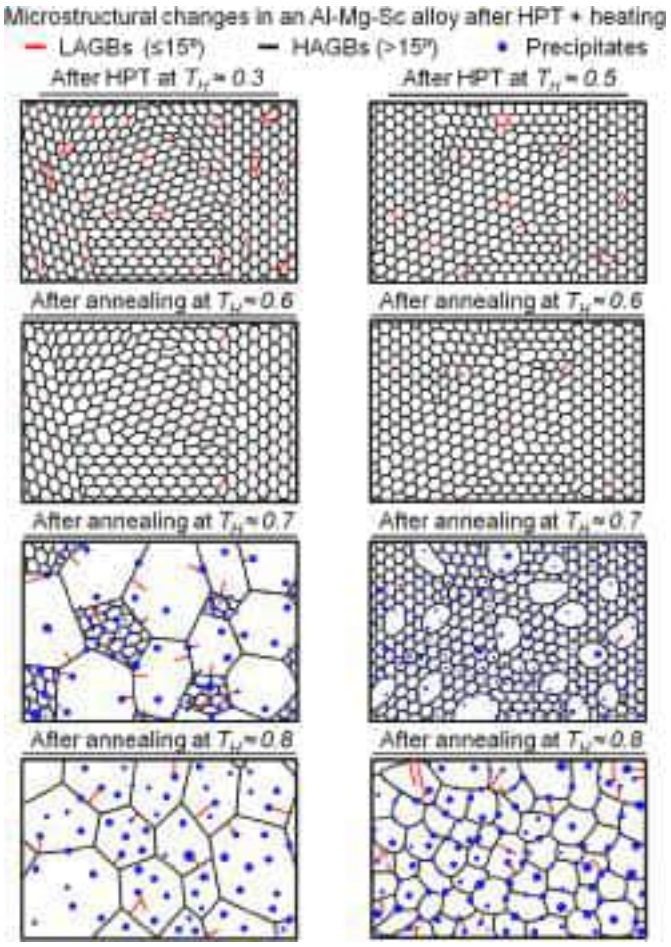

Fig. 13. Schematic illustration of typical microstructural changes in an Al–Mg-Sc alloy after HPT processing at RT or 450 K followed by annealing at different temperatures.

5. Summary and conclusions

1 A solution-treated Al–3Mg-0.2Sc alloy was subjected to 10 HPT revolutions at RT ≈ 300 K or at 450 K to produce a uniform array of grains with an average diameter of ~320 nm. Tensile testing together with XRD, EBSD and TEM analyses were conducted after processing and after subsequent annealing for 1 h at temperatures (T) up to 773 K.

2 After HPT at RT, the alloy achieved yield and tensile strengths of ~590 and 680 MPa, respectively. These values are significantly higher than after HPT at 450 K even though the microstructures of the Al–Mg-Sc alloy displayed nearly the same grain sizes. This is attributed to the higher density of stored dislocations after processing at ~300 K.

3 There was evidence for the occurrence of dynamic strain ageing (DSA) during deformation at RT for the HPT-processed Al–Mg-Sc alloy annealed at $T \geq 523$ K. Type B Portevin-Le Chatelier serrations were recorded in the flow curves after heat treatment at 523–573 K and there was a transition from type B to type C oscillations for $T \geq 623$ K.

4 Grain boundary, dislocation and solid solution strengthening are the main mechanisms operating during tensile testing at RT for the Al–3Mg-0.2Sc alloy after HPT processing and after annealing up to $T \approx 523$ K. For $T \geq 573$ K, the contribution from precipitation becomes relevant as the mean free path for dislocation motion is primarily determined by the interspacing between Al_3Sc particles.

5 HPT at 450 K produces grain structures with greater thermal stability in the Al–3Mg-0.2Sc alloy than processing at 300 K. This may originate from the higher density of heterogeneously distributed dislocations along the microstructure formed during HPT at RT as the local gradients may either trigger grain boundary migration at faster rates or provide conditions for the discontinuous precipitation of Al_3Sc particles during heating.

6 The grain structures of the HPT-processed material underwent abnormal growth during annealing at $623 < T < 673$ K and this was not observed at other temperatures. This is consistent with the values calculated for the boundary stability factor (ψ) using a theoretical model derived for alloys having second-phase particles.

CRediT authorship contribution statement

Pedro Henrique R. Pereira: Conceptualization, Data curation, Formal analysis, Investigation, Methodology, Validation, Visualization, Writing – original draft. **Piotr Bazarnik:** Conceptualization, Investigation, Methodology, Writing – review & editing. **Yi Huang:** Methodology, Supervision, Resources, Writing – review & editing. **Malgorzata Lewandowska:** Methodology, Resources, Funding acquisition, Writing – review & editing. **Terence G. Langdon:** Conceptualization, Resources, Funding acquisition, Methodology, Project administration, Supervision, Writing – review & editing.

Declaration of competing interest

The authors declare that they have no known competing financial interests or personal relationships that could have appeared to influence the work reported in this paper.

Data availability

Data will be made available on request.

Acknowledgements

This research was supported by the European Research Council under ERC Grant Agreement No. 267464-SPDMETALS (TGL and YH), FAPEMIG under Grant APQ-01342–21 (PHRP) and CNPq under Grant No. 443736/2018–9 (PHRP).

Appendix A. Supplementary data

Supplementary data to this article can be found online at https://doi.org/10.1016/j.msea.2023.145766.

References

[1] W.S. Miller, L. Zhuang, J. Bottema, A.J. Wittebrood, P. De Smet, A. Haszler, A. Vieregge, Recent development in aluminium alloys for the automotive industry, Materials Science and Engineering: A 280 (2000) 37–49, https://doi.org/10.1016/S0921-5093(99)00653-X.
[2] C. Gao, S. Wolff, S. Wang, Eco-friendly additive manufacturing of metals: energy efficiency and life cycle analysis, J. Manuf. Syst. 60 (2021) 459–472, https://doi.org/10.1016/J.JMSY.2021.06.011.
[3] M. Kleiner, M. Geiger, A. Klaus, Manufacturing of lightweight components by metal forming, CIRP Ann Manuf Technol 52 (2003) 521–542, https://doi.org/10.1016/S0007-8506(07)60202-9.
[4] O.C. Haase, P.R. Cetlin, R.B. Figueiredo, T.G. Langdon, P.H.R. Pereira, Tailoring a high-strength Al–4Cu alloy through processing of powders by up to 100 turns of high-pressure torsion, Materials Science and Engineering: A 882 (2023), 145454, https://doi.org/10.1016/J.MSEA.2023.145454.
[5] Y.A. Filatov, V.I. Yelagin, V. V Zakharov, New Al–Mg–Sc alloys, Materials Science and Engineering: A 280 (2000) 97–101, https://doi.org/10.1016/S0921-5093(99)00673-5.
[6] X. Yu, D. Yin, Z. Yu, Effects of cerium and zirconium microalloying addition on the microstructures and tensile properties of novel Al-Cu-Li alloys, Rare Met. Mater. Eng. 45 (2016) 1917–1923, https://doi.org/10.1016/S1875-5372(16)30147-3.
[7] J. Røyset, N. Ryum, Scandium in aluminium alloys, Int. Mater. Rev. 50 (2005) 19–44, https://doi.org/10.1179/174328005X14311.
[8] J. Røyset, N. Ryum, Kinetics and mechanisms of precipitation in an Al-0.2wt.% Sc alloy, Mater. Sci. Eng. 396 (2005) 409–422, https://doi.org/10.1016/j.msea.2005.02.015.
[9] E.A. Marquis, D.N. Seidman, Nanoscale structural evolution of Al3Sc precipitates in Al(Sc) alloys, Acta Mater. 49 (2001) 1909–1919, https://doi.org/10.1016/S1359-6454(01)00116-1.
[10] E.A. Marquis, D.N. Seidman, M. Asta, C. Woodward, Composition evolution of nanoscale Al3Sc precipitates in an Al-Mg-Sc alloy: experiments and computations, Acta Mater. 54 (2006) 119–130, https://doi.org/10.1016/j.actamat.2005.08.035.
[11] J. Wang, M. Furukawa, Z. Horita, M. Nemoto, R.Z. Valiev, T.G. Langdon, Enhanced grain growth in an Al-Mg alloy with ultrafine grain size, Mater. Sci. Eng. 216 (1996) 41–46, https://doi.org/10.1016/0921-5093(96)10390-7.
[12] J. Wang, Y. Iwahashi, Z. Horita, M. Furukawa, M. Nemoto, R.Z. Valiev, T. G. Langdon, An investigation of microstructural stability in an Al-Mg alloy with submicrometer grain size, Acta Mater. 44 (1996) 2973–2982, https://doi.org/10.1016/1359-6454(95)00395-9.
[13] S. Lee, A. Utsunomiya, H. Akamatsu, K. Neishi, M. Furukawa, Z. Horita, T. G. Langdon, Influence of scandium and zirconium on grain stability and superplastic ductilities in ultrafine-grained Al-Mg alloys, Acta Mater. 50 (2002) 553–564, https://doi.org/10.1016/S1359-6454(01)00368-8.
[14] T.G. Langdon, Twenty-five years of ultrafine-grained materials: achieving exceptional properties through grain refinement, Acta Mater. 61 (2013) 7035–7059, https://doi.org/10.1016/j.actamat.2013.08.018.
[15] K. Edalati, A. Bachmaier, V.A. Beloshenko, Y. Beygelzimer, V.D. Blank, W.J. Botta, K. Bryła, J. Čížek, S. Divinski, N.A. Enikeev, Y. Estrin, G. Faraji, R.B. Figueiredo, M. Fuji, T. Furuta, T. Grosdidier, J. Gubicza, A. Hohenwarter, Z. Horita, J. Huot, Y. Ikoma, M. Janeček, M. Kawasaki, P. Král, S. Kuramoto, T.G. Langdon, D. R. Leiva, V.I. Levitas, A. Mazilkin, M. Mito, H. Miyamoto, T. Nishizaki, R. Pippan, V.V. Popov, E.N. Popova, G. Purcek, O. Renk, Á. Révész, X. Sauvage, V. Sklenicka, W. Skrotzki, B.B. Straumal, S. Suwas, L.S. Toth, N. Tsuji, R.Z. Valiev, G. Wilde, M. J. Zehetbauer, X. Zhu, Nanomaterials by severe plastic deformation: review of historical developments and recent advances, Mater Res Lett 10 (2022) 163–256, https://doi.org/10.1080/21663831.2022.2029779.
[16] R.Z. Valiev, T.G. Langdon, Principles of equal-channel angular pressing as a processing tool for grain refinement, Prog. Mater. Sci. 51 (2006) 881–981, https://doi.org/10.1016/J.PMATSCI.2006.02.003.
[17] A.P. Zhilyaev, T.G. Langdon, Using high-pressure torsion for metal processing: fundamentals and applications, Prog. Mater. Sci. 53 (2008) 893–979, https://doi.org/10.1016/j.pmatsci.2008.03.002.
[18] K. Edalati, Z. Horita, A review on high-pressure torsion (HPT) from 1935 to 1988, Mater. Sci. Eng. 652 (2016) 325–352, https://doi.org/10.1016/j.msea.2015.11.074.
[19] P.H.R. Pereira, Y. Huang, M. Kawasaki, T.G. Langdon, An examination of the superplastic characteristics of Al–Mg–Sc alloys after processing, J. Mater. Res. 32 (2017) 4541–4553, https://doi.org/10.1557/jmr.2017.286.
[20] P.H.R. Pereira, Y.C. Wang, Y. Huang, T.G. Langdon, Influence of grain size on the flow properties of an Al-Mg-Sc alloy over seven orders of magnitude of strain rate, Mater. Sci. Eng. 685 (2017) 367–376, https://doi.org/10.1016/j.msea.2017.01.020.
[21] T.G. Langdon, A unified approach to grain boundary sliding in creep and superplasticity, Acta Metall. Mater. 42 (1994) 2437–2443, https://doi.org/10.1016/0956-7151(94)90322-0.
[22] T.G. Langdon, Seventy-five years of superplasticity: historic developments and new opportunities, J. Mater. Sci. 44 (2009) 5998–6010, https://doi.org/10.1007/s10853-009-3780-5.
[23] T.G. Langdon, An evaluation of the strain contributed by grain boundary sliding in superplasticity, Mater. Sci. Eng. 174 (1994) 225–230, https://doi.org/10.1016/0921-5093(94)91092-8.
[24] S. Komura, Z. Horita, M. Furukawa, M. Nemoto, T.G. Langdon, Influence of scandium on superplastic ductilities in an Al-Mg-Sc alloy, J. Mater. Res. 15 (2000) 2571–2576, https://doi.org/10.1557/JMR.2000.0367.
[25] G. Sakai, Z. Horita, T.G. Langdon, Grain refinement and superplasticity in an aluminum alloy processed by high-pressure torsion, Materials Science and Engineering: A 393 (2005) 344–351, https://doi.org/10.1016/j.msea.2004.11.007.
[26] P.H.R. Pereira, Y. Huang, T.G. Langdon, Thermal stability and superplastic behaviour of an Al-Mg-Sc alloy processed by ECAP and HPT at different temperatures, IOP Conf. Ser. Mater. Sci. Eng. 194 (2017), 012013, https://doi.org/10.1088/1757-899X/194/1/012013.
[27] P.H.R. Pereira, Y. Huang, T.G. Langdon, Examining the mechanical properties and superplastic behaviour in an Al-Mg-Sc alloy after processing by HPT, Letters on Materials 5 (2015) 294–300.
[28] S. Komura, Z. Horita, M. Furukawa, M. Nemoto, T.G. Langdon, An evaluation of the flow behavior during high strain rate superplasticity in an Al-Mg-Sc alloy, Metall Mater Trans A Phys Metall Mater Sci 32 (2001) 707–716, https://doi.org/10.1007/s11661-001-1006-9.
[29] D.C. Machado, P.C. Alves Flausino, Y. Huang, P.R. Cetlin, T.G. Langdon, P.H. R. Pereira, Influence of processing temperature on microhardness evolution, microstructure and superplastic behaviour in an Al–Mg alloy processed by high-pressure torsion, J. Mater. Res. Technol. 24 (2023) 2850–2867, https://doi.org/10.1016/J.JMRT.2023.03.167.
[30] X. Sauvage, A. Duchaussoy, G. Zaher, Strain induced segregations in severely deformed materials, Mater. Trans. 60 (2019) 1151–1158, https://doi.org/10.2320/matertrans.MF201919.
[31] F. Abdeljawad, S.M. Foiles, Stabilization of nanocrystalline alloys via grain boundary segregation: a diffuse interface model, Acta Mater. 101 (2015) 159–171, https://doi.org/10.1016/j.actamat.2015.07.058.
[32] A. Devaraj, W. Wang, R. Vemuri, L. Kovarik, X. Jiang, M. Bowden, J.R. Trelewicz, S. Mathaudhu, A. Rohatgi, Grain boundary segregation and intermetallic precipitation in coarsening resistant nanocrystalline aluminum alloys, Acta Mater. 165 (2019) 698–708, https://doi.org/10.1016/j.actamat.2018.09.038.
[33] I.C. dos Santos, E.M. Mazzer, R.B. Figueiredo, T.G. Langdon, P.H.R. Pereira, Evidence for two-stage hardening in an Al-Zn-Mg-Cu alloy processed by high-pressure torsion, J. Alloys Compd. 941 (2023), https://doi.org/10.1016/j.jallcom.2023.168839.
[34] G. Sha, L. Yao, X. Liao, S.P. Ringer, Z.C. Duan, T.G. Langdon, Segregation of solute elements at grain boundaries in an ultrafine grained Al-Zn-Mg-Cu alloy, Ultramicroscopy 111 (2011) 500–505, https://doi.org/10.1016/j.ultramic.2010.11.013.
[35] P.H.R. Pereira, Y. Huang, T.G. Langdon, Examining the microhardness evolution and thermal stability of an Al–Mg–Sc alloy processed by high-pressure torsion at a

high temperature, J. Mater. Res. Technol. 6 (2017) 348–354, https://doi.org/10.1016/j.jmrt.2017.05.008.
[36] P. Ghosh, O. Renk, R. Pippan, Microtexture analysis of restoration mechanisms during high pressure torsion of pure nickel, Mater. Sci. Eng. 684 (2017) 101–109, https://doi.org/10.1016/j.msea.2016.12.032.
[37] S.V. Dobatkin, O.V. Rybalchenko, N.A. Enikeev, A.A. Tokar, M.M. Abramova, Formation of fully austenitic ultrafine-grained high strength state in metastable Cr-Ni-Ti stainless steel by severe plastic deformation, Mater. Lett. 166 (2016) 276–279, https://doi.org/10.1016/j.matlet.2015.12.094.
[38] D. Zhemchuzhnikova, R. Kaibyshev, Mechanical behavior of an Al-Mg-Mn-Sc alloy with an ultrafine grain structure at cryogenic temperatures, Adv. Eng. Mater. 17 (2015) 1804–1811, https://doi.org/10.1002/adem.201500138.
[39] D. Zhemchuzhnikova, M. Lebyodkin, T. Lebedkina, A. Mogucheva, D. Yuzbekova, R. Kaibyshev, Peculiar spatiotemporal behavior of unstable plastic flow in an AlMgMnScZr alloy with coarse and ultrafine grains, Metals 7 (2017) 325, https://doi.org/10.3390/MET7090325, 7 (2017) 325.
[40] A. Mogucheva, D. Yuzbekova, R. Kaibyshev, T. Lebedkina, M. Lebyodkin, Effect of grain refinement on jerky flow in an Al-Mg-Sc alloy, Metall Mater Trans A Phys Metall Mater Sci 47 (2016) 2093–2106, https://doi.org/10.1007/s11661-016-3381-2.
[41] R.B. Figueiredo, P.R. Cetlin, T.G. Langdon, Using finite element modeling to examine the flow processes in quasi-constrained high-pressure torsion, Mater. Sci. Eng. 528 (2011) 8198–8204, https://doi.org/10.1016/j.msea.2011.07.040.
[42] P.H.R. Pereira, R.B. Figueiredo, P.R. Cetlin, T.G. Langdon, Using finite element modelling to examine the flow process and temperature evolution in HPT under different constraining conditions, IOP Conf. Ser. Mater. Sci. Eng. 63 (2014), 012041, https://doi.org/10.1088/1757-899X/63/1/012041.
[43] M. Kai, Z. Horita, T.G. Langdon, Developing grain refinement and superplasticity in a magnesium alloy processed by high-pressure torsion, Mater. Sci. Eng. 488 (2008) 117–124, https://doi.org/10.1016/j.msea.2007.12.046.
[44] P.H.R. Pereira, R.B. Figueiredo, P.R. Cetlin, T.G. Langdon, An examination of the elastic distortions of anvils in high-pressure torsion, Mater. Sci. Eng. 631 (2015) 201–208, https://doi.org/10.1016/j.msea.2015.02.052.
[45] H. Shahmir, P.H.R. Pereira, Y. Huang, T.G. Langdon, Mechanical properties and microstructural evolution of nanocrystalline titanium at elevated temperatures, Materials Science and Engineering: A 669 (2016) 358–366, https://doi.org/10.1016/j.msea.2016.05.105.
[46] J. Gubicza, P.H.R. Pereira, G. Kapoor, Y. Huang, S.S. Vadlamani, T.G. Langdon, Annealing-induced hardening in ultrafine-grained Ni-Mo alloys, Adv. Eng. Mater. 20 (2018), 1800184, https://doi.org/10.1002/adem.201800184.
[47] Y. Huang, M. Lemang, N.X. Zhang, P.H.R. Pereira, T.G. Langdon, Achieving superior grain refinement and mechanical properties in vanadium through high-pressure torsion and subsequent short-term annealing, Mater. Sci. Eng. 655 (2016) 60–69, https://doi.org/10.1016/j.msea.2015.12.086.
[48] G.K. Williamson, R.E. Smallman, Dislocation densities in some annealed and cold-worked metals from measurements on the X-ray Debye-Scherrer spectrum, Phil. Mag. 1 (1956) 34–46, https://doi.org/10.1080/14786435608238074.
[49] R.E. Smallman, K.H. Westmacott, Stacking faults in face-centred cubic metals and alloys, Phil. Mag. 2 (1957) 669–683, https://doi.org/10.1080/14786435708242709.
[50] P.H.R. Pereira, Y. Huang, T.G. Langdon, Examining the thermal stability of an Al-Mg-Sc alloy processed by high-pressure torsion, Mater. Res. 20 (2017) 39–45, https://doi.org/10.1590/1980-5373-MR-2017-0207.
[51] J.K. Mackenzie, Second paper on statistics associated with the random disorientation of cubes, Biometrika 45 (1958) 229–240, https://doi.org/10.2307/2333059.
[52] O. Renk, R. Pippan, Transition from thermally assisted to mechanically driven boundary migration and related apparent activation energies, Scripta Mater. 154 (2018) 212–215, https://doi.org/10.1016/j.scriptamat.2018.05.052.
[53] M. Ferry, N.E. Hamilton, F.J. Humphreys, Continuous and discontinuous grain coarsening in a fine-grained particle-containing Al–Sc alloy, Acta Mater. 53 (2005) 1097–1109, https://doi.org/10.1016/J.ACTAMAT.2004.11.006.
[54] E.O. Hall, The deformation and ageing of mild steel: III discussion of results, Proc. Phys. Soc. B 64 (1951) 747–753, https://doi.org/10.1088/0370-1301/64/9/303.
[55] N.J. Petch, The cleavage strength of polycrystals, J. Iron Steel Inst. 174 (1953) 25–28, https://doi.org/10.1007/BF01972547.
[56] R.B. Figueiredo, M. Kawasaki, T.G. Langdon, Seventy years of Hall-Petch, ninety years of superplasticity and a generalized approach to the effect of grain size on flow stress, Prog. Mater. Sci. 137 (2023), 101131, https://doi.org/10.1016/J.PMATSCI.2023.101131.
[57] D.A. Zhemchuzhnikova, M.A. Lebyodkin, T.A. Lebedkina, R.O. Kaibyshev, Unusual behavior of the Portevin-Le Chatelier effect in an AlMg alloy containing precipitates, Mater. Sci. Eng. 639 (2015) 37–41, https://doi.org/10.1016/j.msea.2015.04.094.
[58] Yu Buranova, V. Kulitskiy, M. Peterlechner, A. Mogucheva, R. Kaibyshev, S. V. Divinski, G. Wilde, Al3(Sc,Zr)-based precipitates in Al–Mg alloy: effect of severe deformation, Acta Mater. 124 (2017) 210–224, https://doi.org/10.1016/J.ACTAMAT.2016.10.064.
[59] D.N. Seidman, E.A. Marquis, D.C. Dunand, Precipitation strengthening at ambient and elevated temperatures of heat-treatable Al(Sc) alloys, Acta Mater. 50 (2002) 4021–4035, https://doi.org/10.1016/S1359-6454(02)00201-X.
[60] M.J. Jones, F.J. Humphreys, Interaction of recrystallization and precipitation: the effect of Al3Sc on the recrystallization behaviour of deformed aluminium, Acta Mater. 51 (2003) 2149–2159, https://doi.org/10.1016/S1359-6454(03)00002-8.
[61] H. Chen, Z. Chen, G. Ji, S. Zhong, H. Wang, A. Borbély, Y. Ke, Y. Bréchet, The influence of shearable and nonshearable precipitates on the Portevin-Le Chatelier behavior in precipitation hardening AlMgScZr alloys, Int. J. Plast. 147 (2021), 103120, https://doi.org/10.1016/J.IJPLAS.2021.103120.
[62] J. Røyset, N. Ryum, D. Bettella, A. Tocco, Z. Jia, J.K. Solberg, O. Reiso, On the addition of precipitation- and work-hardening in an Al-Sc alloy, Mater. Sci. Eng. 483–484 (2008) 175–178, https://doi.org/10.1016/j.msea.2006.09.164.
[63] F.J. Humphreys, M. Hatherly, Recrystallization and Related Annealing Phenomena, second ed., Pergamon Press, Oxford, 2004 https://doi.org/10.1016/B978-0-08-044164-1.X5000-2.
[64] F.A. Mohamed, T.G. Langdon, Deformation mechanism maps based on grain size, Metall. Trans. A 5 (1974) 2339–2345, https://doi.org/10.1007/BF02644014.
[65] L.E. Murr, Interfacial Phenomena in Metals and Alloys, Addison-Wesley Pub. Co., Advanced Book Program, Reading (MA), 1975.
[66] Y. Huang, F.J. Humphreys, The effect of solutes on grain boundary mobility during recrystallization and grain growth in some single-phase aluminium alloys, Mater. Chem. Phys. 132 (2012) 166–174, https://doi.org/10.1016/J.MATCHEMPHYS.2011.11.018.
[67] Y. Huang, F.J. Humphreys, Measurements of grain boundary mobility during recrystallization of a single-phase aluminium alloy, Acta Mater. 47 (1999) 2259–2268, https://doi.org/10.1016/S1359-6454(99)00062-2.
[68] F.J. Humphreys, A unified theory of recovery, recrystallization and grain growth, based on the stability and growth of cellular microstructures - II. The effect of second-phase particles, Acta Mater. 45 (1997) 5031–5039, https://doi.org/10.1016/S1359-6454(97)00173-0.
[69] J.D. Robson, M.J. Jones, P.B. Prangnell, Extension of the N-model to predict competing homogeneous and heterogeneous precipitation in Al-Sc alloys, Acta Mater. 51 (2003) 1453–1468, https://doi.org/10.1016/S1359-6454(02)00540-2.

NARODOWE CENTRUM NAUKI

DOW.42.73.15.2024 Kraków, dnia 04-12-2024

DECYZJA
DYREKTORA NARODOWEGO CENTRUM NAUKI
Nr DEC-2024/53/B/ST11/00531

Na podstawie art. 33 ust. 1 i 4 w związku z art. 20 ust. 1 pkt 1) w zw. z art. 21 w zw. z art. 30 ust. 1 - 3 oraz w zw. z art. 24 ust. 1 pkt 4) i 5) ustawy z dnia 30 kwietnia 2010 r. o Narodowym Centrum Nauki (t.j. Dz.U. z 2023 r. poz. 153) po rozpatrzeniu wniosku o finansowanie projektu badawczego o nr rejestracyjnym 2024/53/B/ST11/00531 złożonego w ramach konkursu OPUS 27 na projekty badawcze

przyznaję

podmiotowi będącemu wnioskodawcą:

Politechnika Warszawska

środki finansowe w wysokości: **1 690 900 zł** (słownie: milion sześćset dziewięćdziesiąt tysięcy dziewięćset zł)

na realizację projektu badawczego

pt. Synteza metodą skręcania pod wysokim ciśnieniem niemieszalnych układów wykazujących unikalne właściwości fizyczne i mechaniczne,

który realizować będzie Politechnika Warszawska.

Kierownikiem projektu będzie **Pan/i dr inż. Piotr Marcin Bazarnik**,

z zastrzeżeniem dopełnienia następującej czynności: przedłożenia projektu umowy o realizację i finansowanie projektu badawczego podpisanego przez osobę/y umocowaną/e do podpisywania umów w imieniu wnioskodawcy oraz kierownika projektu.

Projekt umowy należy podpisać w formacie PAdES zaawansowanym podpisem elektronicznym lub kwalifikowanym podpisem elektronicznym zgodnym z Rozporządzeniem Parlamentu Europejskiego i Rady (UE) NR 910/2014 z dnia 23 lipca 2014 r. w sprawie identyfikacji elektronicznej i usług zaufania w odniesieniu do transakcji elektronicznych na rynku wewnętrznym oraz uchylające dyrektywę 1999/93/WE.

Projekt umowy należy przesłać na adres Elektronicznej Skrzynki Podawczej Narodowego Centrum Nauki: /ncn/SkrytkaESP, w terminie 2 miesięcy od dnia doręczenia niniejszej decyzji wnioskodawcy.

Niedotrzymanie ww. terminu skutkować będzie odmową podpisania umowy przez Narodowe Centrum Nauki oraz uchyleniem niniejszej decyzji w trybie art. 162 § 2 ustawy z dnia 14 czerwca 1960 r. Kodeks postępowania administracyjnego (t.j. Dz.U. z 2024 r. poz. 572).

Projekt umowy o realizację i finansowanie projektu badawczego wraz z załącznikami dostępny jest w systemie OSF (Obsługa Strumieni Finansowania) na stronie https://osf.opi.org.pl/.

Adresat niniejszej decyzji, przedkładając ww. umowę zobowiązuje się do niewydatkowania przyznanych niniejszą decyzją środków na wskazane przez Zespół Ekspertów na etapie oceny wniosku koszty niekwalifikowalne, zgodnie z Kosztami w projektach badawczych, które stanowią załącznik nr 2 do Regulaminu przyznawania środków na realizację zadań finansowanych przez Narodowe Centrum Nauki w zakresie projektów badawczych, określonego uchwałą Rady NCN, w brzmieniu mającym zastosowanie dla konkursu OPUS 27, którego tekst jednolity stanowi załącznik do uchwały Rady Narodowego Centrum Nauki nr 23/2024 z dnia 4 marca 2024 r. Wykaz kosztów uznanych za niekwalifikowalne znajduje się w uzasadnieniu oceny wniosku w systemie OSF (Obsługa Strumieni Finansowania) dostępnym na stronie https://osf.opi.org.pl/.

Uzasadnienie

Z uzasadnieniem oceny wniosku można zapoznać się poprzez system OSF (Obsługa Strumieni Finansowania) dostępny na stronie https://osf.opi.org.pl/.

Pouczenie:

Na podstawie art. 33 ust. 2 ustawy z dnia 30 kwietnia 2010 r. o Narodowym Centrum Nauki, w przypadku naruszenia procedury konkursowej lub innych naruszeń formalnych, wnioskodawcy przysługuje odwołanie do Komisji Odwoławczej Rady Narodowego Centrum Nauki, której siedziba mieści się w Krakowie przy ul. Twardowskiego 16, 30-312 Kraków w terminie 14 dni od dnia doręczenia niniejszej decyzji.

Odwołanie składa się za pośrednictwem Dyrektora Narodowego Centrum Nauki, w formie pisemnej, na adres: ul. Twardowskiego 16, 30-312 Kraków albo podpisane w formacie PAdES zaawansowanym podpisem elektronicznym lub kwalifikowanym podpisem elektronicznym zgodnym z Rozporządzeniem Parlamentu Europejskiego i Rady (UE) NR 910/2014 z dnia 23 lipca 2014 r. w sprawie identyfikacji elektronicznej i usług zaufania w odniesieniu do transakcji elektronicznych na rynku wewnętrznym oraz uchylające dyrektywę 1999/93/WE na adres Elektronicznej Skrzynki Podawczej Centrum: /ncn/SkrytkaESP.

Zgodnie z treścią art. 127a ustawy z dnia 14 czerwca 1960 r. Kodeks postępowania administracyjnego (t.j. Dz.U. z 2024 r. poz. 572) przed upływem terminu do wniesienia odwołania strona może zrzec się prawa do wniesienia odwołania wobec organu administracji publicznej, który wydał decyzję. Z dniem doręczenia organowi administracji publicznej oświadczenia o zrzeczeniu się prawa do wniesienia odwołania przez ostatnią ze stron postępowania, decyzja staje się ostateczna i prawomocna.

z upoważnienia Dyrektora Narodowego Centrum Nauki
Kierownik Działu Obsługi Wniosków
Katarzyna Sadowska-Likos

Otrzymują:
1. Politechnika Warszawska
2. dr inż. Piotr Marcin Bazarnik
3. aa

DOW.420.35.83.2020 Kraków, dnia 20-11-2020

DECYZJA
DYREKTORA NARODOWEGO CENTRUM NAUKI
Nr DEC-2020/37/B/ST5/01837

Na podstawie art. 33 ust. 1 ustawy z dnia 30 kwietnia 2010 r. o Narodowym Centrum Nauki (t.j. Dz.U. z 2019 r. poz. 1384) po rozpatrzeniu wniosku o finansowanie projektu badawczego o nr rejestracyjnym 2020/37/B/ST5/01837 złożonego w ramach konkursu OPUS 19 na projekty badawcze

przyznaję

podmiotowi będącemu wnioskodawcą:

Politechnika Warszawska

środki finansowe w wysokości: **1 003 920** zł (słownie: milion trzy tysiące dziewięćset dwadzieścia zł)

na realizację projektu badawczego

pt. Kompozyty na osnowie metalicznej wzmacniane nano-cząstkami 2D i 3D wytwarzane techniką skręcania pod wysokim ciśnieniem,

który realizować będzie Politechnika Warszawska, Wydział Inżynierii Materiałowej.

Kierownikiem projektu będzie **Pan/i dr inż. Piotr Marcin Bazarnik**,

z zastrzeżeniem dopełnienia następującej czynności: przedłożenia w formie elektronicznej, projektu umowy o realizację i finansowanie projektu badawczego podpisanego kwalifikowanym podpisem elektronicznym w standardzie PAdES przez osobę/y umocowaną/e do podpisywania umów w imieniu wnioskodawcy oraz kierownika projektu.

Projekt umowy należy przesłać w formie elektronicznej na adres Elektronicznej Skrzynki Podawczej Narodowego Centrum Nauki: /ncn/SkrytkaESP, w terminie 2 miesięcy od dnia doręczenia niniejszej decyzji wnioskodawcy.

Niedotrzymanie ww. terminu skutkować będzie odmową podpisania umowy przez Narodowe Centrum Nauki oraz uchyleniem niniejszej decyzji w trybie art. 162 § 2 ustawy z dnia 14 czerwca 1960 r. Kodeks postępowania administracyjnego (t.j. Dz.U. z 2020 r. poz. 256 z późn. zm.).

Projekt umowy o realizację i finansowanie projektu badawczego wraz z załącznikami, dostępny jest w systemie ZSUN/OSF (Zintegrowany System Usług dla Nauki/Obsługa Strumieni Finansowania) na stronie www.osf.opi.org.pl.

Adresat niniejszej decyzji, przedkładając ww. umowę zobowiązuje się do niewydatkowania przyznanych niniejszą decyzją środków na wskazane przez Zespół Ekspertów na etapie oceny wniosku koszty niekwalifikowalne, zgodnie z Kosztami w projektach badawczych, które stanowią

załącznik nr 2 do Regulaminu przyznawania środków na realizację zadań finansowanych przez Narodowe Centrum Nauki w zakresie projektów badawczych, określonego uchwałą Rady NCN, w brzmieniu mającym zastosowanie dla konkursu OPUS 19, którego tekst jednolity stanowi załącznik do uchwały Rady Narodowego Centrum Nauki nr 49/2020 z dnia 29 kwietnia 2020 r. Wykaz kosztów uznanych za niekwalifikowane znajduje się w uzasadnieniu oceny wniosku w systemie ZSUN/OSF (Zintegrowany System Usług dla Nauki/Obsługa Strumieni Finansowania) dostępnym na stronie www.osf.opi.org.pl.

Uzasadnienie

Ze szczegółowym uzasadnieniem oceny wniosku, sporządzonym przez Zespół Ekspertów, można zapoznać się poprzez system ZSUN/OSF (Zintegrowany System Usług dla Nauki/Obsługa Strumieni Finansowania) dostępny na stronie www.osf.opi.org.pl.

Pouczenie:

Na podstawie art. 33 ust. 2 ustawy z dnia 30 kwietnia 2010 r. o Narodowym Centrum Nauki, w przypadku naruszenia procedury konkursowej lub innych naruszeń formalnych, wnioskodawcy przysługuje odwołanie do Komisji Odwoławczej Rady Narodowego Centrum Nauki mieszczącej się w Krakowie 30-312, przy ul. Twardowskiego 16, w terminie 14 dni od dnia doręczenia niniejszej decyzji. Odwołanie składa się za pośrednictwem Dyrektora Narodowego Centrum Nauki, pisemnie, na adres: 30-312 Kraków, ul. Twardowskiego 16 albo w formie elektronicznej na adres Elektronicznej Skrzynki Podawczej Centrum: /ncn/SkrytkaESP.

Zgodnie z treścią art. 127a ustawy z dnia 14 czerwca 1960 r. Kodeks postępowania administracyjnego (t.j. Dz.U. z 2020 r. poz. 256 z późn. zm.) w trakcie biegu terminu do wniesienia odwołania strona może zrzec się prawa do wniesienia odwołania wobec organu administracji publicznej, który wydał decyzję. Z dniem doręczenia organowi administracji publicznej oświadczenia o zrzeczeniu się prawa do wniesienia odwołania przez ostatnią ze stron postępowania, decyzja staje się ostateczna i prawomocna.

z upoważnienia Dyrektora Narodowego Centrum Nauki
Katarzyna Sadowska-Likos
Kierownik Działu Obsługi Wniosków

Otrzymują:
1. Politechnika Warszawska
2. dr inż. Piotr Marcin Bazarnik
3. aa

Politechnika Warszawska
Wydział Inżynierii Materiałowej
dr inż. **Piotr Marcin Bazarnik**

Umowa nr **UMO-2017/24/C/ST8/00145**
do wniosku nr **2017/24/C/ST8/00145**
pt. **Synteza nowych materiałów hybrydowych metodą skręcania pod wysokim ciśnieniem**

Niniejszym oświadczam, że dane zawarte na załączonym wydruku umowy są całkowicie zgodne z danymi wprowadzonymi do bazy danych systemu OSF.

Umowa nr UMO-2017/24/C/ST8/00145

o realizację i finansowanie projektu badawczego, który uzyskał finansowanie w ramach konkursu „SONATINA 1”

zawarta w dniu podpisania przez Dyrektora Narodowego Centrum Nauki
w Krakowie pomiędzy:

Narodowym Centrum Nauki w Krakowie, ul. Królewska 57, 30-081 Kraków, NIP 6762429638, REGON 121361537,
zwanym dalej „Centrum”,
reprezentowanym przez Zbigniewa Błockiego - Dyrektora,
zwanego dalej „Dyrektorem”,

a

Politechnika Warszawska
pl. Politechniki 1, 00-661 Warszawa
NIP: 5250005834, REGON: 000001554,

zwaną(ym) dalej „Jednostką”, którą reprezentuje(ą):

prof. dr hab. **Rajmund Bacewicz**, Prorektor ds. Nauki,

oraz

dr inż. Piotr Marcin Bazarnik
Waryńskiego 28 m. 31, Warszawa, 00-650 Warszawa, mazowieckie, Polska
PESEL: 84070400517,

zwaną/ym dalej „Kierownikiem projektu”

na podstawie decyzji Dyrektora nr DEC-2017/24/C/ST8/00145 z dnia 2017-09-21.

UNIVERSITY OF Southampton

Materials Research Group
Faculty of Engineering and the Environment
University of Southampton
Southampton SO17 1BJ
U.K.

Professor Terence G. Langdon, FREng.
Lanchester Building, Room 4029
Tel: +44 (0)23 8059 3766
langdon@soton.ac.uk

21st November, 2013

To whom it may concern:

Mr. Piotr Bazarnik

Piotr Bazarnik is currently a post-graduate student in the Faculty of Materials Science at Warsaw University of Technology where he is undertaking a Ph.D. degree under the supervision of Prof. Malgorzata Lewandowska. In order to gain additional experience, Piotr spent three months working in my research group at the University of Southampton during the autumn of 2013. He is now coming to the end of his stay in the U.K. and he will return to Poland next week.

Piotr has performed exceptionally well during his time in Southampton. He has worked hard on his research project which concerns the processing and properties of ultrafine-grained aluminium 5483 alloy, This alloy is similar to the conventional 5083 alloy except that it has less impurities and a more stabilized chemical composition of the primary compounds of 4.8% Mg and 1.0% Mn.

During his stay, Piotr has processed ultrafine-grained materials using both equal-channel angular pressing (ECAP) and high-pressure torsion (HPT). These processing experiments were conducted using different applied pressures and different amounts of strain. Piotr evaluated the materials by taking extensive microhardness measurements and he determined the mechanical properties by conducting tensile testing. I believe these results will make a valuable addition to his Ph.D. research in Warsaw.

It was a pleasure having Piotr here in Southampton. I am impressed with his hard work and enthusiasm. He is a great credit to Warsaw University of Technology and I am sure he will have a successful career in the field of Materials Science..

Please feel free to contact me by e-mail if additional information is needed.

Terence G. Langdon, FREng
Professor of Materials Science

FACULTE DES SCIENCES DE BASE

CENTRE INTERDISCIPLINAIRE DE
MICROSCOPIE ÉLECTRONIQUE - CIME

EPFL - CIME, BÂTIMENT MXC 132, Station 12, CH - 1015 LAUSANNE
Tel +41.21.693.1111- Fax ++41.21.693.4401

ÉCOLE POLYTECHNIQUE
FÉDÉRALE DE LAUSANNE

Prof. Cécile Hébert
Tél. ++41.21.693.0571, Fax ++41.21.693.4401
E-mail: cecile.hebert@epfl.ch

Lausanne, 26 May, 2016

TO WHOM IT MAY CONCERN

I herewith confirm that mgr inż. Piotr Bazarnik had a 3 month research stay at the interdisciplinary center for electron microscopy, EPFL where he was working full time.

Kind regards,

Prof. Cécile Hébert
Directrice du CIME

UNIVERSITY OF Southampton

Materials Research Group
Faculty of Engineering and the Environment
University of Southampton
Southampton SO17 1BJ
U.K.

Professor Terence G. Langdon, FREng.
Lanchester Building, Room 4029
Tel: +44 (0)23 8059 3766
langdon@soton.ac.uk

26 March, 2018

TO WHOM IT MAY CONCERN:

This letter confirms that Dr. Eng. Piotr Bazarnik of Warsaw Polytechnic University spent two months (February and March 2018) conducting research at the University of Southampton in the Centre for Bulk Nanostructured Materials. During this time, he carried out full-time research within the project "Synthesis of Novel Hybrid Materials Using High-Pressure Torsion", UMO-2017/24/C/ST8/00145.

Please contact me by e-mail at the above address if additional information is required.

Terence G. Langdon, FREng
Professor of Materials Science
University of Southampton

UNIVERSITY OF Southampton

Materials Research Group
Faculty of Engineering and the Environment
University of Southampton
Southampton SO17 1BJ
U.K.

Professor Terence G. Langdon, FREng.
Lanchester Building, Room 4029
Tel: +44 (0)23 8059 3766
langdon@soton.ac.uk

28 August, 2019

TO WHOM IT MAY CONCERN:

This letter confirms that Dr. Eng. Piotr Bazarnik of Warsaw Polytechnic University spent one month (August 2019) conducting research at the University of Southampton in the Centre for Bulk Nanostructured Materials. During this time, he carried out full-time research within the project "Synthesis of Novel Hybrid Materials Using High-Pressure Torsion", UMO-2017/24/C/ST8/00145.

Please contact me by e-mail at the above address if additional information is required.

Yours sincerely,

Terence G. Langdon, FREng
Professor of Materials Science

Politechnika Warszawska

UCZELNIA BADAWCZA
INICJATYWA DOSKONAŁOŚCI

DYPLOM

Best Paper

dla

dr. inż. Piotra Bazarnika

za najlepszą publikację w 2019 roku

„The fabrication of graphene-reinforced Al-based nanocomposites using high-pressure torsion"

14 grudnia 2020 r., Warszawa

Podpis przewodniczącego Komisji

Podpis kierownika Zespołu zarządzającego projektu „Inicjatywa Doskonałości – Uczelnia Badawcza"

REKTOR POLITECHNIKI WARSZAWSKIEJ

NAGRODA

ZESPOŁOWA STOPNIA I

dla

dr. inż.
Piotra Bazarnika

z Wydziału Inżynierii Materiałowej

za osiągnięcia naukowe
w latach 2017–2018

Rektor

Prof. dr hab. inż. Jan Szmidt

Warszawa, dnia 1 października 2019 roku

REKTOR POLITECHNIKI WARSZAWSKIEJ

NAGRODA

ZESPOŁOWA STOPNIA I

dla

dr. inż.
Piotra Bazarnika

z Wydziału Inżynierii Materiałowej

za osiągnięcia naukowe
w latach 2019–2020

Rektor

Prof. dr hab. inż. Krzysztof Zaremba

Warszawa, dnia 1 października 2021 roku

REKTOR POLITECHNIKI WARSZAWSKIEJ

NAGRODA

ZESPOŁOWA STOPNIA I

dla

dr. inż.
Piotra Bazarnika

z Wydziału Inżynierii Materiałowej

za osiągnięcia naukowe
w latach 2021–2022

Rektor

Prof. dr hab. inż. Krzysztof Zaremba

Warszawa, dnia 2 października 2023 roku

MINISTER
NAUKI I SZKOLNICTWA WYŻSZEGO

Warszawa, 2018 -09- 20

DECYZJA NR 0356/E-365/STYP/13/2018

Na podstawie art. 28a ust. 1 i art. 13 ust. 1 ustawy z dnia 30 kwietnia 2010 r. o zasadach finansowania nauki (Dz. U. z 2018 r., poz. 87) oraz art. 104 ustawy z dnia 14 czerwca 1960 r. Kodeks postępowania administracyjnego (Dz. U. z 2017 r. poz. 1257, z 2018 r. poz. 149 i 650), po rozpatrzeniu wniosku **nr rej. 356/STYP/13/2018** z dnia 31 marca 2018 r.

przyznaję

jednostce naukowej:

Politechnika Warszawska

Wydział Inżynierii Materiałowej

środki finansowe w wysokości 194 040 zł (słownie złotych: sto dziewięćdziesiąt cztery tysiące czterdzieści)

na finansowanie w latach 2018 - 2021 stypendium naukowego dla wybitnego młodego naukowca dla:

dr inż. Piotr Marcin Bazarnik

Środki finansowe przekazane będą pod warunkiem złożenia w terminie 30 dni od dnia, w którym niniejsza decyzja stanie się ostateczna, podpisanego projektu umowy określającej szczegółowe warunki finansowania i rozliczenia stypendium. Niezłożenie projektu umowy w wymaganym terminie uważa się za rezygnację z przyznanego finansowania.

Uzasadnienie:

W związku z uwzględnieniem w całości wniosku o przyznanie stypendium naukowego dla wybitnego młodego naukowca, na podstawie art. 107 § 4 ustawy z dnia 14 czerwca 1960 r. – Kodeks postępowania administracyjnego (Dz. U. z 2017 r. poz. 1257, z 2018 r. poz. 149 i 650), odstąpiono od uzasadnienia decyzji.

Pouczenie:

Na podstawie art. 14 ust. 1 ustawy o zasadach finansowania nauki w przypadku naruszenia procedury konkursowej lub innych naruszeń formalnych przy przyznawaniu środków finansowych wnioskodawca może zwrócić się do Ministra Nauki i Szkolnictwa Wyższego z wnioskiem o ponowne rozpatrzenie sprawy w terminie 14 dni od dnia otrzymania decyzji.

ul. Wspólna 1/3, 00-529 Warszawa
tel. (22) 628 19 44, faks: (22) 529 26 21, e-mail: sekretariat.minister@nauka.gov.pl, www.nauka.gov.pl